VNIVERSITAT DE VALÈNCIA

Facultad de Química Departamento de Química Inorgánica

Instituto de Ciencia Molecular (ICMol)

Metal-Organic Frameworks as chemical reactors for new advanced materials: chemistry in confined spaces

Polímeros de coordinación porosos como reactores químicos para nuevos materiales avanzados: química en espacios confinados

Tesis Doctoral

Programa de doctorado en Nanociencia y Nanotecnología RD 99/2011

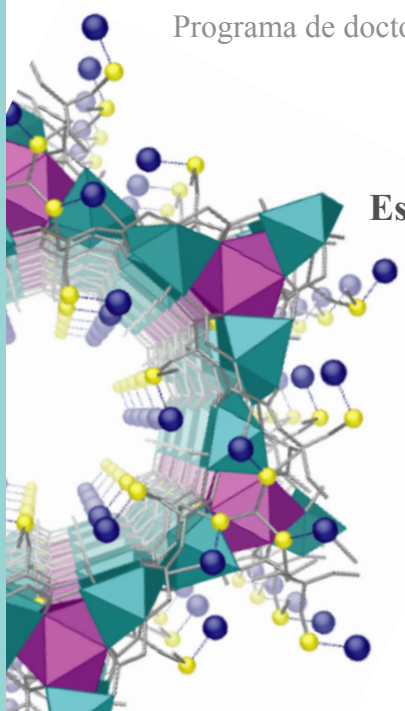

Estefanía Tiburcio Fortes

Junio 2022

Dirigido por Emilio Pardo Marín y

Jesús Ferrando Soria

A mi mujer e hijos

VNIVERSITAT DE VALÈNCIA

Facultad de Química
Departamento de Química Inorgánica
Instituto de Ciencia Molecular (ICMol)

Metal-Organic Frameworks as chemical reactors for new advanced materials: chemistry in confined spaces

Polímeros de coordinación porosos como reactores químicos para nuevos materiales avanzados: química en espacios confinados

Tesis doctoral

Programa de doctorado en Nanociencia y Nanotecnología RD 99/2011

Estefanía Tiburcio Fortes

Junio 2022

Dirigido por Emilio Pardo Marín y Jesús Ferrando Soria

D. **Emilio Pardo Marín**, Doctor en Ciencias Químicas, profesor titular del departamento de Química Inorgánica de la Facultad de Química de la Universitat de València y miembro del Instituto de Ciencia Molecular (ICMol) y D. **Jesús Ferrando Soria**, Doctor en Ciencias Químicas, miembro del Instituto de Ciencia Molecular (ICMol) y del departamento de Química Inorgánica de la Facultad de Química de la Universitat de València.

CERTIFICAN:

Que la memoria que presenta Dña. **Estefanía Tiburcio Fortes**, titulada **"Metal-Organic Frameworks as chemical reactors for new advanced materials: chemistry in confined spaces"**, corresponde al trabajo realizado bajo nuestra dirección en el Instituto de Ciencia Molecular (ICMol), para su presentación como Tesis Doctoral en el Programa de Doctorado en Nanociencia y Nanotecnología de la Universitat de València.

Y así para que conste, firmamos el presente certificado en Paterna, a 3 de Junio de 2022.

Fdo.: Dr. Emilio Pardo Marín Fdo.: Dr. Jesús Ferrando Soria

This thesis has been completed thanks to a PhD research grant funded by the Ministry of Economy and Competitiveness (MINECO) of Spain. Grant BES-2017-081876 funded by MCIN/AEI/10.13039/501100011033 and, as appropriate, by "ERDF A way of making Europe", by "European Union NextGenerationEU/PRTR" (FSE invierte en tu futuro).

ABSTRACT

The central aim of this PhD thesis is to develop synthetic procedures to construct metal organic-frameworks (MOFs) able to host/build up molecular-based species, such as metal ions with particular coordination environments, single atom catalysts (SACs), sub-nanometric metal clusters (SNMCs) and supramolecular coordination complexes (SCCs), otherwise hardly accessible, with high catalytic reactivity and in a multigram scale. The nature of the final assemblies has been characterised with a myriad of physical techniques, where taking advantage of the high crystallinity and structural robustness of the MOFs used as platforms, single-crsytal X-ray crystallography play a promienet role and provide us with unique snapshots of the novel hybrid materials assembled. Here, it is worth to remark that the obtention, stabilization and characterization of such unique hybrid species is an extraordinary challenge. Thus, this in itself reflect the success of the results presented in this PhD thesis.

In order to do so, in this PhD thesis we have worked with oxamate- and oxamidate-based MOFs, derived from robust aromatic diamines and aminoacids, respectively, constructed by applying the rational metalloligand strategy. This strategy consist on the use of dinuclear copper(II) building blocks that act as metalloligands toward transition or alkaline-earth metal ions to assembly the target framework. Then, we have taken advantage of the outstanding crystallinity and structural robustness of these MOFs to use them as chemical nanoreactors by means of different post-synthetic methodologies (PSMs), which enable us to encapsulate and/or in-situ construct within their channels unique molecular-based catalyst.

Besides a general introduction to put in context the results obtained

during this PhD thesis, we have structured them in three different chapters. The first one is focused on the application of post-synthetic partial cation exchange to obtain a material with up to three different metal ions (Cu, Ni and Pd) with potential catalytic activity to explore their use in tandem/cascade catalytic reactions. In the third chapter we move to the obtention of SACs and SNMCs. In particular, we present isolated Ag02 SNMCs and Pd0 SACs, as well as the combination of SACs and SNMCs with $Ag^{0}_{2}Fe^{3+}$. Then, in the fourth chapter we exploit the rich host-guest chemistry of the selected MOF to build SCCs, where the intrinsic catalytic properties of pivotal palladium atoms can be fully exploited. Finally, we have included a general conclusions section together with future perspectives on the basis of the research work developed in this PhD thesis.

RESUMEN

Los marcos metalorgánicos (MOFs) son una clase de materiales cristalinos porosos, compuestos de iones metálicos individuales y/o grupos de metales polinucleares (también conocidos como unidades de construcción secundarias, SBU) unidos a través de ligandos orgánicos. Los MOFs se han revelado como materiales sobresalientes entre otros materiales porosos, como las zeolitas, el carbón activado y la alúmina, como consecuencia de sus características intrínsecas únicas: (i) posibilidad de adaptar, hasta cierto punto, su topología, dimensionalidad y funcionalidades de los poros, (ii) rica química huésped-huésped y (iii) uso de la cristalografía de rayos X como herramienta básica de caracterización.
De hecho, en las últimas tres décadas ha habido un crecimiento exponencial en el interés por los MOF, lo que se ha traducido en el desarrollo de un número creciente de estructuras de gran dimensión estéticamente agradables y funcionales. Esto, en parte, está directamente relacionado con la rica variedad de ligandos orgánicos e iones metálicos/SBU que se pueden combinar para generar redes de alta dimensión con diferentes tamaños de poros, formas y funcionalidades. Además, en la química de MOFs puede ser posible lograr con un control sintético considerable la presencia de dos o más propiedades físico- químicas, lo que conduce a materiales multifuncionales.

Actualmente, en la base de datos de Cambridge Crystal hay depositados ca. 50.000 estructuras MOF. Estos MOF se han sintetizado utilizando una amplia gama de protocolos sintéticos y se han obtenido en diferentes formas, monocristal o polvo policristalino, y escalas, de laboratorio o industriales. El polvo policristalino es el estado en el que

se han reportado la mayoría de los trabajos sobre MOFs, ya que se puede controlar mejor estequiométricamente y hay mayor facilidad de síntesis ya que es más fácil estabilizar nanocristales que requieren menos energía de red. La necesidad de obtener monocristales surge de la necesidad de conocer con exactitud las interacciones interatómicas e intermoleculares tanto intraestructurales como extraestructurales con el medio circundante, los huéspedes o los metales/ligandos incorporados posteriormente. El escalado industrial se lleva a cabo una vez que se ha probado la reproducibilidad a macroescala de un MOF objetivo, así como la viabilidad de su aplicación.

Los MOF se diferencian de otros materiales porosos, como las zeolitas, el carbón activado o la alúmina, en su interacción intraestructural, que se produce a través de enlaces de coordinación. Esto hace que posean menor robustez y resistencia físico-química que las arquitecturas formadas por enlaces covalentes o iónicos. Sin embargo, existen amplias ventajas que pueden ofrecer los compuestos metal-orgánicos.

En términos de preparación, los MOF son más simples que otros materiales porosos. Los MOF generalmente no requieren agentes de plantilla orgánicos o inorgánicos ni condiciones hidrotermales en un sistema de hidrogel de silicato de alúmina rico en álcali, donde el agua actúa como reactivo y medio de reacción, como en las zeolitas. Esto hace que las zeolitas cristalicen impulsadas por la sobresaturación y la nucleación espontánea, que no es estrictamente controlable en condiciones de laboratorio. Sin embargo, también se debe tener en cuenta que los MOF se pueden construir mediante una gran variedad de iones metá-

licos/SBU y enlazadores orgánicos. Por lo tanto, existen posibilidades casi ilimitadas, lo que hizo posible a través de un diseño controlado obtener MOF con diferentes composiciones, tamaños de topologías y entornos químicos para los poros. Además, los MOF poseen una modificación estructural más fácil por intercambio de invitados o reacción química sin pérdida de cristalinidad general, así como una química huésped-huésped más rica, un más flexible naturaleza y accesibilidad de los metales que los materiales inorgánicos cristalinos. Por último, la naturaleza altamente cristalina de los MOF le permite utilizar la difracción de rayos X monocristalinos (SC-XRD) como herramienta de caracterización definitiva. Además, los MOF permiten una determinación estructural precisa mediante métodos experimentales clásicos como la difracción de rayos X en polvo (PXRD), microscopía electrónica de transmisión y barrido (TEM y SEM) y técnicas espectroscópicas como resonancia magnética nuclear (RMN), ultravioleta-visible (UV -Vis) y raman.

La estabilidad estructural y la robustez de los MOF frente a altas temperaturas, presión, humedad y entornos químicos agresivos han sido su característica más débil en comparación con otros materiales porosos. La estabilidad de los MOF se rige por múltiples factores, como el pKa de los ligandos, el estado de oxidación, el potencial de reducción y el radio iónico de los iones metálicos, la geometría de coordinación metal-ligando y la hidrofobicidad de la estructura. En una estructura MOF, el punto químico débil suele ser el enlace metal-enlazador. Sin embargo, se han desarrollado diferentes enfoques sintéticos que permiten mejorar la robustez de los MOF en diversos tipos de disolventes y un amplio rango de pH. En cuanto a la estabilidad térmica de los MOF, debido a la degradación de la parte orgánica a temperaturas entre 300-400 °C (rara vez más de 500 °C), los MOF muestran una menor esta-

bilidad que las zeolitas y los carbones activados. No obstante, ya pesar de la percepción general de baja robustez de los MOFs, especialmente relacionada con la primera generación de MOFs, existen diferentes familias de MOFs altamente robustos.

Los MOFs con los que se ha trabajado en esta línea de investigación se han obtenido siguiendo el concepto de ácidos y bases de Lewis, que se clasifican en especies blandas y duras, en función de su tamaño, polarizabilidad, electronegatividad, potenciales de ionización y energía orbital. El principio establece que los ácidos duros prefieren unirse a bases duras y las bases blandas a ácidos blandos. Tal preferencia puede proporcionar estabilidad adicional en términos de energía de disociación de enlaces entre pares duro-duro o blando-blando y desestabilización entre pares no coincidentes. La energía adicional que implica esta preferencia indica la presencia de otros factores como el efecto de solvatación o la fuerza intrínseca de ácidos y bases.

El ácido duro consiste en un átomo atractor de electrones con baja polarizabilidad, pequeño radio atómico e iónico y alto estado de oxidación. Su orbital molecular desocupado más bajo (LUMO) es altamente energético y carece de electrones externos fácilmente excitables asociados con la afinidad del enlace iónico. Mientras que la base dura consiste en un átomo donador de electrones de baja polarizabilidad, alta electronegatividad y difícil de oxidar, con alta afinidad para la formación de enlaces iónicos, asociado a orbitales inferiores vacíos de alta energía. Por el contrario, el complemento de la base blanda es el ácido duro, es decir, es un átomo de extracción de electrones de gran radio iónico / atómico, estado de oxidación bajo o nulo con electrones externos excitados fácilmente disponibles con alta afinidad para la formación de enlaces covalentes. Por último, la base blanda que es un átomo donador

de electrones con un gran radio iónico/atómico, baja electronegatividad y alta polarizabilidad. Fácilmente oxidable junto con orbitales inferiores vacíos.

También queremos definir un concepto intermedio: línea intermedia duro-blando ácido-base, que son aquellas especies con caracteres entre duro y blando ácido y base.

Una vez internalizados estos conceptos, las reactividades químicas pueden describirse como el ajuste de los electrones de valencia entre los orbitales reactivos en términos del orbital molecular más ocupado HOMO y LUMO según la teoría de la frontera orbital (FOT) (propuesta por Fukui). Por lo tanto, se espera que la reacción suave-blanda esté dominada por el carácter del enlace covalente, mientras que el carácter del enlace iónico predomina en la interacción duro-duro. Sin embargo, la interacción blando-blando consistirá en la interacción entre las dos especies blandas a través de orbitales límite, ya que la carga nuclear está protegida por los electrones del núcleo. Sin embargo, en el caso de la interacción duro-duro, los electrones del núcleo no se escapan. La interacción suave-suave sigue a la interacción "a través del enlace" (límite controlado por orbitales), mientras que la interacción duro-duro sigue a la interacción "a través del espacio" (carga controlada).

Como se señaló anteriormente, la amplia brecha de energía entre HOMO-LUMO dota a la molécula de alta estabilidad, menos reactividad y menos polarizabilidad, mientras que una pequeña brecha (que se produce entre una especie dura y una blanda) las hace menos estables, más reactivas y altamente polarizables.

Por ejemplo, los cationes de alta valencia, como Zr^{4+}, Ti^{4+} , Cr^{3+} , Fe^{3+} o

Al^{3+}, se consideran ácidos duros que pueden formar MOF estables que tienen enlaces M−L fuertes con bases de Lewis duras como carboxilato (por ejemplo, ácido tereftálico o BDC; trimesic ácido o BTC) o fosfonatos tales como (S o R) 3,3'-di-terc-butil-5,5'-dicaboxifenil-6,6- dimetilbifenil-2,2'-dihidrógeno fosfonato.

Numerosos factores influyen en el ensamblaje de un MOF objetivo y, por lo tanto, es un gran desafío obtener un control total de la estructura MOF final. Además, en ocasiones, debido a problemas de estabilidad asociados a las condiciones sintéticas, no es posible obtener un MOF específico mediante síntesis directa. En este contexto, las metodologías post-sintéticas (PSM) emergen como una herramienta sobresaliente para obtener MOF que de otro modo no serían accesibles, y para mejorar o incluso incorporar nuevas propiedades físicas y/o químicas respetando el MOF prístino.

Los materiales MOF son particularmente fascinantes para PSM debido a tres características: (i) la naturaleza lábil de los enlaces de coordinación, que facilitan su formación/rotura, (ii) la naturaleza cristalina, que permite tener la posibilidad de seguir el proceso en un solo - forma de cristal a monocristal (SC a SC) y (iii) la naturaleza porosa y, en consecuencia, la fácil accesibilidad de las moléculas huésped a la estructura. La PSM se puede llevar a cabo modificando el ligando y/o el nodo metálico y adsorción/intercambio de especies huésped. Además, el entorno de la superficie del MOF se puede modificar para aumentar la estabilidad estructural, así como para introducir las propiedades deseadas. Relevantemente, los tratamientos post-sintéticos, no alteran la topología original del MOF, lo que ofrece la posibilidad de establecer relaciones modificaciones-función post-sintéticas.

Como se puede observar en la literatura existen numerosos ejemplos del potencial de PSM. Un tipo importante de PSM se ocupa de la parte inorgánica de los MOF. Los PSM basados en metales relevantes son intercambio de metales, transmetalación, incorporación y metátesis y oxidación post-sintética (PSMO).

Las modificaciones post-sintéticas basadas en ligandos reunieron las más diversas formas de PSM, que consisten en la modificación, instalación, intercambio, remoción de ligandos en el MOF y polimerización post-sintética. Estos PSM se basan en la formación de nuevos enlaces covalentes, normalmente en el ligando orgánico de los MOF, aunque también podría ocurrir en las unidades de construcción secundaria (SBU). Han demostrado ser una buena opción para introducir ligandos orgánicos y/o funcionalidades en MOFs, lo que ha permitido modificar no solo la dimensionalidad estructural, así como su capacidad de unión con centros metálicos, sino también las propiedades de los MOFs resultantes, y en consecuencia su campo de aplicación.

El intercambio simultáneo de la parte orgánica e inorgánica en un MOF representa el nivel más alto de complejidad de las metodologías post-sintéticas. Esto puede conducir a un cambio de imagen total de un material MOF. Pero requiere un diseño químico cuidadoso y lleva bastante tiempo encontrar las condiciones óptimas.

La última parte de la clasificación la constituyen los PSM basados en huéspedes en MOF, que son transformaciones post-sintéticas no covalentes, que incluyen la introducción o intercambio de moléculas huésped alojadas en los poros por difusión. Esto se aplica para el crecimiento o la encapsulación de nanopartículas y clústeres metálicos o, en el caso de los MOF aniónicos, el intercambio de cationes de equilibrio de

carga fuera del marco por complejos metálicos catiónicos.

Los poros de los MOF solían estar ocupados por varias moléculas invitadas, como solventes, iones (cationes/aniones) y moléculas generadas durante la síntesis. Las moléculas invitadas se pueden reemplazar o eliminar mediante diversos métodos para introducir propiedades nuevas y emocionantes en la estructura de MOF. El intercambio de cationes, ubicados como iones fuera del marco, es factible termodinámica y cinéticamente. Para el intercambio activo de cationes, el marco debe ser aniónico. El intercambio de aniones es más complicado y en ocasiones implica el uso de ácidos diluidos. Las inclusiones de invitados dentro de la estructura MOF son una buena estrategia de PSM que abre una oportunidad para una aplicación, o lo hace después de una alteración.
Tras esta breve introducción os presentamos los compuestos objetivo que han podido verificarse con la ayuda de las diferentes técnicas de caracterización. El presente manuscrito se ha organizado de menor a mayor complejidad en términos de las especies nanométricas sintetizadas dentro de los canales del MOF. Se partió del trabajo previo que ejercieron los investigadores predecesores que han trabajado y trabajan en esta línea de investigación que se fundamenta en la síntesis de MOF basados en oxamato y oxamidato, derivados de diaminas y aminoácidos aromáticos robustos, respectivamente, construidos aplicando la estrategia del "metaloligando racional". Esta estrategia consiste en el uso de "bloques de construcción" dinucleares de cobre(II) que actúan como metaloligandos hacia iones metálicos de transición o alcalinotérreos para ensamblar el marco objetivo. A continuación, hemos aprovechado la extraordinaria cristalinidad y robustez estructural de estos MOFs para utilizarlos como nanoreactores químicos mediante diferentes metodologías postsintéticas (PSMs), que nos permiten encapsular y/o construir in-situ dentro de sus canales un catalizador único de base molecular.

Inicialmente, los intereses de mi grupo de investigación se centraron en la preparación de MOF magnéticos basados en oxamato y oxamidato. Sin embargo, la gran versatilidad de estos materiales hizo que se ampliara su aplicabilidad, gracias a sus múltiples propiedades. La sintonizabilidad de su composición, rigidez, cristalinidad y, sobre todo, la variedad de topología, tamaño, distribución y ambiente químico de sus poros son algunas de las propiedades más importantes. En cuanto a aplicaciones, estos MOFs basados en oxamatos y oxamidatos han tenido gran relevancia en múltiples artículos relacionados con la captura de contaminantes (gaseosos y líquidos, como colorantes y metales pesados), captura y liberación de fármacos y complejos alimenticios, magnetismo y catálisis, entre otros. Este último punto es el foco de esta tesis: la catálisis.

La creciente complejidad experimentada a lo largo de la tesis comienza con la inserción parcial de paladio en el MOF basado en oxamato y la amina aromática 2,4,6-trimetil-1,3-fenilendiamina (Capítulo 2).

En cuanto a la producción del material, dada la síntesis y aplicabilidad de **Ni^{2+}@CuNi-Me_3mpba** y sus variantes (como **Fe^{3+}@CuNi- Me_3mpba** o **Ru^{3+}@CuNi-Me_3mpba**), quisimos extrapolar esta metodología post-sintética a la sustitución parcial de cationes Ni^{II} en **Ni2^{+}@CuNi-Me_3mpba** por cationes Pd^{II} para obtener mezclas MOFs metálicos con metales catalíticamente activos, de diferente naturaleza, dentro de sus poros (en este caso Ni y Pd). El PSM aplicado a **$Ni^{2+}Pd^{2+}$@CuNi-Me_3mpba** ha sido estudiado y comprobado su éxito por diferentes métodos de caracterización:

• Análisis elemental: verificó la composición química del compuesto objetivo.

• IR: relacionó el desplazamiento de las señales con el mantenimiento de los sitios fijos de coordinación en la estructura y el ligero cambio en la coordinación producido por la nueva interacción de los grupos funcionales con el metal insertado en los poros del MOF.

• SEM-EDAX: permitió comprobar en continuo el intercambio catiónico parcial producido a partir del Ni por el Pd, mediante los porcentajes estequiométricos de metales, hasta obtener relaciones Cu/Ni de 1,2 correspondientes al mantenimiento de los metales del grupo metal-orgánico. arquitectura NiII4CuII6 que ha de mantenerse fija tras el PSM y el 50% del Ni alojado en los poros sin intercambio y ratios Ni/Pd de 5 correspondientes a los 5 níqueles estequiométricos que hay para cada Pd en la fórmula $[Pd^{II}(NH_3)_4]Ni^{II}\{Ni^{II}_4[Cu^{II}_2(Me_3mpba)_2]_3\}\cdot 52H2O$.

• XPS: confirmó que el estado de oxidación del Pd permanece en +2, cuando la coordinación del metal pasa de interactuar con las especies fuente NH3 y moléculas de Cl- al entorno químico del MOF.

• SC-XRD: confirmó más visualmente que se mantiene la arquitectura en capas cuadradas y octogonales con níquel en los vértices y cobre en los puntos medios de los bordes, así como la disposición espacial de los metales Pd y Ni en los poros octogonales más accesibles.

• XRPD: confirma que tanto los cristales como el polvo cristalino de **$Ni^{2+}Pd^{2+}$@CuNi-Me_3mpba** obtenidos son isoestructurales y que el MOF mantiene la cristalinidad y robustez tras PSM.

• TGA: verificó el número de moléculas de agua con las que cristaliza el MOF y nos dio información sobre la estabilidad del MOF frente a la temperatura.

• La isoterma de adsorción de gas mostró isotermas tipo I características de materiales microporosos y confirmó que después de PSM el MOF conserva su porosidad, siendo mayor para **$Ni^{2+}Pd^{2+}$@CuNi-Me_3mpba** que para **Ni^{2+}@CuNi-Me_3mpba**, sugiriendo que **$Ni^{2+}Pd^{2+}$@CuNi-Me_3mpba** tiene una mayor superficie accesible y una mayor estabilidad estructural.

El intercambio parcial de los cationes de níquel, alojados en sus canales, por paladio permitió una exposición 50/50 de los metales Ni2+ y Pd2+ , de modo que los tres metales con actividad catalíticamente activa (Cu, Ni y Pd) quedaron expuestos, con la intención de realizando catálisis en cascada (reacciones consecutivas). Por separado, Cu tuvo éxito en la hidroalcoxilación de ciclopropenonas donde los rendimientos de las reacciones catalizadas por **Ni^{2+}@CuNi-Me_3mpba** fueron idénticos o ligeramente inferiores a los llevados a cabo en presencia del catalizador homogéneo homogéneo Cu(OAc)2. Además, permitía reutilizar el material mas de 5 veces. En el caso del Ni, su presencia favoreció el acoplamiento Chan-Lam, completando así la funcionalidad de la cascada catalítica **Ni^{2+}@CuNi-Me_3mpba**, donde el Cu se encarga de la reacción de hidratación y el Ni2+ del acoplamiento Chan-Lam. La adición de Pd a la ecuación estuvo dada por la permitividad de la reacción de acoplamiento de hidratación ciclopropenona/Mizoroki-Heck en un solo recipiente que involucró su inclusión en el MOF **Ni^{2+}@CuNi-Me_3mpba.** Esto implicaba que la presencia de Ni^{2+} o Pd^{2+} en el MOF como catalizador heterogéneo estaba determinada por la direccionalidad deseada de la reacción para que el acoplamiento formara ésteres con mayor rendimiento porcentual (favorecidos por Ni) o cetonas (favorecidos por Pd). Finalmente, se concluyó que la presencia de los tres metales Cu, Ni y Pd favorece la reacción de síntesis de los compuestos de la familia de las cumarinas en un solo recipiente, a diferencia del catalizador ho-

mólogo homogéneo.

En el tercer capítulo hemos presentado varios ejemplos de SNMCs@MOFs y SACs@MOFs que constituyen un paso más en el desarrollo de los PSMs y la aplicabilidad de los MOFs como reactores químicos. Es sorprendente cómo el mero hecho de aplicar el proceso de reducción a los metales insertados en el MOF es capaz de formar SACs y SNMCs libres de ligandos y bien definidos dentro de sus canales. En los tres casos presentados, la modificación de la disposición de las especies metálicas insertadas ha dotado al MOF de nuevas propiedades catalíticas, sin olvidar la heterogeneidad y, por tanto, la reutilización que el MOF ya poseía antes de someterse a la reducción.

Partiendo de **Ni^{2+}@CuNi-Me_3mpba**, hemos podido estudiar los SNMC de Ag^0_2 (para el caso de inserción y reducción homometálica) y su cooperación con el SMA de Fe^{3+} (para el caso de inserción heterometálica).

Se caracterizaron los grupos de Ag^0_2 sin ligando dentro de la red **Ag^0_2@CuNi-Me_3mpba** y se utilizaron como catalizadores eficientes y recuperables para la reacción de expansión del anillo de Buchner. El seguimiento de las etapas de producción se llevó a cabo mediante SEM-EDAX, donde la proporción metálica final coincidía prácticamente con los datos proporcionados por el análisis elemental. La XPS pudo corroborar la reducción parcial de los iones Ag^+ insertados en el MOF. Y la perpetuación de la robustez y la cristalinidad tras la fatiga físico-química del MSP se verificó mediante SC-DRX, PDRX e isotermas de adsorción. Sólo con SC-XRD se pudo realizar un seguimiento SC-SC, mostrando en detalle los cambios producidos en el MOF después de cada paso y la disposición de los SNMC de Ag y de los iones Ag^+ sin reducir.

Las técnicas de caracterización utilizadas nos aseguraron que la inserción heterometálica de Ag^{+} y Fe^{3+} , tras el proceso de reducción,sólo fue capaz de formar SNMC de Ag02. Siendo SEM-EDAX (con la presencia estequiométrica de Na^{+} , para compensar las cargas de los metales reducidos), XPS (observando claras diferencias entre los estados de oxidación) y SC-XRD (permitiéndonos visualizar las especies preparadas/incorporadas) las técnicas con las que justificamos la presencia y estabilidad de la especie SNMC de **Ag^{0}_{2}@CuNi-Me_3mpba** y la especie SMA intrínsecamente inestable de Fe^{3+}.

Este metal multimetálico puede obtenerse en cantidades de varios gramos y **$Ag^{0}_{2}Fe^{3+}$@CuNi-Me_3mpba** es un catalizador para el acoplamiento cruzado oxidativo sin TEMPO de estirenos con vinilsulfona para dar vinilsulfonas en rendimientos de hasta >99%. Hemos evaluado que los dímeros de Ag son la especie catalítica activa durante la reacción en solución catalizada por $AgNO_3$ y TEMPO. Las vinilsulfonas pueden convertirse, in situ, en los correspondientes productos de fenilacetileno en altos rendimientos, hasta >99%, después de filtrar el catalizador **Ag^{0}_{2} Fe^{3+}@CuNi-Me_3mpba**, que puede reutilizarse. Así, se consigue una conversión final de estirenos a fenilacetilenos catalizada por $Ag^{0}_{2}Fe^{3+}$@ CuNi-Me_3mpba en un solo paso.

La extrapolación del método post-sintético de inserción desde MOFs aniónicos de oxamatos y Me_3mpba a MOFs neutros basados en oxamidatos y aminoácidos, fue meramente sintética. Ya que la inserción se llevó a cabo mediante la inmersión del MOF en $Pd(NH_3)_4Cl_2$, pero la interacción en lugar de la compensación de carga se debió principalmente a la estabilización a través de los enlaces de coordinación con los ésteres de tiol, que contenían los residuos de cadena del aminoácido modificado metilcisteína. El menor diámetro de los poros del **Pd^{0}@**

CuSr-Mecysmox y su entorno químico permitieron la obtención del SAC para someterse al proceso de reducción tras la inserción del metal.

Esta inserción homometálica del **CuSr-Mecysmox**, junto con su posterior reducción, llevó a cabo la formación in situ de Pd_1 en alcoholes bencílicos puros, que puede catalizar la oxidación aeróbica a ácidos benzoicos. Este MOF basado en metilcisteína con SACs de Pd_1 bien definidos en una distribución homogénea y estabilizados a lo largo de canales funcionales, fue preparado a escala de gramo.

Para la caracterización de los SACs de Pd_1 tuvimos que necesitar un mayor despliegue de herramientas de caracterización para poder demostrar su alta eficacia catalítica en su forma individualizada. Para este caso, SEM-EDAX sólo pudo confirmar la carga de Pd en el MOF y su incorporación estable tras el proceso de reducción. La XPS, además de confirmar la reducción del Pd, confirmó la estabilidad tras la reutilización del MOF catalítico, junto con la PDRX. La SC-XRD de sincrotrón permitió, por primera vez, visualizar claramente los SAC de Pd_1 y sus alrededores. La naturaleza del Pd_1, tanto en solución como en los MOFs, está respaldada por técnicas de microscopía y XAS. Estas últimas nos permiten apoyar los resultados de la SC-XRD revelando las principales interacciones entre los átomos de paladio y la red, así como inferir un mecanismo de formación plausible del Pd_1 SAC.

En el Capítulo 4, retomé el uso de los MOF Ni^{2+}@CuNi-Me_3mpba, después (esta vez) de la inserción completa de cationes Pd(II), se insertaron ligandos bipiridínicos fluorados con la intención de formar SCC dentro del MOF **Pd^{2+}@CuNi-Me_3mpba** que fueron capaces de catalizar la oxidación aeróbica de alcoholes alquílicos a ácidos carboxílicos sin la ayuda de aditivos/bases y manteniendo sus SCC confinados en los po-

ros, con una reutilización mejorada y selectividades interesantes.

El hecho de poder sintetizar SCCs en el interior de MOFs nos ha llevado a obtener un material avanzado con características únicas (en nuclearidad, estabilidad, estructura electrónica, etc.) muy diferentes de los SCCs que se obtendrían fuera de MOFs. En particular, se han insertado diferentes ligandos bis(4-piridilo)acetileno a diferentes grados de fluoración para preparar diferentes SCCs de PdII, donde cada ligando imparte diferentes efectos electrónicos, dentro de **Pd^{2+}@CuNi- Me_3mpba**.

La validación y ampliación de la estrategia sintética -descrita en el apartado 4.1.2- para la síntesis de SCC@MOFs, tal y como pretendíamos, se llevó a cabo mediante diferentes técnicas de caracterización:

- Mediante SEM comprobamos que se mantenía la proporcionalidad metálica, de forma que el MOF no se degradaba y los ligandos fluorados no secuestraban los cationes Pd^{2+} del **Pd^{2+}@CuNi-Me_3mpba**.

- El estado de oxidación de los cationes Pd^{2+} también permaneció intacto tras la inserción postsintética de los ligandos. Esto se verificó mediante XPS.

- Espectroscopia de RMN de ángulo mágico ^{19}F Los espectros de RMN líquida confirmaron la formación de complejos con el sitio PdII del ligando fluorado L_4 dentro del **Pd^{2+}-L_4@CuNi-Me_3mpba**.

-La técnica de SC-XRD, aunque no permitió la resolución de **Pd^{2+}- L_4@ CuNi-Me_3mpba** y **Pd^{2+}-L_5@CuNi-Me_3mpba** debido a su pérdida de cristalinidad tras someterse al PSM, sí fue posible resolver la estructura

de **Pd^{2+}-L_6@CuNi-Me_3mpba**. De este modo, **Pd^{2+}- L_6@CuNi-Me_3mpba**, actuó como figura representativa de los SCC@MOF que se sintetizaron en este trabajo. Mediante esta técnica fue posible confirmar con mayor precisión la formación del SCC dentro del MOF. Se observó que la inserción de los ligandos perfluorados de piridina provocaba una deformación estructural en los poros. Esto podría explicar la no resolución de **Pd^{2+}-L_4@CuNi-Me_3mpba** y **Pd^{2+}- L_5@CuNi-Me_3mpba**, ya que su distribución fluorada no sería lo suficientemente regular como para producir una deformación ordenada en la estructura del MOF.

-PXRD confirmó que la estructura cristalina del monocristal coincidía con la de la muestra de polvo de **Pd^{2+}-L_6@CuNi-Me_3mpba**. Además, la isoestructura de **Pd^{2+}-L_4@CuNi-Me_3mpba** y **Pd^{2+}-L_5@CuNi- Me_3mpba** con respecto a **Pd^{2+}-L_6@CuNi-Me_3mpba**, muestra que la formación de las jaulas dentro del MOF podría llevarse a cabo de forma similar en ambos casos. De este modo, se valida la interpretación del SCC producido en **Pd^{2+}-L_6@CuNi-Me_3mpba**, como figura representativa de **Pd^{2+}-$L_{4\text{-}5}$@CuNi-Me_3mpba**.

- El TGA mostró que la inserción de los ligandos fluorados implicaba la pérdida de la interacción de las moléculas de agua con el MOF de partida para establecer interacciones coordinadas con los ligandos $L_{4\text{-}6}$.

- La isoterma de adsorción de nitrógeno, mostró para los tres casos, **Pd^{2+}-$L_{4\text{-}6}$@CuNi-Me_3mpba**, la disminución del tamaño de poro de **Pd^{2+}@CuNi-Me_3mpba** tras la formación de SCC dentro del MOF.

- XANES y EXAFS confirmaron la electrofilia del Pd^{II} en **Pd^{2+}- L_4@ CuNi-Me_3mpba** y la interacción de los cationes Pd^{2+} con el ligando L_4 (principalmente debido a las interacciones Pd-F), respectivamente.

Finalmente, se validó la actividad catalítica única de los SCC sintetizados dentro del MOF. Se confirma que estos SCC@MOF pueden catalizar la oxidación aeróbica de alcoholes alquílicos a ácidos carboxílicos sin la ayuda de ningún aditivo/base. Se comprobó que los SCC@MOFs superan a los SCCs relacionados compatibles con los MOFs pero sin ligandos de piridina (per)fluorados, ya que estos complejos solubles no pueden realizar dicha transformación de forma eficiente.

Por lo tanto, los SCCs ubicados en los poros del MOF presentan una gran ventaja sobre los SCCs en su forma aislada, ya que se mejora su actividad catalítica, su selectividad (debido al espacio confinado que proporciona el MOF) y su estabilidad (ya que los nodos metálicos que componen la estructura del SCC permanecen ubicados en los poros del

MOF en lugar de producirse una deformación/ruptura del enlace coordinado en los SCCs al participar como catalizador en la reacción). Esta estabilidad proporcionada por la contención de los SCCs en el MOF nos lleva a obtener un catalizador heterogéneo con más de tres usos sin apenas perder su actividad catalítica.

Además, se puede suponer que estos materiales sólidos recuperables no sólo amplían la química organometálica del Pd hacia sitios de Pd^{2+} extremadamente altos y estables, sino que también abren la puerta a su uso como catalizadores en reacciones de activación de C-H desafiantes.

En resumen, en esta tesis hemos profundizado en el uso de MOFs como reactores químicos para la preparación de especies metálicas catalíticamente activas únicas y originales. De hecho, los compuestos reportados en los diferentes capítulos constituyen un paso más en la aplicabilidad de los MOF en un campo tan importante como la catálisis industrial,

ya que algunos de los compuestos reportados muestran propiedades catalíticas sobresalientes y, en algunos casos, son capaces de catalizar reacciones que no se habían presentado antes. se ha logrado antes. Estos resultados también abren la puerta al desarrollo de nuevas especies nanométricas de metal que no se habían logrado antes. En particular, la preparación de grupos heterometálicos subnanómetros libres de ligandos sigue siendo un desafío. Se han logrado algunos resultados preliminares y esta tesis ha sentado las bases para futuras aplicaciones de estas especies únicas sin precedentes.

ABBREVIATIONS

1D: one-dimensional
2D: two- dimensional
3D: three-dimensional
CI: Coordination Index
CPs: Coordination Polymers
CUSs: Coordinatively Unsaturated Metal Sites
DMF: N,N-dimethyl formamide
en: ethylenediamine
EVOH: Ethylene vinyl alcohol polymer
IUPAC: International Union of Pure and Applied Chemistry
Me3mpba: 2,4,6-trimethyl-m-phenylenediamine
MNPs: Metal Nanoparticles
MOF: Metal-Organic Framework
OMC: Organometallic Compound
PSMs: Post-Synthetic Methodologies
SAC: Single-Atom Catalystis
SBUs: Secondary Building Units,
SCCs: Supramolecular Coordination Complexes
SC-XRD: Single-Crystal X-ray Diffraction
SNMCs: Sub-Nanometric Metal Clusters
TMA: Tetramethylammonium

Abstract.....8

Resumen.....10

1. Introduction.....36

1.1. From coordination compounds to Metal-Organic Frameworks (MOFs).....38

1.2. MOFs Classification.....47

1.3. MOFs Synthesis.....53

1.3.1. Crystal MOF.....54

1.3.2. Powder MOF.....58

1.3.2. Industrial MOF.....62

1.4. MOFs properties 70

1.4.1. Tailored Porosity.....70

1.4.2. Benefits and limitations of using MOFs.....79

1.5. MOFs Post-Synthetic modifications (PSMs).....83

1.6. MOFs Applications.....95

1.6.1. Gas storage and separation.....96

1.6.2. Biomedicine.....99

1.6.3. Photoluminescent sensor.....101

1.6.4. Magnetism.....105

1.6.5. Catalysis.....107

1.7. MOFs development within the research line of our group.....111

1.8. References.....125

2. Post-synthetic modification of catalytic properties by cation exchange in MOFs.....156

2.1. Introduction.....157

2.1.1. Common PSM in MOFs.....157

2.1.1.1. Cation exchange 157

2.1.1.2. Transmetalation.....161

2.1.2. Aplications of PSMs in MOFs.....162

2.2. Objectives.....163

2.3. Synthesis.....165

2.4. Characterization.....167

2.4.1. Scanning Electron Microscopy-Energy Dispersive X-ray Spectroscopy (SEM-EDAX) of **$Ni^{2+}Pd^{2+}$@CuNi-Me_3mpba**.....167

2.4.2. X–ray photoelectron spectroscopy (XPS) of **$Ni^{2+}Pd^{2+}$@CuNi-Me_3mpba**.....168

2.4.3. Single-Crystal X-ray diffraction (SC-XRD) of **$Ni^{2+}Pd^{2+}$@CuNi-Me_3mpba**.....169

2.4.4. Powder X–ray Diffraction (PXRD) of **$Ni^{2+}Pd^{2+}$@CuNi-Me_3mpba**.....178

2.4.5. Termogravimetric Analysis (TGA) of **$Ni^{2+}Pd^{2+}$@CuNi-Me_3mpba**.....179

2.4.6. Gas adsorption of **$Ni^{2+}Pd^{2+}$@CuNi-Me_3mpba**.....179

2.5. Catalytic properties of Ni2+Pd2+@CuNi-Me3mpba181

2.5.1. MOFs as suitable solid catalysts for the hydroalkoxylation of cyclopropenones.....181

2.5.2. One–pot hydroalkoxylation of cyclopropenones / cross coupling reactions.....184

2.6. Conclusions.....191

2.7. References.....194

3. MOF-driven synthesis of SACs and SNMCs..204
3.1. Introduction.....205
3.2. Objectives.....214
3.3. Synthesis.....216
3.3.A. Synthesis of homometallic SNMCs (**Ag^0_2@CuNi-Me_3mpba**) 216
3.3.B. Combination of SNMCs and SACs within the same MOF (**$Ag^0_2Fe^{3+}$@CuNi-Me_3mpba**).....218
3.3.C. Synthesis of MOF-driven SACs (**Pd^0@CuSr-Mecysmox**) 221
3.4. Characterization.....228
3.4.1. Scanning Electron Microscopy-Energy Dispersive X-ray Spectroscopy (SEM-EDAX).....228
3.4.1.A. SEM-EDAX of **Ag^0_2@CuNi-Me_3mpba**.....228
3.4.1.B. SEM-EDAX of **$Ag^0_2Fe^{3+}$@CuNi-Me_3mpba**.....229
3.4.1.C. SEM-EDAX of **Pd^0@CuSr-Mecysmox**.....231
3.4.2. X–ray photoelectron spectroscopy (XPS).....232
3.4.2.A. XPS of **Ag^0_2@CuNi-Me_3mpba**.....233
3.4.2.B. XPS of **$Ag^0_2Fe^{3+}$@CuNi-Me_3mpba**234
3.4.2.C. XPS of **Pd^0@CuSr-Mecysmox**.....235
3.4.3. Single-Crystal X-ray Diffraction (SC-XRD).....236
3.4.3.A. XPS of **Ag^0_2@CuNi-Me_3mpba**.....237
3.4.3.B. XPS of **$Ag^0_2Fe^{3+}$@CuNi-Me_3mpba** 244
3.4.3.C. XPS of **Pd^0@CuSr-Mecysmox**.....2
3.4.4. Powder X–ray Diffraction Measurements

(PXRD).....262
3.4.4.A. PXRD of **Ag^0_2@CuNi-Me_3mpba**...263
3.4.4.B. PXRD of
$Ag^0_2Fe^{3+}$@CuNi-Me_3mpba.....264
3.4.4.C. PXRD of
Pd^0@CuSr-Mecysmox.....266
3.4.5. Termogravimetric Analysis (TGA) …….....266
3.4.5.A. TGA of
Ag^0_2@CuNi-Me_3mpba.....267
3.4.5.B. TGA of
$Ag^0_2Fe^{3+}$@CuNi-Me_3mpba.....267
3.4.5.C. TGA of **Pd^0@CuSr-Mecysmox**.....267
3.4.6. Gas adsorption…….....…..…….268
3.4.6.A. Gas adsorption of
Ag^0_2@CuNi-Me_3mpba.....269
3.4.6.B. Gas adsorption of
$Ag^0_2Fe^{3+}$@CuNi-Me_3mpba.....270
3.4.6.C. Gas adsorption of
Pd^0@CuSr-Mecysmox.....270
3.5. Catalytic studies.....272
3.5.A. Catalytic properties of
Ag^0_2@CuNi-Me_3mpba.....272
3.5.B. Catalytic properties of
$Ag^0_2Fe^{3+}$@CuNi-Me_3mpba.....275
3.5.C. Catalytic properties of
Pd^0@CuSr-Mecysmox.....286
3.6. Conclusions…….....…….....306
3.7. References…….....309

4. Post-synthetic construction of Supramolecular Coordination Complexes SCCs……..…….....….324

4.1. Introduction…….....…….....325

4.1.1. MOFs vs SCCs…….....….325

4.1.2. MOF assisted preparation of SCCs……...….329

4.2. Objectives……...……..431

4.3. Synthesis…….……..…..342

4.4. Characterization…….....……346

4.4.1. Scanning Electron Microscopy-Energy Dispersive X-ray Spectroscopy (SEM-EDAX) of **Pd^{2+}-L_{4-6}@CuNi-Me_3mpba**.....346

4.4.2. X–ray Photoelectron Spectroscopy (XPS) of **Pd^{2+}-L_{4-6}@CuNi-Me_3mpba**.....347

4.4.3. Liquid Nuclear Magnetic Resonance (NMR) and Magic Angle Spinning (MAS) Solid 19F NMR Spectroscopy of **Pd^{2+}-L_{4-6}@CuNi-Me_3mpba**.....349

4.4.4. Single-Crystal X-ray Diffraction (SC-XRD) of **Pd^{2+}-L_{4-6}@CuNi-Me_3mpba**…….....350

4.4.5. Powder X–ray Diffraction Measurements (XRPD) of **Pd^{2+}-L_{4-6}@CuNi-Me_3mpba**…….....358

4.4.6. Termogravimetric Analysis (TGA) of **Pd^{2+}-L_{4-6}@CuNi-Me_3mpba** …….....360

4.4.7. Gas adsorption of **Pd^{2+}-L_{4-6}@CuNi-Me_3mpba**….....361

4.4.8. X-Ray Absorption Near Edge Structure (XANES) and Extended X-Ray Absorption Fine Structure (EXAFS) measurements of **Pd^{2+}-L_{4-6}@CuNi-Me_3mpba**…….....362

4.5. Catalysis of Pd^{2+}-L_{4-6}@CuNi-Me_3mpba…….....364

4.6. Conclusions…….....……...374

4.7. References……382

5. General conclusions……390

6. Publications……397

7. Annex……400

Agradecimientos……436

CHAPTER

1

Metal-Organic Frameworks (MOFs) are a class of porous crystalline materials, made up of single metal ions and/or polynuclear metal clusters (also known as secondary building units, SBUs) linked through organic ligands (Figure 1.1).[1-5] MOFs have reveal as outstanding materials among other porous materials, such as zeolites, activated carbon and alumina, as consequence of their unique intrinsic features: (i) possibility to tailor, to a certain extent, their topology, dimensionality and pores functionalities, (ii) rich host-guest chemistry and (iii) use of X-ray crystallography as basic characterization tool.[6,7]

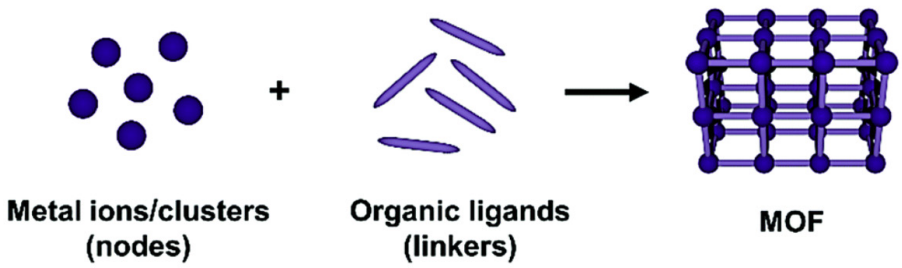

Figure 1.1. Schematic representation of the components parts to assemble metal-organic framework (MOF) [8-10]

In fact, in the last three decades[11], there have been an exponential growth in the interest in MOFs, which has traduced in the development of an increasing number of aesthetically pleasant and functional high-dimensional structures (Figure 1.2). This, in part, is directly related to the rich variety of organic ligands and metal ions/SBUs that can be combined to render high-dimensional networks with different pore sizes, shapes and functionalities. In addition, in MOFs chemistry can be possible to achieve with considerable synthetic control the presence of two or more

physical/chemical properties, leading to multifunctional materials. [12]

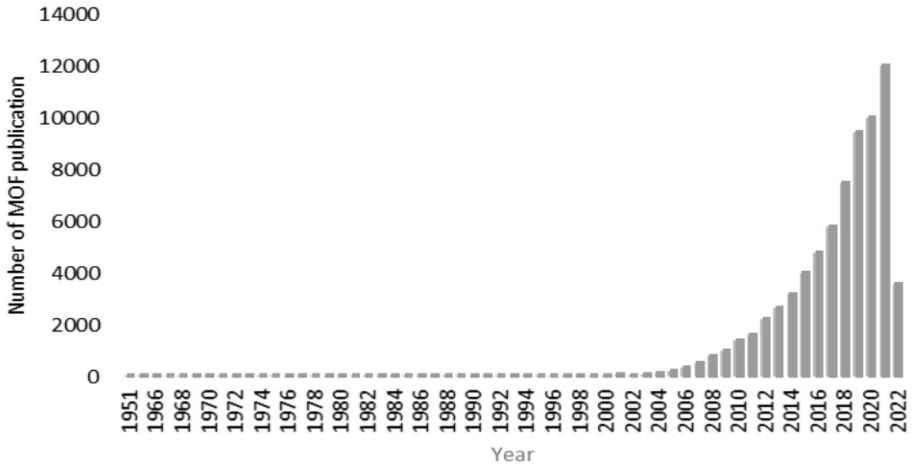

Figure 1.2. Graph depicting the exponential increase in interest in MOFs with the number of publications citing them. Data sourced from Scifindern Search database Search in January 2022.

1.1. From Coordination Compounds to Metal-Organic Frameworks (MOFs)

According to The International Union of Pure and Applied Chemistry (IUPAC), a coordination compound or complex is a chemical species (neutral or ionic) consisting of a central atom (usually a metal, M) and a set of atoms or group of atoms, called ligands, L, which are bonded through a coordinated covalent bond. The ligand provides the pair of electrons of the bond ("lone-pair") and the metal contributes with empty orbitals of low energy, where the pairs of electrons of the L ligands can be accommodated.

Alfred Werner in the period 1893-1913 laid the foundations of coor-

dination chemistry, starting with the publication "Contribution to the Constitution of Inorganic compounds" and culminating with the Nobel Prize13. His work made it possible to explain the "complexity" of the first coordination compounds, obtained by considering that transition metal atoms have a double bonding capacity: primary, based on their ability to share valence electrons, and secondary, responsible for the bonds with the ligand donor atoms. [14,15]

The interactions that exist between the central atom and the ligands are of the Lewis acid-base type. The central atom is an electron acceptor (Lewis acid) and the ligands are capable of donating electron density (Lewis bases)[16], where the atom directly attached to the acceptor is called the "donor atom".

Ligands can be classified according to different features: (i) number of atoms, monoatomic (e.g. Br^- and F^-) or polyatomic, in which case it is essential to know through which atom they coordinate to the central atom. For example, NH_3, H_2O and CO molecules can act as ligands by binding to the central metal atom through the free pair of electrons of the :N, :O and :C atoms, respectively, which will be called donor or coordinator atoms, (ii) charge, anionic (e.g. Cl^-, I^-, NO^{2-}, CN^- and SO_4^{2-}) and neutral (e.g. NH_3, H_2O and CO), and (iii) number of coordination points to the central metal atom, as monodentate (Cl^-, I^-, NO_2^-, NH_3, H_2O and CO) or polydentate (e.g. bidentate, tridentate and tetradentate). Ambidentate ligands are those with more than one donor atom that can be used interchangeably: CN^- (C donor: cyano or cyanide), NC^- (N donor: isocyanane or isocyanide), NO_2^- (N donor: nitro), ONO^- (O donor: nitrite). When a polydentate ligand is bonded to a central metal atom, a ring is formed (generally of 5 or 6 members), the complex is called a chelate, thus giving rise to another way of classifying ligands according to their mode of coordination to the metal, which can be terminal, chelate or bridge.

The atoms of the ligands that are bonded directly to the central ion define the coordination polyhedron (or polygon), so that the number of vertices corresponds to the coordination number or coordination index (CI). The CI corresponds to the number of σ bonds formed between the ligands and the central atom (omitting the π bonds). Depending on CI value, different geometries are generated (linear, flat trigonal, square plane, tetrahedral, square-based pyramid, trigonal bipyramid, octahedral, etc.). The know CI values are in the range of 2 to 12, but the most frequent are 4 and 6. This value depends on several factors, but mainly on the central atom/ligand ratio.

The spatial arrangement (geometry or stereochemistry) of the central metal atom and the ligand donor atoms depends on the coordination index. Table 1.1 shows some examples of geometry according to the coordination index (CI). This geometry is responsible for many characteristics of these compounds, such us magnetic properties, colour and so on.

Table 1.1. Some examples of coordination compound geometries according to the coordination index (CI).

CI	Geometry	
2	Linear 	
3	Trigonal 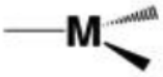	
4	Tetrahedral 	Square planar 
5	Trigonal bipyramidal 	Square piramidal 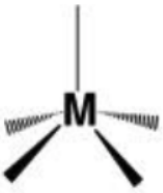
6	Octahedral 	

Also, there are compounds where two or more metals are bonded forming di- or polynuclear metal complexes. It was Robson in 1970 who first coined "dinucleating ligands". Nevertheless, in 1966 F. A. Cotton defined transition metal cluster compounds as "those containing a finite group of metal atoms which are held together as a whole mainly, or at least to a significant extent, by direct bonds between the metal atoms, although some non-metal atoms may be intimately associated with the cluster".[17] So, it excludes polymeric compounds and polynuclear caged or polyhedral compounds, if they lack transition metal-metal bonds, (e.g. polyoxometalates), with fully oxidized transition metal ions/atoms, bridged by heteroatoms such as oxygen or sulphur, lacking "d" electrons and molecular orbitals for transition metal-metal bonds. [18] Since Werner seminal work great advances have been achieved on the controlled design and synthesis of discrete coordination complexes with targeted geometries, stereochemistries and ligand composition. This high-level of control and knowledge treasured, somehow, has been an inspirational source and transferable toolbox for researchers working on develop the area of extended coordination complexes. In this context, following Werner's basis of coordination chemistry, Hofman and Küpert, in 1897, demonstrated the structural concept of framework/network in coordination chemistry with the obtention of the first inorganic clathrate compound, $[Ni(NH_3)_2Ni(CN)_4] \cdot 2C_6H_6$.[19,20] This compound belongs to the latter-known family of Hofmann clathrate, with the general formula $M(NH_3)_2M'(CN)_4 \cdot 2G$, where M is a six-coordinate and M' a four-coordinate divalent metal ion, and G is an aromatic guest molecule.

Following the nomenclature recommendations of IUPAC since 1985, a coordination polymer can be defined as "a coordination compound with repeating coordination entities extending in 1, 2 and 3 dimensions". [21-22]Even so, in 1916, Y. Shibata (founder of coordination chemistry in

Japan and co-worker of Werner) used that term for the first time to describe dimers and trimers of several cobalt(II) amine nitrate. However, it is considered that it appeared for the first time published in 1963, when J. Bailar described bis-(*β*-diketone)-beryllium complexes.

Since then, the term coordination polymer has been used continuously in the scientific literature, but until the development of single-crystal X-ray crystallography, there was no chance to demonstrate the infinite nature of the obtained frameworks. In this context, representative examples were Prussian Blue, $Fe^{III}_4[Fe^{II}(CN)_6]3{\cdot}xH_2O$ (x=14-16), and Hofmann clathrate, $[Ni(NH_3)_2Ni(CN)_4]\cdot 2C_6H_6$. Prussian Blue was discovered by Diesbach and Dippel in 1704 as a blue pigment (substituent of the expensive lapis lazuli), and it was not identified until 1977 as a coordination polymer, when its structure was determined by X-ray diffraction techniques.[23] This three-dimensional coordination polymer, is a mixed-valence compound with a cubic structure, in which alternating octahedral sites of FeII and FeIII ions are linked through cyanide ligands, where carbon and nitrogen are connected to FeII and FeIII, respectively (Figure 1.3a).[24] Similarly, $Ni(NH_3)_2Ni(CN)_4]\cdot 2C_6H_6$ had to wait for its resolution too until Power and Rayner analyzed the structure with X-ray in 1949.25 Consisting of two-dimensional layers of alternating octahedral and square planar NiII, linearly connected through four CN- moieties (Figure 1.3b). The terminal NH3 ligand is axially bound and points towards the adjacent layer, thus forming a cavity that can encapsulate benzene molecules. Years later, Ywamoto's group modified this compound by replacing the hexacoordinate NiII with other divalent ions such as Mn^{II}, Zn^{II}, Cd^{II}, and Cu^{II}, and ammine with other ligands. They introduced ethylenediamine (en) into these types of networks, which enabled the formation of an organic bridge between adjacent layers to make a three-dimensional host lattice. [26,27]

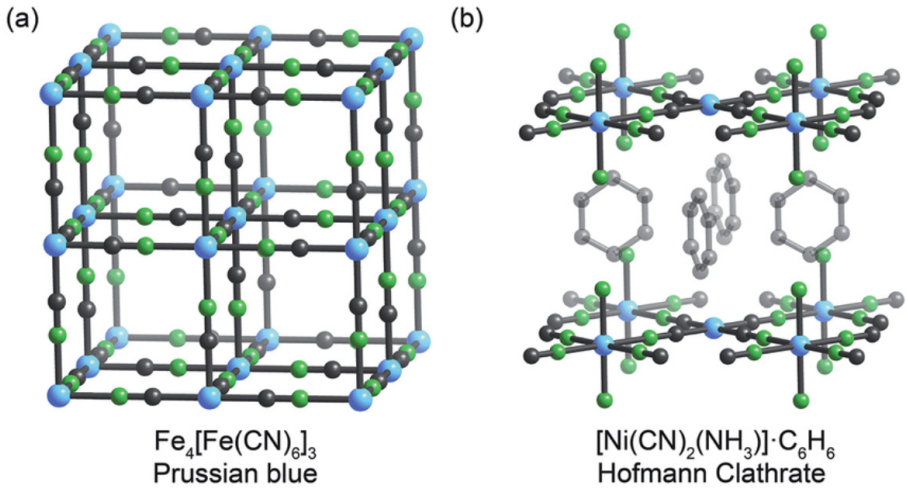

Figure 1.3. a) Prussian blue $Fe^{III}_4[Fe^{II}(CN)_6]_3 \cdot xH_2O$ (x = 14-16) (right) and (b) Hofmann clathrate $[Ni(NH_3)_2Ni(CN)_4]$ ·2C6H6 with benzene molecules occupying the space between the layers. Atom labeling scheme: C, black; N, green; metals, blue. H atoms are omitted for clarity. [28,29]

Saito and co-workers obtained the first crystal structure of a three-dimensional network in 1959, in order to try to get information about the mechanism of cuprous ion dyeing of polyacrylonitrile fibers. The crystallized compound bis(adiponitrile)copper(I) nitrate, belong to the family of bis(alkylnitrilo)copper(I) structures, consists of tetrahedral single-metal building units, $Cu(CN)_4$,[32] (Figure 1.4) connected through organic moieties with different lengths and the NO^{3-} anions occupying its voids. They obtained one-, two- or three-dimensional compounds according to the length and conformation of the organic moieties. [30,31]

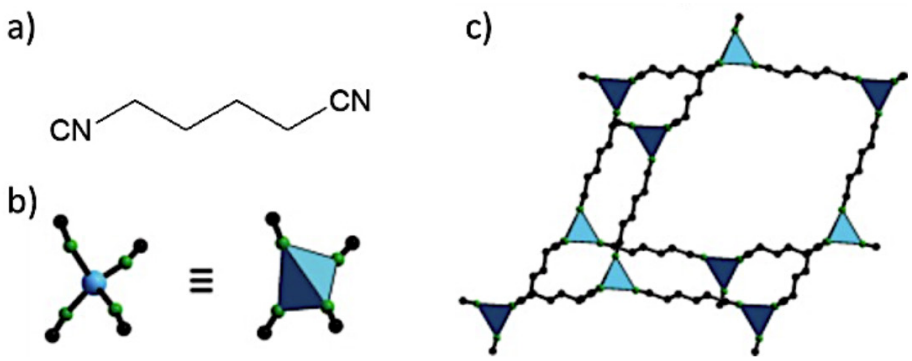

Figure 1.4. a) Adiponitrile formula, b) $Cu(CN)_4$ units c) Bis(adiponitrile)copper(I) nitrate frameworks. Color code: black, C; green, N; blue polyhedra, Cu. Hydrogen atoms, anions, and interpenetrating networks are omitted for clarity. Adapted from ref. 32.

Nevertheless, it was not until the decade of 1980-1990, thanks to the work contributed by Profs. Richard Robson and Bernard F., when coordination polymers had a turning point, and it was envisaged to take advantage on their intrinsic porosity for applications. They applied the geometrical basis of the crystal chemistry of Wells (reported in 1954),[33] to describe crystal structures in terms of networks, and to suggest, pioneeringly, the design of new coordination polymers by a careful assembly of what they referred as secondary units. They considered common coordination environments adopted by metal ions and the directionality that linkers offer to explain the rationale assembly of inorganic-organic subunits, as long as the periodicity and symmetry of the final framework allow it. These compounds showed interesting properties and applications, such as porosity and catalysis. From them, the infinite and non-interpenetrated cationic framework [Cu(TCTPM)]+ is a beautiful exponent. It is based on $Cu(CN)_4$ units linked to tetrahedral organic linker 4,4',4',4'''-tetracyanotetraphenylmethane (TCTPM)32, Figure 1.5.

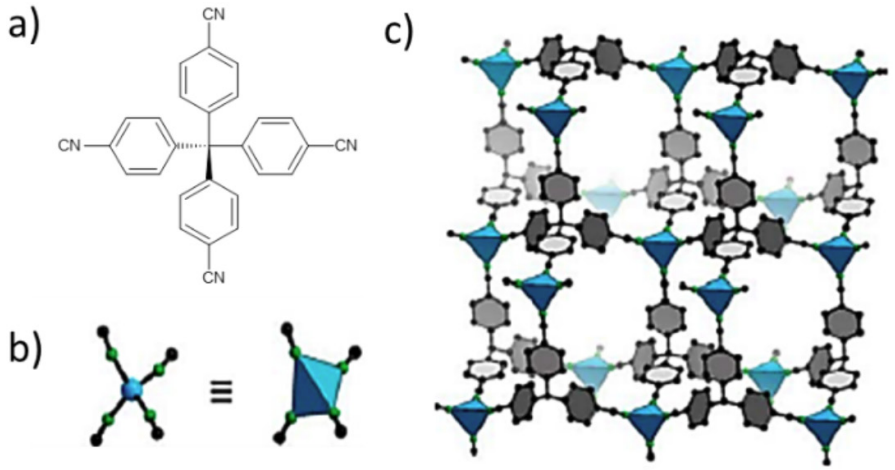

Figure 1.5. a) 4,4',4',4'''-tetracyanotetraphenylmethane (TCTPM) formula b) $Cu(CN)_4$ units c)$[Cu(TCTPM)]^+$ diamond-like framework. Color code as in Figure 3. Adapted from ref. 32.

After this seminal work, the development of porous coordination polymers continued to evolve through the obtention of novel compounds with different structural topologies, made up of distinct multivalency metallic centers and multifunctional ligands.[34] This allowed to increase the knowledge on the controlled design and synthesis of extended 3D networks, in conjunction with the understanding of the influence of different synthetic factors on the final structure, porosity and chemical functionality of the assembled species.

However, it was not until the work done by Prof. Omar M Yaghi, in 1995, when the term metal-organic frameworks (MOFs) was coined, as a differentiating label from coordination polymers, stressing the mixed inorganic-organic nature of components and the porosity of the assembly35. Here, they published the X-ray structure of Cu'(4,4'-bpy)$_{1.5}$ $NO_3(H_2O)_{1.25}$ (4,4'-bpy = 4,4'-bipiridine)[32], which featured an extended cationic framewor with rectangular channels filled by nitrate with a diamond-like structure (Figure 1.6). Also, Prof. Yaghi introduced some-

how the term "host-guest" chemistry into the MOFs field, together with Prof. Susumu Kitagawa,[36] when he showed that the nitrates ions within the channels could be exchanged by other anions such as SO_4^{2-} and BF_4^-, demonstrating the accessibility of the channels. Since then, many MOFs have been synthesized and characterized crystallographically.

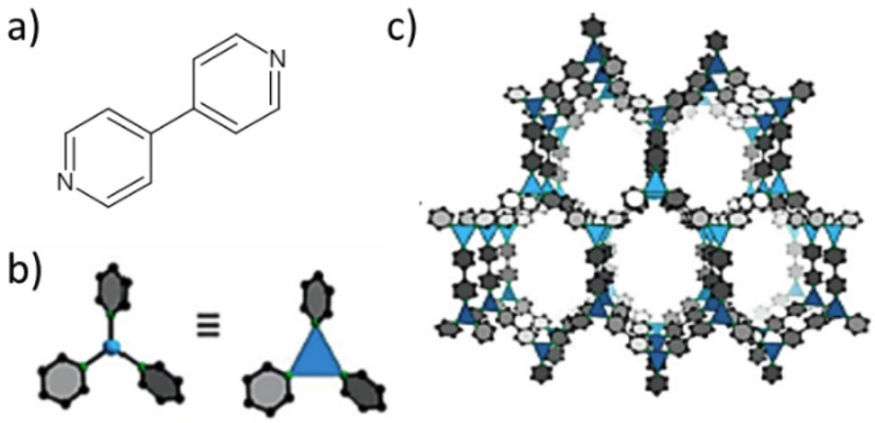

Figure 1.6. a) 4,4'-bpy = 4,4'-bipiridine formula b) $Cu(C_5H_4N)_3$ units c) $CuI(4,4'\text{-bpy})_{1.5}NO_3(H_2O)_{1.25}$. Color code as in Figure 3. Adapted from ref. 32.

1.2. MOFs Classification

The increased use of coordination polymers (CPs) and metal-organic frameworks (MOFs) in many areas of applied science and engineering, together with the appeared confusion in terminology, exerted pressure on IUPAC to establish a classification of coordination compounds in order to avoid misunderstanding and clarify concepts. So, in 2012, a group of researchers presented a classification of solid-state coordination chemistry based on the division of the coordinated compounds into coordination polymers and discrete compounds, see Figure 1.7.

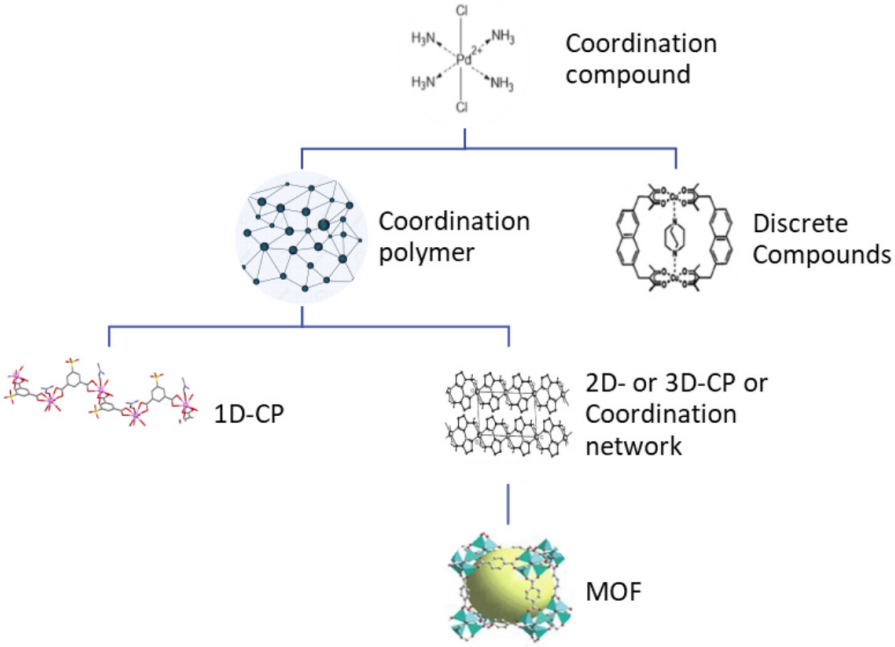

Figure 1.7. IUPAC classification of coordination compounds. [37-41]

Discrete compounds (Figure 1.8), or 0D coordination compounds, are understood as finite entities of metal-organic construction linked by coordination bonds, such as macrocycles, cages and capsules. Meanwhile, a CP is understood to mean a compound with repeating coordination entities extending into an infinite array. So, even though the design and chemistry may be similar, the main difference resides on the nature of the ligand. At this respect, convergent ligand building blocks are used to assembly discrete complexes (Figure 1.8), and divergent ones generate CPs.

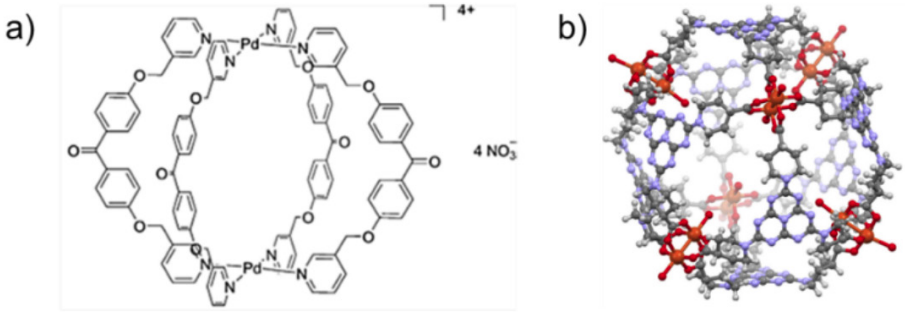

Figure 1.8. Examples of discrete compounds: a) M2L4 coordination cage with two palladium(II) atoms bridged by four bidentate ligands 4,4'-bis(3-pyridinemethoxy) benzophenone. [42] b) Structure of complex $[Cu_{12}(tp4c)_8(H_2O)_{12}]$, where copper(II) paddle-wheels are the SBUs and tp4c is the ligand 1,1',1''-(1,3,3a1,4,6,7,9-heptaazaphenalene-2,5,8-triyl)tris(piperidine-4-carboxylic acid). Color code: orange, blue, gray, and red ellipsoids correspond to Cu, N, C, and O atoms, respectively.[43]

Following the scheme presented in Figure 1.7, coordination polymers are classified into one-dimensional (1D) polymeric compounds (Figure 1.9a) and coordination networks, two- (2D) (Figure 1.9b) and three-dimensional (3D) polymeric compounds (Figure 1.9c). 1D-Coordination Polymer (1D-CP) would consist of entities linked by coordination bonds in one direction and supramolecular interactions (such as hydrogen bonding, π-π stacking and van der Waals) in the two other directions. Meanwhile a structure linked by coordination bonds in two directions and supramolecular interactions in another direction is a 2D-Coordination Polymer (2D-CP), and the one linked by coordination bonds in three directions is a 3D-Coordination Polymer (3D-CP).

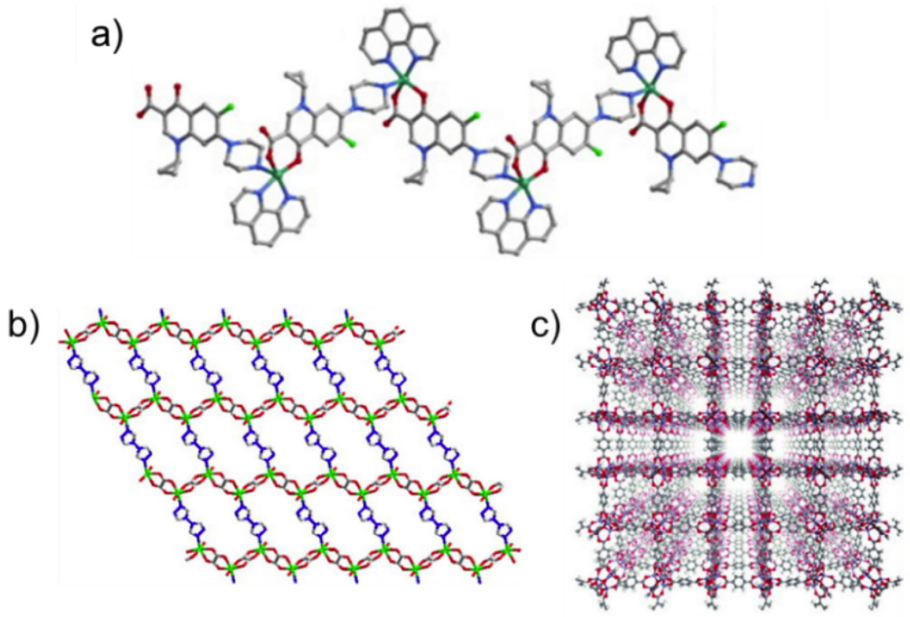

Figure 1.9. Examples of a) 1D-CP: $[Cu(cpx)(phen)]^{+}$, where cpx is ciprofloxacin and phen is 1,10-phenanthroline.[44] b) 2D-CP: $[Mn_2(btr)(\mu\text{-}ox)_2(H2O)_2] \cdot 2H_2O$, where btr is 4,4′-bis-1,2,4-triazole and ox is oxalate anion,[45] and c) 3D-CP: $[Zn_4O(BDC)_3] \cdot (DMF)_8(C_6H_5Cl)$, MOF-5, where the metal center is Zn_4O center, and the organic linker is terephthalate [BDC = 1,4-benzodicarboxylate]. [46]

Finally, MOFs, in turn, belong to a further subclass of coordination networks. According to IUPAC, "a MOF is a coordination network with organic ligands containing potential voids", where "a coordination network is a coordination compound extending, through repeating coordination entities, in one dimension (1D)- that may have cross-links between two or more individual chains, loops, or spiro-links- or a coordination compound extending through repeating coordination entities into two- (2D) or three-dimensions (3D)".[47]

The abbreviation MOF is used as a general term of this class of compounds. However, it is worth to mention that it also designates a subclass of different compounds from Yaghi´s lab, when combined with a

number (e.g. MOF-74, MOF-101, MOF-177, etc.).[48] Also, MOFs are labelled with other names/codes. Analogously to zeolites, existing MOFs are grouped in families of compounds, designated by a name and a number. [49] These families are organized either by similarity in structure and symmetry, like IRMOFs (IsoReticular Metal-Organic Frameworks)[50] and F-MOF (Fluorinated Metal-Organic Frameworks),[51] by similarity to zeolite topology, like ZIF (Zeolite Imidazole Framework)[52], metal-azolate frameworks (MAF),[53] and 'zeolite like MOFs' (ZMOFs);[54] or by abbreviations corresponding to the place of their discovery, like MIL-53 and MIL-101 (Materials of Institute Lavoisier) [55] and HKUST-1 (Hong Kong University of Science and Technology). [56]

Given that MOFs are generally sought for the possibility to tailor their porosity by chemical design, the geometric and connectivity features of the building blocks used to assemble them are of main relevance. On this basis, recently, Prof. Omar M. Yaghi considering the reported examples presented a tentatively classification, (Figure 1.10). Illustrative examples of some of them are shown in Figure 1.11.[57, 58]

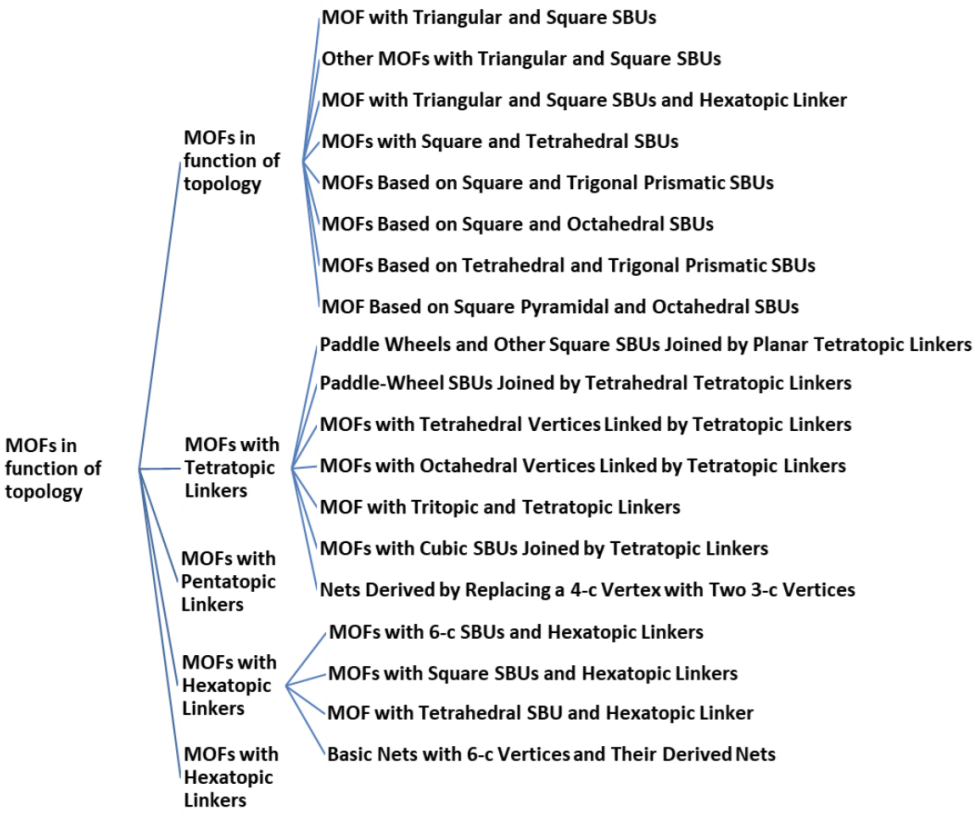

Figure 1.10. MOFs classification in as function of constituting polytopic linkers and/or multiple building units obtained from topological analysis of MOF structure.Adapted from ref. 57.

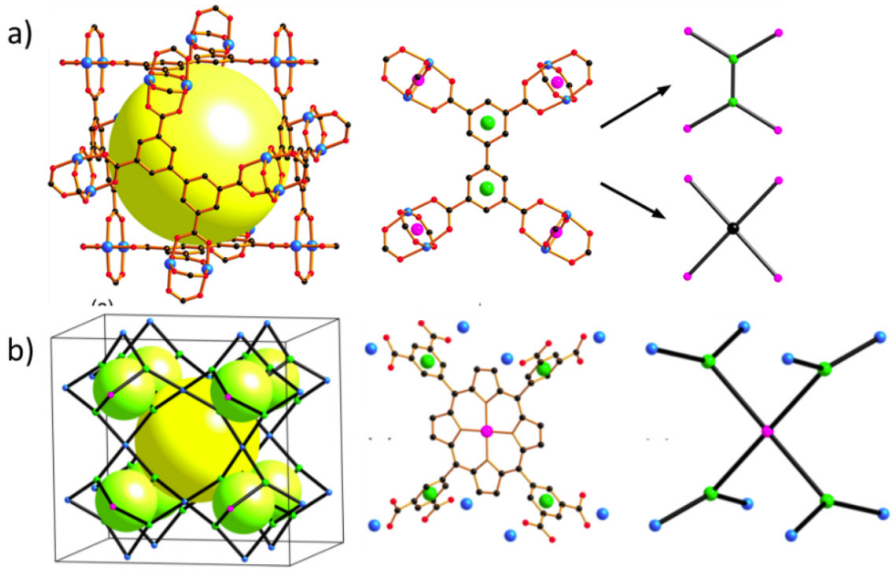

Figure 1.11. a) Representation of a portion of MOF-505 structure, $[Cu_2(PDEB)(H_2O)_2] \cdot xS$ (NJU-Bai12) (left), the linker PDEB = 5,5′-(1,4-phenylenedi-2,1-ethynediyl)bis(1,3-benzenecarboxylic acid) with the basic SBUs (middle) and its schematic representation (right)[58,59] b) Topological representation of ZJU-18, $[Mn_5Cl_2(Mn\text{-}Cl\text{-}OCPP)(DMF)_4(H_2O)_4] \cdot 2DMF \cdot 8CH_3COOH \cdot 14H_2O$ (left), the porfirine linker M-H_8OCPP= 5,10,15,20-tetrakis(3,5-biscarboxylphenyl)porphyrin and basic SBUs (middle). Schematic representation of the nodes and links in the crystal structure.[60,61]

1.3. MOFs Synthesis

Currently, in the Cambridge Crystal Database there are deposited ca. 50,000 MOF structures.[62] These MOFs have been synthesised using quite a wide range of synthetic protocols and obtained in different forms, single crystal or polycrystalline powder, and scales, lab or industrial. The polycrystalline powder is the state in which most works on MOFs have been reported, since it can be better controlled stoichiome-

trically and there is greater ease of synthesis since it is easier to stabilize nanocrystals that require less lattice energy.[63] The need to obtain single crystals arises from the need to know exactly the interatomic and intermolecular interactions both intrastructurally and extrastructurally with the surrounding environment, the guests or the metals/ligands incorporated subsequently. Industrial scaling is carried out once the macro-scale reproducibility of a target MOF as well as the feasibility of their application has been tested. In the following subsections we will describe the main synthetic strategies we have followed for the obtention of MOFs in this PhD thesis, and we will compare and mention with other common methods. The existing MOF structures, on the other hand, suggests a wider variety of preparation methods.

1.3.1 Crystal MOF

In order to understand the molecular interactions of metal-organic frameworks, researchers have set themselves the challenging task of obtaining single crystals suitable for detailed crystallographic analysis. Unlike molecular species, MOFs are insoluble once synthesized (a property which is advantageous for other aspects), and so recrystallization from polycrystalline powders is not an option.

Some MOFs can be obtained in the form of polycrystalline powders directly from the mixing of the precursors. Such MOFs are ideal to be crystallised when the precipitation is slowed down. The most common way to do it is by allowing two separate solutions of metals and ligands to diffuse slowly into each other. A number of different techniques have been established to this end. The simplest method is to layer carefully one solution on top of another in a small vial or tube, Figure 1.12 left.[65] Often a buffer layer of pure solvent is layered between the two solutions

containing the two precursors, where the use of solvents with different densities (e.g. MeOH versus $CHCl_3$) greatly aids separation. The density and polarity of the solvent influence the diffusion to a greater or lesser extent, so it should be noted that the slower the interaction of the precursors, the more slowly some crystal may interact, as long as a time limit is not exceeded in which decomposition or loss of quality of the product or precursor may occur. This can take in the order of 2 weeks, although crystallization can often take much longer (or shorter) times, and so the reaction should be checked regularly, preferably without disturbing the crystal growth through handling. Regular inspection is important as crystals can come and go (for kinetic products) or become flawed, overgrown or otherwise deteriorate in quality over time.

Other variations of this technique include locking one solution into a gel through the addition of a gelling agent such as tetramethoxysilane, Figure 1.12 right. The role of the gel is to slow diffusion through reduction of convection and also provide support for the growing crystals. In this PhD thesis we have taken advantage of a specially designed glassware

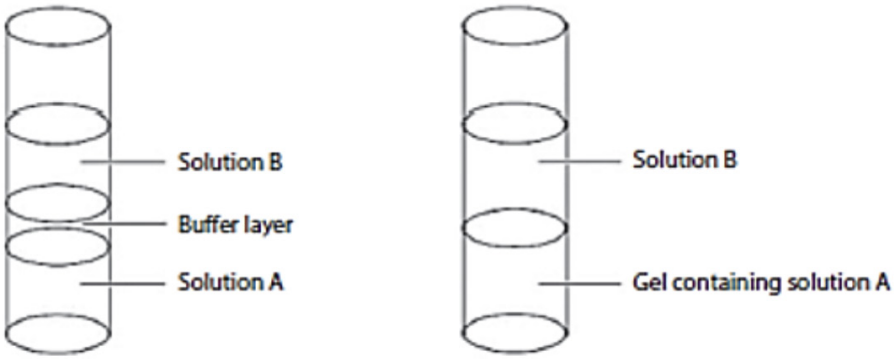

Figure 1.12. Tubes with (right) and without gel (left) for the slow growth of single-crystals of MOFs.

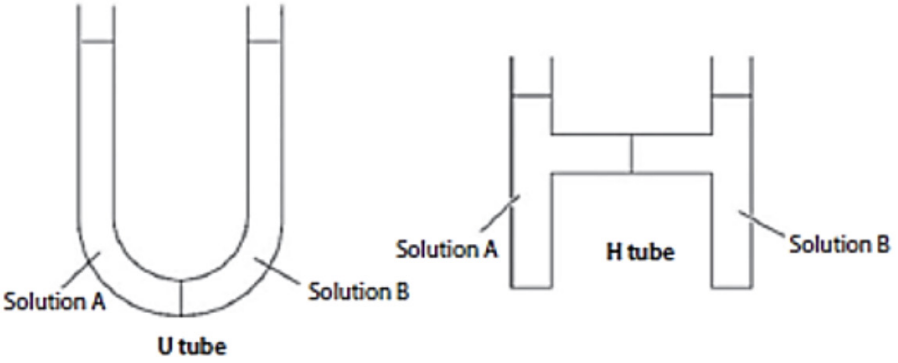

Figure 1.13. H-tubes and U-tubes for the slow growth of single-crystals of MOFs.

The crystallization of MOFs is not an easy task, there are several factors that have a severe influence in the process, such as the polarity of the solvent, counterion or even metal salt choice. Thus, this imply a quite a great synthetic effort to been able to find the optimal synthetic conditions to get suitable crystals to ascertained the structure by means of X-ray crystallography.

One of the key reasons for obtaining crystal structures is to establish relationships between structures and properties, and thus, gain insights that can feed into the design of new materials. So, it has to bear in mind, that the structures obtained from single crystals may be inherently unrepresentative (because the crystallographer chooses the best crystal available) of the bulk material upon which the properties are tested. Furthermore, reactions can often give more than one product, hence researchers have to check the correlation between the single crystals and the bulk product, and this is most easily achieved through the use of techniques such as powder diffraction or (less convincingly) infrared or Raman spectroscopy.

Many other synthetic approaches have been offered for the preparation of MOF,[64,65] such as:

- The slow diffusion of the reagents in a polymeric matrix, where the polymer acts as an additional barrier to slow down the contact between the reagents.

- Evaporation of the solvent at room or reduced temperature, this technique has been widely used in the past due to its simplicity and zero energy cost. As in the case of crystallizing simple inorganic compounds, the dissolved mixture of precursors is simply placed in a crystallization container and evaporation leads to the concentration of the precursors, structurally reorganizing them until they form (or not) the desired MOF.

- Precipitation or recrystallization from a mixture of solvents, this technique is rarely used since, as stated before, once the MOF (insoluble species) is formed, it is difficult to destroy the pre-formed architecture to give rise to a new one. The direct mixing of the precursors gives rise to the production of polycrystalline powder, irregular or amorphous structures or secondary products.

- Cooling at controlled temperature. In the solvent evaporation technique we play with the boiling point of the solvent, here we play with the solidification point. So, it is important to make sure that products that are not target products are not going to be formed.

- Solvothermal methods, which imply the use of solvent above its normal boiling point in a hermetically sealed chemical reactor and depends on different reaction variables (temperature, time, concentration and solubility of the precursor in the solvent, etc). The method results in high product yields and crystallinity. The framework's self-assembly is influenced by the characteristics (geometry and connectivity) of organic ligand, the coordination nature of the metal , the polarity and boiling

point of the solvent, the pH of the solution, and by the presence or not of modulators and other organic ligands.[66]
More recently, solvothermal techniques[67] have become increasingly popular, both as a method of obtaining good single crystals and as a means of obtaining phases that are unavailable through bench-top techniques.

1.3.2. Powder MOF

The preparation methods for MOFs in the form of polycristalline powders (Figure 1.14) can be divided into two groups: traditional, usually referring to classical precipitation, and non-traditional, including microwave and ultrasound-assisted syntheses, mechanochemical and microemulsion methods.[68, 69]
Conventional precipitation from the solution occurs at room temperature or upon heating from the mixture of metallic precursors and organic linkers in an adequate solvent at pH and saturation concentrations adequate for MOF precipitation.[70] The most desired way to prepare MOFs is at ambient pressure and temperature, because allows rapid MOF isolation and avoids energy consumption. But, it sometimes results in poor crystallinity and reproducibility. In this PhD thesis, it would be the method followed to obtain the MOFs in the form of polycrystalline powders.
Solvothermal methods, besides being widely used to obtain single crystals, can be used to obtain the same materials in the form of polycrystalline powders.[71] The organic molecules present in the synthesis (solvents, pH controllers like amines, templates and/or modulators) can play different roles in the MOF structure formation: as a solvent or deprotonation agent, as a template, and as a coordinating ligand to the metal ion, and their concentration influence the formation of polycrys-

talline powders. Crystallinity, crystal size or even the type of structure obtained can be also influenced by changing the synthetic conditions, i.e. time of reaction, temperature and pressure. Usually, synthesis time of solvothermal traditional methods are quite long, and require high-energy consumption and this can be considered a disadvantage from an industrial application point-of-view. Prolonged highly energy-consume in processes and equipment (pressure-sealed vessels) involves higher expense.

Non-traditional methods, are not so developed for MOFs synthesis as traditional precipitation ones. However, an increasing amount of work have been developed in the last years.[72] In this context, microwave- and ultrasound-assisted processes, despite being different in nature, both methods provide ways to accelerate MOF's formation rate in comparison to traditional methods. Microwave (MW) heating offers a reduction of the synthesis time by increasing the efficiency of heating.[73] This is as consequence to provide energy to overcome the activation energy barrier for the framework assembling and, also, influence the metastability of the system and its reactivity in a way that, the less stable the system, the higher the reactivity of the components and the faster the rate of MOF formation. The choice of solvent is an important variable to be controlled because it should absorb the microwave radiation and convert it to heat, unless a metastable point of the system can be achieved at near ambient temperature. So, this method, suppose a simple and energy-efficient strategy to obtain polycrystalline MOFs, owing to their ease to control, reduced crystallization times and increased yield respect traditional methods. Interestingly, this method promotes nanocrystals formation, through rapid and uniform nucleation, which is a consequence of the formation of local hot-spots and a fast heat transfer within the reaction media. In turn, the ultrasound process (or sonoche-

mical synthesis) increases the area of contact between the reactants and, therefore, increases the rate of nucleation and crystal formation.[74] In addition, through the release of air bubbles, formed by the decrease of the pressure in the liquid under condition of acoustic wave propagation, disintegrates the particle agglomerates and results in a homogeneous particle size produced in short reaction times. So, crystal growth followed a simple solid-on-solid model at high reactant concentrations and relatively low energy levels.

Dealing with the mechanochemical method,[75] the synthesis is solvent-free and consists of a solid-solid reaction initiated by mechanical energy, usually ball milling. This method presents the advantage that does not need the application of pressure or temperature. Conversely, the weak point is that sometimes a second phase can be obtained making difficult the isolation of the products. Relevantly, in this method, it has been observed that the presence of a small proportion of liquid components (not a solvent) could offer some benefits, such as an easier crystallization and higher yield of the desired product, due to the improved mobility of the species and their homogenization. Usually, this method has been applied to MOFs whose synthesis is normally made under mild conditions, and cosnequently excludes interesting systems based on Fe, Cr, Al or Ti.

Microemulsion synthesis is based on the thermodynamically stable dispersions of immiscible liquids (water and oil phases) and the presence of emulsifiers or surfactants.[76] The emulsifier is a molecule presenting both polar and non-polar parts. In very diluted water or oil solutions, the emulsifier exists as a monomer, but when its concentration exceeds a certain concentration, called critical micelle concentration (CMC), the emulsifier molecules associate to form aggregates, that is, micelles. These micelles are considered nanoreactors wherein MOF formation

reaction takes place. Thus, the size and the morphology of the resulting MOF particles are greatly influenced by the water/oil phase ratio and the surfactant concentration.

Other synthetic strategies are also available and may offer different advantages depending on the targeted MOF. Such as electrochemical method, in which metal ions are homogeneously supplied by the dissolution of an anode. This is reported as a very clean and fast method, but it is generally applied to Cu-based MOFs, like HKUST.[77] Another one is the continuous flow production method, that should be noted as the first one applied for large-scale industrial preparation, which is based on the induced crystallization from a stream of dissolved precursors in organic solvents.[78]

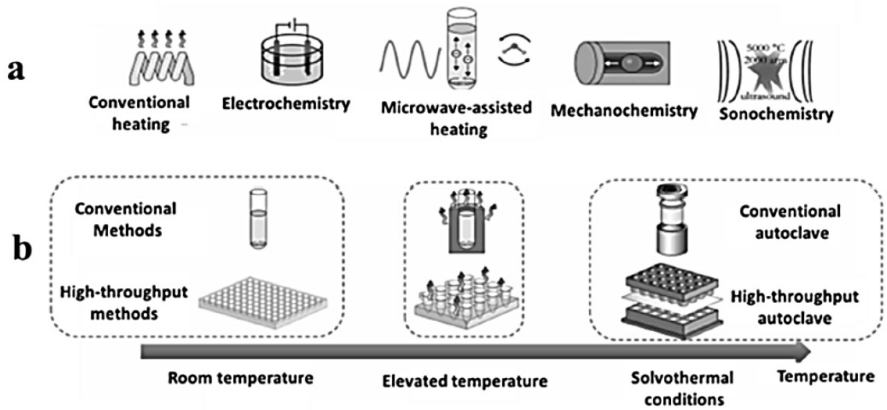

Figure 1.14. Illustration of various reported MOF fabrication methods; conventional hydrothermal and microwave-assisted hydrothermal approaches are the most commonly applied approaches, while electrochemical, mechanochemistry, and ultrasound-assisted methods are quite new techniques in the synthesis of MOFs (a). A wide range of temperatures from room conditions to solvothermal conditions are applied in the fabrication of MOFs (b).[68]

1.3.3. Industrial MOF

The surface chemistry of MOFs can be modulated by in situ or post-synthesis methods, and thus, adapted to different applications. In the last two decades, MOFs have been the most actively studied family of porous materials and great advances in their preparation, modification and stability have been achieved, especially at lab scale. However, MOFs have not been widely applied at industrial scale, and it is somehow consequence of not fulfilling different aspects, such as long stability in relevant environments and moderate production cost. Thus, at industrial scale, zeolites remain unbeatable as heterogeneous catalysts, adsorbents and ion exchangers. Nevertheless, prominent examples exist of MOF materials currently applied in industrial applications, where other porous materials have failed or they do not perform efficently, such as the storage and secure-handling of toxic gases for the electronic industry.[79, 80] The fact that these promising porous materials are still not industrially enough employed may lie in the traditional thinking of applied chemists, which is always biased towards applications where zeolites already have commercial success. In Figure 1.15, it can be seen as until a few years ago zeolites have a higher number of publications per year than MOFs. However, in the last years this situation has changed, as consequence of the exponential growth of MOFs, and most likely this would be translated to the realm of industrial applications in the next decades.

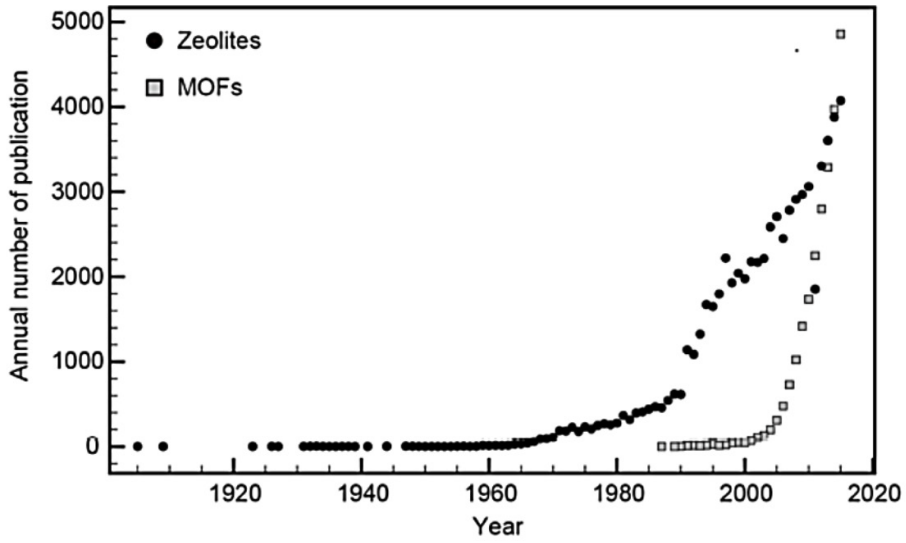

Figure 1.15. Number of publications on zeolites (black circles) and MOFs (squares) in given year.[81]

MOFs have high importance, especially in academia, and the large number of patents reporting these materials (about 1600, retrieved from the Espacenet database) evidence it, particularly for heterogeneous catalysis and gas adsorption applications. But, only a handful of these works consider typical industrial scale-up concepts, despite the fact that several academic reports show the potential application of these materials in a relevant industrial environment. This is attributed to the great difficulty to translate the small laboratory-scale conditions into a large industrial-scale setup. In addition, academia research is more directed toward the details of synthetic route and discovery of novel materials, rather than focus on the synthesis optimization of reported materials. Consequently, patents registered by academic researchers typically report a considerable number and variety of different synthetic methodologies to obtain the same compound. As an example, shown in Table 1.2. the synthetic procedure patented by Hwang et al. describes only

the different approaches used in the hydrothermal synthesis of Fe-BTC (commercial name basolite F300),), with changes in both reaction time and temperature, where the obtained quantities are maintained in the range of milligrams. Despite the fact that some of these academic patents also take into consideration the possible scale-up procedures, in a majority of cases, the simple experimental conditions are patented (with hydrothermal synthesis being the preferred method). In contrast, industrial patents are more interested in the synthetic approach that allows the preparation of a given material with the highest quantity and purity, as well as lowest costs and overall production time. Thus, it is quite common to see industrial patents on the employed synthetic technique used to produce a specific MOF in large quantities.

Table 1.2. A patented general reported method to prepare MOFs, such as basolite F300.[82, 83]

Metal source	Ligand	Reaction conditions	Extraction conditions	MOF	Patent no. Common name References
$Fe(NO_3)_3 \cdot 6H_2O$	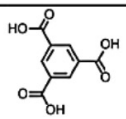 H_3BTC	H_2O/120°C/8 h/1 bar or H_2O/100°C/8 h/1 bar or H_2O/160°C/12 h	Solid washed with distilled water and dried	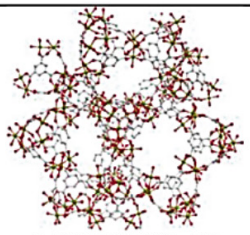 $[Fe_3O(H_2O)_2OH(BTC)_3]_2 \cdot nH_2O$ $0 < n < 50$	US008507399B2 **Basolite F300** [4]
		H_2O/ HF/120°C/12 h/1 bar		$[Fe_3O(H_2O)_2F_{0.85}(OH)_{0.15}(BTC)_3]_2 \cdot nH_2O$ $0 < n < 50$	
$FeCl_3 \cdot 6H_2O$		H_2O/120°C/8 h/1 bar		$[Fe_3O(H_2O)_2Cl_{0.80}(OH)_{0.20}(BTC)_3]_2 \cdot nH_2O$ $0 < n < 50$	
$FeCl_3$		H_2O/160°C/8 h		$[Fe_3O(H_2O)_2Cl(BTC)_3]_2$	

One limitation for the scale-up manufacturing of MOFs concerns the fact that these materials typically nucleate at the surface of the reactor or at the liquid-gas interface (evaporation is the driven force for nucleation, rather than temperature), which ultimately imposes a new variable in the synthesis procedure: the size and shape of the reactor. The increase in the concentration of the starting reagents is also enough to form different materials or mixtures of phases. This also occured at the laboratory scale: as an example, the reaction of 1,4- phenylene-bis(methylene)diphosphonic acid (H4pmd) with La^{3+} ions at 40 °C under simple one-pot conditions originates the 3D network [$La_2(H_2pmd)(pmd)(H_2O)_2$], whereas, if the concentration of both starting materials is doubled, the 1D- assembly [$La_2(H_2pmd)_3(H2O)_{12}$] is obtained instead.[84]

It is important to take into account all the parameters that influence the reaction, regardless of their degree of complexity and involvement, when developing a large-scale production line as part of academic research, since even slight varations (sometimes no visible to the researcher) can be intensified and can lead to unforreseen economic or hazardous events. Though mixing two reagents at the milligram scale could be a slightly exothermic reaction, generating a certain amount of heat that can easily be dissipated within the experimental laboratory environment (e.g. ambient temperature), the same reaction in large quantities could cause an immediate explosion. The high cost of the precursors is also a detrimental aspect for the industry.[85]

In many cases, the large-scale production of very interesting MOFs is economically unfeasible because of the elevated costs of the starting reagents, despite their outstanding application performances.

Large-scale production of a given MOF should achieve the following

prerequisites:

- Low cost and rapid availability of the starting materials.

- Rapid and simple synthetic procedures at low temperature and ambient pressure conditions.

- High yields of the targeted MOF and no formation of secondary products, such as salts, which will increase the production cost due to the necessity for posterior treatment and removal.

- High purity and quality of the product.

- Sustainable procedures, use of small quantities of solvents and reduced production of waste.

Metal sources, such as metal oxides, nitrates, sulfates, and chlorides, are considerably cheap and readily available for purchase from commercial suppliers. However, certain anions should be avoided due to their high-risk and post-production problems.

The organic linker chosen follows the same trend. Simple molecules such as terephthalic, formic, or isophthalic acid are always preferred when compared to more complex ones. However, the versatility of organic synthetic methods, enabled they are not completely discarded.

The employed solvents have a crucial role in large production, mainly because high quantities usually imply a high cost in filtration and separation. Ideally, solvent-free synthesis should be used, where the organic

linker may act both as reagent and solvent, but it is not common. So, synthetic procedures should be optimized to use the minimum amount of solvents and try to be cheap and environmentally friendly, such as water (if the desired material is stable on it).

The final step after filtration, in a typical synthetic procedure, is the drying process that must be performed carefully. So, mild conditions should be used while drying to prevent structural collapse and amorphization of MOFs. Most drying processes involve conventional oven heating, as well as rotator evaporators and/ or using the spray-dry technique.[86]

Figure 1.16 shows a Scheme that summarizes the most important steps and bottlenecks that one could be faced with when trying to transpose the synthesis from the laboratory to the industrial scale.

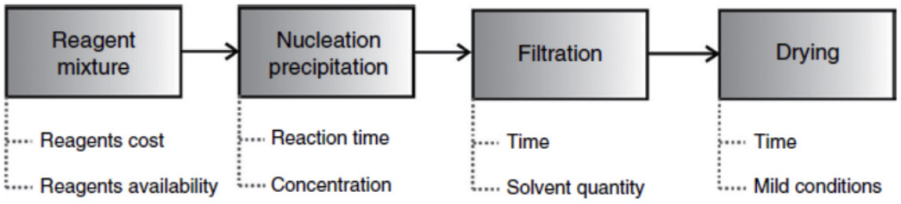

Figure 1.16. Schematic representation of the industrial-scale synthesis of MOFs with emphasis on the important parameters to have in consideration.[87]

The very first scale-up methodologies of MOFs relied mostly upon the use of the same conventional experimental conditions widespread in the academic environment. Solvothermal and one-pot reactions were

preferably selected because of simple equipment requirements. However, several limitations were found when using large reaction vessels and high concentrations of the starting chemicals. This motivated the development, or even improvement, of new techniques for the scale-up production of MOFs. Among them, in the following lines we will describe the most important ones used in industry.

Dealing with electrochemical synthesis, HKUST-1 was the first scaled-up MOF in 2005[88]. This methodology was first reported by the BASF company as an alternative to the conventional synthesis of MOFs on an industrial scale. For their electrochemical preparation copper plates were used as anodes immersed in a solution of methanol with the organic linker 1,3,5-benzenetricarboxylic acid. During 2.5 h, a voltage ranging between 12 and 19 V, and an amperage of 1.3 A, are applied, while a greenish-blue precipitate is simultaneously formed. After BASF success, this method was also used to prepare other MOFs such as ZIF-8, MIL-100, MIL-53,[89] and UiO-66. [90] The electrochemical synthesis was then introduced as a salt-free procedure, where the metal source is the sacrificial metal anode. The reaction allows precise control in the deprotonation of the organic linker in the correct stoichiometry for the MOF preparation. In addition, according to the inventors, the electrochemical synthesis has lower reaction times than conventional synthesis, with no need for separation of anions (such as Cl− and NO3−) at the end of the reaction.

MOFs industrial scale-up has also limitations in terms of the reaction vessel size and shape, as well as on the optimization of synthetic parameters. To overcome these difficulties, a new technique in MOFs field, but used for oxide nanoparticles and organic molecules, coined con-

tinuous flow, was introduced.[91,92] In this methodology, the laboratory conditions are reproduced by means of simultaneously pumping and posteriorly mixing the precursor solutions into a mixer. This is performed in such a way that produces a uniform mixing of reagents and high heat transfer in tubular reactors, independent of the reaction volume. Furthermore, this process is robust enough to be employed in conventional solvothermal synthesis and in microwave-assisted preparations.

HKUST-1 also was one of the first scale-up MOFs using continuous flow by Gimeno-Fabra *et al*..[93] To this end, they used a continuous reactor having a high throughput and very fast reaction process. The synthesis, typically performed at 150 °C, was successfully conducted using a downflow of water at 300 °C, which promoted rapid crystallization. Therefore, this methodology presented a possible scalable process to produce this material, as well as a promising way to fine-tune the crystal morphology itself. Indeed, the process led to nanocrystalline powders with BET and surface areas that exceeded the commercial sample. Later on, the method was further used to scale-up HKUST-1, allowing the preparation of 61.2 g of MOF in just 1 h, approximately 20 times better than that of the commercial analog Basolite C300. In another study, Rubio-Martinez *et al*.[94] studied the synthesis of HKUST-1 ($[Cu_3(BTC)_2 \cdot (H2O)_3]n$, BTC = benzene 1,3,5-tricarboxylate), UiO-66 ($[Zr_6O_4(BDC)_2]$, BDC= benzenedicarboylate), and NOTT-400 ($[Sc_2O_2(BBC)] \cdot 1.25H_2O$, H_4BBC = biphenyl-3,3′,5,5′-tetracarboxylic acid) using the continuous flow method. McKinstry *et al.*[95] also investigated several parameters concerning the synthesis of HKUST-1 in a continuous flow process, and they confirmed that optimized continuous solvothermal processes are viable and can also produce the MOF in high yields, quality, and purity and with the intended surface area.

Mechanochemical synthesis have been proposed as a viable alternative

for industrial scale-up of MOFs. Some examples of compounds obtained using this technique include HKUST-1 and ZIF-8, prepared as highly pure, crystalline, porous solids. However, more work is needed to overcome some of the difficulties mechanochemical approaches faced, such as low rates of production, equipment often undergoing shutdown times, and difficulties in retrieving the product when the physical nature is not a free-flowing powder.

Related to mechanochemical processes is extrusion, a well-developed continuous technique that play a vital role in the manufacturing of food, polymer, and pharmaceutical industries.
Extrusion consists of the forcing of materials through constrained spaces with intensive mixing occurring at the same time. Using this technique, James and coworkers prepared HKUST-1, ZIF-8, and Al(fumarate)(OH) through twin-screw extrusion (TSE), and reached multi-kilogram per hour quantities, with little or no solvent being required. Furthermore, the materials obtained were highly crystalline and with high surface areas. When comparing them with the same compounds prepared by other techniques, researchers showed similar BET surface areas, as well as pore sizes in agreement with those published. Being, the TSE overall efficiency three times better than solvothermal synthesis.

1.4. MOFs properties

1.4.1. Tailored Porosity

The possibility to use X-ray crystallography to unveil with atomic precision the structure of MOFs,[96-98] provide researchers with a key

tool to characterise the main features of MOFs voids. However, this on its own, does not give a real vision of the permanent porosity of a MOF, when solvent molecules were removed. Thus, gas adsorption isotherm on samples where the solvent has been removed is the technique applied routinary to study the permanent porosity of MOFs. This technique allows to gain knowledge on how the adsorption take places and which is the maximum adsorbed amount. On this basis, IUPAC[99] have established a classification with six main different types of isotherms (Figure 1.17).

Reversible Type I isotherms are observed in microporous solids having relatively small external surfaces (e.g. some activated carbons, molecular sieve zeolites, and certain porous oxides), where their limiting uptake is governed by the accessible micropore volume rather than by the internal surface area. The characteristic steep uptake at very low p/p0 is due to enhanced adsorbent-adsorbate interactions in narrow micropores (micropores of molecular dimensions), resulting in micropore filling at very low p/p0. This type of isotherm is the most frequent one for microporous MOFs.

Reversible Type II isotherms are given by the physisorption of most gases on non-porous or macroporous adsorbents. The shape is the result of unrestricted monolayer-multilayer adsorption up to high p/p0. If the knee is sharp, the beginning of the middle almost linear section, usually corresponds to the formation of a monolayer coverage.[100] A more gradual curvature is an indication of a significant amount of overlap between monolayer coverage and the onset of multilayer adsorption. So, in the Type-II isotherms of combined micro/mesoporous adsorbents, the forces involved are the combination of adsorbent–adsorbate and ad-

sorbate–adsorbate interactions.

In the case of a Type III isotherm, there is no knee and therefore no identifiable monolayer formation. In this case, the adsorbent-adsorbate interactions are relatively weak, and the adsorbed molecules are clustered around the most favorable sites on the surface of a non-porous or macroporous solid.

Type IV isotherms are given by mesoporous adsorbents (e.g. many oxide gels, industrial adsorbents and mesoporous molecular sieves). The adsorption behaviour in mesopores is determined by the adsorbent-adsorbate interactions, as well as by the interactions between the molecules in the condensed state. In this case, the initial monolayer-multilayer adsorption on the mesopore walls, which takes the same path as the corresponding part of a Type II isotherm, is followed by pore condensation. A typical feature of Type IV isotherms is a final saturation plateau, of variable length (sometimes reduced to a mere inflexion point). Capillary condensation can be accompanied by hysteresis (the pore width exceeds a certain critical width) or not (with adsorbents having mesopores of smaller width or conical and cylindrical mesopores that are closed at the tapered end). Mesoporous MOFs are characterised by the presence of this type of isotherm.[101]

In the low p/p0 range, the Type V isotherm shape is very similar to that of Type III, and this can be attributed to dominating adsorbate–adsorbate interactions and barely observed purely adsorbent–adsorbate interactions. At higher p/p0, molecular clustering is followed by pore filling. For instance, Type V isotherms are observed for water adsorption on hydrophobic microporous and mesoporous adsorbents.

The reversible stepwise Type VI isotherm present several steps in the adsorption isotherm due to the representative layer-by-layer adsorption on a highly uniform nonporous surface. The step height represents the capacity for each adsorbed layer, while the sharpness of the step is dependent on the system and the temperature. Amongst the best examples of Type VI isotherms are those obtained with argon or krypton at low temperatures on graphitised carbon blacks.

Besides the previous types of isotherms, some MOFs have characterised for exhibiting flexible frameworks with very particular and distinguish isotherms. As consequence of their relevance for gas adsorption and separation, such MOFs have been intensively studied. Despite each flexible MOF is a completely different scenario, the information extracted from these studies enriched greatly the field of soft porous materials and served to develop new avenues of research in MOFs.[102] For example, such materials is MIL-53. The porosity and unit cell volume of these structures change considerably upon guest insertion/removal and also strongly depend on the molecule type – for example structures show very different adsorption isotherms for H_2, N_2, CH_4, CO_2, H_2O or other hyd ved in rigid porous solid

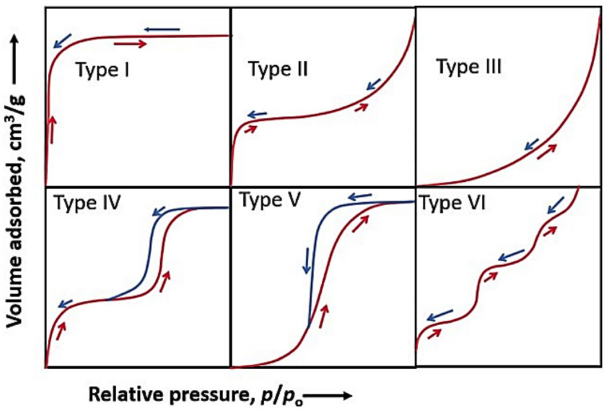

Figure 1 .17. Representation of the different types of IUPAC adsorption isotherms.[104]

The porosity of MOFs was first studied in 1997, based on studies of crystalline zeolites and molecular sieves, when Kondo, Kitawaga and co-workers carried out gas sorption experiments (CH_4, N_2 and O_2) on metal-organic frameworks of formula $\{[M_2(4,4'\text{-bpy})_3(NO_3)_4](H_2O)x\}n$ (M=Co, Ni or Zn). These experiments showed that these MOFs maintained their pore structure, upon guest removal, but the surface area and pore volume could not be determined, since the experiments were carried out at high pressures (1-36 atm).[105]

One year later, Yaghi´s group reported the full characterization of microporosity of Zn(BDC)(DMF)(H_2O) (MOF-2, BDC^{2-}=1,4-benzenedicarboxylate)[32], Figure 1.18, through the determination of the surface area and pore size/volume measuring N_2 and CO_2 adsorption isotherms under low pressure. This was the first proof of the permanent porosity of MOFs.[106]

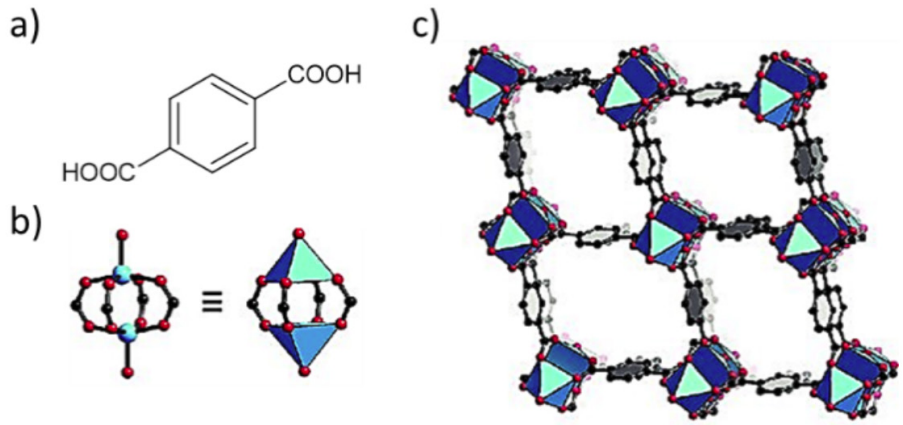

Figure 1.18. Representation of a) 1,4-benzenedicarboxylate formula (BDC), b) $Zn_2(COO)_4(H_20)_2$ SBU and c) Zn(BDC)(DMF)(H_2O), MOF-2. Adapted from ref. 32.

Thereafter, Kitagawa and Kondo (1998) proposed a classification of porous coordination compounds as a function of their porous properties (Figure 1.19):[107,108]

- 1st generation MOFs exhibited a loss of porosity upon solvent removal. This has often been observed in MOFs containing charged frameworks with pores filled by counter anions.

-2nd generation MOFs possess stable and robust porosity and maintain crystallinity against guest removal, typical of neutral and zeolite-like MOFs.

- 3rd generation MOFs display framework flexibility and dynamics, which can respond to guest exchange or chemical/physical external stimuli (pressure, light, electric field, guest molecule, among others) changing their channels or pores reversibly.

- 4th generation MOFs are correlated to the recently developed post-synthetic modifications (PSM) of MOFs, which can maintain underlying topology and structural integrity towards various post-modifications.[109-111] Later Prof. S. Kitagawa[111] proposed that fourth-generation MOFs also include MOFs presenting, anisotropy, hierarchy and defects, including solid solutions and multivariate (MTV) MOFs.[113]

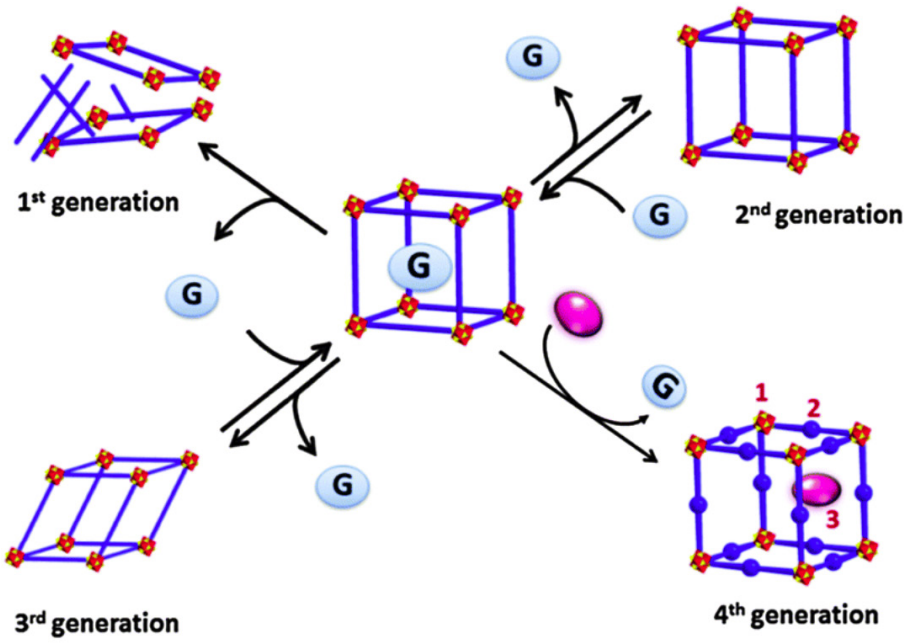

Figure 1.19. Classification of MOFs: 1st generation MOFs collapse on guest removal, 2nd generation MOFs have permanent porosity against guest removal, 3rd generation MOFs show flexible and dynamic properties, and 4th generation MOFs can sustain post-processing (modifiable positions: (1)metal/cluster sites, (2) organic linkers, and (3) vacant space).[114]

In Figure 1.20 are presented the different possibilities that the 4th generation present, such as: the post-synthetic modification (Figure 1.20a), the containment of defects (Figure 1.20b), the non-stoichiometry (solid solution) (Figure 1.20c), the rearrangement capacity of out-of-frame counter ions (Figure 1.20d) and the reorientation capacity of flexible ligand substituents (Figure 1.20e). These last two belong to 4th generation materials that combine a rigid structure with self-changing pores, which can adapt to a particular host through extrastructural counterions that can move freely within the pore space (Figure 1.20d) or flexible ligand

substituents (Figure 1.20e).

In this way 4th generation "hard-soft" materials could combine the advantages of 2nd and 3rd generation MOFs: (a) retention of topology and structural integrity during gas or vapor adsorption, (b) smooth pore surfaces that respond to external stimuli, leading to diverse sorption profiles, and (c) the self-adaptive ability of pore size and pore chemistry to adapt to different host species.

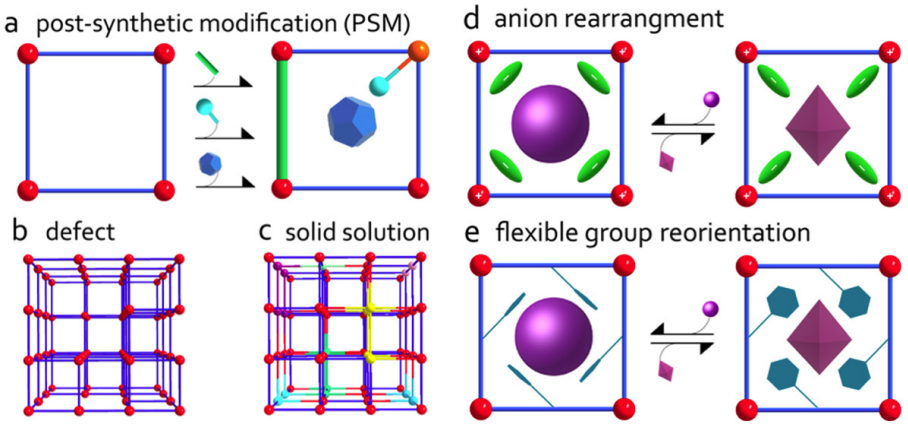

Figure 1.20. Fourth-generation porous materials are modifiable using (a) postsynthetic approaches that chemically modify their pore structure, or they are complex systems that (b) contain defects or (c) are nonstoichiometric (solid solution). A different type of fourth-generation porous materials exhibits rigid frameworks with self-switching pores that adapt to a particular guest through (d) rearrangement of extraframework counterions or (e) reorientation of flexible ligand substituents.[115]

An important highlight for the study of the porosity in MOFs was when MOF-5 (Figure 1.9C), was reported in 1999. Its success was justified because, in their day, it was a structure with higher surface area and pore volume than most porous crystalline zeolites, together with an easy and versatile preparation. It was the first MOF based on linking octahedral zinc acetate building units, $Zn4O(-COO)_6$, with six chelating

1,4-benzenedicerboxylate (BDC^{2-}) units to give a cubic framework. Later, in 2002, it was reported that MOF-5 has a modular structure, and 16 isoreticular frameworks (IRMOF-1 to IRMOF-16) were synthesized by changing the length and functionality of the linkers, and thus, the concomitant void space (Figure 1.21). This work was used to demonstrate that pore size and functionality could be varied systematically, providing a large number of topologically identical architectures.

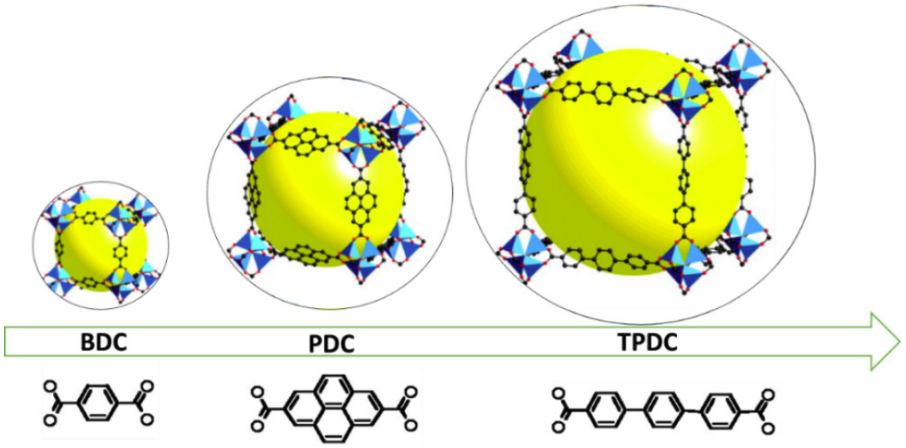

Figure 1.21. Single crystal X-ray structure of MOF-5 and IRMOF-n (n = 14 and 16). The large spheres represent the largest Van der Waals spheres that would fit in the cavities without touching the frameworks.[116]

Besides the type of isotherm and the response of MOFs to the removal of guests, the size of the pores has been also used to define and classified MOFs. Thus, it has been established the following types: macropores (>500 Å), mesopores (20-500 Å), micropores (5-20 Å) and ultramicropores (<5 Å).

As has been shown, the adsorption of the guest molecules in the solid surfaces permits determining the properties of porous compounds.

However, it also allows the study of the confined molecules.[117] For example, it has been observed that these molecules or atoms can have interesting properties, which are not observed or are different in bulk state, just by being confined in nano-spaces.[118] For this purpose, the understanding of the interaction between guest molecules and surfaces is crucial, as well as the control of pore size and shape.

1.4.2. Benefits and limitations of using MOFs

MOFs differ from other porous materials, such as zeolites, activated carbon or alumina, in their intrastructural interaction, which is through coordination bonds. This makes them possess lower robustness and physical-chemical resistance than architectures formed by covalent or ionic bonds. However, there are extensive advantages that metal-organic compounds can offer.

In terms of preparation, MOFs are simpler than other porous materials. MOFs do not usually require organic or inorganic templating agents nor hydrothermal conditions in an alkali-rich alumina silicate hydrogel system, where water acts as a reagent and reaction medium, such as in zeolites. This makes zeolites crystallize driven by supersaturation and spontaneous nucleation, which is not strictly controllable under laboratory conditions. However, it should also be noted that MOFs can be built up by a great variety of metal ions/SBUs and organic linkers. Thus, there are almost unlimited possibilities, which made possible through a controlled design to obtain MOFs with different compositions, topologies sizes, and chemical environments for the pores. In addition, MOFs possess an easier structural modification by guest exchange or chemical reaction without loss of overall crystallinity, as well as a richer host-guest chemistry, a more flexible nature and metals accessibility than

crystalline inorganic materials. Finally, the highly crystalline nature of MOFs allows it to use single-crystal x-ray diffraction (SC-XRD) as the definitive characterization tool. Besides, MOFs permits a precise structural determination by classical experimental methods such as powder X-ray diffraction (PXRD), transmission and scanning electron microscopy (TEM and SEM) and spectroscopic techniques such as nuclear magnetic resonance (NMR), ultraviolet-visible (UV-Vis) and Raman.

The structural stability and robustness of MOFs toward high temperature, pressure, moisture and harsh chemical environments have been their weakest feature in comparison to other porous materials. MOFs stability is governed by multiple factors, such as pKa of ligands, oxidation state, reduction potential and ionic radius of the metal ions, metal-ligand coordination geometry, and hydrophobicity of the structure. In a MOF structure, the chemical weak spot is usually the metal-linker bond. However, different synthetic approaches have been developed allowing to improve the robustness of MOFs in a diverse type of solvents and a wide range of pH. Dealing with MOFs thermal stability, due to the degradation of the organic part at temperatures between 300-400 °C (rarely more than 500 °C), MOFs show a lower one than zeolites and activated carbons. Nevertheless, and despite of the general perception of low robustness of MOFs, specially related to the first generation of MOFs, there are different families of highly robust MOFs.

They have been obtained following the concept of Lewis acids and bases[119], which are classified into soft and hard species, depending on their size, polarizability, electronegativity, ionization potentials and orbital energy. The principle states that hard acids prefer to bond with hard bases and soft bases with soft acids (Figure 1.22).[120] Such preference may

provide additional stability in terms of bond dissociation energy between hard-hard or soft-soft pairs and destabilization between mismatched pairs. The additional energy that this preference implies indicates the presence of other factors such as the solvation effect or the intrinsic strength of acids and bases.[120-123]

The hard acid consists of an electron-withdrawing atom with low polarizability, small atomic and ionic radius, and high oxidation state. Its lowest unoccupied molecular orbital (LUMO) is highly energetic and lacks easily excitable outer electrons associated with ionic bond affinity. While the hard base consists of an electron donor atom of low polarizability, high electronegativity and difficult to oxidize, with high affinity for the formation of ionic bonds, associated with high energy empty lower orbitals.

In contrast, the soft acid complements the hard acid, that is, it is an electron-withdrawing atom of large ionic/atomic radius, low or no oxidation state with readily available excited external electrons with high affinity for bond formation. covalent.

Lastly, the soft base which is an electron donor atom with a large ionic/atomic radius, low electronegativity and high polarizability. Easily oxidizable together with empty lower orbitals.

We also want to define an intermediate concept: borderline hard-soft acid-base, are those species with characters between hard and soft acid-base.

Once these concepts are internalized, chemical reactivities can be des-

cribed as the adjustment of the valence electrons between the reactive orbitals in terms of the highest occupied molecular orbital HOMO and LUMO according to the orbital frontier theory (FOT) (proposed by Fukui[124]). Thus, the soft-soft reaction is expected to be dominated by the covalent bond character, while the ionic bond character predominates in the hard-hard interaction.[125] However, the soft-soft interaction will consist of the interaction between the two soft species through boundary orbitals, since the nuclear charge is shielded by the electrons in the nucleus. However, in the case of hard-hard interaction, electrons from the nucleus do not leak out. The soft-soft interaction follows the " through the bond" interaction (orbital-controlled boundary), while the hard-hard interaction follows the " through space " interaction (controlled charge).[126]

As noted above, the wide energy gap between HOMO-LUMO endows the molecule with high stability, less reactivity and less polarizability, while a small gap (produce between a hard and a soft species) makes them less stable, more reactive and highly polarizable.[127,128]

For example, high valent cations, such as Zr^{4+}, Ti^{4+}, Cr^{3+}, Fe^{3+} or Al^{3+} are regarded as hard acids, that can form stable MOFs having strong M−L bonds with hard Lewis bases such as carboxylate (e.g. terephthalic acid or BDC; trimesic acid or BTC) or phosphonates such as (S or R) 3,3'-di-tert-butyl-5,5'-dicaboxyphenyl-6,6-dimethylbiphenyl-2,2'-dihydrogen phosphonate. [129]

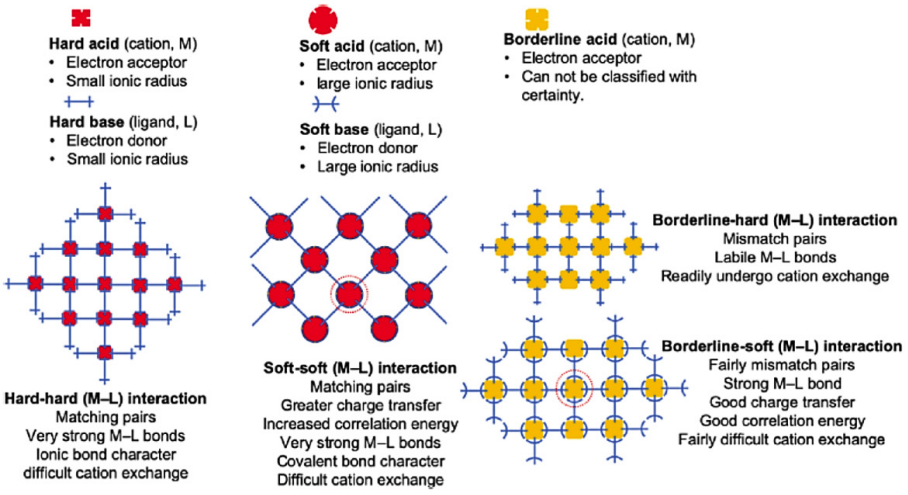

Figure 1.22. Typical interactions of hard, soft and borderline Lewis acid-base in MOF.[130]

1.5.MOFs Post-Synthetic modifications (PSMs)

Numerous factors influence the assembly of a target MOF, and thus, it is highly challenging to obtain a total control of the final MOF structure. Besides, sometimes, due to stability issues associated with synthetic conditions, it is not possible to obtain a specific MOF by direct synthesis. In this context, post-synthetic methodologies (PSMs) emerge as an outstanding tool to obtain otherwise not accessible MOFs, and to improve or even incorporate new physical and/or chemical properties respect the pristine MOF.[131]

MOF materials are particularly mesmerizing for PSM due to three fea-

tures: (i) the labile nature of the coordination bonds, which facilitate their formation/breaking, (ii) the crystalline nature, which allow to have the possibility of follow the process in a single-crystal to single crystal (SC-to-SC) manner and (iii) the porous nature, and consequently easy accessibility of guest molecules to the framework.

PSM can be carried out by modifying the ligand and/or metal node, and adsorption/exchange of guest species. Also, the surface environment of the MOF can be modified to increase structural stability, as well as to introduce desired properties. Relevantly, post-synthetic treatments, do not alter the original topology of the MOF, which offer the possibility to establish post-synthetic modifications-function relationships. Figure 1.23 shows a schematic classification of different post-synthetic methods. [132]

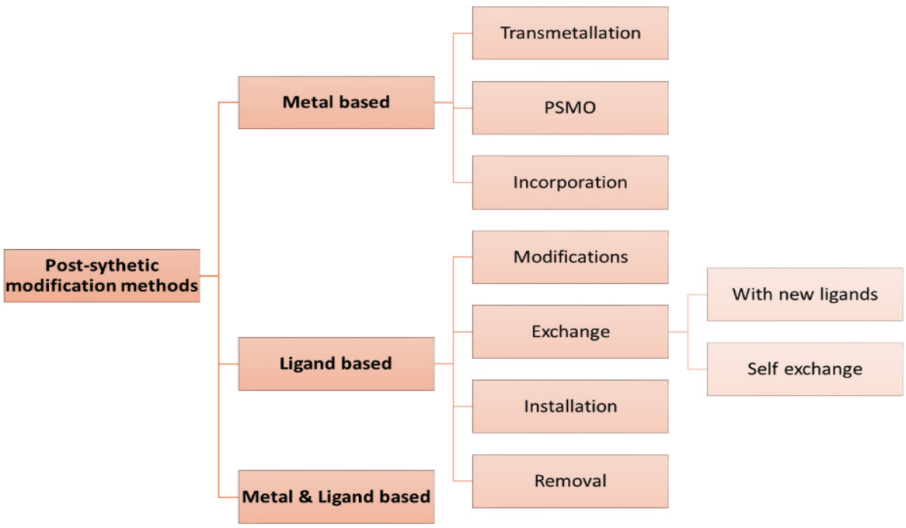

Figure 1.23. Classifications of post-synthetic methods. Adapted from ref.132.

As it can be observed in the literature numerous examples exist of the

potential of PSM. An important type of PSMs deals with the inorganic part of MOFs. Relevant metal-based PSM are metal exchange, transmetallation, incorporation and post-synthetic metathesis and oxidation (PSMO).

Metal exchange (Figure 1.24) consist on the replacement of the metal ions hosted within MOFs channels, which act as countercations. The metal exchange reactions, particularly with bivalent transition metal ions, sometimes follow the Irving–Williams series, where the order of the stability of the divalent first-row transition elements increases across the period is Mn(II) < Fe(II) < Co(II) < Ni(II) < Cu(II) > Zn(II).[133,134]

This process constitutes the most elemental form of metal-based PSMs. However, it has demonstrated as a very relevant tool to obtain MOFs with outstanding physical properties.[135-143]

Figure 1.24. Possible pathways of cation exchange in MOFs.[144]

Transmetalation (Figure 1.25) involves the replacement of the metal ions hosted in the channels acting as countercations and the ones constituting the network. Thus, it implies breaking of bonds between the organic ligands and metal ions, and the formation of new bonds with the incoming metal ions. So, it requires more energy compared to the metal

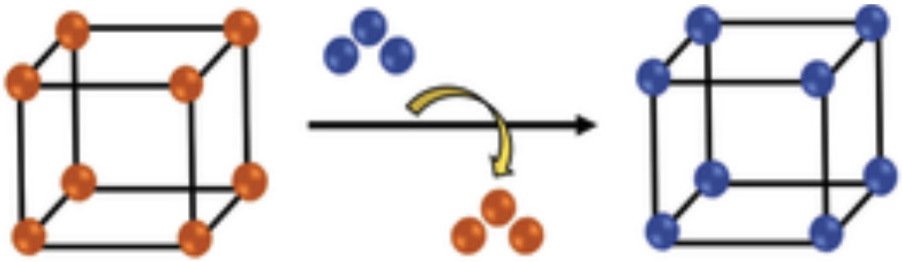

Figure 1.25. Possible pathways of transmetallation in MOFs. [144]

exchange of guest ions, involving no bond breakage and formation. As consequence, this process is not so frequent.[145]

Partial or complete metal exchange/transmetalation depends on the lability of the metal ions to be exchanged, the valence and coordination of the incoming metal ion, the solvent used, and the chemical stability of the resultant MOF. Partial metal exchange/transmetallation is produced, mainly, in systems where fast early exchange (with a quick equilibrium) is followed by saturation after some time. To move toward complete exchange/transmetallation, the solution containing the incoming metal ions needs to be refresh several times. Most likely, the stability of the MOFs depends considerably on the exchangeability of the metal ions, so, to replace a metal ion, one needs to consider the crystal field stabilization energy (CFSE) and the ionic radius of the incoming ion[146]. The smaller the size of the ion, higher will be the stability of resultant MOF. For Cu^{2+} octahedral or square-planar coordination, the Jahn–Teller effect has to be considered as well[147]. Another factor that influences these processes deals with the nature of the solvents. This was evidenced in a work of Wang and co-workers[148], where they employed various coordinating solvents (amide and ketone-based solvents) to obtain Cr(III) MOFs, which are difficult to synthesize by direct methods, by complete transmetalation of the Fe(III) MOFs. A partial metal exchange/transmetalation enable also the possibility to led to materials

with a higher degree of heterogeneity and complexity. This, in turn, open the way to obtain synergetic behaviour between metals ions, and then novel functionalities.[149]

The incorporation of an additional metal ion or metal complex into the framework (Figure 1.26) could be carried out by the direct coordination at a specific coordination site in the framework. An illustrative example is the addition of Ni(II) ions into an eight coordinated Zr_6-based MOF (PCN-700, PCN stands for porous coordination network), which resulted in the formation of Zr_6Ni_4 SBUs. Ni(II) ions coordinate to the terminal -OH− and H_2O ligands exposed to the channel followed by the carboxylate group migration to form bridges between Zr and Ni, through the oxygen atoms. The bridge formation involves the creation of new Zr–O–Ni bonds through the breaking of the original Zr–O bonds.[150] Another representative example includes the metalation of porphyrin rings.[151]

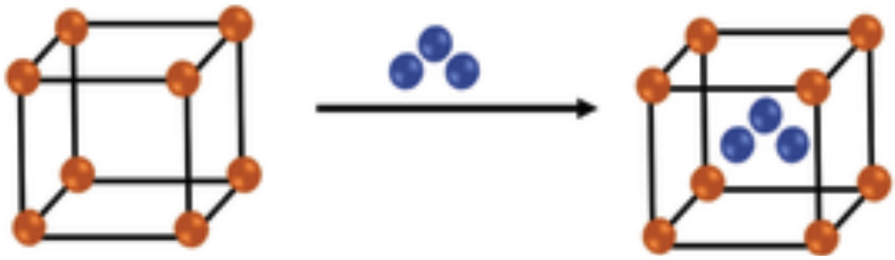

Figure 1.26. Possible pathways of metal incorporation in MOFs. [144]

Post-synthetic metathesis and oxidation (PSMO) is a little-known, but effective, pathway to obtain high-valence MOFs. This was reported for the first time with PCN-426-Mg, where Mg(II) were exchanged with Fe(II) and Cr(II) in an SCSC manner (under anhydrous and inert conditions) and then oxidized in air to produce the corresponding Fe(III)

and Cr(III) MOF single crystals.[152] This method allow to circumvent the kinetic inertness of Cr(III), and at the same time represent a soft method that avoid the partial collapse of the framework due to the acidity of chromium(III) salts.

Ligand-based post-synthetic modifications (Figure 1.27) gathered the most diverse forms of PSMs, which consist on the modification, installation, exchange, removal of ligands in the MOF and post-synthetic polymerization. These PSMs are based on the formation of new covalent bonds, usually in the organic ligand of the MOFs, although it could also occur in the secondary building units (SBUs).

They have proven to be a good option to introduce organic ligands and/or functionalities in MOFs, which have allowed to modify not only the structural dimensionality as well as its ability to bind with metal centers, but also the properties of the resulting MOFs, and consequently their application field. A special form of post-synthetic modification is post-synthetic deprotection. This is based on the formation of MOFs with organic linkers that have protected functional groups and after its synthesis, the protecting groups are removed.

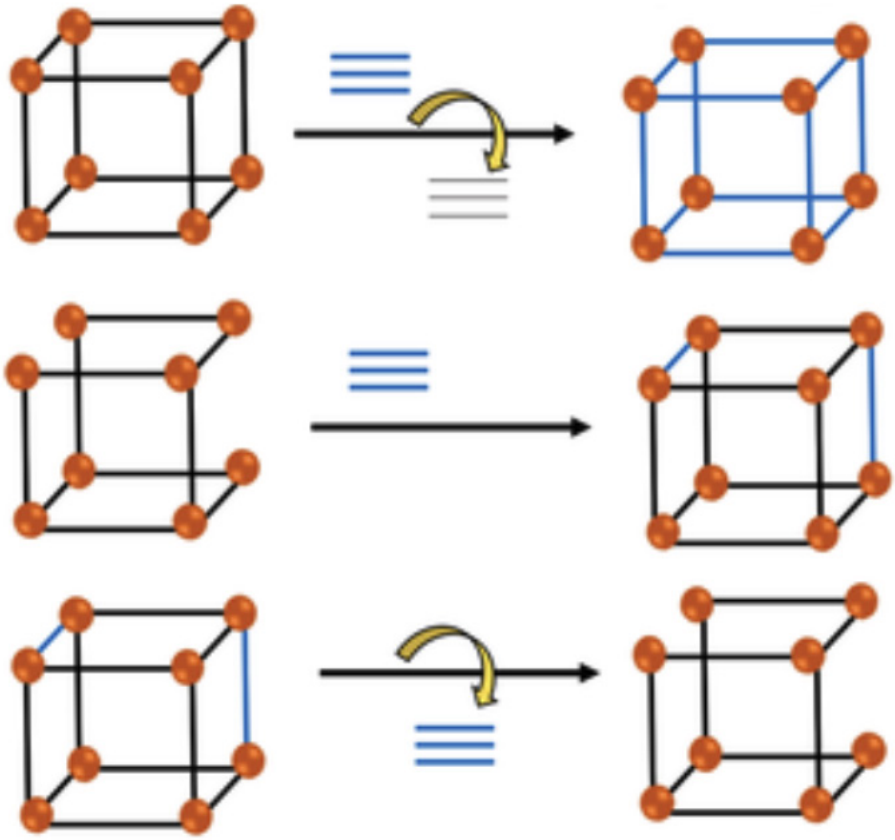

Figure 1.27. Possible pathways of ligand-based post-synthetic modifications in MOFs: ligand exchange (top), ligand installation (middle) and ligand removal (bottom). [144]

Ligand modification of MOFs accounts for the incorporation of novel functionalities in non-functionalize MOFs and the chemical transformation of existing ones. Here, special care has to be taken in the synthetic procedure applied to avoid structural collapse. For example, the new functional groups can act as adsorption sites for various target molecules. This is exemplified on the grafting of molecules into the ZIF-90, leading to a structure with a pyrimidine-thione fragment which is active toward the Hg^{2+} adsorption. [153]

Solvent-assisted linker incorporation (SALI) is a process consisting on the integration of new struts in a preformed MOF. SALI takes advantage of the defect sites and porosity of the original structure to build new features, especially for tailored applications. Several MOFs have been successfully modified using this approach by Hupp and coworkers.[154] For example, by electropolymerizing the polythiophene molecules on the walls of NU-1000, a semiconducting material was produced without compromising the superior porosity of the original MOF. In the same way, ferrocene-functionalised ligands, which act as redox shuttle species, have also been incorporated into the same scaffold and were used as a thin-film coating for the electrodes, which shows activity near the ferrocenium/ferrocene redox potential. Other groups have taken advantage of this approach for the obtention of multivariate and multicomponent MOFs.[155] This is illustrated with PCN-700, a 8-connected Zr_6 MOF with inherent missing linker sites and bcu topology, where up to three different functionalities have been incorporated by means of installing selected dicarboxylic acids. The new linkers replace the terminal OH^-/H_2O ligands of adjacent $Zr_6O_4(OH)_8(H_2O)_4$ clusters to get assimilated into the structure in an SCSC manner. Interestingly, it was observed in the resulting multicomponent MOF that the network complexity is translated in improved functionality respect the pristine MOF.

Solvent-assisted ligand exchange (SALE) is another useful strategy for obtaining MOFs with ligands that could not form frameworks *in-situ.* The rate of exchange and the factors affecting it are the object of study in this field. One of the factors is the pKa values of the incoming and outgoing ligands. Thus, it appears that the kinetic rate of exchange can be enhanced with increasing acidity of the incoming ligands. An illustrative example of this type of PSM is the N1,N3-di (pyridine-4-yl)

malonamide linker (S) which does not easily enter into the structure during the synthesis of MOFs. Ali Morsali et al. designed amide-functionalized benzene-core ligand derivatives as linkers to obtain [Co(oba)(bpta)]·(DMF)2 TMU-50 and [Co2(oba)2(bpfn)]·(DMF)2.5 TMU-51, which can catalyze the methanolysis reaction of epoxides. To increase the MOF catalytic efficiency, they designed the N1,N3-di (pyridine-4-yl) malonamide linker (S) as a malonamide ligand, which contains acidic hydrogen that is suitable for catalyzing an epoxide ring-opening reaction. But the MOF synthesis with this linker was not successful, so they designed new structures by incorporating different percentages of S linkers by exchanging the acylamide functional group with malonamide via the SALE pathway. The acylamide functional group was successfully replaced and produced daughter MOFs TMU-50S and TMU-51S eficientes to catalize the target reaction.[156]

Usually, this ligand exchange is partially, which inherently induce the formation of heterogenous and complex materials, as with SALI. Terminal ligands removal is a simple approach for creating defective frameworks in several robust MOF scaffolds, which in turn offer the possibility to tune and improve MOF properties.[157] Recently, other PSM have been applied to try to control the number of defects at MOFs, based on ligand removal/labilization.[158] This approach consists on the use of a MOF with a pro-labile ligand and a non-labile ligand, and where pro-labile ligand is subsequently cleaved into several parts to get the defective MOF. Among them, a recent example is the ozonization of mixed-ligand Zr-fcu-MOFs based on organic ligand pairs. Here Daniel Maspoch et al. obtained one ligand that has ozone-cleavable olefin bonds and the other ligand is ozone-resistant, they could selectively break the cleavable ligand via ozonolysis to trigger the fusion of micro-

pores into mesopores within the MOF framework. This solid-gas phase method was performed at room-temperature, and, depending on the cleavable ligand used, the resultant ligand-fragments could be removed from the ozonated MOF by either washing or sublimation.[159] Another one, is the reported by Zhou et al.[160] with PCN-100, a multicomponent MOF constructed with the ligand AZDC (azobenzene-4,4′-dicarboxylate) and the pro-labile linker CBAB (4-carboxybenzylidene-4-aminobenzate), which has similar length and connectivity that AZDC. In this study it is reported that once the MOF is assembled with both ligands, CBAB was severed into 4-amino benzoic acid and 4-formylbenzoic acid by acid hydrolysis, removed from the framework by washing, while the MOF network retain the structural integrity.

Post-synthetic polymerization (PSP) at MOFs, focused on MOFs transformations into polymer materials or into polymer-MOF composites. This modification could be carried out, for example, by means of multiple organic reactions to connect the ligands buildings the MOFs within each other or by the growth of a polymer on the surface or within the channels of a MOF. Recent work has demonstrated that polymers can enhance MOF stability and even improve other important properties like electrical conductivity. In addition, in other studies have been reported how the addition of external polymer coatings or the insertion or grafting of polymer species inside the MOF pores can lead to noticeable performance enhancement in a variety of applications including water treatment, catalysis, small molecule adsorption/separation, small molecule/ion sensing, and bio-delivery[161]An important work reported recently describes the formation of a cross-linked polymer-MOF composite, with a uniform distribution of MOFs over the polymer, by the replacement of some initial ligands (such as 1,4-benzene dicarboxylic

acid, BDC) on the MOF surface with a polymeric ligand (polyamic acid).[162]

The simultaneous exchange of the inorganic and organic part on a MOF represents the highest level of complexity of post-synthetic methodologies. This can lead to a total makeover of a MOF material. But it requires a careful chemical design and it is quite time-consuming to find the optimal conditions. This degree of complexity makes this subclass of PSMs do not have so many examples. However, the existence of some of them represent in itself strong evidence of the potential of MOFs to create highly heterogenous and complex materials while retaining the order. An elegant example is the SCSC transformation of the MOF $Zn_4O(PyC)_3$ (PyC = 4-pyrazolecarboxylate) to a defective framework by the elimination of both Zn^{2+} ions and PyC ligands and the successive incorporation of a different metal ion and organic linker.[163]

The last part of the classification is constituted by guest-based PSM in MOFs (Figure 1.28), 164 which are non-covalent post-synthetic transformations, which include the introduction or exchange of guest molecules hosted in the pores by diffusion. This is applied for the growth or encapsulation of metal nanoparticles and clusters, or in the case of anionic MOFs, exchange of extra-framework charge balancing cations by cationic metal complexes.

Figure 1.28. Possible pathways of guest-based PSM in MOFs. [144]

As stated in the section on porosity (Section 1.3.1.), this MOF property is widely celebrated. The pores of MOFs used to be occupied by various guest molecules such as solvents, ions (cations/anions), and molecules generated during the synthesis. The guest molecules can be replaced or removed by diverse methods to introduce new and exciting properties to the MOF structure.

The exchange of cations, located as extra-framework ions, is thermodynamically and kinetically feasible. For the active exchange of cations, the framework needs to be anionic. There are works that have shown the Mn(II) ions, present in the pores, were replaced by several other metal ions, generating stable frameworks with high H_2 adsorption. The enhanced binding of H_2 is attributed to the presence of the improved electrostatic field in the cavity of the framework.

The exchange of anions is more complicated and sometimes the use of dilute acids is involved. There is an interesting work where the modulator formate ions are exchanged with chloride and sulfate ions employing dilute acids in which the product MOF functions as a catalyst for esterification reactions have been reported.

The guest inclusions inside the MOF structure are a good strategy of PSM that opens an opportunity for an application, or it does so after an alteration. The guest molecules can be either solvent or reactive molecules. In a nanoporous MOF, the exchange of DMF molecules by solvents such as methanol, ethanol, propanol, benzene, or I2 changes its magnetic properties. When 7,7,8,8-tetracyanoquinodimethane (TCNQ) molecule, derived from a porphyrin ligand, in a 2D MOF suffers a solvent replacement their electrical conductivity is enhanced with respect

to starting framework. The guest inclusion, followed by an alteration of the guest, also generates better quality MOFs for precise applications. A ninefold increase in the electrical conductivity of a cadmium-based MOF was reported when redox-active pyrrole monomers were introduced into the nanochannels and subjected to oxidative polymerization by I_2.

1.6. MOFs Applications

At the end of the last century, MOFs emerged with great impact and constituted a new family in the field of porous materials. As stated in section 1.1., MOFs research was driven by the research groups of Robson and Hoskins –which initially named them as porous coordination polymers, PCPs– and later by Yaghi, Ferey, Kitagawa and others, the first of which coined them as MOFs. The interest in MOFs comes from their crystallinity and their high and regular porosity, which provides them with exceptional chemical and physical properties[165-168]suitable for applications in many different fields (Figure 1.29).

Initially, due to their porosity and metal sites accessibility, they were explored for adsorption of different gases[169,170] and catalytic applications[171,172] Currently, these two applications continue to be the most investigated ones. However, other developed, but promising applications have also been developed, such as ion exchange, drug transport and delivery, sensor technology, luminescence, non-linear optics, magnetism,[173,174] ferroelectricity, conductivity, water remediation[175-180] among others. In addition, due to their unique intrinsic properties, they have also been used as chemical nanoreactors, templating the growth of nanoparticles and constructing small metal clusters. Thus, acting as hosts

for a wide variety of guest molecules due to their large functional channels/pores.

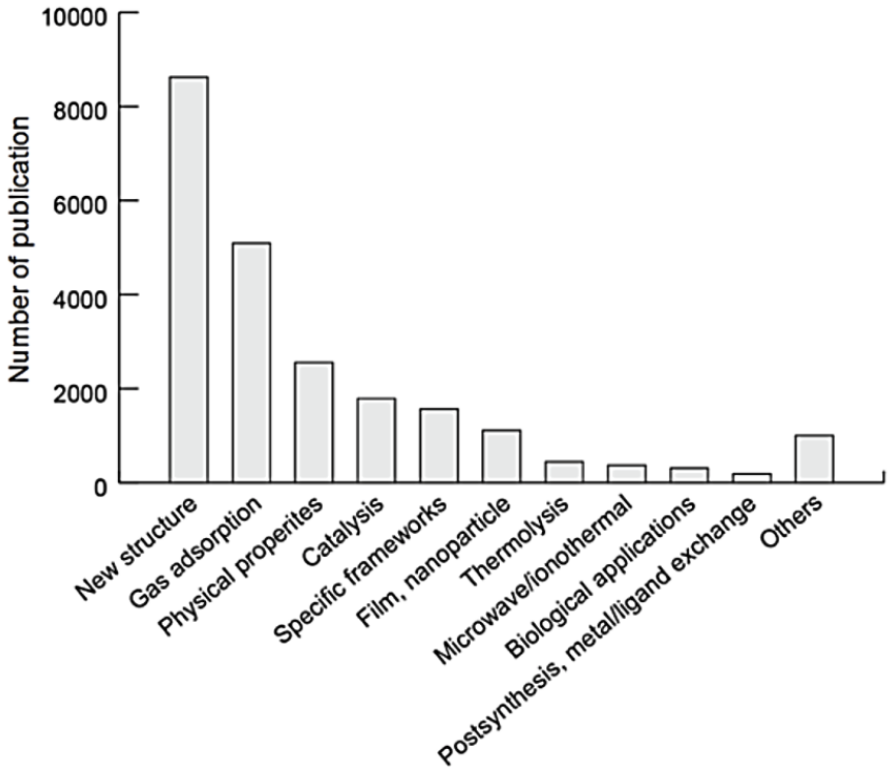

Figure 1.29. Research areas for MOFs from citation network analysis.[180]

1.6.1. Gas storage and separation

Gas storage and separation are one of the most visible and studied applications in MOFs due to the dimensionality and tunability of the pores. The high porosity and large surface areas of MOF allowed Kitagawa, in 1997, to open the way for the search for materials able to store gases with the introduction at high pressures of methane in a coordination polymer.[181]

MOFs gas capture is based on the specific interactions that are established between the adsorbed gases and MOFs channels, as consequence of their particular pore shapes, sizes, and chemical environments. In this sense, the control on the MOFs pore size allows the exclusion of gases by molecular size. The exclusion/recognition and selective uptake of gases are also determined by the functionalities decorating the pores sites[182,183], as well as by the shape of the pores.

The uptake and storage of gases is an application that can be extended to areas such as sustainable energy, environmental (removal of pollutants), and health-related. For the area of energy, it is important the use of MOFs as intermediaries in the generation of clean energies. MOFs have shown as efficient materials in controlled capture and release processes of gases such as hydrogen (H_2), methane (CH_4) and carbon dioxide (CO_2) or, in gas separation[184,185] as for example CO_2 from CH_4 in natural gas, and olefins from paraffins. The importance of H2 and CH_4 capture and release resides in its use as an alternative to fuel oil (with declining stocks). While CO_2 sequestration helps to reduce the environmental impact of the greenhouse effect[186-189]. In addition, MOFs have shown remarkable capture properties for toxic industrial chemicals such as NH_3 and H_2S, volatile organic compounds such as benzene and xylenes, and environmentally hazardous gases such as NO_x, SO_x, CO and CO_2, MOFs also capture chemical warfare agents.

Molecular separations are based on thermodynamic, kinetic, conformational or molecular exclusion factors. It is considered thermodynamic if the separation of two or more components is produced by the differences in affinity between adsorbates and MOFs. For example, in different MOFs it has been observed that CO_2 interact more efficiently than CH_4,

N_2 or C_2H_2, which facilitates CO2 sequestration and separation form the rest of gases. Figure 1.30 shows the CO_2 permeability of different known MOFs.[190] The kinetic separation is produced when there are differences in diffusivity of the adsorbate molecules. This ability or difficulty of molecules to move along the MOFs channels can be found in molecules that display similar size and functionality, such as hydrocarbons. Separation based on steric effects that depend on the efficient packing in a pore is considered conformational separation. This has been observed in olefins/paraffins separations. Last of all, separation based on molecular exclusion permits a full-size exclusion of one component from others according to pore aperture size and shape.

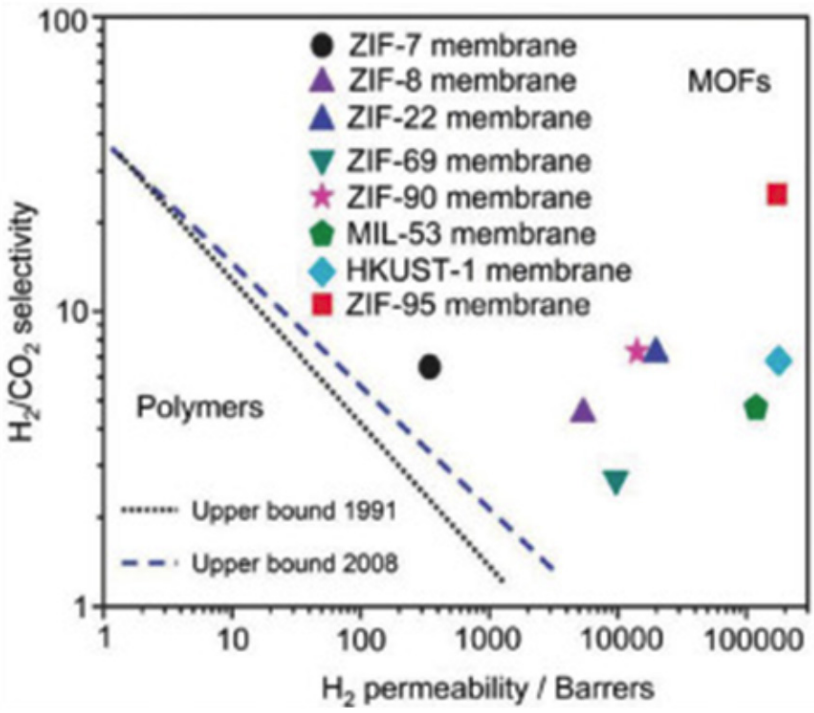

Figure 1.30. Comparison of the H_2/CO_2 separation performances of early MOF membranes with polymeric membranes.[190]

1.6.2. Biomedicine

One of the main applications of MOFs in biomedicine is their use as drug carriers, which somehow is closely related to the first-named application. In this case their high and regular porosity, organic groups within their networks, hydrophilic-hydrophobic cavities and tunable host-guest properties are used to achieve high drug loading as well as its controlled release. This allows solving problems that some therapeutic molecules present, such as instability in biological media and low solubility, among others. Additionally, the well-defined crystalline structures of MOFs, characterizable by SCXRD, allow to obtain unique snapshots of the main interactions behind the drug insertion, and in an indirect manner of the release process.

The first example of a MOF for biomedical application appeared more than a decade before, as drug carrier. Horcajada and co-workers, proposed the use of MOF nanoparticles for drug delivery[191,192] specifically, Cr-based MIL-100 and MIL-101 (Figure 1.31, left). They demonstrated that it was possible to adsorb the anti-inflammatory molecule ibuprofen into the large porosities of these MOF structures, showing extremely high drug storage capacities –up to 1.4 g of drug per gram of MIL-101. In addition, they showed their controlled release under physiological conditions, using simulated body fluid, 3 days for MIL-100 and up to six days in MIL-101 (Figure 1.31, right).

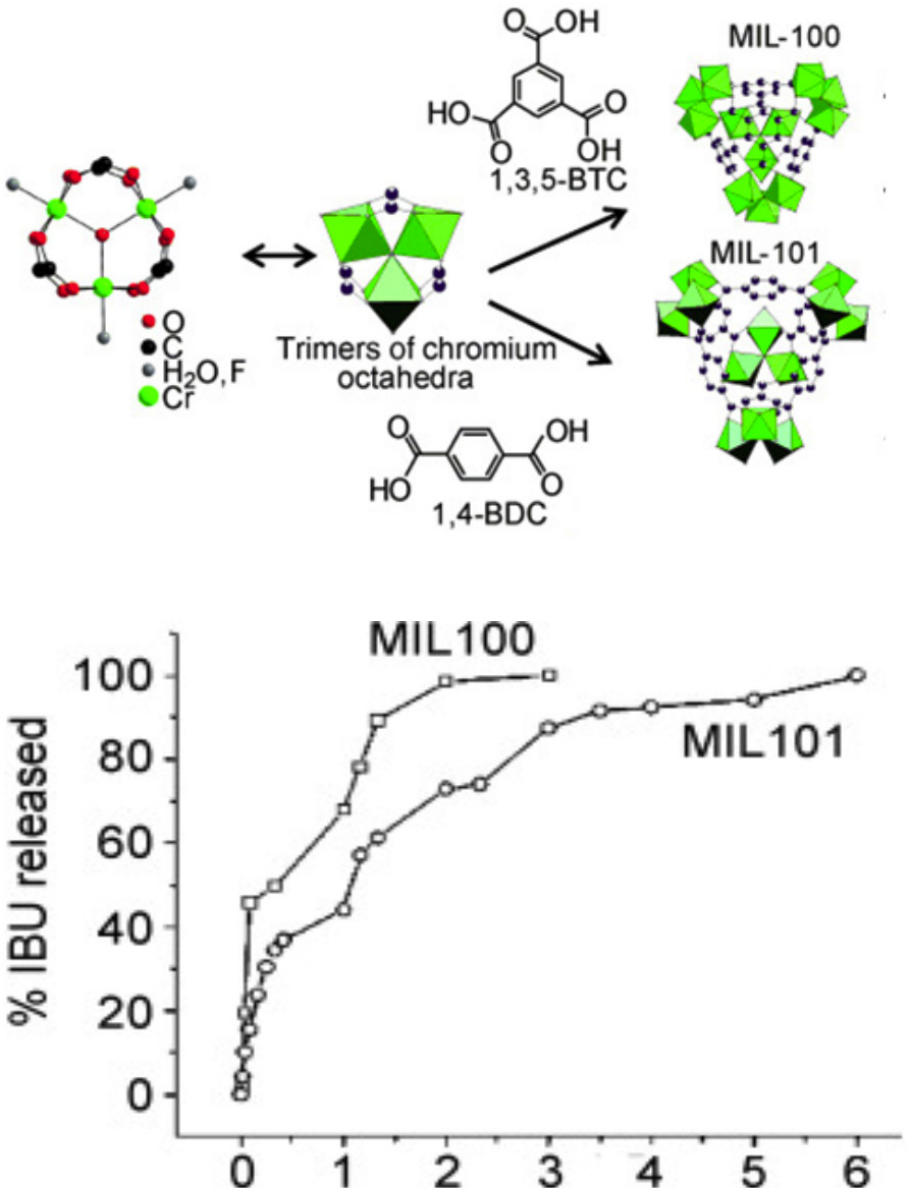

Figure 1.31. Obtention (top) and sustained release (bottom) of ibuprofen under physiological conditions from MIL-100(Cr) and MIL-101(Cr).[193]

Another biomedical application of MOFs is their use for contrast

imaging. This requires the use of nanoscale metal-organic frameworks (NMOFs) to been able to cross the cellular membranes. Different approaches have been followed to this application, starting with the simplest one where the inorganic part or the organic linker are behind the property, going through the encapsulated guest species and ending with a combination of both of them.[194] Related to this application is the use of MOFs with nanoparticles of paramagnetic metals as contrast agents for magnetic resonance (MR) imaging.[195]

Besides MOFs goodness in a particular biomedical application, it is important their constituents have biologically friendly character. In this context, metals such as calcium, magnesium, and to a lesser extent, zinc and iron would be appropriate. Respect the organic linker, the most favourable are the ones derived from biomolecules, such as amino acids, sugars and peptides. For all these mentioned biomedical uses, MOFs must be adapted as a dosimetric release material that can take the form of pellets, films or stable solutions of nanoparticles, among others. At this respect, it is worthy to mention that the structuration of MOFs has advanced considerably during the last years, which apart from being beneficial for biomedical applications is equally important in all the others applications of MOFs.

1.6.3. Photoluminescent sensors

The rich host-guest chemistry MOFs exhibited is consequence of the great level of tunability of their structure, where a wide variety of organic linkers and metal nodes can be used in order to increase sensitivity and selectivity towards certain analytes. MOFs could be used directly as a functional sensing element or as an auxiliary filtering element. At

this respect, MOFs are useful in a wide range of areas as chemical sensors and adsorbents for environmental monitoring, occupational safety, medical diagnostics, chemical threat detection, quality controlling or industrial process management. In addition, it is important to highlight that their porous nature, besides to selectively capturing the analyte, allows to adsorb and pre-concentrate the analytes at the sensor, which increases host-guest interactions and improves sensing performance. Here, it is worth to note that to be useful MOF-based sensors, MOFs must be selective, sensitive, stable, reusable, and have adequate response times.

The most studied types of MOF sensors are based on photoluminescence due to the quick and easy colorimetric response to stimuli, so the signal can be recognised easily either by eyes or by fluorescence spectrometers[196]. The luminescence can arise from their organic linkers (generally aromatic or conjugated organic compounds), metal ions (generally d^{10} transition metals or lanthanoid metal ions), guest molecules and a combination of them. As the organic ligands are part of the network, they have restricted mobility, and as consequence, the nonradioactive relaxation caused by the free rotation and vibration of the ligand can be reduced, improving the quantum efficiency of the system. In the case of the guest molecules, which can either be emitters or sensitizers, they can alter their own emission properties and the ones of the host molecules, resulting in changes that can be detected in their emission profiles such as displacements of wavelength, changes in intensity, or a completely different emission.

The efficiency and versatility of luminescent MOFs based sensors have been demonstrated with the detection of different analytes such as ions,

volatile organic compounds (VOCs), explosives, biomolecules, toxic species, gas, humidity, temperature or pH. Also, it has been used for the detection of mercury(II), which is considered as one of the most toxic and hazardous metal. Bioaccumulation of mercury in the food chain has led to several fatal diseases in humans. That is why several researchers have located their studies on obtaining MOF-based sensory probes for the detection of this toxic water pollutant. In a very nice work, it was reported an efficient chemosensor for Hg2+ ions in a water medium based on a functionalized MOF, UiO-66@butyne (isoreticular with UiO-66), featuring an active butyne functionality (Figure 1.32, left). In this study, the researchers found, the luminescence quenching process involved an oxymercuration reaction-based chemodosimetric pathway with high sensitivity and good selectivity in the presence of interfering metal cations (Figure 1.32, right).

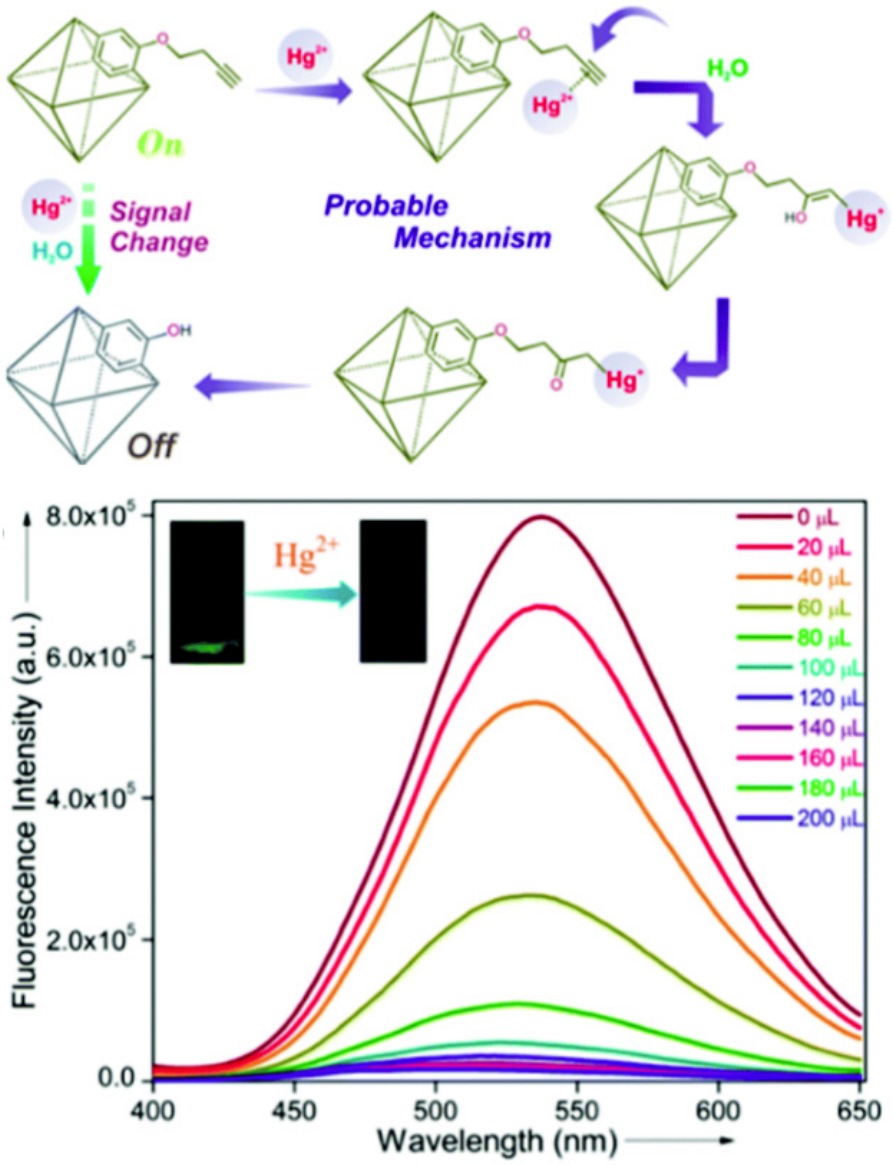

Figure 1.32. Schematic representation for the plausible mechanism of Hg2+ ion sensing with UiO-66@butyne (left) and fluorescence quenching of UiO-66@butyne upon the addition of Hg^{2+} ion solution in water (right).[197]

1.6.4. Magnetism

Magnetic MOFs represent an exciting class of multifunctional materials in which magnetic properties coexist with porosity. This make of them ideal candidates to be used as magnetic sensors, molecular magnets or to carry out magnetic separations. Despite being highly challenging, the magnetic properties of MOFs can be tuned by modifiying/exchanging the organic ligands that act as linkers between the paramagnetic metal centers, and thus the magnetic interaction, acting directly over the magnetic centers and by guest inclusion within MOFs channels.

Depending on the class of exhibited magnetic properties, MOFs can be classified, mainly, into four types (Figure 1.33): (*i*) porous magnets, where magnetic exchange through the ligands led to a MOF with a magnetic order, *(ii*) spin-crossover MOFs, where the nodes have suitable coordination environments for this phenomenon to exist, (*iii*) MOFs with slow magnetic relaxation, where the nodes are single metal ions or SBUs possessing an anisotropic spin ground state; with single-molecule magnet behaviour, and (*iv*) MOFs with magneto-caloric effect, where the nodes are SBUs possessing an isotropic spin ground state.

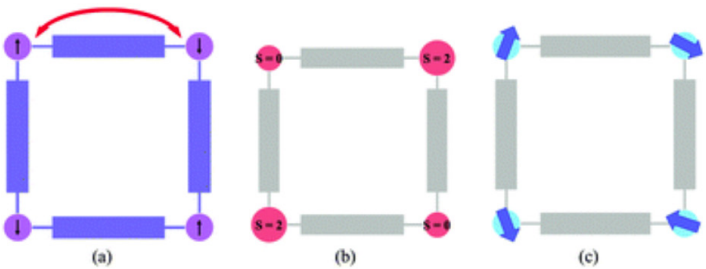

Figure 1.33. Schematic representation of the different strategies to incorporate magnetic functionalities into MOFs: (a) magnetic exchange via the ligands; (b) spin-crossover at the nodes; (c) MOFs with magnetic clusters in the nodes (anisotropic spin for SMM, isotropic spin for magnetocaloric).[198]

Here, it is important to note that the magnetic interactions, their sign and the strength, depend on both the nature and coordination environment of the magnetic carriers. Indeed, coexistence between porosity and magnetism in MOFs requires a design counterpart because whereas magnetic exchange interactions require short distances between the metal centres, which are most commonly the spin carriers, porosity is typically favoured with the use of long linkers, which are often too long for efficient magnetic exchange. Thus, to combine both properties, diverse synthetic strategies have been used in literature: (*i*) short linkers (*i.e*. cyanides, azolates, and lactates) combined with longer linkers that can provide large pore apertures, (*ii*) preformed complexes such as metalloligands, and (*iii*) radical ligands.

An example of magnetic MOF is Co(imidazolate)$_2$ (Figure 1.34, left), where imidazolate can form strong and directional coordination bonds serving as bridges between metal ions. Despite the short nature of the linker, a highly porous solid Despite imidazolates transmit antiferromagnetic couplings between Co^{II} ions (Figure 1.34, right), the uncompensated antiferromagnetic couplings that result from non-centrosymmetric structures produced weak ferromagnets due to spin-canting. [189]

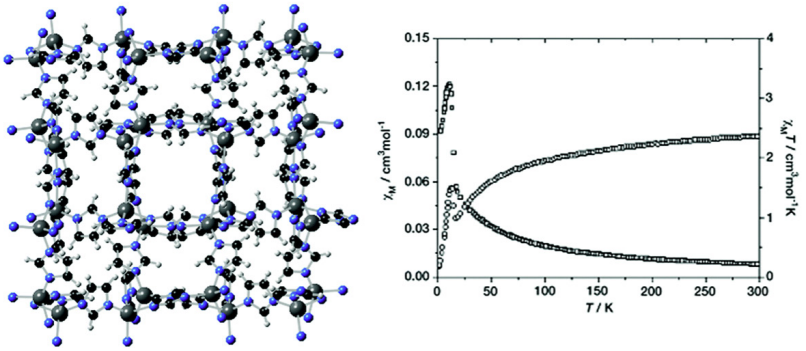

Figure 1.34. (a) Crystal structure of Co(imidazolate)2; (b) plots of temperature dependence of χM and χMT for Co(imidazolate)$_2$ measured at a field of 10 kOe (left).[199]

Hofmann-type MOF {Fe(bpb)[MII(CN)4]}·xGuest (bpb = bis(4-pyridyl) is a representative example of Spin-crossover (SCO) MOF.200 Such system shows a characteristic transition between FeII high-spin a low-spin near room temperature, which is affected by the adsorption of guest molecules (gases, solvents, halogens, and organic molecules) through host-guest interactions.

The magnetic behaviour of MOFs can be produced by the presence of single-molecule magnets (SMMs) or single ion magnets (SIMs) as constituting inorganic part or in the organic nodes, producing a slow relaxation of the magnetization at low temperatures. Also, preformed SMMS/SIMs can be encapsulated as guests, where it has been observed a change in their magnetic properties due to confinement effects within MOFs channels.[201] Polynuclear clusters with a high magnetic anisotropy, normally constituted SMMs, while SIMs are usually based on lanthanides or transition metals. The latter ones have the advantage that they can combine huge magnetic anisotropies with strong quantum effects. A beautiful example of Single-Molecule Magnets (SMMs) is the incorporation of the nanostructuration Mn_3 into mesoporous aluminum-based metal-organic framework (MOF) [Al(OH)(SDC)]n (H2SDC = 4,4′-stilbenedicarboxylic acid), known as CYCU-3.[202]

1.6.5. Catalysis

Catalyst are materials characterised by increase the rate of a chemical reaction without its consumption during the reaction. They can be classified by function of the physical phase of the catalyst and the reactants: (*i*) homogeneous when they are in the same physical phase, and (*ii*) heterogeneous when they are in different phases, where normally the re-

actants are in the gas or solution phase and the catalyst in a solid phase. The chemical industry relies on catalytic processes, usually using heterogeneous catalysts, because they offer many advantages over homogeneous catalysts, such as the ability to separate catalysts from reaction products, the capability of applying them to continuous-flow processes, and the ease of recycling them (often by simply heating in the presence of air or hydrogen). [203]

The multiple opportunities of MOFs to create one or more active catalytic sites within the pores made of catalysis, since the early ages of MOFs, an important application to be explored. Indeed, due to their ability to remain intact during catalytic processes[204] and their confinement capacity, MOFs show promise for heterogeneous catalysis in industrial applications, as they can be recycled and reused several times, showing economically and environmentally advantageous properties for industries as compared to homogeneous catalysts.

Metal centers (as node points) and ligands (as skeletons) are MOFs constituents. But, also can act as catalytic centers, if metal ions have available active positions and/or ligands have active functional groups for catalysis.[205] Open metal sites in the framework can be generated by removing guest solvent molecules coordinated to these metal centres without collapse of the structures, getting unsaturated coordination environments, to be utilized as active catalyst sites. Many MOFs have been obtained with open metal sites, such as MOF-11, HKUST-1, MIL-100, MIL-101 and UiO-66- and they can be used as mild Lewis acids. In addition, catalytically active organic functional groups can be incorporated using the open metal sites as anchoring points by PSM. The active organic functional groups from ligands of the MOF or anchored

to the metal centres, have reveal as versatile catalyst as can act as either Lewis acids or bases, as well as be active species for anchoring metallic catalyst. An example of this is MIL-101 (Cr) functionalized with ethylenediamine, where the free amine group immobilizes palladium nanoparticles to be applied in coupling reactions. Also, if chiral organic ligands are incorporated into a MOF structure, the MOF is endowed with chiral centers with the capacity to do asymmetric catalysis.

Besides these options, MOFs can exhibit catalytic activity by incorporating active guest species in their pores, such as complexes or inorganic nanoparticles. Finally, MOFs can also serve as templates for the preparation of catalytically active nanoclusters (NCs) and nanoparticles (NPs) through the use of post-synthetic methods (PSMs). This last option represents the investigated central core of the works constituting my PhD thesis.

Examples of catalytic MOFs are NH_2-UMCM-1 and NH_2-MOF-5 (top of Figure 1.35), which were used for the formation of C-C bonds based on the Morita–Baylis–Hillman reaction. In this work, the authors were able to identify the expected triphenylphosphonium intermediate trapped inside the pore and proposed a concerted mechanism (bottom of Figure 1.35), where the active intermediate interacts with the amino functional groups decorating the pore surface forming stable noncovalent interactions. Also, they found the three phenyl groups of the trapped intermediate cause significant steric hindrance, while conformational freedom is limited by the MOF. Thus, the tetrahedral configuration of the phosphonium moiety is distorted, opening the door for a completely unprecedented electrophilic attack and leading to an unexpected aldol-Tischenko product (bottom of Figure 1.35).

Relevantly, control experiments show that this result cannot be achieved with homogeneous catalysts. Indeed, the most interesting aspect of this work is that the selectivity-switch by confinement is observed only with some MOF topologies. Like the ones UMCM-1 and NH_2-MOF-5 that can impose the necessary geometric constraints, but also bear the chemical functionalities necessary to stabilize the reactive intermediate. This work represents a splendid example of the correlation between pore environment (geometry and functional groups) and reaction pathway.

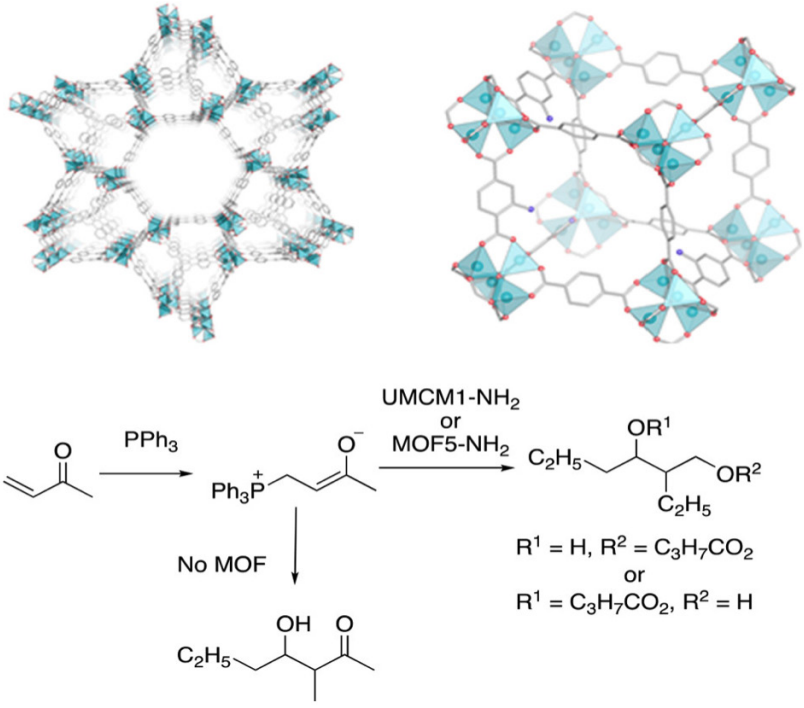

Figure 1.35. Top: Crystal structures of NH_2-UMCM-1 (left) and NH_2-MOF-5 (right). Bottom: Diverging reaction pathways from a common triphenylphosphonium intermediate in the presence and absence of MOF.[206]

1.7. MOFs development within the research line of our group

In this thesis, we have focused on oxamate- and oxamidate-based MOFs build up following the metalloligand design strategy, where preformed complexes are used as metalloligands toward transition metals, and alkaline earth metals to assembly the target MOF During the last years, our group have treasured a wide knowledge about using oxamate and oxamidate-based ligands to build, in the first days, magnetic coordination polymers and MOFs, and later on by tuning pores functionalities, MOFs with such diverse applications[207] as chemical reactors, catalysis, gas adsorption and water remediation.

Oxamate (Figure 1.36a) and oxamidate (Figure 1.36b) dianions can adopt bidentate and bis(bidentate) coordination modes in metallic complexes to obtain mono- (Figure 1.36c) and dinuclear complexes (Figure 1.36d). These metalloligands have high stability in solution, as direct consequence of the strong-donating capacity of the *N,O*-oxamate and *N,N*-oxamidate groups[208] and their coordination affinity towards the divalent metal ions of the first transition series (Cu^{II}, Ni^{II} and Co^{II}). In addition, they present free carbonyl-oxygen atoms capable of binding other divalent transition or alkaline earth metal ions (Sr^{II}, Ca^{II} and Ba^{II}), enabling the formation of stable and robust heterobimetallic MOFs.[209,210]

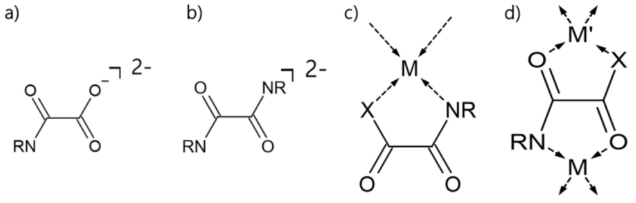

Figure 1.36. Oxamate (a) and oxamidate dianions (b); mono- (c) and dincuclear complexes (d).

The interest in oxamate-based mono- and dinuclear Cu^{II} complexes could be said to have started in 1986 by the group led by O. Kahn.[211] This work being somehow inspired in the publication of Nonoyama and co-workers about *N*-monosubstituted oxamide derivates coordinating with Cu^{II} and Ni^{II} to design polymetallic systems with predictable molecular magnetics properties.[212] Later on, Journaux´s and Lloret's groups further extended Kahn' group knowledge to oxamidato complexes, using aliphatic and aromatic group-substituted bis(oxamato)- and bis(oxamidato)-copper(II) complexes as metalloligands (Figure 1.37). These metalloligands were linked to other metal ions in such a way that they could obtain molecule based-magnets with crescent dimensionality, and allowing to move l T_C towards higher temperatures.

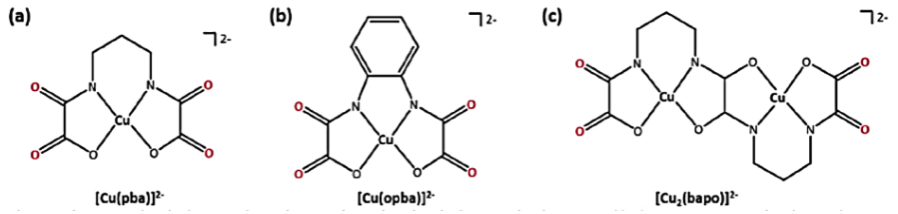

Figure 1.37. Some oxamato and oxamidato copper(II) precursors used by the groups of Kahn, Journaux and Lloret. a) $[Cu(pba)]^{2-}$ (pba =N,N'-1,3-propylenebis(oxamato) b) [Cu(opba)] 2- (opba =N,N'-1,2-phenylenebis(oxamato) and c) $[Cu(bapo)]^{2-}$ (bapo = N,N'- bis(oxamatos-1,3-propylene)oxamido.

Then, different mono-, di-, and trinuclear complexes were obtained from a wide variety of *N*-substituted aromatic oligo(oxamate) ligands (Figure 1.38).[213-216] The development of oxamato/oxamidato bridged polymetallic complexes as metalloligands have helped our group to obtain a wide variety of magnetic materials, as well as unlocked multiple functionalities to these materials.

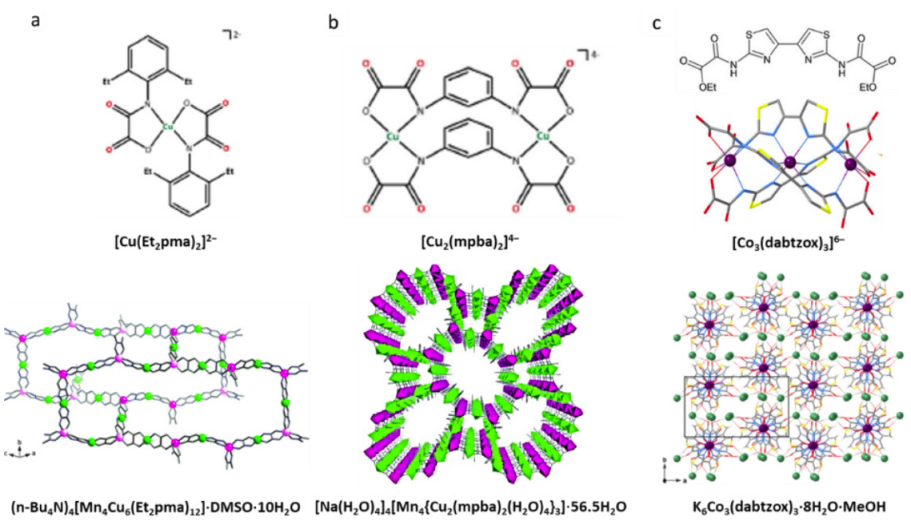

Figure 1.38. a) Mononuclear complex $[Cu(Et_2pma)_2]^{2-}$ (Et_2pma =N-2,6-diethylphenyloxamate) (top) and perspective view of coordination polymer $(n\text{-}Bu_4N)_4[Mn_4Cu_6(Et_2pma)_{12}]\cdot DMSO\cdot 10H_2O$ (bottom) [217], b) dinuclear complex $[Cu_2(mpba)_2]^{4-}$ (mpba=N,N′-1,3-phenylenebis(oxamate)) and its corresponding MOF $[Na(H_2O)_4]_4[Mn_4\{Cu_2(mpba)_2(H_2O)_4\}_3]\cdot 56.5H_2O$ [218], and c) trinuclear cobalt(III) complex $[Co_3(dabtzox)_3]^{6-}$ (dabtzox=N,N′-2,2′-(4,4′-bithiazole)bis(oxamate)) and its corresponding MOF $K_6Co_3(dabtzox)_3\cdot 8H_2O\cdot MeOH$. [219]

So, when we have used dianionic oxamatos-containing mononuclear copper(II) complexes, $[CuL_2]^{2-}$, as bis(bidentate) metalloligands toward transition metal cations in a 1:1 ratio, heterobimetallic one-dimensional chains have been built. However, also high dimensionality compounds (2D and 3D) was possible to be obtained if we play with the metalloligand:transition metal ratio and the influence of the length of the alkyl-substituents in the aromatic ring of oxamate ligands. In the case of anionic dinuclear copper(II) complexes, $[Cu_2L2]^{4-}$, with π-conjugated phenylene spacers, as tetrakis(bidentate) metalloligand towards M^{2+} ion, our group have reported bidimensional (2D) and tridimensional (3D) magnetic MOFs.

Our research group, led by Emilio Pardo and Jesús Ferrando Soria, has followed this line of research by exploiting the chemistry of oxamate complexes to the maximum. My work focuses on two distinct families of MOFs, on the basis of the starting ligand, one based in oxamidate ligands derived from chiral amino acids and the other where the organic ligand are oxamate-derived from aromatic amines, and the application on them of PSMs to endow the resulting MOFs with interesting catalytic properties.

Firstly, we focus in MOFs obtained from oxamates and aromatic amines, specifically 2,4,6-trimethyl-1,3-phenylenediamine, that lead to highly robust and crystalline structures. Following a previously reported method,220 an equivalent of the initial compound 2,4,6-trimethyl-m-phenylenediamine, with two active amino groups, can react with two equivalents of ethyl chlorooxoacetate in THF at 0 °C, to led after one hour of reflux, to the organic proligand 2,4,6-trimethyl-*N,N*'-1,3-phenylenebis(oxamate), called **$H_2Et_2Me_3mpba$**. The dicopper(II) metalloligand $Na^{I}_4[Cu^{II}_2(Me_3mpba)_2] \cdot 4H_2O$ is obtained by the slow addition of cooper nitrate over the proligand in an aqueous basic environment. Then, adding dropwise a second metal ion, magnesium, over dinuclear precursor in neutral aqueous medium, polycrystalline powder of $Mg^{I}_2\{Mg^{II}_4[Cu^{II}_2(Me_3mpba)_2]_3\} \cdot 45\ H_2O$ **(Mg^{2+}@CuNi-Me_3mpba)** is obtained, which consist in an anionic bimetallic $[Cu_6^{II}Mg4^{II}]^{2-}$ ordered porous framework together with water and magnesium ions hosted in the pores. The obtention of bright-green tiny single-crystals of this MOF is achieved by H-shaped tube. Figure 1.39 show the MOF synthetic route.

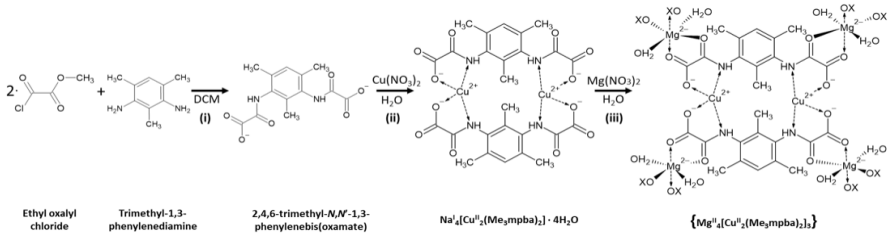

Figure 1.39. MgII2{MgII4[CuII2(Me3mpba)2]3} · 45 H2O MOF's Synthetic route

In the formation of MOFs, several parameters are involved, such as nature and coordination preferences of metal ions, nature of the counter anion, metal-to-ligand ratio and flexibility of the organic building blocks. The possibility to perform post-synthetic ion exchange is one of the interesting properties of anionic or cationic MOFs that do not have neutral frameworks.

Metal exchange is a powerful approach to obtain novel functional materials and can involve metal nodes and/or countercations residing within MOFs cavity. In the presented example, dicopper metalloligands ($Na^{I}_{4}[Cu^{II}_{2}(Me_3mpba)_2]$) are the "blocks" that are linked by a divalent metal (Mg^{2+}). Here it is worthy to clarify that when we refer about transmetallation we mean that all magnesium (nodes and countercations) is replaced, while copper remain in the framework. When we used the term insertion, we mean exchange of only metal hosted in the pores.

In this context, transmetallation and metal-exchange have been used to introduce or improve physical properties on preformed MOFs. [221-226] For example, transmetallation of **Mg^{2+}@CuNi-Me_3mpba** with nickel(II), by prolonged immersión of that MOF in a NiNO3 solution, lead to obtain the MOF of formula $Ni^{II}_{2}\{Ni^{II}_{4}[Cu^{II}_{2}(Me_3mpba)_2]_3\}\cdot 54H_2O$ **(Ni^{2+}@CuNi-Me_3mpba)**[227], Figure 1.40. Due to the substitution of diamagne-

tic Mg^{II} ions by paramagnetic Ni^{II} ions, it was observed the occurrence of a long-range magnetic ordering in **Ni^{2+}@CuNi-Me_3mpba**, and an improvement of the structural stability, cristallinity and porosity respect the pristine magnesium MOF. This transmetallation process was monitored by scanning electron microscopy-energy dispersive X-ray analizer (SEM-EDAX), showing there are two steps: the substitution of those metal ions hosted in pores and the replacement of the ones building the coordination network.

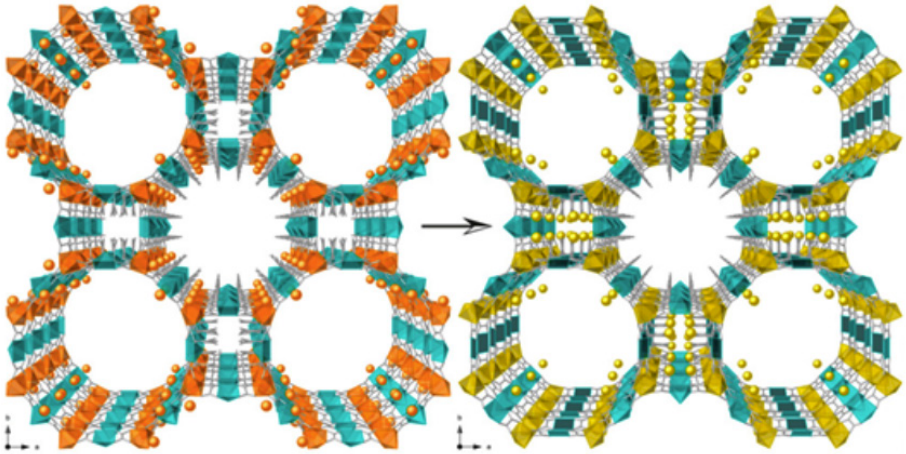

Figure 1.40. Transmetallation of $Mg^{II}_2\{Mg^{II}_4[Cu^{II}_2(Me_3mpba)_2]_3\} \cdot 45\ H_2O$ to $Ni^{II}_2\{Ni^{II}_4[Cu^{II}_2(Me_3mpba)_2]_3\} \cdot 54H_2O$ with $NiNO_3$.[228]

Later on, based on the improved physical properties of **Ni^{2+}@CuNi-Me_3mpba**, it was explored the use of this MOF as starting material to obtain other functional MOFs by the cation exchange of the nickel atoms present in the pores with other metal ions, such as Sr^{2+}, Pt^{2+}, Ag^{+}, Pd^{2+}, Fe^{3+}, Au^{3+}, Cu^{2+} ...The selection of the metal cation used for PSM of **Ni^{2+}@CuNi-Me_3mpba** was not arbitrary, it was determined by the type of catalytic activity/application that we want to endow our resulting porous material. This process was also monitored by SEM-EDAX,

where it is was observed, that the Cu^{2+}:Ni^{2+} ratio increases and the Ni^{2+}:Mn^{+} ratio decreases due to the substitution of the nickel(II) ions hosted in the channels.

Then, widening the applications of MOFs and taking advantage of the highly robust and crystalline nature and rich host-guest chemistry of oxamate- and oxamidate-based MOFs, they have been used as chemical nanoreactors to synthesise species that otherwise would be hardly accessible. Oxamato- and oxamidato-based MOFs have shown able to resist a wide variety of solvents and conditions, while maintaining their structure and crystallinity. Thus, this makes them capable of suffering the straight insertion and stabilization of highly reactive catalytic species, as well as the step-by-step preparation of functional catalytically active species within their confined functional space (Figure 1.41).

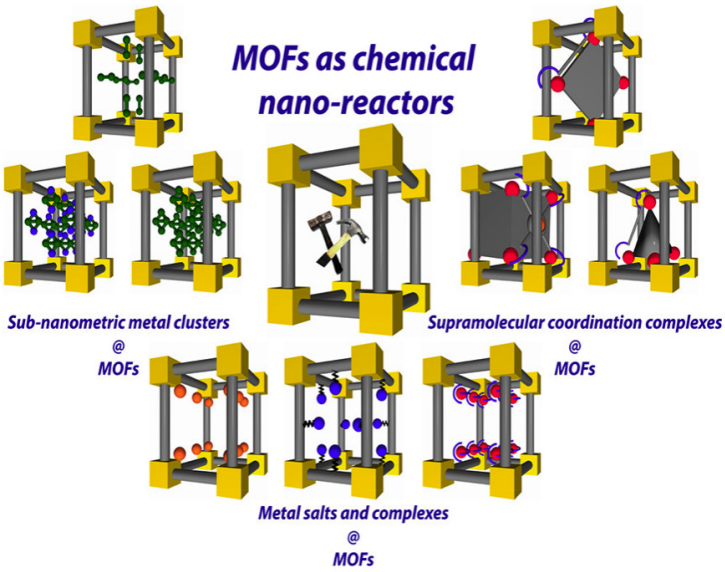

Figure 1.41. Overview of the three main blocks where MOFs support catalytically active species.[229]

Dealing with the family of MOFs constructed with oxamidate-derived amino acids, the intrinsic chirality of asymmetric α-carbon atoms offers the possibility of forming in a controlled manner chiral MOFs.

Amino acids are organic compounds formed by carboxyl (-COOH) and amine ($-NH_2$) functional groups connected by a carbon called an alpha-carbon, Cα. This alpha carbon is also linked to a specific side chain (R group) (Figure 1.42), which brings each amino acid a set of properties: charge, polarity, aromatic/aliphatic character, etc. Oxamidate-derived amino acid MOFs offer also many other advantages, such as biocompatibility, stability in water, rich structural diversity, and more relevantly, the specific properties offered by the side chain.

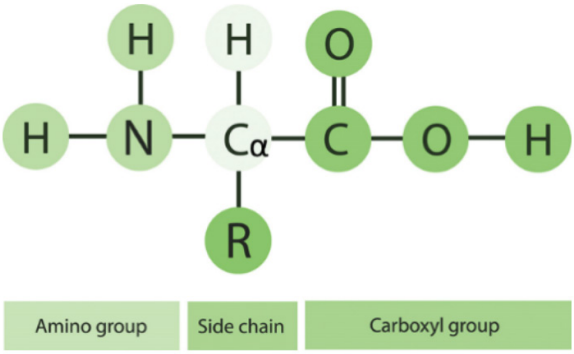

Figure 1.42. Amino acid structure.

To synthesize disubstituted oxamidate organic ligands, it makes necessary to esterify amino acids previously, and thus, when they are not commercially available in the synthetic procedure it has to be added this pre-synthetic step, –using thionyl chloride ($SOCl_2$) and methanol under N_2, firstly, at 0°C to alleviate the temperature produced by this exothermic reaction and, then, at 80°C reflux. Then, two equivalents of methyl ester derivative react with an equivalent of oxalyl chloride to obtain the desired proligand, which reacting with copper(II) chlori-

de in basic conditions led to the formation of the dinuclear precursor. Table 1.3 shows ligands and the respective copper(II) metalloligands to obtain MOFs. The interaction between copper precursors, acting as metalloligands toward alkaline earth metal ions (Ca^{2+}, Ba^{2+} o Sr^{2+}) led to the assembly of heterobimetallic three-dimensional MOFs with functional pores decorated with the residues of the amino acid used to form the metalloligand. Figure 1.43 shows the scheme of the synthetic route used to obtain these 3D heterobimetallic MOFs. An example is the MOF $\{Ba^{II}Cu^{II}_6[(S,S)\ valmox]_3(OH)_2(CH_3OH)_6\}\cdot 6H_2O$, shown in Figure 1.44a, wherein the left side it shows the environment of copper metal ions and the residue - $CH(CH_3)_2$, and the right one the view of the sheets in the ab plane. Alternatively, It has been demonstrated it is also possible to obtain 3D homometallic MOFs modifying the pH of the copper precursor solution until precipitates, like in the case of the MOF Cu^{II}_2(S,S)-hismox$\cdot 5H_2O$ (Figure 1.44b) with only copper nodes and histidine-base proligand. These MOFs have been structurally characterized and studied for different applications, such as gas-adsorption, pollutants removal, chemical nanoreactors and catalysis. Remarkably, it was observed the properties of these MOFs were somehow controlled depending on the starter aminoacid R-group, as consequence of the different pore size and functionality decorating the channels.

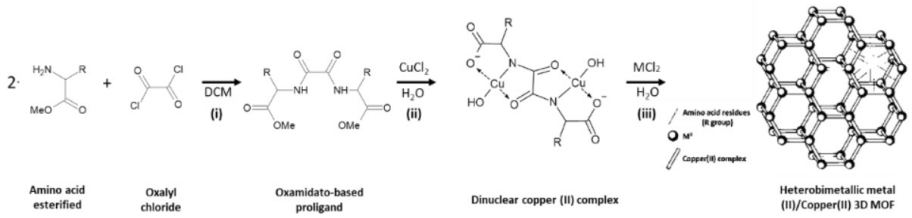

Figure 1.43. Scheme of the synthetic route used to obtain 3D heterobimetallic MOFs

Table 1.3. Sintetized ligands and Cu^{2+} to obtain chiral MOFs.

Aminoacid	Side chain	Ligand	Cu^{II} Metalloligand
S-Methyl-L-cysteine	Thioether $-CH_2SCH_3$	H_2Me_2-(S,S)-CH_3cysteine	$(Me_4N)_2\{Cu_2[(S,S)$-CH_3Cysteine$](OH)_2\}$ $4H_2O$
L-Histidine	Imidazole 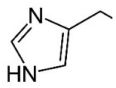	H_2Me_2-(S,S)-hismox	$(Me_4N)_2\{Cu_2[(S,S)$-hismox$](OH)_2\}$ $4H_2O$
L-Methionine	Thioether $-CH_2CH_2SCH_3$	H_2Me_2-(S,S)-methox	$(Me_4N)_2\{Cu_2[(S,S)$-methox$](OH)_2\}$ $4H_2O$
L-Serine	Hydroxyl -OH	H_2Me_2-(S,S)-serimox	$(Me_4N)_2\{Cu_2[(S,S)$-serimox$](OH)_2\}$ $5H_2O$

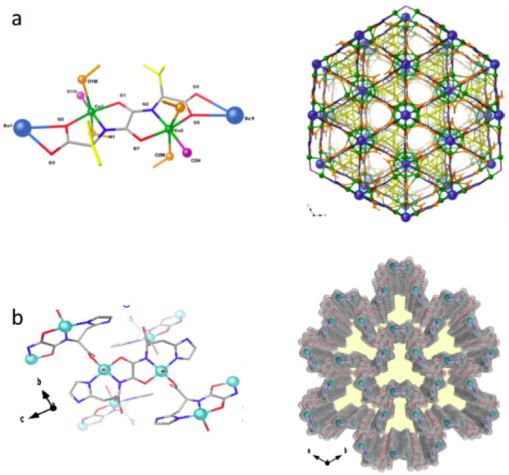

Figure 1.44. (a) Left, details of coordination mode and environment of copper metal ions in $\{Ba^{II}Cu^{II}_6[(S,S)\ valmox]_3(OH)_2(CH_3OH)_6\}\cdot 6H_2O$; right, view of the sheets in ab plane (Cu, green; Ba, blue; methanol molecules, orange; hydroxo oxygen, purple; isopropyl chains, yellow; oxygen from ligands, red sticks; nitrogen, blue sticks). (b) Left, Perspective view of a fragment of MOF Cu^{II}_2(S,S)-hismox$\cdot 5H_2O$ in the bc plane, showing the dinuclear units coordination modes, and right, perspective view of the 3D open-framework (110 K) along the c axis (the crystallization water molecules are omitted for clarity). Color codes: Cu: cyan; O: red; C: gray; N: blue.

Cu^{II}_2(S,S)-hismox·$5H_2O$ (Figures 1.44b and 1.45) represent an interesting example of MOF with qtz-e-type topology (due to unidimensional trapezoidal nanosized channels growing along the [001] direction) which exhibits a continuous and reversible breathing behavior, can adsorb CO_2, N_2, Ar, and C_3H_6 and can separate efficiently mixtures of CO_2/N_2, CO_2/CH_4 and C_3H_8/C_3H_6. Dealing with water decontamination, for example, our group have reported the efficient capture of four distinct dyes –pironine Y (PY), auramine O (AO), brilliant green (BG) and methylene blue (MB)– using the MOF $\{Ca^{II}Cu^{II}_6[(S,\ S)$-serimox$]_3(OH)_2(H_2O)\}\cdot 39H_2O$ Figure 1.46.

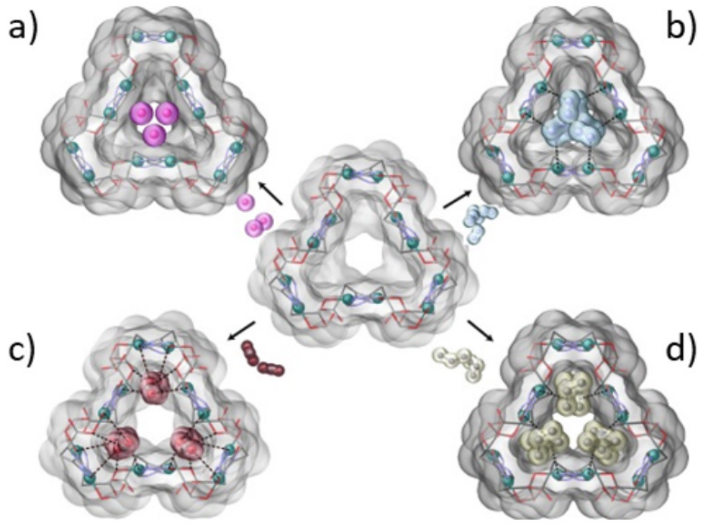

Figure 1.45. Perspective views of the porous structures Cu^{II}_2(S,S)-hismox·5H2O determined by single-crystal X-ray diffraction of the host-guest adsorbates containing Ar (a, 120 K and 10 bar), N2 (b, 110 K and 7. 4 bar), CO_2 (c, 235 K and 9.4 bar) and C_3H_6 (d, 290 K and 7.5 bar). Copper(II) atoms are depicted as spheres and sticks whereas ligands are represented as sticks. The guest gases are represented as spheres and sticks with surfaces. The host guest interactions are shown in detail (dashed lines) in the right side of the porous structures. Color codes: Ar: pink; Cu: cyan; O: red; C: gray; N: blue.)

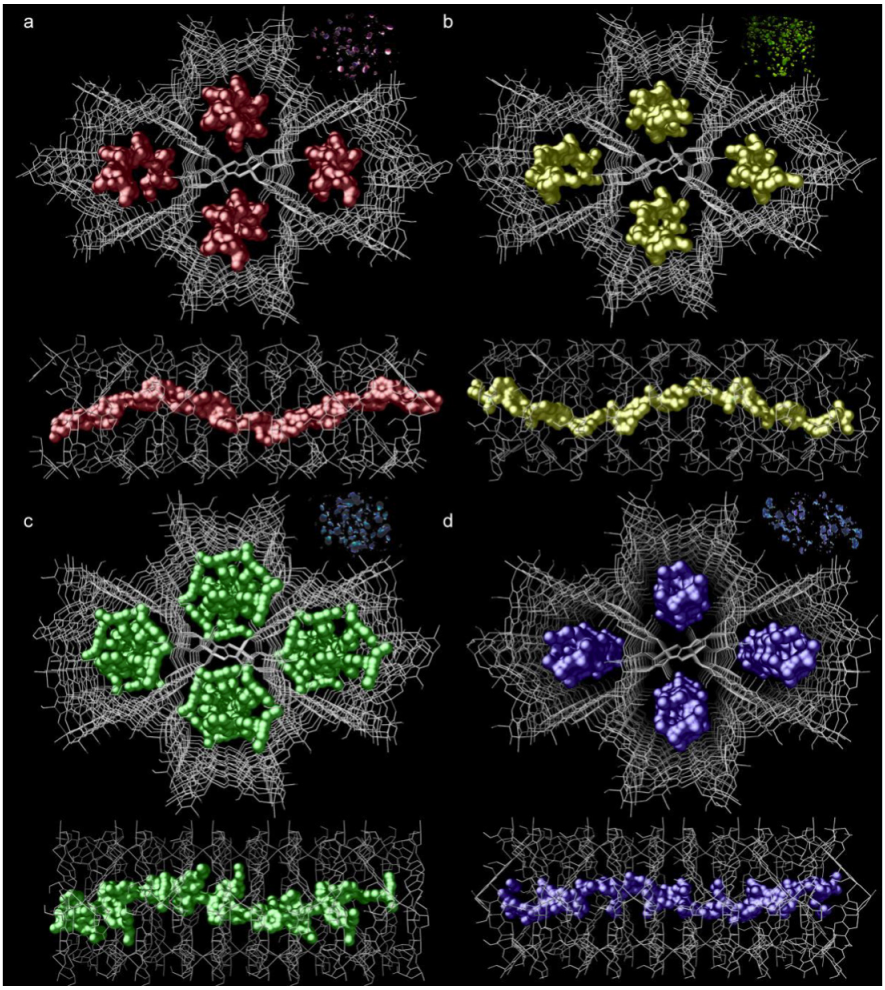

Figure 1.46. Perspective views in the ab (top) and bc (bottom) planes of the porous structures of $\{Ca^{II}Cu^{II}_6[(S,\ S)\text{-serimox}]_3(OH)_2(H_2O)\}\cdot 39H_2O$ dyes (pironine Y (PY), auramine O (AO), brilliant green (BG) y Methilene Blue (MB)) inside MOF: $PY@\{Ca^{II}Cu^{II}_6[(S,S)\text{-serimox}]_3(OH)_2(H_2O)\}\cdot 15H_2O\cdot CH_3CN$ (a), $AO@@\{Ca^{II}Cu^{I-I}_6[(S,S)\text{-serimox}]_3(OH)_2(H_2O)\}\cdot 15H_2O\cdot 2CH_3CN$ (b), $BG@@\{Ca^{II}Cu^{II}_6[(S,S)\text{-serimox}]_3(OH)_2(H_2O)\}\cdot 17H_2O\cdot 2CH_3CN$ (c) and $MB@@\{Ca^{II}Cu^{II}_6[(S,S)\text{-serimox}]_3(OH)_2(H_2O)\}\cdot 19H_2O$ (d). The networks are depicted as light grey sticks whereas guest organic dyes are represented as red (Pyronin Y), yellow (Auramine O), green (Brilliant green) and blue (Methylene blue) solid surfaces, respectively. Free water solvent molecules are omitted for clarity.

In our group, recently, it has been opened a new research line devoted to the obtention of multivariant MOFs (MTV-MOFs), which are characterised by being composed of more than one different metalloligand. This was done with the aim of both to increase pore complexity and to obtain synergetic effects on the applications as consequence of the coexistence of different functional groups (amino acid residues) within the same pore. Figure 1.47 show the MTV-MOF assembled from metalloligands derived from amino acids *L*-methionine and *L*-serine of formula, $\{Ca^{I}{}^{I}Cu^{II}{}_{6}[(S,S)\text{-methox}]_{1.43-1.46}(S,S)\text{-serimox}]_{1.57-1.54}(OH)_{2}(H_{2}O)\}\cdot 30H_{2}O$, which is able to capture dyes contaminants (PY, AO, BG and MB) and heavy metals (Hg^{2+}, T^{l+} y Pb^{2+} in a solution which contain too Cu^{2+}, Ni^{2+}, Ca^{2+}, Mg^{2+}, K^{+}, and Na^{+}) simultaneously.

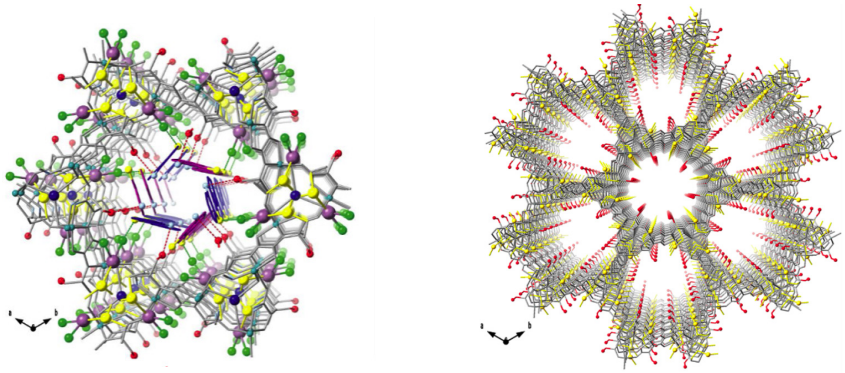

Figure 1.47. $\{Ca^{II}Cu^{II}{}_{6}[(S,S)\text{-methox}]_{1.43-1.46}$ $(S,S)\text{-serimox}]_{1.57-1.54}$ $(OH)_{2}(H_{2}O)\}$ $\cdot 30H_{2}O$ crystalline structure (left) and the same structure interacting with mercury and Methyl Blue dye (MB)$\cdot HgCl_{2}\{Ca^{II}Cu^{II}{}_{6}[(S,S)\text{-methox}]_{1.46}(S,S)\text{serimox}]_{1.54}$ $(OH)_{2}(H_{2}O)\}$ $\cdot 6H_{2}O[(MB)\cdot HgCl_{2}@2]$ (right).

Next, after having made a review of the knowledge that has led us to the completion of this thesis. We will continue in later chapters the analysis of the new compounds obtained after the PSM produced on the MOF

based on the aromatic ligand, discussed in this section 1.7, **Ni^{2+}@Cu-Ni-Me_3mpba** and the MOF based on the amino acid methylcysteine, **CuSr-Mecysmox**. Both will undergo PSM transmetalation, homo- and heterometallic cation exchange, and reduction. These processes will lead us to the stabilization of the MOF and the provision of catalytic activity through the incorporation of catalytically active metals. The reduction will take us one step further in terms of catalytic activity, developing systems that change their catalytic activity depending on their state of aggregation, from the so-called single crystal molecule (SAC) to the subNanometer Cluster (SNMC). Finally, a PSM that differs from the metallic PSM will be added: the insertion of ligands. These ligands will form molecular cages in the confined space of the MOF pores, which in its stable form does not present that structural stability during its catalysis of specific reactions.

1.8. References

1. H. Furukawa et al., Science 341, 1230444 (2013).

2. Moha med Eddaoudi, Jaheon Kim, Nathaniel Rosi, David Vodak, JosephWachter, Michael O'ÕKeeffe, Omar M. Yaghi. Science Vol 295 18 January 2002

3. Xuan Zhang, Zhijie Chen, Xinyao Liu, Sylvia L. Han na, Xingjie Wang, Reza Taheri-Ledari, Ali Maleki, Peng Li and Omar K. Farha. Chem. Soc. Rev., 2020, 49, 7406

4. Hong-Cai Zhou, Jeffrey R. Long, and Omar M. Yaghi. Chem. Rev. 2012, 112, 673−674

5. Jeffrey R. Longa and Omar M. Yaghi. Chem. Soc. Rev., 2009, 38, 1213–1214

6. Takaya Ogawa, Kenta Iyoki, Tomohiro Fukushima and Yuya Kajikawa. Materials 2017, 10, 1428; doi:10.3390/ma10121428.

7. Shuai Cao. Johnson Matthey Technol. Rev., 2015, 59, (2)

8. Do Yeon Heo, Ha Huu Do, Sang Hyun Ahn, and Soo Young Kim. Polymers 2020, 12(9), 2061

9. Eram Sharmin and Fahmina Zafar. Introductory Chapt er: Metal Organic Frameworks (MOFs). Reviewed: July 4th,

2016 Published: October 12 th, 2016.

10. Timothy A. Goetjen, Jian Liu, Yufang Wu, Jingyi Sui, Xuan Zhang, Joseph T. Hupp and Omar K. Farha. Chem. Com mun., 2020, 56, 10409.

11. Shan Dai, Antoine Tissot, and Christian Serre. Bull. Chem. Soc. Jpn. 2021, 94, 2623-2636.

12. Q. Fang, J. Sculley, H.-C.J. Zhou, G. Zhu, 5.01 - Po rous Metal–Organic Frameworks, Editor(s): David L. Andrews, Gre gory D. Scholes, Gary P. Wiederrecht, Compre hensive Nanoscience and Technology, Academic Press, 2011, Pages 1-20, ISBN 9780123743961.

13. W. A. Smeaton. Platinum Metals Rev., 1966, 10, (4), 140

14. G. B. Kauffman, Alfred Werner Founder of Coordina tion Theory, Springer, Berlin, 1966, 127 pp. G. B. Kauffman (ed.) Coordination Chemistry: A Century of Progress, ACS Symposium Series 565, Washington DC, 1994, 464.

15. N.N. Greenwood, A. Earnshaw. 19 - Coordination and Organometallic Compounds. Chemistry of the Ele ments (Second Edition), Butterworth-Heinemann, 1997, Pages 905-943, ISBN 9780750633659.

16. F. A. Cotton. Q. Rev. Chem. Soc., 1966,20, 389-401

17. W. H. Brock, K. A. Jensen, C. K. Jorgensen And G. B. Uljffman. Coordination and Organometallic Compounds. Am bix 27, 171-83 (1981).

18. James C. Earl, Louis Messerle. Organometallic Tri- and Polynuclear Clusters of Tantalum, Niobium and Group 6 and 7 Transition Metals. Reference Module in Chemistry, Molecular Sciences and Chemical Engineering. Elsevier, 2021

19. Hofmann, K. A.; Kuspert, F., "Verbindungen von Ko hlenwasserstoffen mit Metallsalzen," Z. Anorg. Alig. Chem. 1897, 15, 204-207.

20. Iwamoto, T., In Inclusion Compounds; 1. L. Atwood, 1. E. Davies and D. D. MacNicol Eds.; Academic Press Inc.: London, 1984; Vol. 1, pp. 29-57.

21. L. G. Donaruma, B. P. Block, K. L. Loening, N. Plate, T. Tsuruta, K. Ch. Buschbeck, W. H. Powell, J. Reedijk. Pure Appl. Chem., 1985, Vol. 57, No. 1, pp. 149-168.

22. Stuart R. Batten, Neil R. Champness, Xiao-Ming Chen, Javier Garcia-Martinez, Susumu Kitagawa, Lars Öhrström, Michael O'Keeffe, Myunghyun Paik Suh and Jan Reedijk. CrystEngComm, 2012, 14, 3001-3004.

23. H. J. Buser, D. Schwarzenbach, W. Petter, and A. Ludi. Inorg. Chem. 1977, 16, 11, 2704–2710

24. Piernas Muñoz, M., Castillo Martínez, E. (2018). Prus sian Blue and Its Analogues. Structure, Characterization and Applications. In: Prussian Blue Based Batteries. SpringerBrie fs in Applied Sciences and Technology. Springer, Cham. ISBN: 978-3-319-91487-9.

25. Alexander Kraft, Gesimat GmbH, Berlin. Bull. Hist. Chem., VOLUME 33, Number 2 (2008)

26. T. Iwamoto, T. Nakano, M. Morita, T. Miyoshi, T. Miya moto and Y. Sasaki. Inorganica Chimica Acta. Volume 2, March 1968, Pages 313-316.

27. H. G. Büttner and G. J. Kearley. Acta Cryst. (1994). B50, 431-435

28. Bunyarat Rungtaweevoranit, Christian S. Diercks, Mar kus J. Kalmutzkia and Omar M. Yaghi. Spiers Memorial Lec ture: Progress and prospects of reticular chemistry. Faraday Discuss., 2017, 201, 9.

29. J. H. Rayner and H. M. Powell. J. Chem. Soc., 1952, 319-328

30. Yukio Kinoshita, Ikuo Matsubara, Taiichi Higuciu and Yoshihiko Saito. The Crystal Structure of Bis(adiponitrilo) co pper(I) Nitrate. Vol. 32, No. 11, November, 1959.

31. Michael Jewess, Susan Lee-Bechtold and Lionel A. K.

Staveley. J.C.S. Faraday 11, 1980, 76, 803-811.

32. Reed M. Izatt. Alexander Schoedel and Omar M. Ya ghi. Porosity in Metal–Organic Compounds. Macrocyclic and Supramolecular Chemistry: How Izatt–Christensen Award Win ners Shaped the Field, First Edition. Ltd. Published 2016 by John Wiley & Sons, pg 200-219.

33. A. F. Wells. Acta Cryst. (1954). 7, 535-544

34. Structural Design and Properties of Coordination Poly mers. George E. Kostakis www.mdpi.com/journal/crystals Edi ted by Collected Articles from the Special Issue Published in Crystals. ISBN 978-3-03842-802-2 (PDF)

35. Jesse L.C. Rowsell, Omar M. Yaghi. Microporous and Mesoporous Materials 73 (2004) 3–14

36. Megumu Munakata, Liang Ping Wu, Mikiko Yamamo to, Takayoshi Kuroda-Sowa, Masahiko Maekawa, Satoshi Kawata and Susumu Kitagawa. J. Chem. Soc., Dalton Trans., 1995, 4099-4106

37. Zoi-Christina Kampouraki, Dimitrios A. Giannakouda kis, Vaishakh Nair, Ahmad Hosseini-Bandegharaei, Juan Car los Colmenares and Eleni A. Deliyanni. Molecules 2019, 24(24), 4525.

38. Makoto Fujita and Katsuyuki Ogura. Bull. Chem. Soc.

Jpn., 69. 1471-1482 (1996).

39. Pavel N. Gaponik, Sergei V. Voitekhovich, Alexander S. Lyakhov, Vadim E. Matulis, Oleg A. Ivashkevich, Manuel Quesada, JanReedijk. Inorganica Chimica Acta 358 (2005) 2549–2557.

40. Franco, C.H.J., Aglio, R.C., de Almeida, T.G. et al. J In org Organomet Polym 28, 978–989 (2018).

41. Stuart R. Batten, Neil R. Champness, Xiao-Ming Chen, Javier Garcia-Martinez, Susumu Kitagawa, Lars Öhrström, Michael O'Keeffe, Myunghyun Paik Suh and Jan Ree dijk. CrystEngComm, 2012, 14, 3001.

42. Andrea Schmidt, Angela Casini, Fritz E. Kühn. Coordi nation Chemistry Reviews 275 (2014) 19–36.

43. Lindley Maxwell, Héctor Martínez, Alejandro Mar tín-Rodríguez, Silvia Gómez-Coca, Kari Rissanen, and Eliseo Ruiz. Inorganic Chemistry 2021 60 (2), 570-573.

44. Maria J. Feio, Isabel Sousa, Mariana Ferreira, Luís Cun ha-Silva, Raúl G. Saraiva, Carla Queirós, José G. Alexandre, Vasco Claro, Adélia Mendes, Rosa Ortiz, Sandra Lopes, Ana Luísa Amaral, João Lino, Patrícia Fernandes, Ana João Silva, Lisete Moutinho, Baltazar de Castro, Eulália Pereira, Lourdes Perelló, Paula Gameiro. Journal of Inorganic Biochemistry 138 (2014) 129–143.

45. Yong-Quan Huang and Peng Cheng. Inorganic Chemist ry Communications 11 (2008) 66–68.

46. David S. Bell. The Promise of Metal–Organic Fra meworks for Use in Liquid Chromatography. LCGC North America (June 2018) Volume 36 Number 6.

47. Stuart R. Batten, Neil R. Champness, Xiao-Ming Chen, Javier Garcia-Martinez, Susumu Kitagawa, Lars Öhrström, Mi chael O'Keeffe, Myunghyun Paik Suh, and Jan Reedijk. Pure Appl. Chem., Vol. 85, No. 8, pp. 1715–1724, 2013.

48. Andrew R. Millward and Omar M. Yaghi. J. Am. Chem. Soc. 2005, 127, 51, 17998–17999.

49. Francisco G. Cirujano. Catal. Sci. Technol. 2017, 7. 5482

50. Zehan MaiZehan Mai and Dingxin Liu. Cryst. Growth Des. 2019, 19, 12, 7439–7462.

51. Pradip Pachfule, Chandan Dey, Tamas Panda and Ra hul Banerjee. CrystEngComm, 2010,12, 1600-1609

52. Binling Chen, Zhuxian Yang, Yanqiu Zhua and Yong de Xia. J. Mater. Chem. A, 2014,2, 16811-16831

53. Miriam de J. Velásquez-Hernández, Efwita Astria, Sa rah Winkler, Weibin Liang, Helmar Wiltsche, Arpita Poddar,

Ravi Shukla, Glenn Prestwich, John Paderi, Pablo Salce do-Abraira, Heinz Amenitsch, Patricia Horcajada, Christian J. Doonan and Paolo Falcaro. Chem. Sci., 2020, 11, 10835-10843.

54. Mohamed Eddaoudi, Dorina F. Sava, Jarrod F. Eubank, Karim Adil and Vincent Guillerm. Chem. Soc. Rev., 2015,44, 228-249.

55. Mitra Bahri, Fariborz Haghighat, Sohrab Rohani, Hos sein Kazemian. Chemical Engineering Journal, Volume 320, 2017, 308-318.

56. Kuen-Song Lin, Abhijit Krishna Adhikari, Chi-Nan Ku, Chao-Lung Chiang, Hua Kuo. International Journal of Hydro gen Energy, Volume 37, Issue 18, 2012, 13865-13871.

57. Mian Li, Dan Li, Michael O'Keeffe, and Omar M. Ya ghi. Chem. Rev. 2014, 114, 1343−1370

58. Chen, B.; Ockwig, N. W.; Millward, A. R.; Contreras, D. S.; Yaghi, O. Chem., Int. Ed. 2005, 44, 4745.

59. Baishu Zheng, Ruirui Yun, Junfeng Bai, Zhiyong Lu, Liting Du, and Yizhi Li. Inorg. Chem. 2013, 52, 6, 2823–2829.

60. Xiu-Li Yang, Ming-Hua Xie, Chao Zou, Yabing He, Banglin Chen, Michael O'Keeffe, and Chuan-De Wu. J. Am. Chem. Soc. 2012, 134, 25, 10638–10645

61. Gulzhian I. Dzhardimalieva and Igor E. Uflyand. RSC Adv.,2017,7, 42242.

62. Butova, V.V., Soldatov, M.A., Guda, A.A., Loma chenko, K.A, Lamberti, C. Russian Chem. Rev. 2016, 85, 280.

63. Atkins; et al. (2010). Química inorgánica de Shriver y Atkins(quinta ed.). Nueva York: WH Freeman and Company. ISBN 978-1-4292-1820-7.

64. Kamran Akhbaria, Ali Morsalia and Pascal Retailleau. Ultrasonics Sonochemistry. Volume 20, Issue 6, November 2013, Pages 1428-1435.

65. IBM T. J. Watson Research Center, P. O. Journal of So lid State Chemistry 145, 694}704 (1999)

66. Peter Klaus Sawinski and Richard Dronskowski. Inorg. Chem. 2012, 51, 13, 7425–7430.

67. Peng Liang, Wen-Xiu Xia, Wei-Man Tian and Xian-Hong Yin. Molecules 2013, 18, 14826-14839.

68. Coordination Polymers and Metal Organic Framewor ks: Properties, Types and Applications : Properties, Types and Applications, edited by Oscar L. Ortiz, and Luis D. Ramírez, Nova Science Publishers, Incorporated, 2011. ISBN 978-1-61470-913-8 (E-BOOK)

69. Xiang-Jing Kong, Jian-Rong Li, An Overview of Me tal–Organic Frameworks for Green Chemical Engineering, En gineering, Volume 7, Issue 8, 2021, Pages 1115-1139, ISSN 2095-8099.

70. Manuel Sánchez-Sánchez, Negash Getachew, Kenya Díaz, Manuel Díaz-García, Yonas Chebude and Isabel Díaz Green. Chem., 2015,17, 1500-1509

71. Yang Zhao, Zhongxin Song, Xia Li, Qian Sun, Niancai Cheng, Stephen Lawes, Xueliang Sun. Materials, Volume 2, 2016, 35-62.

72. Amin Hamed Mashhadzadeh, Ali Taghizadeh, Mohsen Taghizadeh, Muhammad Tajammal Munir, Sajjad Habibzadeh, Azam Salmankhani, Florian J. Stadler and Mohammad Reza Saeb. J. Compos. Sci. 2020, 4, 75.

73. Stephen Caddick, Richard Fitzmaurice, Tetrahedron, Volume 65, Issue 17, 2009, 3325-3355.

74. Farrukh Israr, Daye Chun, Yeongmin Kim, Duk Kyung Kim, Ultrasonics Sonochemistry, Volume 31, 2016, 93-101.

75. Sylwia Głowniak, Barbara Szczęśniak, Jerzy Choma, Mietek Jaroniec,Materials Today, Volume 46, 2021,109-124.

76. Wenting Shang, Xinchen Kang, Hui Ning, Jianling Zhang, Xiaogang Zhang, Zhonghua Wu, Guang Mo, Xueqing

Xing, and Buxing Han. Langmuir 2013, 29, 43, 13168–13174

77. Witri Wahyu Lestari, Marisa Adreane, Candra Pur nawan, Hamzah Fansuri, Nurul Widiastuti and Sentot Budi Ra hardjo. Mater. Sci. Eng. 107, 012030.

78. Michael P Batten, Marta Rubio-Martinez, Trevor Had ley,Keri-Constanti Carey, Kok-Seng Lim, Anastasios Polyzos and Matthew R Hill. Current Opinion in Chemical Engineering 2015, 8:55–59

79. Metal-Organic FrameworkS: Applications in Separa tions and Catalysis. Edited by Hermenegildo García and Sergio Navalón. Print ISBN: 978-3-527-34313-3.

80. Sherman, J.D. PNAS 1999, 96, 3471.

81. Takaya Ogawa, Kenta Iyoki, Tomohiro Fukushima, and Yuya Kajikawa. Review: Materials 2017, 10, 1428.

82. Hwang, Y.K., Chang, J.-S., Seo, Y.-K., and Hwang, D.W. (2013) Porous organic–inorganic hybrid materials with crystallinity and method for preparing thereof. US Patent US008507399B2.

83. Book Title: Zeolites and Metal-Organic Frameworks. From lab to industry. Book Editor(s): Vincent Blay, Luis F. Bo badilla, Alejandro Cabrera García. Published by: Amsterdam

University Press. (2018). ISBN: 978 94 6298 556 8.
84. Sérgio M. F. Vilela, Ricardo F. Mendes, Patrícia Silva, José A. Fernandes, João P. C. Tomé, and Filipe A. Almeida Paz. Cryst. Growth Des. 2013, 13, 2, 543–560

85. Book Title: Zeolites and Metal-Organic Frameworks. From lab to industry. Book Editor(s): Vincent Blay, Luis F. Bo badilla, Alejandro Cabrera García. Published by: Amsterdam University Press. (2018). ISBN: 978 94 6298 556 8.

86. Linjian Zhang, Fangqin Liand and Liangfei Luo. Earth Environ. Sci. 108 042104

87. Metal-Organic FrameworkS: Applications in Separa tions and Catalysis. Edited by Hermenegildo García and Sergio Navalón. Print ISBN: 978-3-527-34313-3.

88. Nicolò Campagnol, Tom Van Assche, Tom Boudewijns, Joeri Denayer, Koen Binnemans, Dirk De Vos and Jan Fran saer. J. Mater. Chem. A, 2013,1, 5827-5830

89. Millange, F., Serre, C., and Férey, G. (2002) Chem. Commun., 822–823.

90. Férey, G., Serre, C., Mello-Draznieks, C., Millange, F., Surblé, S., Dutour, J., and Margiolaki, I. (2004) Angew. Chem. Int. Ed., 43, 6296–6301.

91. Prashant L. Suryawanshi, Shirish H. Sonawane, Bharat

A. Bhanvase, Muthupandian Ashokkumar, Makarand S. Pim plapure and Parag R. Gogate. Green Process Synth 2018; 7: 1–11

92. Peter A. Bayliss, Ilich A. Ibarra, Eduardo Pérez, Si hai Yang, Chiu C. Tang, Martyn Poliakoff and Martin Schröder. Green Process Synth 2018; 7: 1–11.

93. Colin McKinstry, Edmund J. Cussen, Ashleigh J. Flet cher, Siddharth V. Patwardhan, Jan Sefcik. Chemical Enginee ring Journal, Volume 326, 2017, 570-577.

94. Rubio-Martinez, M., Batten, M., Polyzos, A. et al. Sci Rep 4, 5443 (2014).

95. Colin McKinstry, Edmund J. Cussen, Ashleigh J. Flet cher, Siddharth V. Patwardhan, Jan Sefcik. Chemical Enginee ring Journal, Volume 326, 2017, 570-577.

96. Inokuma, Y.; Yoshioka, S.; Ariyoshi, J.; Arai, T.; Hito ra, Y.; Takada, K.; Matsunaga, S.; Rissanen, K.; Fujita. Nature 2013, 495, 461−466.

97. Bloch, W. M.; Champness, N. R.; Doonan, C. J. An gew. Chem., Int. Ed. 2015, 54, 12860−12867.

98. Mon, M.; Bruno, R.; Ferrando-Soria, J.; Bartella, L.; Di Donna, L.; Talia, M.; Lappano, R.; Maggiolini, M.; Armen tano, D.; Pardo, E. Mater. Horiz. 2018, 5, 683−690.

99. K. S. W. Sing, D. H. Everett, R. A. W. Haul, L. Mos cou, R. A. Pieroti, J. Rouquerol, T. Siemieniewska. Pure Appl. Chem. 57, (1985).

100 .J. Rouquerol, F. Rouquerol, K. S. W. Sing, P. Llewellyn, G. Maurin. Adsorption by Powders and Porous Solids: Princi ples, Methodology and Applications, Academic Press (2014).

101. P. A Monson. Microporous Mesoporous Mater. 160, 47 (2012).

102 .K. Vasanth Kumar, Srinivas Gadipelli, Barbara Wood, Ki ran A. Ramisetty, Andrew A. Stewart, Christopher A. Howard, Dan J. L. Brett and F. Rodriguez-Reinoso. J. Mater. Chem. A, 2019, 7, 10104–10137.

103. M. Thommes, K. Kaneko, A. V Neimark, J. P. Olivier,F. Rodriguez-Reinoso, J. Rouquerol and K. S. W. Sing. Pure Appl. Chem., 2015,87(9–10), 1051–1069.

104. K. Vasanth Kumar, Srinivas Gadipelli, Barbara Wood, Ki ran A. Ramisetty, Andrew A. Stewart, Christopher A. Howard, Dan J. L. Brett and F. Rodriguez-Reinoso. J. Mater. Chem. A, 2019, 7, 10104–10137.

105. Hiroshi Kajiro, Atsushi Kondo 2, Katsumi Kaneko and Hirofumi Kanoh. Int. J. Mol. Sci. 2010, 11, 3803-3845

106. Hailian Li, Mohamed Eddaoudi, Thomas L. Groy, andO.

M. Yaghi. J. Am. Chem. Soc. 1998, 120, 8571-8572

107. Horike, S., Shimomura, S. & Kitagawa, S. Soft porous crystals. Nature Chem 1, 695–704 (2009).

108. Evans, J.D., Bon, V., Senkovska, I. et al. Four-dimen sional metal-organic frameworks. Nat Commun 11, 2690 (2020).

109. Wang, Z.; Cohen, S. M. Chem. Soc. Rev. 2009, 38, 1315.

110. Cohen, S. M. Chem. Rev. 2012, 112, 970.

111. Cohen, S. M. J. Am. Chem. Soc. 2017, 139, 2855.

112. Susumu Kitagawa and Kazuhiro Uemura. Chem. Soc. Rev., 2005,34,109–119

113. Kitagawa, S. New Dimensions of Porous Coordination Polymers/Metal-Organic Frameworks. Presented at the 43rd In ternational Conference on Coordination Chemistry, Sendai, Ja pan, July 30−August 4, 2018; Abstract A00584-SK.

114. Jiewei Liu, Lianfen Chen, Hao Cui, Jianyong Zhang, Li Zhang and Cheng-Yong Su. Chem.Soc.Rev.,2014,43,6011

115. Shi-Yuan Zhang, Stephanie Jensen, Kui Tan, Lukasz Woj tas, Matthew Roveto, Jeremy Cure, Timo Thonhauser, Yves J. Chabal, and Michael J. Zaworotko. J. Am. Chem. Soc. 2018,

140, 12545−12552.

116. Mohamed Eddaoudi, Jaheon Kim, Nathaniel Rosi, David Vodak, Joseph Wachter, Michael O'Keeffe and Omar M. Ya ghi. Science , 18 Jan 2002, Vol 295, Issue 5554. pp. 469-472.

117. Nobuhiko Hosono, Takashi Uemura. Matter, Volume 3, Is sue 3, 2020, 652-663.

118. Jaison Jeevanandam, Ahmed Barhoum, Yen S Chan, Alain Dufresne, and Michael K Danquah. Beilstein J Nanotechnol. 2018; 9: 1050–1074.

119. R.G. Pearson, J Am Chem Soc 85 (1963) 3533–3539.

120. P.W. Ayers, R.G. Parr, R.G. Pearson, J Chem Phys 124 (2006).

121. R.G. Pearson, Cc/Eng Tech Appl Sci (1986) 18 18.

122. R.G. Pearson, Inorg. Chim. Acta 240 (1995) 93–98.

123. R.G. Pearson, Chemical hardness, Wiley-VCH, 1997.

124. K. Fukui, Theory of orientation and stereoselection, in: Orientation and Stereoselection, Springer, 1970, pp. 1-85.

125. R. Kostyk, M. Whitehead, J. Mol. Struct. (Thoechem) 230 (1991) 83–125.

126. G Klopman. Chemical reactivity and reaction paths. Edi tor Wiley-interscience, 1974.

127. P. Chattaraj, D. Roy, M. Elango, V. Subramanian, The Journal of Physical Chemistry A 109 (2005) 9590–9597.

128. J.-I. Aihara, The Journal of Physical Chemistry A 103 (1999) 7487–7495.

129. Considerations for the Specification of Enzyme Assa ys Involving Metal Ions Richard Cammack1 and Martin N. Hu ghes. ESCEC, September 23rd – 26th, 2007, Rü desheim/Rhein, Germany.

130. Aliyu M. Hamisua, Azhar Ariffina, Arief C. Wibowob. Inorganica Chimica Acta 511 (2020) 119801.

131 .Sukhendu Mandal, Srinivasan Natarajan, Prabu Mani, and Asha Pankajakshan. Adv. Funct. Mater. 2021, 31, 2006291.

132. Sukhendu Mandal, Srinivasan Natarajan, Prabu Mani, and Asha Pankajakshan. Adv. Funct. Mater. 2021, 31, 2006291.

133. Housecroft, C. and Sharpe, A.G. (2007) Inorganic Che mistry. Prentice Hall, New Jersey

134.P. Deria, J. E. Mondloch, O. Karagiaridi, W. Bury, J. T. Hupp, O. K. Farha, Chem. Soc. Rev. 2014, 43, 5896

135 .Sukhendu Mandal, Srinivasan Natarajan, Prabu Mani, and Asha Pankajakshan. Adv. Funct. Mater. 2021, 31, 2006291.

136. Zhenqiang Wang and Seth M. Cohen. Chem. Soc. Rev., 2009, 38, 1 3 1 5 ~ 1329.

137. Mark Kalaj and Seth M. Cohen. ACS Cent. Sci. 2020, 6, 1046−1057

138. Joshua D. Sosa, Timothy F. Bennett, Katherine J. Nelm sO , Brandon M. LiuO , Roberto C. Tovar and Yangyang Liu. Crystals 2018,8, 325; doi:10.3390/cryst8080325

139. Kristine K. Tanabea and Seth M. Cohen. Chem. Soc. Rev., 2011,40, 498-519

140. Adeel H. Chughtai, Nazir Ahmad, Hussein A. Younus, A. Laypkov

141. Francis Verpoort. Chem. Soc. Rev., 2015, 44, 6804—6849.

142. Seth M. Cohen. Chem. Rev. 2012, 112, 970–1000.

143. Pravas Deria, Joseph E. Mondloch, Olga Karagiaridi, Wojciech Bury

144 .Jie Li, Wenling Ye, Changlun Chen. Chapter 5 - Removal of toxic/radioactive metal ions by metal-organic framework-ba sed materials. Interface Science and Technology, Elsevier,

Volume 29, 2019, Pages 217-279, ISSN 1573-4285, ISBN 9780081027271.

145. K. S. Asha, R. Bhattacharjee, S. Mandal, Angew. Chem., Int. Ed. 2016, 55, 11528.

146. J. H. Wang, Y. Zhang, M. Li, S. Yan, D. Li, X. M. Zhang, Angew. Chem., Int. Ed. 2017, 56, 6478.

147. L. L. Lv, J. Yang, H. M. Zhang, Y. Y. Liu, J. F. Ma, Inorg. Chem. 2015, 54, 1744.

148 .Jun-Hao Wang, Ying Zhang, Mian Li,Shu Yan, Dan Li,. Xian-Ming Zhang. Angewandte chemie international Edition Volume56, Issue23 June 1, 2017 Pages 6478-6482

149. L. Li, H. Xue, Y. Wang, P. Zhao, D. Zhu, M. Jiang, X. Zhao, ACS. Appl. Mater. Interfaces 2015, 7, 25402.

150. S. Yuan, Y. P. Chen, J. Qin, W. Lu, X. Wang, Q. Zhang, M. Bosch, T. F. Liu, X. Lian, H. C. Zhou, Angew. Chem., Int. Ed. 2015, 54, 14696.

151. H. Zhang, J. Wei, J. Dong, G. Liu, L. Shi, P. An, G. Zhao, J. Kong, X. Wang, X. Meng, J. Zhang, J. Ye, Angew. Chem., Int. Ed. 2016, 55, 14310.

152. T. F. Liu, L. Zou, D. Feng, Y. P. Chen, S. Fordham, X. Wang, Y. Liu, H. C. Zhou, J. Am. Chem. Soc. 2014, 136, 7813.

153. W. H. Yin, Y. Y. Xiong, H. Q. Wu, Y. Tao, L. X. Yang, J. Qiang Li, X. L. Tong, F. Luo, Inorg. Chem. 2018, 57, 8722.

154. T. C. Wang, I. Hod, C. O. Audu, N. A. Vermeulen, S. T. Nguyen, O. K. Farha, J. T. Hupp, ACS Appl. Mater. Interfaces 2017, 9, 12584

.

155. Marta Viciano-Chumillas, Xiangyu Liu, Antonio Ley va-Pérez, Donatella Armentano, Jesús Ferrando-So ria and Emilio Pardo. Coordination Chemistry Reviews, Volu me 451, 2022, 214273, ISSN 0010-8545

156. Maniya Gharib, Leili Esrafili, Ali Morsali and Pascal Re tailleau. Dalton Trans., 2019,48, 8803-8814

157. S. J. D. Smith, K. Konstas, C. H. Lau, Y. M. Gozukara, C.D. Easton, R. J. Mulder, B. P. Ladewig, M. R. Hill, Cryst. Grow th Des. 2017, 17, 4384.

158. S. Dissegna, K. Epp, W. R. Heinz, G. Kieslich, R. A. Fis cher, Adv. Mater. 2018, 30, 1704501.

159. Vincent Guillerm, Heng Xu, Jorge Albalad, Inhar Imaz, and Daniel Maspoch. J. Am. Chem. Soc. 2018, 140, 44, 15022–15030

160. Qian-Rong Fang, Da-Qian Yuan, Julian Sculley, Jian-Rong Li, Zheng-Bo Han, Hong-Cai Zhou. Inorg Chem. 2010 Dec 20;49(24):11637-42. doi: 10.1021/ic101935f. Epub 2010

Nov 17.

161. Shuliang Yang, Vikram V. Karve, Anita Justin, Ilia Koche tygov, Jordi Espín, Mehrdad Asgari, Olga Trukhina, Daniel T. Sun, Li Peng, Wendy L. Queen. Coordination Chemistry Re views 427 (2021) 213525.

162. V. J. Pastore, T. R. Cook, J. Rzayev, Chem. Mater. 2018, 30, 8639.

163. B. Tu, Q. Pang, D. Wu, Y. Song, L. Weng, Q. Li, J. Am. Chem. Soc. 2014, 136, 14465.

164. Shuliang Yang, Vikram V. Karve, Anita Justin, Ilia Koche tygov, Jordi Espín, Mehrdad Asgari. Coordination Chemistry Reviews 427 (2021) 213525.

165. Olga Trukhina a, Daniel T. Sun a, Li Peng b, Wendy L. Queen, Li, P.; Vermeulen, N. A.; Malliakas, C. D.; Gómez-Gual drón, D. A.; Howarth, A. J.; Mehdi, B. L.; Do hnalkova, A.; Browning, N. D.; O'Keeffe, M.; Farha, O. K. Science 2017, 356, 624− 627.

166. Kim, H.; Yang, S.; Rao, S. R.; Narayanan, S.; Kapustin, E. A.; Furukawa, H.; Umans, A. S.; Yaghi, O. M.; Wang, E. N. Science 2017, 356, 430−434.

167 .Reed, D. A.; Keitz, B. K.; Oktawiec, J.; Mason, J. A.; Runčevski, T.; Xiao, D. J.; Darago, L. E.; Crocellà, V.; Bordi

ga, S.; Long, J. R. Nature 2017, 550, 96−100.

168 .Shen, K.; Zhang, L.; Chen, X.; Liu, L.; Zhang, D.; Han, Y.; Chen, J.; Long, J.; Luque, R.; Li, Y.; Chen, B. Science 2018, 359, 206−210.

169. Cadiau, A.; Adil, K.; Bhatt, P. H.; Belmabkhout, Y.; Ed daoudi, M. Science 2016, 353, 137−140.

170. Li, H.; Wang, K.; Sun, Y.; Lollar, C.; Li, J.; Zhou, H.-C. Mater. Today 2018, 21, 108−121.

171. Belmabkhout, Y.; Bhatt, P. M.; Adil, K.; Pillai, R. S.; Ca diau, A.; Shkurenko, A.; Maurin, G.; Liu, G.; Koros, W. J.; Ed daoudi, M. Nat. Energy 2018, 3, 1059−1066.

172 Zhang, X.; Huang, Z.; Ferrandon, M.; Yang, D.; Robison, L.; Li, P.; Wang, T. C.; Delferro, M.; Farha, O. K. Nat. Catal. 2018, 1, 356−362.

173. Li, W.; Sun, L.; Qi, J.; Jarillo-Herrero, P.; Dincă, M.; Li, J. Chem. Sci. 2017, 8, 2859−2867.

174. Pedersen, K. S.; Perlepe, P.; Aubrey, M. L.; Woodruff, D. N.; Reyes-Lillo, S. E.; Reinholdt, A.; Voigt, L.; Li, Z.; Bo rup, K.; Rouzières, M.; Samohvalov, D.; Wilhelm, F.; Roga lev, A.; Neaton, J. B.; Long, J. R.; Clérac, R. Nat. Chem. 2018, 10, 1056−1061.

175. Y. Inokuma, M. Kawano and M. Fujita, Nat. Chem., 2011, 3 (5), 349–358.

176. M. Mon, X. Qu, J. Ferrando-Soria, I. Pellicer-Carreño, A. Sepúlveda-Escribano, E. V. Ramos-Fernandez, J. C. Jansen, D. Armentano and E. Pardo, J. Mater. Chem. A, 2017, 5, 20120–20125.

177. M. Mon, R. Bruno, J. Ferrando-Soria, L. Bartella, L. Di Donna, M. Talia, R. Lappano, M. Maggiolini, D. Armenta no and E. Pardo, Materials Horizons, 2018, DOI: 10.1039/C8MH00302E.

178. R. J. Drout, K. Otake, A. J. Howarth, T. Islamoglu, L. Zhu, C. Xiao, S. Wang, O. K. Farha, Chem. Mater., 2018, 30, 1277-1284.

179. Kobielska, P. A.; Howarth, A. J.; Farha, O. K.; Nayak, S. Metalorganic frameworks for heavy metal removal from water. Coord. Chem. Rev. 2018, 358, 92−107.

180. Mon, M.; Bruno, R.; Ferrando-Soria, J.; Armentano, D.; Pardo, E. Metal-organic framework technologies for water re mediation: towards a sustainable ecosystem. J. Mater. Chem. A 2018, 6, 4912− 4947.

181. Susumu Kitagawa, Ryo Kitaura, Shin-ichiro Noro. An gew. Chem. Int. Ed. 2004, 43, 2334 –2375.

182 .Pang, J.; Yuan, S.; Qin, J.; Wu, M.; Lollar, C. T.; Li, J.; Huang, N.; Li, B.; Zhang, P.; Zhou, H.-C. Enhancing Pore-En vironment Complexity Using a Trapezoidal Linker: Toward Stepwise Assembly of Multivariate Quinary Metal-Organic Frameworks. J. Am. Chem. Soc. 2018, 140, 12328−12332.

183. Guillerm, V.; Grancha, T.; Imaz, I.; Juanhuix, J.; Mas poch, D. Zigzag ligands for Transversal Design in Reticular Chemistry: Unveiling New Structural Opportunities for Me tal-Organic Frameworks. J. Am. Chem. Soc. 2018, 140, 10153−10157.

184. T. Grancha, M. Mon, J. Ferrando-Soria, J. Gascon, B. Seoane, E. V. Ramos-Fernandez, D. Armentano and E. Pardo, J. Mater. Chem. A, 2017, 5, 11032–11039.

185. L. H. Wee, M. Meledina, S. Turner, G. Van Tendeloo, K. Zhang, L. M. Rodriguez-Albelo, A. Masala, S. Bordiga, J. Jiang, J. A. R. Navarro, C. E. A. Kirschhock and J. A. Martens, J. Am. Chem. Soc., 2017, 139 (2), 819–828.

186. S. Yang, X. Lin, W. Lewis, M. Suyetin, E. Bichoutskaia, J. E. Parker, C. C. Tang, D. R. Allan, P. J. Rizkallah, P. Hub berstey, N. R. Champness, K. Mark Thomas, A. J. Blake and M. Schröder, Nat. Mater., 2013, 11, 710–716.

187. N. S. Bobbitt, M. L. Mendonca, A. J. Howarth, T. Isla moglu, J. T. Hupp, O. K. Farha, R. Q. Snurr, Chem. Soc. Rev., 2017, 46, 3357-3385.

188. F. Luo, C. Yuan, L. Dang, R. Krishna, W. Zhou, H. Wu, X. Dong, Y. Han, T. L. Hu, M. O'Keeffe, L. Wang, M. Luo, R.-B. Lin and B. Chen, J. Am. Chem. Soc., 2016, 138, 5678–5684.

189. E. López-Maya, C. Montoro, L. M. Rodriguez-Albelo, S. D. Aznar Cervantes, A. A. Lozano-Pérez, J. L. Cenís, E. Ba rea and J. A. R. Navarro, Angew. Chem., Int. Ed., 2015, 54, 6790–6794.

190 .Hakan Demir, Gokhan Onder Aksu, Hasan Can Gul balkan, Seda Keskin. Carbon Capture Science & Technology. Volume 2, March 2022, 100026

191.Simon-Yarza, T.; Giménez-Marqués, M.; Mrimi, R.; Miel carek, A.; Gref, R.; Horcajada, P.; Serre, C.; Couvreur, P. A Smart Metal- Organic Framework Nanomaterial for Lung Tar geting. Angew. Chem., Int. Ed. 2017, 56, 15565−15569.

192.Dong, Z.; Sun, Y.; Chu, J.; Zhang, X.; Deng, H. Multivaria te Metal-Organic Frameworks for Dialing-in the Binding and Programming the Release of Drug Molecules. J. Am. Chem. Soc. 2017, 139, 14209−14216.

193.Patricia Horcajada, Christian Serre, María Vallet-Regí, Mu riel Sebban, Francis Taulelle and Gérard Férey. Angewandte Chemie International Edition. Volume45, Issue36. September 11, 2006. Pages 5974-5978.

194. Fatma Demir Duman and Ross S. Forgan. J. Mater. Chem. B, 2021, 9, 3423-3449

195. Mohammad A Chowdhury. ChemBioEng Reviews 4(4):225–239

196. L. Shang, S. Dong and G. U. Nienhaus, Nano Today, 2011, 6, 401–418.

197. Yuanqiang Hao, Shu Chen,Yanli Zhou,,Yintang Zhang and Maotian Xu. Nanomaterials 2019, 9, 974; doi:10.3390/nano9070974.

198. Guillermo Mínguez Espallargas and Eugenio Coronado. Chem. Soc. Rev., 2018,47, 533-557.

199. Yun-Qi Tian, Chen-Xin Cai, Xiao-Ming Ren, Chun-Ying Duan, Yan Xu, Song Gao, and Xiao-Zeng You. Chem. Eur. J.2003,9, 5673-5685.

200. Lucía Piñeiro-López, Maksym Seredyuk, M. Carmen Mu ñoz, José A. Real. Eur. J. Inorg. Chem.2020, 764–769.

201. Julia Vallejo, Isabel Castro, Rafael Ruiz-García, Joan Cano, Miguel Julve, Francesc Lloret, Giovanni De Munno, Wolfgang Wernsdorfer, and Emilio Pardo. J. Am. Chem. Soc. 2012, 134, 38, 15704–15707.

202. Tongxin Liu, Zhenjun Fan, Zhenyu Mi, Weijun Du, Xiao

hui Song, Rongzhao Liu, Haocheng Wang, Yanjing Du. Jour nal of Solid State Chemistry, Volume 305, 2022, 122697, ISSN 0022-4596.

203. Christophe Copéret, Aleix Comas-Vives, Matthew P. Con ley, Deven P. Estes, Alexey Fedorov, Victor Mougel, Haruki Nagae, Francisco Núñez-Zarur, and Pavel A. Zhizhko. Chemic al Reviews 2016, 116 (2), 323-421.

204 .Ben S. Pilgrim and Neil R. Champness. Chem Plus Chem 2020, 85, 1842–1856.

205. Shikha Gulati. Metal-Organic Frameworks (MOFs) as Ca talysts. Buch Hardcover, 789 Seiten, 2022. 1st ed. 2022, Sprin ger Verlag, Singapore, 978-981-16-7958-2 (ISBN)

206. Vlad Pascanu, Greco González Miera, A. Ken Inge, and Belén Martín-Matute. J. Am. Chem. Soc. 2019, 141, 18, 7223-7234.

207 .Hiroyasu Furukawa, Kyle E. Cordova, Michael O'Kee ffe, Omar M. Yaghi. Science 341, 1230444 (2013).

208. Francisco Ramón Fortea-Pérez, Isabel Schlegel, Miguel Julve, Donatella Armentano, Giovanni De Munno, Salah-Eddi ne Stiriba. Journal of Organometallic Chemistry, Volume 743, 2013, Pages 102-108, ISSN 0022-328X.

209 .Emilio Pardo, Rafael Ruiz-García, Joan Cano, Xavier

Ottenwaelder, Rodrigue Lescouëzec, Yves Journaux, Fran cesc Lloret and Miguel Julve. Dalton Trans., 2008, 2780-2805.

210. Marie-Claire Dul, Emilio Pardo, Rodrigue Lescouëzec, Yves Journaux, Jesús Ferrando-Soria, Rafael Ruiz-García, Joan Cano, Miguel Julve, Francesc Lloret, Danielle Cangus su, Cynthia L.M. Pereira, Humberto O. Stumpf, Jorge Pasán, Catalina Ruiz-Pérez. Coordination Chemistry Reviews, Volu me 254, Issues 19–20, 2010, 2281-2296.

211. Yu. Pei, Olivier. Kahn, and Jorunn. Sletten. J. Am. Chem. Soc. 1986, 108, 11, 3143–3145

212. Kiyoko Nonoyama, Heijiro Ojima, Matsuo Nonoyama. Inorganica Chimica Acta, Volume 20, 1976,127-132.

213. Ferrando-Soria, J.; Pasán, J.; Ruiz-Pérez, C.; Journaux, Y.; Julve, M.; Lloret, F.; Cano, J.; Pardo, E. Inorg. Chem. 2011, 50, 8694−8696.

214. Ferrando-Soria, J.; Grancha, T.; Julve, M.; Cano, J.; Llo ret, F.; Journaux, Y.; Pasán, J.; Ruiz-Pérez, C.; Pardo, E. Chem. Commun. 2012, 48, 3539−3541.

215. Grancha, T.; Mon, M.; Lloret, F.; Ferrando-Soria, J.; Jour naux, Y.; Pasán, J.; Pardo, E. Inorg. Chem. 2015, 54, 8890−8892.

216. Grancha, T.; Qu, X.; Julve, M.; Ferrando-Soria, J.; Armen tano, D.; Pardo, E. Inorg. Chem. 2017, 56, 6551−6557.

217. Jesús Ferrando-Soria, Thais Grancha, Miguel Julve, Joan Cano, Francesc Lloret, Yves Journaux, Jorge Pasán, Catali na Ruiz-Pérez and Emilio Pardo. Chem. Commun., 2012, 48, 3539–3541.

218. Jesús Ferrando-Soria, Rafael Ruiz-García, Joan Cano, Sa lah Eddine Stiriba [Julia Vallejo/ Isabel Castro] Miguel Julve, Francesc Lloret, [Pedro Amorós/ Jorge Pasán/ Catalina Ruiz-Pérez, Y ves Journaux,, and Emilio Pardo]. Chem. Eur. J. 2012, 18, 1608- 1617

219. Lucas H. G. Kalinke, Renato Rabelo, Ana K. Valdo, Feli pe T. Martins, Nicolás Moliner, Jesus Ferrando-Soria, Mi guel Julve, Francesc Lloret, Joan Cano, and Danielle Cangus su. Inorganic Chemistry 2022 61 (15), 5696-5700.

220. Thais Graneha, Jesús Ferrando-Soria, Hong-Cai Zhou, Jorge Gasean, Beatriz Seoane, Jorge Pasán, Osear Fabelo, Mi guel Julve, and Emilio Pardo. Angew. Chem. lnt. Ed. 2015, 54, 6521 – 6525.

221. Sukhendu Mandal, Srinivasan Natarajan, Prabu Mani, and Asha Pankajakshan. Adv. Funct. Mater. 2021, 31, 2006291.

222. Joshua D. Sosa, Timothy F. Bennett, Katherine J. Nelm sO , Brandon M. LiuO , Roberto C. Tovar and Yangyang Liu. Crystals 2018,8, 325; doi:10.3390/cryst8080325

223. Kristine K. Tanabea and Seth M. Cohen. Chem. Soc. Rev., 2011,40, 498-519

224. Adeel H. Chughtai, Nazir Ahmad, Hussein A. Younus, A. Laypkov and Francis Verpoort. Chem. Soc. Rev., 2015, 44, 6804—6849.

225. Seth M. Cohen. Chem. Rev. 2012, 112, 970–1000.

226. Pravas Deria, Joseph E. Mondloch, Olga Karagiaridi, Wojciech Bury,Joseph T. Hupp and Omar K. Farha. Chem. Soc. Rev., 2014, 43, 5896

227. Grancha, T.; Ferrando-Soria, J.; Zhou, H.-C.; Gascon, J.; Seoane, B.; Pasán, J.; Fabelo, O.; Julve, M.; Pardo, E. Angew. Chemie Int. Ed. 2015, 54 (22), 6521–6525.

228. Thais Grancha, Jesús Ferrando-Soria, Hong-Cai Zhou, Jorge Gascon, Beatriz Seoane, Jorge Pasán, Oscar Fabelo, Mi guel Julve, and Emilio Pardo. Angew. Chem. Int. Ed. 2015, 54, 6521 –6525.

229. Marta Viciano-Chumillas, Marta Mon, Jesus Ferrando-So ria, Avelino Corma, Antonio Leyva-Pérez, Donatella Armenta no, and Emilio Pardo. Acc. Chem. Res. 2020, 53, 2, 520–531.

CHAPTER

2

2.1. Introduction

After the information provided in the general introduction (chapter 1), it can be anticipated that in this thesis we will work with MOFs based on oxamato- and/or oxamidato-based copper(II) secondary building units (SBUs) bound to divalent metals giving rise to robust and crystalline structures with ordered pores decorated by functional groups. The robustness and crystallinity make them suitable candidates to resist the consecutive application of different post-synthetic methods (PSMs), to acquire novel functionalities, without losing their crystallinity and integrity. In the general introduction, I have showed several examples describing this methodology. In particular, the MOF with formula $Mg^{II}_2\{Mg^{II}_4[Cu^{II}_2(Me_3mpba)_2]_3\} \cdot 45\ H_2O$ **(Mg^{2+}@CuNi-Me_3mpba)**, is a very illustrative example. This MOF –possessing Mg^{II} cations in both the heterometallic anionic $Cu_6Mg_4^{4-}$ framework and also hosted in its channels– experiences a double and simultaneous PS processes consisting on a cation exchange of Mg^{II} cations located in the pores by Ni^{II} ones and also a transmetalation of the network, resulting in the total substitution of Mg^{II} cations and giving rise to the final novel material with formula $Ni^{II}_2\{Ni^{II}_4[CuII_2(Me_3mpba)_2]_3\}\cdot 54H_2O$ **(Ni^{2+}@Cu-Ni-Me_3mpba).**

2.1.1. Common PSM in MOFs

2.1.1.1 Cation exchange

In this subsection of this introduction, I will focus on describing the most common PSM[1-3] in MOFs, which is the cation exchange[4] of me-

tal cations situated within their pores. In particular, I have selected a quite recent work, in which we reported a solid-state single-crystal to single-crystal (SC to SC) cation-exchange of the nickel(II) cations in **Ni^{2+}@CuNi-Me_3mpba**[5] (see above) with barium(II) cations to afford a novel heterotrimetallic **Ba^{2+}@CuNi-Me_3mpba** and increase our knowledge on these processes. This PS process consisted in suspending **Ni^{2+}@CuNi-Me_3mpba** on a saturated aqueous solution of $Ba(NO_3)_2$ for 48h (for both crystal and powder MOFs) in order to obtain the MOF $[Ba^{II}(H_2O)_4][Ba^{II}(H_2O)_5]\{Ni^{II}_4[Cu^{II}_2(Me_3mpba)_2]_3\} \cdot 58H_2O$ **(Ba^{2+}@CuNi-Me_3mpba)**, which is highly performant in the capture of SO_2 from the air.

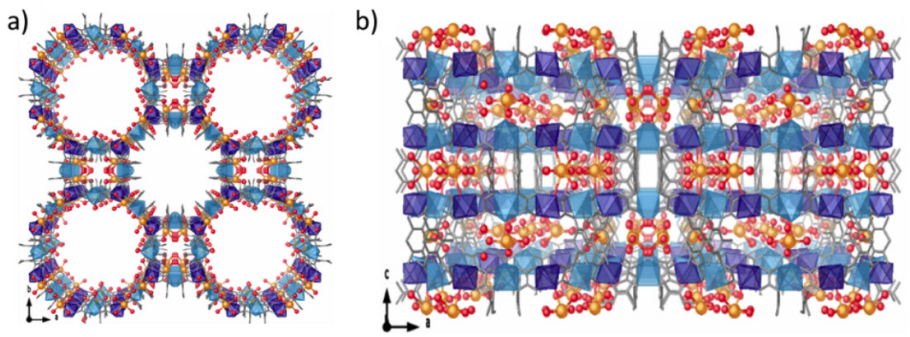

Figure. 2.1. Perspective view of the 3D anionic network of **Ba^{2+}@CuNi-Me_3mpba** along the crystallographic *c* (a) and *b* (b) axis showing the pillared square/octagonal layer architecture and the site occupation of the channels by the Ba^{II} countercations. Copper and nickel atoms from the covalent network are represented by cyan and blue polyhedra, respectively, whereas barium atoms occupying the channels are depicted as orange spheres, respectively. The coordinated water molecules are depicted as red spheres whereas the free H_2O molecules are omitted for clarify.[6]

The crystal structure of **Ba^{2+}@CuNi-Me_3mpba** could be determined by single-crystal X-ray diffraction and could be compared to the previously reported **Ni^{2+}@CuNi-Me_3mpba**. Both **Ni^{2+}@CuNi-Me_3mpba** and **Ba^{2+}@CuNi-Me_3mpba** are isomorphous and crystallize in the *P*4/

mmm space group. **Ba^{2+}@CuNi-Me_3mpba** exhibited a pillared oxamato-bridged $Ni^{II}_4Cu^{II}_6$ square/octagonal layer architecture growing in the *ab* plane, whose layers are interconnected through the two trimethyl substituted *m*-phenylene spacers constituting the Cu^{II} SBUs. This structure exhibits hydrated BaII counterions occupying the channels together with crystallization water molecules (Figures 2.1 and 2). It features three types of pores propagating along the *c* axis: Square-shaped small pores with a virtual diameter of *ca* 0.4 nm and two octagonal-like large pores of ca. 1.5 and 2.2 nm, respectively (Figure 2.1a). Ba^{II} cations are situated in the smaller ones and also in the larger octagonal ones, being the former the only ones accessible for gas adsorption.

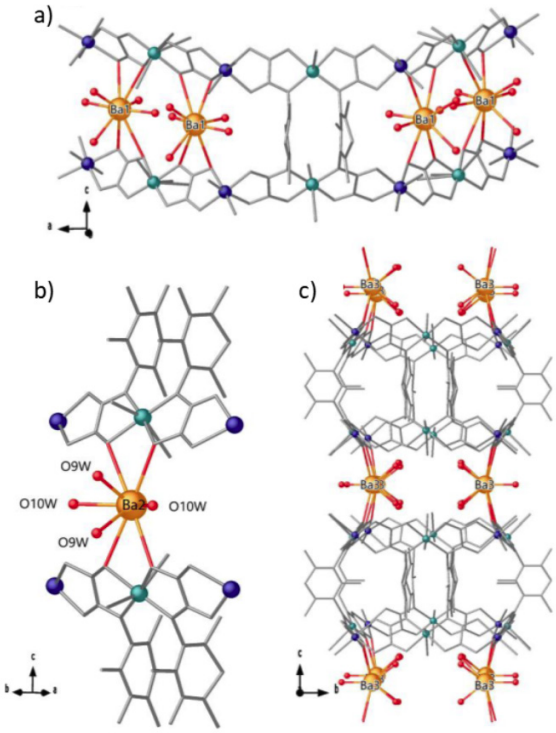

Figure 2.2. Details of host-guest interactions in **Ba^{2+}@CuNi-Me_3mpba**, showing the three crystallographically distinct Ba^{2+} ions. (a) Direct visualization by crystallography of Ba^{2+} ions detailed environments comprising carbonyl–oxygen atoms from the coordination network and water molecules for Ba1 (a), Ba2 (b) and Ba3 (c).

BaII insertion in **Ni^{2+}@CuNi-Me_3mpba** provides it with the capacity to capture SO_2. [7-9] This gas has a high impact on global air quality, harming the environment and human health. The current flue-gas desulfurization (FGD), by wet scrubbing with limestone slurry or wet sulphuric acid process, requires large amounts of water and further treatment of the resultant wastewater[10-15] Thus, it is needed the development of novel materials able to perform this capture in a more efficient manner. By breakthrough experiments of simulated flue-gas we obtained respective uptakes for **Ni^{2+}@CuNi-Me_3mpba** and **Ba^{2+}@CuNi-Me_3mpba**, of 2.0 and 2.5 mmol g^{-1} at 303 K and low SO_2 partial pressure, indicative of an improvement of SO_2 adsorption upon barium(II) incorporation (Figure 2.3). Also, we found the adsorption reversibility up to 10 successive adsorption/desorption cycles of SO_2. Thus, the macro-scale production of **Ba^{2+}@CuNi-Me_3mpba** MOF could lead to a more sustainable disposal of this gas, given its SO_2 uptake and recyclability.

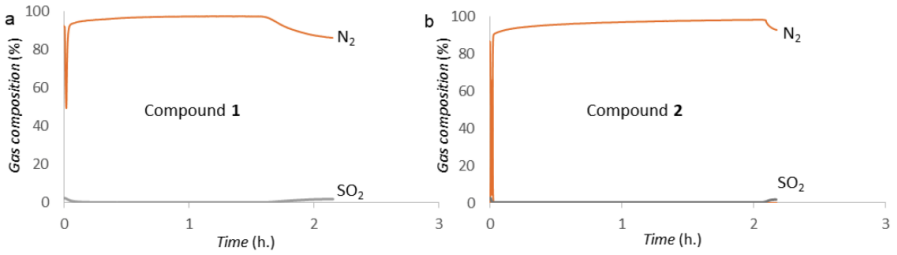

Figure 2.3. N_2/SO_2 separation breakthrough curves at 303 K for **Ni^{2+}@CuNi-Me_3mpba** (a) and **Ba^{2+}@CuNi-Me_3mpba** (b) using 20 mL min-1 flow of N_2/SO_2 (97.5/2.5) gas mixture at 303 K.

2.1.1.2. Transmetalation

Another illustrative example of how PSMs may originate novel properties in a given MOF is briefly described hereafter. In particular, a new MOF was synthesised using cobalt(III) SBUs with formula $Na_{12}\{Co_4(tpatox)_4\}\cdot 6H_2O$ (where tpatox are oxamato-based ligands derived from the aromatic amine tris(4-aminophenyl)amine, Figure 2.4a), which further coordinates to Ca^{2+} to create the diamagnetic MOF $\{Ca^{II}\ 6(H_2O)_{24}[Co^{III}\ _4(tpatox)_4]\}\cdot 44H_2O$ (Figure 2.4b). In a second step, the transmetallation of Ca^{2+} by terbium (Tb^{3+}), dysprosium (Dy^{3+}), holmium (Ho^{3+})16-18or erbium (Er^{3+}) led to the obtention of the following MOFs: $\{[Tb^{III}_6(H_2O)_{24}[Co^{III}_4(tpatox)_4]](NO_3)_6\}\cdot 49H_2O$, $\{[Dy^{III}_6(H_2O)_{24}[Co^{III}_4(tpatox)_4]](NO_3)_6\}\cdot 53H_2O$, $\{[Ho^{III}_6(H_2O)_{30}[Co^{III}_4(tpatox)_4]](NO_3)_6\}\cdot 44H_2O$ and $Er^{III}_6(H_2O)24[Co^{III}_4(tpatox)_4]](NO_3)_6\}\cdot 58H_2O$, respectively (Figure 2.4c). The presence of these cations, together with the appropriate coordination geometries, resulted on the appearance of slow magnetic relaxation effects, typical of single-molecule magnets, for the MOFs with dysprosium and erbium.[19]

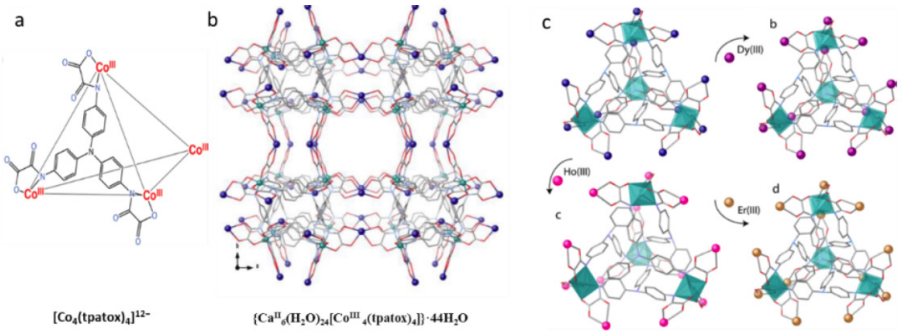

Figure 2.4. a) Tetranuclear metallogand $Na_{12}\{Co_4(tpatox)_4\}\cdot 6H_2O$ $[Co_4(tpatox)_4]^{12-}$, b) MOF $\{Ca^{II}_6(H_2O)_{24}[Co^{III}_4(tpatox)_4]\}\ \cdot\ 44H_2O$, c) Transmetallation of MOF $\{Ca^{II}_6(H_2O)_{24}[Co^{III}\ _4(tpatox)_4]\}\cdot 44H_2O$ Transmetallation from Ca^{2+} to Dy^{3+} (purple), Ho^{3+}(-pink) and Er^{3+}(orange) (right), respectively.

2.1.2. Applications of PSMs in MOFs

Once described two of the most common PSMs in MOFs, we should question what advantages they offer. Indeed, PSMs offer the possibility to maintain the MOF architecture, but include novel functionalities associated to the introduced metal species and, thus, expand the range of applications of MOFs. For example, as a direct consequence of the use of PSMs, they can acquire interesting properties such as magnetism,[20] gas adsorption/separation,[21] ferroelectricity/multiferroism,[22,23] conductive properties[24] and catalysis. [25,26] In particular, we will briefly discuss a nice example of how PSMs can modify/introduce catalytic properties in a MOF, given that catalysis will be the properties we seek in the MOFs presented in this chapter.

The anionic MOF ZJU-28 was reported to experiment a partial exchange of the endogenous H_2NMe^{2+} cations with cationic complexes of $[Rh(dppe)(COD)]BF_4$ (Figure 2.5a), which catalyzes the hydrogenation of 1-octene to *n*-octane. It was observed that this supported catalyst improves the catalytic properties of the homogeneous counterpart (Figure 2.5b), and can be recycled at least four times.[27]

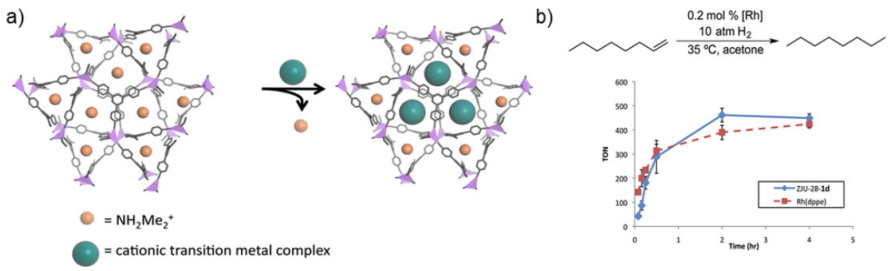

Figure 2.5. a) Proposed heterogenization of single-site transition-metal catalysts in ZJU-28 via cation exchange. b) Hydrogenation of *n*-octene to n-octane in acetone catalyzed by ZJU-28-1d (blue) and homogeneous 1d (red).[28]

2.2. Objectives

On the basis of the previous results, detailed in the introduction, we pretended to go one step further, by synthesizing catalytically active MOFs containing metal cations, of different nature, within their channels. Thus, the main objectives of this chapter can be summarized as:

* Preparation of MOFs containing different metal atoms of different nature using PSMs (partial cation exchange). In particular, we focused on the partial substitution of Ni^{II} cations hosted in the channels of **Ni^{2+}@CuNi-Me_3mpba**, by Pd^{II} ones to give a novel MOF named **$Ni^{2+}Pd^{2+}$@CuNi-Me_3mpba.**

* Characterization of the obtained material, paying particular attention to SCXRD methods, Figure 2.6.

* Study of their catalytic application. In particular, considering, the presence of accessible metals of different nature, we explored the possibility to have consecutive (cascade) catalytic reactions mediated by the different metal cations.

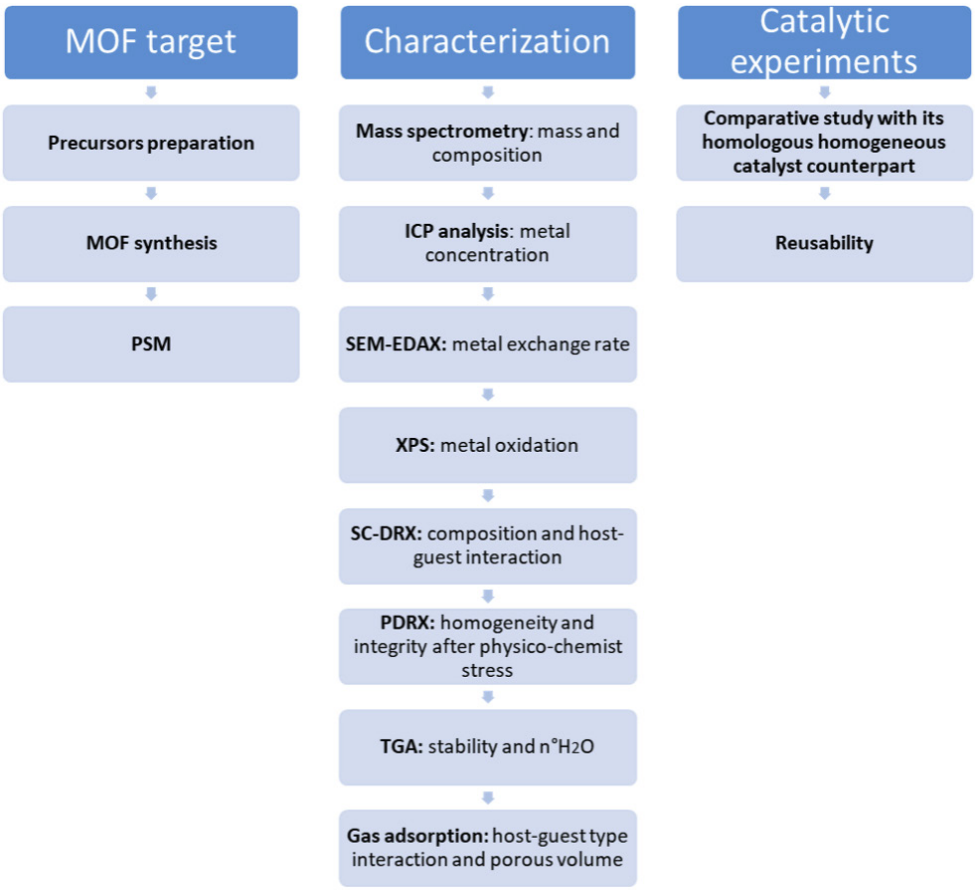

Figure 2.6. Synthesis procedure and structural and functional study of the MOF. In the characterization methods, the main function for which each technique has been used has been listed, omitting the rest of the information it may provide.

2.3. Synthesis

Synthesis of **$[Pd^{II}(NH_3)_4]Ni^{II}\{Ni^{II}_4[Cu^{II}_2(Me_3mpba)_2]_3\} \cdot 52H_2O$ ($Ni^{2+}Pd^{2+}$@CuNi-Me_3mpba)**. After transmetallation of Mg for Ni in the Mg^{2+}@CuNi-Me_3mpba structure described in the introduction, a second post-treatment step takes place, where a cation exchange of the Ni ions hosted in the pores for Pd cations occurs, thus forming **$[Pd^{II}(NH_3)_4]Ni^{II}\{Ni^{II}_4[Cu^{II}_2(Me_3mpba)_2]_3\} \cdot 52H_2O$ ($Ni^{2+}Pd^{2+}$@CuNi-Me_3mpba)**. It is obtained on a multigram scale by immersing 5 g of the reported **Ni^{2+}@CuNi-Me_3mpba**[29] compound powder (1.45 mmol) in a solution (5mL) of 1.067 g of the $[Pd(NH_3)_4]Cl_2$ species (2.9 mmol) for 24 hours, in high yield (4.91 g, 96%).

In order to obtain **$Ni^{2+}Pd^{2+}$@CuNi-Me_3mpba** crystals of high crystallinity and minimal physico-chemical stress to be suitable for single-crystal X-ray diffraction studies, the insertion conditions have to be milder. For this purpose, **Ni^{2+}@CuNi-Me_3mpba** crystals (about 5 mg, 0.0015 mmol) are immersed for 24 hours in 5 mL of aqueous solutions of $[Pd(NH_3)_4]Cl_2$ (0.003mmol) to obtain well-formed dark green prisms of **$Ni^{2+}Pd^{2+}$@CuNi-Me_3mpba.**

The elemental analysis shows a molecular weight for $Cu_6Ni_5PdC_{78}H_{176}N_{16}O_{88}$ **($Ni^{2+}Pd^{2+}$@CuNi-Me_3mpba)** of Mw 3527.45 g/mol and an elemental percentage of C, 25.68; H, 5.01; N, 6.34, is found (C, 26.56; H, 5.03; N, 6.35 was expected). IR (KBr) shows the signals ν of 3011, 2956 and 2917 cm^{-1} (C–H) and 1607 cm^{-1} (C=O).

Figure 2.7 illustrates a first stage of transmetallation and cation exchange of all Mg for Ni, and a second stage of partial cation exchange of Ni

for Pd. The starting point is a structure with copper atoms (purple balls) in its network and magnesium atoms in its network (orange balls) and lodged in the pores (orange balls with sticks). After prolonged immersion in a $NiNO_3$ cation solution, a complete substitution of all Mg by Ni occurs (green balls in both forms). The second stage would only involve the 50% of replacement of the Ni atoms in the pores (green balls with sticks) by Pd (pink balls with sticks).

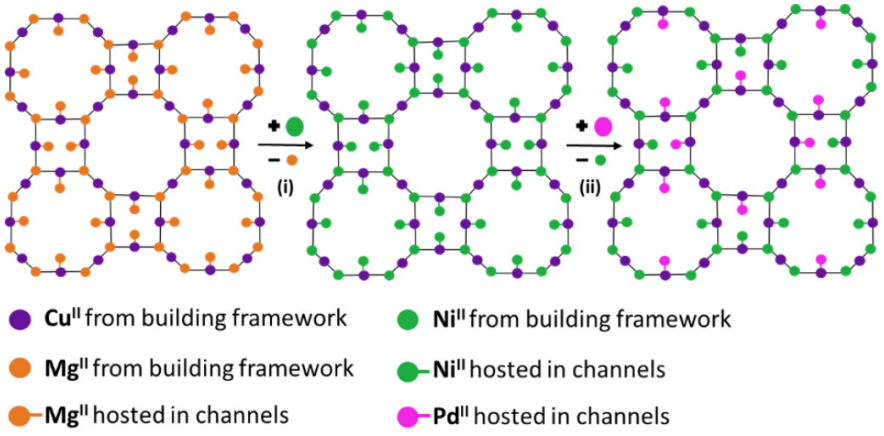

Figure 2.7. Scheme of the synthetic procedure of total $Mg^{II} \rightarrow Ni^{II}$ transmetallation (i) and partial $Ni^{II} \rightarrow Pd^{II}$ cation exchange in pores (ii).

2.4. Characterization

2.4.1. Scanning Electron Microscopy-Energy Dispersive X-ray Spectroscopy (SEM-EDAX) of $Ni^{2+}Pd^{2+}$@Cu-Ni-Me_3mpba

Once carried out the cation exchange, I use SEM/EDX as a fast and cheap tool to follow the exchange process (Table 2.1) and verify the metal ratios (Table 2.2) in order to see if all the nickel atoms in the pores have been replaced. Since the MOF is anionic, the structure is supposed to change from $Ni^{II}_2\{Ni^{II}_4[Cu^{II}_2(Me_3mpba)_2]_3\}$ to $Pd^{II}Ni^{II}\{Ni^{II}_4[Cu^{II}_2(Me_3mpba)_2]_3\}$, so the Cu/Ni ratios should be around 1.2 and Ni/Pd 5.

Table 2.1. SEM/EDX analyses of **$Ni^{2+}Pd^{2+}$@CuNi-Me_3mpba**

Metal	% mass	Metal stoichiometry
Cu	12.33	5.31
Ni	10.21	4.39
Pd	2.05	0.88

Table 2.2. SEM/EDX metal stoichiometry ratios of **$Ni^{2+}Pd^{2+}$@CuNi-Me_3mpba**

Ratio	Value
Cu/Ni	1.21
Ni/Pd	4.98

The values obtained in the tables confirm that the cation exchange has been carried out correctly since the expected ratios correspond to the ratios obtained.

2.4.2. X–ray photoelectron spectroscopy (XPS) of $Ni^{2+}Pd^{2+}$@CuNi-Me_3mpba

In order to ascertain the oxidation states of the metal cations hosted in the channels of **$Ni^{2+}Pd^{2+}$@CuNi-Me_3mpba**. I carried out X–ray photoelectron spectroscopy (XPS) measurements. In particular, we have focused on determining the oxidation state of palladium metals. Figure 2.8 shows the XPS spectra of **$Ni^{2+}Pd^{2+}$@CuNi-Me_3mpba**. The Pd3d line is the typical doublet with binding energies (BE) for the $Pd3d_{5/2}$ and $Pd3d_{3/2}$ peaks of 338.6 and 343.0 eV, respectively, typical of Pd^{2+} cations, which is in agreement to other reported values.[29] In conclusion, XPS measurements confirm that palladium oxidation state is still +2, which indicates that the insertion process did not alter its oxidation state. Here, it is important to remark that ascertaining oxidation state of potential catalytically active sites is crucial in order to find the appropriate organic reaction to be catalysed.

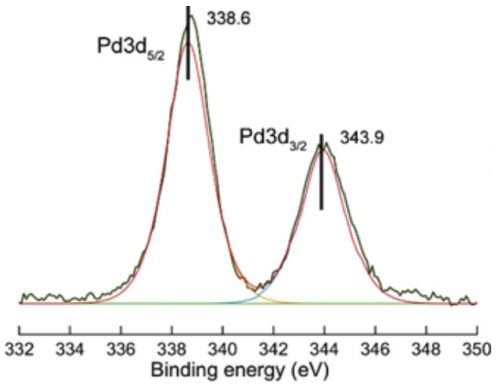

Figure 2.8. X–ray photoelectron spectroscopy (XPS) of **$Ni^{2+}Pd^{2+}$@CuNi-Me_3mpba.**

2.4.3. Single-Crystal X-ray diffraction (SC-XRD) of $Ni^{2+}Pd^{2+}$@CuNi-Me_3mpba

In order to fully characterize the hybrid material, we carried out single crystal X-Ray diffraction. The robustness and crystallinity of the 3D network, allowed the resolution of the crystal structure of **$Ni^{2+}Pd^{2+}$@CuNi-Me_3mpba** even after a two–step PS process consisting on a transmetallation (replacing Mg cations by Ni ones) and Pd insertion. It allows a direct visualization of the catalytic species, stabilized within MOF channels. For that reasons, it is worth to underline that structural parameters such as thermal factors are sometimes high due to disorder related to the high degrees of freedom expected in highly porous nanospace. A summary of the most important crystallographic data, for **$Ni^{2+}Pd^{2+}$@CuNi-Me_3mpba** (and also **Ni^{2+}@CuNi-Me_3mpba** for the sake of comparison) is collected in Table 2.3

Table 2.3. Summary of Crystallographic Data for $[Pd^{II}(NH_3)_4]Ni^{II}\{-Ni^{II}_4[Cu^{II}_2(Me_3mpba)_2]_3\} \cdot 52H_2O$ **($Ni^{2+}Pd^{2+}$@CuNi-Me_3mpba)** and **Ni^{2+}@CuNi-Me_3mpba.**

Compound	**Ni^{2+}@CuNi-Me_3mpba**	**$Ni^{2+}Pd^{2+}$@CuNi-Me_3mpba**
Formula	$C_{78}H_{90}Cu_6Ni_6N_{12}O_{53}$	$C_{78}Cu_6H_{176}N_{16}O_{88}Ni_5Pd$
***M* (g mol^{-1})**	2780.82	3527.53
Crystal system	Tetragonal	Tetragonal
λ (Å)	0.6889	0.6889
Space group	*P4/mmm*	*P4/m*
***a* (Å)**	36.1886(6)	35.8876(4)
***b* (Å)**	36.1886(6)	35.8876(4)
***c* (Å)**	14.8134(2)	15.2635(3)
***V* (Å^3)**	19399.8(7)	19658.2(6)
Z	4	4
ρ calc (g cm^{-3})	0.940	1.192
***M* (mm^{-1})**	1.073	1.117
***T* (K)**	45.0	90
Unique reflections (R_{int})	8917 (0.1140)	17343 (0.0658)
Observed reflections [$I > 2\sigma(I)$]	5545	11623
Goof	1.415	1.211
***R*^{A} [$I > 2\sigma(I)$] (all data)**	0.1173 (0.1533)	0.0979 (0.1244)
***wR*^{B} [$I > 2\sigma(I)$] (all data)**	0.3673 (0.3936)	0.3059 (0.3262)

[a] $R = \sum(|F_o| - |F_c|)/\sum|F_o|$. [b] $wR = [\sum w(|F_o| - |F_c|)^2/\sum w|F_o|^2]^{1/2}$.

The robustness and crystallinity of this MOF allowed to solve crystal structure of **$Ni^{2+}Pd^{2+}$@CuNi-Me_3mpba** and comparison with the previously reported oxamato–based[31-33] three–dimensional (3D) **Ni^{2+}@CuNi-Me_3mpba**. Once 50% of NiII cations are replaced with PdII ones, the anionic $Ni^{II}_4Cu^{II}_6$ open-framework structure, in **$Ni^{2+}Pd^{2+}$@CuNi-Me_3mpba**, exhibits the same pillared square/octagonal layer architecture, where nickel(II) and copper(II) ions are located on the vertices and midpoints of the edges, respectively, featuring three types of pores, different in size and shape, propagating along the *c* axis. **$Ni^{2+}Pd^{2+}$@CuNi-Me_3mpba** framework is built up of regularly spaced, almost square sized small pores (virtual diameter of ca 0.4 nm) and two octagonal-type large pores (virtual diameters of ca. 1.5 and 2.2 nm, respectively), hydrophobic and hydrophilic, depending on the disposition of the trimethyl-substituted phenylene spacers, pointing inwards or outwards of the voids, respectively (Figure 2.9). The presence of $[Ni(H_2O)_6]^{2+}$ and $[Pd(NH_3)_4]^{2+}$ cationic complexes inside the new nanoporous **$Ni^{2+}Pd^{2+}$@CuNi-Me_3mpba** material were underpinned by SC-XRD, and its crystal structure unambiguously shows that the $[Pd(NH_3)_4]^{2+}$ and $[Ni(H_2O)_6]^{2+}$ units are hosted in the two types of channels present in the anionic framework.

The larger octagonal pores –also accessible for catalysis (*vide infra*)– host both $[Ni(H_2O)_6]_{2+}$ and $[Pd(NH_3)_4]^{2+}$ units with the latter stabilized in sites close to the walls of the network. This evidence further supports an intrinsic stabilizing effect of MOF's confined space. The small square hindered channels retain only $[Ni(H_2O)_6]^{2+}$ as in the structure of the precursor **Ni^{2+}@CuNi-Me_3mpba**, confirming the less accessibility of these pores for cation exchange.

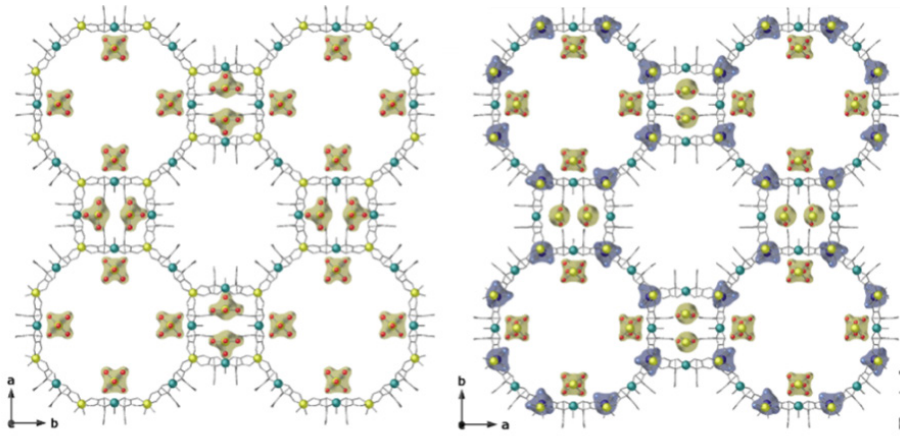

Figure 2.9. Views along the c of the crystal structures, of the previously reported **Ni^{2+}@CuNi-Me_3mpba**[30] (left) and the novel **$Ni^{2+}Pd2^{+}$@CuNi-Me_3mpba** (right). The ligands of the coordination 3D network are depicted as grey sticks, whereas copper and nickel atoms are represented as cyan and yellow spheres. For the guest species hosted in the channels, nickel and palladium atoms and water and ammonia molecules are represented as yellow, dark blue, red and light blue spheres, respectively. Yellow and blue surfaces are used to highlight the guest Ni and Pd species, respectively, within MOFs channels.

Figure 2.10 shows the intercalation of the layers of the metal-organic network. For **Ni^{2+}@CuNi-Me_3mpba** (Figure 2.10 left), an intercalation of horizontal layers occupied with or without $[Ni(H_2O)_6]^{2+}$ is observed. While for **$Ni^{2+}Pd^{2+}$@CuNi-Me_3mpba** there is an intercalation of $[Ni(H_2O)_6]^{2+}$ and $[Pd(NH_3)_4]^{2+}$ species (Figure 2.10 right).

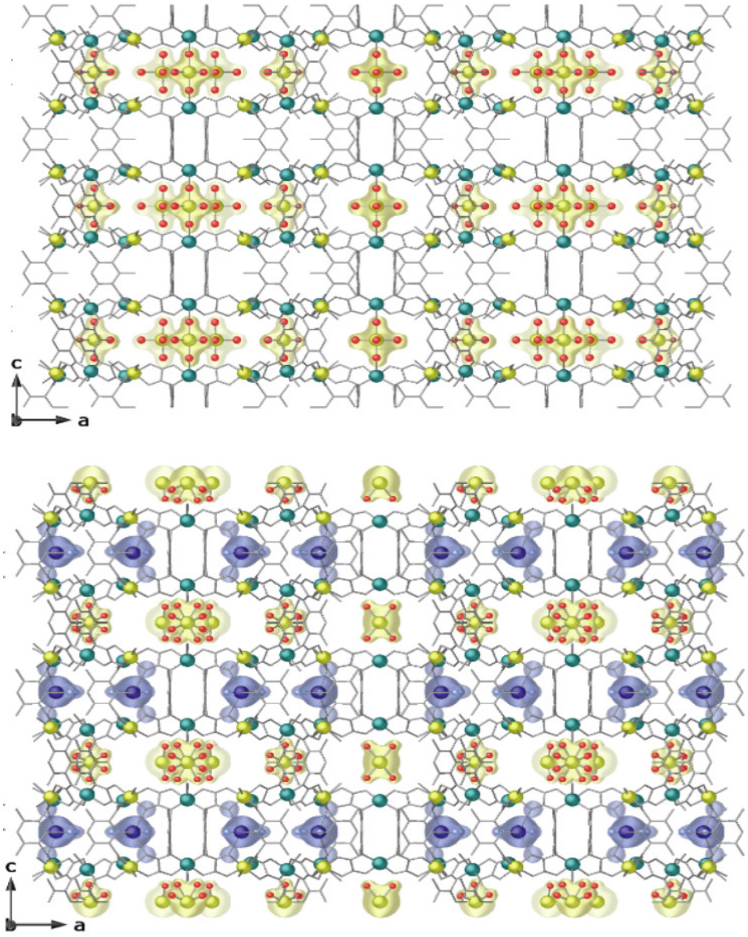

Figure 2.10. Views along the b axes of the crystal structures, determined by synchrotron X–ray diffraction, of the previously reported **Ni^{2+}@CuNi-Me_3mpba**[30](up) and the novel **$Ni^{2+}Pd^{2+}$@CuNi-Me_3mpba** (bottom). The ligands of the coordination 3D network are depicted as grey sticks whereas copper and nickel atoms are represented as cyan and yellow spheres. For the guest species hosted in the channels, nickel and palladium atoms and water and ammonia molecules are represented as yellow, dark blue, red and light blue spheres, respectively. Yellow and blue surfaces are used to highlight the guest Ni and Pd species, respectively, within MOFs channels.

Ni^{2+}@CuNi-Me_3mpba (and also **$Ni^{2+}Pd^{2+}$@CuNi-Me_3mpba**) possesses accessible Cu^{2+}sites, which are located in the anionic coordination framework, and Ni^{2+} cations situated in the channels. Figure 2.11 highlights the immutable arrangement of $[Ni(H_2O)_6]^{2+}$ after tetraaminopalladium insertion. The larger octagonal hydrophilic channels of the MOF contain a much larger accessible void space (size of ca. 2.2 nm), which makes them as the first candidate to cation exchanges, leaving the small square channels fully occupied by the $[Ni(H_2O)_6]^{2+}$ monomers exactly as in **Ni^{2+}@CuNi-Me_3mpba**.

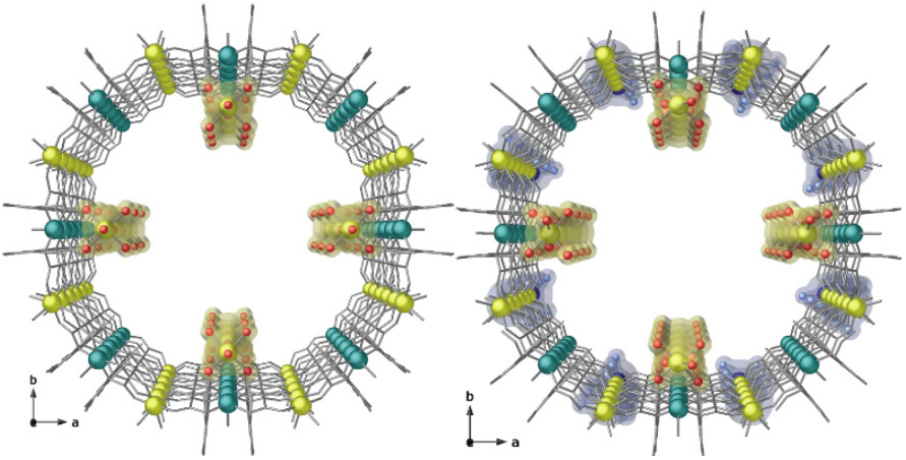

Figure 2.11. Perspective views of one single channel of **Ni^{2+}@CuNi-Me_3mpba** (Left) and **$Ni^{2+}Pd^{2+}$@CuNi-Me_3mpba** (Right). The ligands of the coordination 3D network are depicted as grey sticks whereas copper and nickel atoms are represented as cyan and yellow spheres. For the guest species hosted in the channels, nickel and palladium atoms and water and ammonia molecules are represented as yellow, dark blue, red and light blue spheres, respectively. Yellow and blue surfaces are used to highlight the guest Ni and Pd species, respectively, within MOFs channels.

The tetraammonium Pd(II) monomers exhibit Pd–NH3 bond distances [1.86(2) to 1.98(2) Å], very similar to those previously reported.[30] Apart

from electrostatic interactions between Pd(II) units and the anionic framework, all $[Pd(NH_3)_4]^{2+}$ cations are hydrogen–bonded through the carboxylate oxygen atoms of the framework and ammonia molecules of the Pd(II) environment [$N_{ammonia}\cdots O_{oxamate}$ varying in the range 2.93(2) and 3.07(2) Å] to the anionic framework which further fixes and stabilizes them within the pores (Figure 2.12).

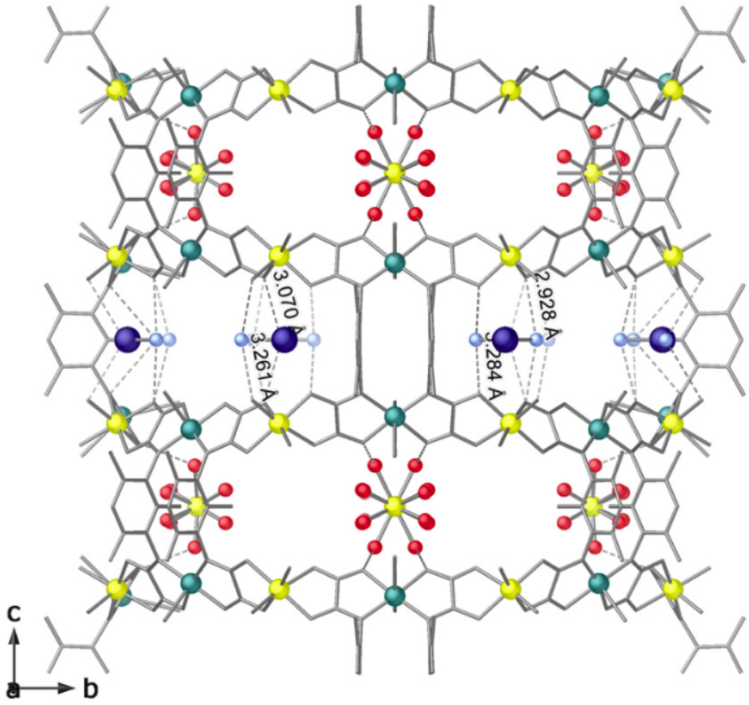

Figure 2.12. Views of a fragment of **$Ni^{2+}Pd^{2+}$@CuNi-Me_3mpba** in the bc planes showing $[Ni(H_2O)_6]^{2+}$ and $[Pd(NH_3)_4]^{2+}$ inside the nanoporous material. Copper, nickel and palladium ions are represented by green, yellow and blue spheres, respectively, whereas the ligands are depicted as grey sticks. Oxygen from water molecules and nitrogen atoms from ammonia molecules coordinated to Ni^{2+} and Pd^{2+} are depicted as red and light blue spheres, respectively. [Hydrogen atoms are omitted for clarity].

Figure 2.13 top evidences the regular alternation of $[Ni(H_2O)_6]^{2+}$ and $[Pd(NH_3)_4]^{2+}$ inside the nanoporous, where water molecules of

$[Ni(H_2O)_6]^{2+}$ complex ions in pores exhibit positional disorder (Figure 2.13 bottom).

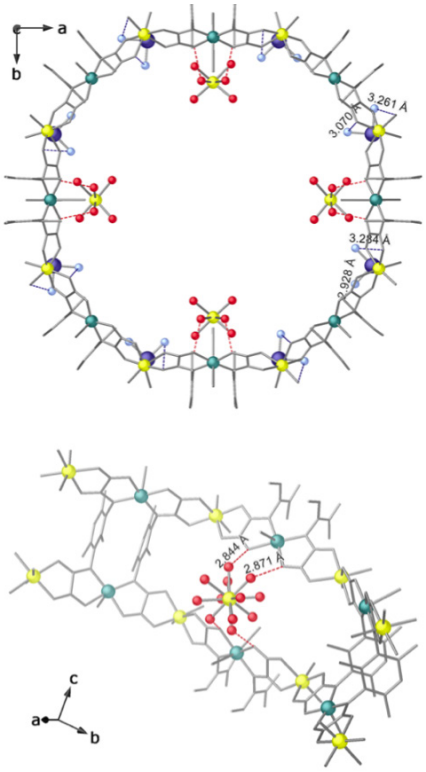

Figure 2.13. (Top) Perspective view along c crystallographic axis of the single channel in $Ni^{2+}Pd^{2+}$**@CuNi-Me$_3$mpba**. (Bottom) Details of $[Ni(H_2O)_6]^{2+}$ complex ions in pores where water molecules exhibit positional disorder. Copper, nickel and palladium ions are represented by green, yellow and blue spheres, respectively, whereas the ligands are depicted as grey sticks. Oxygen from water molecules and nitrogen atoms from ammonia molecules coordinated to Ni^{2+} and Pd^{2+} are depicted as red and light blue spheres, respectively. [Hydrogen atoms are omitted for clarity].

Finally, Figure 2.14 shows details of $[Pd(NH_3)_4]^{2+}$ cations interactions hydrogen-bonded through the carboxylate oxygen atoms of the framework and ammonia molecules of the Pd(II) environment of a channel. A further interaction involving a water molecule and $[Pd(NH_3)_4]^{2+}$ moieties contribute to uniform distribution of catalytically active species within pores [symmetric H-Bond, Nammonia···OWater 3.26(2) Å].

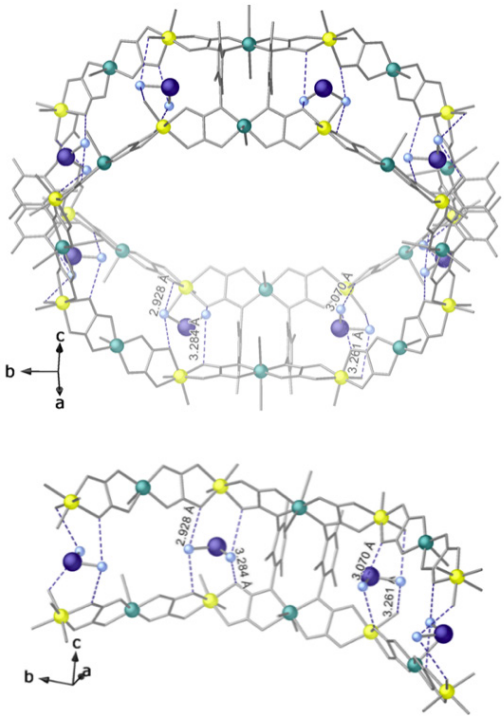

Figure 2.14. (Top) Perspective view of a portion of one single channel of **$Ni^{2+}Pd^{2+}$@CuNi-Me_3mpba** showing details of $[Pd(NH_3)_4]^{2+}$ cations. (Bottom) Deep perspective view of details for $[Pd(NH_3)_4]^{2+}$ cations interactions in pores of **$Ni^{2+}Pd^{2+}$@CuNi-Me_3mpba**. Copper, nickel and palladium ions are represented by green, yellow and blue spheres, respectively, whereas the ligands are depicted as grey sticks. Nitrogen atoms from ammonia molecules coordinated to Pd^{2+} are depicted as light blue spheres. [Hydrogen atoms are omitted for clarity].

2.4.4. Powder X–ray Diffraction Measurements (PXRD) of $Ni^{2+}Pd^{2+}$@CuNi-Me_3mpba

In order to confirm the crystallinity of **$Ni^{2+}Pd^{2+}$@CuNi-Me_3mpba** and the isostructurality of single crystals with bulk polycrystalline samples X–ray Powder Diffraction Measurements (XRPD) were carried out. A polycrystalline sample of **$Ni^{2+}Pd^{2+}$@CuNi-Me_3mpba** was introduced into a 0.5 mm borosilicate capillary prior to being mounted and aligned on a Empyrean PANalytical powder diffractometer, using Cu Kα radiation (λ = 1.54056 Å). Five repeated measurements were collected at room temperature (2θ = 2–60°) and merged in a single diffractogram.

The experimental powder X–ray diffraction (PXRD) patterns of **$Ni^{2+}Pd^{2+}$@CuNi-Me_3mpba**, together with those of the previously reported **Ni^{2+}@CuNi-Me_3mpba**[34] for the sake of comparison, can be observed in Figure 2.15. In each case, the experimental patterns (solid lines) are identical to the theoretical ones (bold lines), confirming the pureness and homogeneity of the samples. The similarities between the diffraction patterns of **Ni^{2+}@CuNi-Me_3mpba**[3] and **$Ni^{2+}Pd^{2+}$@CuNi-Me_3mpba** indicate that the MOF retains its integrity after suffering the physico-chemical stress of PSM.

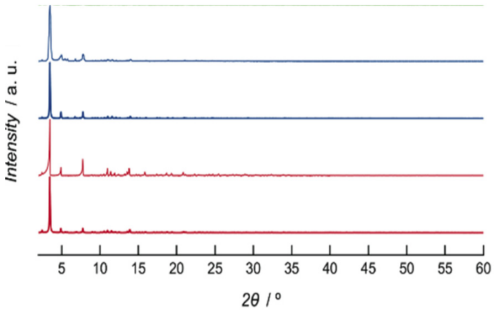

Figure 2.15. Calculated (bold lines) and experimental (solid lines) PXRD pattern profiles of **Ni^{2+}@CuNi-Me_3mpba** (red) and **$Ni^{2+}Pd^{2+}$@CuNi-Me_3mpba** (blue) in the 2θ range 2.0–60.0°.

2.4.5. Termogravimetric Analysis (TGA) of $Ni^{2+}Pd^{2+}$@Cu-Ni-Me_3mpba

In order to determine the water contents of **$Ni^{2+}Pd^{2+}$@CuNi-Me_3mpba**, the thermogravimetric analyses were performed on crystalline samples under a dry N_2 atmosphere with a Mettler Toledo TGA/STDA 851^e thermobalance operating at a heating rate of 10 ºC min^{-1}. The first step of the graphic allows confirming the 52 water molecules of **$Ni^{2+}Pd^{2+}$@ CuNi-Me_3mpba** by calculating the lost mass and the second one shows the MOF decomposition as a function of temperature (Figure 2.16).

2.4.6. Gas adsorption of $Ni^{2+}Pd^{2+}$@CuNi-Me_3mpba

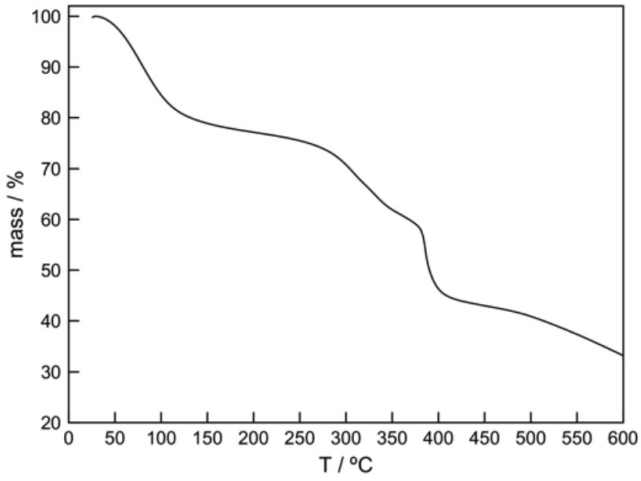

Figure 2.16. Thermo-Gravimetric Analysis (TGA) of **$Ni^{2+}Pd^{2+}$@CuNi-Me_3mpba** under dry N2 atmosphere.

The permanent porosity of **$Ni^{2+}Pd^{2+}$@CuNi-Me_3mpba** was confirmed by gas adsorption measurements. In particular, the N_2 adsorption–desorption isotherms at 77 K were carried out on crystalline samples of

Ni^{2+}@CuNi-Me_3mpba and **$Ni^{2+}Pd^{2+}$@CuNi-Me_3mpba** with a Micromeritics ASAP2020 instrument. Samples were evacuated at 70 °C during 24 hours under 10-6 Torr prior to their analysis. Water adsorption is common to expect secondary events like cluster formation, co-adsorption, creation of new active sites due to the adsorbed water molecules, so it is important to remove it from MOF pores.

Figure 2.17 shows the N_2 adsorption isotherm of **Ni^{2+}@CuNi-Me_3mpba** and **$Ni^{2+}Pd^{2+}$@CuNi-Me_3mpba** that present a type I sorption behavior characteristic of microporous compounds. Both **$Ni^{2+}Pd^{2+}$@CuNi-Me_3mpba** (blue line) and **Ni^{2+}@CuNi-Me_3mpba** (red line) were compared confirming their permanent porosity. Remarkably, the porosity for **$Ni^{2+}Pd^{2+}$@CuNi-Me_3mpba** is higher than **Ni^{2+}@CuNi-Me_3mpba**. This feature suggests higher accessible surface and structural stability for **$Ni^{2+}Pd^{2+}$@CuNi-Me_3mpba**.

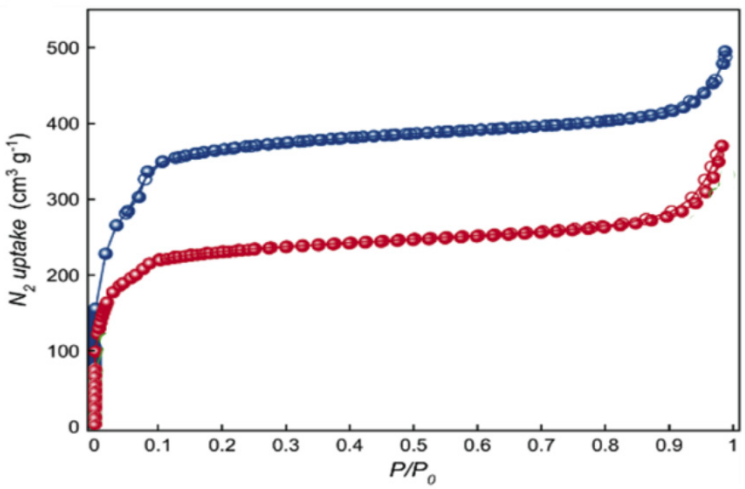

Figure 2.17. N2 (77 K) adsorption isotherms for the activated compounds **Ni^{2+}@CuNi-Me_3mpba** (red) and **$Ni^{2+}Pd^{2+}$@CuNi-Me_3mpba** (blue). Filled and empty symbols indicate the adsorption and desorption isotherms, respectively.

2.5. Catalytic properties of Ni2+Pd2+@Cu-Ni-Me3mpba

As mentioned in the crystal structure section, we have several metals in **$Ni^{2+}Pd^{2+}$@CuNi-Me_3mpba** which are, potentially, catalytically active. In a first initial step, we verified that both Cu^{2+} metal nodes from the framework and Pd^{2+} entities were catalytically active for hydroalkoxylation of cyclopropenones[35] and cross-coupling reactions, respectively. Therefore, we planned a series of consecutive cascade reactions that are described below.

2.5.1. Metal organic frameworks (MOFs) as suitable solid catalysts for the hydroalkoxylation of cyclopropenones.

To confirm the described catalytic activity of Cu^{2+} cations[36,37] can be extended to heterogeneous catalysis, and to extend such results to cascade catalysis, we used the previously described[38-42] **$Ni^{2+}Pd^{2+}$@CuNi-Me_3mpba**, which contains three potential different metal active sites (Cu, Ni, Pd), located either in the framework (Cu) or in the channels (Pd) and in both sites (Ni).

In this first catalytic section we study the hydroalkoxylation of cyclopropenones catalyzed by either soluble $Cu(OAc)_2$ (2 mol%) and/or insoluble **Ni^{2+}@CuNi-Me_3mpba** (10 mol%), Figure 2.18.

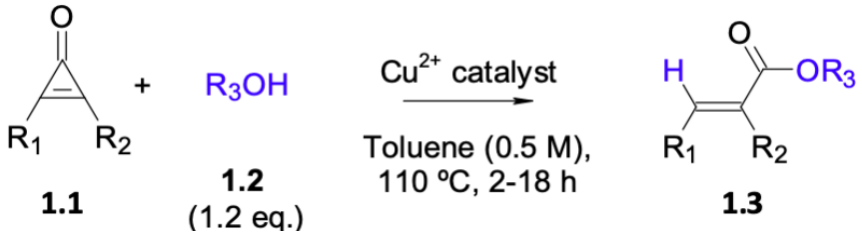

Figure 2.18. Reaction scheme of hydroalkoxylation of cyclopropenones.

Table 2.4 shows the isolated yields of different esters catalyzed by Cu^{2+} catalyst unsupported (yields between parentheses) or supported by **Ni^{2+}@CuNi-Me_3mpba** (yields in bold and without parentheses). The catalized reaction of diphenylcyclopropenone was performed with water (1.2a), phenols (1.2b-e and 1.2i-k), benzyl (1.2f-g), phenethyl (1.2h), allyl (1.2l), homopropargyl (1.2m), amine alkyl (1.2n) and linear primary alcohols containing sensitive functionalities (1.2o-p), secondary alcohols either linear (1.2q) or cyclic (1.2r), and natural products such as geraniol (1.2s). Bigger products do not penetrate in the microporous MOF solid. The alcohol is added in all cases selectively across the cyclopropenone bond in good to excellent yields, with easy–to–migrate alkenes and chiral carbon–oxygen bonds remaining untouched during the course of the reaction. Remarkably, we observed that the catalytic activity of the framework Cu^{2+} cations persisted in **$Ni^{2+}Pd^{2+}$@CuNi-Me_3mpba** but not in the related fully-nickel exchanged and palladium reduced material **Pd^0_4@CuNi-Me_3mpba (**Pd^{2+}**@CuNi-Me_3mpba** reduced with $NaBH_4$),[30] in line with the higher accessibility to the Cu2+ sites for the former, observed during the characterization measurements (*vide supra*). This is strongly supporting that the Cu^{2+} cations of the MOFs are the catalytic active species for the hydroalkoxylation reaction because other Ni and Pd catalysts including NiX_2 (X = OAc, NO_3, SO_4) and $PdCl_2(PPh_3)_2$, $Pd(PPh_3)_4$, $Pd[P(o\text{–}tolyl)_3]_4$, $PdOAc_2(SPhos)_2$, and also oxime palladacycles, were tested without success (yield <1%).

Table 2.4. Synthesis of cinnamate products by hydroalkoxylation of cyclopropenones, catalyzed by either soluble $Cu(OAc)_2$ (2 mol%, yields between parentheses) and/or insoluble **Ni^{2+}@CuNi-Me_3mpba** (10 mol%, yields in bold and without parentheses). Isolated yields. The major product for non–symmetric cyclopropenones is shown.

<table>
<tr><th colspan="4">Diphenylcyclopropenone (1.1a)</th></tr>
<tr><td colspan="4"> 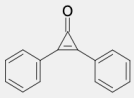
(1.1a)</td></tr>
<tr><td colspan="2">1.1a + H_20</td><td colspan="2">1.1a + [Phenols (n = 0), benzyl alcohol (n = 1), phenethyl alcohol (n = 2)]</td></tr>
<tr><td colspan="2"> 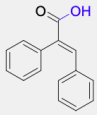
1.3a
99%
(99%)</td><td colspan="2"> 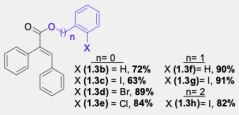
n= 0
X (1.3b) = H, 72%
X (1.3c) = I, 63%
X (1.3d) = Br, 89%
X (1.3e) = Cl, 84%
n= 1
X (1.3f)= H, 90%
X (1.3g)= I, 91%
n= 2
X (1.3h)= I, 82%</td></tr>
<tr><td colspan="2">1.1a + Functionalised benzyl alcohols</td><td colspan="2">1.1a + Allyl alcohol</td></tr>
<tr><td colspan="2"> 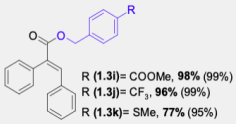
R (1.3i)= COOMe, 98% (99%)
R (1.3j)= CF_3, 96% (99%)
R (1.3k)= SMe, 77% (95%)</td><td colspan="2"> 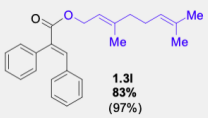
1.3l
83%
(97%)</td></tr>
<tr><td>1.1a + Homopro-pargyl</td><td>Ph_2C + Amine alkyl alcohols</td><td colspan="2">1.1a + Linear primary alcohols containing sensitive functionalities</td></tr>
<tr><td> 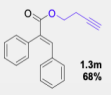
1.3m
68%</td><td> 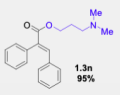
1.3n
95%</td><td> 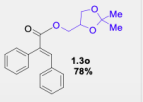
1.3o
78%</td><td> 
1.3p
62%</td></tr>
<tr><td>1.1a + Secondary alcohols linear</td><td>1.1a + Secondary alcohols cyclic</td><td>1.1a + Geraniol</td><td></td></tr>
<tr><td> 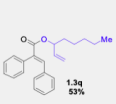
1.3q
53%</td><td> 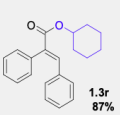
1.3r
87%</td><td> 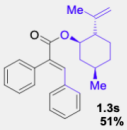
1.3s
51%</td><td></td></tr>
</table>

The fact of having the Cu^{2+} in the solid framework immobilised and using non–polar toluene as solvent of the reaction, precludes a significant leaching of the active species (Figure 2.19), which allowed to reuse **Ni^{2+}@CuNi-Me_3mpb**a at least five times without significant depletion in the final yield of product **1.3r** in which a secondary alcohol cyclic is involved (75% after 5 uses).

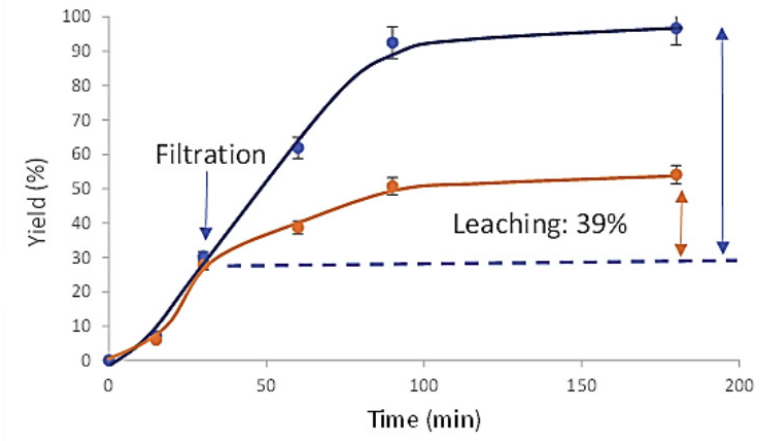

Figure 2.19. Leaching test for the hydroalkoxylation of diphenylcyclopropenone with alcohol secondary alcohol cyclic (**1.3r**) catalyzed by **Ni^{2+}@CuNi-Me_3mpba** (10 mol%). For reaction conditions, see Figure 2.18. Error bars account for a 5% uncertainty.

2.5.2. One–pot hydroalkoxylation of cyclopropenones / cross coupling reactions.

The presence of different catalytically active metal sites in **Ni^{2+}@CuNi-Me_3mpba** and **$Ni^{2+}Pd^{2+}$@CuNi-Me_3mpba** offers us the possibility of carrying out consecutive cascade–like reactions where each metal catalyzes one step, *i.e.* one–pot hydroalkoxylation/cross coupling reactions. Figure 2.20 shows that the one–pot diphenylcyclopropenone

(**1.1a**) hydration/Chan–Lam coupling reaction proceeds with catalytic amounts of **Ni^{2+}@CuNi-Me_3mpba**, to give the corresponding aromatic esters (**1.6a-d**, Table 2.5), after formation of intermediate 1.3a (Figure 2.21).

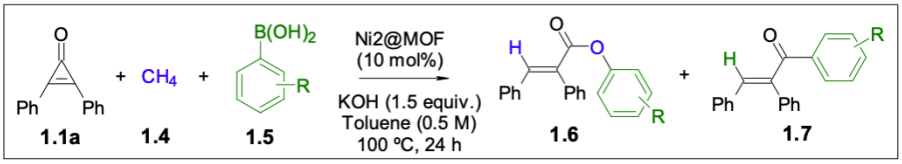

Figure 2.20. **Ni^{2+}@CuNi-Me_3mpba**–catalyzed one–pot cyclopropenone hydration/Chan–Lam reaction.

Table 2.5. Compounds and derivates of **1.6** and **1.7** from **Ni^{2+}@CuNi-Me_3mpba**–catalyzed one–pot cyclopropenone hydration/Chan–Lam reaction.

Diphenylcyclopropenone (1.1a)			
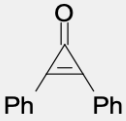			
1.6a (R = Ph)	**1.6b** (R= *p*-MePh)	**1.6c** (*R*=*m*-NO_2Ph)	**1.6d** + (*R*= *p*-OMePh)
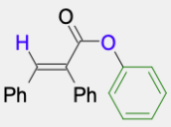 **61%**	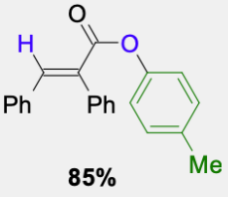 **85%**	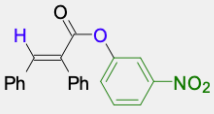 **15%**	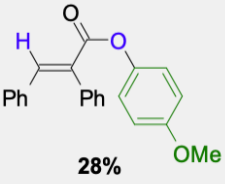 **28%**
1.7a (R=Ph)	1.7b (R = *p*-MePh)	1.7c (*R* = *m*-NO_2Ph)	1.7d + (*R* = *p*-OMePh)
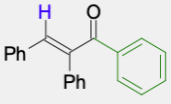 **<10%**	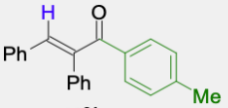 **<10%**	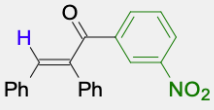 **<10%**	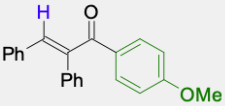 **<10%**

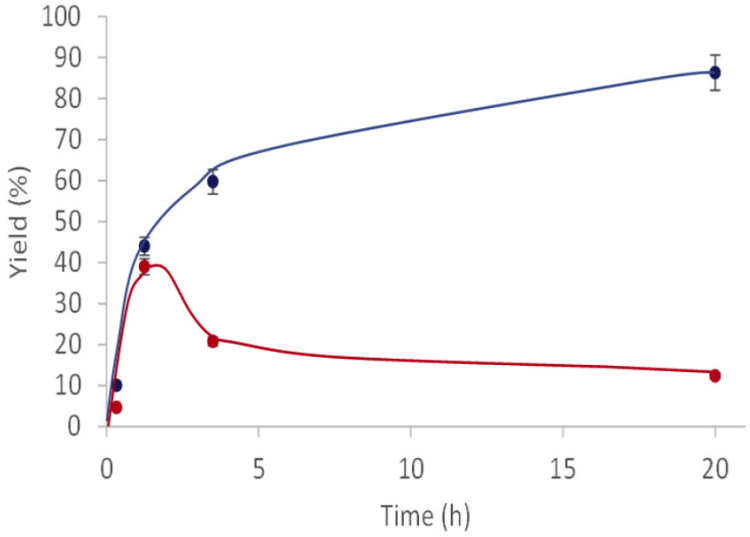

Figure 2.21. Kinetics for the one–pot cyclopropenone hydration/Chan–Lam coupling reaction of diphenylcyclopropenone with boronic acid to obtain **1.6b** (blue line), forming during a pre-stage the intermediate **1.3a** (red line), catalyzed by **Ni^{2+}@Cu-Ni-Me_3mpba** (20 mol%). For reaction conditions, see Figure 2.20. Error bars account for a 5% uncertaintity

The Chan–Lam coupling is severelly inhibited after exchanging Ni^{2+} by either Fe^{3+} or Pd^{2+} in the MOF (Table 2.6, Yield of **1.6a**),43which confirms the catalytic action of Ni^{2+} for the coupling.[43] Also it is shown in Table 2.6, the direct coupling of the boronic acid with either the alkene moiety of **1.3a (1.1a+$H_2$0)**[44] or of **1.1a**,[46] to give product **1.7a**, occurs, and the latter only occured in great extent when Pd^{2+} was the exchanged cation (**$Ni^{2+}Pd^{2+}$@CuNi-Me_3mpba**, Table 2.6). KOH was the base of choice from all the bases tested due to its higher yields (Table 2.6). It is therefore concluded despite Cu^{2+} is traditionally active as a catalyst for the Chan–Lam reaction,[47] the Cu^{2+} cations, from the framework in **Ni^{2+}@CuNi-Me_3mpba**, can not accomodate two different aromatic molecules in its rigid metal coordination sphere and neither perform re-

dox switches, thus being merely inactive for the coupling. Thus, **Ni^{2+}@ CuNi-Me_3mpba** acts here as a bifunctional solid metal catalyst where Cu^{2+} catalyzes the hydration reaction and Ni^{2+} the Chan–Lam coupling.

Table 2.6. Results for the one-pot cyclopropenone hydration/Chan-Lam reaction with cyclopropenone and the boronic acid. For reaction conditions, see Figure 2.20.

Entry	Catalyst	Base	Yield of 1.6a / 1.7a (%)
1	**Ni^{2+}@CuNi-Me_3mpba**	**KOH**	**61 / 6**
2	**Fe^{3+}@CuNi-Me_3mpba**	KOH	12 / 0
3	**$Ni^{2+}Pd^{2+}$@CuNi-Me_3mpba**	KOH	8 / 89
4	**Ni^{2+}@CuNi-Me_3mpba**	K_2CO_3	22 / 3
5	**Ni^{2+}@CuNi-Me_3mpba**	K_3PO_4	44 / 5
6	**Ni^{2+}@CuNi-Me_3mpba**	Pyridine	11 / 3
7	**Ni^{2+}@CuNi-Me_3mpba**	Et_3N	<1 / <1

Knowing that **$Ni^{2+}Pd^{2+}$@CuNi-Me_3mpba** is catalytically active for the direct coupling of diphenylcyclopropenone (**1.1a**) and boronic acid (**1.5a**) to give **1.7a** (89%, entry 3 in Table 2.6), a one–pot cyclopropenone hydration/Mizoroki–Heck coupling reaction was tested. In this approach, the direct coupling of the alkene with the cyclopropenone cannot occur, thus giving an opportunity for the cascade reaction to proceed.

The deficiency of straightforward, atom economical and chemoselective synthetic methods for cinnamates translates into the unfeasibility of a straightforward synthesis for medium size lactones by intramolecular Heck reaction[48-53] since the preparation of cinnamates containing an aryl halide functionality at 5 to 8 carbon atom distance, ready for coupling, is difficult to find.[54-57] Figure 2.22 shows the products belonging to the cumerine family whose synthesis has been catalyzed by the homogeneous catalyst $Pd(OAc)_2$ (2 mol%) and the heterogeneous catalyst discussed in this chapter, **$Ni^{2+}Pd^{2+}$@CuNi-Me_3mpba** (10 mol%). The main difference is that starting from monophenylcyclopropenone, for the first case a pre-synthesis of the cinnamates and an intramolecular Heck reaction is required, whereas with the MOF it has been obtained in a single step the regioirregular Heck products in reasonable yields, called one–pot reaction. These results confirm and significantly expand previous work[58,59] with sterically–hindered organopalladium complexes where the high electron–withdrawing nature of acrylates is overridden by the severe steric effects on the catalytic Pd site, which forces the coupling to occur on the electronically–disfavored alpha position.[60-64]

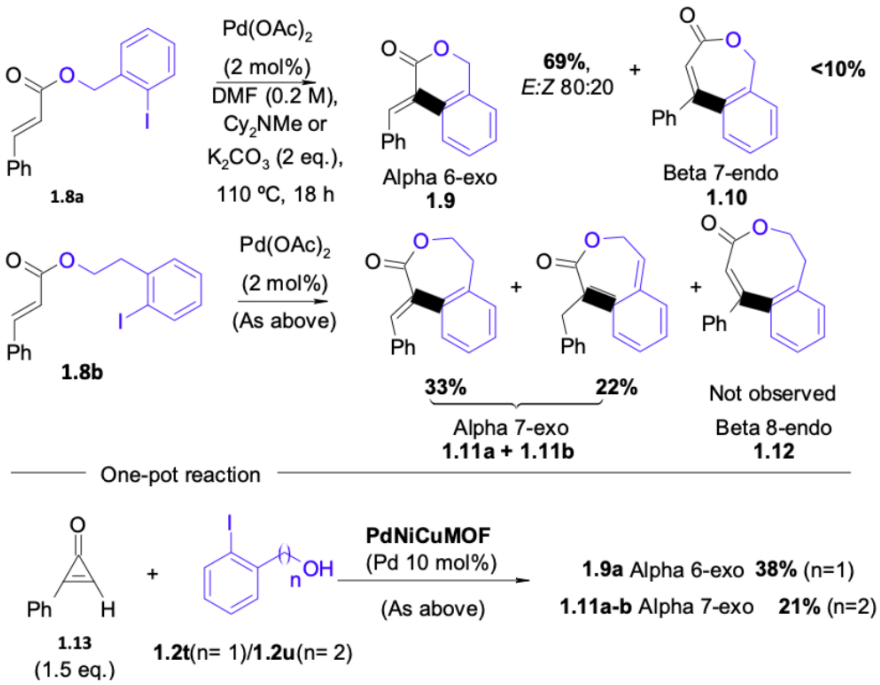

Figure 2.22. Intramolecular Heck reaction of ortho–iodo substituted cinnamates **1.8a** and **1.8b** (formed by iodo substituted monophenylcyclopropenone, **1.13**, and benzyl alcohol radical, **1.2t-u**) with the catalyst $Pd(OAc)_2$ (2mol%), and one–pot hydroalkoxylation of monophenylcyclopropenone 1.13 with iodo substituted benzyl alcohol/ intramolecular Mizoroki–Heck reaction catalyzed by **$Ni^{2+}Pd^{2+}$@CuNi-Me_3mpba** (10 mol%).

Given the irrelevant role of Ni^{2+} cations in the one–pot hydroalkoxylation / Mizoroki–Heck coupling reaction, seemed reasonable to replace, completely, Ni^{2+} cations by Pd^{2+} ones in order to increase the efficiency of the catalyst. When Ni^{2+} cations hosted in the pores are replaced by Pd^{2+} cations and reduced with $NaBH_4$, subnanometer Pd_4 clusters are formed, and the corresponding MOF **$Pd0_4$@CuNi-Me_3mpba** was not active even for the esterification, which did not proceed. It is due to the lack of activity of **$Pd^0{}_4$@CuNi-Me_3mpba** for the hydration of the

cyclopropenone, which can be associated with the inaccessibility of the reagents to the Cu^{2+} sites after the Pd cations have been reduced and agglomerated in clusters.

2.6. Conclusions

Given the synthesis and applicability of **Ni^{2+}@CuNi-Me_3mpba** and its variants (such as **Fe^{3+}@CuNi-Me_3mpba** or **Ru^{3+}@CuNi-Me_3mpba**), we wanted to extrapolate this post-synthetic methodology to the partial substitution of Ni^{II} cations in **Ni^{2+}@CuNi-Me_3mpba** by Pd^{II} ones to obtain mixed metal MOFs with catalitically active metals, of different nature, within their pores (in this case Ni and Pd). The PSM applied to **$Ni^{2+}Pd^{2+}$@CuNi-Me_3mpba** has been studied and its success verified by different characterisation methods:

- Elemental analysis: verified the chemical composition of the target compound.

- IR: related the displacement of the signals to the maintenance of the fixed coordination sites in the structure and the slight change in the coordination produced by the new interaction of the functional groups with the metal inserted in the pores of the MOF.

- SEM-EDAX: allowed the continuous checking of the partial cation exchange produced from the Ni by the Pd, by means of the steichimetric metal percentages, until obtaining Cu/Ni ratios of 1.2 corresponding to the maintenance of the metals of the metal-organic architecture $Ni^{II}_4Cu^{II}_6$ that has to be kept fixed after the PSM and 50% of the Ni lodged in the pores without exchanging and Ni/Pd ratios of 5 corresponding to the 5 steichimetric nickels that there are for each Pd in the formula $[Pd^{II}(NH_3)_4]Ni^{II}\{Ni^{II}_4[Cu^{II}_2(Me_3mpba)_2]_3\} \cdot 52H_2O$.

- XPS: confirmed that the oxidation state of Pd remains at

+2, when the metal coordination shifts from interacting with the source species NH_3 and Cl^- molecules to the chemical environment of the MOF.

- SC-XRD: confirmed more visually that the square and octagonal layered architecture with nickel at the vertices and copper at the midpoints of the edges is maintained, as well as the spatial arrangement of Pd and Ni metals in the more accessible octagonal pores.

- XRPD: confirmed that both the crystals and the crystalline powder of **$Ni^{2+}Pd^{2+}$@CuNi-Me_3mpba** obtained are isostructural and that the MOF maintains crystallinity and robustness after PSM.

- TGA/STDA: verified the number of water molecules with which the MOF crystallises and gave us information about the stability of the MOF against temperature.

- Gas adsorption isotherm showed type I isotherms characteristic of microporous materials and confirmed that after PSM the MOF retains its porosity, being higher for **$Ni^{2+}Pd^{2+}$@CuNi-Me_3mpba** than for **Ni^{2+}@CuNi-Me_3mpba**, suggesting that **$Ni^{2+}Pd^{2+}$@CuNi-Me_3mpba** has a larger accessible surface area and greater structural stability.

After verifying the obtaining of this compound, its catalytic qualities have been tested and have given very positive results.

The different metals contained in **$Ni^{2+}Pd^{2+}$@CuNi-Me_3mpba** (Cu, Ni, Pd) have been shown to be catalytically active sites. Cu has been found

to be very important in the hydroalkoxylation of cyclopropenones where the yields of the reactions catalysed by **Ni^{2+}@CuNi-Me_3mpba** were identical or slightly lower than those carried out in the presence of the homogeneous homologous catalyst $Cu(OAc)_2$. In the case of Ni, its presence led to the Chan-Lam coupling, thus completing the catalytic cascade functionality of **Ni^{2+}@CuNi-Me_3mpba**, where Cu is in charge of the hydration reaction and Ni^{2+} of the Chan-Lam coupling. The reason for the deliberate insertion of Pd is given by the permittivity of the one-pot cyclopropenone hydration/Mizoroki-Heck coupling reaction. This implies that the selection of **Ni^{2+}@CuNi-Me_3mpba** or **$Ni^{2+}Pd^{2+}$@CuNi-Me_3mpba** as heterogeneous catalyst will be determined by the desired directionality of the reaction so that the coupling will form more esters (favoured by Ni) or ketones (favoured by Pd), after a previous study of their activity in different solvents and insertion metals. Finally, we focused on the synthesis of coumarin family compounds, where it was observed that the presence of the three metals Cu, Ni and Pd favours the one-pot reaction, as opposed to the homogeneous homologous catalyst $Pd(OAc)_2$ which requires the prior synthesis of the cinnamates.

2.7. References

1. S. M. Cohen, J. Am. Chem. Soc., 2017, 139, 2855–2863.

2. M. Tejeda-Serrano, M. Mon, B. Ross, F. Gonell, J. Fe rrando-Soria, A. Corma, A. Leyva-Perez, D. Armentano and E. Pardo, J. Am. Chem. Soc., 2018, 140, 8827.

3. M. Mon, M. A. Rivera-Crespo, J. Ferrando-Soria, A. Vi dal-Moya, M. Boronat, A. Leyva-Pérez, A. Corma, J. C. Hernández-Garrido, M. López-Haro, J. J. Calvino, G. Raga zzon, A. Credi, D. Armentano and E. Pardo, Angew. Chem., Int. Ed., 2018, 57, 6186–6191.

4. Beheshtia and Ali Morsali. Saeideh RSC Adv., 2014,4, 41825-41830.

5. T. Grancha, J. Ferrando-Soria, H.-C. Zhou, J. Gascon, B. Seoane, J. Pasa´n, O. Fabelo, M. Julve and E. Pardo, An gew. Chem., Int. Ed., 2015, 54, 6521.

6. Marta Mon, Estefanía Tiburcio, Jesús Ferrando-Soria, Rodrigo Gil San Millán, Jorge A. R. Navarro, Donatella Armen tano and Emilio Pardo. Chem. Commun., 2018, 54, 9063.

7. L. Marleny Rodríguez-Albelo, E. López-Maya, S. Ha mad, A. Rabdel Ruiz-Salvador, S. Calero and J. A. R. Navarro, Nat. Commun., 2017, 8, 14457.

8. M. Savage, Y. Cheng, T. L. Easun, J. E. Eyley, S. P. Argent, M. R. Warren, W. Lewis, C. Murray, C. C. Tang, M. D. Frogley, G. Cinque, J. Sun, S. Rudić, R. T. Murden, M. J. Benham, A. N. Fitch, A. J. Blake, A. J. Ramirez-Cuesta, S. Yang and M. Schröder, Adv. Mater., 2016, 28, 8705–8711.

9. X. Cui, Q. Yang, L. Yang, R. Krishna, Z. Zhang, Z. Bao, H. Wu, Q. Ren, W. Zhou, B. Chen and H. Xing, Adv. Mater., 2017, 29, 1606929.

10. D. Britt, D. Tranchemontagne and O. M. Yaghi, Proc. Natl. Acad. Sci. USA, 2008, 105(33), 11623-11627.

11. Z. Arcís-Castillo, F. J. Muñoz-Lara, M. Carmen Muñ0z, D. Aravena, A. B. Gaspar, J. F. Sánchez-Royo, E. Ruiz, M. Ohba, R. Matsuda, S. Kitagawa and J. A. Real, Inorg. Chem., 2013, 52, 12777–12783.

12. S. Yang, L. Liu, J. Sun, K. M. Thomas, A. J. Davies, M. W. George, A. J. Blake, A. H. Hill, A. N. Fitch, C. C. Tang and M. Schröder, J. Am. Chem. Soc., 2013, 135, 4954–4957.

13. K. Tan, P. Canepa, Q. Gong, J. Liu, D. H. Johnson, A. Dyevoich, P. K. Thallapally, T. Thonhauser, J. Li and Y. J. Chabal, Chem. Mater., 2013, 25, 4653–4662.

14. S. Yang, J. Sun, A. J. Ramirez-Cuesta, S. K. Callear, W. I. F. David, D. P. Anderson, R. Newby, A. J. Blake, J. E. Parker, C. C. Tang and M. Schröder, Nat. Chem., 2012,

4, 887–894

15. T. G. Glover, G. W. Peterson, B. J. Schindler, D. Britt, O. Yaghi, Chem. Eng. Sci., 2011, 66, 163–170.

16. Zabrodsky, H.; Peleg, S.; Avnir, D. J. Am. Chem. Soc. 1992, 114, 7843−7851.

17. Pinsky, M.; Avnir, D. Continuous Symmetry Measures. 5. The Classical Polyhedra. Inorg. Chem. 1998, 37, 5575−5582.

18. Llunell, M.; Casanova, D.; Cirera, J.; Alemany, P.; Al varez, S. SHAPE 2.1, Program for Calculating Continuous Sha pe Measures of Polyhedral Structures; Universitat de Barcelo na: Barcelona, Spain, 2013.

19. Lucas H. G. Kalinke, Danielle Cangussu, Marta Mon, Rosaria Bruno, Estefania Tiburcio, Francesc Lloret, Donatella Armentano, Emilio Pardo, and Jesus Ferrando-Soria. Inorganic Chemistry 2019 58 (21), 14498-14506. DOI: 10.1021/acs.inorgchem.9b02086

20. Min Guo, Hong-Ling Cai, Ren-Gen Xiong, Inorganic Chemistry Communications,Volume 13, Issue 12,2010, 1590-1598.

21. Yinina Ma and Young Sun. Journal of Applied Physics 127, 080901 (2020)

22. Qin, J.-S.; Yuan, S.; Zhang, L.; Li, B.; Du, D.-Y.; Huang, N.; Guan, W.; Drake, H. F.; Pang, J.; Lan, Y.-Q.; Alsal me, A.; Zhou, H.-C. J. Am. Chem. Soc. 2019, 141, 2054−2060.

23. Belmabkhout, Y.; Bhatt, P. M.; Adil, K.; Pillai, R. S.; Cadiau, A.; Shkurenko, A.; Maurin, G.; Liu, G.; Koros, W. J.; Eddaoudi, M. Nat. Energy 2018, 3, 1059−1066.

24. Raghavender Medishetty, Jan K. Zaręba, David Ma yer, Marek Samoć and Roland A. Fischer. Chem. Soc. Rev., 2017,46, 4976-5004.

25. Robert J. Comito, Keith J. Fritzsching, Benjamin J. Sun dell, Klaus Schmidt-Rohr, and Mircea Dincă. J. Am. Chem. Soc. 2016, 138, 32, 10232–10237.

26. Elsa Quartapelle Procopio, Fátima Linares,Carmen Montoro,Valentina Colombo, Angelo Maspero, Elisa Barea, Jorge A. R. Navarro. Angew. Chem.2010,122, 7466 –7469.

27. Douglas T. Genna, Antek G. Wong-Foy, Adam J. Matz ger, and Melanie S. Sanford. J. Am. Chem. Soc. 2013, 135, 29, 10586–10589.

28. Jack D. Evans , Christopher J. Sumby and Christian J. Doonan. Chem. Soc. Rev., 2014, 43, 5933-5951.

29. Thais Grancha, Jesús Ferrando-Soria, Hong-Cai Zhou, Jorge Gasean, Beatriz Seoane, Jorge Pasán, Osear Fabelo, Mi

guel Julve, and Emilio Pardo. Angew. Chem. lnt. Ed. 2015, 54, 6521 – 6525.

30. Fortea–Pérez, F. R.; Mon, M.; Ferrando–Soria, J.; Boro nat, M.; Leyva–Pérez, A.; Corma, A.; Herrera, J. M.; Osadchii, D.; Gascon, J.; Armentano, D.; Pardo, E., Nat. Mater. 2017, 16 (7), 760–766.

31. Grancha, T.; Ferrando–Soria, J.; Castellano, M.; Julve, M.; Pasán, J.; Armentano, D.; Pardo, E., Chem. Com mun. 2014, 50 (57), 7569–7585.

32. Adam, R.; Mon, M.; Greco, R.; Kalinke, L. H. G.; Vi dal–Moya, A.; Fernandez, A.; Winpenny, R. E. P.; Doménech–Carbó, A.; Leyva–Pérez, A.; Armentano, D.; Pardo, E.; Fer-ran do–Soria, J., J. Am. Chem. Soc. 2019, 141 (26), 10350–10360.

33. Mon, M.; Adam, R.; Ferrando−Soria, J.; Corma, A.; Ar men-tano, D.; Pardo, E.; Leyva−Pérez, A., ACS Catal. 2018, 8 (11), 10401–10406.

34. Grancha, T.; Ferrando–Soria, J.; Zhou, H. C.; Gascon, J.; Seoane, B.; Pasán, J.; Fabelo, O.; Julve, M.; Pardo, E., Angew. Chem. Int. Ed.. Engl. 2015, 54 (22), 6521–5.

35. Breslow, R.; Posner, J.; Krebs, A., J. Am. Chem. Soc. 1963, 85 (2), 234–234.

36. He, C.; Guo, S.; Huang, L.; Lei, A., J. Am. Chem. Soc.

2010, 132 (24), 8273–8275.

37. Syu, J.-R.; Lin, C.-H.; Kuo, C.-W.; Yang, D.-Y., Tetra hedron Lett. 2014, 55, 1207–1211

38. Viciano–Chumillas, M.; Mon, M.; Ferrando–Soria, J.; Corma, A.; Leyva–Pérez, A.; Armentano, D.; Pardo, E., Acc. Chem. Res. 2020, 53 (2), 520–531.

39. Young, R. J.; Huxley, M. T.; Pardo, E.; Champness, N. R.; Sumby, C. J.; Doonan, C. J., Chem. Sci. 2020, 11 (16), 4031–4050.

40. Yang, D.; Gates, B. C., ACS Catal. 2019, 9 (3), 1779–1798.

41. Dhakshinamoorthy, A.; Li, Z.; Garcia, H. Chem. Soc. Rev. 2018, 47 (22), 8134–8172.

42. Gascon, J.; Corma, A.; Kapteijn, F.; Llabrés i Xamena, F. X., ACS Catal. 2014, 4 (2), 361–378.

43. Tejeda–Serrano, M.; Mon, M.; Ross, B.; Gonell, F.; Fe rrando–Soria, J.; Corma, A.; Leyva–Pérez, A.; Armentano, D.; Pardo, E., J. Am. Chem. Soc. 2018, 140 (28), 8827–8832.

44. Wang, J.; Qin, T.; Chen, T.-G.; Wimmer, L.; Edwards, J. T.; Cornella, J.; Vokits, B.; Shaw, S. A.; Baran, P. S. Angew. Chem. Int. Ed. Engl. 2016, 55 (33), 9676-9679.

45. Chen, W.; Sun, L.; Huang, X.; Wang, J.; Peng, Y.; Song, G., Adv. Synth. Catal. 2015, 357, 1474–1482.

46. Shan, L.; Wu, G.; Liu, M.; Gao, W.; Ding, J.; Huang, X.; Wu, H., Org. Chem. Front. 2018, 5, 1651–1654.

47. Vijayan, A.; Rao, D. N.; Radhakrishnan, K. V.; Lam, P. Y. S.; Das, P., Synthesis 2021, 53, 805–847.

48. Martins, A.; Marquardt, U.; Kasravi, N.; Alberico, D.; Lautens, M., J. Org. Chem. 2006, 71 (13), 4937–4942.

49. Denieul, M.–P.; Laursen, B.; Hazell, R.; Skrydstrup, T., J. Org. Chem. 2000, 65 (19), 6052–6060.

50. Li, X.; Zhou, B.; Yang, R.–Z.; Yang, F.–M.; Liang, R.–X.; Liu, R.–R.; Jia, Y.–X., J. Am. Chem. Soc. 2018, 140 (42), 13945–13951.

51. Lautens, M.; Paquin, J. F.; Piguel, S., J. Org. Chem. 2002, 67 (11), 3972–4.

52. Coya, E.; Sotomayor, N.; Lete, E., Adv. Synth. Catal. 2014, 356 (8), 1853–1865.

53. Beller, M.; Zapf, A., Intermolecular Heck reaction: Pa lladium–catalyzed coupling reactions for industrial fine chemi cals syntheses. In Handbook of Organopalladium Chemistry for Organic Synthesis; Negishi, E., Ed.; John Wiley & Sons,

Inc. 2002; pp 1209–1222.

54. Alami, M.; Liron, F.; Gervais, M.; Peyrat, J.–F.; Brion, J.–D., Angew. Chem. Int. Ed.. Engl. 2002, 41 (9), 1578–1580.

55. Kadnikov, D. V.; Larock, R. C., J. Org. Chem. 2003, 68 (24), 9423–32.

56. Kwak, S. H.; Lim, S.–J.; Yoo, H.–J.; Ha, J.–E.; Gong, Y.–D. Synthesis 2016, 48 (23), 4131–4142.

57. Madhurima, H.; Krishna, J.; Satyanarayana, G., Synthe sis 2015, 47 (09), 1245–1254.

58. Garnes–Portolés, F.; Greco, R.; Oliver–Meseguer, J.; Castel-lanos–Soriano, J.; Consuelo Jiménez, M.; López–Haro, M.; Hernández–Garrido, J. C.; Boronat, M.; Pérez–Ruiz, R.; Leyva–Pérez, A., Nat. Catal. 2021, 4 (4), 293–303.

59. Wucher, P.; Caporaso, L.; Roesle, P.; Ragone, F.; Cava llo, L.; Mecking, S.; Göttker–Schnetmann, I.,Proc. Natl. Acad. Sci. USA 2011, 108 (22), 8955–8959.

60. Beletskaya, I. P.; Cheprakov, A. V., J. Organomet. Chem. 2004, 689 (24), 4055–4082.

61. Nájera, C., ChemCatChem 2016, 8 (11), 1865–1881.

62. Mo, J.; Xiao, J., Angew. Chem. Int. Ed.. Engl. 2006, 45

(25), 4152–4157.

63. Qin, L.; Ren, X.; Lu, Y.; Li, Y.; Zhou, J., Angew. Chem..Int. Ed. Engl. 2012, 51 (24), 5915–9.

64. Fardost, A.; Lindh, J.; Sjöberg, P. J. R.; Larhed, M., Adv. Synth. Catal. 2014, 356 (4), 870–878

CHAPTER

3

3.1. Introduction

Once verified the potential catalytic application of MOFs, by the insertion of catalytically active metal species, studied in chapter 2, we will focus, in this third chapter, on the preparation and study of their catalytic properties of ultrasmall metal nanosized species such as single-atom catalyst (SACs) and subnanometer metal clusters[1-6] (SNMCs).

Even though there may be differences in catalysts, reaction environments, and reaction scopes among the disciplines, the atomic structure of active sites can be used as a bridge to link the mechanisms of different reactions. It has been thought that active sites in homogeneous catalysis systems are mononuclear metal complexes whose ligands or reactants coordinate with the metal centres, which are derived from metal complexes added during the reaction mixture. But also is used to propose binuclear or multinuclear metal species as working active sites. During catalytic reactions, metal species are formed from molecular precursors into metal clusters or nanoparticles by nucleation-growth processes, which have been extensively studied in the preparation of colloid metal nanocrystals. Solvents and reactants are reducing agents that promote the transformation of the molecular metal catalysts into clusters or nanoparticles.

The idea of catalyst activation consisted in increasing the amount of the surface atoms which are in a state of unsaturation relative to the main body of the catalyst material, however, numerous studies have confirmed that the key is the catalyst size, considering the number of metal atoms composing the active sites[7]. In fact, size reduction of metal particles can improve the performance of catalysts due to coordination

environment diminution of the metal centres8 and, especially, that all metal atoms should be outer exposed.

According to their sizes, [9] we can differenciate (Figure 1) among metal nanoparticles (MNPs), Metal clusters (including SNMCs) and single atoms (SACs), [10] which could be considered as the best active sites because they are totally unsaturated and then completely exposed to the reaction environment[11,12]. However, it should be taken into account that both the shape and chemical composition of the catalyst, as well as the metal-support/reactants interaction, are also determining factors.

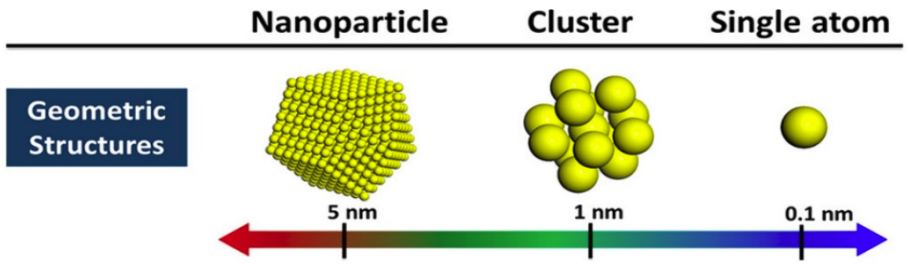

Figure 3.1. Size and nuclearity of single atoms, clusters, and nanoparticles.

Metal clusters (MCs) are isolated metal particles, between 1-10 nm, considered to be formed from three up to twenty atoms.[12,13] Considering their thermodynamical instability, these small metallic entities tend to aggregate, consequently, the synthesis and their following storage must avoid this undesired process. The synthetic approaches can be "bottom-up" or "top-down" methods. In "bottom-up" methodologies, metal salts undergo reduction, nucleation and following growth of the desired particles, while, in "top-down", the nanosized metal particles result from the mechanical downsizing of bulk metals or nanoparticles and subsequent stabilization by the addition of blocking protective agents

that avoid the deactivation of the catalyst.

The metal atoms in the MC can cooperate during the catalysis, unfortunately, MCs stabilized by ligands are poorly effective in catalysis due to the fatal destabilization exerted by reactant coordination and subsequent ligand displacement. However, ligands can act as blocking protective agents14 and supporting material that strongly interacts with the particles, which allows the dispersion and isolation of the active sites from each other, and therefore their stabilization. Here is where MOFs come into play since are promising support materials for nanosized metals, offering many advantages in comparison with the traditional supports[15] (zeolites, carbons, and aluminosilicates).

Relevant examples of the catalytic applicability of MCs[16-18] would be oxidation, hydrogenation, dehydrogenation, and photocatalytic and electrocatalytic reactions.

In the 90s, Single Atoms Catalysts (SACs) were considered "single-site heterogeneous catalysts", where the isolated active sites consisted of one or more atoms[19,20]. But in the 2000s, the concept evolved into the idea of SAC as an individual atom. Of the three catalytic forms described, it is the one with the highest surfaces/volume ratio and tendency to aggregate (being necessary to maintain these entities well isolated and stable), and they are a priori those with the highest catalytic activity if they are stabilized with suitable support materials.

Most of the uses of SACs were initially dedicated to the activation of carbon-free small molecules such as O_2, H_2 or H_2O, frequently in electrochemical and photochemical processes. Other relevant examples of

the catalytic applicability of SACs are oxidation, hydrogenation, dehydrogenation, hydroformylation, photocatalysis, electrocatalysis and even cross-coupling reactions.[21]

MOFs are interesting porous materials due to their ability to be tuned and versatility. They are also crystalline enough to be measured by single-crystal X-ray diffraction (SC-XRD) before and after post-synthetic methods. The principal interest of MOFs is their network composition which appeals properties to act as chemical nanoreactors and be used to synthesize and stabilize, within their channels, catalytically active species that otherwise could be hardly accessible. Highly robust and crystalline oxamato- and oxamidato-MOFs features with tailored channels (in terms of size, charge and functionality) can be exploited for the incorporation and stabilization of metals salts and complexes, and the in situ synthesis of subnanometric metal clusters[22-24] (SNMCs) and single-atom catalysts[25-30] (SACs). The challenge to be exceeded is to obtain materials with a high catalytic activity that are sufficiently crystalline to study their intra-structural interactions, selectivity, and catalytic mechanisms and sufficiently stable to reproduce their synthesis at gram-scale and be reused.

By using so-called post-synthesis methods (PSMs)31, guest molecules can either be inserted[32] or constructed within the channels of the MOFs, acting as chemical nanoreactors[33]. Among the wide range of possible functional entities that can be incorporated or synthesized within MOFs, catalytically active species tend to be the most suitable given the inherent characteristics of these porous materials. MOFs[34] exhibit catalytic activity resulting from the catalytic activity of their constituting building blocks, open metal sites and organic links, of the coordination

network, or of the guests embedded inside their pores. With regard to guest species, MOFs offer advantages to support catalytically active metal cations[35], complexes[36], small clusters[37], and nanoparticles[38,39]. MOFs, as compared to other solid catalysts such as zeolites and other microporous silico-alumino materials with embedded metal species[40-42], show thermal and chemical stability limitations, they offset these limitations with a rich structural variety, due to a large number of known metal centers/secondary building units (SBUs) and organic linkers, and high tuneable porosity, which eases the accessibility of active sites for catalysis, facilitate the transport of substrates and products, and offer size- and shape-selective catalysis.

The modified anionic oxamato-based MOF of formula $Ni^{II}_2\{Ni^{II}_4[CuII_2(Me_3mpba)_2]_3\} \cdot 54H_2O$, **$Ni^{2+}$@CuNi-$Me_3$mpba** (Figure 1.35), discussed in chapter 2, was used also to transform in situ the metals embedded in the MOF into isolated (SACs) or aggregated (SNMCs) entities. These transformations gave the material other equally interesting catalytic properties.

In a previous work of my group, **Ni^{2+}@CuNi-Me_3mpba** used as a nanoreactor, allowed the obtention of Pd_4 clusters with mixed-valence oxidation states, stabilized and homogeneously organized within the walls of a MOF. To obtain well-defined ligand-free Pd_4 clusters within the channels of **Ni^{2+}@CuNi-Me_3mpba**[43] it was necessary to carry out three PS steps: A transmetalation and cation exchange processes involving the replacement of all magnesium(II) cations in an ancestor **Mg^{2+}@CuNi-Me_3mpba** to give the **Ni^{2+}@CuNi-Me_3mpba**, exchange of the nickel(II) cations within the pores by palladium(II) ones to give $[Pd^{II}_2(\mu\text{-}O)(NH_3)_6(NH_4)_2]_{0.5}\{Ni^{II}_4[Cu^{II}_2(Me_3mpba)_2]_3\}\cdot 52H_2O$, **$Pd^{2+}$@**

CuNi-Me$_3$mpba, and the controlled insertion of the reducing agent (NaBH4) to synthesize in situ the naked Pd_4 NCs and give $[Pd_4]_{0.5}$@ $Na_3\{Ni^{II}_4[Cu^{II}_2(Me_3mpba)_2]_3\}\cdot 56H2O$, **Pd04@CuNi-Me3mpba**, (Figure 3.2). These PS steps were studied before, chapter 2, except for the last one. The study of the crystal structure in every step, by SC-XRD[44-46], allowed controlling of the formation of SMNCs, i.e., the number of inserted cations and their organization in the confined space.

Pd^{2+}@CuNi-Me$_3$mpba possesses a homogeneous distribution of Pd^{2+} cations along the channels, which are situated in specific positions interacting with the carboxylate-oxygen atoms from the network and limited in number by the anionic charge of the MOF. In this way, MOF restrains the movement capacity of the palladium atoms, favoring the formation of SMNCs and preventing their aggregation into larger MNPs. These rare linear Pd4 NCs are also stabilized by weak supramolecular interactions (Figure 3.2b) that prevent their leaching during catalysis.

The resulting solid catalyst **Pd0$_4$@CuNi-Me$_3$mpba** outperformed state-of-the-art metal catalysts in carbene-mediated reactions of diazoacetates with high yields, such as the inter- and intramolecular Buchner ring expansion reaction, the alcohol insertion and the dimerization of diazocompounds, to give some unique naturally occurring and synthetically useful products.[47-49]

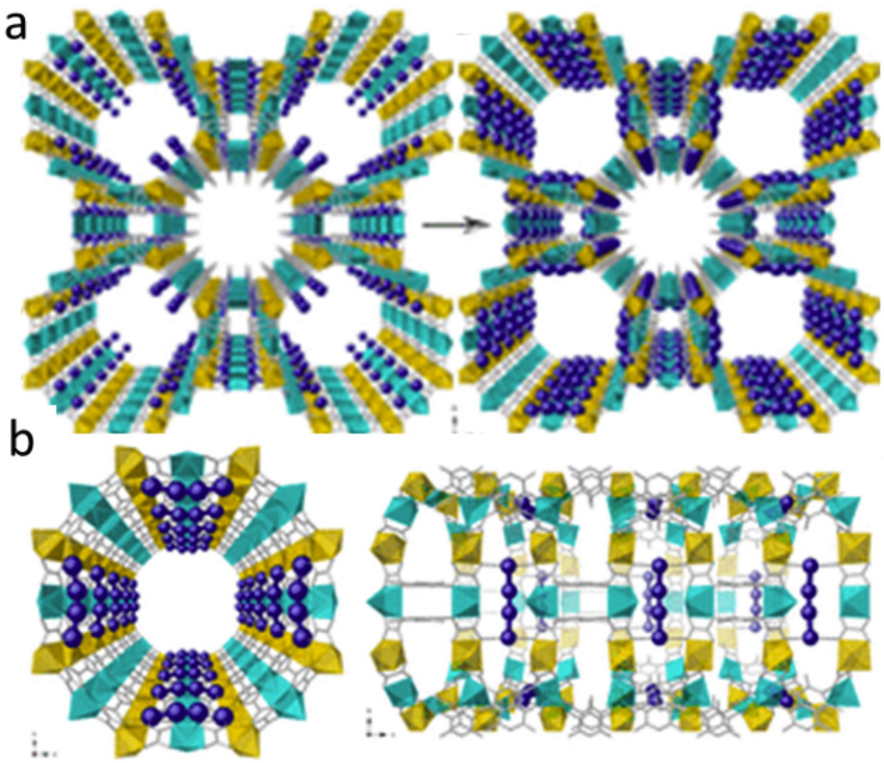

Figure 3.2. a) **Pd^{2+}@CuNi-Me_3mpba** reduces the process to obtain **Pd^0_4@CuNi-Me_3mpba.** b) Perspective views of a channel of **Pd^{04}@CuNi-Me_3mpba** emphasizing the stabilizing interactions.[45]

Their impressive catalytic behaviour of Pd is due to the stabilization of intermediate Pd valence within the supported-MOF cluster and enables carbene bonding to give a catalytic activity that exceeds by one order of magnitude that of the state-of-the-art catalysts for these reactions. In addition, the solid catalyst can be recovered and reused up to 20 times in batch without any reactivation treatment or depletion of the catalytic activity, or operated in flow with solvent recycling during hours.

The versatility of **Ni^{2+}@CuNi-Me_3mpba** was also extrapolated to the

preparation of platinum SACs. They are obtained in a similar way to Pd_4 SNMCs but with the insertion of Pt. So, the **Ni^{2+}@CuNi-Me_3mpba** (Figure 3.3a) was exchanged with $[Pt(NH_3)]_4^{2+}$ to give the intermediate hybrid material $[Pt^{II}_2(\mu\text{-}OH_2)(NH_3)_6)]_{0.65}[Pt^{II}(NH_3)_4]_{0.7}\{Ni^{II}_4[Cu^{II}_2(Me_3mpba)_2]_3\} \cdot 65H_2O$ (**Pt^{2+}@CuNi-Me_3mpba**) (Figure 3.3b), which was then treated with $NaBH_4$ to give the final solid material $[Pt^{I-}_2(\mu\text{-}O)(OH)_2(NH_3)_4]_{0.5}Pt^{I}_1@Na_3$ {Ni $^{II}_4$ [Cu II2(Me3mpba)2]3} $\cdot 79H_2O$ (**$Pt^{2+}Pt^{+}$@CuNi-Me_3mpba**) (Figure 3.3c).

The MOF-supported Pt^{I}_1 [50,51] constituted an exceptional case of a single-atom catalyst (SAC) without strong coordinating ligands or surfaces where Pt^{I}_1 complexes are structurally and electronically well-defined stabilized by water clusters, homogeneously distributed along the channels of an anionic 3D MOF (Figure 3.3).

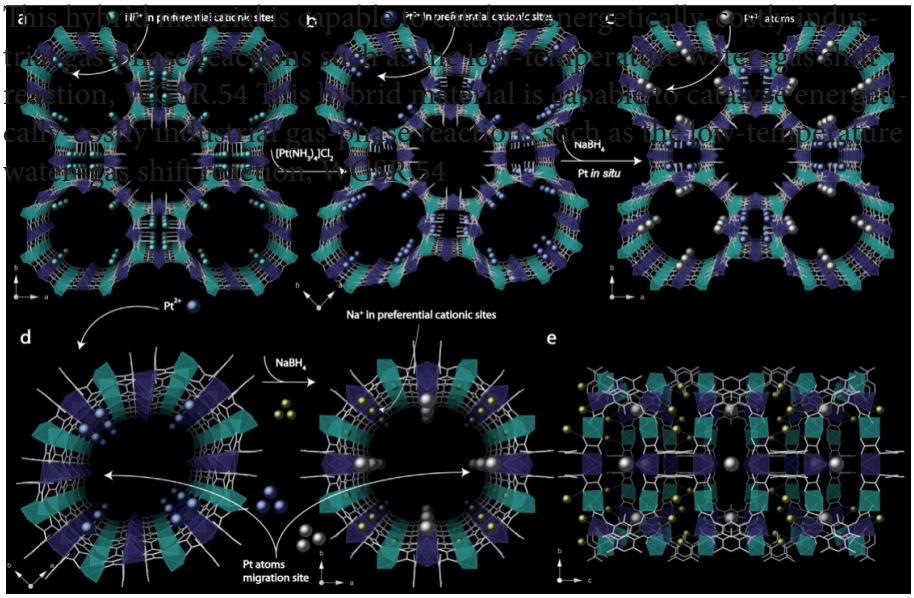

Figure 3.3. Experimental crystal structures of MOFs **Ni^{2+}@CuNi-Me_3mpba** (a), **Pt^{2+}@CuNi-Me_3mpba** (b) and **$Pt^{2+}Pt^{+}$@CuNi-Me_3mpba** (c), and perspective views along different axes (d,e) for **Pt^{2+}@CuNi-Me_3mpba** and **$Pt^{2+}Pt^{+}$@CuNi-Me_3mpba**, respectively, showing in detail the **Pt^{II} (Pt^{2+}@CuNi-Me_3mpba)** and the Na^{I} and Pt^{I}_{1} (**$Pt^{2+}Pt^{+}$@CuNi-Me_3mpba**) sites.[52] Cu atoms from the network are represented by cyan polyhedra. Ni atoms from the network are represented by purple polyhedra. Green Ni^{II}, blue Pt^{II}, gray Pt^{I}, yellow Na^{I} atoms, organic ligands are depicted as sticks.[53]

This hybrid material is capable to catalyze energetically-costly industrial gas-phase reactions such as the low-temperature water–gas shift reaction, WGSR.[54]

3.2. Objectives

The main objective of this chapter focuses on the validation and expansion of the previously developed synthetic strategy consisting on using MOFs, as chemical reactors, for the preparation of ligand-free and well-defined SACs and SNMCs within their channels. Secondly, these metal nanosized species are expected to show outstanding catalytic activity, which will be studied accordingly.

In particular, for **Ni^{2+}@CuNi-Me_3mpba** (see chapter 2), we will focus on the obtention of both homo- and heterometallic SNMCs after one or consecutive insertion metal species. The insertion of silver (homometallic SNMCs) and the insertion of silver and iron into **Ni^{2+}@ CuNi-Me_3mpba** (heterometallic SNMCs) will be presented in this chapter, being necessary the application of a reducing environment that facilitates the formation of clusters after the insertion of the desired metals incorporated into the structure.

So far we have only presented Me_3mpba oxamates as organic ligands forming the MOF. In this section, we want to include also MOFs based on oxamidates and amino acids, in particular with the modified amino acid methylcysteine. The selection of methylcysteine is not accidental. It is well-known the affinity of sulfur atoms for soft metals (like Pd). The palladium insertion will be the one to be studied in these MOFs of smaller pore diameter. Obtaining the SACs also required a reduction process after the metal insertion.

As stated in the introduction (Section 1.7), amino acids linked to oxamate groups to obtain MOF's precursors provide them multiple coor-

dination sites through the carbonyl and the deprotonated amidate and carboxylate donors groups offering advantages such as biocompatibility, stability in water, rich structural diversity, chirality, and specific properties offered by side chain. Specifically, the methyl cysteine-based MOFs, together with methionine, possess methylated thionyl groups as a side chain that can be exposed in the pores of the MOF and have the ability to interact strongly with various metals. This has been exploited by our group for the capture of metal contaminants and the purposeful insertion of catalytically active metals. Image 5 shows the procedure to obtain the SACs and SNMCs in **Ni^{2+}CuNi-Me_3mpba** and **CuSr-Me-cysmox**.

Multiple homo- and hetero-metallic insertions were performed on the oxamate- and oxamidate-based MOFs (discussed in the introduction Section 1.7) which could not be covered in this chapter. Section 7, future work and perspectives, reports some of the structures that have been obtained and could not be included in the thesis report due to lack of complete characterization and catalytic study.

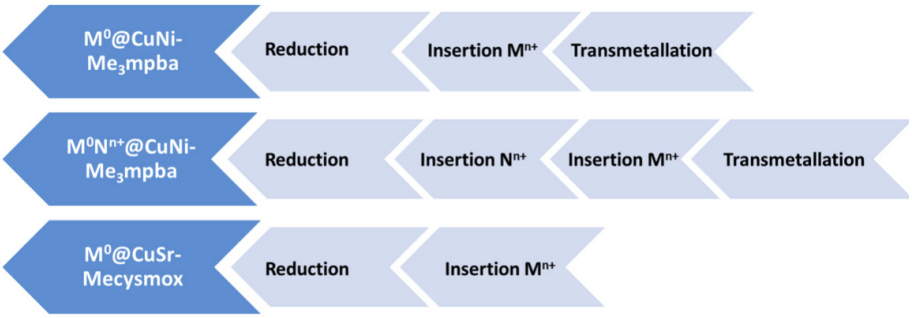

Figure 3.5. Scheme of the MOFs obtained in this chapter.

3.3. Synthesis

As mentioned in the objectives, the synthesis method of homometallic and bimetallic **Ni^{2+}@CuNi-Me_3mpba** SNMCs and **CuSr-Mecysmox** SACs will be explained.

3.3.A. Synthesis of homometallic SNMCs (Ag^0_2@Cu-Ni-Me_3mpba).

Synthesis of $Ag^I_4\{Ni^{II}_4[Cu^{II}_2(Me_3mpba)_2]_3\} \cdot 51H_2O$ (Ag^+@Cu-Ni-Me_3mpba). Similar to the procedure followed for **Pd^{2+}@Cu-Ni-Me_3mpba** but with greater amounts, a silver insertion occurred after Mg-Ni transmetallation. [55] A cation exchange of the Ni ions hosted in the pores for Ag cations occurs, thus forming $Ag^I_4\{Ni^{II}_4[Cu^{II}_2(Me3mpba)_2]_3\} \cdot 51H_2O$ (**Ag^+@CuNi-Me_3mpba**). It is obtained on a multigram scale by immersing *ca*. 20 g of the **Ni^{2+}@CuNi-Me_3mpba** compound powder (5.8 mmol) in a solution of 2.378 g/5mL of the $AgNO_3$ species (14.0 mmol) for 24 hours, in high yield (20.33 g, 96%).

In order to obtain well-formed deep green prisms crystals of **Ag^+@Cu-Ni-Me_3mpba**, which were suitable for single-crystal X-ray diffraction, the insertion conditions have to be also milder. For this purpose, **Ni^{2+}@ CuNi-Me_3mpba** crystals, about 5 mg (ca. 0.0015 mmol) are immersed for 48 hours in 5 mL of aqueous solutions of $AgNO_3$ (0.004mmol), which were replaced three times.

The elemental analysis shows a molecular weight for $Cu_6Ni_4Ag_4C_{78}H_{162}N_{12}O_{87}$ (**Ag^+@CuNi-Me_3mpba**) of Mw 3707.7 g/mol and an elemental percentage of C, 25.27; H, 4.40; N, 4.53, is found (C, 25.34; H, 4.37;

N, 4.59 was expected). IR (KBr) shows the signals ν of = 3008, 2961 and 2926 cm^{-1} (C–H), 1601 cm^{-1} (C=O).

Synthesis of $[Ag^0_2]Ag^I_2Na^I_2\{Ni^{II}_4[Cu^{II}_2(Me_3mpba)2]3\} \cdot 48H_2O$ (Ag^{02}@CuNi-Me_3mpba). The reduction of **Ag^+@CuNi-Me_3mpba**, for both polycrystalline powder (ca. 10 g) and crystal (ca. 5 mg) form, gives $[Ag^0_2]Ag^I_2Na^I_2\{Ni^{II}_4[Cu^{II}_2(Me_3mpba)_2]_3\} \cdot 48H_2O$ (**Ag^0_2@CuNi-Me_3mpba**). It consists of suspending **Ag^+@CuNi-Me_3mpba** in an excess solution of $NaBH_4$ in H_2O/CH_3OH (1:2) (1 mol NaBH4 per mol **Ag^+@CuNi-Me_3mpba** approx.), where after each addition, the mixture is left to react for 1.5 hours and gently washed with H_2O/CH_3OH solution (to retire better $NaBH_4$ with more water content). This operation was repeated a total of 26 times, after which the mixture was filtered on paper giving high yields (ca. 98%).

The elemental analysis shows a molecular weight for $Cu_6Ni_4Ag_4Na_2C_{78}H_{156}N_{12}O_{84}$ (**Ag^0_2@CuNi-Me_3mpba**) of Mw 3699.61 g/mol and an elemental percentage of C, 25.28; H, 4.17; N, 4.59, is found (C, 25.32; H, 4.25; N, 4.54 was expected). IR (KBr) shows the signals ν of = 3011, 2971 and 2928 cm–1 (C–H), 1605 cm–1 (C=O).

This schematic version (Figure 3.6) briefly explains the homometallic insertion of Ag into **Ni^{2+}@CuNi-Me_3mpba**, which after reduction the species obtained a cluster conformation.

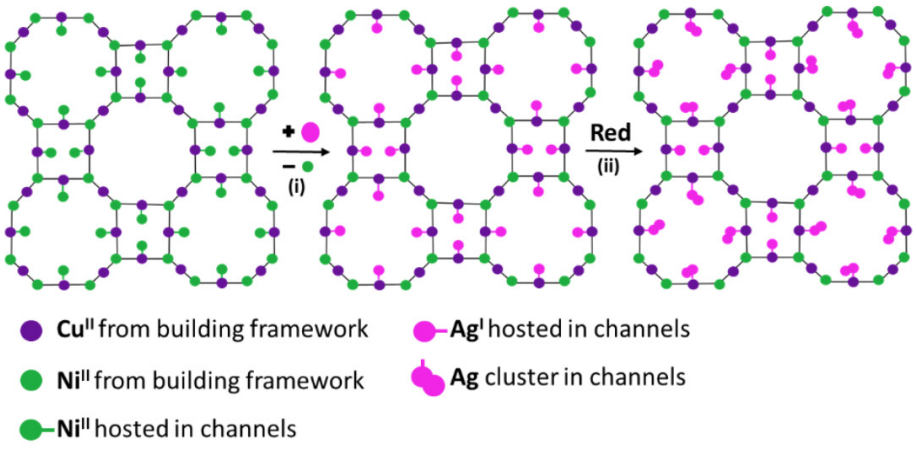

Figure 3.6. Scheme of the synthetic procedure of NiII ⟶ AgI cation exchange in pores (i) and obtaining Ag_2 clusters after reduction (ii).

3.3.B. Combination of SNMCs and SACs within the same MOF ($Ag^0_2Fe^{3+}$@CuNi-Me^3mpba).

Synthesis of $[Ag^+_{3.44}Fe^{III}_{0.66}]$@$\{Ni^{II}_4[Cu^{II}_2(Me_3mpba)_2]_3\}$ · $63H_2O$ (Ag^+Fe^{3+}@CuNi-Me_3mpba). Based on the reported $[Fe^{III}(H_2O)_6]$ $[Fe^{III}_2(\mu\text{-}O)_2(H_2O)_6]_{1/2}\{Ni^{II}_4[Cu^{II}_2(Me_3mpba)_2]_3\}$ · $72H_2O$ (**Fe^{3+}@Cu-Ni-Me_3mpba**)[56] and the recently mentioned [Ag02]@AgI2NaI2{NiI-I4[CuII2(Me3mpba)2]3} · $48H_2O$ (**Ag^0_2@CuNi-Me3mpba**), an intermediate version between the two species was created in order to merge the properties of **Fe^{3+}@CuNi-Me_3mpba** and **Ag^0_2@CuNi-Me_3mpba** in a novel MOF with formula $[Ag^0_2(Ag^0)_{1.44}Fe^{III}_{0.66}]$@$Na^I_2\{Ni^{II}_4[Cu^{II}_2$(-Me3mpba)2]3} · $63H_2O$ (**$Ag^{02}Fe^{3+}$@CuNi-Me3mpba**).

The first stage of a multigram scale of $[Ag^+_{3.44}Fe^{III}_{0.66}]$@$\{Ni^I_{I4}[Cu^{II}_2$(-$Me_3$mpba)$_2]_3\}$ · $63H_2O$ (**Ag^+Fe^{3+}@CuNi-Me_3mpba**) synthesis consists, rationionaly, of the first stage of **Ag^+@CuNi-Me_3mpba** production: ca-

tion exchange of nickel hosted in **Ni^{2+}@CuNi-Me_3mpba** pores by silver. Their obtention consists in was also carried out by using a powder sample of compound **Ni^{2+}@CuNi-Me_3mpba** (5 g) which were suspended, for 24 hours, in 1 g /5 mL of $AgNO_3$ aqueous solutions (6 mmol), until complete replacement of Ni^{2+}, cations hosted in the pores, by Ag^+ ones. Then, the resulting material was resuspended in a $(NH_4)_2Fe(SO_4)_2 \cdot 6H_2O$ water/methanol (1:1) solution (1.2 g, 3 mmol) under aerobic conditions. The process was repeated several times until Fe percentage was near Ag percentage every 24 h.

Synthesis of $[Ag^0_2(Ag^0)_{1.44}Fe^{III}_{0.66}]@Na^I_2\{Ni^{II}_4[Cu^{II}_2(Me_3mpba)_2]_3\} \cdot 63H_2O$ ($Ag^0_2Fe^{3+}$@CuNi-Me_3mpba). The second step consists on the reduction of **Ag^+Fe^{3+}@CuNi-Me_3mpba** to give the novel MOF with formula $[Ag^0_2(Ag^0)_{1.44}Fe^{III}_{0.66}]@Na^I_2\{Ni^{II}_4[Cu^{II}_2(Me_3mpba)_2]_3\} \cdot 63H_2O$ (**$Ag^0_2Fe^{3+}$@CuNi-Me_3mpba**). 5 g of **Ag^+Fe^{3+}@CuNi-Me_3mpba** were soaked in a H_2O/CH_3OH (1:1) solution to which $NaBH_4$, divided 3 g in 15 fractions (4 mmol of $NaBH_4$ per mmol of MOF each), were added progressively in the space of 72 hours, each fraction was allowed to react for 1.5 h, and the same successful results occurs and a high yield (5.13 g, 96%).

The elemental analysis shows a molecular weight for $Cu_6Ni_4Fe_{0.66}Ag_{3.44}Na_2C_{78}H_{186}N_{12}O_{99}$ (**$Ag^0_2Fe^{3+}$@CuNi-Me_3mpba**) of Mw 3946.29 g/mol and an elemental percentage of C, 23.88; H, 4.72; N, 4.23 is found (C, 23.74; H, 4.75; N, 4.26 was expected). IR (KBr) shows the signals ν of 3011, 2956 and 2917 cm–1 (C–H), 1607 cm–1 (C=O).

Alternatively, the procedure was also carried out by using the same synthetic procedure but with smaller amounts of both, where well-formed dark green prisms of $[Ag^+_{3.44}Fe^{III}_{0.66}]@\{Ni^{II}_4[Cu^{II}_2(Me_3mpba)_2]_3\}$

· $63H_2O$ (**$Ag^{+}Fe^{3+}$@CuNi-Me_3mpba**) were suitable for X-ray diffraction, were obtained in a Three-step PS process:

First, ca. 5 mg crystals of **Ni^{2+}@CuNi-Me_3mpba** (0.0015 mmol) were suspended, for 24 hours, in 1 mg /5 mL of $AgNO_3$ aqueous solutions (0.006 mmol), Ni^{2+} cations exchange by Ag^{+} hosted in the pores occurs. Then, the resulting material was resuspended in a $(NH_4)_2Fe(SO_4)_2.6H_2O$ water/methanol (1:1) solution (1.2 mg, 0.003 mmol) under aerobic conditions. The process was repeated several times but the iron contents were identical to those obtained after 24 h. The crystals were isolated by filtration on paper and air-dried.

After this double PS process, the resulting crystals (ca. 5 mg) were soaked in a H_2O/CH_3OH (1:1) solution to which $NaBH_4$, divided in 15 fractions (0.4 mmol of NaBH4 per mmol of MOF each), were added progressively in the space of 72 hours. Each fraction was allowed to react for 1.5 h. After this period, samples were gently washed with a H_2O/CH_3OH solution and filtered on paper.

The elemental analysis shows a molecular weight for $Cu_6Ni_4Fe_{0.66}Ag_{3.44}Na_2C_{78}H_{186}N_{12}O_{99}$ (**$Ag^{0}_{2}Fe^{3+}$@CuNi-Me_3mpba** of Mw 3946.29 g/mol and an elemental percentage of C, 23.79; H, 4.73; N, 4.36, is found (C, 23.74; H, 4.75; N, 4.26 was expected). IR (KBr) shows the signals ν of 3008, 2967 and 2923 cm–1 (C–H), 1611 cm–1 (C=O).

This schematic version (Figure 3.7) briefly explains the heterometallic insertion of Ag and Fe into **Ni^{2+}@CuNi-Me_3mpba**, where, firstly, was necessary to insert completely Ag in pores and later displace a half Ag cation by Fe, being necessary also a reduction process to obtain clusters.

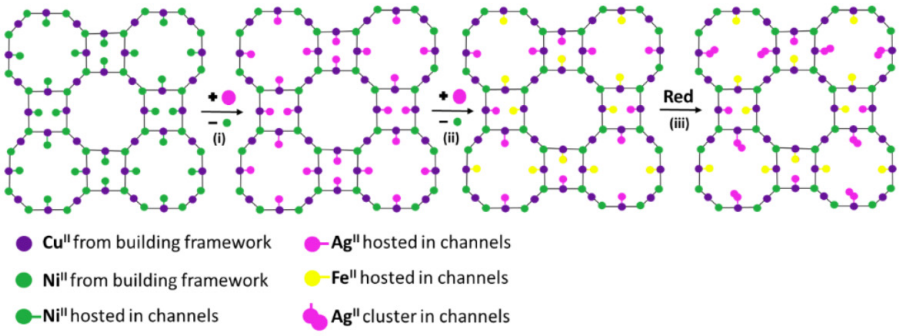

Figure 3.7. Scheme of the synthetic procedure of $Ni^{II} \longrightarrow Ag^{I}$ complete cation exchange in pores (i), $Ag^{II} \longrightarrow Fe^{III}$ partial cation exchange (ii) and obtaining Ag^{2} clusters after reduction (iii).

3.3.C. Synthesis of MOF-driven SACs (Pd0@CuSr-Mecysmox)

As mentioned in the objectives, we added a different MOF to the one we have been working with so far. In this case, instead of using MOFs based on oxamates and an aromatic ligand, we use oxamidates and amino acids, in this case esterified methylcysteine (Figure 3.31 in the introduction chapter). In the following synthetize process, similarities with respect to Me3mpba-based MOFs (such as the use of a cuprous dinuclear precursor) and differences (such as no need for transmetallation) will be noted.

Synthesis of H_2Me_2-(*S,S*)-Mecysmox = bis[(*S*)-methyl-(*L*)-cysteine] oxalyl diamide. In the case of this methylcysteine-based bioMOF, obtaining the proligand required a prior esterification step. The esterification procedure consists in, first, under a N_2 atmosphere, an excess of thionyl chloride (13.10 mL, 180 mmol $SOCl_2$) was added dropwise,

under stirring at 0°C on an ice-bath, to a solution of 8.11 g (*S*)-methyl-(*L*)-cysteine amino acid (60 mmol) in 150 mL of MeOH. The low addition temperature is highly recommended because the mixture causes an exothermic reaction. Once all the $SOCl_2$ solution was added, the colorless mixture was refluxed in 80°C for 6 hours. Then, the excess of thionyl chloride was distilled with MeOH (3 x 150 mL). The reaction mixture was washed with acetone (150 mL) and diethyl ether (100 mL) and further concentrated, under reduced pressure, to afford the methyl ester derivative of the (*S*)-methyl-(*L*)-cysteine amino acid, which was used in the next step without further purification.

After aminoacid esterification, 8.95 g of the resulting methyl ester derivative of the (*S*)-methyl-(*L*)-cysteine (60 mmol) was dissolved in 250 mL of dichloromethane. To neutralise the HCl molecules formed during the interaction of the oxalyl with the modified amino acid, 8.4 mL triethylamine (60 mmol) was used as a base, giving a colorless reaction mixture. As mentioned in advance, it was added drop by drop another solution containing 2.54 mL of oxalyl chloride (30.0 mmol) in 150 mL dichloromethane under vigorous stirring at 0 °C on an ice-bath. The resulting solution was further stirred for two hours. The small amount of white solid (Et_3NHCl) formed was filtered off and the resulting solution was then concentrated in a rotatory evaporator to a final volume of 100 mL. The purification was carried out by extraction of the obtained pale yellow solution was washed three times with water (3x50 mL). Finally, the target product was separated of the solvent DCM with a rotatory evaporator to afford a white solid, which was collected with water and dried under vacuum to obtain a yield of 9.62 g (91%) of **H_2Me_2-(S,S)-Mecysmox** = bis[(*S*)-methyl-(*L*)-cysteine]oxalyl diamide. The elemental analysis shows a molecular weight for $C_{12}H2_0S_2N_2O_6$

(H_2Me_2-(*S,S*)-Mecysmox) of Mw 352.4 g/mol and an elemental percentage of C 40.97, H 5.68, S 18.26, N 7.99, is found (C 40.98, H 5.72, S 18.20, N 7.95 was expected). ^{1}H NMR ([D_6]DMSO) confirms that the compound was obtained correctly: 2.20 (s, 6H; SCH3), 2.97 (m, 2H; CH2), 3.17 (m, 2H; CH2), 3.62 (s, 6H; OCH3), 4.78 (t, 2H; CH), 9.01 (d, 2H; NH from CONH). IR (KBr) shows the signals ν of 1763, 1751and 1656 cm^{-1} (C=O).

Synthesis of $(Me_4N)_2\{Cu_2[(S,S)\text{-Mecysmox}](OH)_2\}.\ 5H_2O$. To produce the metalloligands **$(Me_4N)_2\{Cu_2[(S,S)\text{-Mecysmox}](OH)_2\}.\ 5H_2O$**, it was necessary for the -OCH_3 groups to be free to interact with the Cu. To remove the methyl protector group, 10.572 g of H_2Me_2-(*S,S*)-Mecysmox (30 mmol) was suspended in water (60 mL) and treated with 36 mL of 25% methanolic solution of Me_4NOH (125 mmol) until complete dissolution. In order to be able to make a slow addiction of Cu (to avoid polymeric aggregates), 8.07 g of $CuCl_2$ (60 mmol) was solved in 25 mL of water and, then, added dropwise while the reaction mixture was stirred. The resulting deep green solution was concentrated to a volume of *ca*. 5-10 mL in a rotary evaporator affording a green polycrystalline solid that was gently washed with acetone filtered off and dried under vacuum, yielding a performance of 14.77 g (68%). The elemental analysis shows a molecular weight for $C_{18}H_{48}Cu_2S_2N_4O_{13}$ ($(Me_4N)_2\{Cu_2[(S,S)\text{-Mecysmox}](OH)_2\}.\ 5H_2O$) of Mw 719.8 g/mol and an elemental percentage of C, 30.13; H, 6.63; S, 8.93; N, 7.75% is found (C, 30.03; H, 6.72; S, 8.91; N, 7.78%was expected). IR (KBr) shows the signals ν of 3621 cm–1 (O-H), 3023, 2964 cm^{-1} (C-H), 1608 cm^{-1} (C=O).

Synthesis of $\{Cu_6Sr[(S,S)\text{-Mecysmox}]_3(OH)_2(H_2O)\}\ .\ 15H_2O$

(CuSr-Mecysmox). The corresponding MOF, $\{Cu_6Sr[(S,S)\text{-Mecysmox}]_3(OH)_2(H_2O)\} \cdot 15H_2O$ (CuSr-Mecysmox), was obtained merely by precipitation, in the case of polycrystalline powder. So, 4.32 g of de dinuclear metalloligands $(Me_4N)_2\{Cu_2[(S,S)\text{-methox}](OH)_2\} \cdot 4H_2O$ (6.0 mmol) was dissolved in 50 mL of water, it was added dropwise under stirring 0.42 g of $Sr(NO_3)_2$ (2.0 mmol) in 10 mL of aqueous solution and it is left with further stirring for 10h, at room temperature. On this way, a green polycrystalline powder was obtained and collected via filtration and dried with ethanol, acetone and diethyl ether with a yield of 2.91 g (83%). The elemental analysis shows a molecular weight for $C_{30}Cu_6SrH_{70}S_6N_6O_{36}$ ($\{Cu_6Sr[(S,S)\text{-Mecysmox}]_3(OH)_2(H_2O)\} \cdot 15H_2O$) of Mw 1752.2 g/mol and an elemental percentage of C, 20.51; H, 4.00; S, 10.99; N, 4.83% is found (C, 20.56; H, 4.03; S, 10.98; N, 4.80% was expected). IR (KBr) shows the signals ν of 1605 cm^{-1} (C=O). Unlike the crystals of **Ni^{2+}@CuNi-Me_3mpba** and derivatives, the crystals formed from methylcysteine were hexagonal prisms. Well-shaped hexagonal prisms of **CuSr-Mecysmox** suitable for X-ray structural analysis could be obtained by slow diffusion, in an H-shaped tube, of H_2O/DMF (1:9) solutions containing stoichiometric amounts of 0.13 g solved in 0.5ml of solvent $(Me_4N)_2\{Cu_2[(S,S)\text{-Mecysmox}](OH)_2\} \cdot 5H_2O$ (0.18 mmol) in one arm and 0.012 g $Sr(NO_3)_2$ (0.06 mmol) in 1ml of the solvent in the other, about 1.5-2 months is the time that we have to wait normally to obtain it. They were isolated by filtration on paper and air-dried.

Figure 3.8 describes the synthetic route to obtain de target MOF, starting with (i) the proligand obtention by merging the esterified methyl cysteine with oxalyl chloride, continuing with (ii) their coordination with copper and finishing with (iii) the link of dinuclear copper complex and strontium.

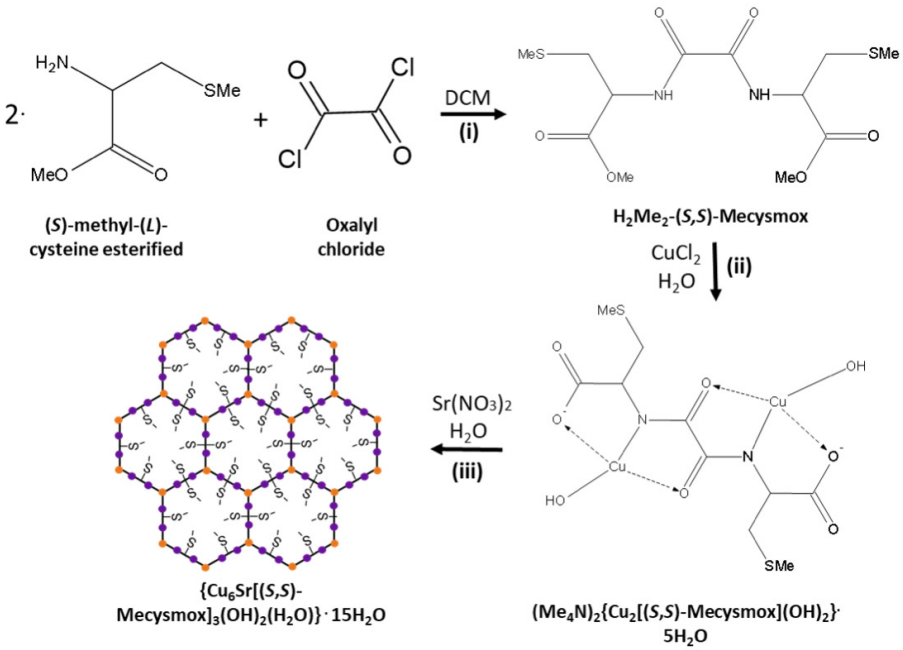

Figure 3.8. The synthetic process to obtain the **MOF CuSr-Mecysmox**: i) oxamidato bond is produced between oxylil chloride and the specific amino acid, ii) coordination bond is produced between the synthesized proligand and cooper and, finally, (iii) it was produce the directional growing of the MOF when building blocks interact with strocium as metal nodes.

Synthesis of $[Pd_2(H_2O)(NH_3)_6]_{0.5}Cl_2$@$\{Sr^{II}Cu^{II}_6[(S,S)$–Mecysmox$]_3(OH)_2(CH_3OH)\}$. $12H_2O$ (Pd^{2+}@CuSr-Mecysmox). The MOF obtained, unlike the anionic MOF based on Me_3mpba, is neutral, so although the insertion is carried out in the same way as during the cation exchange (immersing the MOF in the metal of interest), its interaction with the metal-organic network is by the interaction of the methyl thioether groups.

Therefore, the resulting MOF $[Pd_2(H_2O)(NH_3)_6]_{0.5}Cl_2$@ $\{Sr^{II}Cu^{II}{}_6$ $[(S,S)$–Mecysmox$]_3(OH)_2(CH_3OH)\}$. $12H_2O$ (**Pd^{2+}@CuSr-Mecysmox**) in multigram scale was developed by using 2 g of the polycrystalline powder SrCuMecys (1.15 mmol) to be suspended in a solution of $[Pd(NH_3)_4]Cl_2$ (1.1 mmol) with H_2O/CH_3OH (1:1) for 1 hour under a mild stirring. The process was repeated 5 times with cleaning cycles with the solvent. Finally, the product was collected by filtration, washed with the solvent too and air–dried. The elemental analysis shows a molecular weight for $C_{31}Cl_2Cu_6SrH_{76}PdS_6N_9O_{33.5}$ (**Pd^{2+}@CuSr-Mecysmox**) of Mw 1949.6 g/mol and an elemental percentage of C, 19.02; H, 3.87; S, 9.91; N, 6.47% is found (C, 19.10; H, 3.93; S, 9.87; N, 6.47% was expected). IR (KBr) shows the signals ν of 1602 cm^{-1} (C=O).

After the repeating 5 cycles of soaking crystals of ca. 25 mg **CuSr-Mecysmox** (0.015 mmol) in solution of $[Pd(NH_3)_4]Cl_2$ (0.015 mmol) with H_2O/CH_3OH (1:1) for 6 hours and washing with the solvent, well–formed hexagonal green prisms of **Pd^{2+}@CuSr-Mecysmox** were suitable for X–ray diffraction. To be characterized, crystals were washed with the solvent several times, isolated by filtration on paper and air–dried. The elemental analysis shows a molecular weight for $C^{31}Cl_2Cu_6SrH_{76}PdS_6N_9O_{33.5}$ (**Pd^{2+}@CuSr-Mecysmox**) of Mw 1949.6 g/mol and an elemental percentage of C, 19.07; H, 3.89; S, 9.91; N, 6.45% is found (C, 19.10; H, 3.93; S, 9.87; N, 6.47% was expected). IR (KBr) shows the signals ν of 1603 cm^{-1} (C=O). Figure 3.9 shows schematically the palladium insertion in bioMOF, interacting with the thionyl groups.

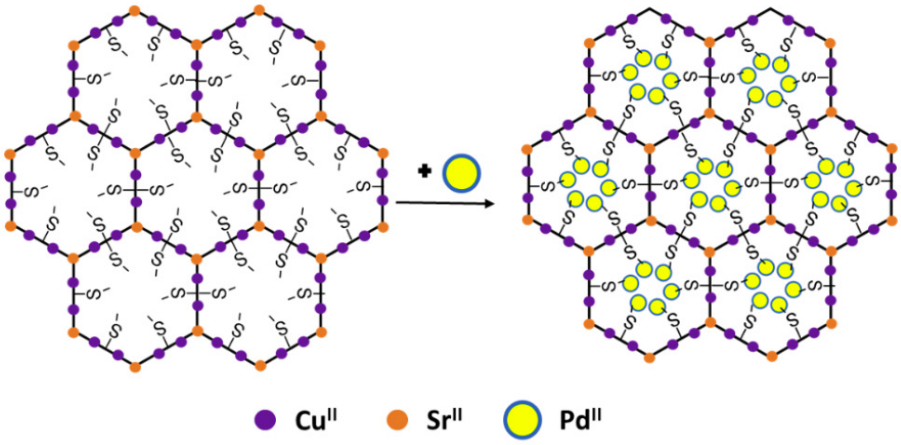

Figure 3.9. Schematic of the palladium insertion in the MOF $\{Cu_6Sr[(S,S)\text{-Mecysmox}]_3(OH)_2(H_2O)\}\ .\ 15H_2O$.

Synthesis of $(Pd^0)_{0.5}([Pd^{II}(H_2O)(NH_3)_3]Cl_2)_{0.5}$@$\{Sr^{II}Cu^{II}_6[(S,S)\text{-Mecysmox}]_3(OH)_2(CH_3OH)\}\cdot 13H_2O$ (Pd^0@CuSr-Mecysmox). A second PS was suffered by the **CuSr-Mecysmox** glass: the reduction with the corresponding **$(Pd^0)_{0.5}([Pd^{II}(H_2O)(NH_3)_3]Cl_2)_{0.5}$@ $\{Sr^{II}Cu^{II}_6[(S,S)\text{-Mecysmox}]_3(OH)_2(CH_3OH)\}\cdot 13H_2O$ (Pd^0@CuSr-Mecysmox)** obtained. This procedure was applied successfully to both, crystals (*ca*. 25 mg) and a powder polycrystalline **Pd^{2+}@CuSr-Mecysmox** (*ca*. 2 g). They suffer 15 cycles of $NaBH_4$ solutions suspensions (0.4 mmol of $NaBH_4$ per mmol of MOF) with the solvent H_2O/CH_3CH_2OH (1:1) for 1.5 hour and washing with the solvent. After this period, samples were gently washed with a H_2O/CH_3OH solution and filtered on paper. The elemental analysis shows a molecular weight for $C_{31}ClCu_6SrH_{73.5}PdS_6N_{7.5}O_{34.5}$ (**Pd^0@CuSr-Mecysmox**) of Mw 1906.6 g/mol and an elemental percentage of C, 19.48; H, 3.87; S, 10.03; N, 5.49% is found (C, 19.53; H, 3.89; S, 10.01; N, 5.51%. was expected). IR (KBr) shows the signals ν of 1601 cm^{-1} (C=O).

3.4. Characterization

3.4.1. Scanning Electron Microscopy-Energy Dispersive X-ray Spectroscopy (SEM-EDAX)

As in chapter 2, the amount of inserted metal and the metals that form part of the intra-structure were checked again by SEM-EDAX.

3.4.1.A. SEM-EDAX of Ag^0_2@CuNi-Me_3mpba

Cation exchange and reduction of target compound $[Ag^0_2]Ag^I_2Na^I_2\{Ni^{II}_4[Cu^{II}_2(Me_3mpba)_2]_3\} \cdot 48H_2O$ **Ag^0_2@CuNi-Me_3mpba** was followed by SEM/EDX (Table 3.1). In the first stage, Ag insertion gave rise to *$Ag^I_4\{Ni^{II}_4[Cu^{II}_2(Me_3mpba)_2]_3\} \cdot 51H_2O$* **$Ag^+$@CuNi-Me3mpba**, if we observe its formula the expected ratios have to coincide with the one shown in the elemental analysis Cu/Ni 1,5 and Ni/Ag 1 (Table 3.2 left). Whereas, once the Ag atoms were reduced, the charge compensation was performed with the sodium cations provided by $NaBH_4$, where the Cu/Ni 1.5 and Ni/Ag 1 ratios should be maintained and the Ni/Na 2 ratio should also be taken into account (Table 3.2 right).

Table 3.1. SEM/EDX analyses of **Ag^+@CuNi-Me_3mpba** y **Ag^0_2@CuNi-Me_3mpba.**

	Ag^+@CuNi-Me_3mpba		**Ag^0_2@CuNi-Me_3mpba**	
Metal	**% mass**	**Metal stoichiometry**	**% mass**	**Metal stoichiometry**
Cu	11.17	4.81	11.03	4.75
Ni	7.41	3.19	7.36	3.17
Ag	7.55	3.25	7.01	3.02
Na	-	-	3.71	1.60

Table 3.2. SEM/EDX metal stoichiometry ratios of **Ag^{+}@CuNi-Me_3mpba** y **Ag^{0}_{2}@CuNi-Me_3mpba**.

Ratio	Ag^{+}@CuNi-Me_3mpba	Ag^{0}_{2}@CuNi-Me_3mpba
Cu/Ni	1.51	1.5
Ni/Ag	0.98	1.05
Ni/Na	-	1.98

The values obtained in the tables confirm that the cation exchange has been carried out correctly, as the expected ratios practically correspond to those obtained. Some silver is lost during the reduction due to the aggressiveness of the reductant, so, if there is less silver there is more sodium to compensate charges in the anionic MOF.

3.4.1.B. SEM-EDAX of $Ag^{0}_{2}Fe^{3+}$@CuNi-Me_3mpba

After verifying that complete Ag insertion has been performed in the **Ni^{2+}@CuNi-Me_3mpba** by SEM/EDX, values corresponding to those of the **Ag^{+}@CuNi-Me_3mpba** (Section 3.4.1.A), the partial displacement of Ag by Fe insertion was observed (Table 3.3 left). The creation of the cluster will be given by the reduction of the MOF, leading to ratios from **$Ag^{+2}Fe^{3+}$@CuNi-Me_3mpba**, formula $[Ag^{+}_{3.44}Fe^{III}_{0.66}]@\{Ni^{II}_{4}[Cu^{I}_{2}(Me_3mpba)_2]_3\} \cdot 63H_2O$, of Cu/Ni around 1.5, Ni/Ag of 1.15 and Ni/Fe around 6 to **$Ag^{0}_{2}Fe^{3+}$@CuNi-Me_3mpba** network, formula $[Ag^{0}_{2}Ag^{I}_{1.72}Na^{I}_{1.72}Fe^{III}_{0.66}]@\{Ni^{II}_{4}[Cu^{II}_{2}(Me_3mpba)_2]_3\} \cdot 48H_2O$, and thus Cu/Ni ratios around 1.5 (confirming the non-alteration of the metal-organic network composition), Ni/Ag around 1.1, Ni/Fe around 6 and Ni/Na around 2.3, Table 3.4.

Table 3.3. SEM/EDX analyses of **$Ag^{+}_{2}Fe^{3+}$@CuNi-Me_3mpba** and **$Ag^{0}_{2}Fe^{3+}$@CuNi-Me_3mpba.**

	$Ag^{+}_{2}Fe^{3+}$@CuNi-Me_3mpba		$Ag^{0}_{2}Fe^{3+}$@CuNi-Me_3mpba	
Metal	**% mass**	**Metal stoichiometry**	**% mass**	**Metal stoichiometry**
Cu	14.14	6.05	14.08	6.02
Ni	9.42	4.03	9.07	3.88
Ag	7.97	3.41	6.83	2.92
Fe	1.54	0.66	1.48	0.63
Na	-	-	3.83	1.64

Table 3.4. SEM/EDX metal stoichiometry ratios of **$Ag^{+}_{2}Fe^{3+}$@CuNi-Me_3mpba** and **$Ag^{0}_{2}Fe^{3+}$@CuNi-Me_3mpba.**

Ratio	**$Ag^{+}_{2}Fe^{3+}$@CuNi-Me_3mpba**	**$Ag^{0}_{2}Fe^{3+}$@CuNi-Me_3mpba**
Cu/Ni	1.5	1.55
Ni/Ag	1.18	1,33
Ni/Fe	6.11	6.16
Ni/Na	-	2.37

The values obtained in the tables confirm that the cation exchange has been carried out correctly, as the expected ratios practically correspond to those obtained. Some silver and iron are also lost (as expected) during the reduction, with a corresponding slight gain of sodium.

3.4.1.C. SEM-EDAX of Pd0@CuSr-Mecysmox

In the case of this neutral MOF, as stated in the objectives, what is studied is the number of thionyl positions that can be occupied by palladium by SEM/EDX (Table 3.5). Since it is not necessary for a charge compensation to occur, the reduction did not involve incorporation of Na atoms in its structure, so the ratios should be practically identical for both **{$Cu_6Sr[(S,S)$-Mecysmox$]_3(OH)_2(H_2O)$} . $15H_2O$** and $[Pd_2(H_2O)(NH_3)_6]_{0.5}Cl_2$@{$Sr^{II}Cu^{II}_6[(S,S)$–Mecysmox$]_3(OH)_2(CH_3OH)$} . $12H_2O$ (Table 3.6). The Cu/Sr (ca 6) and Cu/S (ca 1) ratios will be the indicators of the stability of the MOF instead of the Cu/Ni in base MOF of the Me3mpba. Since we don't have a reference metal to exchange cations for (such as Ni), copper also serves as a reference to check the amount of palladium in the MOF, Cu/Pd 6.

Table 3.5. SEM/EDX analyses of **Pd^{2+}@CuSr-Mecysmox** and **Pd^0@CuSr-Mecysmox**

	Pd^{2+}@CuSr-Mecysmox		**Pd^0@CuSr-Mecysmox**	
Metal	**% mass**	**Metal stoichiometry**	**% mass**	**Metal stoichiometry**
Cu	16.99	6.00	17.12	6.00
S	15.44	5.45	14.26	5
Sr	1.58	0.88	1.43	0.79
Pd	17.98	2.07	18.34	2.10

Table 3.6. SEM/EDX metal stoichiometry ratios of **Pd^{2+}@CuSr-Mecysmox** and **Pd^{0}@CuSr-Mecysmox**.

Ratio	Pd^{2+}@CuSr-Mecysmox	Pd^{0}@CuSr-Mecysmox
Cu/S	1.1	1.2
Cu/Sr	6.82	7.59
Cu/Pd	2.90	2,10

The values obtained in the tables confirm that the insertion has taken place correctly, although they do not fit perfectly with the data obtained, this is due to the possible overestimation of the copper that may have been carried out by the measurement apparatus or because during the insertion some areas of the MOF structure may have been slightly degraded. In the case of Cu/Pd the estimation is almost double or triple, compared to that calculated by elemental analysis, this may be due to the fact that Pd is not only retained by the thionyl groups but also by interaction with other functional groups that constitute the MOF or intermolecular interaction Pd-Pd.

3.4.2. X–ray photoelectron spectroscopy (XPS)

As previously observed, the formation of SNMCs and SACs from the metals of interest inserted in the MOF required a final reduction post-treatment step. Monitoring of the oxidation states before and after reduction was carried out by XPS.

3.4.2.A. XPS of Ag^0_2@CuNi-Me_3mpba

In order to ascertain the oxidation states of the metal cations hosted in the channels of **Ag^+@CuNi-Me_3mpba** and **Ag^0_2@CuNi-Me_3mpba**. I carried out XPS measurements, focusing on the oxidation state of silver metals (Figure 3.10). **Ag^+@CuNi-Me_3mpba** signals only two bands at 368.9 and 374.5 eV corresponding to Ag^+ cations, ascribed to Ag $3d_{5/2}$ and Ag $3d_{3/2}$ binding energies,[57,58] are observed (Figure 3.10a). On the other, **Ag^0_2@CuNi-Me_3mpba** signals, apart from the same Ag 3d5/2 and Ag 3d3/2 bands at 368.4 and 374.4 eV, indicative of Ag^+, two additional peaks at 370.0 and 375.9 eV can be observed, which are attributed to reduced Ag^0 atoms. The SC-RDX results discussed in the following section and other analyses will suggest that coexist Ag^+ cations and Ag^0_2 nanoclusters, where the ratio of Ag^0 respect Ag^+ correspond with a 1:1 ratio. This point confirms that 50% of Ag^+ present in **Ag^0_2@CuNi-Me_3mpba** are reduced by $NaBH_4$ forming Ag^0_2 nanoclusters, whereas 50% of Ag^+ cations remain untouched occupying inaccessible sheltered interstitial positions where the reducing agent cannot accede.

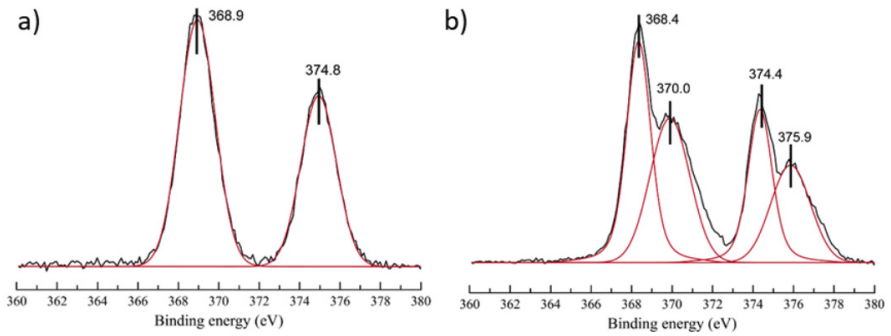

Figure. 3.10. X–ray photoelectron spectroscopy (XPS) of **Ag^+@CuNi-Me_3mpba (a)** and **Ag^0_2@CuNi-Me_3mpba (b).**

3.4.2.B. XPS of $Ag^0_2Fe^{3+}$@CuNi-Me_3mpba

In the case of **Ag^+@CuNi-Me_3mpba** and **$Ag^0_2Fe^{3+}$@CuNi-Me_3mpba**, the iron XPS signals had to be analyzed in addition to the silver signals studied for unreduced (Figure 3.11a) and reduced **Ag^+@CuNi-Me_3mpba** (Figure 3.11b). So we start from the prior knowledge of both Ag^0_2-subNMCs and Ag^0-SMAs within the same MOF and of Iron signals in isolated Fe^{3+}-SMAs of FeNiCuMOF were also previously reported.

Before reduction, Ag $3d_{5/2}$ and Ag $3d_{3/2}$ bands are observed at 368.6 and 374.6 eV, which are indicative of Ag^+(Figure 3.11a left), while after reduction, peaks at 370.1 and 375.8 eV can be observed (Figure 3.11b left), which are attributed to reduced Ag^0 atoms. This confirms the full reduction of Ag^+ atoms after reacting with $NaBH_4$, in contrasts with the case of the homometallic **Ag^0_2@CuNi-Me_3mpba** where only 50% of Ag^+ cations (those located in larger channels) where reduced by $NaBH_4$ forming Ag^0_2 nanoclusters, which could be explained by the higher content of Ag^+ present in the previously reported MOF. In turn, the analysis of the iron bands before (Figure 3.11a right) and after (Figure 3.11b right) introduction of $NaBH_4$, allows to confirm that Fe^{3+} cations are either not reduced by $NaBH_4$ or re-oxidized upon exposed to air. Indeed, the fitting of the Fe($2p_{3/2}$) and Fe($2p_{1/2}$) shows well-known peaks for Fe^{III}.[60] In particular, peaks at 711.2/711.1 eV and 713.8/713.9 eV, before and after reduction, respectively, can be clearly associated with Fe^{III} $2p_{3/2}$, while peaks at 724.9/724.2 eV and 726.9/726.7 eV are associated with Fe^{III} $2p_{1/2}$. Additionally, other satellite peaks, typical of Fe^{III} ions, can be also observed (Figure 3.11 right).

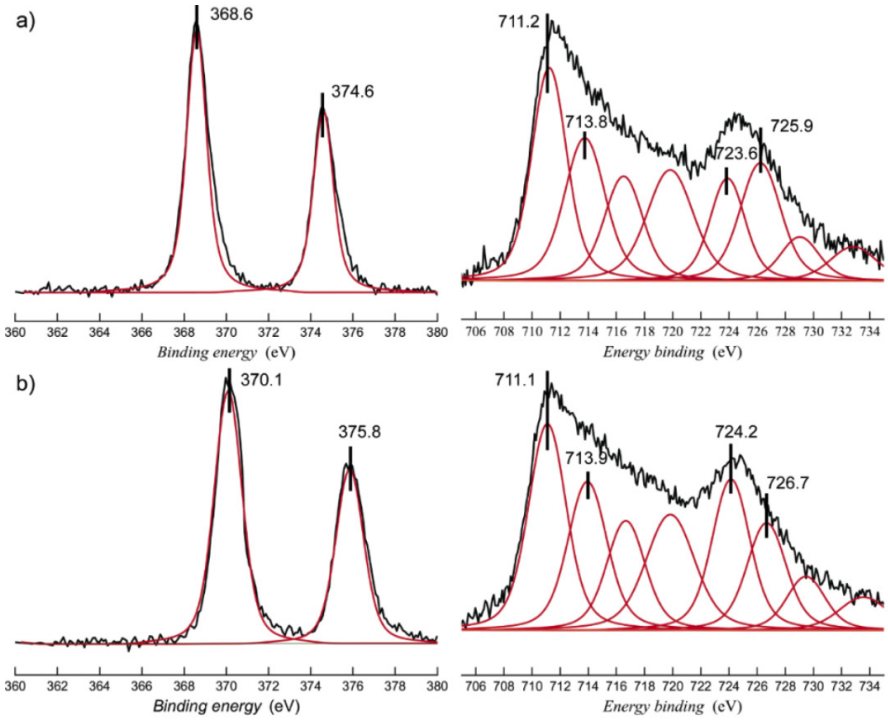

Figure 3.11. X–ray photoelectron spectroscopy (XPS) of **$Fe^{3+}Ag^{+}$@MOF** (a) and **$Fe^{3+}Ag^{0}_{2}$@MOF** (b), where the silver signals correspond to those on the left, while the iron signals correspond to those on the right.

3.4.2.C. XPS of Pd^{0}@CuSr-Mecysmox

In this work we focus again on the metal inserted via XPS, in this case Pd. The Pd signals in **Pd^{2+}@CuSr-Mecysmox** (Figure 3.12a) practically coincide with the **Pd^{2+}@CuNi-Me3mpba** signals (Chapter 2, section 2.4.2). The Pd3d line of **Pd^{2+}@CuSr-Mecysmox** is only one doublet with a binding energy (BE) of the $Pd3d_{5/2}$ peak of 337.8 eV, typical of Pd^{2+} cations which is close enough to other reported values.[30] In turn, Figure 3.12b clearly shows, apart from the same $Pd3d_{5/2}$ doublet with a BE of 337.7 eV, an additional peak at 335.8 eV, attributed to reduced

Pd^0@CuSr-Mecysmox SACs,[30] with a 1:1 ratio respect to Pd^{2+}. This feature indicates that only a 50% of Pd^{2+} –those occupying accessible positions– are reduced when in contact with reducing agent, whereas those Pd^{2+} cations situated in inaccessible sheltered interstitial positions remain in their original oxidation state. These values are close enough to those observed for other Pd^{2+}/ Pd_1 species.[44,60] Therefore, they suggest that the thioether groups do not alter significantly either the native electronics nor the open-shell structure of the Pd^1 site, which is ready to catalyze the aerobic oxidation target for this compound: benzyl alcohol to benzoic acid.

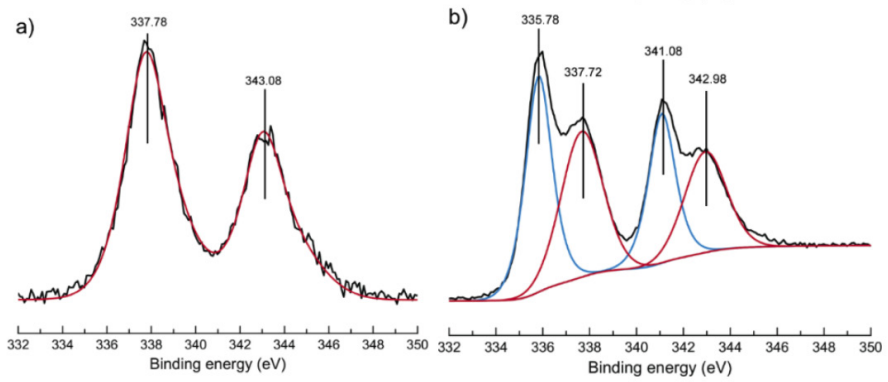

Figure 3.12. X–ray photoelectron spectroscopy (XPS) of **Pd^{2+}@CuSr-Mecysmox** (a) and **Pd^0@CuSr-Mecysmox** (b).

3.4.3. Single Crystal X-ray diffraction (SC-XRD)

To fully characterize the three post-treated metal-organic structures in this thesis, we carried out single crystal X-ray diffraction. The robustness and crystallinity of each 3D lattice presented after each post-treatment step allowed the necessary resolution to be produced to interpret the multiple interactions they incorporate.

3.4.3.A. SC-XRD of Ag^0_2@CuNi-Me_3mpba

In chapter 2, SC-SC monitoring of the two post-synthetic stages: transmetallation of Mg by Ni and cation exchange of pore-hosted Ni by Pd using the SC-XRD technique. As we have been studying in this chapter, here we are presented with another stage: reduction. This stage is decisive for the formation of SNMCs[61] or SACs.

For the formation of Ag^0_2 nanoclusters, we have extended our knowledge applied to the **Pd^{2+}@CuNi-Me_3mpba** MOF, starting with the same previous stage of transmetallation and differing in a complete insertion of silver (more affordable metal than palladium) and a reduction by its treatment with $NaBH_4$. Detailed SC-SC follow-up of the PSMs applied to **Ni^{2+}@CuNi-Me_3mpba** was performed by SC-XRD with synchrotron radiation.

So, starting from our host matrix $Ni^{II}_2\{Ni^{II}_4[Cu^{II}_2(Me_3mpba)_2]_3\} \cdot 54H_2O$ (**Ni^{2+}@CuNi-Me_3mpba**) the nickel(II) cations (Figure 3.13 left), located in the pores of **Ni^{2+}@CuNi-Me_3mpba**, were exchanged for Ag^I cations giving rise to the new compound $Ag^I_4\{Ni^{II}_4[Cu^{II}_2(Me_3mpba)_2]_3\} \cdot 51H_2O$ (**Ag^+@CuNi-Me_3mpba**) (Figure 3.13 middle). Since nickel has a double valence compared to silver, the charge compensation required a double amount of silver cations. Then, after the introduction of $NaBH_4$, the reduction process takes place to give the final compound $[Ag^0_2]@Ag^I_2Na^I_2\{Ni^{II}_4[Cu^{II}_2(Me_3mpba)_2]_3\} \cdot 48H_2O$ (**Ag^0_2@CuNi-Me_3mpba**) (Figure 3.13 right). This formula already allows us to guess that the reduction partially took place, as well confirmed by XPS and SEM-EDAX.

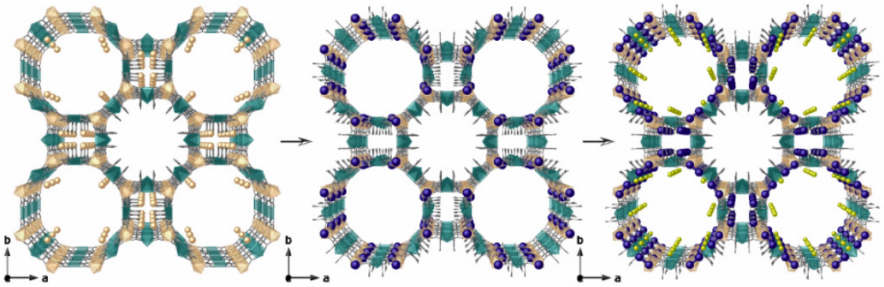

Figure 3.13. Design approach showing the crystal structures of **Ni^{2+}@CuNi-Me_3mpba** (left), **Ag^{+}@CuNi-Me_3mpba** (middle) and **Ag^{0}_{2}@CuNi-Me_3mpba** (right) showing the two–step PS process consisting of the exchange of the Ni^{II} cations in the pores of **Ni^{2+}@CuNi-Me_3mpba** by Ag^{I} ones to yield **Ag^{+}@CuNi-Me_3mpba** and the reduction process to form the Ag^{0}_{2} clusters in **Ag^{0}_{2}@CuNi-Me_3mpba**. Copper and nickel atoms from the network are represented by cyan and orange polyhedral, respectively, whereas organic ligands are depicted as grey sticks. Orange, yellow and blue spheres represent Ni, Na and Ag atoms, respectively.

Table 3.7. jointly with Figure 3.13, confirms that the crystal structure resolution of **Ag^{+}@CuNi-Me_3mpba** and **Ag^{0}_{2}@CuNi-Me_3mpba** was successfully performed showing isoreticularity and belonging to the P4/mmm space group of the tetragonal system. This allows us to describe the observations we have been able to make of these ultra-small silver dinuclear entities and their surroundings within the solid in **Ag^{0}_{2}@ CuNi-Me_3mpba**.

Table 3.7. Summary of Crystallographic Data for **Ag^{+}@CuNi-Me_3mpba** and **Ag^{0}_2@CuNi-Me^3mpba**.

Compound	**Ag^{+}@CuNi-Me_3mpba**	**Ag^{0}_2@CuNi-Me_3mpba**
Formula	$C_{78}H_{162}Ag_4Cu_6N_{12}Ni_4O_{87}$	$C_{78}H_{156}Ag_4Cu_6N_{12}Na_2Ni_4O_{84}$
M **(g mol^{-1})**	3707.75	3699.68
Crystal system	Tetragonal	Tetragonal
λ(Å)	0.6889	0.6889
Space group	P4/mmm	P4/mmm
a **(Å)**	35.7978(7)	36.037(6)
b **(Å)**	35.7978(7)	36.037(6)
c **(Å)**	15.0057(3)	15.311(2)
V **(Å^3)**	19229.5(8)	19884(7)
Z	4	4
ρ_{calc} (g cm^{-3})	1.281	1.236
M **(mm^{-1})**	1.507	1.460
T **(K)**	90	90
Unique reflections (R_{int})	7686 (0.0931)	5730(0.2125)
Observed reflections [$I > 2\sigma(I)$]	5325	3335
GOOF	1.273	1.937
R ^{A} **[$I > 2\sigma(I)$] (all data)**	0.1220 (0.1594)	0.1562 (0.2124)
wR ^{B} **[$I > 2\sigma(I)$] (all data)**	0.3424 (0.3686)	0.3565 (0.3749)

$^aR = \sum(|F_o| - |F_c|)/\sum|F_o|$. $^bwR = [\sum w(|F_o| - |F_c|)^2/\sum w|F_o|^2]^{1/2}$.

In order to study the lead metal in this section, the silver atoms for **Ag^{+}@CuNi-Me_3mpba** (Figure 3.14a) and **Ag^{0}_{2}@CuNi-Me_3mpba** (Figure 3.14b) were highlighted in Figure 3.14 in blue and grey. In this Figure 3.14, it can be seen how the crystal structure of **Ag^{+}@CuNi-Me_3mpba** has channels, both octagonal and square, full of Ag^{+} complexes, while for **Ag^{0}_{2}@CuNi-Me_3mpba** only the square pores contemplate it because in the octagonal pores (with greater accessibility) a reduction and, therefore, a formation of NCs of Ag^{0}_{2}.

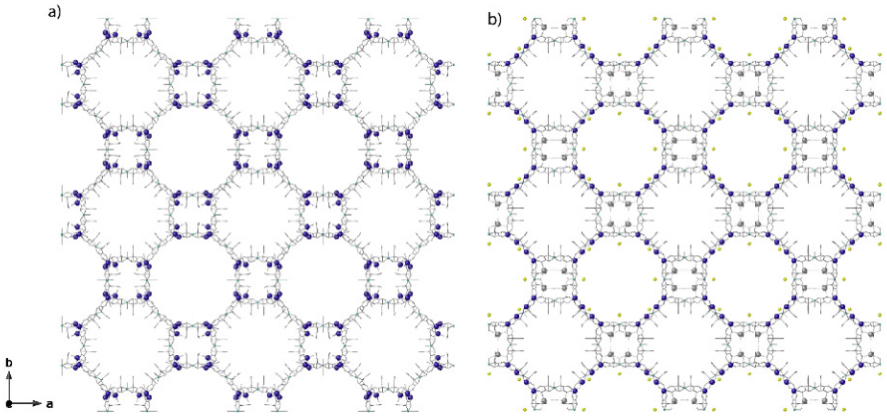

Figure 3.14. Perspective view along c crystallographic axis of crystal structures of **Ag^{+}@CuNi-Me_3mpba** (a) and **Ag^{0}_{2}@CuNi-Me_3mpba** (b). Lattice water molecules and hydrogen atoms have been omitted for clarity. Color scheme: Silver, blue sphere (octagonal pores of **Ag^{+}@CuNi-Me_3mpba** and **Ag^{0}_{2}@CuNi-Me_3mpba**) and grey spheres (Ag^{+} ions not reduced in square pores in **Ag^{0}_{2}@CuNi-Me_3mpba**); sodium, yellow spheres, ligands atoms and metal ions of the whole net have been depicted as grey sticks.

The Ag^{I} cations incorporated in the **Ag^{+}@CuNi-Me_3mpba** structure are located within the hydrophilic octahedral pore walls [virtual diameter of 2.2 nm] (Figure 3.15) where they are stabilized by non-covalent interactions involving oxamate oxygen atoms [$Ag^{+}\cdots O_{oxamate}$ from 2.72(1) - 2.79(1) Å] (Figure 3.16). The fact that there is no trace of Ni^{II} cations

above **Ni^{2+}@CuNi-Me_3mpba** indicates that the NiII in the pores have been completely exchanged for Ag^{I} (Figure 3.13b). The surroundings of the Ag^{I} ions reveal interacting oxygen atoms that probably belong to nitrate anions (whose complete fragments were not found in the ΔF-map) or to solvent water molecules [$Ag^{+}\cdots O$ distance of 2, 38(3)-2.56(3) Å], together with $Ag^{+}\cdots Ag^{+}$ with a separation of 2.74(2) Å which is shorter than the Van der Waals contact distance and which could be considered as precursors of the Ag^{0}_{2} dimers observed in **Ag^{0}_{2}@CuNi-Me_3mpba**.

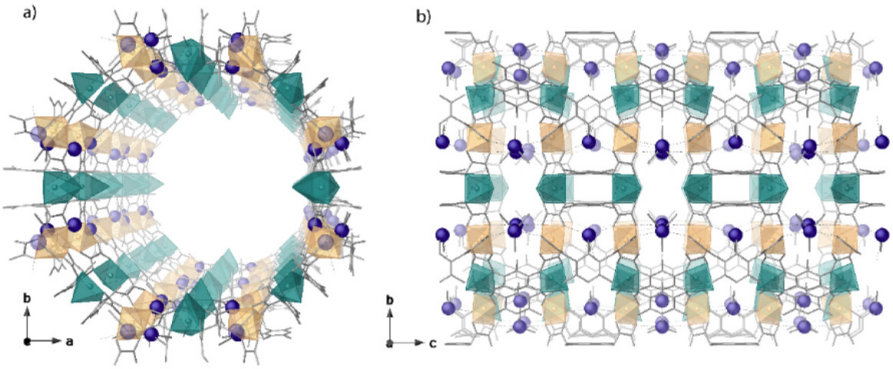

Figure 3.15. Details along c (a) and a (b) crystallographic axis of a single octagonal pore in **Ag^{+}@CuNi-Me_3mpba**. Color scheme: Silver, blue sphere; Copper and nickel, cyan and orange polyhedral, respectively; ligands atoms of the whole net have been depicted as grey sticks.

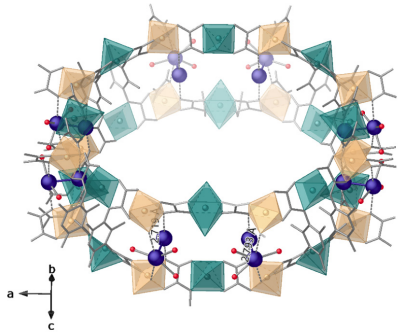

Figure 3.16. One single channel of **Ag^{+}@CuNi-Me_3mpba** showing supramolecular interactions involving oxamate ligands of the network stabilizing Ag^{+} dimers. Color scheme: Silver, blue sphere; Copper and nickel, cyan and orange polyhedral, respectively; ligands atoms of the whole net have been depicted as grey sticks. Modelled oxygen atoms (likely belonging to NO_{3^-} anions) surrounding Ag^{+} ions are depicted as red spheres.

On the other hand, the crystal structure of **Ag^0_2@CuNi-Me_3mpba** provides stability to the synthesized Ag^0_2 dimers thanks to the nano-confinement on the walls of the hydrophilic octagonal channels of the anionic $Ni_4^{II}Cu_6^{II}$ open-framework network (Figures 3.13c and 17-18). The confinement of the unreduced Ag^I---Ag^I dimers in smaller square pores prevented access of the solvated $NaBH_4$ species (Figures 3.13c and 3.18), these were blocked by Ag^I---Ooxamate interactions at a distance of 2.84(1) Å. In addition, the hydrated alkali NaI cations counteracting the charge are retained on the preferential cationic sites, which stabilise the final material showing a much higher robustness (Figures 3.17-3.18).

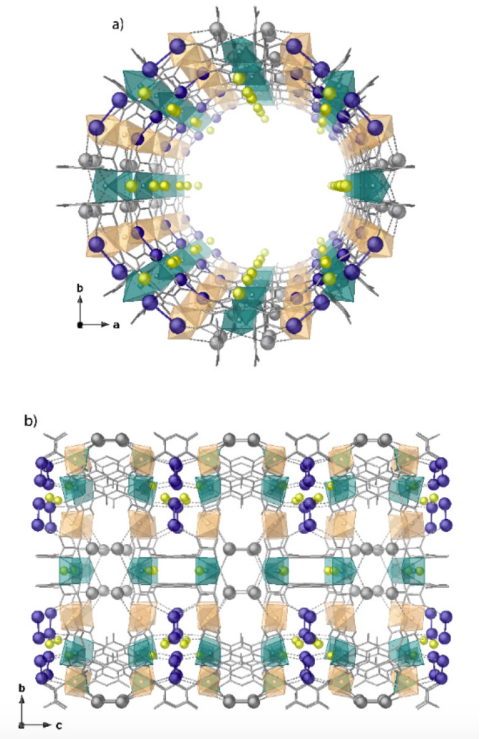

Figure 3.17. Details along c (a) and a (b) crystallographic axis of a single octagonal pore in **Ag^0_2@CuNi-Me_3mpba**. Color scheme: Silver, blue sphere; Sodium, yellow spheres. Copper and nickel, cyan and orange polyhedral, respectively; ligands atoms of the whole net have been depicted as grey sticks.

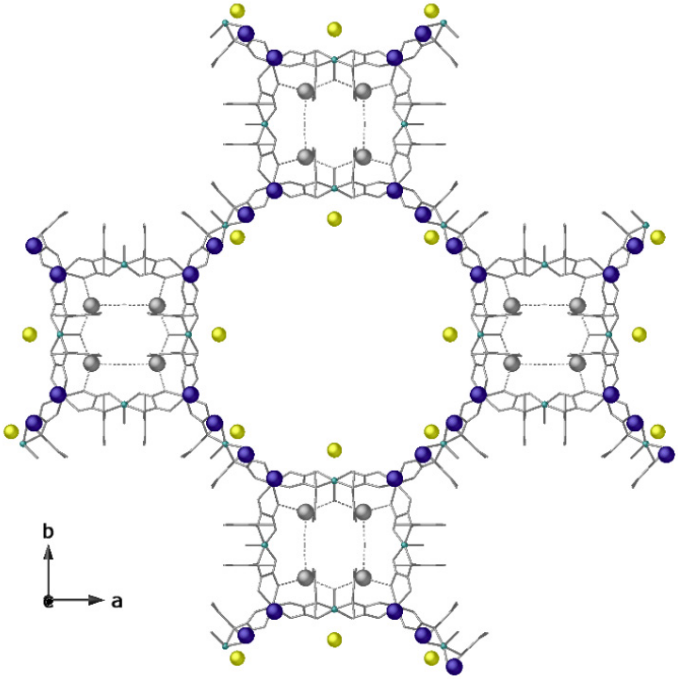

Figure 3.18. Details along c crystallographic axis of a portion of crystal structure of **Ag^0_2@CuNi-Me_3mpba** showing disposition of Ag^+ ions (grey spheres) residing in poorer accessible small square pores. Color scheme: Silver, blue and grey spheres (Ag^+ ions not reduced in square pores); sodium, yellow spheres. Copper and nickel, cyan and orange polyhedral, respectively; ligands atoms of the whole net have been depicted as grey sticks.

Figure 3.19 shows that the Ag^0_2 dimers [Ag---Ag intradimer distance of 3.19(1) Å] are well attached and stabilised within the larger pore walls of the network by supramolecular interactions involving oxamate ligands [Ag---Ooxamate range 2.93(1) - 3.05(1) Å] and very weak connections with solvent molecules [Ag0---O_{water} distance of 3.25(1) Å].

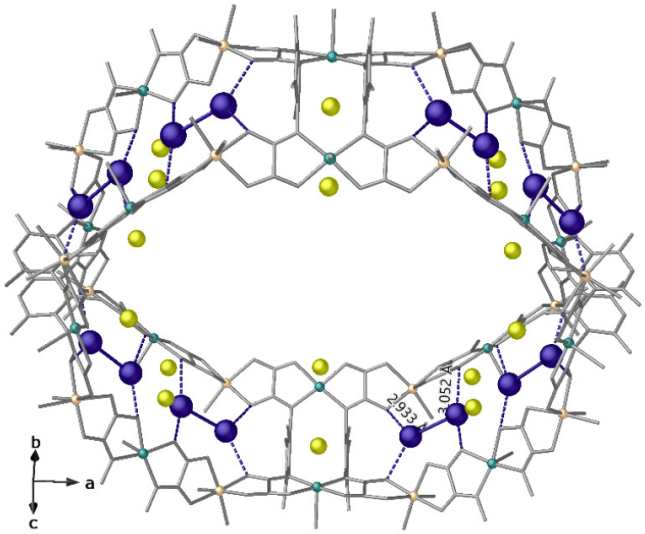

Figure 3.19. One single channel of **Ag^0_2@CuNi-Me_3mpba** showing supramolecular interactions involving oxamate ligands of the network (distances are reported in Å).

3.4.3.B. SC-XRD of **$Ag^0_2Fe^{3+}$@CuNi-Me_3mpba**

The following structure involves a PS stage plus[62] the recently discussed **Ag^+@CuNi-Me_3mpba**, i.e. a complete cation exchange of Ni for Ag of the pores is necessary in order to incorporate iron cations and reduce it to form heterometallic SNMCs. So the starting crystalline MOF underwent a transmetallation (obtaining **Ni^{2+}@CuNi-Me_3mpba**),[63] a complete cation exchange (obtaining **Ag^+@CuNi-Me_3mpba**), a partial cation exchange of the inserted silvers by iron (obtaining **Ag^+Fe^{3+}@CuNi-Me_3mpba**) and, finally, a reduction(**$Ag^0_2Fe^{3+}$@CuNi-Me_3mpba**). Thus, the four PS steps resulted in the formation of a single crystal of $[Ag^0_2(Ag^0)_{1.34}Fe^{III}_{0.66}]@Na^I_2\{Ni^{II}_4[Cu^{II}_2(Me_3mpba)_2]_3\} \cdot 63H_2O$ (**$Ag^0_2Fe^{3+}$@CuNi-Me_3mpba**) which has sufficient stability and crystallinity to be measured sequential SC to SC by SC-DRX (Table 3.8 and Figure 3.20c). This hybrid MOF integrates Fe^{3+}-SMAs and both Ag^0_2-subN-

MCs and Ag^0-SMAs within the same channels[18, 64] . The final structure fulfils the expectations created after the study of the reported SMAs[65] from FeNiCuMOF (Figure 3.20a) and the previously performed study of SMAs and subNMCs from the unreduced and reduced **Ag^+@Cu-Ni-Me_3mpba** (Figure 3.20b).

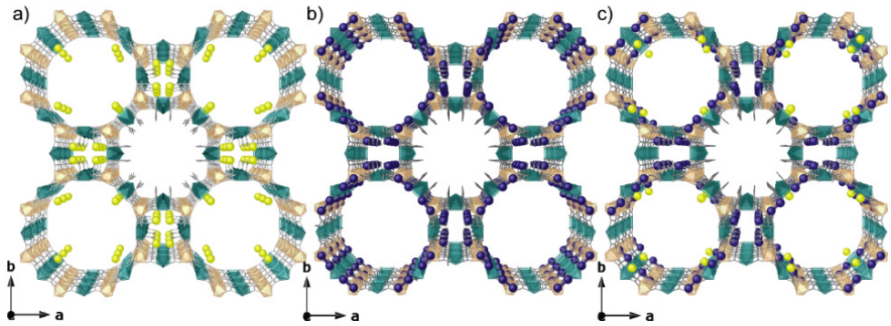

Figure 3.20. Crystal structures of **Fe^{3+}@CuNi-Me_3mpba**70 (a), **Ag^0_2@CuNi-Me_3mpba** (b) and **$Ag^0_2Fe^{3+}$@CuNi-Me_3mpba** (c). Copper and nickel atoms from the network are represented by cyan and orange polyhedral, respectively, whereas organic ligands are depicted as grey sticks. Yellow and dark blue spheres represent Fe and Ag atoms, respectively.

Table 3.8. Summary of Crystallographic Data for **$Ag^0_2Fe^{3+}$@Cu-Ni-Me_3mpba.**

Compound	$Ag^0_2Fe^{3+}$@CuNi-Me_3mpba
Formula	$C_{78}H_{186}Ag_{3.44}Fe_{0.66}Na_2Cu_6Ni_4N_{12}O_{99}$
***M* (g mol^{-1})**	3946.37
Crystal system	Tetragonal
λ (Å)	0.71073
Space group	P4/mmm
***a* (Å)**	35.8023(16)
***b* (Å)**	35.8023(16)
***c* (Å)**	15.2143(9)
***V* (Å^3)**	19502(2)
Z	4
ρ calc (G CM–3)	1.344
***M* (MM–1)**	1.492
***T* (K)**	150
Unique reflections (R_{int})	5756(0.1219)
Observed reflections [$I > 2\Sigma(I)$]	2992
Goof	0.951
***R*^{A} [$I > 2\sigma(I)$] (all data)**	0.0872 (0.1469)
***WR*^{B} [$I > 2\sigma(I)$] (all data)**	0.2363 (0.2619)

[a] $R = \sum(|F_o| - |F_c|)/\sum|F_o|$. [b] $wR = [\sum w(|F_o| - |F_c|)^2/\sum w|F_o|^2]^{1/2}$.

These predecessor species, separately, already gave a detailed structural analysis of the MOF accommodation network, and revealed that the metallic entities do not undergo significant changes in atomicity, oxidation state (except Ag^{+} and Ag^{0} in the small square pores for **Ag^{0}_{2}@CuNi-Me$_3$mpba** and **$Ag^{0}_{2}Fe^{3+}$@CuNi-Me$_3$mpba**, respectively), chemical environment and relative position in the channels, as well as no structural distortion of the MOF network.

In the **$Ag^{0}_{2}Fe^{3+}$@CuNi-Me$_3$mpba** MOF it can be highlighted that, compared to previously reported methods in porous materials where mixtures of different metallic species with random distribution are more commonly obtained, we have obtained defined and ordered metallic entities of different metallic ions and with different number of atoms constituting each entity within the same MOF. It can be said that the difficulty of forming Ag^{0}_{2} clusters in the presence of another metal has also been overcome, since silver atoms have a highly reactive nature towards other metals leading to redox reaction and alloying under a wide variety of reaction conditions. In addition to presenting a strong tendency to reduce and form nanoparticles even under the simple action of light.

The SCXRD data of **Ag02Fe3+@CuNi-Me3mpba**, provided in Table 3.8. manifest an anionic $Ni^{II}_{4}Cu^{II}_{6}$ open–framework structure isoreticular to ancestor, which crystallized in the P4/mmm space group of the tetragonal system. Significant statistical and dynamic clutter may affect the visualization of metal positions in large pores, however, crystallography clearly reveals the formation of Ag^{0}_{2} dimers,[66-69] stabilized near the walls of hydrophilic octagonal channels [virtual diameter of 2.2 nm], (crystallographically) mixed with Fe^{III} cations that also reside in

the largest accessible hydrophilic octagonal channels, in the vicinity of the already discovered preferred cationic sites in **Fe^{3+}@CuNi-Me_3mpba** (Figure 3.20a).

Inside the large octagonal channels, both Ag^0_2 dimers and Fe^{III} cations are mixed with a population of 34 and 67% respectively, and are stabilized by non-covalent interactions involving oxamate oxygen atoms. In fact, the disorder that FeAgNiCuMOF presents gives a mixed view of the spatial arrangement of the atoms in its structure quite understandable, considering that a crystal structure is the spatial average of all the chemical fragments averaged in the crystal via only one-unit cell. Figure 3.21 (Left) displays Ag^0_2 dimers [intradimer Ag···Ag distance of 2.67(3) Å] are trapped and stabilized nearby the walls of the largest pores of the network by Ag···Ooxamate interactions [Ag^0_2···Ooxamate of 2.87(2) and 3.09(3) Å]. Further Ag^0_2 dimers [intradimer Ag···Ag distance of 2.93(3) Å] are formed and blocked in the small and thus less accessible square pores of the porous network, stabilized by Ag^0 ···Ooxamate interactions at a distance of 2.83(2) Å] (Figure 3.21, right).

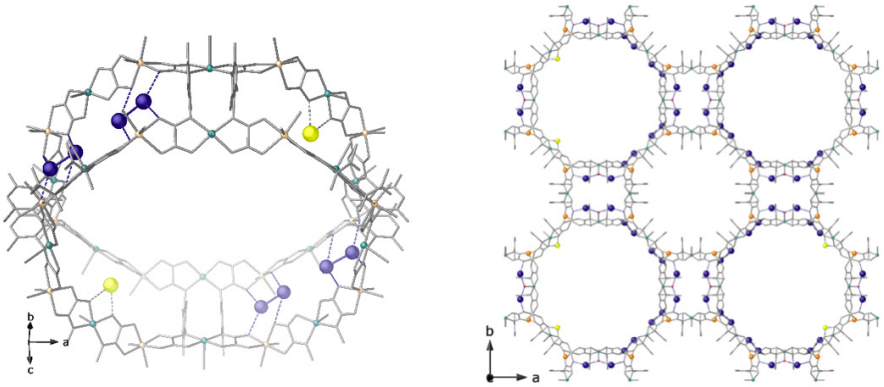

Figure 3.21. (Left) Details of $Fe^{3+}Ag^{0}_{2}$@MOF X-ray structure showing supramolecular interactions stabilizing Ag^{0}_{2} dimers and $Fe3^{+}$ ions in hydrophilic octagonal channels (intradimer Ag···Ag distance of 2.67(3) Å). Copper and nickel atoms from the network are represented by cyan and orange spheres respectively, whereas organic ligands are depicted as grey sticks. Yellow and dark blue spheres represent Fe and Ag atoms, respectively. (Right) View along c crystallographic axis of $Fe^{3+}Ag^{0}_{2}$@MOF crystal structures showing randomly distribution of Fe^{3+} (yellow spheres) and Ag^{0}_{2} dimers (blue spheres) inside octagonal hydrophilic pores together with Ag^{0}_{2} dimers formed and blocked in the small square pores of the porous network

The Fe^{3+} surrounding in **$Ag^{0}_{2}Fe^{3+}$@CuNi-Me_3mpba** crystal structure can be retained via $Fe^{3+\cdots}O_{oxamate}$ contacts [$Fe^{3+\cdots}O_{oxamate}$ of 2.53(2) Å]. Hydrated charge–counterbalancing alkali Na^{+} cations, are retained, as constantly found for this hosting matrix, in the preferential cationic sites, further contributing to the outstanding robustness of the final material (Figures 3.22-3.23).

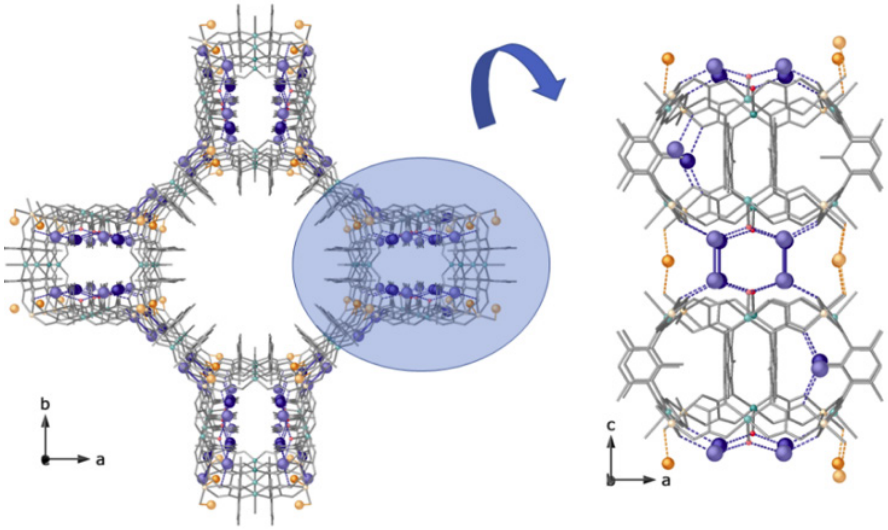

Figure 3.22. Perspective view along c and b axis of Ag^0_2 dimers (blue spheres) residing in the small square pores of the porous network stabilized by $Ag^0 \cdots O_{oxamate}$ interactions at a distance of 2.83(2) Å (blue dashed lines) and Na+ alkali metal ions (orange spheres) connected to the walls of the network by means of non-covalent interactions.

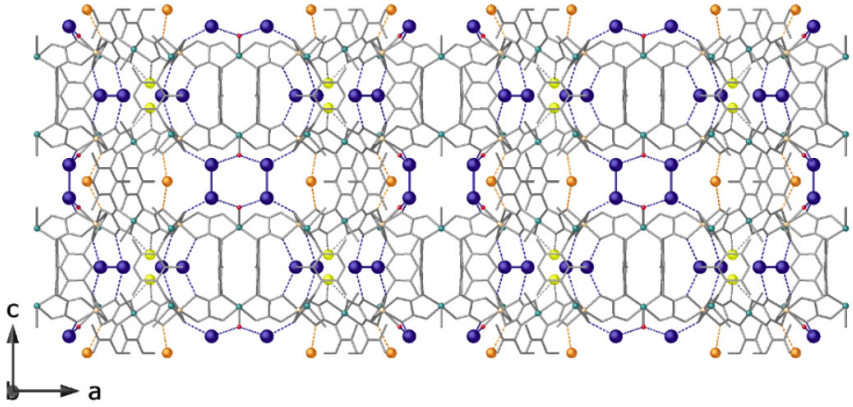

Figure 3.23. Perspective view of **$Ag^0_2Fe^{3+}$@CuNi-Me_3mpba** crystal structures along *b* crystallographic axis clearly showing distribution of Ag^0 dimers (blue spheres) and Fe^{3+} metal ions (yellow spheres) together with hydrated alkali Na^+ cations (orange spheres), retained in preferential cationic sites, further contributing to the robustness of the final material.

It is important to emphasize both the similarities and differences between the presented structure **$Ag^0_2Fe^{3+}$@CuNi-Me_3mpba** and the structures previously reported **Fe^{3+}@CuNi-Me_3mpba** and **Ag^0_2@CuNi-Me_3mpba**, certain similarities can be observed along with important differences. If we observe at FeNiCuMOF, the interaction $Fe^{III}\cdots$MOF comes into contact, stabilizing metal ions, where it is mediated by water.[70] In fact, $[Fe^{III}(H_2O)_6]^{3+}$ monomers can establish strong hydrogen bonds with the oxygen atoms in the pore walls of the oxamate ligands and the water molecules surrounding the Fe^{III} ions. In the FeAgNiCuMOF crystal structure, Fe^{III} ions are also located at the same preferential cationic sites, but exhibit shorter $Fe^{III}\cdots$Oxamate separation, suggesting direct contact with the walls of the networks (probably at the origin of the highly disordered and undetected by ΔFmaps the water molecules completing the FeIII coordination sphere).

Another point of review is the comparison between **$Ag^0_2Fe^{3+}$@CuNi-Me_3mpba** and **Ag^0_2@CuNi-Me_3mpba**, which are highly alike, even in terms of structural parameters (i.e. intradimer Ag···Ag distances). This confirms the same intrinsic capability of the anionic $Ni^{II}_4Cu^{II}_6$ open–framework to synthesize and stabilize Ag^0_2 dimers. So, apart from the structural richness gained with **$Ag^0_2Fe^{3+}$@CuNi-Me_3mpba**, these systems are excellent test benches to study, without structural/electronic ambiguities, the activity of each metallic entity, either isolated or integrated in the same MOF, for a given catalytic reaction. Offering a singular opportunity to investigate the potential cooperative/symbiotic effect of having simultaneously two different and well-defined metallic species at a molecular distance in a solid support.

3.4.3.C. SC-XRD of Pd^0@CuSr-Mecysmox

In this section, we work with a bioMOF based on S-methyl-L-cystei-

ne, with formula {Cu6Sr[(S,S)-Mecysmox]3(OH)2(H2O)} . 15H2O (CuSr-Mecysmox) (Mecysmox = bis[S-methylcysteine]oxalyl diamide), Figure 3.24 and 3.26a. This MOF, although it is not anionic (like Ni2+@CuNi-Me3mpba) to be able to capture cations by cation exchange, already contains functional groups with the capacity to capture metals, as was reported for the case of methiomox (with shorter thioalkyl chains), being unnecessary to functionalize the ligands.

The conformation of the thioalkyl arms of the MOF shows the intrinsic flexibility of the chain, which gives it that ability to grasp guest molecules and, together with the size of the pore, to be able to confine more effectively than with the Me_3mpba-based MOF (comparing the hexagonal pores of the **CuSr-Mecysmox** with the large octagonal pores of the **Ni^{2+}@CuNi-Me_3mpba**). Contrary to the example reported in the introduction to this chapter 3, **Pd^0_4@CuNi-Me_3mpba** PdNiCuMOF_red, its smaller pore size was predicted to exert an insulating effect, preventing the appearance of aggregates during the reduction of the inserted metal.

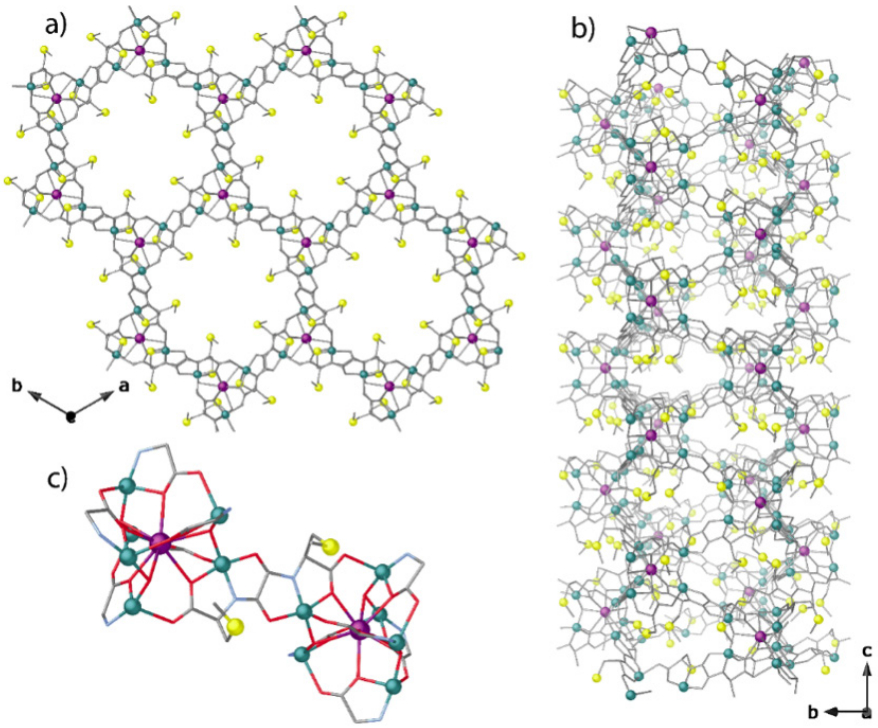

Figure 3.24. a) Views of a fragment of **CuSr-Mecysmox** in the ab and bc (c) planes, respectively. c) Fragment of **CuSr-Mecysmox** showing the dianionic bis(hydroxo) dicopper(II) building blocks. Copper, strontium and sulfur atoms are represented by green, purple and yellow spheres, respectively, whereas the ligands (except sulfur) are depicted as grey sticks [carbon: gray, oxygen: red and nitrogen: blue in fragment represented in c)]. Hydrogen atoms are omitted for clarity.

In **CuSr-Mecysmox**, thioether chains from **H_2Me_2-(*S,S*)-Mecysmox** ligand show as basic conformation one of the two distinct moieties in a distended conformation towards the center of the pores, and the other one regularly bent, with the terminal methyl groups pointing towards the smaller interstitial voids residing along a axis (Figures 3.25).

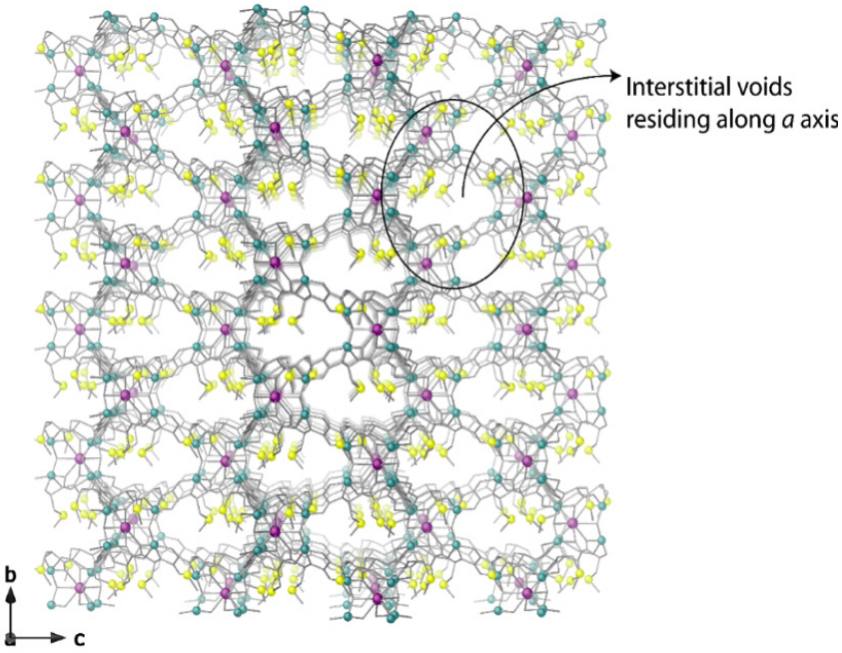

Figure 3.25. (a) Perspective view along a crystallographic axis of the 3D chiral porous network of **CuSr-Mecysmox** evidencing the regularly bent dymethyl thioether arm of the H_2Me_2-(*S,S*)-**Mecysmox** ligand with the terminal methyl groups pointing towards the smaller interstitial voids residing along a axis. Copper, strontium and sulfur atoms are represented by green, purple and yellow spheres, respectively, whereas the ligands (except sulfur) are depicted as grey sticks [carbon: gray, oxygen: red and nitrogen: blue in fragment represented in c)]. Hydrogen atoms are omitted for clarity.

The PSM used to obtain **Pd^0@CuSr-Mecysmox** are similar to those previously described, except for the transmetallation, which is not necessary in this case. It is important to emphasize that the first stage of insertion, the uptake of Pd cations, is not given by cation exchange but by coordinated capture of Pd by the thionyl groups.

CuSr-Mecysmox, featuring pores densely decorated with dimethyl thioether groups, allows the sequential formation and stabilization

of Pd1 SACs within their functional channels (Figure 3.26c). In order to do so, as stated, firstly $Pd(NH_3)_4Cl_2$ was inserted to obtain [PdI-I2(H2O)$(NH_3)_6]_{0.5}Cl_2$@{$Sr^{II}Cu^{II}_6$[(*S,S*)–Mecysmox]$_3(OH)_2$ $CH_3OH)$}} . $12H_2O$ (**Pd^{2+}@CuSr-Mecysmox**) (Figure 3.26b) and, then, their reduction allows obtain two palladium species (unreduced and reduced), $(Pd^0{}_1)_{0.5}([Pd^{II}(H_2O)(NH_3)_3]Cl_2)_{0.5}$@{$Sr^{II}Cu^{II}_6$[(*S,S*)-Mecysmox]$_3(OH)_2$ CH_3OH)}} . $13H_2O$ (**Pd^0@CuSr-Mecysmox**), (Figure 3.26c).

From the SACs formation route, we can appreciate the concomitant in-situ reduction of half of the Pd^{2+} cations to form the mixed valence Pd^{2+}/ Pd_1 hybrid compound (**Pd^0@CuSr-Mecysmox**), where sulfur groups no only retain the Pd^{2+} cations in specific positions after the insertion process but also allows their homogeneous distribution along the channels, and prevent their agglomeration forming NCs or NPs during the reduction process. This MOF also has the crystallinity and robustness[71-76] enough to be unveiled by SC-XRD (Figure 3.26 and Table 3.9).

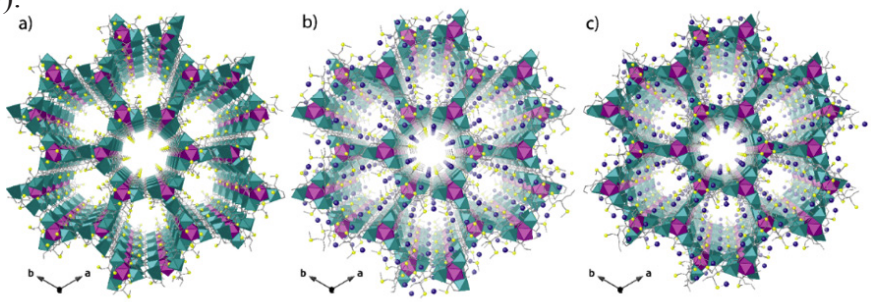

Figure 3.26. PS approach showing the structures of **CuSr-Mecysmox**, **Pd^{2+}@CuSr-Mecysmox** and **Pd^0@CuSr-Mecysmox** determined by single–crystal X–ray diffraction which consists of two con-secutive processes. First, the insertion of $[Pd(NH_3)_4]^{2+}$ cations within the channels of **CuSr-Mecysmox** (a) to give **Pd^{2+}@CuSr-Mecysmox** (b) and second the reduction of Pd^{2+} cations to form the Pd^0 single atoms in **Pd^0@CuSr-Mecysmox** (c). Copper and strontium atoms from the network are represented by cyan and purple polyhedra, respectively, whereas organic ligands are depicted as gray sticks. Yellow and blue spheres represent S and Pd atoms. Dual color sticks represent the Pd···S interactions.

Compounds **CuSr-Mecysmox**, **Pd^{2+}@CuSr-Mecysmox** and **Pd^{0}@CuSr-Mecysmox** are isomorphous –crystallizing in the chiral $P6_3$ space group (Table 3.9) and exhibit a chiral 3D strontium(II)–copper(II) network, featuring hexagonal channels where the dimethyl thioether chains from methylcysteine residues are confined. These functional arms exploit their intrinsic flexibility adopting different most stable conformations depending on the nature of target: *i.e.* solvent molecules in **CuSr-Mecysmox** (Figures 3.24, 3.25 and 3.26a), Pd^{2+} in **Pd^{2+}@CuSr-Mecysmox** (Figures 3.26b and 3.27a) or both Pd^{2+} cations and Pd^{0}_{1} SACs in **Pd^{0}@CuSr-Mecysmox** (Figures 3.26c and 3.27b)

Table 3.9. (right) Summary of Crystallographic Data for $\{Cu_6Sr[(S,S)\text{-Mecysmox}]_3(OH)_2(H_2O)\}.15H_2O$(**CuSr-Mecysmox**), $[Pd_2(H_2O)(NH_3)_6]_{0.5}Cl_2$@$\{Sr^{II}Cu^{II}_6[(S,S)\text{–Mecysmox}]_3(OH)_2(CH_3OH)\}.12H_2O$ (**Pd^{2+}@CuSr-Mecysmox**) and $(Pd^0)_{0.5}([Pd^{II}(H_2O)(NH_3)_3]Cl_2)_{0.5}$@ $\{Sr^{II}Cu^{II}_6[(S,S)\text{-Mecysmox}]_3(OH)_2(CH_3OH)\}$. $13H_2O$ (**Pd^{0}@CuSr-Mecysmox**).

Compound	CuSr-Mecysmox	Pd^{2+}@CuSr-Mecysmox	Pd^{0}@CuSr-Mecysmox
Formula	$C_{30}Cu_6H_{70}N_6O_{36}S_6Sr$	$C_{31}Cu_6H_{76}N_9O_{33.5}S_6SrPdCl_2$	$C_{31}Cu_6H_{73.5}N_{7.5}O_{34.5}S_6SrPdCl$
M (g mol^{-1})	1752.14	1949.52	1906.54
Crystal system	Hexagonal	Hexagonal	Hexagonal
λ (Å)	0.71073	0.6889	0.6889
space group	$P6_3$	$P6_3$	$P6_3$
a (Å)	18.057(4)	17.86780(10)	17.8206(2)
b (Å)	18.057(4)	17.86780(10)	17.8206(2)
c (Å)	12.800(3)	12.80840(10)	12.7821(3)
V (Å^3)	3614.6(17)	3541.34(5)	3515.42(11)
Z	2	2	2
ρ calc (g cm^{-3})	1.610	1.828	1.801
M (mm^{-1})	2.719	2.760	2.742
T (K)	100	100	100
Unique reflections(R_{int})	4808 (0.1620)	11688 (0.0424)	11614 (0.1080)
Observed reflections [$I > 2\sigma(I)$]	2375	8552	3420
GOOF	0.994	1.293	0.916
R^A [$I > 2\sigma(I)$] (all data)	0.0752 (0.1446)	0.0566 (0.0702)	0.0694 (0.1616)
wR^B [$I > 2\sigma(I)$] (all data)	0.1809 (0.2007)	0.1783 (0.1858)	0.1819 (0.1983)

$^a R = \sum(|F_o| - |F_c|)/\sum|F_o|$. $^b wR = [\sum w(|F_o| - |F_c|)^2/\sum w|F_o|^2]^{1/2}$.

If we zoom in the pores of **Pd^{2+}@CuSr-Mecysmox** and **Pd^{0}@CuSr-Mecysmox**, we can observe the change in the interaction of the palladium atoms with the alkylthionyl groups when Pd is oxidized from II to 0, forcing the thionyl groups to change their special disposition (Figure 3.27).

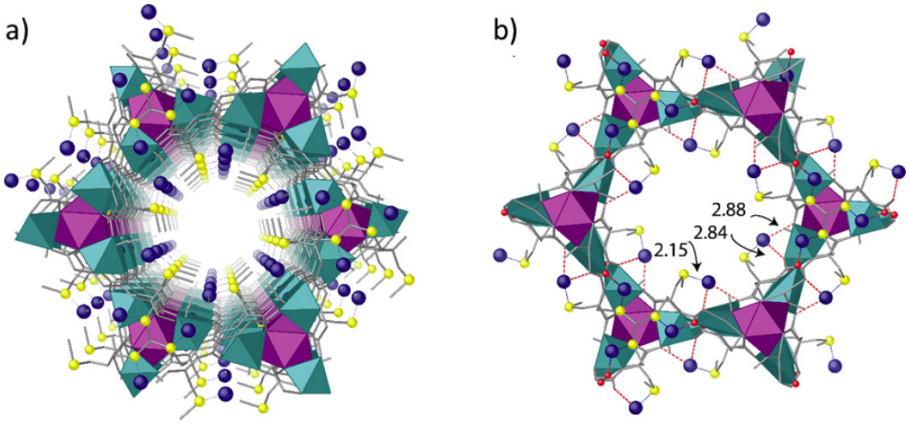

Figure 3.27. Details of pores in **Pd^{2+}@CuSr-Mecysmox** (a) and **Pd^{0}@CuSr-Mecysmox** (b) viewed along c crystallographic axis in polyhedral (copper and strontium) ball and stick for Pd^{2+} and sulfur ions/atoms, and stick (ligand) model. Copper and strontium atoms from the network are represented by cyan and purple polyhedra, respectively, whereas organic ligands are depicted as gray sticks. Yellow and blue spheres represent S and Pd atoms. In the first picture, little blue color sticks represent the Pd···S interactions, while in the second one, blue dashed lines represent the Pd···S interactions whereas red dashes lines represent $Pd^{2+}\cdots O_{ligand}$ interactions.

The Pd^{2+}–S bond distances [1.96(4) and 2.17(2) Å (**Pd^{2+}@CuSr-Mecysmox**] (Figure 3.28a) are close enough to those observed previously,[64] and similar to the Pd^{0}–S bond distance observed in **Pd^{0}@CuSr-Mecys-**

mox 2.16(2) Å] (Figures 3.28b). This apparently insignificant change in the interaction distance from Pd^{2+}-S to Pd^{0}_{1}-S means the breaking of the bridge between two-coordinated Pd^{II} anions linked by a water molecule (belonged to $[Pd_2(H_2O)(NH_3)_6]$, where he unreduced Pd^{II} maintains its interaction with the water molecule and the sulfur of the amino chain, while the Pd^0 SAC needs to be stabilized by additional interaction with oxygens belonging to the oxamate oxygen of the ligand, as well as with the sulfur of the amino acid chain. The suggestion made from SC-XRD data allows to know the Pd^1 formation mechanism, being the bridging water molecule might play a crucial role during the SACs formation process (**Pd^0@CuSr-Mecysmox**), acting synergistically with the flexible dimethyl thioether chains from methylcysteine residues stabilizing Pd^{II} metal ions in **Pd^{2+}@CuSr-Mecysmox**. The reduction process of Pd^{II} –S units located inside the most accessible pores breaks water bonds from one side, meanwhile generates the Pd^0 –S ones in **Pd^0@ CuSr-Mecysmox**. This leaves the water molecule still coordinated and stabilizing the unreduced mononuclear Pd^{II} complexes residing in hindered interstitial voids (Figures 3.28b). As a consequence of the breaking linkage after Pd^1 SAC formation [Pd-Ow 2.00(6) and 3.03(7) Å in **Pd^{2+}@CuSr-Mecysmox** and 1.99(2) Å in **Pd^0@CuSr-Mecysmox**] (Figure 3.28) (*vide infra*). Pd^{0}_{1} weakly interact also with oxamate moieties with Pd···O distances of 2.84(1) and 2.88(1) Å (see also Figures 3.27b and 3.28b). As far as we know, no examples of crystallographically precise Pd^1 SACs have been reported so far. Nevertheless, this Pd···O distance is close enough to that previously reported for Pd nanoclusters (2.9 Å).[64]

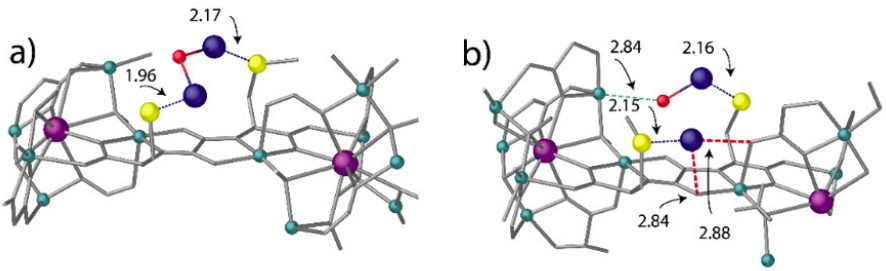

Figure 3.28. Details of the Pd···S interactions in **Pd^{2+}@CuSr-Mecysmox** (a) and **Pd^{0}@CuSr-Mecysmox** (b) underlining the detected water molecule acting as bridge between two-coordinated Pd^{2+} ions in **Pd^{2+}@CuSr-Mecysmox** still remains coordinated in **Pd^{0}@CuSr-Mecysmox**, as terminal ligand, only to Pd^{2+} metal ions as a consequence of the breaking linkage after Pd^{0} SAC formation. Copper, strontium, palladium, oxygen and sulfur atoms are represented by green, purple, blue, red and yellow spheres, respectively, whereas the ligands (except sulfur) are depicted as grey sticks. Hydrogen atoms are omitted for clarity.

As **CuSr-Mecysmox** crystal structure, both **Pd^{2+}@CuSr-Mecysmox** and **Pd^{0}@CuSr-Mecysmox** have also two conformations of thioether chains pointing Pd^{2+} ions by S binding sites,[77,78] towards the smaller interstitial voids residing along a axis (Figures 3.25, 3.29 and 3.30). If we compare the positions of the Pd^{2+} ions in **Pd^{2+}@CuSr-Mecysmox** and **Pd^{0}@CuSr-Mecysmox**, it is observed that they reside both in large pores and in smaller interstitial voids for the first case (Figure 3.29), while for the reduced structure they only remain unreducible in the interstitial voids (Figure 3.30) offered by the peculiarity structure that presents the MOF CuSr-Mecysmox (Figure 3.25). In the **Pd^{0}@CuSr-Mecysmox** structure, in addition to the Pd^{2+} ions relying on the interstitions, the single-atom catalyst Pd^{0} is accommodated in the larger hexagonal pores. But only the Pd^{2+} ions residing in the most accessible pores [50% of total Pd^{2+} ions] could be chemically reduced to Pd^{0}, as confirmed by XPS spectrum of **Pd^{0}@CuSr-Mecysmox** (*vide infra*).

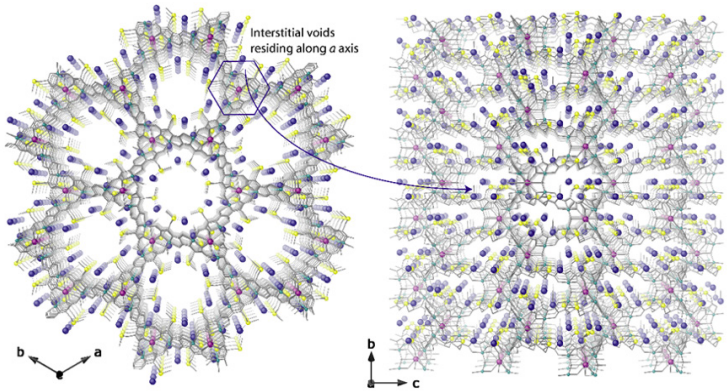

Figure 3.29. Details of fragments of the net along c (left) and a (right) crystallographic axis for **Pd^{2+}@CuSr-Mecysmox**, where Pd^{2+} cation are depicted as blue spheres. Copper, strontium and sulfur atoms of the MOF are represented by green, purple and yellow spheres, respectively, whereas the ligands (except sulfur) are depicted as grey sticks [carbon: gray, oxygen: red and nitrogen: blue]. Hydrogen atoms are omitted for clarity.

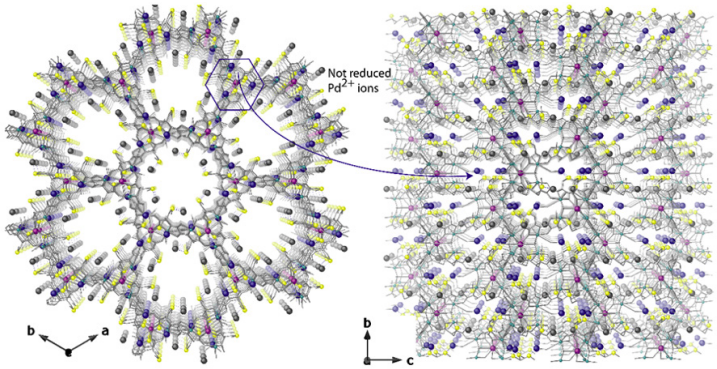

Figure 3.30. Details of fragments of the net along c (left) and a (right) crystallographic axis for **Pd^{0}@CuSr-Mecysmox**, where Pd^{0} single atom catalysts are depicted as grey spheres and Pd^{2+} cations are depicted still as blue spheres. Copper, strontium and sulfur atoms of the MOF are represented by green, purple and yellow spheres, respectively, whereas the ligands (except sulfur) are depicted as grey sticks [carbon: gray, oxygen: red and nitrogen: blue]. Hydrogen atoms are omitted for clarity.

Lastly, the length of the amino acid residue also seems to play a key role in the nuclearity of the metal species formed. Thus, in the present MOF, where Pd^{2+} cations are connected to shorter dimethyl thioether chains within the channels, Pd_1 SACs are formed during the reduction process. In turn, in a previously reported work with an isoreticular MOF prepared from the amino acid L-methionine,[79,80] the larger length of the ethylmethyl thioether chains decorating the channels allows a closer approach of the metal species, and dinuclear Pt2 nanoclusters could be obtained.

The virtual diameter of the channels only slightly decreases from ca. 0.9 nm in the precursor material **CuSr-Mecysmox** to *ca*. 0.7 nm in **Pd^{2+}@CuSr-Mecysmox** and **Pd^{0}@CuSr-Mecysmox**. This is in total agreement with adsorption measurements.

3.4.4. Powder X–ray Diffraction (PXRD)

In order to confirm the crystallinity of unreducible and reducible **Ag^{+}@CuNi-Me_3mpba, $Ag^{0}_2Fe^{3+}$@CuNi-Me_3mpba** and MecysPd, and the isostructurality of corresponding single crystals with bulk polycrystalline samples X–ray Powder Diffraction Measurements (XRPD) were carried out. A polycrystalline sample of **Pd^{2+}@CuNi-Me_3mpba** was introduced into a 0.5 mm borosilicate capillary prior to being mounted and aligned on an Empyrean PANalytical powder diffractometer, using Cu Kα radiation (λ = 1.54056 Å). Five repeated measurements were collected at room temperature (2θ = 2–60°) and merged in a single diffractogram.

3.4.4.A. PXRD of Ag^0_2@CuNi-Me_3mpba

Figure 3.31 shows the experimental X-ray diffraction (PXRD) patterns of **Ag^+@CuNi-Me_3mpba** (bottom spectra) and **$Ag^0_2Fe^{3+}$@CuNi-Me3mpba** (top spectra). In each case, the experimental diffraction patterns (solid lines) are identical to the theoretical ones extracted from the SC-DRX data (bold lines), confirming the crystallinity and purity of the samples, after undergoing the aggressiveness of the silver inserting agent. It is also worth noting that Figure 3.31 indicates that that the bulk samples are crystalline and pure, without typical Ag^0 nanoparticle peaks.

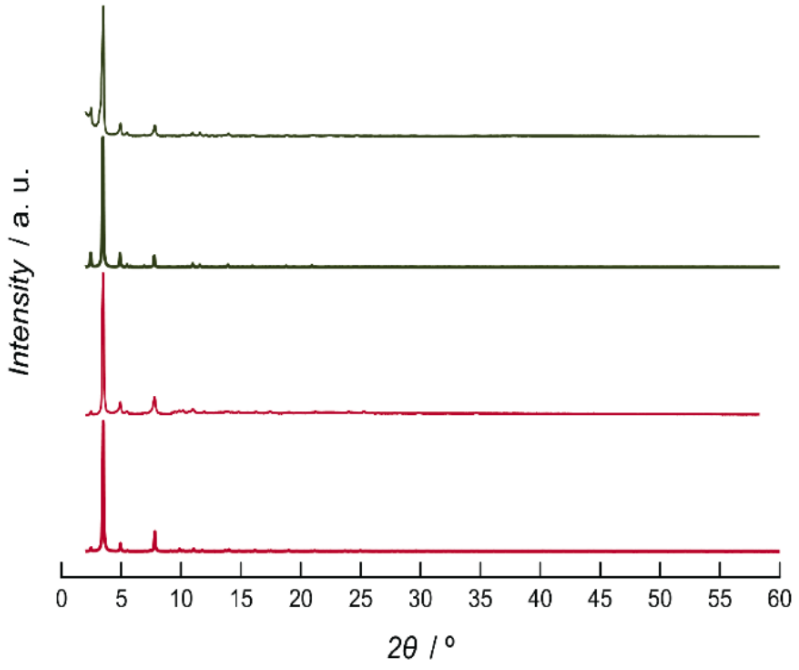

Figure 3.31. Theoretical (bold lines) and experimental (solid lines) PXRD pattern profiles of **Ag^+@CuNi-Me_3mpba** (red) and **Ag^0@CuNi-Me_3mpba** (dark green) in the 2θ range 2–60°

3.4.4.B. PXRD of $Ag^0_2Fe^{3+}$@CuNi-Me_3mpba

The experimental PXRD pattern of **$Ag^0_2Fe^{3+}$@CuNi-Me_3mpba** (top spectra), as well as those of previously reported **Fe^{3+}@CuNi-Me_3mpba** (bottom spectra) and **Ag^0_2@cuNi-Me_3mpba** (middle spectra), are identical to the calculated ones (Figure 3.32), which confirm both the homogeneity of the samples and the isostructurality to the single-crystals selected for SCXRD.

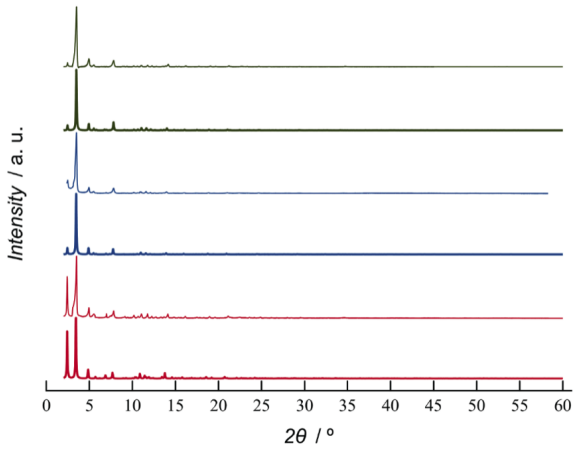

Figure 3.32. Theoretical (bold lines) and experimental (solid lines) PXRD pattern profiles of **Fe^{3+}@CuNi-Me_3mpba** (red), **Ag^0_2@CuNi-Me_3mpba** (blue) and **$Ag^0_2Fe^{3+}$@CuNi-Me_3mpba** (dark green) in the 2θ range 2–60°.

3.4.4.C. PXRD of Pd^0@CuSr-Mecysmox

Figure 3.33 shows the experimental powder X-ray diffraction (PXRD) patterns of **CuSr-Mecysmox**, **Pd^{2+}@CuSr-Mecysmox**, and **Pd^0@CuSr-Mecysmox** (solid lines), which are identical to the theoretical ones (bold lines), demonstrating high purity, homogeneity, and isostructurality in these bulk samples. Since the intensities of the diffraction patterns were weak, an extension of the range 10-45° is given in Figure 3.33b.

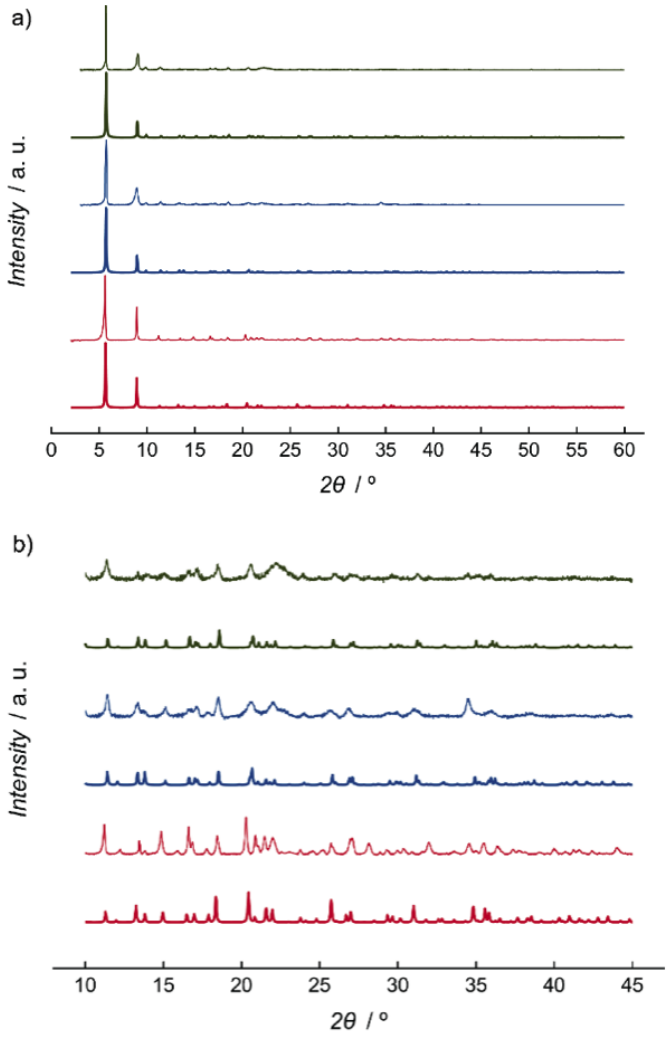

Figure 3.33. a) Calculated (bold lines) and experimental (solid lines) PXRD pattern profiles of **CuSr-Mecysmox**(red), Pd^{2+}@**CuSr-Mecysmox** (blue) and Pd^{0}@**CuSr-Mecysmox** (green) in the 2θ range 2.0–60.0°. b) Calculated (bold lines) and experimental (solid lines) PXRD pattern profiles of **CuSr-Mecysmox**(red), Pd^{2+}@**CuSr-Mecysmox** (blue) and Pd^{0}@**CuSr-Mecysmox** (green) are shown in the 2θ

3.4.5. Thermogravimetric analysis (TGA)

Thermogravimetric analyzes were performed on crystalline samples in a dry N_2 atmosphere with a Mettler Toledo TGA/STDA 851e thermobalance operating at a heating rate of 10 ºC min-1. The following ATG graphs will give us information about the number of solvent molecules, specifically water molecules, that contain the MOFs in the structure (obtained from the percentage of weight lost during the first decay) and the thermostability they present.

3.4.5.A. TGA of **Ag^0_2@CuNi-Me_3mpba**

TGA analyses for **Ag^+@CuNi-Me_3mpba** and **Ag^0_2@CuNi-Me_3mpba** (Figure 3.34) established the solvent contents for both materials. The mass loss was around 20% for both, corresponding to 51 water molecules for the **Ag^+@CuNi-Me_3mpba** and 48 for the **Ag^0_2@CuNi-Me_3mpba** _red, coinciding with the elemental analysis.

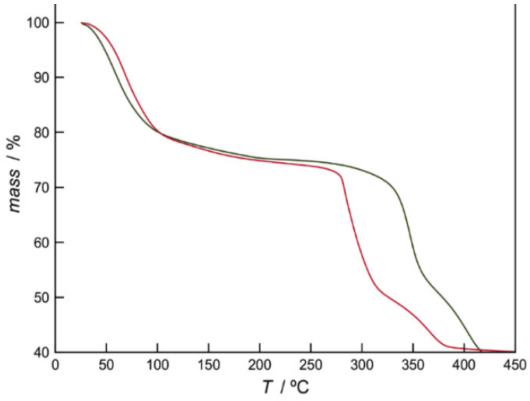

Figure 3.34. Thermo-Gravimetric Analyses (TGA) of **Ag^+@CuNi-Me_3mpba** (red) and **Ag^0_2@CuNi-Me_3mpba** (green) under a dry N_2 atmosphere.

Regarding thermal stability, it can be observed how the formation of clusters within the confined octagonal spaces of the MOF reinforces its structure.

3.4.5.B. TGA of $Ag^0_2Fe^{3+}$@CuNi-Me_3mpba

In order to establish the solvent content of **$Ag^0_2Fe^{3+}$@CuNi-Me_3mpba**, TGA analysis was performed under a dry N_2 atmosphere (Figure 3.35). The observed weight loss corresponds to 63 water molecules, which agree with the CHN analysis.

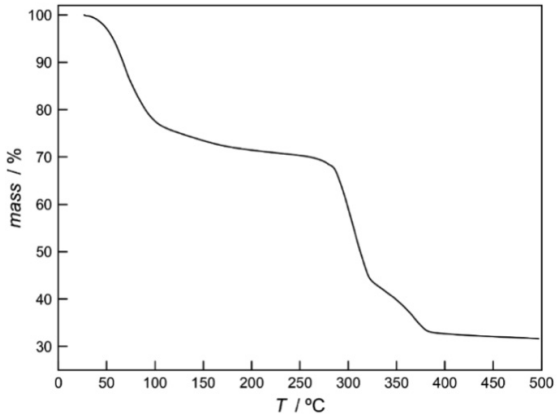

Figure 3.35. Thermo-Gravimetric Analyses (TGA) of **$Ag^0_2Fe^{3+}$@CuNi-Me_3mpba** under a dry N_2 atmosphere.

3.4.5.C. TGA of Pd^0@CuSr-Mecysmox

The solvent contents of **CuSr-Mecysmox**, **Pd^{2+}@CuSr-Mecysmox** and **Pd^0@CuSr-Mecysmox** were, on the other hand, definitively established by thermogravimetric analysis (TGA) (Figure 3.36). Where the water molecules calculated by ATG correspond to those given by CHN analysis:

- The loss of 15.4% of the mass of the **CuSr-Mecysmox** corresponds to 15 water molecules.

- The loss of 11.1% of the mass of **Pd^{2+}@CuSr-Mecysmox** corresponds to 12 water molecules.

- The loss of 12.3% of the mass of the **Pd^0@CuSr-Mecysmox** corresponds to 13 water molecules.

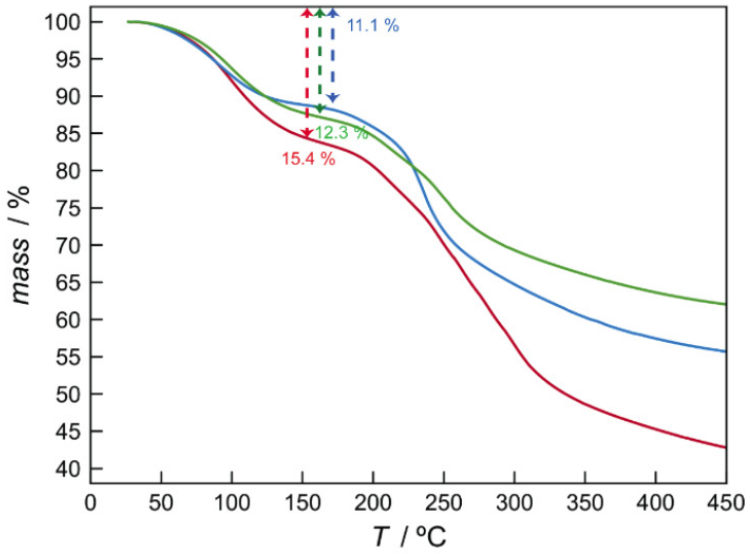

Figure 3.36. Thermo-Gravimetric Analysis (TGA) of **CuSr-Mecysmox** (red), **Pd^{2+}@CuSr-Mecysmox** (blue) and **Pd^0@CuSr-Mecysmox** (green) under dry N_2 atmosphere.

3.4.6. Gas adsorption

The permanent porosity of the presented MOFs was confirmed by gas adsorption measurements. Adsorption-desorption isotherms of N_2 at 77 K were carried out on crystalline powder samples with a Micromeritics ASAP2020 instrument. The samples were evacuated at 70 °C for 24 hours at 10^{-6} Torr before analysis. This technique mainly gives us an idea of the size and surface area of the regular pores contained in MOFs. The BET model to which it fits gives us an idea about the type of interaction that is exerted between the MOF and the bimolecular nitrogen molecules, which for all cases was type 1 sorption behavior characteristic of microporous compounds.

3.4.6.A. N_2 Adsorption isotherm of Ag^0_2@CuNi-Me_3mpba

The N_2 adsorption isotherms for **Ni^{2+}@CuNi-Me_3mpba**, **Ag^+@CuNi-Me_3mpba** and **Ag^0_2@CuNi-Me_3mpba** confirm their permanent porosity (Figure 3.37). The N_2 adsorption isotherms for **Ni^{2+}@CuNi-Me_3mpba** and **Ag^0_2@CuNi-Me_3mpba** are very similar, suggesting a very similar accessible pore space. Therefore, these adsorption graphs tell us how the starting MOF (**Ni^{2+}@CuNi-Me_3mpba**, blue dates), suffers partial obstruction of the pore with the insertion of Ag ions that decreases the pore size of the MOF (**Ag^+@CuNi-Me^3mpba**, red dates) and the nanoconfinement of the cations, together with the reduction of Ag^+ to $Ag_2{}^0$, provides a greater accessibility of the pores (**Ag^0_2@CuNi-Me_3mpba**, green dates). The slight difference in N_2 adsorption between **Ni^{2+}@CuNi-Me_3mpba** and **Ag^0_2@CuNi-Me_3mpba** could be due to the fact that the positions of the metals housed in octagonal accessible pores in the case of **Ni^{2+}@CuNi-Me_3mpba** are not aggregated to form a cluster, as is the case with **Ag^0_2@CuNi-Me_3mpba**.

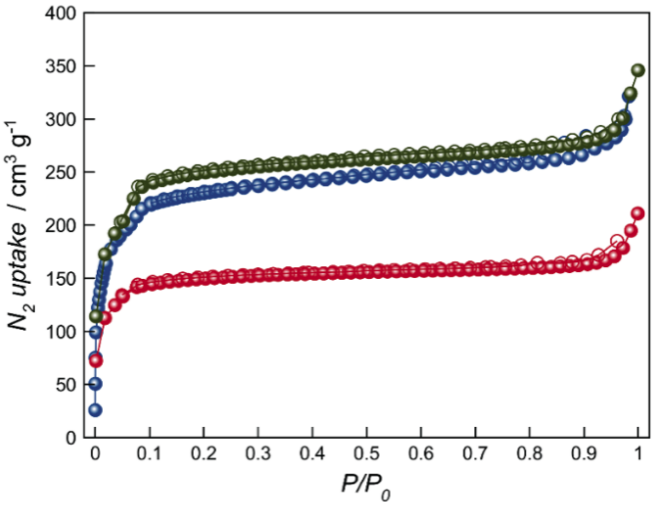

Figure 3.37. N2 sorption (filled circles) and desorption (empty circles) isotherms for the activated compounds **Ni^{2+}@CuNi-Me_3mpba** (blue), **Ag^+@CuNi-Me_3mpba** (red) and **Ag^0_2@CuNi-Me3mpba** (green) at 77 K.

3.4.6.B. N_2 Adsorption isotherm of **$Ag^0_2Fe^{3+}$@CuNi-Me_3mpba**

The N_2 adsorption isotherm at 77 K, for **Fe^{3+}@CuNi-Me_3mpba**, **Ag^0_2@CuNi-Me_3mpba** and **$Ag^0_2Fe^{3+}$@CuNi-Me_3mpba** is shown in Figure 3.38. Relevantly, despite the increased complexity within the MOF channels and the aggressiveness of the PSMs, the hybrid material it maintained the required porosity to be able to accommodate catalytic events within its channels.

For this case, what was expected occurred, the **Fe^{3+}@CuNi-Me_3mpba** (blue) had a smaller pore size due to the non-compaction of the ions housed in the octagonal pores to form a cluster, which does occur for **Ag^0_2@CuNi-Me_3mpba** and **$Ag^0_2Fe^{3+}$@CuNi-Me_3mpba**.

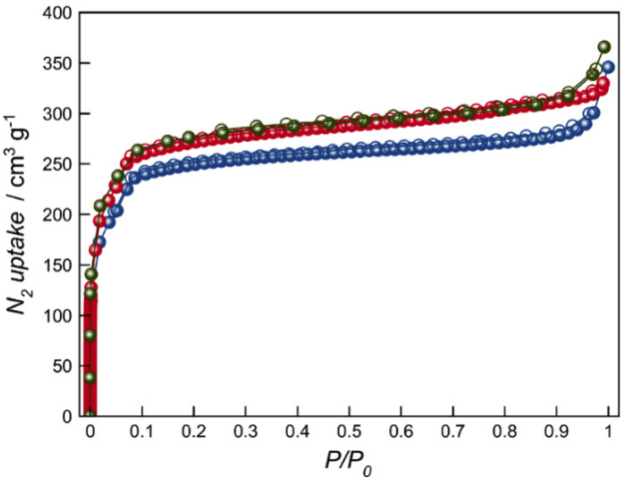

Figure 3.38. N_2 sorption (filled circles) and desorption (empty circles) isotherms for the activated compounds **Fe^{3+}@CuNi-Me_3mpba** (blue), **Ag^0_2@CuNi-Me_3mpba** (red) and **$Ag^0_2Fe^{3+}$@CuNi-Me_3mpba** (green) at 77 K.

3.4.6.C. N_2 Adsorption isotherm of **Pd^0@CuSr-Mecysmox**

The permanent porosity of the samples –particularly important in the case of **Pd^{2+}@CuSr-Mecysmox** and **Pd^0@CuSr-Mecysmox** for catalytic applications– was verified by measuring their N_2 adsorption

isotherms at 77 K. They confirm permanent porosity for **CuSr-Mecysmox**, **Pd^{2+}@CuSr-Mecysmox** and **Pd^{0}@CuSr-Mecysmox** (Figure 3.39), which is slightly lower for **Pd^{2+}@CuSr-Mecysmox** and **Pd^{0}@CuSr-Mecysmox**, as expected from the decrease of their accessible void due to the presence of the Pd guests within the channels (calculated Brunauer-Emmett-Teller (BET) surface areas[69] for **CuSr-Mecysmox**, **Pd^{2+}@CuSr-Mecysmox** and **Pd^{0}@CuSr-Mecysmox** are 719, 548 and 572 m^2/g, respectively). These ratios correspond to the virtual diameter of the channels, which decrease slightly from ca. 0.9 nm in the CuSr-Mecysmox precursor material at ca. 0.7 nm in **Pd^{2+}@CuSr-Mecysmox** and **Pd^{0}@CuSr-Mecysmox.**

Since this is a case of SAC and not of SNMC, no clusters are formed in the pores that group the atoms, optimizing the pore size, but the diameter practically does not change after the reduction of the Pd atoms.

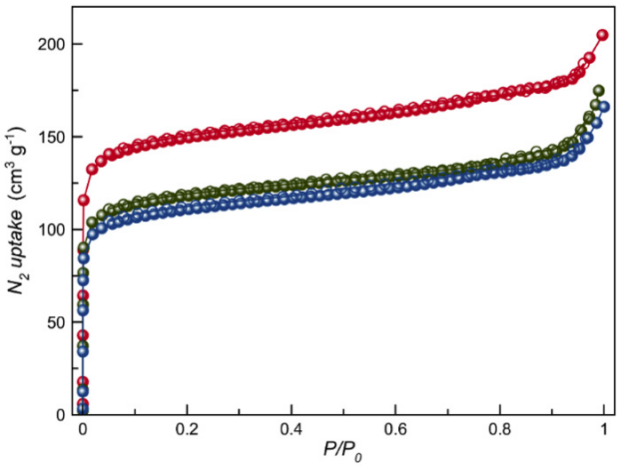

Figure 3.38. N_2 (77 K) adsorption isotherms for the activated compounds **CuSr-Mecysmox** (red), **Pd^{2+}@CuSr-Mecysmox** (blue) and **Pd^{0}@CuSr-Mecysmox** (green). Filled and empty symbols indicate the adsorption and desorption isotherms, respectively. The samples were activated at 70 °C under reduced pressure for 16 h prior to carry out the sorption measurements.

3.5. Catalytic studies

3.5.A. Catalytic properties of Ag^0_2@CuNi-Me_3mpba

After obtaining clusters of Ag_2^0 confined in the accessible pores of the MOF, their catalytic properties were studied. Despite the multiple options that **Ag^0_2@CuNi-Me_3mpba** could contemplate, we have focused on the expansion reaction of the Buchner ring with catalytic amounts of said MOF. Previous results show that the reaction between toluene and ethyl diazoacetate (EDA) proceeds rapidly (30 min) in very high yield, under standard reaction conditions (Figure 3.39)[46,81]and **2.3a** was obtained with optimum >95% yield. This **2.3a** corresponds to the typical mixture of cycloheptatriene isomers, in accordance with previous results. [44,88] Their obtaining was produced after maintaining a low concentration of EDA during reaction, which was achieved by adding a solution of EDA (in toluene or DCM) into the reaction mixture with a syringe pump, instead of addition at once; which produce unwanted dimerization reaction of EDA.

A hot filtration test, where the solid MOF catalyst **Ag^0_2@CuNi-Me_3mpba** is removed from the reaction mixture at the reaction temperature (60 °C) at early conversion (~30%), shows that the catalytic active species are not present in solution within the experimental error (< 10%, Figure 3.40), which supports the stability of the solid catalyst.

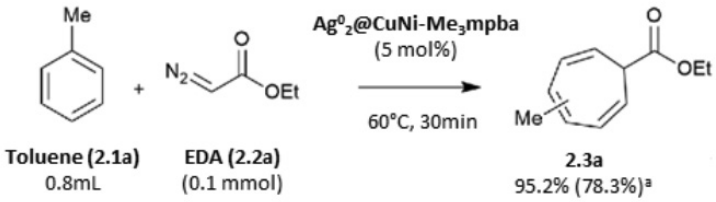

Figure 3.39. Buchner ring expansion reaction between toluene and ethyl diazoacetate EDA catalyzed by MOF **Ag^0_2@CuNi-Me_3mpba**. a GC yield after syringe pump addition of EDA, the result after addition of EDA at once is between parentheses.

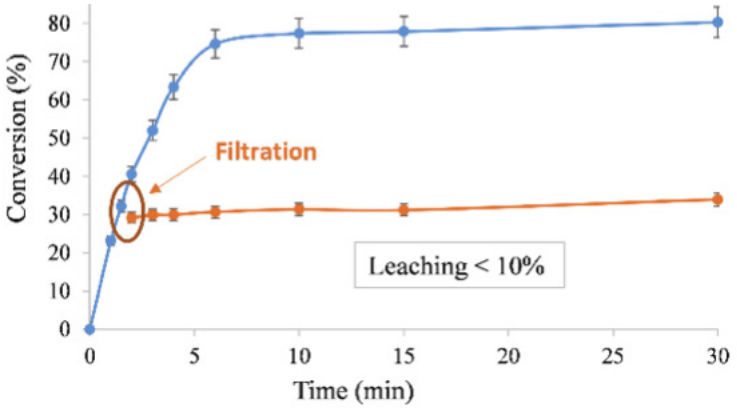

Figure 3.40. Hot filtration test after adding EDA at once in Buchner ring expansion reaction between toluene and ethyl diazoacetate EDA catalyzed by MOF **Ag^0_2@CuNi-Me_3mpba**, error bars account for 5% uncertainty.

Figure 3.41 shows MOF **Ag^0_2@CuNi-Me_3mpba** can be recovered at the end of the reaction by centrifugation, washed, and reused six times, keeping a good catalytic activity.

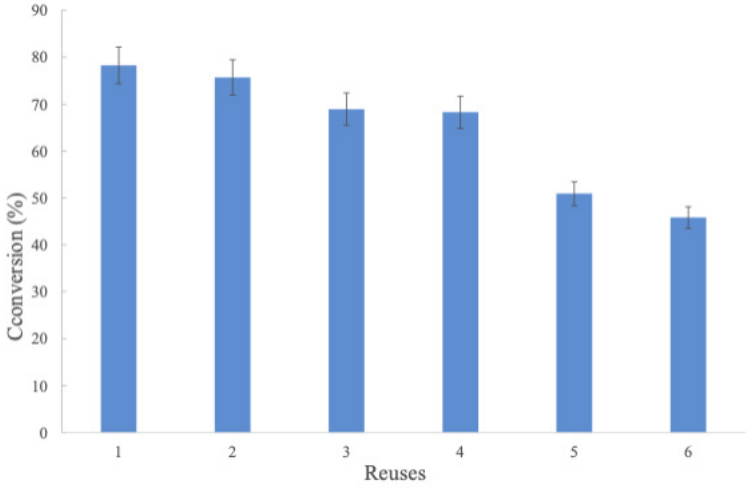

Figure 3.41. Catalytic results for the Buchner ring expansion reaction between toluene and EDA catalyzed by MOF Ag^0_2@CuNi-Me_3mpba under the reaction conditions indicated in the main text. EDA is added at once. **Ag^0_2@CuNi-Me_3mpba** is recovered from the reaction mixture by centrifugation, washed with dichloromethane, and reused. Error bars account for 5% uncertainty.

The Buchner ring expansion reaction catalysed by Ag^0_2@CuNi-Me_3mpba could be expanded to other aromatic substrates (Figure 3.42 and Table 3.10). Halogenated (entry 1, 2 and 5 in Table 3.10), cyano (entry 3 in Table 3.10), methoxy (entry 4 in Table 3.10) and ortho-disubstituted (entry 6 in Table 3.10) aromatic compounds react with **EDA** in good to excellent yields, and still in short reaction times (<2 h).

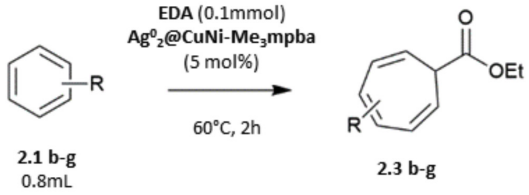

Figure 3.42. The Buchner ring expansion reaction catalysed by **Ag^0_2@CuNi-Me_3mpba** expanded to other aromatic substrates.

Table 3.10. Results for the Buchner ring expansion reaction between different aromatics and EDA, catalyzed by MOF **Ag^0_2@CuNi-Me_3mp-ba**. a GC yields after syringe pump addition of EDA.

ENTRY	ARYL SUBSTRATE SUBSTITUENT(S)	YIELD OF THE PRODUCT (%)[A]
1	Cl	66.5 (2.3b)
2	Br	64.9 (2.3c)
3	CN	92.8 (2.3d)
4	OMe	82.6 (2.3e)
5	CH_2Br	50.2 (2.3f)
6	Me-*ortho*-F	72.7 (2.3g)

These results should be remarked in view that is difficult to find in the open literature Ag-catalyzed Buchner ring expansion reactions.[83-84] Therefore, as for MOF- or zeolite-stabilized Pd clusters,[86] the formation of Ag_2 clusters in micro-structured solids enables not only the catalytic use of this metal in this complex organic synthetic reaction, but also its recovery and reuse.[87]

3.5.B. Catalytic properties of $Ag^0_2Fe^{3+}$@CuNi-Me_3mpba

During the search for systems that represent an exceptional opportunity to study in a neat manner, without structural/electronic ambiguities, the catalytic role and activity of each metallic entity for a given reaction, the potential that **$Ag^0_2Fe^{3+}$@CuNi-Me_3mpba** can offer was studied. This MOF was challenged to do conversion of styrenes to phenylace-

tylenes in one-pot (Figure 3.43). The path of obtaining was based on the metal-catalyzed oxidative cross-coupling of styrenes with phenyl sulfone to give phenylacetylenes, after elimination of the sulfone moiety of intermediates vinyl sulfones–incompatible procedure in homogenous phase with previously reported methods.[88,90]Vinyl sulfones have been previously prepared by a variety of methods.[18, 91-93]However, the engagement of vinyl sulfones with a base-mediated elimination, to form the corresponding alkyne, is not easy with any of these methods. For instance, the synthesis of vinyl sulfones has been reported with large amounts of the catalytic system $AgNO_3$/TEMPO [TEMPO: (2,2,6,6-tetramethylpiperidin-1-yl)oxyl, 15-20 mol%].94 Although, this is incompatible with the elimination step. Thus, there is a necessity to found novel catalysts able to circumvent the existing drawbacks on the synthesis of more complex alkynes, and consequently expand the library of available alkynes in industry.

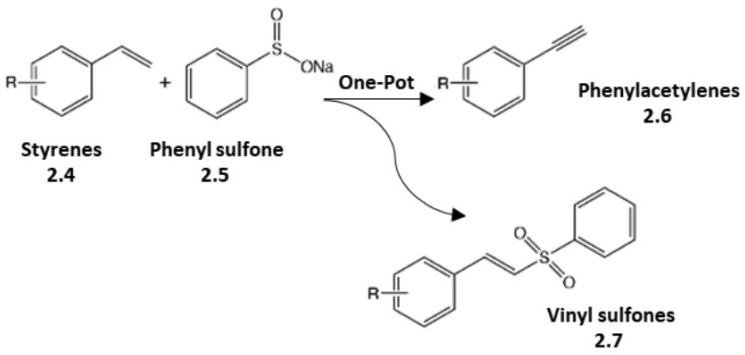

Figure 3.43. Proposed approach for the one-pot conversion of alkenes into alkynes, based on the metal-catalyzed oxidative cross-coupling of styrenes (**2.4**) with phenyl sulfone (**2.5**) to give phenylacetylenes (**2.6**), after elimination of the sulfone moiety of intermediates vinyl sulfones (**2.7**).

In the study of the catalytic applications of SMAs and subNMCs, we encountered in the literature that the true catalytic species for the coupling of styrenes with phenyl sulfone are Ag dimers, and not the starting $AgNO_3$ salt.[95] Thus, firstly, to check this finding or even if silver could transform in other metallic species of higher atomicity, as well as if other metal ions could behave as suitable catalyst, the synthesis of the vinyl sulfone intermediate **2.7a** was studied, from the reaction of styrene **2.4a** and phenyl sulfone **2.5** in the presence of different homogenous metal catalyst and using or not TEMPO as organic oxidant (Figure 3.44, Table 3.11 entries 1-9), and performed an in deep characterization when using $AgNO_3$ and TEMPO to unveiled the nature of the true silver catalyst. So, as expected, we found the oxidative coupling of styrene **2.4a** and phenyl sulfone **2.5** barely proceeded without $AgNO_3$ or TEMPO (entries 1-2), but gave 74% of **2.7a** when both $AgNO_3$ (15 mol%) and TEMPO (20 mol%) were combined (entry 3 in Table 3.11), suggesting the formation of the active dinuclear silver species in the presence of TEMPO. However, different copper and iron metal salts were not found catalytically active (entries 4-6), with the exception of $Fe_2(SO_4)_3$, which gave ~25% product either in the presence of TEMPO or not (entries 7-8). Also notice that the combination of $AgNO_3$ and $Fe_2(SO_4)_3$ did not produce any catalytic action (5% product), which is in accordance with the easy reactivity between both metal salts in solution, precluding them to play as catalyst (entry 9 in Table 3.11).

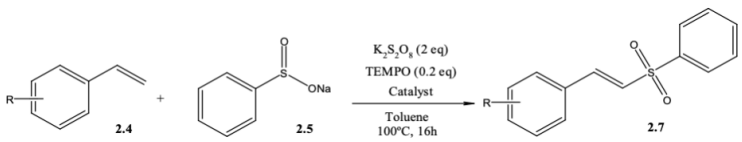

Figure 3.44. Schematic representation of the oxidative cross-coupling reaction of styrene **2.4a** with phenyl sulfone **2.5** to yield the vinyl sulfone **2.7a**. (i) Catalyst: Metal (15 mol%) / TEMPO (20 mol%), $K_2S_2O_8$ (2 equivalents), toluene (0.2 M), 100 °C, 24h.

Table 3.11. Catalytic results for the oxidative cross-coupling reaction of styrene **2.4a** with phenyl sulfone **2.5**. GC yields; average of, at least, two runs. The total metal loading was consistently 15 mol%, *i.e.* 7.5 mol% of Ag plus 7.5 mol% of Fe when combined.

Entry	Catalyst	TEMPO	2.7a (Yield, %)
1	None	Yes	6
2	$AgNO_3$	None	8
3		Yes	74
4	$CuCl_2$	Yes	7
5	$Cu(OAc)_2$	Yes	6
6	$Fe(acac)_3$	Yes	3
7	$Fe_2(SO_4)_3$	Yes	28
8	$AgNO_3$ + $Fe_2(SO_4)_3$	None	22
9		None	5
10	Ag^0_2@CuNi-Me_3mpba	Yes	48
11		None	45
12	Ni^{2+}@CuNi-Me_3mpba	None	11
13	$AgNO_3$ + Ni^{2+}@CuNi-Me_3mpba	None	61
14	Fe^{3+}@CuNi-Me_3mpba	Yes	63
15		None	61
16	Ag^0_2@CuNi-Me_3mpba + Fe^{3+}@CuNi-Me_3mpba	Yes	53
17		None	73
18	$Ag^0_2Fe^{3+}$@CuNi-Me_3mpba	Yes	73
19		None	95
20	$Fe_2(SO_4)_3$ + Ag^0_2@CuNi-Me_3mpba	None	6
21	$AgNO_3$ + Fe^{3+}@CuNi-Me_3mpba	None	32

[a]Please note that the catalytic results of Table 3.11 were obtained under the optimized reaction conditions reported in the literature and following the reactants disappearance and product appearance by gas-chromatography (gc).

After assimilating this information obtained from the homogeneous catalysts, we move on to the heterogeneous phase (entries 10-21 in Table 3.11). Firstly, we investigated the catalytic activity of **Ag^0_2@ CuNi-Me_3mpba**, possessing subNMCs Ag^0_2 within MOFs channels. We observed that **Ag^0_2@CuNi-Me_3mpba** showed a moderate catalytic activity for the reaction (ca. 45%, entries 10-11 in Table 3.11), with and without TEMPO. The fact that **Ag^0_2@CuNi-Me_3mpba** was able to catalyze the reaction without TEMPO can be explained by the co-catalysis exerted by the framework of the MOF itself, which was able to trigger the catalytic activity even with $AgNO_3$ in solution (entries 12-13 in Table 3.11), but, with moderate yields of **2.7a**. Then, on the basis of the results obtained by homogeneous solutions of $Fe_2(SO_4)_3$, we investigated the catalytic performance of **Fe^{3+}@CuNi-Me_3mpba**, obtaining moderately good yields (ca. 62%) in the presence or not of TEMPO (entries 14-15 in Table 3.11), which evidenced the suitability of Fe^{3+}-SMAs to substitute TEMPO.[96]

In this context, we envisioned the heterogenization of metallic species in **$Ag^0_2Fe^{3+}$@CuNi-Me_3mpba** would be an appealing candidate to catalyze efficiently the required chemical events for the oxidative cross-coupling of **2.4a** and **2.5**. In fact, we can boast that **$Ag^0_2Fe^{3+}$@ CuNi-Me_3mpba** outperforms all the tested catalyst (entry 19 in Table 3.11), due it showed a very efficient performance that exceeds not only the individual MOF-supported metallic entities (**Fe^{3+}@CuNi-Me_3mpba** and **Ag^0_2@CuNi-Me_3mpba**, entries 10-11 and 14-15 in Table 3.11), but also a 1:1 physical mixture of them (entries 16-17 in Table 3.11) and any soluble catalyst under the same reaction conditions (entries 2-9 in Table 3.11), to give **2.7a** in 95% yield (entry 19 in Table 3.11). In addition, we further confirmed TEMPO is not needed for the reaction when

the catalyst contains Fe^{3+}-SMAs, since in **$Ag^0_2Fe^{3+}$@CuNi-Me_3mpba** only hampers the final reaction yield (compare entries 18-19 in Table 3.11). Thus, the heterogenization within MOFs channels, integrating SMAs and subNMCs of different metal ions, represent an exceptional exponent of how structural complexity/diversity could be transformed in evolved catalytic functionality.

The superior catalytic performance of **$Ag^0_2Fe^{3+}$@CuNi-Me_3mpba** respect to any other catalyst can be explained on the basis of its unique chemical structure, where isolated Fe^{3+}-SMAs and **Ag^0_2-subNMCs** are firmly supported within the same MOF, and noteworthy, coexisting at molecular distances. In one hand, the fixed position of the isolated metallic entities avoids metal interaction and reactivity within the MOF channels, which explains the dramatic increase in catalytic action compared to the corresponding silver(I) and iron(III) salts in solution (5% yield of **2.7a**, entry 10 in Table 3.11). This point was further confirmed when we studied the reaction using one of the individual MOFs together with the corresponding salt of the other metal ($Fe_2(SO_4)^{3+}$ **Ag^0_2@CuNi-Me_3mpba** and $AgNO_3$ + **Fe^{3+}@CuNi-Me_3mpba**, entries 20-21 in Table 3.11), where we found an abrupt decrease of the catalytic activity respect to **$Ag^0_2Fe^{3+}$@CuNi-Me_3mpba**. Thus, one can soundly affirm that supporting both Fe^{3+}-SMAs and Ag^0_2-subNMCs metallic entities within the MOFs walls is essential for having an efficient reaction. In the other hand, the proximity between metal sites in **$Ag^0_2Fe^{3+}$@CuNi-Me_3mpba** is of key relevance to allow a much better co-catalysis. This was supported with the study of the 1:1 physical mixture of **Ag^0_2@CuNi-Me_3mpba** + **Fe^{3+}@CuNi-Me_3mpba** –where the metallic entities in each of these materials are structurally identical to the ones in **Ag^0_2 Fe^{3+}@CuNi-Me_3mpba** but just residing in distinct MOF particles–,

that gave a significant lower yield of **2.7a** (73 vs 95%, compare entries 17 and 19 in Table 3.11), since intermediates must diffuse interparticle.

Once we confirmed the superiority of the hybrid assembly **$Ag^0_2Fe^{3+}$@ CuNi-Me_3mpba** to obtain the intermediate vinyl-sulfone **2.7a**, we studied independently the elimination step to led to phenylacetylene **2.6a** under basic conditions (Figure 3.45 and Table 3.12). The results show that KOtBu in tetrahydrofurane (THF) solvent is the only effective system from those studied, which include different carbonates, phosphonates and tert-butoxides in toluene or acetonitrile. Being **2.5** equivalents of KO^{t}Bu in THF (1M) solution, at 70 ºC, the optimized conditions to convert all the vinyl sulfone **2.7a** to phenylacetylene **2.6a** in 1 h reaction time We also found commercially available KO^{t}Bu in THF gives the same result as solid KO^{t}Bu dispersed in THF, thus, both can be used indistinctly.

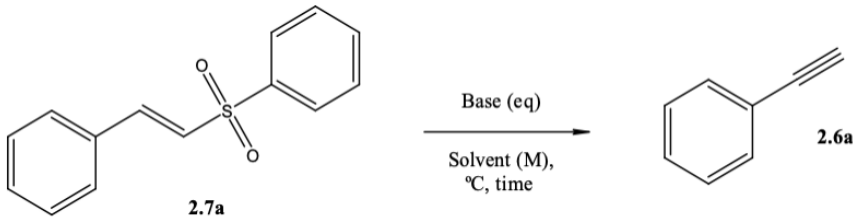

Figure 3.45. Synthesis of alkyne **2.6a** from vinyl sulfone **2.7a** under basic conditions

Table 3.12. Results for the synthesis of alkyne **2.6a** from vinyl sulfone **2.7a** under basic conditions. GC yields; average of, at least, two runs. aSome oligomers of **2.6a** were also found and are included in the yield. [b]Commercially available KO^{t}Bu in THF gives the same result than solid KO^{t}Bu dispersed in THF.

Entry	Base (Equivalents)	Solvent (M)	Temperature (^{o}c)	Time (Min)	2.6a (Yield, %)[A]
1	K_2CO_3 (2)	THF (2)	70	60	<1
2	Cs_2CO_3 (2)				<1
3	K_3PO_4 (2)				<1
4	NaO^{t}Bu (2)				8
5[b]	KO^{t}Bu (2)				>99
6	KO^{t}Bu (1.5)				>99
7			40		93
8			25		80
9			0		6
10		THF (3M)	25		85
11		THF (1M)			62
12		THF (0.75M)			20
12	NaO^{t}Bu (1.5)				2
14	KO^{t}Bu (1)	THF (3M)	70		68
15	KO^{t}Bu (2)				>99
16				15	>99
17		Toluene (3M)		60	<5
18		Acetonitrile (3M)			<5

After knowing the catalytic properties of the obtained MOF, **$Ag^0_2Fe^{3+}$@CuNi-Me_3mpba**, and the best reaction conditions, we proceed to study the one-pot conversion of styrene **2.4a** to phenylacetylene **2.6a** through intermediate vinyl-sulfone **2.7a** (Figure 3.46 and Table 3.13). We observed the one-pot synthesis of phenylacetylene **2.6a** from styrene **2.4a** was not possible when the soluble catalytic system $AgNO_3$ + TEMPO is employed (entries 1-3 in Table 3.12), even if the remaining salts after the oxidative coupling of the toluene solvent are removed prior to K^{t}O-Bu treatment in THF. In contrast, **$Ag^0_2Fe^{3+}$@CuNi-Me_3mpba** allows the one-pot synthesis of phenylacetylene **2.6a** from styrene **2.4a**, after filtration of the catalyst and toluene removal, to give phenylacetylene **2.6a** together with some heavier molecules in >99% isolated yield –after water/ethyl acetate washings, drying and solvent removal. Here we would like to remark the relevance of this result. In fact, it is difficult to find in the literature any procedure that directly converts an alkene to an alkyne in the same flask[97-99] and, to our knowledge, a catalytic version of this transformation has only previously reported with Pd supported in polyamine,[19, 100] which we could not reproduce in our hands. Besides, the **$Ag^0_2Fe^{3+}$@CuNi-Me_3mpba** catalyst could be reused after filtration, being able to be recycled up to 5 times retaining moderately good yields (Figure 3.46). Dealing with the structure of the heavier molecules, they could be assigned to the corresponding oligomers of alkyne **2.6a**, according to gas chromatography-mass spectrometry (GC-MS) analysis of the product mixture, in order to complete the mass balance. The **2.6a**/oligomer mixture was also characterized by FTIR and ^{1}H nuclear magnetic resonance (^{1}H-NMR, Figure 3.47), which confirmed the total conversion of the intermediate vinyl sulfone **2.7a** and the unambiguous formation of **2.6a** and the corresponding oligomers.

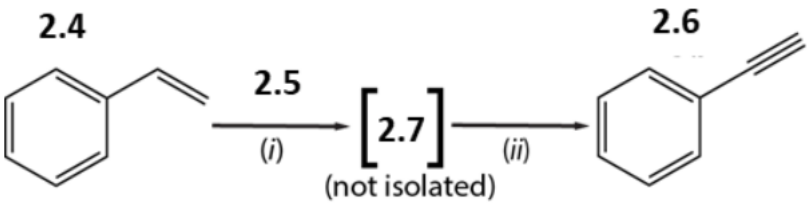

Figure 3.46. Schematic representation of the one-pot reaction to obtain phenylacetylene **2.6a** from styrene **2.6a**, after oxidative cross-coupling reaction with phenyl sulfone **2.5** and *in-situ* base treatment, under optimized conditions. (i) Same conditions as in Table 3.12; (ii) KO^{t}Bu (1.5 equivalents), THF (3M), 70 °C, 1h.

Table 3.13. Results for the one-pot synthesis of phenylacetylene **2.6a** from styrene **2.4a**, after oxidative cross-coupling reaction with phenyl sulfone **2.5** and base treatment, under optimized conditions (see Table 3.11). GC yields; average of, at least, two runs.

Entry	Coupling Catalyst	Filtration prior to KO^{T}BU reaction	Solvent For KO^{T}BU	2.6A (Yield, %)[A]
1	$AgNO_3$ + TEMPO	No	Toluene + THF	<5
2		Yes		<5
3		Yes	THF	<5
4	$Ag^0_2Fe^{3+}$@CuNi-Me_3mpba	No	Toluene + THF	<5
5		Yes		<5
6		Yes	THF	>99

[A]Isolated yield; some oligomers of 2.6a were also found and are included in the yield.

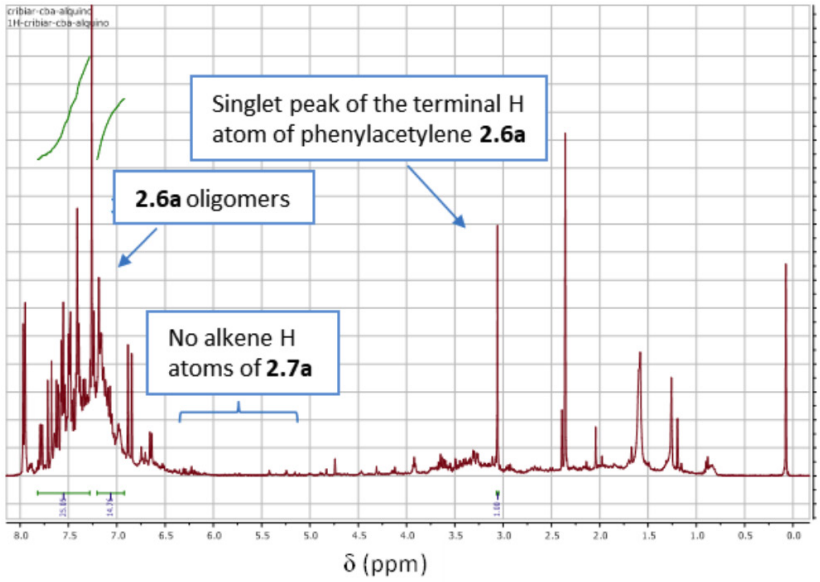

Figure 3.47. ^{1}H nuclear magnetic resonance (^{1}H-NMR) of the product mixture obtained after the one-pot oxidative cross-coupling reaction of styrene **2.4a** with phenyl sulfone **2.5** and in-situ base treatment.

Experiments with neat phenylacetylene **2.6a** under the KO^{t}Bu conditions in Table 3.13 confirmed that the base-triggered oligomerization reaction is faster than the deprotonation/elimination of vinyl sulfone **2.7a**, which explains the irremediably appearance of these oligomerizes at the end of the reaction.[101,102] Finally, we explored the performance of **$Ag^{0}_{2}Fe^{3+}$@CuNi-Me$_3$mpba** for the one-pot oxidative cross-coupling reaction of different styrenes **2.4b-g** with phenyl sulfone **2.5** and *in-situ* KO^{t}Bu treatment (Figure 3.48). It can be seen that ~70% yields for phenylacetylenes **2.6b-f** were consistently obtained, with a quantitative yield (>99%) for alkyne **2.6e.** Thus, aldehyde, halogen and methyl substitutions in different positions of the aromatic ring are tolerated, in contrast to the anisole derivative **2.7g** that does not engage in the final elimination reaction, however, it reacts well (96.8%) during the **$Ag^{0}_{2}Fe^{3+}$@CuNi-Me$_3$mpba** catalyzed oxidative coupling.

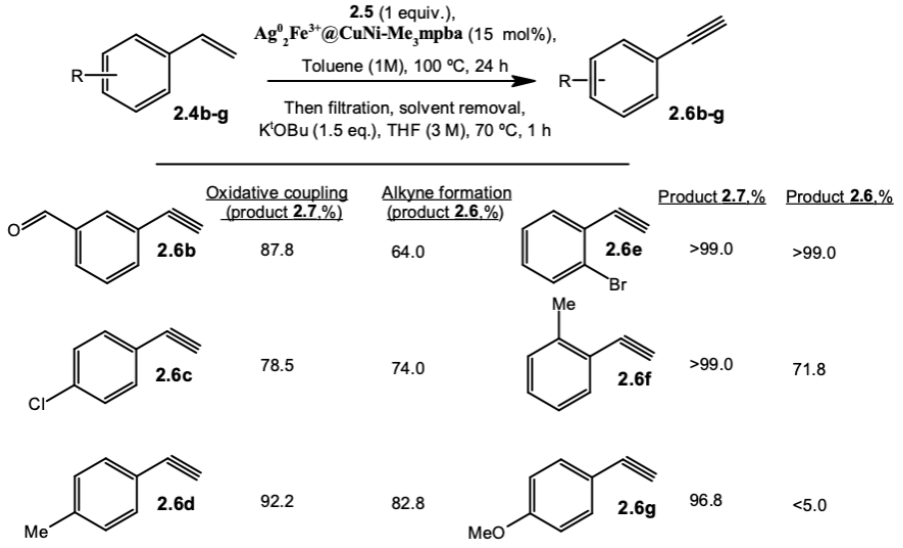

Figure 3.48. Results for the one-pot synthesis of alkynes **2.6b-g** from styrenes **2.4b-g**, after oxidative cross-coupling reaction with phenyl sulfone **2.5** catalyzed by $\mathbf{Ag^0_2Fe^{3+}}$**@CuNi-Me$_3$mpba** and in-situ ^{t}BuOK treatment. GC yields for products **2.7b-g** and isolated yields for products **2.6b-g**, taking in account the oligomers formed.

3.5.C. Catalytic properties of Pd0@CuSr-Mecysmox

We want to work in this section with the applicability of **Pd^0@CuSr-Mecysmox** SACs, in particular the reduction of noble metal salts (e.g., Pd, Au, ...)[103] to nanoparticles by using the industrial reagent benzyl alcohol leading to the corresponding formation of benzaldehyde. The dissolution of a metal salt into tiny amounts of neat benzyl alcohols might be sufficient to generate a single metal atom for catalytic oxidation of benzyl alcohols to benzoic acid under air. Due to its high reactivity, this single atom would, in principle, offer the coordination sites necessary for the different chemical events occurring during the reaction, such as dehydrogenation and oxygen activation,[104-106] without actually poisoning

the benzyl alcohol. Materials synthesis-wise, SAC could be considered a quiescent state of the metal during the reduction/aggregation process in benzyl alcohol, which keeps the metal seeds alive and catalytically active for the oxidation process without solvents, ligands or additives, even though other metal species may be present.[107.108]

Figure 3.49 shows the catalytic results for the aerobic oxidation of neat benzyl alcohol **2.8a** to benzoic acid **2.9a** with a 0.03-0.3 mol% of dissolved $Pd(OAc)_2$, and it can be observed that a high initial turnover frequency (TOF0) for **2.9a** is achieved with <0.1 Pd mol% but not with higher amounts of Pd, with yields of **2.9a** around 50-80% after 4h reaction time. Although, interestingly, started to slightly increase after 0.15 mol%. We supposed that the catalytic species at concentrations lower than 0.1 mol% were Pd SAs, whereas at higher amounts of palladium bigger species were formed, i.e., metal clusters and nanoparticles.[109,110]

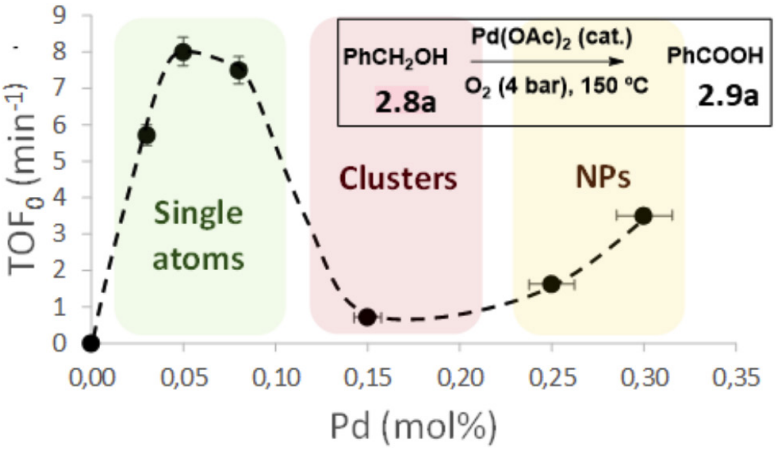

Figure 3.49. a) Initial turnover frequency (TOF_0) and final yields for the aerobic oxidation of neat benzyl alcohol 2.8a in the presence of different amounts of $Pd(OAc)_2$ at 150 ∞C under 4 bars of O_2.

Similar results were observed with other Pd spieces, including K_2PdCl_4, $Pd_2(dba)_3$ and $Pd(acac)_2$, but not with Pd complexes having a stronger ligand such as a phosphine, i.e. $Pd(PPh_3)_4$ or $Pd(PPh_3)_2Cl_2$ (Table 3.14 and Figure 3.50).

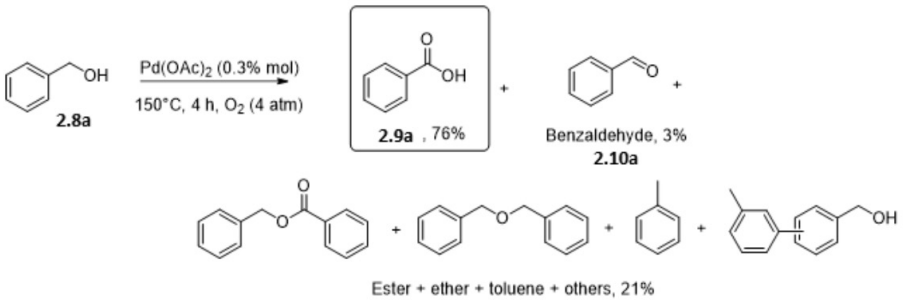

Figure 3.50. Yields for the aerobic oxidation of neat benzyl alcohol **2.8a** to benzoic acid **2.9a** catalyzed by $Pd(OAc)_2$ at 150 ºC and 4 bars of O_2.

Table 3.14. Catalytic results for different Pd compounds.

Catalyst	2.9a	Benzaldehyde	Other products
$Pd(OAc)_2$	75%	3.6%	6.9%
K_2PdCl_4	55.6%	15.5%	15.7%
$Pd_2(dba)_3$*	37.9%	18.2%	9.9%
$Pd(acac)_2$	51.4%	15.8%	9.6%
Pd^0@CuSr-Mecysmox	41.1%	26.4%	7.6%
Pd(PPh3)4	7.2%	24.1%	8.8%
$Pd(PPh_3)_2Cl_2$	0.7%	4.5%	7.0%

Reaction conditions: 1.96 mmol substrate, 0.3% mol Pd, 4 atm O2, 150°C, 450 rpm, h. GC yields. *15 h

Figure 3.51 shows that **2.9a** starts to be formed at intermediate conversions, when >50% of **2.8a** still remains in solution. These results confirm that the Pd catalyst formed under these conditions is able to override the poisoning of **2.8a** under aerobic conditions, and is not behaving as a quencher for the radical oxidation of **2.8a** to **2.9a**.[111] An acceptorless dehydrogenation pathway can be ruled out since an open vial reaction gave very conversion of **2.8a**, thus confirming the need of O2 to facilitate the one-pot oxidation.[112,113]

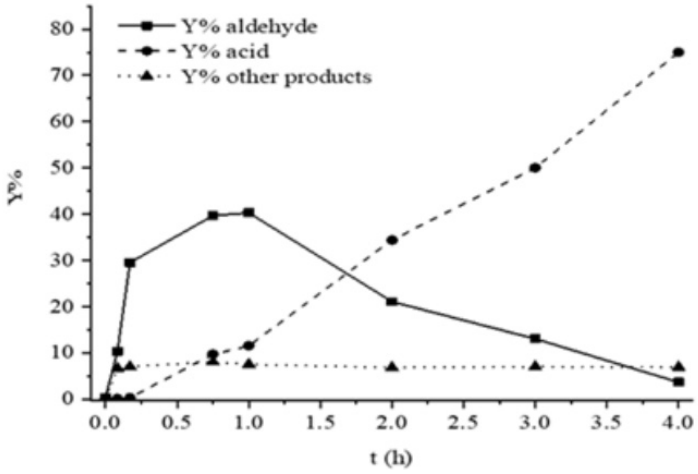

Figure 3.51. b) Representative time-yield kinetic plot of the reaction, for 0.05 mol% $Pd(OAc)_2$.

A quenching test with triphenylphosphine (Figure 3.52), under the indicated reaction conditions, showed that the concentration was not crucial for the reaction to happen and the catalytic activity comes from species in solution, *i.e.*, SAs were catalyzing the reaction. This is supported by the fact that when PPh_3 was use as a quencher of the possible monometallic active species in solution and the formation of **2.8a** could not proceed after the addition of the phosphine

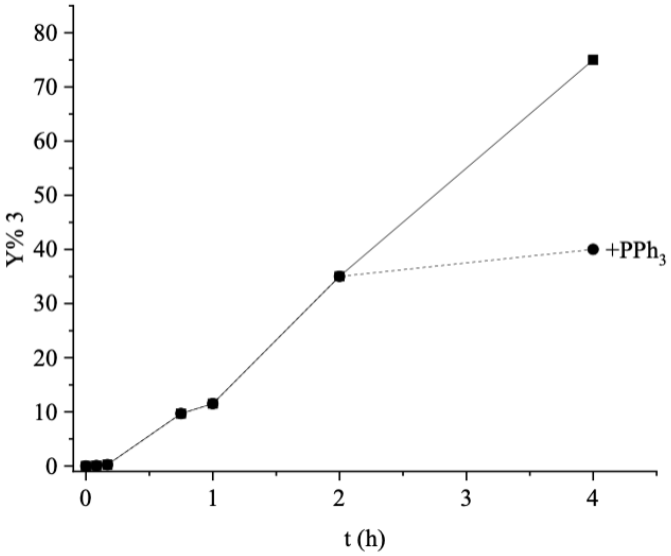

Figure 3.52. Quenching test with triphenylphosphine for the oxidation of neat benzyl alcohol **2.8a** to benzoic acid **2.9a** at 150 ºC and 4 bars of O_2, catalyzed by Pd(OAc)2.

This hypothesis of the in-situ formation of SAs had to be proven by studying metal species formed during the reaction at concentrations lower than 0.1 mol%, using Aberration-corrected High-angle Annular Dark Field Scanning-transmission Electron Microscopy (AC HAADF-STEM), which confirmed the presence of Pd SAs, Figure 3.53. Since AC HAADF-STEM imaging114 is proportional in good approximation to the squared atomic number, Z2, Pd species can be reliably identified as the brightest contrasts in the image (some of them have been marked with yellow circles). While Pd single atoms are the main species present at <0.1 Pd mol%, in the cases of concentrations higher than 0.1 mol%, clusters (MCs) and nanoparticles (NPs) were found in the images at concentrations of 0.15 mol% and 0.30 mol%, respectively.

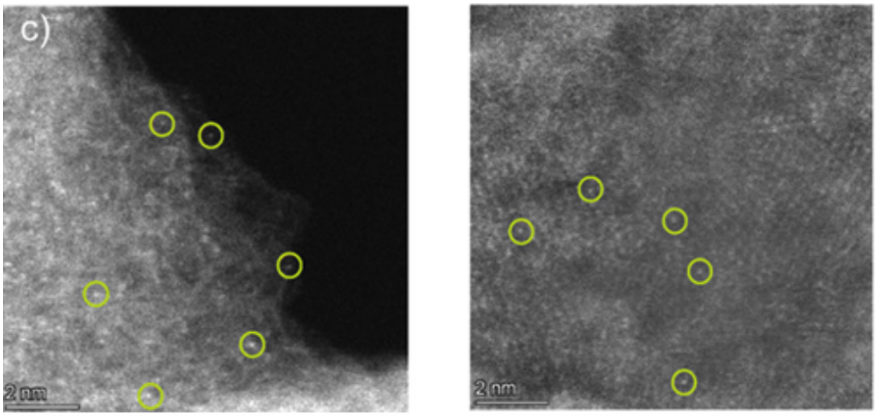

Figure 3.53. Two different AC-HAADF-STEM images of the Pd species in solution during reaction, after being trapped in active charcoal. Some Pd SACs are marked with yellow circles.

Figure 3.54 shows X-ray absorption near edge structure (XANES) and extended X-ray absorption fine structure (EXAFS) measurements of the solution, which confirm the partial reduction of Pd and the generation of very small agglomerates, with an average number of ~6 Pd-Pd bonds (Table 3.15), much lower than in Pd foil (12 Pd-Pd bonds). Moreover, the flattening in the XANES spectrum after (Figure 3.54, left) is related to the quantum size effect generated by the presence of SAs and very small agglomerated.

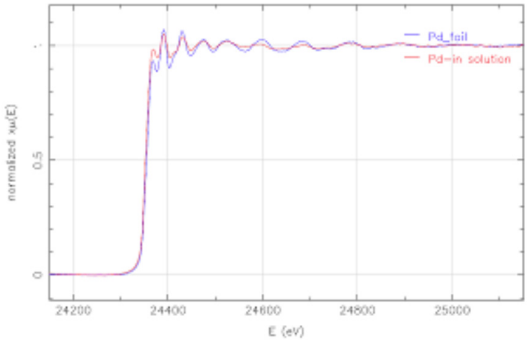

Figure 3.54. X-ray absorption near edge structure (XANES, top) and extended X-ray absorption fine structure (EXAFS, bottom) spectra of the solution (red lines), compared to Pd foil (blue lines).

Table 3.15. EXAFS results for Pd(0) foil, Pd SACs in solution and supported in the MOF.

Sample	NPd-Pd	NPd-S	σ2 (Å2)	ΔE0 (eV)	R
Pd foil	12 (fixed)	--	0.005 ±0.0004	3.03 ± 1.01	2.736 ± 0.007
Pd in solution	6.25 ± 1.62	--	0.006 ±0.002	3.56 ±1.80	2.759 ± 0.013
Pd SAC-MOF	--	3.77 ± 0.45	0.003 ±0.0008	-2.95 ±1.47	2.291 ± 0.014

Ultraviolet-visible (UV-Vis) spectrophotometric titrations with PPh_3 confirm the progressive disappearance of Pd^{II} in solution during reaction (Figure 3.55). These results strongly support that partially reduced Pd_1 species could be the catalytic active species for the direct aerobic oxidation of **2.8a** to **2.9a**.

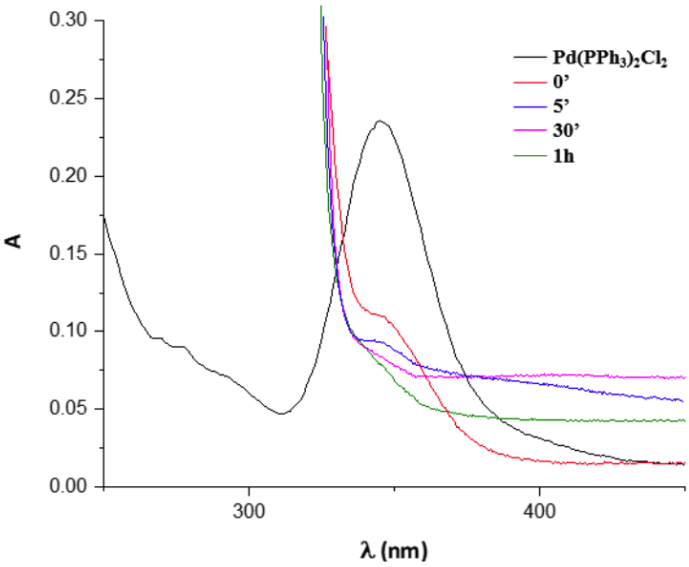

Figure 3.55. Ultraviolet-visible (UV-Vis) spectrophotometric titrations with PPh_3 during the oxidation of neat benzyl alcohol **2.8a** to benzoic acid **2.9a** at 150 ºC and 4 bars of O_2, catalyzed by $Pd(OAc)_2$. Complex $Pd(PPh_3)_2Cl_2$ is used as a reference. Complex $Pd(PPh_3)_4$ absorbs at higher energies.

The very low catalytic activity of intermediate Pd amounts (0.1-0.25 mol%) is related to the formation of sub-nanometric Pd clusters, catalytically inactive in this case.[115] To check this hypothesis, sub-nanometric Pd clusters in solution were independently prepared by two reported methods: endogenous reduction in aqueous DMF and supporting, reduction and leaching from ethylene vinyl alcohol polymer (EVOH),[116] and tested as catalyst for the oxidation of **2.8a** under the same conditions than Pd salts and complexes. The results (Table 3.16) show that these clusters are inactive as catalysts for the oxidation of **2.8a** to **2.9a**, therefore strongly supporting that Pd1 is the main catalytic active species for the oxidation reaction.

Table 3.17. Yields for the aerobic oxidation of neat benzyl alcohol **2.8a** to benzoic acid **2.9a** catalyzed by two differently prepared Pd clusters in solution (0.1 mol%), at 150 ºC and 4 bars of O_2.

Catalyst	Benzaldehyde	2.9a	Other products
Pd(**CuSr-Mecysmox and Pd^{2+}@CuSr-Mecysmox**) in DMF	40.5%	2.7%	2.2%
Pd (**CuSr-Mecysmox, Pd^{2+}@CuSr-Mecysmox and Pd^{0}@CuSr-Mecysmox**) in EVOH	5.1%	0.0%	2.1%

The combination of a mild reductant agent (benzyl alcohol) can act as a stabilizer and a support/strong reductant system for the preferential formation of Pd_1 species.[11, 117,118] In fact, the Pd clusters may unable not only to catalyze the redox reaction but also to dislodge Pd single atoms, according to the canonical Ostwald ripening mechanism. So that the formation of **2.9a** starts to be observed again at Pd concentrations where NPs are formed (>0.3 mol%). This is in good agreement with the reported catalytic activity of some metal NPs for this reaction,[119-124] as well as with the ability of metal NPs to dissociate O_2 and dislodge single atoms in solution.[125] Commercially available samples of Pd/C with different Pd loadings (1-10 wt%) and particle size (5-50 nm average diameter) were tested as catalyst for the reaction and only the sample with highest loading and biggest NP size was active for the formation of **2.9a** (Figure 3.56). These results strongly support that the oxidation of **2.8a** to **2.9a** in the neat reagent is catalyzed by soluble Pd_1 species, regardless the amount of Pd employed.[126]

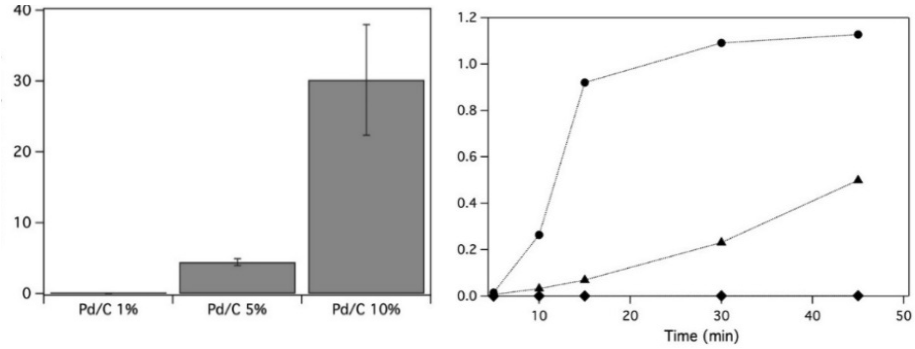

Figure 3.56. Oxidation of neat benzyl alcohol 1a to benzoic acid **2.9a** at 150 ºC and 4 bars of O_2, catalyzed by commercially available samples of Pd/C (1-10 wt% Pd loading and 5-50 nm average particle diameter). The leached amount of Pd in solution is the same for all three initial rate experiments. TOF (left) and representative kinetic profile for the formation of benzoic acid **2.9a** (right).

Fourier transform infrared under CO (FTIR–CO), XANES and EXAFS spectroscopic measurements were carried out in order to further confirm the presence of partially reduced Pd SACs within Pd^0@CuSr-Mecysmox. Figure 3.57 shows the low-temperature (-196 ºC) FTIR-CO results of **Pd^0@CuSr-Mecysmox**, where no signals above 2150 cm^{-1}, corresponding to bare Pd^{II}, can be observed, which supports the partial reduction of Pd. However, two clear broad signals centered at 2114 and 2012 cm^{-1}, attributable to unreduced $Pd^{\delta+}$ and highly dispersed, partially reduced $Pd^{\delta+}$ atoms (δ=0-1),[44] respectively, can be clearly seen, together with the increasing sharp signal of free CO (2137 cm^{-1}) at high CO doses. These peaks are accompanied by a very broad signal at 1820 cm^{-1}, which can be assigned to Pd^0 nanoparticles.

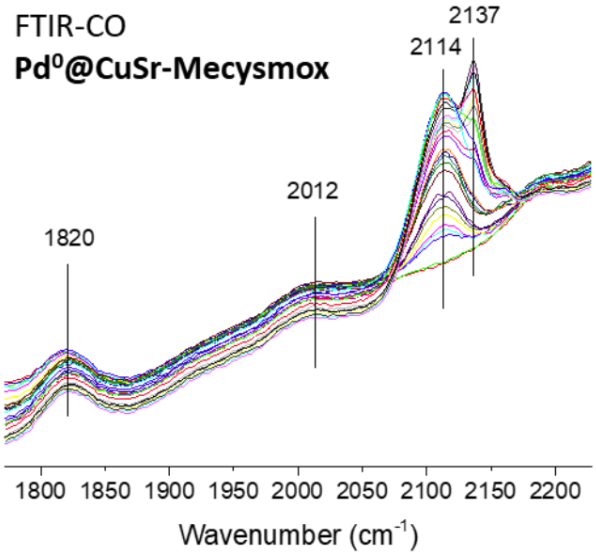

Figure 3.57. Low-temperature Fourier transform infrared spectrum, under CO (FTIR-CO), of fresh Pd^0@CuSr-Mecysmox. Peak assignments: free CO (2137 cm^{-1}), $Pd^{\delta+}$ (2114 cm^{-1}), $Pd^{\delta+}$ (2012 cm^{-1}, δ=0-1), Pd0 NPs (1820 cm^{-1}).

EXAFS and XANES spectra of **Pd^0@CuSr-Mecysmox** results (Figure 3.58), compared to Pd foil, confirm the partial reduction of Pd, as occurred for the Pd catalyst in solution (see Figure 3.54 above and Figure 3.59 for comparison and fitting). It can be observed in both cases, *i.e*. in solution and in **Pd^0@CuSr-Mecysmox,** that the first oscillations beyond the edge are flattened respect to the foil due to quantum size effects of the single atoms, also indicating a large fraction of low coordination Pd atoms, more intensified in the case of **Pd^0@CuSr-Mecysmox**. No Pd-Pd bond signals can be detected for the latter, but an average of **CuSr-Mecysmox** Pd-S bonds (Table 3.15), in agreement with the SCXRD structure. These results, combined, strongly support the single atom nature of Pd within **Pd^0@CuSr-Mecysmox**.

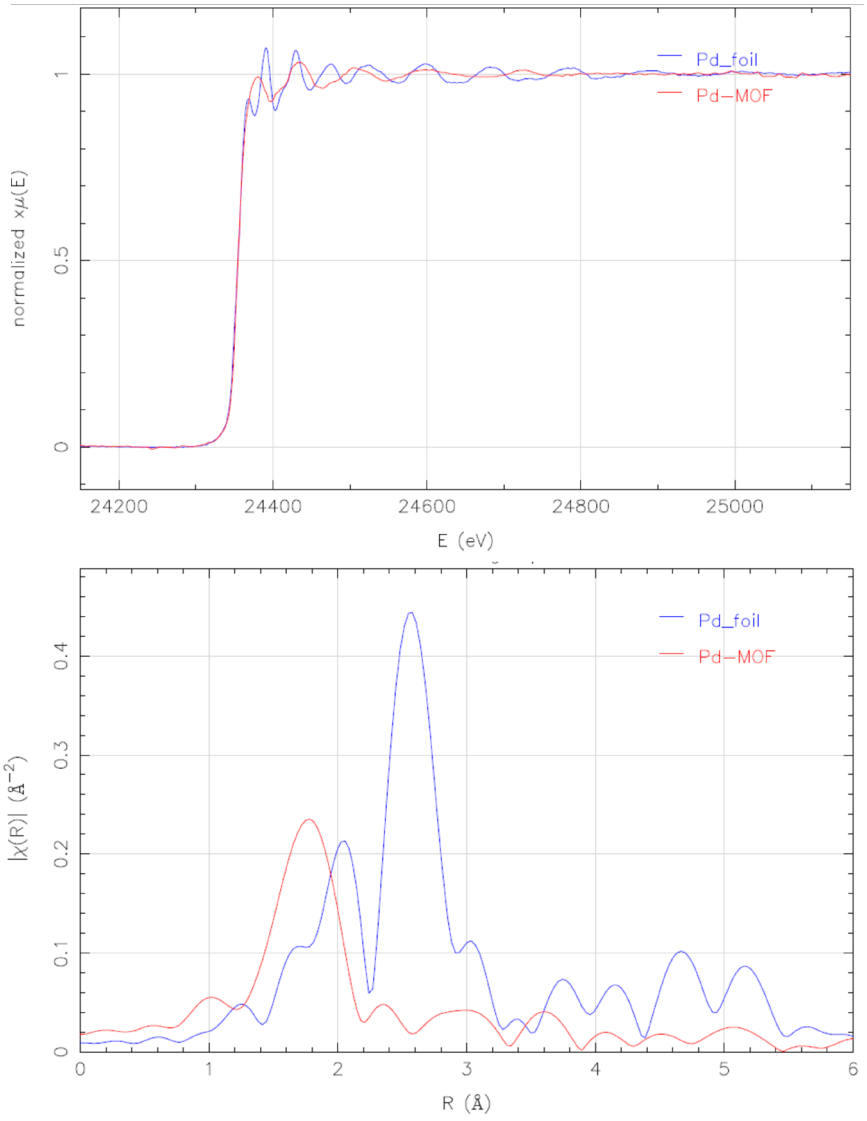

Figure 3.58. XANES (top) and EXAFS (bottom) spectra of fresh **Pd^0@CuSr-Mecys-mox** (red lines), compared to Pd foil (blue lines).

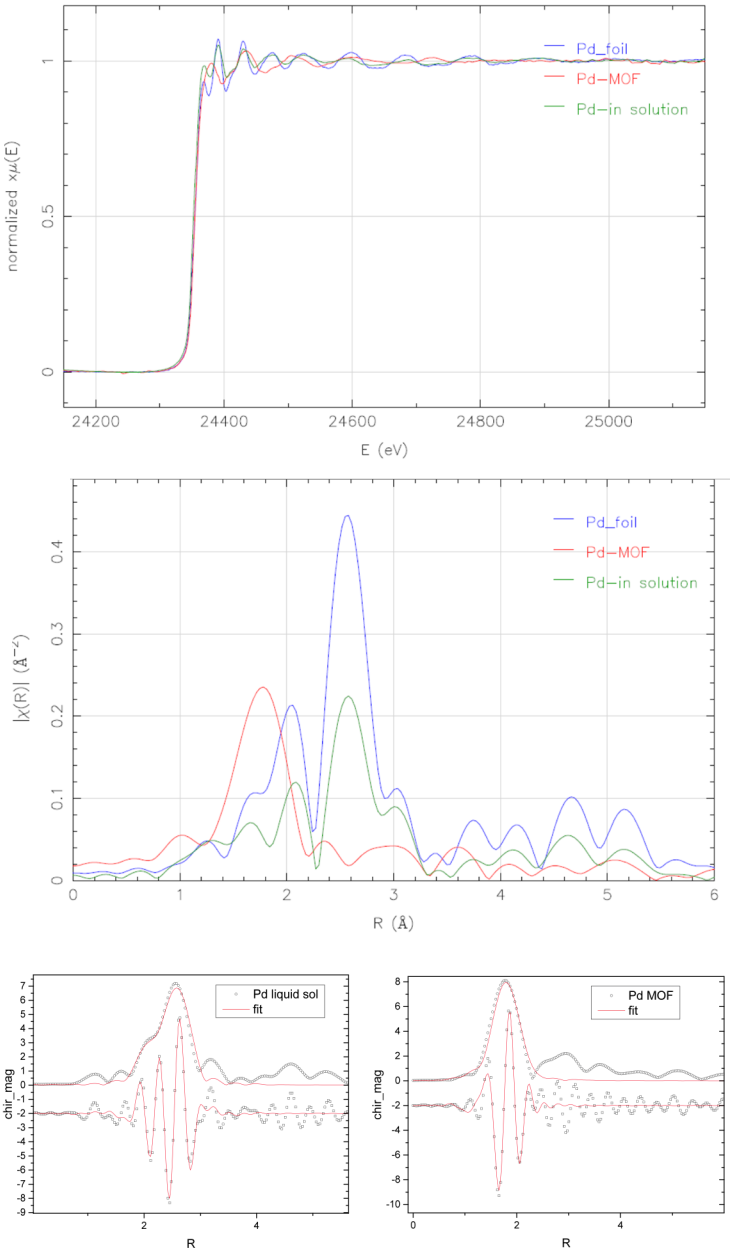

Figure 3.59. XANES (top) and EXAFS (middle) spectra of Pd in solution (green lines) and fresh **Pd^0@CuSr-Mecysmox** (red lines), compared to Pd foil (blue lines). Fitting (bottom) for both Pd catalysts.

Among **CuSr-Mecysmox**, **Pd^{2+}@CuSr-Mecysmox** and **Pd^{0}@CuSr-Mecysmox**, only the last one gave favorable catalytic results for the aerobic oxidation of benzyl alcohol **2.8a**, showing that only Pd1 SACs-MOF (**Pd^{0}@CuSr-Mecysmox**) catalyzes the oxidation with good efficiency (28% of benzaldehyde and 43% of benzoic acid **2.9a**) while, in contrast, **Pd^{2+}@CuSr-Mecysmox** barely catalyzes the reaction and **CuSr-Mecysmox** is completely inactive. The inactivity of **Pd^{2+}@CuSr-Mecysmox** can be explained by the need of using a reducing agent stronger than **2.8a** to obtain the catalytically active Pd_1 species within the MOF, which then show a catalytic activity comparable to the Pd(0) complex $Pd_2(dba)_3$ (Table 3.14). Figure 3.60 shows that **Pd^{0}@CuSr-Mecysmox** is recyclable, without minimal depletion of the catalytic activity after 3 reuses. In order to verify the integrity of the SACs in **Pd^{0}@CuSr-Mecysmox**, electronic microscopy experiments were carried out after the catalytic experiments, where no SC-XRD measurements could be carried out due to the loss of the crystallinity of the material.

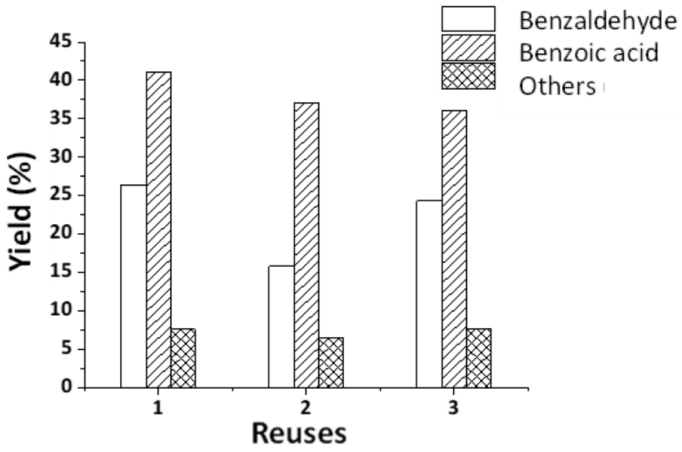

Figure 3.60. a) Reusability of Pd01 SACs- **Pd^{0}@CuSr-Mecysmox**; reaction conditions: 1.96 mmol substrate, 0.1% mol Pd^{0}_1 SACs-MOF, 4 atm O2, 150°C, 450 rpm, 15 h; GC yields.

Figures 3.61 shows representative AC-HAADF-STEM images of **Pd^0@CuSr-Mecysmox**. Note how highly dispersed Pd species are clearly observed. In particular, they show a 0.135 nm average diameter, which is in a good agreement with isolated atomic species. Only very scarcely, small agglomerations could be observed in some areas, with diameters <0.5 nm, thus confirming that the Pd atoms do not aggregate into large NCs.

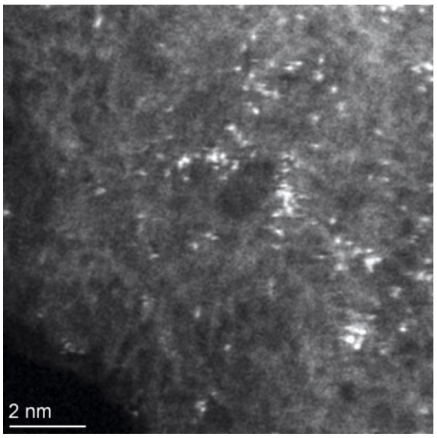

Figure 3.61. AC-HAADF-STEM image of reused **Pd^0@CuSr-Mecysmox** showing the presence of Pd SACs.

In the same vein, PXRD pattern of **Pd^0@CuSr-Mecysmox**, recovered after catalysis (Figure 3.62 top), confirm that the material remains crystalline and that no characteristic XRD peaks of Pd NPs or oxides are observed, further confirming the integrity of Pd_1 SACs. Moreover, the XPS spectra of **Pd^0@CuSr-Mecysmox** after catalytic experiments (**post-Pd^0@CuSr-Mecysmox'**) is very similar to that of the starting material (Figure 3.62 bottom), confirming that a 1:1 ratio for Pd^0 and Pd^{2+} remains after catalysis.

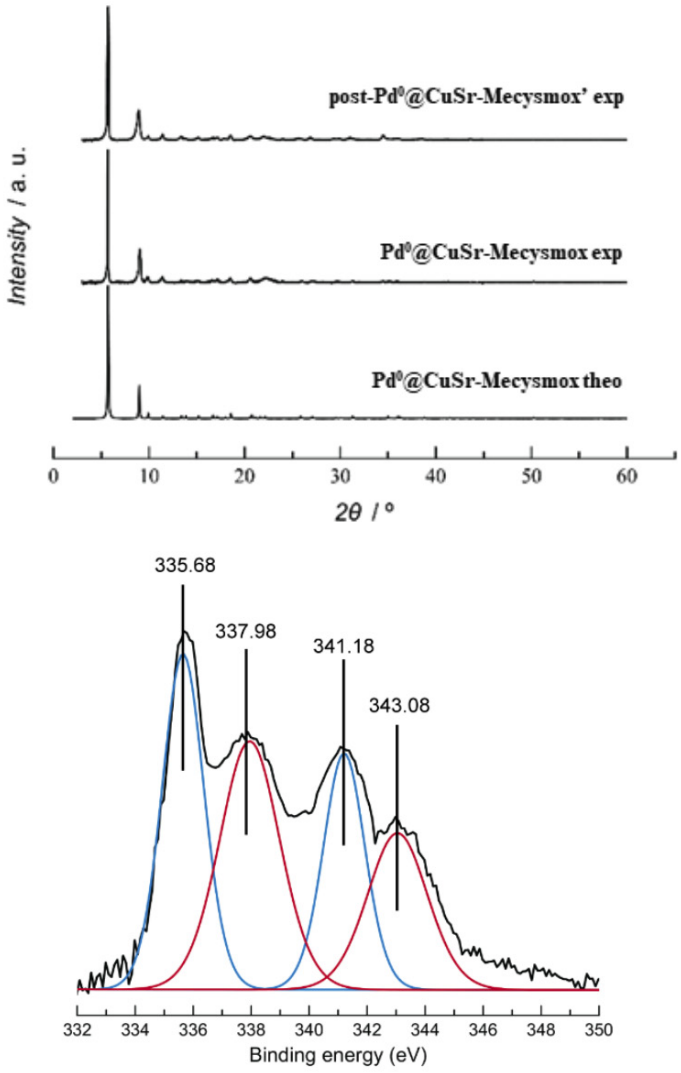

Figure 3.62. Top: Calculated (**Pd⁰@CuSr-Mecysmox** theo) and experimental (**Pd⁰@CuSr-Mecysmox** exp and **post-Pd⁰@CuSr-Mecysmox'** exp) PXRD pattern profiles of **Pd⁰@CuSr-Mecysmox** in the 2θ range 2.0–60.0°. Experimental PXRD patterns are given before (**Pd⁰@CuSr-Mecysmox** exp.) and after (**post-Pd⁰@CuSr-Mecysmox'** exp.) the catalytic experiments. Bottom: X–ray photoelectron spectroscopy (XPS) of Pd0@CuSr-Mecysmox after catalytic experiments (post- Pd0@CuSr-Mecysmox ').

In accordance with all the characterization made to the used **Pd^0@ CuSr-Mecysmox** sample, leaching tests after filtration in hot of the catalyst (Figure 3.63) reveal that no reaction occurs after filtration of the solid catalyst, neither for the benzaldehyde intermediate nor product **2.9a**, which discards the presence of catalytically active Pd species in solution from **Pd^0@CuSr-Mecysmox**.

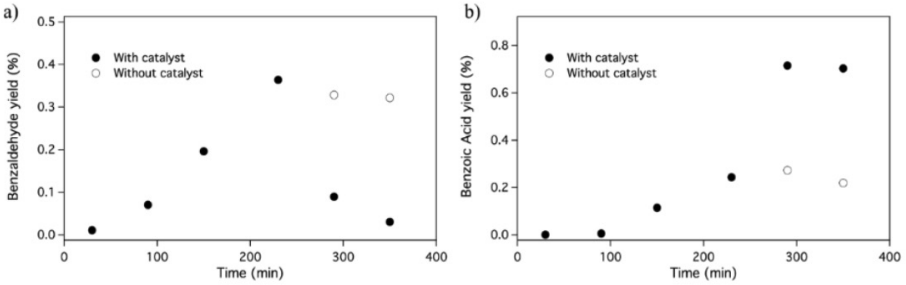

Figure 3.63. Hot filtration test (without catalyst refers to filtrated catalyst) for the aerobic oxidation of **2.8a** catalyzed by **Pd^0@CuSr-Mecysmox** under optimized reaction conditions. Reaction conditions: 1.96 mmol substrate, Pd_1 SACs-MOF 0.3% mol [Pd], 4 atm O2, 150°C, 450 rpm. GC yields.

The potential co-catalysis by the Cu atoms in the MOF was discarded on the basis of comparative experiments (Table 3.18), since $Cu(OAc)_2$ merely does not catalyze the reaction (0.6% of **2.9a** and 2.8% of benzaldehyde under optimized reaction conditions) while a Cu-MOF treated under reduction conditions ($NaBH_4$ in methanol) and not having any Pd, showed a similar catalytic activity than $Cu(OAc)_2$ (0.8% of 2.9a and 5.0% of benzaldehyde). These results discard Cu, in its own, as a catalyst of the reaction, and when $Cu(OAc)_2$ was put together with $Pd(OAc)_2$, the yield of benzoic acid **2.9a** was lower than with Pd alone. These results, together, confirm that Pd is the only metal catalyst for the reaction here. Overall, these results nicely fit the observations during

the reactions in solution, and strongly support that ligand-free Pd_1 are the catalytically active species during the one-pot oxidation of benzyl alcohols to benzoic acids under additive- and solvent-free conditions. Figure 3.64 shows the plausible reaction mechanism for Pd in solution.

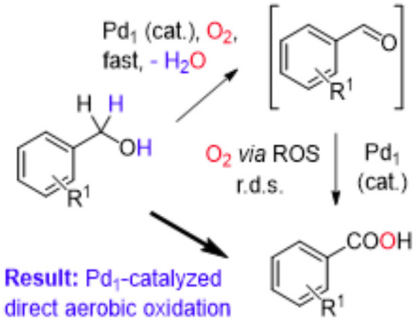

Figure 3.64. Plausible reaction mechanism for Pd in solution.

Table 3.18. Effect of Cu into the catalytic reaction.

Entry	Catalyst	**2.9**	Benzaldehyde	Other products
1	$Pd(OAc)_2$	75%	3.6%	6.9%
2	$Cu(OAc)_2$	0.6%	2.8%	0.2%
3	$Pd(OAc)_2/Cu(OAc)_2$	38.7%	33.4%	11.4%
4	**Pd^0@CuSr-Mecysmox**	41.1%	26.4%	7.6%
5	**Cu^{2+}@CuSr-Mecysmox**	0.8%	5.0%	9.9%

The fact that different Pd sources work well as catalysts in solution (Table 3.14) suggests that the dynamic system drives to a common catalytically active reduced Pd species in variable amounts, while, in contrast, the reduced Pd species are directly obtained within the MOF **Pd^0@CuSr-Mecysmox** during the reduction treatment and not during reaction, since MOF **Pd^{2+}@CuSr-Mecysmox** does not work well. The-

se results illustrate the stability conferred by the MOF structure to the confined Pd single atoms, at expenses of losing substrate availability. Nevertheless, Figure 3.65 shows the reaction scope for the Pd_1 catalyst in neat benzyl alcohols **2.8a-i**, which provides a limited number of benzoic acids **2.9a-i** in moderate yields, however, fairly comparable to most of the catalytic metal systems previously reported.[127]

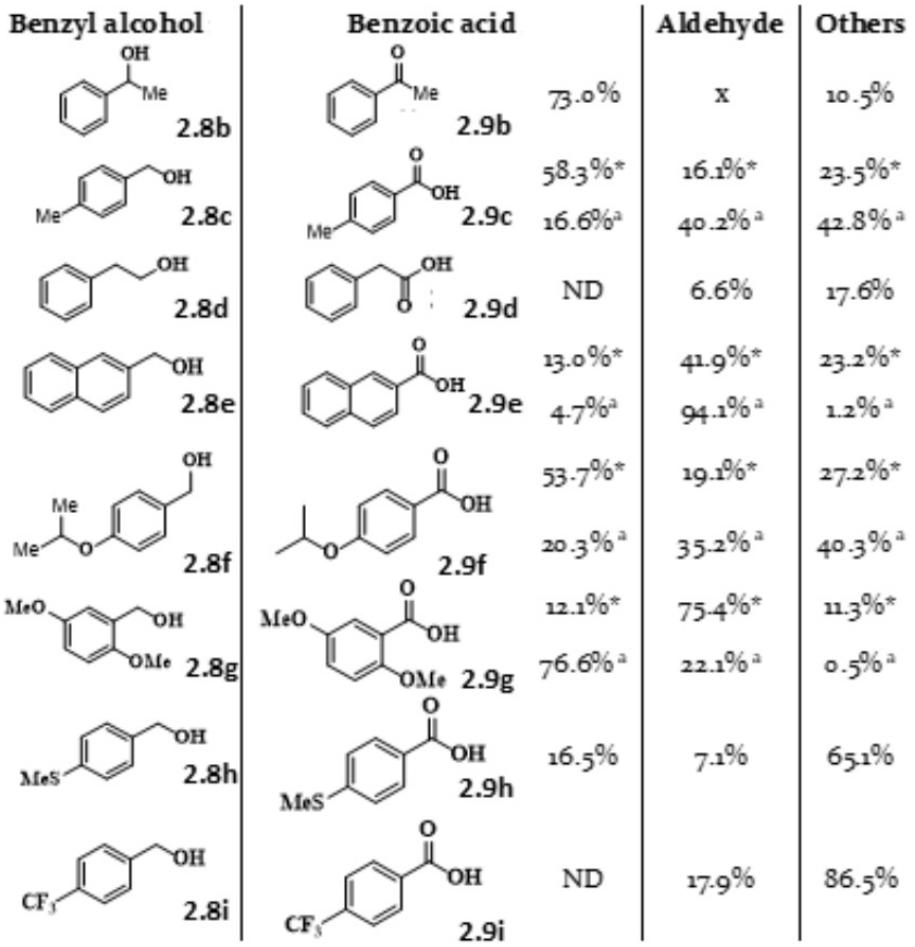

Figure 3.65. Reaction scope with $Pd(OAc)_2$ (0.3 mol%); Reaction conditions: 1.96 mmol substrate, 0.3% mol $Pd(OAc)_2$, 4 atm O2, 150°C, 450 rpm, 4 h. GC yields. * 15 h. a 0.1% mol Pd01 SACs-MOF, 24 h.

Besides, the calculated turnover frequency for product **2.9a** under optimized conditions is 7.95 min^{-1}, which is a 50-fold increases respect to any other catalytic system previously reported for this reaction (Table 3.19).

Table 3.19. Comparison of the turnover frequency (TOF) for previously reported catalysts and the catalyst reported here for the aerobic oxidation of benzyl alcohol **2.8a** and cinnamyl alcohol to the corresponding acids.

Entry	Product	Catalyst	Conditions	Additives/ Solvent	TOF (min^{-1})
1	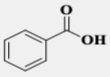	Pd(II)-biquinoline[128]	Air (40 atm) 125°C	NaOAc· $3H_2O$, $NaOH/H_2O$	$8 \cdot 10^{-2}$
2		Azobenzene[129]	O_2 (1 atm) 80°C	NaOH/1,4-dioxane	$2 \cdot 10^{-4}$
3		Au@PVP[130]	air (1 atm) 25°C	KOH/H_2O	0.12
4		Pd@ P-E15[131]	O_2 (1 atm) 90°C	K_2CO_3/ H_2O	0.21
5		$Pd(OAc)_2$	O_2 (4 atm) 150°C	-	7.95
6	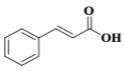	$Au@CeO_2$ [132]	O_2 (1 atm) 80°C	Na_2CO_3/ H_2O	0.82

3.6. Conclusions

In the present chapter, we have presented several examples of SNMCs@MOFs and SACs@MOFs that constitute a further step in the development of PSMs and the applicability of MOFs as chemical reactors. It is amazing how the mere fact of applying the reduction process to the metals inserted in the MOF is able to form ligand-free and well-defined SACs and SNMCs within their channels. For the three cases presented, the modification of the arrangement of the inserted metal species has endowed the MOF with new catalytic properties, not to mention the heterogeneity and thus the reusability that the MOF already possessed before undergoing reduction.

Starting from **CuNi-Me3mpba**, we were able to study Ag^0_2 SNMCs (for the case of homometallic insertion and reduction) and their cooperation with Fe^{3+} SMA (for the case of heterometallic insertion).

The ligand-free Ag^O_2 groups within the **Ag^0_2@CuNi-Me3mpba** network was characterised and used as efficient and recoverable catalysts for the Buchner ring expansion reaction. The follow-up of the production steps was carried out by SEM-EDAX, where the final metallic ratio practically matched the data provided by the elemental analysis. XPS was able to corroborate the partial reduction of the Ag^+ ions inserted in the MOF. And the perpetuation of the robustness and crystallinity after the physico-chemical fatigue of the PSM was verified by SC-DRX, PDRX and adsorption isotherms. Only with SC-XRD could a SC-SC follow-up be carried out, showing in detail the changes produced in the MOF after each step and the disposition of the Ag SNMCs and the Ag^+ ions without reducing.

The characterization techniques used assured us that the heterometallic insertion of Ag^{+} and Fe^{3+}, after the reduction process, was only capable of forming SNMC of Ag^{0}_{2}. Being SEM-EDAX (with the stoichiometric presence of Na^{+}, to compensate the charges of the reduced metals), XPS (observing clear differences between the oxidation states) and SC-XRD (allowing us to visualize the prepared/incorporated species) the techniques with which we justify the presence and stability of the SNMC species of Ag^{0}_{2} and the intrinsically unstable SMA species of Fe^{3+}.

This multimetallic metal can be obtained in quantities of several grams and **$Ag^{0}_{2}Fe^{3+}$@CuNi-Me_3mpba** is a catalyst for the TEMPO-free oxidative cross-coupling of styrenes with vinylsulfone to give vinylsulfones in yields up to >99%. We have evaluated that Ag dimers are the active catalytic species during the reaction in solution catalyzed by AgNO3 and TEMPO. Vinylsulfones can be converted, in situ, to the corresponding phenylacetylene products in high yields, up to >99%, after filtering off the **$Ag^{0}_{2}Fe^{3+}$@CuNi-Me_3mpba** catalyst, which can be reused. Thus, a final one-pot AgFe-MOF catalyzed conversion of styrenes to phenylacetylenes is achieved.

Extrapolation of the post-synthetic method of insertion from anionic mofs of oxamates and Me_3mpba to neutral MOFs based on oxamidates and amino acids, was merely synthetic. Since the insertion was carried out by immersing the MOF in $Pd(NH_3)_4Cl_2$, but the interaction instead of charge compensation was mainly due to stabilization through coordination bonds with the thiol esters, which contained the chain residues of the modified amino acid methylcysteine. The smaller pore diameter

of the **Pd^0@CuSr-Mecysmox** and its chemical environment allowed the obtaining of the SAC to undergo the reduction process after the insertion of the metal.

This homometallic insertion of the **CuSr-Mecysmox**, together with its subsequent reduction, carried out the in situ formation of Pd_1 in pure benzyl alcohols, which can catalyze aerobic oxidation to benzoic acids. This methylcysteine-based MOF with well-defined Pd_1 SACs in a homogeneously distributed and stabilized along functional channels, was prepared at gram scale.

For the characterization of the SACs of Pd_1 we had to need a greater deployment of characterization tools to be able to demonstrate its high catalytic effectiveness in its individualized form. For this case, SEM-EDAX could only confirm the loading of Pd in the MOF and its stable incorporation after the reduction process. XPS, in addition to confirming the reduction of Pd, confirmed the stability after reuse of the catalytic MOF, together with PDRX. Synchrotron SC-XRD allowed, for the first time, to clearly visualize the SACs of Pd_1 and its surroundings. The nature of Pd_1 both in solution and in MOFs is supported by microscopic and XAS techniques. The latter allow us to support the SC-XRD results revealing the main interactions between the palladium atoms and the lattice, as well as to infer a plausible formation mechanism of Pd1 SAC.

3.7. References

1. Z. Li, S. Ji, Y. Liu, X. Cao, S. Tian, Y. Chen, Z. Niu and Y. Li, Chem. Rev., 2020, 120, 623–682.

2. S. Mitchell, R. Qin, N. Zheng and J. Pérez-Ramírez, Nat. Nanotechnol., 2021, 16, 129–139.

3. N. Wang, Q. Sun and J. Yu, Adv. Mater., 2019, 31, 1803966.

4. L. Xu, W. Ma, L. Wang, C. Xu, H. Kuang and N. A. Ko tov, Chem. Soc. Rev., 2013, 42, 3114.

5. M. Grzelczak, J. Pérez-Juste, P. Mulvaney and L. M. Liz-Marzán, Chem. Soc. Rev., 2008, 37, 1783.

6. J. Pérez-Juste, I. Pastoriza-Santos, L. Liz-Marzán and P. Mulvaney, Coord. Chem. Rev., 2005, 249, 1870–1901.

7. Ozin, G. A., Metal atom matrix chemistry. Correlation of bonding with chemisorbed molecules. Acc. Chem. Res. 1977, 10 (1), 21-26.

8. Burda, C.; Chen, X.; Narayanan, R.; El-Sayed, M. A. Chem. Rev. 2005, 105 (4), 1025–1102.

9. Aiken, J. D.; Finke, R. G. J. Mol. Catal. A Chem. 1999, 145 (1-2), 1-44.

10. Yang, X. F.; Wang, A.; Qiao, B.; Li, J.; Liu, J.; Zhang, T. Acc. Chem. Res. 2013, 46 (8), 1740-1748.

11. Liu, L.; Corma, A. Chem. Rev. 2018, 118 (10), 4981–5079.

12. Schmid, G., General features of metal nanoparticles physics and chemistry, in Metal nanoclusters in catalysis and material science: the issue of size control, Corain, B., Schmid, G., Toshima, N., Editors. 2008, Elsevier.

13. Bönnemann, H.; Nagabhushana, K. S., Metal nanoclus ters: Synthesis and strategies for their size control, in Metal na noclusters in catalysis and material science: the issue of size control, Corain, B.; Schmid, G.; Toshima, N., Editors. 2008, El sevier.

14. X. Kang, S. Wang, Y. Song, S. Jin, G. Sun, H. Yu and M. Zhu, Angew. Chem. Int. Ed., 2016, 55, 3611–3614.

15. L. Liu, M. Lopez-Haro, C. W. Lopes, C. Li, P. Concep cion, L. Simonelli, J. J. Calvino and A. Corma, Nat. Mater., 2019, 18, 866–873.

16. Lu, Y.; Chen, W.Chem. Soc. Rev. 2012, 41, 3594-3623

17. M. Viciano-Chumillas, M. Mon, J. Ferrando-Soria, A. Corma, A. Leyva-Pérez, D. Armentano and E. Pardo, Acc. Chem. Res., 2020, 53, 520–531.

18. R. J. Young, M. T. Huxley, E. Pardo, N. R. Champness,

C. J. Sumby and C. J. Doonan, Chem. Sci., 2020, 11, 4031–4050.

19. Thomas, J. M.; Raja, R.; Lewis, D. W. Angew. Chem. Int. Ed. 2005, 44 (40), 6456-6482.

20. Ji, S.; Chen, Y.; Wang, X.; Zhang, Z.; Wang, D.; Li, Y., Chem. Rev. 2020, 120 (21), 11900-11955.

21. Ji, S.; Chen, Y.; Wang, X.; Zhang, Z.; Wang, D.; Li, Y., Chem. Rev. 2020, 120 (21), 11900-11955.

22. Oliver-Meseguer, J.; Cabrero-Antonino, J. R.; Domin guez, I.; Leyva-Perez, A.; Corma, A. Science 2012, 338, 1452–1455.

23. Argo, A. M.; Odzak, J. F.; Lai, F. S.; Gates, B. C. Nature 2002, 415, 623–626.

24. M. Boronat, A. Leyva-Pérez and A. Corma, Acc. Chem. Res., 2014, 47, 834–844.

25. Yang, X.-F.; Wang, A.; Qiao, B.; Li, J.; Liu, J.; Zhang, T. Acc. Chem. Res. 2013, 46, 1740–1748.

26. C. Bilanin, E. Tiburcio, J. Ferrando-Soria, D. Armen tano, A. Leyva-Pérez and E. Pardo, ChemCatChem, 2021, 13, 195–1200.

27. E. Tiburcio, R. Greco, M. Mon, J. Ballesteros-Soberanas, J. Ferrando-Soria, M. López-Haro, J. C. Hernández-Garrido, J. Oliver-Meseguer, C. Marini, M. Boronat, D. Armentano, A. Leyva-Pérez and E. Pardo, J. Am. Chem. Soc., 2021, 143, 2581–2592.

28. M. A. Rivero-Crespo, M. Mon, J. Ferrando-Soria, C. W. Lopes, M. Boronat, A. Leyva-Pérez, A. Corma, J. C.

Hernández-Garrido, M. López-Haro, J. J. Calvino, E. V. Ramos-Fernandez, D. Armentano and E. Pardo, Angew. Chem. Int. Ed., 2018, 57, 17094–17099.

29. F. R. Fortea-Pérez, M. Mon, J. Ferrando-Soria, M. Boro nat, A. Leyva-Pérez, A. Corma, J. M. Herrera, D. Osadchii, J. Gascon, D. Armentano and E. Pardo, Nat. Mater., 2017, 16, 760–766.

30. M. Mon, M. A. Rivero-Crespo, J. Ferrando-Soria, A. Vidal-Moya, M. Boronat, A. Leyva-Pérez, A. Corma, J. C. Hernández-Garrido, M. López-Haro, J. J. Calvino, G. Ragazzon, A. Credi, D. Armentano and E. Pardo, Angew. Chem. Int. Ed., 2018, 57, 6186–6191.

31. Cohen, S. M. J. Am. Chem. Soc. 2017, 139,2855–2863.

32. Dhakshinamoorthy, A.; Garcia, H. Chem. Soc. Rev. 2012, 41, 5262

33. Juan-Alcañiz, J.; Ramos-Fernandez, E. V.; Kapteijn, F.; Gascon, J. MOFs as Nano-reactors. In Metal–Organic Frameworks as Heterogeneous Catalysts; Editors: Llabres i Xamena, F. X. and Gascon. J.; Royal Society of Chemis try: Cambridge, U.K., 2013; Chapter 10, pp 310–343.

34. Dhakshinamoorthy, A.; Li, Z.; Garcia, H. Chem. Soc. Rev. 2018, 47 8134–8172.

35. Li, B.; Leng, K.; Zhang, Y.; Dynes, J. J.; Wang, J.; Hu, Y.; Ma, D.; Shi, Z.; Zhu, L.; Zhang, D.; Sun, Y.; Chrzanowski, M.; Ma, S. J. Am. Chem. Soc. 2015, 137, 4243–4248.

36. Pullen, S.; Fei, H.; Orthaber, A.; Cohen, S. M.; Ott, S. J. Am. Chem. Soc. 2013, 135, 16997–17003.

37. Wang, N.; Sun, Q.; Yu, J. Adv. Mater. 2019, 31, 1803966.

38. Li, G.; Zhao, S.; Zhang, Y.; Tang, Z. Adv. Mater. 2018, 30, 1800702.

39. Wang, S.; McGuirk, C. M.; D'Aquino, A.; Mason, J. A.; Mirkin, C. A. Adv. Mater. 2018, 30, 1800202.

40. Zhai, Y.; Pierre, D.; Si, R.; Deng, W.; Ferrin, P.; Nilekar, A. U.; Peng, G.; Herron, J. A.; Bell, D. C.; Saltsburg, H.; Mavri kakis M.; Flytzani-Stephanopoulos, M. Alkali-Stabilized Scien ce 2010, 329, 1633–1636.

41. Flytzani-Stephanopoulos, M.; Gates, B. C. Annu. Rev. Chem. Biomol. Eng. 2012, 3, 545–574.

42. Kistler, J. D.; Chotigkrai, N.; Xu, P.; Enderle, B.; Praser thdam, P.; Chen, C.-Y.; Browning, N. D.; Gates, B. C. Angew. Chemie Int. Ed. 2014, 53, 8904–8907.

43. Fortea-Pérez, F. R.; Mon, M.; Ferrando-Soria, J.; Bo ronat, M.; Leyva-Pérez, A.; Corma, A.; Herrera, J. M.; Osadchii, D.; Gascon, J.; Armentano, D.; Pardo, E. Nat. Mater. 2017, 16, 760–766.

44. Burgun, C. J. Coghlan, D. M. Huang, W. Chen, S. Hori ke, S. Kitagawa, J. F. Alvino, G. F. Metha, C. J. Sumby and C. J. Doonan, Angew. Chem. Int. Ed., 2017, 56, 8412–8416.

45. Y. Inokuma, S. Yoshioka, J. Ariyoshi, T. Arai, Y. Hitora, K. Takada, S. Matsunaga, K. Rissanen and M. Fujita, Nature, 2013, 495, 461–466.

46. M. Mon, R. Bruno, J. Ferrando-Soria, L. Bartella, L. Di Donna, M. Talia, R. Lappano, M. Maggiolini, D. Armentano and E. Pardo, Mater. Horizons, 2018, 5, 683–690.

47. M. Mon, R. Bruno, J. Ferrando-Soria, L. Bartella, L. Di Donna, M. Talia, R. Lappano, M. Maggiolini, D. Armentano and E. Pardo, Mater. Horizons, 2018, 5, 683–690.

48. Flytzani-Stephanopoulos, M.; Gates, B. C. Annu. Rev. Chem. Biomol. Eng. 2012, 3, 545–574.

49. Kistler, J. D.; Chotigkrai, N.; Xu, P.; Enderle, B.; Praser thdam, P.; Chen, C.-Y.; Browning, N. D.; Gates, B. C. Angew. Chemie Int. Ed. 2014, 53, 8904–8907.

50. Mon, M.; Bruno, R.; Ferrando-Soria, J.; Bartella, L.; Di Donna, L.; Talia, M.; Lappano, R.; Maggiolini, M.; Armenta no, D.; Pardo, E. Mater. Horizons 2018, 5, 683–690

51. L. Liu, U. D&az, R. Arenal, G. Agostini, P. Concepciln, A. Corma, Nat. Mater. 2016, 16, 132–138.

52. M. S. Nashner, A. I. Frenkel, D. L. Adler, J. R. Shapley, R. G. Nuzzo, J. Am. Chem. Soc. 1997, 119, 7760–7771.

53. CCDC 1841392 and 1841391 (Pt2+@CuNi-Me3mpba and Pt2+Pt+@CuNi-Me3mpba) contain the supplementary crystallographic data for this paper. These data can be obtained free of charge from The Cambridge Crystallographic Data Cent re.

54. Miguel A. Rivero-Crespo, Marta Mon, Jesús Ferran do-Soria, Christian W. Lopes, Mercedes Boronat, Anto nio Leyva-Pérez, Avelino Corma, Juan C. Hernández-Garrido, Miguel López-Haro, Jose J. Calvino, Enrique V. Ramos-Fernán dez, Donatella Armentano, and Emilio Pardo. Angew. Chem. Int. Ed. 2018, 57, 17094 –17099.

55. Cristina Bilanin, Estefanía Tiburcio, Jesús Ferrando-So ria, Donatella Armentano, Antonio Leyva-Pérez, and Emilio

Pardo. ChemCatChem 2020, 12, 1–7.

56. Thais Grancha, Jesús Ferrando-Soria, Hong-Cai Zhou, Jorge Gasean, Beatriz Seoane, Jorge Pasán, Osear Fabelo, Mi guel Julve, and Emilio Pardo. Angew. Chem. lnt. Ed. 2015, 54, 6521 – 6525.

57. María Tejeda-Serrano, Marta Mon, Bethany Ross, Francisco Gonell, Jesús Ferrando- Soria, Avelino Cor ma, Antonio Leyva-Pérez, Donatella Armentano, and Emilio Pardo. J. Am. Chem. Soc. 2018, 140, 28, 8827–8832.

58. L. He and S. C. Tjong, RSC Adv., 2017, 7, 2058–2065.

A. M. Ferraria, A. P. Carapeto and A. M. Botelho do Rego, Vacuum, 2012, 86, 1988–1991.

59. Lin, L.; Husek, J.; Biswas, S.; Baumler, S. M.; Adel, T.; Ng, K. C.; Baker, L. R.; Allen, H. C. J. Am. Chem. Soc. 2019, 141 (34), 13525–13535. https://doi.org/10.1021/jacs.9b05231.

60. Saikia, K.; Dutta, D. K. J. Mol. Catal. A Chem. 2015, 408, 20–25.

61. B. Ni and X. Wang, Chem. Sci., 2016, 7, 3978–3991.

62. Kalaj, M.; Cohen, S. M. ACS Cent. Sci. 2020, 6 (7), 1046–1057. https://doi.org/10.1021/acscentsci.0c00690.

63. Grancha, T.; Ferrando-Soria, J.; Zhou, H.-C.; Gas con, J.; Seoane, B.; Pasán, J.; Fabelo, O.; Julve, M.; Par do, E. Angew. Chemie Int. Ed. 2015, 54 (22), 6521–6525. https://doi.org/10.1002/anie.201501691.

64. Young, R. J.; Huxley, M. T.; Pardo, E.; Champness, N.

R.; Sumby, C. J.; Doonan, C. J. Chem. Sci. 2020, 11 (16), 4031–4050. https://doi.org/10.1039/D0SC00485E.

65. Tejeda-Serrano, M.; Mon, M.; Ross, B.; Gonell, F.; Fe rrando-Soria, J.; Corma, A.; Leyva-Pérez, A.; Armentano, D.; Pardo, E. J. Am. Chem. Soc. 2018, 140 (28), 8827–8832. https://doi.org/10.1021/jacs.8b04669.

66. Tyo, E. C.; Vajda, S. Nat. Nanotechnol. 2015, 10 (7), 577–588. https://doi.org/10.1038/nnano.2015.140.

67. Buceta, D.; Busto, N.; Barone, G.; Leal, J. M.; Domín guez, F.; Giovanetti, L. J.; Requejo, F. G.; García, B.; López-Quintela, M. A. Angew. Chemie Int. Ed. 2015, 54 (26), 7612–7616. https://doi.org/10.1002/anie.201502917.

68. Malola, S.; Häkkinen, H. Nat. Commun. 2021, 12 (1), 2197. https://doi.org/10.1038/s41467-021-22545-x.

69. Zaker, Y.; Ashenfelter, B. A.; Bhattarai, B.; Diemler, N. A.; Brewer, T. R.; Bigioni, T. P. Small 2021, 17 (27), 2002238. https://doi.org/10.1002/smll.202002238.

70. Chenghui Zhang, Huaizhong Shi, Libo Sun, Yan Yan, Bolun Wang, Zhiqiang Liang, Li Wang, and Jiyang Li. Cryst. Growth Des. 2018, 18, 12, 7683–7689.

71. Blay, G.; Fernández, I.; Giménez, T. Chem. 2001, 919, 2102–2103.

72. Adam, R.; Mon, M.; Greco, R.; Kalinke, L. H. G.; Vi dal-Moya, A.; Fernandez, A.; Winpenny, R. E. P.; Do ménech-Carbó, A.; Leyva-Pérez, A.; Armentano, D.; Pardo, E.; Ferrando-Soria, J. J. Am. Chem. Soc. 2019, 141, 10350–10360.

73. Mon, M.; Adam, R.; Ferrando–Soria, J.; Corma, A.; Armentano, D.; Pardo, E.; Leyva–Pérez, A. ACS Catal. 2018, 8, 10401–10406.

74. Rivero-Crespo, M. A.; Mon, M.; Ferrando-Soria, J.; Lopes, C. W.; Boronat, M.; Leyva-Pérez, A.; Corma, A.; Hernández-Garrido, J. C.; López-Haro, M.; Calvino, J. J.; Ramos-Fernandez, E. V.; Armentano, D.; Pardo, E. Angew. Chem. Int. Ed. 2018, 57, 17094–17099.

75. Mon, M.; Rivero-Crespo, M. A.; Ferrando-Soria, J.; Vidal-Moya, A.; Boronat, M.; Leyva-Pérez, A.; Corma, A.; Hernández-Garrido, J. C.; López-Haro, M.; Calvino, J. J.; Ragazzon, G.; Credi, A.; Armentano, D.; Pardo, E. Synthesis of Densely Packaged, Angew. Chem. Int. Ed. 2018, 57 (21), 6186–6191. https://doi.org/10.1002/anie.201801957.

76. Tejeda-Serrano, M.; Mon, M.; Ross, B.; Gonell, F.; Fe rrando-Soria, J.; Corma, A.; Leyva-Pérez, A.; Armentano, D.; Pardo, E. J. Am. Chem. Soc. 2018, 140 (28), 8827–8832. https://doi.org/10.1021/jacs.8b04669.

77. Mon, M.; Bruno, R.; Tiburcio, E.; Viciano-Chumillas, M.; Kalinke, L. H. G.; Ferrando-Soria, J.; Armentano, D.; Pardo, E. J. Am. Chem. Soc. 2019, 141, 13601–13609.

78. Mon, M.; Qu, X.; Ferrando-Soria, J.; Pellicer-Carreño, I.; Sepúlveda-Escribano, A.; Ramos-Fernandez, E. V.; Jansen, J. C.; Armentano, D.; Pardo, E. J. Mater. Chem. A 2017, 5, 20120–20125

79. Mon, M.; Lloret, F.; Ferrando-Soria, J.; Martí-Gastaldo, C.; Armentano, D.; Pardo, E. Angew. Chem. Int. Ed. 2016, 55, 11167–11172.

80. Mon, M.; Ferrando-Soria, J.; Grancha, T.; Fortea-Pé rez, F. R.; Gascon, J.; Leyva-Pérez, A.; Armentano, D.; Pardo, E. J. Am. Chem. Soc. 2016, 138, 7864–7867

81. M. M. Díaz-Requejo and P. J. Pérez, J. Organomet. Chem., 2005, 690, 5441–5450.

82. C. J. Lovely, R. G. Browning, V. Badarinarayana and H. V. R. Dias, Tetrahedron Lett., 2005, 46, 2453–2455.

83. Y. Deng, C. Jing, P. Y. Zavalij and M. P. Doyle, Org. Lett., 2015, 17, 4312–4315.

84. S. Radhika, C. M. A. Abdulla, T. Aneeja and G. Anilku mar, New J. Chem., 2021, 45, 15718–15738.

85. F. Garnes-Portolés, R. Greco, J. Oliver-Meseguer, J. Castellanos-Soriano, M. Consuelo Jiménez, M. López-Haro, J. C. Hernández-Garrido, M. Boronat, R. Pérez-Ruiz and A. Leyva-Pérez, Nat. Catal., 2021, 4, 293–303.

86. J. Oliver-Meseguer, M. Boronat, A. Vidal-Moya, P. Con cepción, M. Á. Rivero-Crespo, A. Leyva-Pérez and A. Corma, J. Am. Chem. Soc., 2018, 140, 3215–3218.

87. Li, X.; Xu, Y.; Wu, W.; Jiang, C.; Qi, C.; Jiang, H. Chem. Eur. J. 2014, 20 (26), 7911–7915. https://doi.org/10.1002/chem.201402815.

88. Bao, W.-H.; Ying, W.-W.; Xu, X.-D.; Zhou, G.-D.; Meng, X.-X.; Wei, W.-T.; Liu, Y.-Y.; Li, Q. Tetrahedron Lett. 2019, 60 (1), 55–58. https://doi.org/10.1016/j.tetlet.2018.11.059.

89. Ueda, M.; Kamikawa, K.; Fukuyama, T.; Wang, Y.; Wu, Y.; Ryu, I. Angew. Chemie Int. Ed. 2021, 60 (7), 3545–3550. https://doi.org/10.1002/anie.202011992.

90. Chen, Z.; Song, J.; Peng, X.; Xi, S.; Liu, J.; Zhou, W.; Li, R.; Ge, R.; Liu, C.; Xu, H.; et al. Adv. Mater. 2021, 33 (34), 2101382. https://doi.org/10.1002/adma.202101382.

91. Gascon, J.; Corma, A.; Kapteijn, F.; Llabrés i Xamena, F. X. ACS Catal. 2014, 4, 361–378.

92. Dhakshinamoorthy, A.; Li, Z.; Garcia, H. Chem. Soc. Rev. 2018, 47, 8134–8172.

93. Yang, D.; Gates, B. C. ACS Catal. 2019, 9, 1779–1798.

94. Gui, Q.; Han, K.; Liu, Z.; Su, Z.; He, X.; Jiang, H.; Tian, B.; Li, Y. Org. Biomol. Chem. 2018, 16 (32), 5748–5751. https://doi.org/10.1039/C8OB01502C.

95. Deng, X.; Qin, B.; Liu, R.; Qin, X.; Dai, W.; Wu, G.; Guan, N.; Ma, D.; Li, L. J. Am. Chem. Soc. 2021, 143 (49), 20898–20906. https://doi.org/10.1021/jacs.1c09535.

96. Garnes-Portolés, F.; Greco, R.; Oliver-Meseguer, J.; Cas tellanos-Soriano, J.; Consuelo Jiménez, M.; López-Haro, M.; Hernández-Garrido, J. C.; Boronat, M.; Pérez-Ruiz, R.; Ley va-Pérez, A. Nat. Catal. 2021, 4 (4), 293–303. https://doi.org/10.1038/s41929-021-00592-3.

97. Cum, G.; Gallo, R.; Ipsale, S.; Spadaro, A. J. Chem. Soc. Chem. Commun. 1985, No. 22, 1571. https://doi.org/10.1039/c39850001571.

98. Abidi, S. L. J. Org. Chem. 1986, 51 (14), 2687–2694. https://doi.org/10.1021/jo00364a013.

99. Akiyama, S.; Nakatsuji, S.; Nomura, K.; Matsuda, K.; Nakashima, K. J. Chem. Soc., Chem. Commun. 1991, No. 14, 948–950. https://doi.org/10.1039/C39910000948.

100.Gao, R.; Wang, J.; Huang, Z.-F.; Zhang, R.; Wang, W.; Pan, L.; Zhang, J.; Zhu, W.; Zhang, X.; Shi, C.; et al. Nat. Energy 2021, 6 (6), 614–623. https://doi.org/10.1038/s41560-021-00826-5.

101.Dai, W.; Petersen, J. L.; Wang, K. K. Org. Lett. 2004, 6 (23), 4355–4357. https://doi.org/10.1021/ol0481434.

102.Ahmed, J.; Swain, A. K.; Das, A.; Govindarajan, R.; Bhunia, M.; Mandal, S. K. A K. Chem. Commun. 2019, 55 (92), 13860–13863. https://doi.org/10.1039/C9CC07833A.

103.J. R. Reimers, M. J. Ford, A. Halder, J. Ulstrup, N. S. Hush, Proc. Natl. Acad. Sci. USA 2016, 113, E1424–E1433.

104.Juárez, R.; Concepción, P.; Corma, A.; Fornés, V.; García, H. Angew. Chem. Int. Ed. 2010, 49, 1286–1290.

105.Schultz, M. J.; Adler, R. S.; Zierkiewicz, W.; Privalov, T.; Sigman, M. S. J. Am. Chem. Soc. 2005, 127, 8499–8507.

106.Steinhoff, B. A.; Guzei, I. A.; Stahl, S. S. J. Am. Chem. Soc. 2004, 126, 11268–11278.

107.Polynski, M. V.; Ananikov, V. P. ACS Catal. 2019, 9, 3991–4005.

108.Geiger, Y.; Achard, T.; Maisse-François, A.; Bellemin-La ponnaz, S. Nat. Catal. 2020, 3, 422–426.

109.Savara, A.; Chan-Thaw, C. E.; Rossetti, I.; Villa, A.; Prati, L. ChemCatChem 2014, 6, 3464–3473.

110.Karimi, B.; Khorasani, M.; Vali, H.; Vargas, C.; Luque, R. ACS Catal. 2015, 5, 4189–4200

111.Buffin, B. P.; Belitz, N. L.; Verbeke, S. L.. J. Mol. Catal. A Chem. 2008, 284, 149–154.

112.Ananikov, V. P.; Beletskaya, I. P. Organometallics 2012, 31, 1595–1604.

113.Eremin, D. B.; Ananikov, V. P.. Coord. Chem. Rev. 2017, 346, 2–19

114.R. F. Egerton, P. Li and M. Malac, Micron, 2004, 35, 399–409.

115.Leyva-Pérez, A.; Oliver-Meseguer, J.; Rubio-Marqués, P.; Corma, A. Angew. Chem. Int. Ed. 2013, 52, 11554–11559.

116.Fernández, E.; Rivero-Crespo, M. A.; Domínguez, I.; Ru bio-Marqués, P.; Oliver-Meseguer, J.; Liu, L.; Cabrero-Antoni no, M.; Gavara, R.; Hernández-Garrido, J. C.; Boronat, M.; Ley va-Pérez, A.; Corma, A. J. Am. Chem. Soc. 2019, 141, 1928–1940.

117.Yang, X.-F.; Wang, A.; Qiao, B.; Li, J.; Liu, J.; Zhang, T. Acc. Chem. Res. 2013, 46, 1740–1748.

118.Flytzani-Stephanopoulos, M.; Gates, B. C. Annu. Rev. Chem. Biomol. Eng. 2012, 3, 545–574.

119.Abad, A.; Concepción, P.; Corma, A.; García, H. A Angew. Chem. Int. Ed. 2005, 44, 4066–4069.

120.Tsunoyama, H.; Sakurai, H.; Negishi, Y.; Tsukuda, T. J. Am. Chem. Soc. 2005, 127, 9374–9375.

121.Abad, A.; Corma, A.; García, H. Chem. Eur. J. 2008, 14, 212–222

122.García-Suárez, E. J.; Tristany, M.; García, A. B.; Collière, V.; Philippot, K. Microporous Mesoporous Mater. 2012, 153, 155–162

123.Savara, A.; Chan-Thaw, C. E.; Rossetti, I.; Villa, A.; Prati, L. ChemCatChem 2014, 6, 3464–3473.

124.Karimi, B.; Khorasani, M.; Vali, H.; Vargas, C.; Luque, R. ACS Catal. 2015, 5, 4189–4200.

125.Boronat, M.; Leyva-Pérez, A.; Corma, A. Acc. Chem. Res. 2014, 47, 834–844.

126.Kaiser, S. K.; Fako, E.; Manzocchi, G.; Krumeich, F.; Hauert, R.; Clark, A. H.; Safonova, O. V.; López, N.; Pérez-Ra mírez, J. Nat. Catal. 2020, 3, 376–385.

127.Chen, Y.; Guo, Z.; Chen, T.; Yang, Y. J. Catal. 2010, 275, 11–24.

128.Buffin, B. P.; Belitz, N. L.; Verbeke, S. L.. J. Mol. Catal. A Chem. 2008, 284, 149–154.

129.Liu, C.; Fang, Z.; Yang, Z.; Li, Q.; Guo, S.; Guo, K. RSC Adv. 2015, 5, 79699–79702.

130.Tsunoyama, H.; Sakurai, H.; Negishi, Y.; Tsukuda, T. J. Am. Chem. Soc. 2005, 127, 9374–9375.

131.Karimi, B.; Khorasani, M.; Vali, H.; Vargas, C.; Luque, R. ACS Catal. 2015, 5, 4189–4200.

132.Abad, A.; Concepción, P.; Corma, A.; García, H. A Angew. Chem. Int. Ed. 2005, 44, 4066–4069.

CHAPTER

4

POST-SYNTHETIC FORMATION OF SCCs

4.1. Introduction

4.1.1. MOFs vs SCCs

When guests (substrates) are confined in an isolated cavity, they experience unique environments that are hardly accessible in a bulk solution. This is beautifully exemplified in the active centres of enzymes in living beings, which have served as seminal inspiration for chemist to develop the field of Supramolecular Chemistry.[1] In this context, during the last decades, molecular self-assembly have produced an extraordinary number of elegant examples, demonstrating the influence of the confined space on the physico-chemical properties of the substrates.[2,3] Among these systems, metal-organic frameworks (MOFs) and supramolecular coordination compounds (SCCs) are of particular interest. MOFs are ordered-pore crystalline metal-organic polymers, while SCCs possess a discrete (or finite) internal void. These finite structures present shapes fall into such geometrical configurations as polygons, polyhedra, prisms/antiprisms, tubes, helicates, bowl-shaped, organic-pillared, porphyrin-prism, and so on.[4,5] These metal-organic structures have clear synergies between them. However, the two fields have been rarely connected in a synergistic manner.

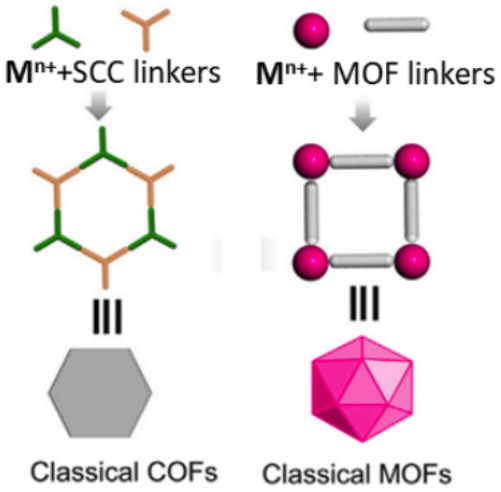

Figure 4.1. Illustrative scheme of the differences between the metal-organic cages and the metal organic framework after the interaction of organic ligands with metal ions or clusters. Adapted from ref. 6.

From a compositional point of view, SCCs have the same constituent parts of MOFs, but they are assembled into distinct individual complexes, instead of extended structures. In MOFs, reactant metal cations are usually uncapped, leaving the coordination sites free for ligand coordination, and ligands are chosen to facilitate lattice propagation. Due to the wide variation of ligand types within MOFs, neutral, cationic and anionic MOFs can be easily prepared depending on the specific desired target. SCCs can host impressive cavities with sizes approaching those of MOF cavities. Like MOFs, SCCs can be constructed from a wide variety of ligands and metals from across the Periodic Table. In particular, Fe^{II}, Pd^{II}, Pt^{II}, Zn^{II}, Co^{II}, and Ga^{III} have been widely used[7-10]. As far as organic ligands are concerned, pyridine is unrivalled in terms of ubiquity. It is frequently combined as part of bidentate and tridentate coordination motifs, including bipyridyls, pyridyl imines, pyridyl tria-

zoles and pyridyl pyrazoles.[11] Catechol, phosphines and thioethers (especially in weak/reversible coordination) should also be mentioned[12]. Due to neutral nature of most N-based ligands metal ions, most SCCs are cationic. However, when the ligand is anionic, SCCs, with overall negative charge, can also be constructed. Interestingly, in both systems, the cavities force the guests to adopt a more compact conformation and/or temporarily adhere to the metal-organic structure, increase the intermolecular collision rate and increase the local catalyst concentration, which is ideal for the enhancement of metal catalytic properties.[13-15]
At this respect, remarkable advances have been obtained in supramolecular catalysis with SCCs.[16] However, it is considered that its full potential has not been reached. The self-assembly of SCCs takes place in homogeneous chemistry in solution. Therefore, SCCs are formed with isolated fully-coordinated metal atoms as structural nodes, which hampers any activation of external reagents on the metal sites without destroying the assembly. Thus, limiting their use in metal-based supramolecular catalysis. In fact, there are few reported metal-based reactions with the approximately spherical polyhedra of general formula Pd_nL_2n in catalytic quantities, and in the existing examples the integrity of the systems is difficult to be secured. Therefore, the metallocatalysis of metal atoms constituting SCCs could be exploited by developing SCCs with non-fully coordinated metals.

MOFs have proven to be versatile platforms leading to a wide range of applications due to their rich host-guest chemistry[17], which can be tailored by fine control of the size, shape and functionality of the MOF channels, and the possibility to use single-crystal X-ray diffraction (SCXRD) as basic characterization tool, which offers the possibility to test the success of synthetic methodologies and to follow/understand what is actually happening within MOFs channels. SCCs are also able

to be characterized by SCXRD too[18]. However, in general, the techniques used for MOFs are based on techniques more focused on solid state materials (e. g. powder X-ray diffraction, neutron diffraction and adsorption) and for SCCs, techniques for small molecules in solution can be applied (e. g. NMR, UV-vis, MS without fragmentation and ESI). In contrast to SCCs, MOFs are widely regarded as stable materials in the solid state. The stability of MOFs has allowed them to be obtained on an industrial scale; in contrast, SCCs are often difficult to prepare and distribute as bulk materials due to aggregation problems. However, despite the improvements achieved during the last years in terms of the structural robustness of MOFs, they still have some limitations. For example, one of the most studied MOFs, HKUST-1, is known to be stable with respect to the presence of ethanol, but is not stable in water. In fact, studies have shown that some MOFs undergo reversible dissolution and re-growth in some solvents. Unlike MOFs, SCCs are predominantly self-assembled and studied in solution. Thus, despite MOFs may be more suitable for solid-state materials, SCCs are very promising as soft matter/materials[19]. Post-assembly modification of SCCs is a particularly active area.[20] For MOFs, the modification of exposed functional groups not involved in the structure is also on the rise, as well as the insertion of metal ions or clusters for their catalytic applications.

So far, MOFs have developed considerably in fields such as the adsorption and separation of guest gases or small molecules, and catalysis. Also, great advances have been done related to molecular recognition and/or encapsulation of complex molecular systems. But, there is still much work to be done in relation to the use of MOFs as chemical nanoreactors. In fact, only very few examples have been reported aiming at

the MOF-driven formation of supramolecular complexes within MOFs channels, which lack of a proper structural characterization and just models could be delivered.[21,22]

4.1.2. MOF assisted preparation of SCCs

Inspired by the high efficiency and specificity of enzymes in living systems, the development of artificial catalysts as mimetic enzymes has emerged as an active field. The inspiration eventually slanted towards the abiotic catalytic process merging environment catalysis with traditional homogeneous organotransition metal catalyst.

Recent advances in supramolecular chemistry have shown that coordination cages are a good selection as non-covalent coordination bonds buildings. Their confined cavity, resembles the binding pocket of an enzyme, and their facile tunability (of functional groups, complexes dimensions, metal ions with specific size, coordination geometries and oxidation state, etc.) are essential for substrate isolation (from external species like solvent molecules), substrate recognition[23,24] (analyte discrimination and sensing), control of molecular conformation (conformational manipulation), precise aggregation of molecules or functional groups (preorganization), transition-state stabilization, kinetic trapping of metastable species (to prevents further reaction or deformation), and product release.

Supramolecular coordination cages are good candidates for supramolecular nanoreactors due to, providing specific cavities to bind substrates, stabilize the transition state, and avoid product inhibition through collective noncovalent interactions to accomplish specific and selective

catalysis.

As supramolecular nanoreactors, coordination cages have presented some characteristics in catalysis, such as accelerating the reaction rate, enhancing reactivity and selectivity, changing the reaction mechanism, and stabilizing otherwise unstable intermediates. Also both chiral and achiral supramolecular coordination cages can be employed for asymmetric catalysis.

The major problem with SCCs is that their discrete structure usually implies that the catalytically active positions are part of the construction of their supramolecular architecture, so they are fully coordinated. Therefore, compared to MOFs, SCCs have fewer molecules in their chemical environment with which to stabilize themselves during the dedication of the metal node to their particular catalytic behaviour, so that its catalytic activity is mitigated.

As mentioned above (chapters 2 and 3), Metal-Organic Frameworks (MOFs) show features capable of acting as chemical nanoreactors for the in-situ synthesis and stabilization of functional species (normally difficult to access).

Therefore, one promising approach consists of using the confined space offered by a MOF reactor to synthesise, in situ, supramolecular coordination complexes (SCCs), by means of PSMs. In so doing, both structures fusion so that the SCCs benefit from the stability provided by the MOF chemical environment and the confinement provided by the MOF pores and the MOF increases its confinement, selectivity and catalytic activity with the incorporation of the SCCs in its interior, by decreasing

the MOF pore and inserting the metals and functional groups of the SCC ligand.

In our group, recently, a research line has been developed to explore the use of post-synthetic methodologies for the in-situ construction of SCCs within MOFs channels. As a relevant example for this chapter, we will discuss a precedent reported devoted to this end. It concerns three mechanically-bonded SCCs of Pd(II) within the unique confined space of a previously described MOF (**Ni^{2+}@CuNi-Me_3mpba**, Chapter 1) channels. The resulting hosted SCCs (SCCs@MOF), had never been obtained before, and a post-assembly metalation from one to give a heterobimetallic PdII-AuIII supramolecular cage. These SCCs@MOF consist on a novel Pd_8 square metal-organic polygon, a discrete Pd_{16} supramolecular cage, and a heterobimetallic Au^{III}-Pd^{II} cage. All these robust SCCs catalyse, heterogeneously, the homocoupling of boronic acids, alkynes, and the cross-coupling between them, with higher catalytic activity and selectivity than homogeneous Pd catalysts while retaining their structural integrity, in contrast to traditional coordination cages assembled in solution. This behaviour emerges from the synergetic hybridization between SCCs and MOFs, which enables both the formation of otherwise not accessible supramolecular assemblies and its stabilization under catalytic conditions by mechanical-bonds to exploit the metal-based catalysis of pivotal metal atoms.

In particular, I have used as chemical nanoreactor, a highly crystalline MOF, $[Pd^{II}(NH_3)_4][Pd^{II}_2(\mu\text{–}O)(NH_3)_6)(NH_4)_2]_{0.5}\{Ni^{II}_4[Cu^{II}_2(Me_3mpba)_2]_3\} \cdot 52H_2O$ (**Pd^{2+}@CuNi-Me_3mpba**), developed in chapter 2. This MOF was subjected to a second Post-Synthetic Methodology (PSM), in which organic ligands were inserted into the structure in order to

form the SCCs@MOF. As it has already been mentioned, the **Pd^{2+}@CuNi-Me_3mpba** features large octagonal pores which are occupied by Pd_2^{II} dimers, stabilized and defined, with atomic precision, to reside on preferential positions of the channels (Figure 4.2 left and Figure 4.3, 4.4 and 4.5). After analysing the available void space, the distance between Pd2 units and the amount of available PdII ions, crystals of **Pd^{2+}@CuNi-Me_3mpba** were soaked with a solution of, appropriately selected, linear (L_4) and bended ($L_{5,6}$) ligands (Figure 4.2) to yield unprecedented MOF-templated in-situ heterogeneous self-assembled SCCs within channels.

The Pd^{II}_8 square metal-organic polygon of formula $[Pd^{II}_2(\mu\text{–}OH_2)_2(NH_3)_4)]_{0.5}[Pd^{II}_8(\mu\text{–}OH_2)_8(NH_3)_8(L_1)_4]_{0.125}\{Ni^{II}_4[Cu^{II}_2(Me_3mpba)_2]_3\} \cdot 43H_2O$ (**Pd^{2+}-L_1@CuNi-Me_3mpba**) - was grown when using the linear ligand L_1 (Figure 4.3), and with the tripodal bended ligand L_2 (Figure 4.4) a water-assisted PdII supramolecular assembly of formula $[Pd^{I}_{16}(H_2O)_8(NH_3)_{24}(\mu\text{–}OH_2)_4(H_2O)_{24}(L_2)]_{0.125}\{Ni^{II}_4[Cu^{II}_2(Me_3mpba)_2]_3\} \cdot 30H_2O$ (**Pd^{2+}-L_2@CuNi-Me_3mpba**) was obtained. Notice that L_3 has a thioether-functional group, which can act as a secondary point of coordination, once a SCC@MOF has been assembled. With L_3, the consecutive self-assembly of the supramolecular complex within MOF channels and the post-assembly metalation of the preformed SCC@MOF (Figure 4.5b) lead to the formation of a heterobimetallic assembly of formula $[Au^{III}_2(\mu\text{–}OH)_2(OH)_4)]_{0.5}[Au^{III}_2Cl_6Pd^{II}_2(NH_3)_6(L_3)_2]_{0.5}[Pd^{II}_2(\mu\text{-}OH_2)(NH_3)_6)]_{0.5}\{Ni^{II}_4[Cu^{II}_2(Me_3mpba)_2]_3\} \cdot 37H_2O$ (**Pd^{2+}-L_3@CuNi-Me_3mpba**) (Figure 4.5).

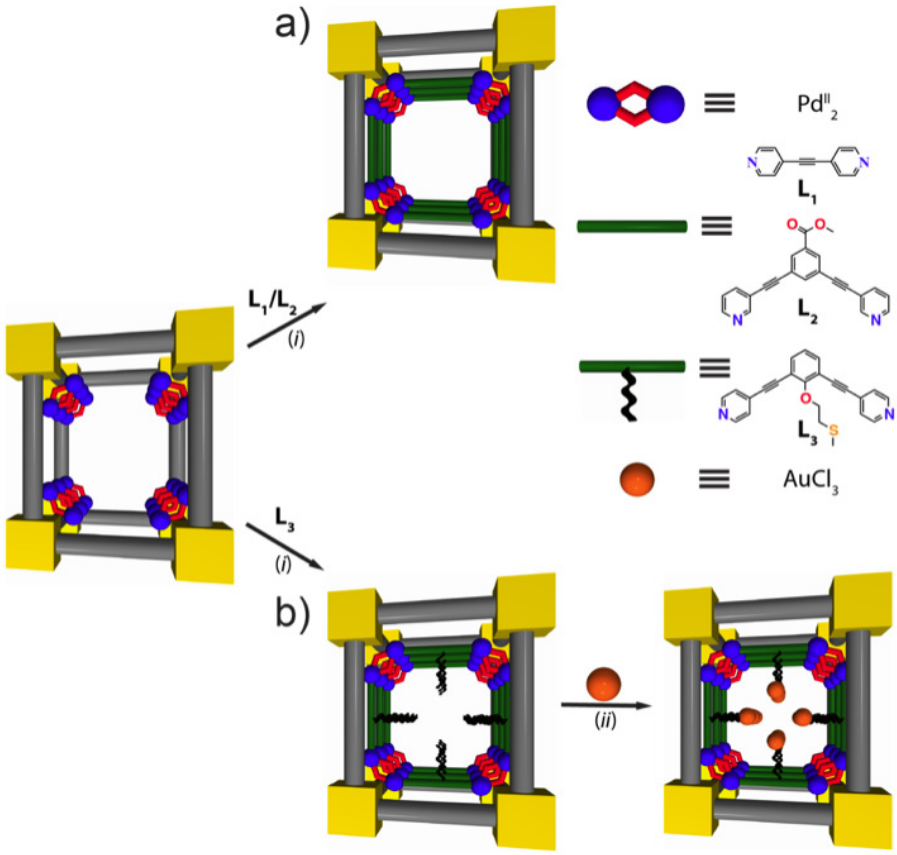

Figure 4.2 Template-directed strategy, involving the use of post-synthetic methodologies for the step-wise sequential synthesis of original homo- (a) and heterobimetallic (b) mechanically-bonded catalytically-active SCCs within the confined space of MOFs channels (SCCs@MOFs). (*i*) Incorporation of desired organic ligand with suitable encoded structural and coordination information and (*ii*) post-assembly metalation of preformed SCCs@MOFs.[25]

The crystal structure of **Pd^{2+}-L_1@CuNi-Me_3mpba** was obtained by SCXRD. Moreover, for **Pd^{2+}-L_2@CuNi-Me_3mpba** it was possible to refine a structural model which gives the most probable organization of entities self-assembled within pores. For **Pd^{2+}-L_3@CuNi-Me_3mpba**, the quality of the SCXRD data was not good enough for the comple-

te structural resolution, but the crystallographic positions of the metal ions, building up the SCCs, and some ligand's fragments determined from Fourier maps, suggest precious insights about the most probable structure of the growth assemblies in the confined space of **Pd^{2+}@Cu-Ni-Me_3mpba**.

The SCXRD data of **Pd^{2+}-L_{1-3}@CuNi-Me_3mpba** evidences that the 3D network remained crystalline during the MOF-templated in-situ heterogeneous self-assembly process. The anionic $Ni_4^{II}Cu_6^{II}$ open-framework in **Pd^{2+}-L_{1-3}@CuNi-Me_3mpba** retains the known structure of **Pd^{2+}@ CuNi-Me_3mpba**. Both, the biggest hydrophobic octagonal channels and the square smallest pores, accommodate Pd(II) **Pd^{2+}-L_{1-2}@Cu-Ni-Me_3mpba** and Pd(II)/Au(III) **Pd^{2+}-L_3@CuNi-Me_3mpba** complexes as result of L_1–L_3 binding to either mononuclear, $[Pd^{II}(NH_3)_4]^{2+}$, or dinuclear complexes, $[Pd^{II}_2(\mu\text{–O})(NH_3)_6]^{2+}$, of **$Pd^{2+}$@CuNi-$Me_3$mpba** (Figures 4.3, 4.4 and 4.5).In **Pd^{2+}-L_1@CuNi-Me_3mpba**, half of the Pd^{2+} ions from the mononuclear and dinuclear entities in **Pd^{2+}@ CuNi-Me_3mpba** are self-assembled by L_1 giving $[Pd^{II}_8(\mu\text{–}OH_2)_8(NH_3)_8(L_1)_4]^{16+}$ square polygons, with $[Pd^{II}_2(\mu\text{-}OH_2)_2(NH_3)_4]$ dimers residing at the corners of the quadrangular SCC (Figures 4.3) and stabilized by H-bonds to the MOF. Each Pd^{II} exhibits regular square planar geometry, with Pd–N [2.02(2) and 2.09(2) Å for Pd-NL1 and Pd-NH_3, respectively] and Pd-OH_2 [1.99(2) and 2.05(2) Å] bond distances similar to those found in the literature.[26-29] The Pd^{II} separations through H_2O and L_1 bridges are 2.840(6) and 13.49(1) Å, respectively. Square polygons are regularly pillared along *c* crystallographic axes, with a Pd(II)···Pd(II) separation among adjacent polygons of 15.15(1) Å, being stabilized by mechanical-bonds with the walls of the net involving terminal NH_3 molecules and oxamate residues belonging to the

net [$H_3N\cdots O_{oxamate}$ of 2.913(9) Å]. The synergic stabilizations ensured by hosting matrix strongly support the robustness of such assembled SCCs, with high activity in heterogeneous metal-based supramolecular catalysis (*vide infra*).

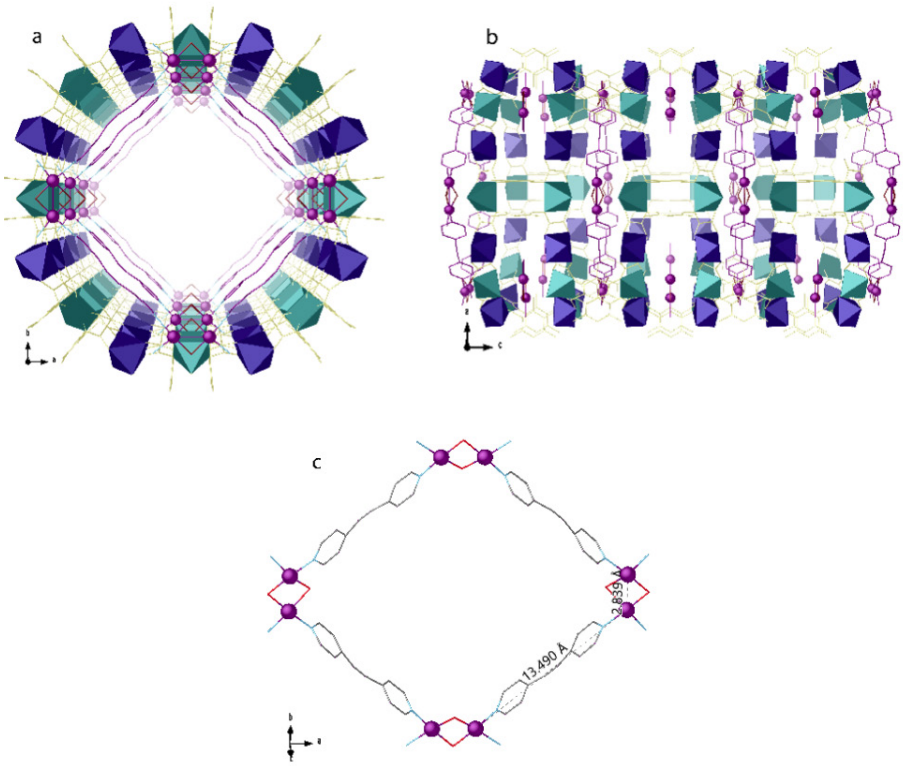

Figure 4.3. A portion of crystal structures of **Pd^{2+}-L_1@CuNi-Me_3mpba** obtained by SCXRD. (a-b) Perspective views of a channel of **Pd^{2+}-L_1@CuNi-Me_3mpba** along the *c* or *b* axes showing, in detail, the Pd^{II}_8 and Pd^{II}_2 complexes. (c) Perspective view of a Pd^{II}_8 SCC underlining the intra-assembly structural parameters related to $Pd^{II}\cdots Pd^{II}$ separations. Color scheme: Cu and Ni atoms from the network are represented by cyan and blue polyhedra, respectively, whereas organic ligands are depicted as yellow and purple sticks (in a-b) for ligand of the whole net and L_1 ligand, respectively. Purple spheres represent Pd^{2+}, whereas red, blue and grey sticks represent oxygen, nitrogen and carbon atoms, respectively (in c).

The different nature and symmetry of ligand L_2 imposes a totally different assembly in **Pd^{2+}-L_2@CuNi-Me_3mpba**, yielding a $[Pd^{II}_{16}(H_2O)_8(NH_3)_{24}(\mu\text{–}OH_2)_4(H_2O)_{24}(L_2)]$ supramolecular assembly, where $[Pd^{II}_2(NH_3)_6(L_2)]$ dimers are linked by strong hydrogen bonds, through the carboxylate group of L2 and H_2O molecules, to $[Pd^{II}_2(\mu\text{–}OH_2)_4(H_2O)_6]$ dimers for which not all waters have been found from density maps [O···O of 2.89(4) and 2.89(3) Å for -COO···O_{water} and O_{water}···O_{water}, respectively] (Figure 4.4). Despite thermal and positional disorder detected for L_2 ligand –that clearly does not fit the space group of hosting matrix – the crystal structure of SCC was solved, where Pd(II) ions exist in distorted square planar geometries with Pd-N in the $[Pd^{II}_2(NH_3)_6(L_2)]$ dimers and Pd-OH_2 distances of the $[Pd^{II}_2(\mu\text{–}OH_2)_4(H_2O)_6]$ moieties falling in the expected values [1.99(1) and 2.00(1) Å for Pd-N_{L2} and Pd-NH_3, respectively, and Pd-OH_2 of 2.05(3) and 2.47(3) Å].30-33 The Pd(II)···Pd(II) separation within $[Pd^{II}_2(NH_3)_6(L_2)]$ dimers is of 6.1 Å whereas 8.3 Å is the shortest Pd(II)···Pd(II) distance detected in Pd_{16} assemblies. The strength of H-bonds observed in Pd_{16} assembly of **Pd^{2+}-L_2@CuNi-Me_3mpba**, together with its stabilization by mechanical-bonds with the network, underpins the role of supramolecular interactions in nanosolvated space, which should be most likely able to preserve Pd_{16} aggregates during catalysis as well.

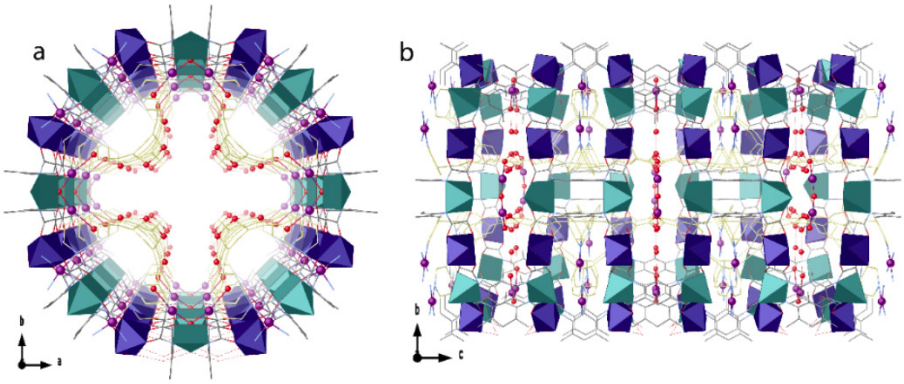

Figure 4.4. A portion of crystal structures of **Pd^{2+}-L_2@CuNi-Me_3mpba** obtained by SCXRD. (a-b) Perspective views of a channel of **Pd^{2+}-L_2@CuNi-Me_3mpba** along the c or b axes showing, the Pd^{II}_{16} and Pd^{II}_{2} complexes. Color scheme: Cu and Ni atoms from the network are represented by cyan and blue polyhedra, respectively, whereas organic ligands are depicted as grey and yellow sticks for ligand of the whole net and L_2 ligand, respectively. Purple spheres represent Pd^{2+}, whereas red, blue and grey sticks represent oxygen, nitrogen and carbon atoms, respectively.

The quality of the SCXRD data did not allow the same precision for the complete visualization of SCCs' crystal structure of **Pd^{2+}-L_3@CuNi-Me_3mpba**. However, many local maxima attributable to Pd^{2+} and Au^{3+} metal ions in the channels together with few peaks related to L_3 ligand's fragments were located in the observed structure factor Fourier maps, providing evidence of the localization of the SCCs (Figure 4.5). Looking at their disposition, it is rationale to hypothesize a self-assembly, in a similar manner as observed in **Pd^{2+}-L_1@CuNi-Me_3mpba**, producing $[Pd^{II}_2(NH_3)_6(L_3)_2]$ dimers (for which no peaks related to the aromatic moiety has been found from electron density maps) remaining in big hydrophobic pores with Pd(II) in square planar geometry [average Pd-N of 2.10(2) Å]. The Pd···Pd and $N_{L3}\cdots N_{L3}$ separations within dimers of 11.36 and 13.97(1) Å fit very-well with those found

for complexes constructed with similar ligands (ca. 14 Å).[34-36] These dimers further grasp $AuCl_3$ complexes exploiting the high affinity for soft metal ions of the thioether moiety[37] featured by L_3, generating, finally, self-assembled heterometallic SCCs of the type $[Au^{III}_2Cl_6Pd^{II}_2(NH_3)_6(L_3)_2]$ showing Pd···Au and Au···Au separations of 13.50(1) and 11.89(1) Å, respectively. Interestingly the found position of Au(III) ions, consistent with L_3 symmetry, is displaced towards the centre of the big pores, suggesting a high accessibility for reactants. Furthermore, the solved crystal structure clearly evidences thioether fragments, allowing to unveil the Au-S distance of 2.34(1) Å.

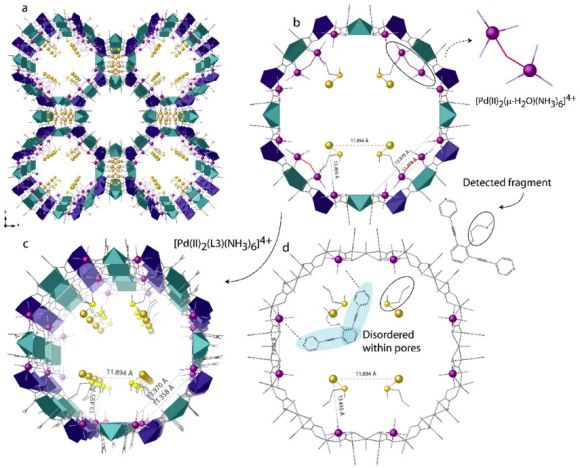

Figure 4.5. Details of crystal structure of **Pd^{2+}-L_3@CuNi-Me_3mpba**. (a) Perspective view along c crystallographic axis of the overall distribution of metal ions within pores. (b) Details of a single hydrophilic pore showing the detected fragments, by SCXRD, of $[Pd^{II}_2(\mu\text{-}OH_2)(NH_3)_6)]$ dimers and $[Au^{III}_2Cl_6Pd^{II}_2(NH_3)_6(L_3)_2]$ heterometallic SCCs. (c-d) Views of a single pore along *c* axis representing only $[Au^{III}_2Cl_6Pd^{II}_2(NH_3)_6(L_3)_2]$ fragments with parameters details related to Pd···Pd and Pd···Au separations and ligand scheme. Color scheme: Cu and Ni atoms from the network are represented by cyan and blue polyhedra, respectively, whereas organic ligands are depicted as grey sticks. Palladium, gold and sulfur, purple, gold and yellow spheres respectively, whereas red, blue and grey sticks represent oxygen, nitrogen and carbon atoms, respectively.

Once characterised this family of SCC@MOFs, the catalytic activity of the three hybrid compounds **Pd^{2+}-L_{1-3}@CuNi-Me_3mpba**, was evaluated. This SCC@MOF coupling allowed to heterogeneously catalyze the homocoupling of boronic acids and alkynes, maintaining the structural integrity of the SCC. As an even more favorable contribution of this SCC@MOF coupling, it surpassed the catalytic activity and selectivity offered by standard homogeneous Pd catalysts and in traditional coordination cages assembled in solution, specifically the soluble Pd^{II}_4 (L_1) 4 squares that are readily decompose under reaction conditions.

On the basis on the unique catalytic results of **Pd^{2+}-L_{1-3}@CuNi-Me_3mpba**, it is clear that novel SCCs@MOFs with new functionalities could offer outstanding perspectives in the field. The use of fluorinated pyridinic ligands as ancillary ligands - ligands that stabilise the metal complex without providing catalytic activity - of catalytic metal complexes has emerged as an idea for the formation of complexes with moderate lifetime and high electrophilicity involved in aromatic C-H activation[38-40] and oxidation reactions[41]. In general, the more sigma (σ) electron-donating the ligand is, the more stable the complex becomes, but also the lower the lewis acidity/catalytic activity. Therefore, the synthesis strategy of the metal complex/network is focused on the design of a ligand that provides stability and, at the same time, decreases the electron donation of the ligand to the metal with the help of the fluoride due to its strong inductive effect.

As seen in the introduction of this chapter, previously reported palladium SCCs@MOFs[42] exhibited high structural stability under reaction conditions –due to the formation of stabilizing mechanical interactions between the SCCs and the MOF network– and improved catalytic ac-

tivities and selectivities for metal–catalysed reactions, as consequence of the limited, but tunable, accessible void space for catalysis. Based on this previous result, we take advantage of the same synthetic strategy and MOFs pore´s chemistry to construct catalytically active fluorinated pyridine–type Pd^{2+} SCCs@MOFs, showing enhanced catalytic activity respect homogenous complexes in the base–free oxidation of aliphatic primary alcohols to carboxylic acids.

This chapter will show how I have managed to obtain another nice example of hybrid MOF-SCC obtained following the same synthetic approach. The same post-processed MOF, **Pd^{2+}@CuNi-Me_3mpba**, was used as the MOF recipient. However, the construction of the molecular cages was performed with bis(4-pyridyl) acetylene ligands at different degrees of fluorination. [43]

4.2. Objectives

* Our first objective is to validate and extend the synthetic strategy –described in 4.1.2– for the synthesis of SCC@MOFs, by preparing novel examples of unprecedented SCCs within MOFs (Figure 4.6)

* Preparation of novel functional organic ligands suitable for the formation of new SCCs being capable to modify the electronic structure (and thus the catalytic properties) of the formed SCCs. In particular we pretended to synthesise/insert different bis(4-pyridyl)acetylene ligands at different degrees of fluorination to prepare different PdII SCCs where each ligand impart different electronic effects.

* Validate the unique catalytic activity –in terms of efficiency or selectivity– of the resulting SCCs. In particular, we envision that the resulting Pd^{II} SCCs with fluorinated ligands can be useful for the aerobic oxidation of aliphatic alcohols.

* On the basis of the exposed above, I will evaluate the electronic effects imparted by the substituted functional groups in the general catalytic activity of supported SCCs.

Figure 4.6. Schematic of the working procedure for the formation of supramolecular cages within the MOF.

4.3. Synthesis

To form the fluorinated cages, we started with **Pd^{2+}@CuNi-Me_3mpba**, which was partially obtained in chapter 2. For this case, a total cationic exchange of the Ni^{II} of the pores by Pd was necessary, obtaining $[Pd^{I}{}^{I}(NH_3)_4][Pd^{II}{}_2(\mu\text{–}O)(NH_3)_6)(NH_4)_2]_{0.5}\{Ni^{II}{}_4[Cu^{II}{}_2(Me_3mpba)_2]_3\} \cdot 52H_2O$ (**Pd^{2+}@CuNi-Me_3mpba**). The second post-synthetic step involves the insertion of fluorinated aromatic ligands (Figure 4.7).

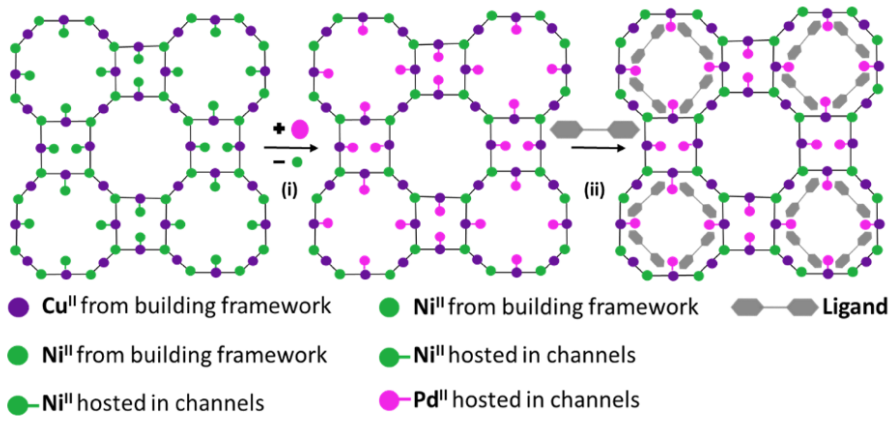

Figure 4.7. Scheme of the synthetic procedure of $Ni^{II} \longrightarrow Pd^{II}$ cation exchange in pores (i) and ligand insertion (ii).

A collaborating group (led by Antonio Fernandez Mato, Loughborough University in UK) carried out the synthesis, by Sonogashira coupling/silane deprotection of the corresponding iodides and silyl acetylenes, and characterisation of the ligands $L_{4\text{-}6}$ inserted into the **Pd^{2+}@CuNi-Me_3mpba**, to led to the formation of **Pd^{2+}-$L_{4\text{-}6}$ @CuNi-Me_3mpba**, respectively:

-Bis(3-fluoro-pyridin-4-yl)acetylene (L4).

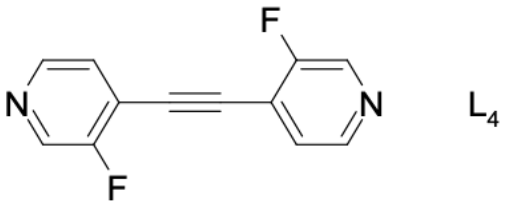

-Bis(2,3-difluoro-pyridin-4-yl)acetylene (L5).

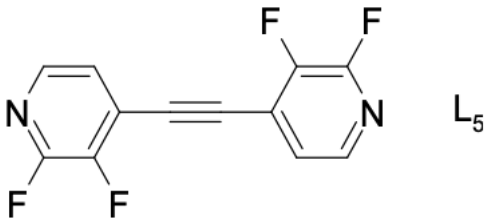

-Bis(2,3,5,6-tetrafluoro-pyridin-4-yl)acetylene (L6).

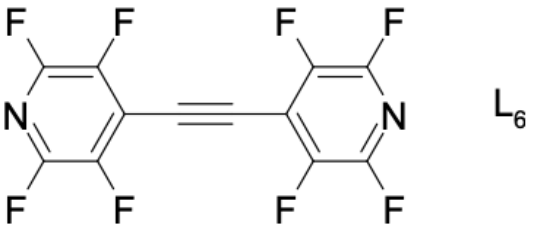

The formation of the molecular cages **Pd^{2+}-L_{4-6}@CuNi-Me_3mpba** was performed in the same way for all cases: immersion of the MOF in a solution containing the ligand to be inserted. Taking into account that the Mg-Ni transmetalation and the cation exchange located in the octagonal Ni-Pd pores were already explained. We can start the synthesis from the reported **Pd^{2+}@CuNi-Me_3mpba** structure, where the insertion was total, instead of partial at 50% as in chapter 2.

Synthesis of $[Pd^{II}(NH_3)_4)]_{1.5}[Pd^{II}_6(\mu–HOAc)_2(H_2O)_{12}(L_4)_4]_{0.08333}$

$\{Ni^{II}_4[Cu^{II}_2(Me_3mpba)_2]_3\}\cdot 25H_2O$ (Pd^{2+}-L_4@CuNi-Me_3mpba). $[Pd^{II}(NH_3)_4)]_{1.5}$ $[Pd^{II}_6(\mu–HOAc)_2(H_2O)_{12}(L_4)_4]_{0.08333}$ $\{Ni^{II}_4[Cu^{II}_2(Me^3mpba)_2]_3\} \cdot 25H_2O$ (**Pd^{2+}-L_4@CuNi-Me_3mpba**) was prepared by immersing crystals of **Pd^{2+}@CuNi-Me^3mpba** (ca. 43 mg, 0.012 mmol) in hot (50 ºC) acetonitrile/water (2:1) solutions of L_1 (7 mL, 12 mM) containing sodium acetate (0.98 mg, 0.012 mmol) for one week. Then, the supernatant solution was removed, and the crystals were washed with an acetonitrile solution (3 x 10 mL), isolated by filtration on paper and air-dried. Despite retaining a nice crystallinity, unfortunately, it was not possible to solve its crystal structure by single-crystal X-ray diffraction, and a multitechnique approach (ICP-MS, SEM-EDAX, PDRX, XPS, Magic Angle Spinning Solid 19F NMR Spectroscopy Liquid NMR spectra, TGA, N_2 isotherm, XANES and EXAFS measurements) has been applied. Elemental analysis [% calcd., % found for $Cu_6Ni_4Pd_2C_{82.3}H_{132.5}N_{18.6}O_{62.3}F_{0.6}$ (3222.70)]: C, 30.68; H, 4.14; N, 8.11; F, 0.39 %. Found: C, 30.60; H, 4.06; N, 8.31; F, 0.43 %. IR (KBr): ν = 1601 cm_{-1} (C=O).

Synthesis of $[Pd^{II}(NH_3)_4)]_{1.5}[Pd^{II}_6(\mu–HOAc)_2(H_2O)_{12}(L_5)_4]_{0.08333}$ $\{Ni^{II}_4[Cu^{II}_2(Me_3mpba)_2]_3\} \cdot 26H_2O$ (Pd^{2+}-L_5@CuNi-Me_3mpba). In an analogous synthetic procedure to that for **Pd^{2+}-L_4@CuNi-Me_3mpba,** but using L_5 instead of L_4, it was obtained **Pd^{2+}-L_5@CuNi-Me_3mpba**. Elemental analysis [% calcd., % found for $Cu_6Ni_4Pd_2C_{82.3}H_{133.8}N_{18.6}O_{63.3}F_{1.3}$ (3252.72)]: C, 30.40; H, 4.15; N, 8.04; F, 0.78 %. Found: C, 30.55; H, 4.12; N, 8.11; F, 0.80 %. IR (KBr): ν = 1603 cm^{-1} (C=O).

Synthesis of $[Pd^{II}(NH_3)_4)]_{1.5}[Pd^{II}_6(\mu–HOAc)_2(H_2O)_{12}(L_6)_4]_{0.08333}$ $\{Ni^{II}_4$[-

$Cu^{II}_2(Me_3mpba)_2]_3\} \cdot 28H_2O$ (Pd^{2+}-L_6@CuNi-Me_3mpba). Well-formed deep green prisms of **Pd^{2+}-L_6@CuNi-Me_3mpba**, suitable for X-ray diffraction, were synthesized by immersing crystals of **Pd^{2+}@CuNi-Me_3mpba** (ca. 43 mg, 0.012 mmol) in hot (50 ºC) acetonitrile/water (2:1) solutions of L_6 (7 mL, 12 mM) containing sodium acetate (0.98 mg, 0.012 mmol) for one week. Then, the supernatant solution was removed, and the crystals were washed with an acetonitrile solution (3 x 10 mL), isolated by filtration on paper and air-dried. Elemental analysis [%calcd., % found for $Cu_6Ni_4Pd_2C_{82.3}H_{136.6}N_{18.6}O_{65.3}F_{2.6}$ (3309.73)]: C, 29.85; H, 4.16; N, 7.89; F, 1.53 %. Found: C, 29.75; H, 4.12; N, 7.71; F, 1.50 %. IR (KBr): $\nu = 1605$ cm^{-1} (C=O).

In an alternative manner, large scale syntheses of **Pd^{2+}-$L_{4\text{-}6}$@CuNi-Me_3mpba**, were also carried out by using the same synthetic procedure that for crystals, but with stirring greater amounts of powder sample of **Pd^{2+}-$L_{4\text{-}6}$@CuNi-Me_3mpba** (1g, 0.275 mmol) and the respective ligand $L_{4–6}$ (20 mL, 27 mM) containing sodium acetate (22.55 mg, 0.275 mmol). Then, the product was collected by filtration, washed with acetonitrile solution (3 x 20 mL) and air-dried.

Elemental analysis [% calcd., % found for large scale syntheses of **Pd^{2+}-$L_{4\text{-}6}$@CuNi-Me_3mpba**]. **Pd^{2+}-L_4@CuNi-Me_3mpba**: C, 30.68; H, 4.14; N, 8.11; F, 0.39 %. Found: C, 30.50; H, 4.26; N, 8.41; F, 0.45 %. **Pd^{2+}-L_5@CuNi-Me_3mpba**: C, 30.40; H, 4.15; N, 8.04; F, 0.78 %. Found: C, 30.45; H, 4.11; N, 8.03; F, 0.76 %. **Pd^{2+}-L_6@CuNi-Me_3mpba**: C, 29.85; H, 4.16; N, 7.89; F, 1.53 %. Found: C, 29.89; H, 4.20; N, 7.96; F, 1.62 %.

4.4. Characterization

4.4.1. Scanning Electron Microscopy-Energy Dispersive X-ray Spectroscopy (SEM-EDAX) of Pd^{2+}-L_{4-6}@Cu-Ni-Me_3mpba

Cation exchange and ligand insertion of compound **Pd^{2+}@CuNi-Me_3mpba** and **Pd^{2+}-L_{4-6}@CuNi-Me_3mpba** was followed by SEM/EDX (Table 4.1 and Table 4.2). In the first stage, Pd insertion gave rise to $[Pd^{I}{}^{I}(NH_3)_4][Pd^{II}{}_2(\mu\text{–}O)(NH_3)_6)(NH_4)_2]_{0.5}\{Ni^{II}{}_4[Cu^{II}{}_2(Me_3mpba)_2]_3\} \cdot 52H_2O$ (**Pd^{2+}@CuNi-Me_3mpba**), and later, L_{4-6} insertion give us **Pd^{2+}-L_{4-6}@CuNi-Me3mpba.** If we observe its formula the expected ratios have to coincide with the one shown in the elemental analysis Cu/Ni 1,5 and Ni/Pd 2 (Table 4.3), and palladium content is maintained afeter ligand insertion.

Table 4.1. Selected data from SEM/EDX analyses for **Pd^{2+}@CuNi-Me_3mpba** and **Pd^{2+}-L_4@CuNi-Me_3mpba**.

	Pd^{2+}@CuNi-Me3mpba		**Pd^{2+}-L4@CuNi-Me3mpba**	
M	**% mass**	**Metal stoichiometry**	**% mass**	**Metal stoichiometry**
Cu	10.43	5.92	11.80	5.98
Ni	6.47	3.98	7.29	4.00
Pd	5.77	1.95	6.54	1.98

Table 4.2. Selected data from SEM/EDX analyses for **Pd^{2+}-L_{5-6} @Cu-Ni-Me_3mpba.**

	Pd^{2+}-L_5@CuNi-Me_3mpba		Pd^{2+}-L_6@CuNi-Me_3mpba	
M	**% mass**	**Metal stoichiometry**	**% mass**	**Metal stoichiometry**
Cu	11.74	6.02	11.51	6.01
Ni	7.30	4.05	7.11	4.02
Pd	6.57	2.01	6.48	2.02

Table 4.3. SEM/EDX metal stoichiometry ratios of **Pd^{2+}@CuNi-Me_3mpba** and **Pd^{2+}-L_{4-6}@CuNi-Me_3mpba.**

Ratio	**Pd^{2+}@CuNi-Me_3mpba**	**Pd^{2+}-L_4@CuNi-Me_3mpba**	**Pd^{2+}-L_5@CuNi-Me_3mpba**	**Pd^{2+}-L_6@CuNi-Me_3mpba**
Cu/Ni	1.49	1.50	1.49	1.49
Ni/Pd	2.04	2.02	2.01	1.99

The values obtained in the tables confirm that the cation exchange has been carried out correctly, and the maintenance of its compositional integrity after the insertion of the fluorinated ligands.

4.4.2. X–ray photoelectron spectroscopy (XPS) of Pd^{2+}-L_{4-6}@CuNi-Me_3mpba

To validate the maintenance of the oxidation state of the Pd^{2+} cations, XPS was used. In figure 4.9, we can compare the XPS spectra

of **Pd^{2+}-L_{4-6}@CuNi-Me_3mpba**, with the starting **Pd^{2+}@CuNi-Me_3mpba**. These spectra reveal a very slight shift of the Pd $3d_{5/2}$ peak of the Pd^{II} atoms in **Pd^{2+}-L_4@CuNi-Me3mpba** (338.8 eV), **Pd^{2+}-L_5@CuNi-Me_3mpba** (338.9 eV), and Pd2+-L6@CuNi-Me3mpba (338.8 eV) relative to **Pd^{2+}@CuNi-Me_3mpba** (338.6 eV), as expected due to the low coordination of the fluorinated L_{4-6} ligands. With practically no difference between the SCC@MOFs.

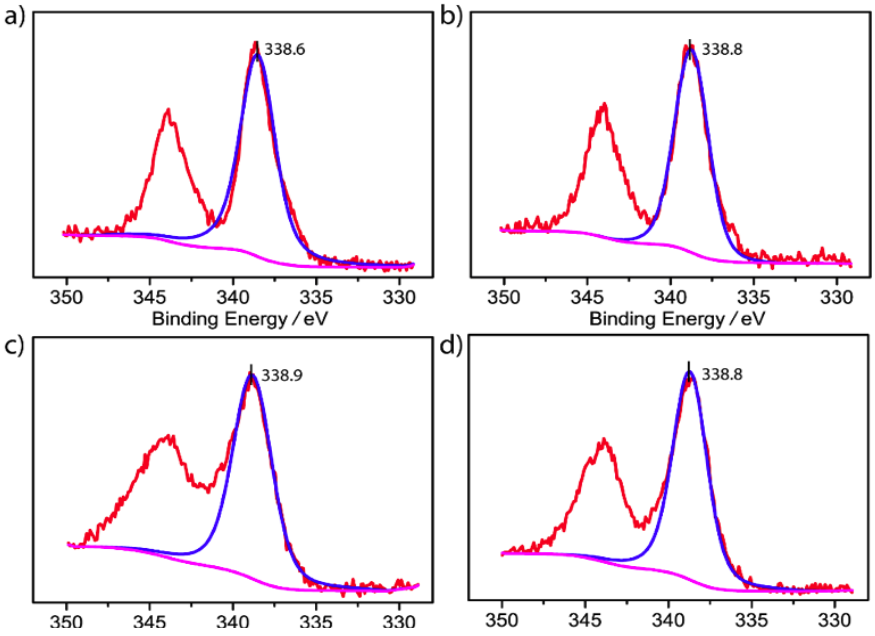

Figure 4.9. X-ray photoelectron spectroscopy (XPS) of **Pd^{2+}@CuNi-Me_3mpba** (a), **Pd^{2+}-L_4@CuNi-Me3mpba** (b), **Pd^{2+}-L_5@CuNi-Me_3mpba** (c) and **Pd^{2+}-L_6@CuNi-Me_3mpba (d).**

4.4.3. Liquid Nuclear Magnetic Resonance (NMR) and Magic Angle Spinning (MAS) Solid 19F NMR Spectroscopy of Pd^{2+}-$L_{4\text{-}6}$@CuNi-Me_3mpba

Combined liquid NMR and SS MAS 19F–NMR confirmed the complexation to the Pd^{II} site of the fluorinated ligand L_4 within the Pd^{2+}-L_4@CuNi-Me_3mpba, since the expected downshift of the signal of free L_4 from ~-126 to ~-118 ppm when complexed to the metal, can be seen, beyond the presence of an impurity coming from the starting material (Figure 4.10).

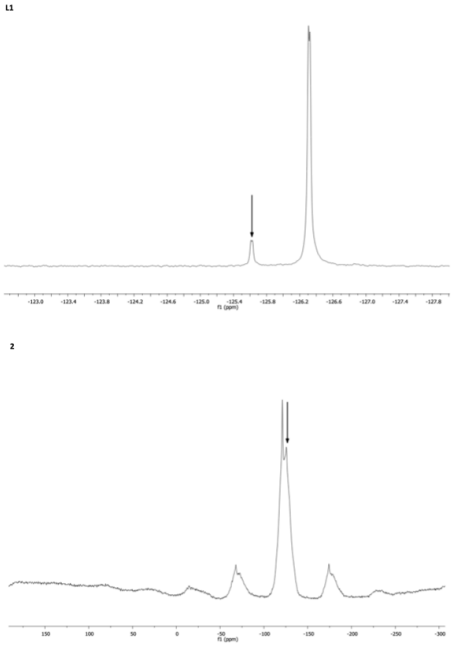

Figure 4.10. Liquid and solid–state magic–spinning ^{19}F nuclear magnetic resonance (NMR and SS MAS 19F–NMR) spectra of ligand L_4 (top) and the corresponding **Pd^{2+}-L_4@CuNi-Me_3mpba** (bottom). The arrow points a typical impurity present in the starting ligand, the other signals correspond to L_4 complexed or not with Pd^{II}, and the corresponding spinning bands.

4.4.4. Single-Crystal X-ray diffraction (SC-XRD) of Pd^{2+}-L_{4-6}@CuNi-Me_3mpba

Diffraction measurements were carried out by another collaborating group at the University of Calabria specialised in SC-XRD (Prof. Donatella Armentano, Universidad de Calabria).

Attempts to solve the crystal structure of **Pd^{2+}-L_4@CuNi-Me_3mpba** and **Pd^{2+}-L_5@CuNi-Me_3mpba** were unsuccessful. Despite not having the security of the atomic resolution provided by SCXRD, the multi–technique approach used –commonly applied in solving highly complex architectures, when SCXRD is not possible– and the similarities of the ligands allowed us to propose tentatively formulae for **Pd^{2+}-L_4@CuNi-Me_3mpba** and **Pd^{2+}-L_5@CuNi-Me3mpba** $[Pd^{II}(NH_3)_4)]_{1.5}[Pd^{II}_6(\mu\text{–HOAc})_2(H_2O)_{12}(L_4)_4]_{0.08333}$ $\{Ni^{II}_4[Cu^{II}_2(Me_3mpba)_2]_3\} \cdot 25H_2O$ (**Pd^{2+}-L_4@CuNi-Me_3mpba**) and $[Pd^{II}(NH_3)_4)]_{1.5}[Pd^{II}_6(\mu\text{–HOAc})_2(H_2O)_{12}(L_5)_4]_{0.08333}\{Ni^{II}_4[Cu^{II}_2(Me_3mpba)_2]_3\} \cdot 26H_2O$ (**Pd^{2+}-L_5@CuNi-Me_3mpba**). Conversely for **Pd^{2+}-L_6@CuNi-Me_3mpba**, application of cutting–edge X–ray crystallography techniques, allowed us to unveil that the 3D network of the anionic $Ni^{II}_4Cu^{II}_6$ porous framework acts in response to perfluorinated pyridine ligand insertion simply with a distortion of the pores' shape, accounting for a phase transition from the tetragonal (P4/*mmm* space group of **Pd^{2+}@CuNi-Me_3mpba**) to the orthorhombic system (Table 4.4). Indeed, **Pd^{2+}-L_6@CuNi-Me_3mpba** crystallizes in the *Cmmm* space group, with the $[Pd^{II}_6(\mu\text{–HOAc})_2(H_2O)_{12}(L_6)_4]$ cages located in the hydrophilic distorted octagonal pores [virtual diameter of ca. 2.2 nm] previously occupied by the Pd^{2+} dimers of **Pd^{2+}@CuNi-Me_3mpba**.

Table 4.4. Summary of crystallographic data for Pd^{2+}-L_6@CuNi-Me_3m-pba.

Compound	Pd^{2+}-L_6@CuNi-Me_3mpba
Formula	$C_{80.50}H_{163}Cu_6F_2N_{13.50}Ni_4O_{81}Pd_2$
M (g mol^{-1})	3483.11
λ (Å)	0.6889
Crystal system	orthorhombic
Space group	*Cmmm*
a (Å)	48.7991(8)
b (Å)	52.1147(9)
c (Å)	14.93830(10)
V (Å^3)	37990.3(9)
Z	8
ρ_{calc} (g cm^{-3})	1.218
μ (mm^{-1})	1.146
T (K)	100(2)
θ range for data collection (°)	0.981 - 26.999
Completeness to θ = 25.0	100
Measured reflections	145893
Unique reflections (Rint)	23713 (0.1821)
Observed reflections [$I > 2\sigma(I)$]	9750
Goof	1.058
R^a [$I > 2\sigma(I)$] (all data)	0.1415 (0.2142)
wR^b [$I > 2\sigma(I)$] (all data)	0.3771 (0.4079)
CCDC code	2107391

$^aR = \sum(|F_o| - |F_c|)/\sum|F_o|$. $^bwR = [\sum w(|F_o| - |F_c|)^2/\sum w|F_o|^2]^{1/2}$.

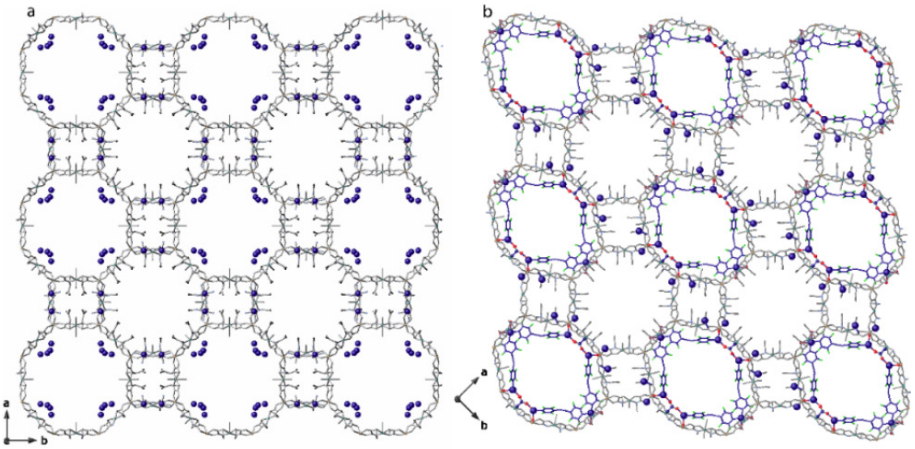

Figure 4.11. (a) View along c crystallographic axis of crystal structure of the precursor **Pd^{2+}@CuNi-Me_3mpba**,[44] featuring channels filled by $[Pd^{II}(NH_3)_4][Pd^{II}_2(\mu–O)(NH_3)_6)(NH_4)_2]$. (b) View of the crystal structure, determined by synchrotron X–ray diffraction, of **Pd^{2+}-L_6@CuNi-Me_3mpba**, where $[Pd^{II}_6(\mu–HOAc)_2(H_2O)_{12}(L_6)_4]$ cages are self–assembled within the confined spaces by perfluorinated ligand L_6. Ligands atoms of the heterobimetallic $Ni^{II}_4Cu^{II}_6$ 3D anionic network are depicted as grey sticks, with cyan or orange spheres for copper and nickel metal ions, respectively. Pd(II) cations in the pores and ligands forming the cages, are represented by blue spheres and blue sticks (with fluorine in green), respectively, with oxygen atoms as red spheres.

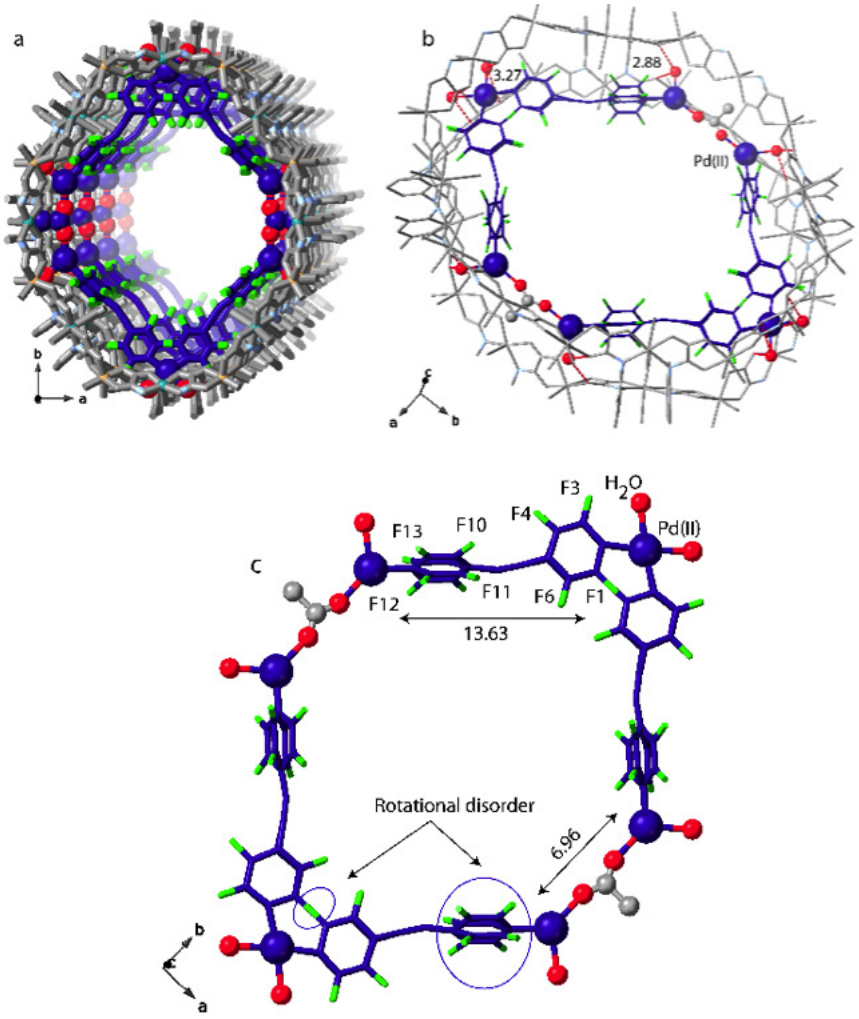

Figure 4.12. Details of a single pore in crystal structure of Pd^{2+}-L_6@CuNi-Me_3mpba. Perspective views of a portion of single pores along the [001] direction showing the $[Pd^{II}_6(\mu\text{–}HOAc)_2(H_2O)_{12}(L_6)_4]$ cages (a) and (b) cages stabilized within MOF's pores by symmetric OH2 ⋯O interactions. (c) View of the structure of the cages and related structural parameters. The heterobimetallic $Ni^{II}_4Cu^{II}_6$ 3D anionic network is depicted as grey sticks. Pd(II) cations in the pores and ligands forming the cages, are represented by blue spheres and blue sticks (with fluorine in green), respectively, with oxygen atoms as red spheres. Hydrogen–bonds are represented as red dashed lines.

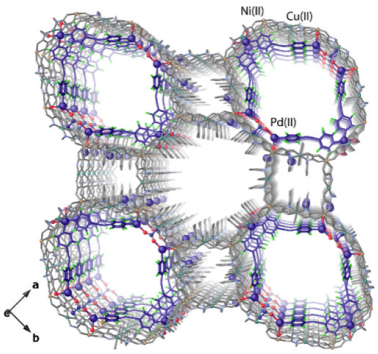

Figure 4.13. Perspective view along c crystallographic axis of crystal structure of **Pd^{2+}-L_6@CuNi-Me_3mpba** featuring channels filled by $\{[Pd^{II}(NH_3)_4)]^{2+}/[Pd^{II}(H_2O)x(NH_3)_{4-x})]^{2+}\}$ and $[Pd^{II}{}_6(\mu\text{–}HOAc)_2(H_2O)_{12}(L_6)_4]^{10+}$ moieties. Lattice water molecules and hydrogen atoms have been omitted for clarity. Color scheme: palladium, blue sphere; oxygen from cage, red spheres, ligand L_6, blue sticks (with F green). Ligand atoms of the whole net have been depicted as grey sticks, and cyan or orange sphere for copper and nickel, respectively.

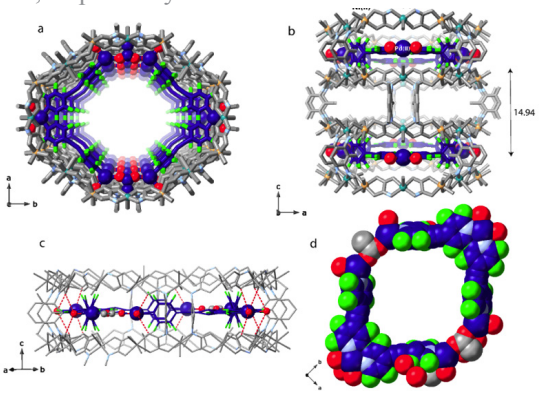

Figure 4.14. Views of fragments of crystal structure of **Pd^{2+}-L_6@CuNi-Me_3mpba**. (a-b) Perspective views along c and b crystallographic axes of a portion of hydrophilic single channel filled with $[Pd^{II}{}_6(\mu\text{–}HOAc)_2(H_2O)_{12}(L_6)_4]^{10+}$ cages. (c) Perspective view along the [111] direction showing the $[Pd^{II}{}_6(\mu\text{–}HOAc)_2(H_2O)_{12}(L_6)_4]^{10+}$ cages, stabilized by symmetric $OH_2\cdots O$ interactions [$H_2O\cdots O_{oxamate}$ of 2.88(1) and 3.27(1) Å]. (d) View of $[Pd^{II}{}_6(\mu\text{–}HOAc)_2(H_2O)_{12}(L_6)_4]^{10+}$ cages represented with space filling model (Van der Waals radii). Color scheme: palladium, blue sphere; oxygen, red spheres, carbon, grey spheres, ligand L_6, blue sticks (with F green). Ligand atoms of the whole net have been depicted as grey sticks, and cyan or orange sphere for copper and nickel, respectively.

Monomeric $\{[Pd^{II}(NH_3)_4]^{2+}/[Pd^{II}(H_2O)x(NH_3)_{4-x}]^{2+}\}$ complexes still reside both in the square smallest pores and octagonal hydrophobic pores (Figure 4.15). The nature and size of pores accounts for formulae uncertainties, indeed some NH_3 and H_2O molecules were not found from ΔF map (Figures 4.15 and 4.18). The confined assemblies are finely stabilized by interactions with the MOF network, which, due to their flexibility, *adapts* pores, in terms of shape in relation to the nature of the linker of the cages.

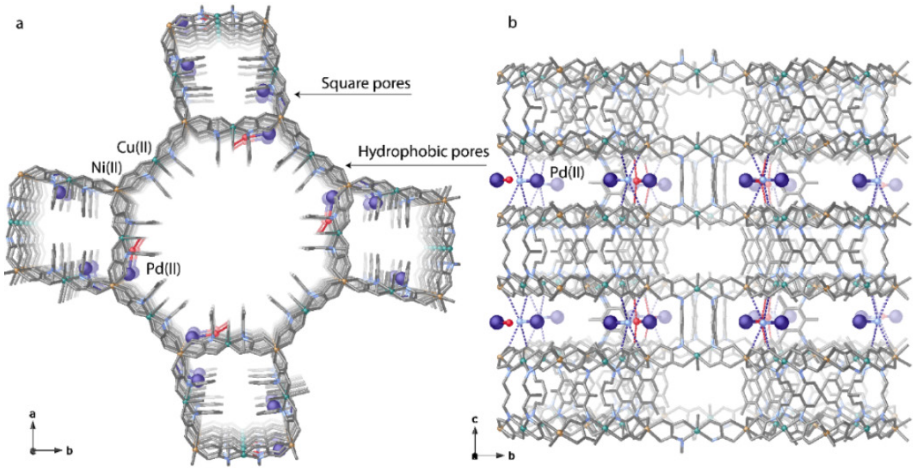

Figure 4.15. Perspective views of a fragment of crystal structure of **Pd^{2+}-L_6@Cu-Ni-Me_3mpba** along c and a axes (a-b) showing square and octogonal hydrophobic pores filled by $\{[Pd^{II}(NH_3)_4)]^{2+}/ [Pd^{II}(H_2O)x(NH_3)_{4-x})]^{2+}\}$ monomeric units, stabilized by hydrogen bonds involving oxygen atoms from oxamate ligand. Color scheme: palladium, blue sphere; oxygen, red spheres, carbon, grey spheres, ligand L_6, blue sticks (with F green). Ligand atoms of the whole net have been depicted as grey sticks, and cyan or orange sphere for copper and nickel, respectively.

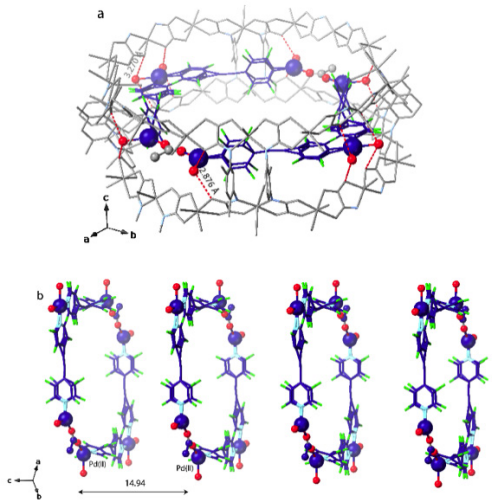

Figure 4.16. Further details of crystal structure of **Pd^{2+}-L_6@CuNi-Me_3mpba**. (a) Perspective views of a portion of the hydrophilic pore (a) showing the stabilized Pd^{II}_6 cages and related structural parameters. (b) Perspective view of cages distribution within a single channel, underlining the inter-assembly structural parameters related to $Pd^{II}\cdots Pd^{II}$ separations. Color scheme: palladium, blue sphere; oxygen, red spheres, carbon, grey spheres, ligand L_6, blue sticks (with F green). Ligand atoms and metal ions of the whole net have been depicted as grey sticks.

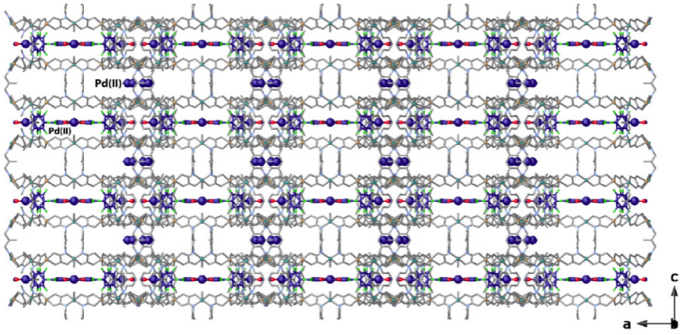

Figure 4.17. View along b crystallographic axis of crystal structures of **Pd^{2+}-L_6@ CuNi-Me_3mpba** featuring channels filled by $\{[Pd^{II}(NH_3)_4)]^{2+}/ [Pd^{II}(H_2O)_x(NH_3)_{4-x})]^{2+}\}$ monomeric units and $[Pd^{II}_6(\mu\text{–HOAc})_2(H_2O)_{12}(L_6)_4]^{10+}$ cages. Lattice water molecules and hydrogen atoms have been omitted for clarity. Color scheme: palladium, blue sphere; oxygen, red spheres, ligand L_6, blue sticks (with F green). Ligand atoms of the whole net have been depicted as grey sticks and cyan or orange sphere for copper and nickel, respectively.

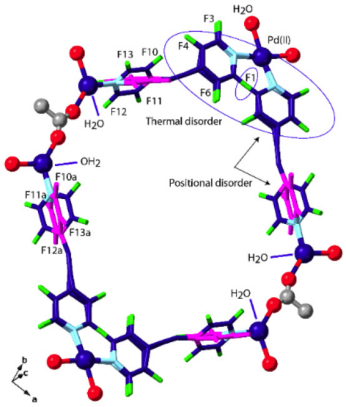

Figure 4.18. View of $[Pd^{II}_6(\mu\text{–HOAc})_2(H_2O)_{12}(L_6)_4]^{10+}$ cages, with thermal and statistically disordered fragments underlined in blue and purple colors, respectively. The region characterized by high dynamical disorder did not permit to resolve the statistical disorder on one of the rings, causing the overlap of fluorine atoms. Color scheme: palladium, blue sphere; oxygen, red spheres, carbon, grey spheres, nitrogen, light blue sticks, ligand L_6, blue sticks (with F green), different conformations of ligand have been depicted as in blue and purple colors, respectively.

Figure 4.12 shows that the $[Pd^{II}_6(\mu\text{–HOAc})_2(H_2O)_{12}(L_6)_4]$ cages are self–assembled within the confined spaces of **Pd^{2+}-L_6@CuNi-Me_3mpba**, resulting from the reaction of half of the Pd^{2+} ions, from the mononuclear and dinuclear entities stabilized by the precursor (**Pd^{2+}@CuNi-Me_3mpba**), with the perfluorinated ligand. The templating action of the MOF is undersigned with the final polygon shape, which follows pore's distortion, exhibiting an elliptic geometry. The corners of the $[Pd^{II}_6(\mu\text{–HOAc})_2(H_2O)_{12}(L_6)_4]$ cages can be located on $[Pd^{II}_2(\mu\text{–HOAc})(H_2O)_2]$ dimeric fragments, which reside at the sides of the elliptic assembly (Figures 4.13 and 4.14) and interact with the MOF by means of water–mediated H–bonds. Each Pd(II) exhibits regular square planar geometry, with Pd–N [2.13(2) and 2.077(11) Å for Pd–NL_6 and 2.070(10) Å for detected Pd–NH_3, respectively], Pd–OH_2 [2.35(2) and 2.30(2) Å for detected Pd–OH_2] and Pd–OAc [2.34(2) Å] bond distances similar, or longer for the latter, to those found in the literature.[45] Fi-

gure 4.12c shows that Pd(II) separations through AcOH and L_6 bridges are 6.96(1) and 13.63(1) Å, respectively. Elliptic polygons are regularly pillared along c crystallographic axes, with a Pd(II)···Pd(II) separation among adjacent polygons of 14.94(1) Å (Figure 4.14 and 16b). Figure 4.12b shows that the polygons are well–stabilized by mechanical–bonds with the walls of the net, involving terminal H_2O molecules and oxamate residues belonging to the porous network [H2O···Ooxamate of 2.88(1) and 3.27(1) Å] (Figures 4.14 and 4.15). Figure 4.12b also shows that further stabilization is ensured by interactions involving terminal water molecules coordinated to copper metal ions of the network [H–OH···O_{water} 3.15(1) Å] (Figure 4.14c). The synergic stabilizations, ensured by a such MOF, allow the framework to act as impeccable platform to efficiently safeguard the robustness of the assembled cages, which in turn exhibit high activity in heterogeneous metal–based supramolecular catalysis (*vide infra*). Furthermore, it is worth to note that their size and shape, stabilized near to the walls of the hosting matrix, preserve the available nano–confined spaces, needed for reactants access (Figure 4.13 and 4.14a–d).

4.4.5. Powder X–ray Diffraction (PXRD) of Pd^{2+}-L_{4-6}@ CuNi-Me_3mpba

The experimental PXRD pattern of **Pd^{2+}-L_6@CuNi-Me_3mpba** is identical to the corresponding calculated one (Figure 4.19). This confirms the homogeneity of the bulk sample, which is isostructural to the crystal selected for single crystal X-ray diffraction. Since the crystals of **Pd^{2+}-L_4@CuNi-Me_3mpba** and **Pd^{2+}-L_5@CuNi-Me_3mpba** could not be resolved by SC-XRD, their isocrystallinity was tested by their similarities to **Pd^{2+}-L_6@CuNi-Me_3mpba** in the experimental diffractograms.

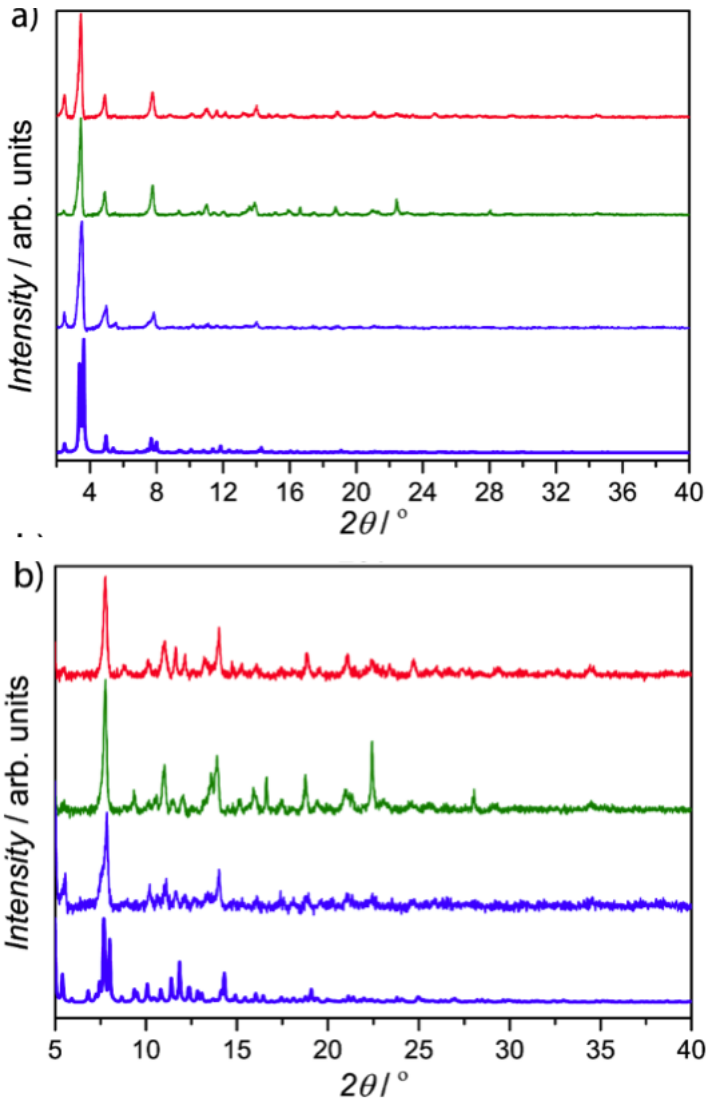

Figure 4.19. Calculated (bold lines) and experimental (solid lines) PXRD pattern profiles of SCCs@MOFs **Pd^{2+}-L_4@CuNi-Me_3mpba** (red), **Pd^{2+}-L_5@CuNi-Me_3mpba** (green) and **Pd^{2+}-L_6@CuNi-Me_3mpba** (blue) in the 2θ range 2.0–40.0∞ (a) and enlarged image in the range 5.0–40.0º (b).

4.4.6. Termogravimetric Analysis (TGA) of Pd^{2+}-L_{4-6}@ CuNi-Me_3mpba

The solvent contents of **Pd^{2+}-L_{4-6}@CuNi-Me_3mpba** were determined by TGA under a dry N_2 atmosphere and compared with pristine MOF **Pd^{2+}@CuNi-Me_3mpba** (Figure 4.20).

All four materials showed a fast mass loss from room temperature, being lower for **Pd^{2+}-L_{4-6}@CuNi-Me_3mpba** than in **Pd^{2+}@CuNi-Me_3mpba**, which agree with the fact that the cavities of these materials are partially occupied by the in–situ constructed SCCs. Then, there is a pseudo plateau until decomposition starts in **Pd^{2+}@CuNi-Me_3mpba** and **Pd^{2+}-L_{4-6}@CuNi-Me_3mpba**. The observed weight losses were 25.72 (**Pd^{2+}@CuNi-Me_3mpba**), 13.96 (**Pd^{2+}-L_4@CuNi-Me_3mpba**), 14.65 (**Pd^{2+}-L_5@CuNi-Me_3mpba**) and 15.45% (P**d^{2+}-L_6@CuNi-Me_3mpba**), respectively, and correspond to 52, 25, 26 and 28 water molecules, respectively, which is in line with CHN analyses.

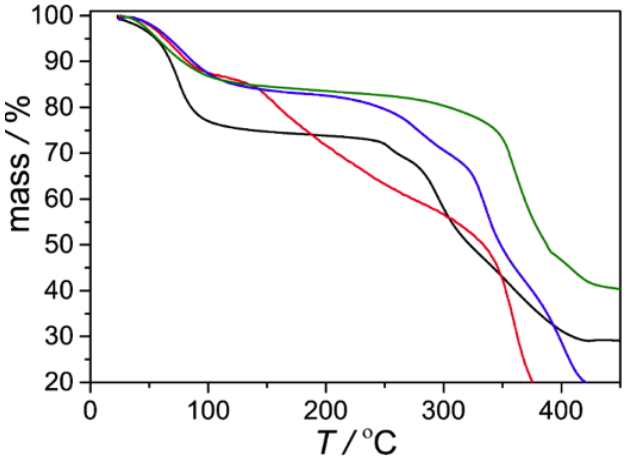

Figure 4.20. Thermo-Gravimetric Analyses (TGA) of MOF **Pd^{2+}@CuNi-Me_3mpba** (black), **Pd^{2+}-L_4@CuNi-Me_3mpba** (red), **Pd^{2+}-L_5@CuNi-Me_3mpba** (green) and **Pd^{2+}-L_6@CuNi-Me_3mpba** (blue).

4.4.7. Gas adsorption of Pd^{2+}-L_{4-6}@CuNi-Me_3mpba

N2 adsorption isotherms helped us to verify the formation of SCC within the pores of **Pd^{2+}@CuNi-Me_3mpba** with the insertion of any of the three L_{4-6} ligands. In the N2 adsorption isotherms of **Pd^{2+}-L_{4-6}@CuNi-Me_3mpba** at 77 K (Figure 4.21) there is a decrease in the empty space accessible to the channels as a consequence of the formation of SCCs@MOF, which is consistent with TGA and the crystal structure. In addition, the amount adsorbed is similar to that of previously reported related non-fluorinated SCC@MOFs.[46]

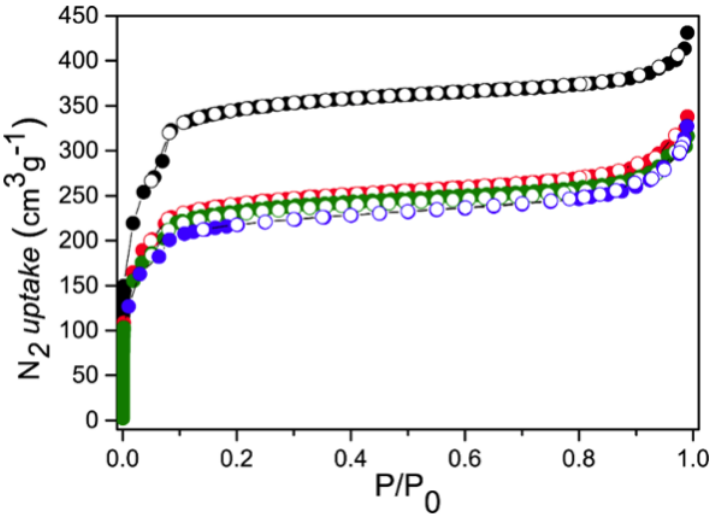

Figure 4.21. N_2 (77 K) adsorption isotherm for the activated compounds **Pd^{2+}@CuNi-Me_3mpba**(black), **Pd^{2+}-L_4@CuNi-Me_3mpba** (red), **Pd^{2+}-L_5@CuNi-Me_3mpba** (green) and **Pd^{2+}-L_6@CuNi-Me_3mpba** (blue). Filled and empty symbols indicate the adsorption and desorption isotherms, respectively. The sample was activated at 80 ∞C under reduced pressure for 16 h prior to carry out the sorption measurements.

4.4.8. X-Ray Absorption Near Edge Structure (XANES) and Extended X-Ray Absorption Fine Structure (EXAFS) measurements of Pd^{2+}-L_{4-6}@CuNi-Me_3mpba

XANES and EXAFS measurements were carried out in ALBA synchrotron by Prof. Carlo Marini, in order to extract further information about the chemical environments of Pd atoms.

XANES results confirm the electrophilicity of Pd^{II} in **Pd^{2+}-L_4@CuNi-Me_3mpba**, similar to **Pd^{2+}@CuNi-Me_3mpba** without any ligand (Figure 4.22 and Table 4.5), with respect to Pd foil.

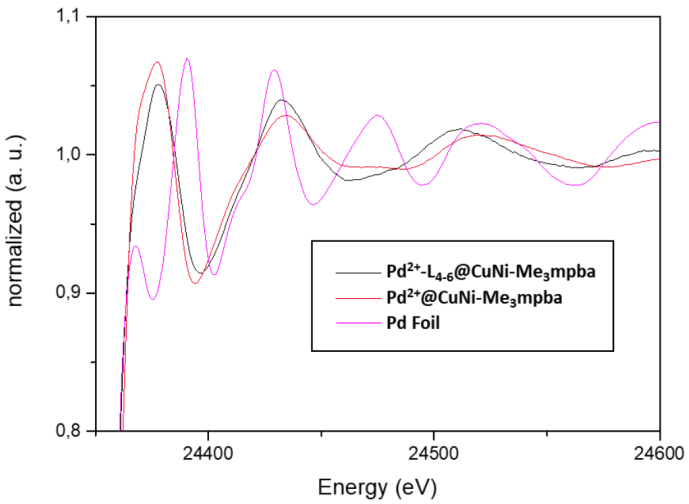

Figure 4.22. X–ray absorption near edge structure (XANES) of **Pd^{2+}@CuNi-Me_3mpba** (a), **Pd^{2+}-L_4@CuNi-Me_3mpba** and Pd foil.

EXAFS results for **Pd^{2+}-L_4@CuNi-Me_3mpba** strongly support the formation of the SCCs inside the MOF, with coordination numbers (CN) and estimated distances (Å) for oxygen atoms (CN: 2.35±0.93 and 2.02 Å), nitrogen atoms (CN: 4.40±0.73 and 2.19 Å) and fluorine atoms

(CN: 1.50±0.86 and 2.45 Å) in good agreement with the SC–XRD of **Pd^{2+}-L_4@CuNi-Me_3mpba** (Figure 4.23 and Table 4.5).

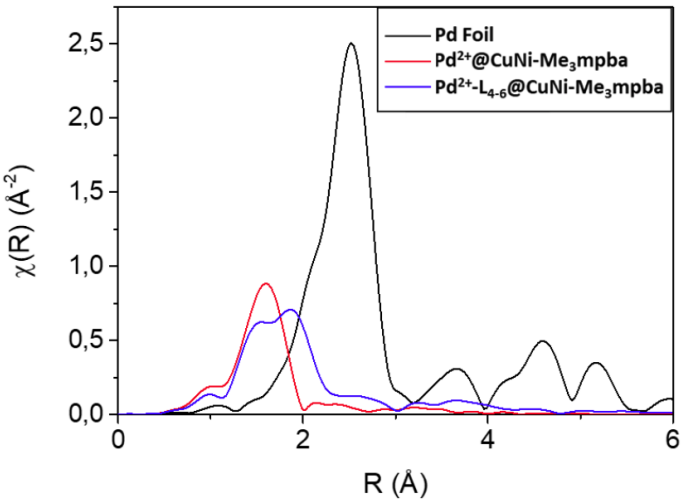

Figure 4.23. Extended X–ray absorption fine structure (EXAFS) of **Pd^{2+}@CuNi-Me_3mpba, Pd^{2+}-L_4@CuNi-Me_3mpba** and Pd foil.

Table 4.5. EXAFS fitting results for the fluorinated cages **Pd^{2+}-L_4@CuNi-Me_3mpba** compared to the Pd foil used for the measurements.

Sample	CN Pd-Pd and R(Å)	CN Pd-O And R(Å)	CN Pd-N and R(Å)	CN Pd-F and R(Å)	ΔE0 (eV)
Pd foil	12 (fixed) 2.74	--	--	--	2.88 ± 0.42
Pd^{2+}@CuNi-Me_3mpba_L_4	--	2.35±0.93 2.01	4.40±0.72 2.19	1.49±0.86 2.44	7.98 ± 2.35

4.5. Catalytic properties of Pd^{2+}-L_{4-6}@Cu-Ni-Me_3mpba

As mentioned above, these Pd^{II} SCCs with fluorinated ligands can be useful for the aerobic oxidation of aliphatic alcohols. We have checked this hypothesis and compared to traditional catalysts. Table 4.6 shows the results for the aerobic oxidation of hexanol **3.1a** to caproic acid **3.2a** with $Pd(OAc)_2$/2-fluoro-pyridine (^{2}F-py)[47] as a catalyst and different solvents, atmospheres and pressures. The best results were obtained with dioxane as a solvent under 4 bars of O2 (48.9% yield with >97% selectivity, entry 5 in table 4.6). The intermediate aldehyde **3.3a** was barely detected at the end of the reaction under these conditions and, remarkably, the addition of NaOAc, a typical base for this reaction, does not significantly change neither the yield nor selectivity to **3.2a** (entry 11 in table 4.6), in accordance with the potential ability of Pd^{2+} to catalyze the whole process without base assistance. The lack of base does not adversely affect the reaction progress, since the formed acid does not apparently poison the catalytic system and can be easily isolated after chromatographic separation. The N:Pd ratio in the MOF analyses, corresponding to the expected pyridine to Pd site stoichiometry, excludes the action of any excess of pyridine ligands as a base, which in any case would correspond to an amount of base marginal to improve the catalytic reaction. The formation of high–valence Pd complexes can be excluded on the basis of oxidation experiments with m–chloroperbenzoic acid (MCPBA), which do not show any increase in the oxidation yield (entry 8 in table 4.6), and control experiments also exclude any role of water during reaction (entry 9 in table 4.6). The reaction yield is proportional to the pressure of O_2 (compare entries 10–12 in table 4.6). Thus, air can replace pure O_2 as an oxidant, provided that the right

partial pressure of O_2 is set, otherwise the oxidation tends to stop in the intermediate aldehyde **3.3a.** Notice that the oxidation reaction does not evolve without O_2, which discards acceptorless dehydrogenative mechanisms.

Table 4.6. (a) Aerobic oxidation of hexanol **3.1a** to caproic acid **3.2a** with $Pd(OAc)_2$/^{2}F–py catalyst under different reaction conditions. Turnover number (TON) equals yield in this case (1 mol% catalyst).

Entry	Solvent	Additive	Atmosphere	TON	
				3.2a	3.3a
1	-*	-	O_2 (4atm)	0.2	0.2
2	toluene	-	O_2 (4atm)	8.6	n.d.
3	dodecane	-	O_2 (4atm)	5.6	0.4
4	THF	-	O_2 (4atm)	4.2	4.2
5	dioxane	-	O_2 (4atm)	48.9	0.8
6	butyric anhydride	-	O_2 (4atm)	n.d.	0.3
7	dioxane	NaOAc	O_2 (4atm)	57.0	2.2
8	dioxane	MCPBA	O_2 (4atm)	43.0	1.5
9	dioxane	H_2O	O_2 (4atm)	55.8	1.1
10	dioxane	-	N_2 (4atm)	2.1	3.3
11	dioxane	-	reflux	9.4	10.6
12	dioxane	-	air (4atm)	10.1	6.9

Figure 4.24 shows the results for different pyridine–Pd^{2+} complexes under optimized reaction conditions, including fluorinated linear alkynyl bispyridines (L_1-L_3). Yields of **3.2a** can be correlated with the pKa value of the ligand, which constitutes a valid estimation for the σ electron donation of the pyridine to the Pd^{2+} atom,[48] and the constant of formation for each complex in solution, calculated by ^{1}H– and ^{19}F–NMR measurements of each complex.

These correlations show that the catalytic activity increases linearly with the electron donor weakness of the pyridine ligand, reaching a maximum for ^{2}F–py, in accordance with previous reports for other reactions.[49-51] This volcano–type is explained by the lack of formation of the Pd^{2+}–pyridine complex beyond the monofluorinated pyridine, which is confirmed here by the formation constants of the different complexes, drastically decreasing for perfluorinated pyridines (blue squares). Notice that the relationship between k_f for electron-poor pyridines and catalytic activity is qualitative, just to confirm that the formation of the palladium complex is directly related to the catalytic activity, but not quantitative, and the better formation of the MOF-supported fluoropyridine Pd complexes is not assessed here with kfs. The blank experiment without any ligand also gives a significant amount of oxidation product, since acetates are relatively low–coordinating ligands, however, a lower amount of oxidation products are found for many of the electron poor ligands. It must be noticed that the formation of the corresponding fluorobispyridine–Pd^{2+} cages in solution did not occur under standard synthetic conditions for the non–fluorinated cage,[52] which contrast with their formation within MOFs channels (see above).

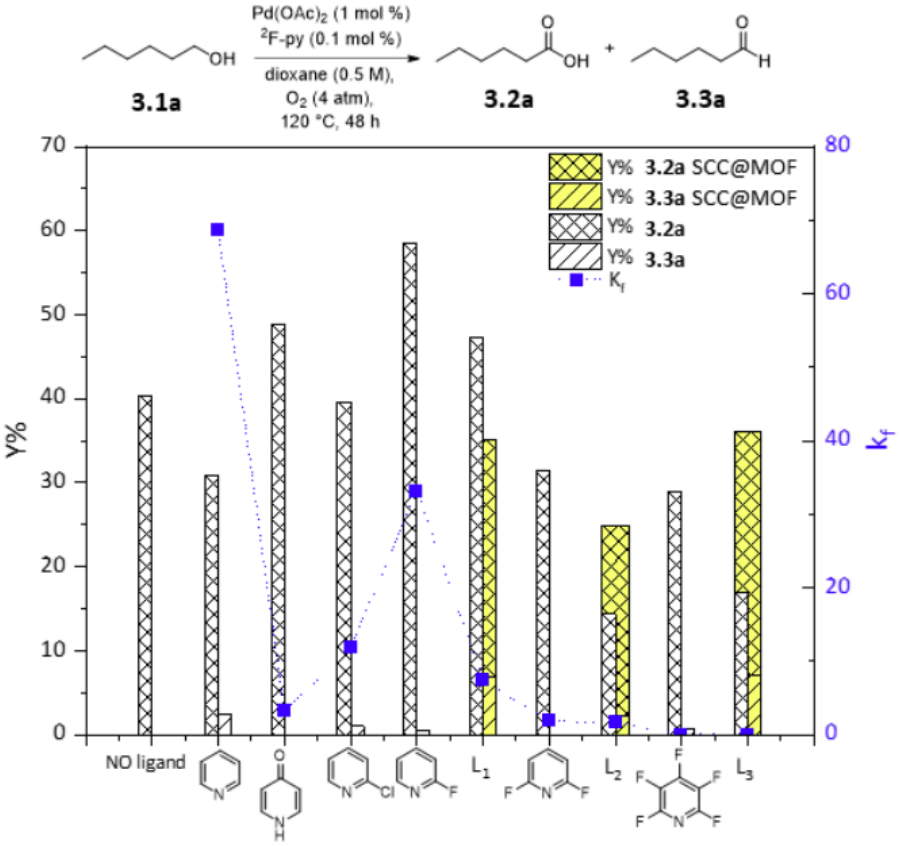

Figure 4.24. (b) Correlation between catalytic activity, pyridine σ electron donation and complex stability for different pyridine–Pd^{2+} complex catalysts. The yields obtained are correlated with the pK_a value of the ligand, which constitutes a valid estimation of the σ electron donation to the Pd^{2+} atom, and the constant of formation for each complex in solution (kf, square points). Reaction conditions: **3.1a** 0.25 mmol; [Pd] 1% mol; [pyridine ligand] 0.1% mol; dioxane 0.5M; 120 °C; 48 h; O2 4 bar. * No solvent.

Kinetic experiments with different amounts of NaOAc confirmed that the absence of NaOAc is beneficial for the formation of **3.2a** (Figure 4.25). The catalytic results for the oxidation of **3.1a** to **3.2a** with the different **Pd^{2+}-$L_{4\text{-}6}$@CuNi-Me_3mpba** can also be found in Figure 4.24. It

can be seen that, in contrast to the corresponding fluoro-pyridine–Pd^{2+} complexes in solution, the yield of **3.2a** is kept to a maximum value with the perfluorinated cage in **Pd^{2+}-L_6@CuNi-Me_3mpba.** Here, the catalytic activity is defined by a subtle balance between the number of F atoms in the pyridine ligand (electronic effect) and the associated limited diffusion within the microporous framework (steric and coordinating impediments).

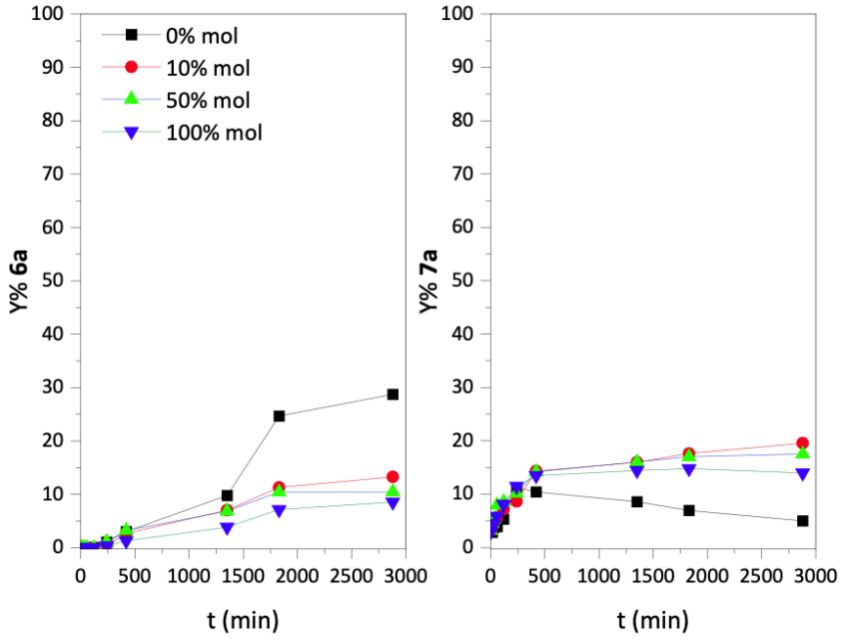

Figure 4.25. Time dependence for the formation of the acid **3.2a** and the aldehyde **3.3a** with different amounts of NaOAc. Reaction conditions: 3.1a 0.5 mmol; $Pd(OAc)_2$ 1% mol; ^{2}F-py 2% mol; dioxane 0.5M; 120 °C; O_2 4 bar.

Indeed, the position of the F atoms in the pyridine ligand also can play a role, beyond the total number of F substituents. For that reason, 2,3–difluoropyridine and 2,3,5,6–tetrafluoropyridine were additionally tested as ligands in solution and the catalytic results (Figure 4.26) show that it is difficult to establish a sound relationship between number/position of

F atoms on the pyridine ligand and catalytic activity in solution, beyond the rough increase in catalytic activity for F–substituted ligands.

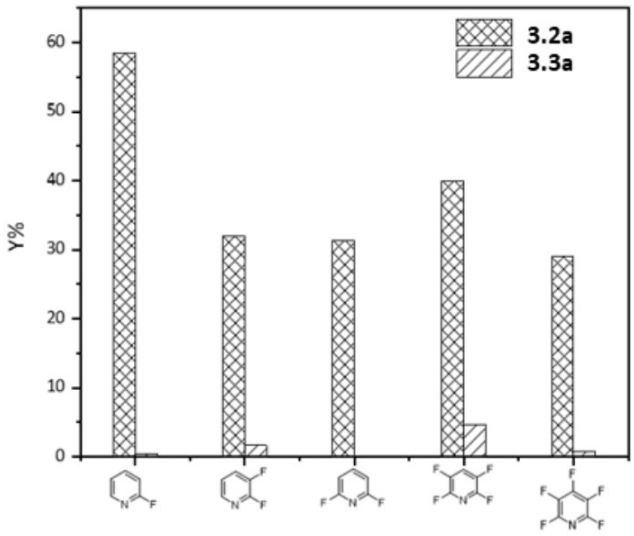

Figure 4.26. Yields of **3.2a** and **3.3a** obtained from the oxidation reaction of hexanol **3.1a**, using $Pd(OAc)_2$ and additional fluorinated pyridines.

The formation of the cage is paramount for the catalytic activity within the MOF, since the combination of the ancestor **Pd^{2+}@CuNi-Me_3mpba**, with bare Pd^{2+} sites, and different soluble pyridine ligands, only catalyze properly the oxidation of **3.1a** when the appropriate ligand for cage formation is employed (Table 4.7). The catalytic results with **Pd^{2+}-$L_{4\text{-}6}$@CuNi-Me_3mpba** do not exceed the soluble monofluorobipyridine–Pd^{2+} complex, however, they reflect the higher activity of the perfluorinated ligand when forming SCCs@MOF. Also, it will showcase the advantages of translating unrecoverable homogenous catalysts into nanoparticulated recoverable solid catalysts (see next page).[53-59]

Table 4.7. Oxidation of **3.1a** to **3.2a** with various $Pd(OAc)_2$ or **Pd^{2+}@CuNi-Me_3mpba** with different ligands. Reaction conditions: **3.1a** 0.25 mmol; [Pd] 1% mol; [L] 0.1% mol; dioxane 0.5M; 120 °C; 48 h; O_2 4 bar.

Entry	Catalyst	Ligand	TON	
			3.2a	**3.3a**
1	$Pd(OAc)_2$	-	40.4	0.0
2	**Pd^{2+}@CuNi-Me_3mpba**		6.6	0.9
3	$Pd(OAc)_2$	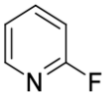	58.5	0.5
4	**Pd^{2+}@CuNi-Me_3mpba**		22.6	0.0
5	$Pd(OAc)_2$	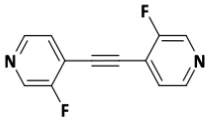	47.2	0.0
6	**Pd^{2+}-L_4@CuNi-Me_3mpba**		15.4	1.3
7	$Pd(OAc)_2$	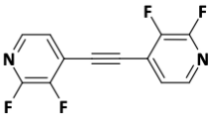	14.4	0.0
8	**Pd^{2+}-L_5@CuNi-Me_3mpba**		6.4	2.4
9	$Pd(OAc)_2$		17.0	0.0
10	**Pd^{2+}-L_6@CuNi-Me_3mpba**		25.1	0.0

Figure **4.27** shows the aerobic oxidation of different aliphatic alcohols of increasing chain length **3.1a–h** catalyzed by **Pd^{2+}-L_6@CuNi-Me_3mpba**, under optimized conditions. It can be seen that ~30% and ~20% yields, in average, are obtained for <8 atom carbon acids **3.2a–d** and >8 atom carbon acids **3.2e–h**, respectively. These results are in accordance with the channels topology and dimensions (~0.8 nm) of **Pd^{2+}-L_6@CuNi-Me_3mpba**, which allows the better diffusion of small linear alkyl

chain reactants and products not only through the MOF channels but also through the cages, and complicates the traffic of longer chain molecules. The aerobic oxidation of alkyl alcohols to carboxylic acids is plagued with multiple by-reactions such as ester or ether formation and decarboxylation, and moreover, the absence of base provokes the acidification of the reaction medium, which could trigger more undesired reactions. Thus, the final reaction yields obtanied here with a MOF solid catalyst can be considered reasonable.

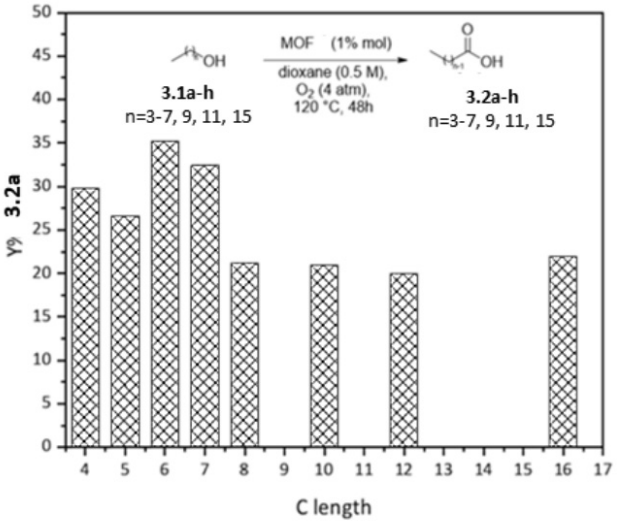

Figure 4.27. (a) Results for the aerobic oxidation of aliphatic alcohols of increasing chain length catalyzed by solid **Pd^{2+}-L_6@CuNi-Me_3mpba**. Selectivity to the carboxylic acid is >97%. Reaction conditions: **3.1a–h** 0.25 mmol; **Pd^{2+}-L_6@CuNi-Me_3mpba,** [Pd] 1% mol; dioxane 0.5M; 120 °C; 48 h; O_2 4 bar.

Figure **4.28a** shows the hot filtration test for **Pd^{2+}-L_6@CuNi-Me_3mpba**, which excludes the presence of catalytically active species in solution, and Figure 4.28b shows that **Pd^{2+}-L_6@CuNi-Me_3mpba** keeps its catalytic activity throughout different reuses.

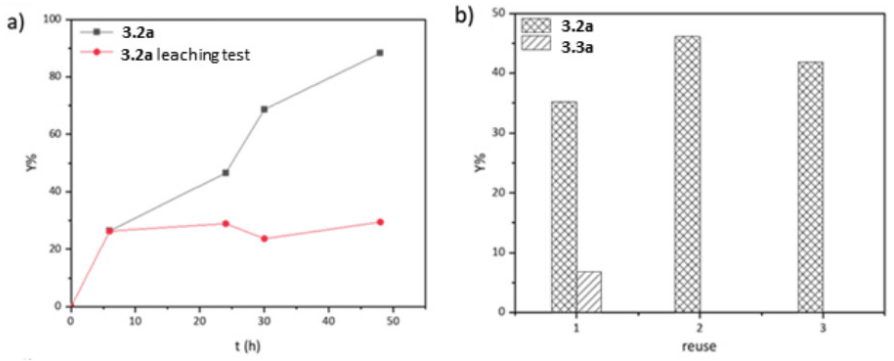

Figure 4.28. (a) Hot filtration test and (b) reuses of **Pd^{2+}-L_6@CuNi-Me_3mpba** for the oxidation of **3.1a** under optimized conditions.

PXRD analysis of the fresh and spent solid catalyst confirmed the integrity of the structure (Figure 4.29). It seems that the catalyst becomes more selective after the first use, nevertheless notice that the yield for **3.2a** is <10% and **3.2a** is a potential intermediate of **3.2a**, thus some variability in the final yield of **3.2a** may be expected. This variability could come, for instance, from different O_2 pressure during the reuses or slightly modifications of the solid catalyst material during reaction. However, it should be considered that the yields are 35, 45 and 42% for the three reuses, respectively, and a 7% by-product is found in the first use, and none in the second two uses.

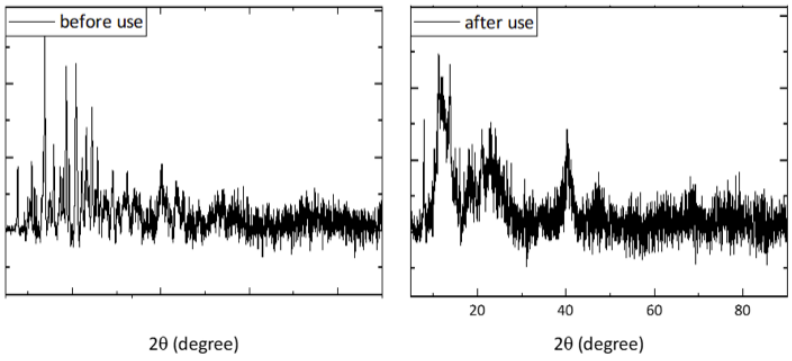

Figure 4.29. PXRD patterns of **Pd^{2+}-L_4@CuNi-Me_3mpba** before and after the oxidation reaction of hexanol.

Thus, the variability for both yield and selectivity is < 10% overall, thus it is a reasonable value for a reused solid catalyst. In addition, we have observed that the results with the catalytic **Pd^{2+}-L_4@CuNi-Me_3mpba** are not far from the parent monofluorinated complex in solution (Figure 4.30). These results showcase a clear practical advantage of the solid SCCs@MOFs respect to the homogeneous soluble counterparts, beyond the electronic effects imparted by the perfluorinated ligand.[60-63]

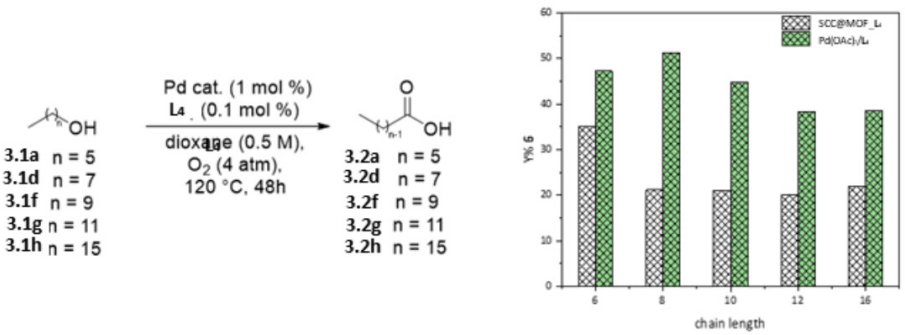

Figure 4.30. Results for the aerobic oxidation of aliphatic alcohols of increasing chain length catalyzed by solid **Pd^{2+}-L_4@CuNi-Me_3mpba** or soluble $Pd(OAc)_2/L_4$ complex catalyst. Selectivity to the carboxylic acid is > 97%. Reaction conditions: 5 0.25 mmol; [Pd] 1% mol; [L_4] 0.1% mol; dioxane 0.5 M; 120 °C; 48 h; O_2 4 atm.

Figure 4.31d shows the kinetics for the oxidation of intermediate hexanal **3.3a**, catalyzed by **Pd^{2+}-L_6@CuNi-Me_3mpba**, under optimized conditions. Each point corresponds to an individual experiment, where O_2 is released and filled back to the reaction to keep the same starting pressure. The formation of caproic acid **3.2a** perfectly matches with the disappearance of hexanal **3.3a**, which explains that the intermediate aldehyde is not detected under reaction conditions, since **3.3a** rapidly oxidizes to **3.2a** as soon as the former is formed (indeed, the final yield of **3.2a** is > 10% higher when starting from **3.1a** than **3.3a**, compare Figures **4.28b** and 4.31). These results suggest that the rate–determining step during the oxidation of **3.1a** to **3.2a** is the dehydrogenation of **3.1a** to **3.3a**. Blank experiments showed that no conversion for any of both reactions occurs if **Pd^{2+}-L_6@CuNi-Me_3mpba** is not present (not shown).

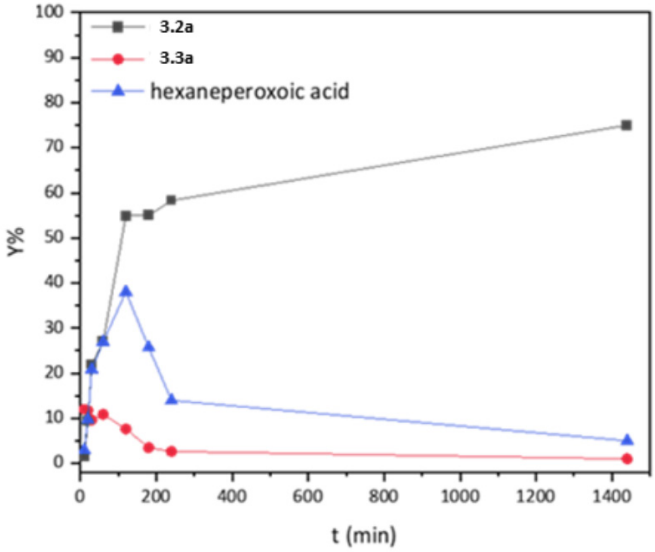

Figure 4.31. Time dependence for the formation of acid **3.2a** during the oxidation of intermediate aldehyde **3.3a**. Reaction conditions: **3.3a** 0.25 mmol; **Pd^{2+}-L_6@Cu-Ni-Me_3mpb**a, [Pd] 1% mol; dioxane 0.5M; 120 °C; O_2 4 bar.

Figure 4.32 shows a plausible mechanism for the oxidation of **3.1a** to **3.2a**. Kinetic studies reveal that the rate for the oxidation of hexanol **3.1a** to caproic acid **3.2a** follows the equation r0 = [**3.1a**][Pd][L]$^{-1}$ at low concentrations of **3.1a** and for any pyridine ligand tested.

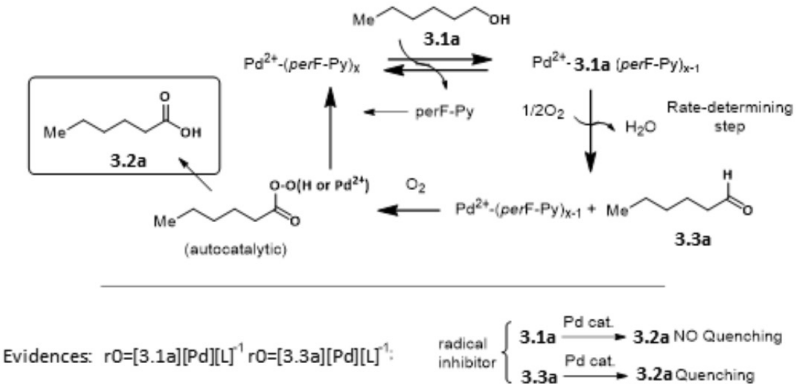

Figure 4.32. Plausible mechanism for the oxidation of **3.1a** to **3.2a.**

A numerical reaction order O_2 pressure does not appear in the rate equation, in accordance with the rapid oxidation of hexanal **3.3a** to caproic acid **3.2a**, and the reaction order for hexanal **3.3a** matches **3.1a** under similar reaction conditions, which further confirms the intermediary character and rapid oxidation of **3.3a** (Figure 4.33).

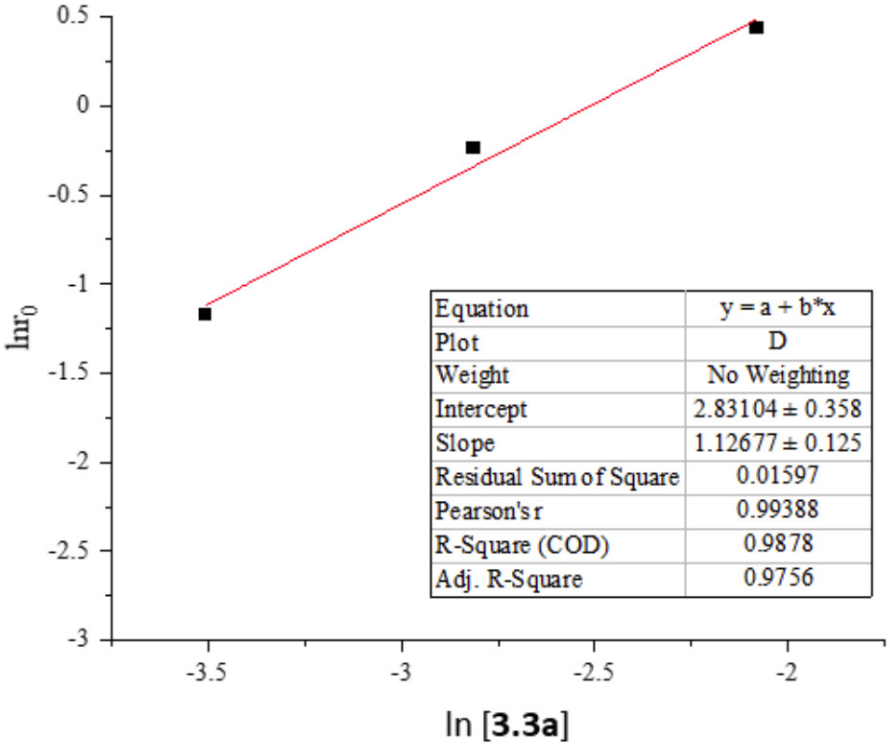

Figure 4.33. Initial rates vs the amount of hexanal **3.3a** in the oxidation reaction with $Pd(OAc)_2$/^{2}F-py. Reaction conditions: [Pd] 1 mol %; [^{2}F-py] 0.1 mol %; dioxane 0.5 mL; 120 °C; O_2 4 atm.

Besides, [**3.1a**] has no influence on the reaction rate at concentrations > 3:1 respect to [Pd^{2+}], thus when the Pd complex is already saturated by the alcohol. These results strongly suggest that the catalytic species corresponds to a Pd^{2+} complex where the alcohol has replaced the pyridine ligand, to be efficiently dehydrogenated by the electrophilic $Pd2^{+}$ site. This cationic Pd site is now available to receive the hydroperoxy mo-

lecule (see ahead). The highly competitive coordination of the pyridine ligand explains why the perfluorinated Pd^{2+} cages in **Pd^{2+}-L_{4-6}@Cu-Ni-Me_3mpba**, despite having the optimal electronics in the ligands, are only slightly more efficient that the monofluoropyridine–Pd^{2+} complex in solution, since the forced ligand–to–metal interaction in the confined coordination cage must severely impede the coordination of alcohol **3.1a.** However, the catalytic results obtained by the solid **Pd^{2+}-L_{4-6}@ CuNi-Me_3mpba** have to be put in context and remarked, if one considers not only the intrinsic steric and coordination hindrance of the cage but also the lower mobility of the reactants/products inside the micro–structured SCCs@MOFs compared to the open catalytic Pd^{2+} complexes in solution.

Considering that the aldehyde is the undiscussed precursor of the acid, and in order to unveil the rapid oxidation mechanism operating during the reaction, the rate equation and possible transient species during the oxidation of hexanal **3.3a** to caproic acid **3.2a** was studied.

The results with different fluoropyridine–Pd^{2+} catalysts show that hexanehydroperoxy acid is formed in all cases, and it rapidly collapses into the final acid **3.2a**, with a rate equation $r_0 = [\mathbf{3.3a}][Pd][L]^{-1.}$ This rate equation is identical to the direct oxidation process, from hexanol **3.1a** to caproic acid **3.2a**. The use of radical inhibitors (Figure 4.34) quenches the oxidation of aldehyde **3.3a** to **3.2a**, and the dehydrogenation of alcohol **3.1a** to **3.3a**.

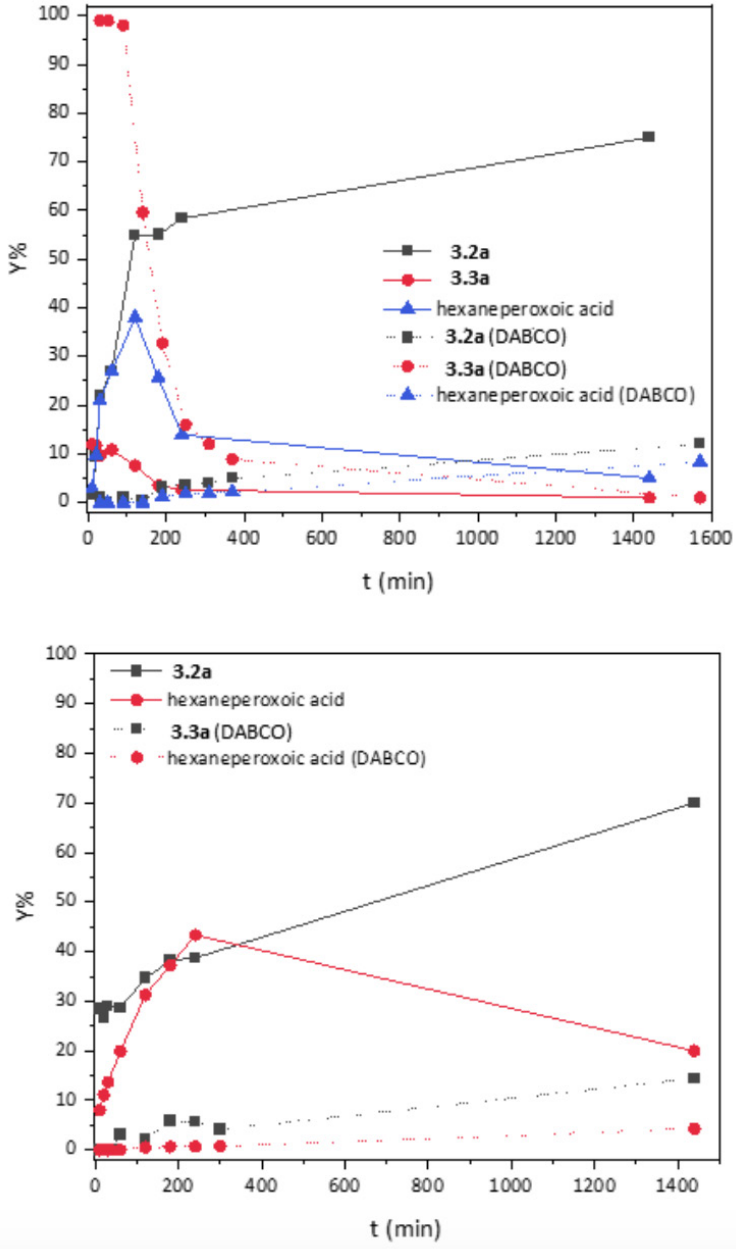

Figure 4.34. Radical inhibitors experiments starting from **3.1a** (top) and **3.3a** (bottom) performed using DABCO as a radical inhibitor, with $Pd(OAc)_2$/^{2}F-py as a catalyst.

These results strongly support alkylhydroperoxy acids as intermediates during the oxidation of the aldehyde, which are accepted intermediates during the autocatalyzed oxidation of aldehydes to carboxylic acids.[64] These peroxy acids join the potential formation of explosive peroxide intermediates with solvent dioxane under O_2, which probably makes the system unsuitable at the industrial level but certainly promising and worthy of further exploration.

4.6. Conclusions

The fact of being able to synthesise SCCs inside MOFs led us to obtain an advanced material with unique characteristics (in nuclearity, stability, electronic structure, etc.) very different from the SCCs that would be obtained outside MOFs. In particular, different bis(4-pyridyl)acetylene ligands have been inserted at different degrees of fluorination to prepare different Pd^{II} SCCs, where each ligand imparts different electronic effects, inside **Pd^{2+}@CuNi-Me_3mpba**.

The validation and extension of the synthetic strategy - described in section 4.1.2 - for the synthesis of SCC@MOFs, as we aimed to do, was carried out using the following methods of different characterisation techniques:

- By means of SEM we verified that the metallic proportionality was maintained, so that the MOF was not degraded and the fluorinated ligands did not sequester the Pd^{2+} cations of the **Pd^{2+}@CuNi-Me_3mpba.**

- The oxidation state of the Pd^{2+} cations also remained intact after the post-synthetic insertion of the ligands. This was verified using XPS.

- Magic Angle Spinning Solid ^{19}F NMR Spectroscopy Liquid NMR spectra confirmed the formation of complexes with the Pd^{II} site of the fluorinated ligand L_4 within **Pd^{2+}-L_4@CuNi-Me_3mpba**.

-The SC-XRD technique, although it did not allow the resolution of **Pd^{2+}-L_4@CuNi-Me_3mpba** and **Pd^{2+}-L_5@CuNi-Me_3mpba** due to its loss of crystallinity after undergoing the PSM, it was possible to resol-

ve the structure of **Pd^{2+}-L_6@CuNi-Me_3mpba**. So that **Pd^{2+}-L_6@CuNi-Me_3mpba**, acted as a representative figure of the SCC@MOF that were synthesized in this work. Through this technique it was possible to confirm with greater precision the formation of the SCC within the MOF. It was observed that the insertion of the perfluorinated pyridine ligands caused a structural deformation in the pores. This could explain the non-resolution of **Pd^{2+}-L_4@CuNi-Me_3mpba** and **Pd^{2+}-L_5@CuNi-Me_3mpba**, since their fluorinated distribution would not be regular enough to produce an ordered deformation in the MOF structure.

-PXRD confirmed that the crystal structure of the single crystal matched that of the **Pd^{2+}-L_6@CuNi-Me_3mpba** powder sample. In addition, the isostructurality of **Pd^{2+}-L_6@CuNi-Me_3mpba** and **Pd^{2+}-L_5@CuNi-Me_3mpba** with respect to **Pd^{2+}-L_6@CuNi-Me_3mpba**, shows that the formation of the cages within the MOF could be carried out in a similar way in both cases. In this way, the SCC interpretation produced in **Pd^{2+}-L_6@CuNi-Me_3mpba**, as a representative figure of **Pd^{2+}-$L_{4\text{-}5}$@CuNi-Me_3mpba**, is validated.

- TGA showed that the insertion of the fluorinated ligands involved the loss of interaction of water molecules with the starting MOF to establish coordinated interactions with the $L_{4\text{-}6}$ ligands.

- The nitrogen adsorption isotherm, showed for the three cases, **Pd^{2+}-$L_{4\text{-}6}$@CuNi-Me_3mpba**, the decrease in the pore size of **Pd^{2+}@CuNi-Me_3mpba** after the formation of SCC inside the MOF.

- XANES and EXAFS confirmed the electrophilicity of Pd^{II} in **Pd^{2+}-L_4@CuNi-Me_3mpba** and the interaction of Pd^{2+} cations with the L_4 ligand

(mainly due to Pd-F interactions), respectively.

Finally, the unique catalytic activity of the SCCs synthesised inside the MOF was validated. It is confirmed that these SCC@MOFs can catalyse the aerobic oxidation of alkyl alcohols to carboxylic acids without the aid of any additives/bases. It was found that SCC@MOFs outperform related SCCs compatible with MOFs but without (per)fluorinated pyridine ligands, since such soluble complexes cannot perform such transformation efficiently.

Therefore, SCCs located in the MOF pores present a great advantage over SCCs in their isolated form, since their catalytic activity (as seen in section 4.5), selectivity (due to the confined space provided by the MOF) and stability (since the metal nodes that make up the SCC structure remain located in the MOF pores instead of a deformation/breakage of the coordinated bond in the SCCs when participating as catalyst in the reaction) are improved. This stability provided by the containment of the SCCs in the MOF leads us to obtain a heterogeneous catalyst with more than three uses without hardly losing its catalytic activity.
Furthermore, it can be assumed that these solid recoverable materials not only expand the organometallic chemistry of Pd towards extremely high and stable electrophilic Pd^{2+} sites, but also open the door to their use as catalysts in challenging C-H activation reactions.

4.7. References

1. Michael J Wiester 1, Pirmin A Ulmann, Chad A Mirkin. Angew. Chem. Int. Ed.2011,50, 114 – 137.

2. Hiroki Takezawa and Makoto Fujita. Bull. Chem. Soc. Jpn. 2021, 94, 2351–2369.

3. Makoto Fujita and Katsuyuki Ogura. Bull. Chem. Soc. Jpn., 69, 1471–1482 (1996).

4. Mei Pan, Kai Wu, Jian-Hua Zhang, Cheng-Yong Su. Coordination Chemistry Reviews 378 (2019) 333–349.

5. Chunxia Tan, Dandan Chu, Xianhui Tang, Yan Liu, Weimin Xuan, and Yong Cui. Chem. Eur. J. 2019, 25, 662 – 672. DOI:10.1002/chem.201802817

6. Yang Li, Meghdad Karimi, Yun-Nan Gong, Nan Dai, Vahid Safarifard, and Hai-Long Jiang. Matter 4, 1–36, July 7, 2021

7. Toshinobu Korenaga, Ryo Sasaki and Kazuaki Shima da. Dalton Trans., 2015, 44,19642.

8. Liping Cao, Pinpin Wang, Xiaran Miao, Yunhong Dong, Heng Wang, Honghong Duan, Yang Yu, Xiaopeng Li, and Peter J. Stang. J. Am. Chem. Soc. 2018, 140, 7005−7011.

9. Andrea Schmidta, Angela Casinib, Fritz E. Kühn. Coordination Chemistry Reviews 275 (2014) 19–36.

10. Marina Frank, Mark D. Johnstone, and Guido H. Cle ver. Chem. Eur. J. 2016, 22, 14104 – 14125.

11. Stephen P. Argent, Harry Adams, Thomas Riis-Johan nessen, John C. Jeffery, Lindsay P. Harding, Olimpia Mamula, and Michael D. Ward. Inorganic Chemistry, Vol. 45, No. 10, 2006

12. Nilanjan Dey, Cally J. E. Haynes. ChemPlusChem / Volume 86, Issue 3 / p. 418-433

13. Sarita Yadav, Palanisamy Kannan and Guanyinsheng Qiu. Org. Chem. Front. , 2020, 7, 2842-2872.

14. Xuezhao Li, Jinguo Wu, Cheng He, Qingtao Meng, and Chunying Duan. Small 2019, 15, 1804770.

15. Dr. Liubov I. Panferova,Mikhail O. Zubkov,Dr. Vladi mir A. Kokorekin,Dr. Vitalij V. Levin. Angew Chem Int Ed, Volume: 60, Issue: 6, Pages: 2849-2854.

16. Chunxia Tan, Dandan Chu, Xianhui Tang, Yan Liu, Weimin Xuan, and Yong Cui. Supramolecular Coordination Cages for Asymmetric Catalysis. Chem. Eur. J. 2019, 25, 662 – 672

17. Felix J. Rizzuto, Larissa K. S. von Krbek, Jonathan R.

Nitschke. Nature Reviews Chemistry volume 3, pages204–222 (2019).

18. Fan-Fan Zhu, Li-Jun Chen, Shangjun Chen, Gui-Yuan Wu, Wei-Ling Jiang, Ji-Chuang Shen, Yi Oin,1 Lin Xu, and Hai-Bo Yang. Chem 6, 2395- 2406, Se ptembe r 10, 2020.

19. Nobuhiko Hosono and Susumu Kitagawa. Acc. Chem. Res. 2018, 51, 2437–2446.

20. Sarita Yadav, Palanisamy Kannan and Guanyinsheng Qiu. Org. Chem. Front. , 2020, 7, 2842-2872

21. Hiroki Takezawa and Makoto Fujita. Bull. Chem. Soc. Jpn. 2021, 94, 2351–2369. doi:10.1246/bcsj.20210273

22. Kevin Byrne, Muhammad Zubair, Nianyong Zhu, Xiao-Ping Zhou1, Daniel S. Fox, Hongzhou Zhang, Brendan Twamley, Matthew J. Lennox, Tina Düren & Wolfgang Schmitt. Nat Commun. 2017; 8: 15268.

23. Navarro-Sánchez, J.; Argente-García, A. I.; Moli ner-Martínez, Y.; Roca-Sanjuán, D.; Antypov, D.; Campíns-Fal có, P.; Rosseinsky, M. J.; Martí-Gastaldo, C. J. Am. Chem. Soc. 2017, 139, 4294–4297.

24. Martell, J. D.; Porter-Zasada, L. B.; Forse, A. C.; Siegel man, R. L.; Gonzalez, M. I.; Oktawiec, J.; Runčevski, T.; Xu, J.; Srebro- Hooper, M.; Milner, P. J.; Colwell, K. A.; Autschbach, J.; Reimer, J. A.; Long, J. R. J. Am. Chem. Soc. 2017, 139, 16000–16012.

25. Rosa Adam, Marta Mon, Rossella Greco, Lucas H. G. Kalinke, Alejandro Vidal-Moya, Antonio Fernandez, Richard E. P. Winpenny, Antonio Doménech-Carbó, Antonio Leyva-Pé rez, Donatella Armentano, Emilio Pardo, and Jesús Ferran

do-Soria. J. Am. Chem. Soc. 2019, 141, 10350−10360.

26. Tominaga, M.; Suzuki, K.; Kawano, M.; Kusukawa, T.; Ozeki, T.; Sakamoto, S.; Yamaguchi, K.; Fujita, M. Angew. Chem., Int. Ed. 2004, 43, 5621−5625

27. Sun, Q.-F.; Iwasa, J.; Ogawa, D.; Ishido, Y.; Sato, S.; Oze ki, T.; Sei, Y.; Yamaguchi, K.; Fujita, M Science 2010, 328, 1144−1147.

28. Fujita, D.; Ueda, Y.; Sato, S.; Mizuno, N.; Kumasaka, T.; Fujita, M. Nature 2016, 540, 563−566.

29. Martinez, C.; Muñiz, K. Chem. - Eur. J. 2016, 22, 7367−7370.

30. Tominaga, M.; Suzuki, K.; Kawano, M.; Kusukawa, T.; Ozeki, T.; Sakamoto, S.; Yamaguchi, K.; Fujita, M. Angew. Chem., Int. Ed. 2004, 43, 5621−5625

31. Sun, Q.-F.; Iwasa, J.; Ogawa, D.; Ishido, Y.; Sato, S.; Oze ki, T.; Sei, Y.; Yamaguchi, K.; Fujita, M. Science 2010, 328, 1144−1147.

32. Fujita, D.; Ueda, Y.; Sato, S.; Mizuno, N.; Kumasaka, T.; Fujita, M. Nature 2016, 540, 563−566.

33. Martinez, C.; Muñiz, K. Chem. - Eur. J. 2016, 22, 7367−7370.

34. Tominaga, M.; Suzuki, K.; Kawano, M.; Kusukawa, T.; Ozeki, T.; Sakamoto, S.; Yamaguchi, K.; Fujita, M. Angew. Chem., Int. Ed. 2004, 43, 5621−5625

35. Sun, Q.-F.; Iwasa, J.; Ogawa, D.; Ishido, Y.; Sato, S.; Oze ki, T.; Sei, Y.; Yamaguchi, K.; Fujita, M. Science 2010, 328,

1144–1147.

36. Fujita, D.; Ueda, Y.; Sato, S.; Mizuno, N.; Kumasaka, T.; Fujita, M. Nature 2016, 540, 563–566.

37. Mon, M.; Ferrando-Soria, J.; Grancha, T.; Fortea-Pé rez, F. R.; Gascon, J.; Leyva-Pérez, A.; Armentano, D.; Pardo, E. J. Am. Chem. Soc. 2016, 138, 7864–7867.

38. D. Zhao, P. Xu, T. Ritter, Chem 2019, 5, 97–107.

39. C. A. Salazar, K. N. Flesch, B. E. Haines, P. S. Zhou, D. G. Musaev, S. S. Stahl, Science 2020, 370, 1454–1460.

40. J. Vercammen, M. Bocus, S. Neale, A. Bugaev, P. Tom kins, J. Hajek, S. Van Minnebruggen, A. Soldatov, A. Krajnc, G. Mali, et al., Nat. Catal. 2020, 3, 1002–1009.

41. G. t. Brink, Science 2000, 287, 1636–1639.

42. R. Adam, M. Mon, R. Greco, L. H. G. Kalinke, A. Vidal-Moya, A. Fernandez, R. E. P. Winpenny, A. Do ménech-Carbó, A. Leyva-Pérez, D. Armentano, et al., J. Am. Chem. Soc. 2019, 141, 10350–10360.

43. Makoto Fujita and Katsuyuki Ogura. Bull. Chem. Soc. Jpn., 69. 1471-1482 (1996)

44. F. R. Fortea-Pérez, M. Mon, J. Ferrando-Soria, M. Boro nat, A. Leyva-Pérez, A. Corma, J. M. Herrera, D. Osadchii, J. Gascon, D. Armentano, et al., Nat. Mater. 2017, 16, 760–766

45. J.-H. Chu, Z.-H. Su, K.-W. Yen, H.-I. Chien, Organome tallics 2020, 39, 3168–3179.

46. R. Adam, M. Mon, R. Greco, L. H. G. Kalinke, A.

Vidal-Moya, A. Fernandez, R. E. P. Winpenny, A. Do ménech-Carbó, A. Leyva-Pérez, D. Armentano, et al., J. Am. Chem. Soc. 2019, 141, 10350–10360.

47. R. Sheldon, I. W. C. Arends, A. Dijksman, Catal. Today 2000, 57, 157–166.

48. K. Noweck, W. Grafahrend, in Ullmann's Encycl. Ind. Chem., Wiley-VCH Verlag GmbH & Co. KGaA, Weinheim, Germany, 2006.

49. D. L. Bruns, D. G. Musaev, S. S. Stahl, J. Am. Chem. Soc. 2020, 142, 19678–19688.

50. D. C. Powers, E. Lee, A. Ariafard, M. S. Sanford, B. F. Yates, A. J. Canty, T. Ritter, J. Am. Chem. Soc. 2012, 134, 12002–12009

51. C. C. Roberts, E. Chong, J. W. Kampf, A. J. Canty, A. Ariafard, M. S. Sanford, J. Am. Chem. Soc. 2019, 141, 19513–19520.

52. M. Fujita, O. Sasaki, T. Mitsuhashi, T. Fujita, J. Yazaki, K. Yamaguchi, K. Ogura, Chem. Commun. 1996, 1535

53. S. Mitchell, R. Qin, N. Zheng, J. Pérez-Ramírez, Nat. Nanotechnol. 2021, 16, 129–139.

54. Abad, P. Concepción, A. Corma, H. García, Angew. Chem. Int. Ed. 2005, 44, 4066–4069.

55. Abad, C. Almela, A. Corma, H. García, Tetrahedron 2006, 62, 6666–6672.

56. D. I. Enache, J. K. Edwards, P. Landon, B. Solsona-Es priu, A. F. Carley, A. A. Herzing, M. Watanabe, C. J. Kiely, D.

W. Knight, G. J. Hutchings, Science 2006, 311, 362–365.

57. Karimi, F. Mansouri, H. Vali, ACS Appl. Nano Mater. 2020, 3, 10612–10627.

58. A. Steinhoff, S. R. Fix, S. S. Stahl, J. Am. Chem. Soc. 2002, 124, 766–767.

59. B. A. Steinhoff, S. S. Stahl, J. Am. Chem. Soc. 2006, 128, 4348–4355.

60. Dhakshinamoorthy, H. Garcia, ChemSusChem 2014, 7, 2392–2410.

61. Dhakshinamoorthy, A. M. Asiri, H. Garcia, Chem. Commun. 2017, 53, 10851–10869.

62. Dhakshinamoorthy, A. M. Asiri, H. Garcia, Trends Chem. 2020, 2, 454–466.

63. Dhakshinamoorthy, A. M. Asiri, H. Garcia, ChemCat Chem 2020, 12, 4732–4753.

64. M. Sankar, E. Nowicka, E. Carter, D. M. Murphy, D. W. Knight, D. Bethell, G. J. Hutchings, Nat. Commun. 2014, 5, 3332

CHAPTER

GENERAL CONCLUSIONS AND FUTURE PERSPECTIVES

Overall, the present manuscript has been organised from lower to higher complexity in terms of the nanosised especies synthesised within the channels of the MOF. First, the introduction covers the most relevant features of MOFs, such as background, classification, synthetic variants, properties, different post-synthetic methods and applications. In particular, I have also focused on showing relevant examples of oxamate- and oxamidate-based MOFs –which have been prepared recently by my research group– as they have been chosen to be used as chemical in my thesis work. They offer great advantages –necessary to accomplish the objectives of my thesis– such as high robustness and crystallinity and the possibility to tune, easily, their porosity in terms of size, shape and, especially, functionality. Moreover, oxamate- and oxamidate-based MOFs are prepared by using "rational programmed" self-assembly methods, based on the previous preparation of stable "building blocks" which incorporate the desired functionalities that will be ultimately translated to the final MOF. This original approach –that shows clear advantages to direct precipitation methods in order to obtain MOFs with the mentioned requirements– has been also discussed in the introduction.

Initially, my research group interests were focused on the preparation of magnetic oxamate- and oxamidate-based MOFs. However, the great versatility of these materials led to an extension of their applicability, thanks to their multiple properties. The tunability of their composition, rigidity, crystallinity and, above all, the variety of topology, size, distribution and chemical environment of their pores are some of the most important properties. In terms of applications, these MOFs based on oxamates and oxamidates have had great relevance in multiple articles

related to the capture of pollutants (gaseous and liquid, such as dyes and heavy metals), capture and release of drugs and food complexes, magnetism and catalysis, among others. This last point is the focus of this thesis: catalysis.

The increasing complexity experienced throughout the thesis begins with the partial insertion of palladium into the oxamate-based MOF and the aromatic amine 2,4,6-trimethyl-1,3-phenylenediamine (Chapter 2). Partial exchange of the nickel cations, hosted in their channels, for palladium allowed a 50/50 exposure of the Ni^{2+} and Pd^{2+} metals, so that all three metals with catalytically active activity (Cu, Ni and Pd) were exposed, with the intention of carrying out cascade catalysis (consecutive reactions). Separately, Cu was successful in the hydroalkoxylation of cyclopropenones where the yields of the reactions catalysed by **Ni^{2+}@CuNi-Me_3mpba** were identical or slightly lower than those carried out in the presence of the homogeneous homogeneous catalyst $Cu(OAc)_2$. Moreover, it allowed a reuse of the material up to 5 times. In the case of Ni, its presence favoured the Chan-Lam coupling, thus completing the **Ni^{2+}@CuNi-Me_3mpba** catalytic cascade functionality, where Cu is in charge of the hydration reaction and Ni^{2+} of the Chan-Lam coupling. The addition of Pd to the equation was given by the permittivity of the cyclopropenone/Mizoroki-Heck hydration coupling reaction in a single vessel which involved its inclusion in the **Ni^{2+}@CuNi-Me_3mpba** MOF. This implied that the presence of Ni^{2+} or Pd^{2+} in the MOF as a heterogeneous catalyst was determined by the desired directionality of the reaction for the coupling to form esters in higher percentage yield (favoured by Ni) or ketones (favoured by Pd). Finally, it was concluded that the presence of the three metals Cu, Ni and Pd favours the synthesis reaction of coumarin family compounds in a single vessel, unlike the

homogeneous homologous catalyst.

Once the total or partial insertion of transition metals into the pores of the oxamate-based MOF and the said aromatic amine was controlled, the next level of complexity of post-synthetic modification was taken to the creation of SACs and SNMCs. The **Ni^{2+}@CuNi-Me_3mpba** MOF underwent complete insertion of silver cations into the MOF pores and subsequent reduction to create Ag^0_2 clusters. To add catalytic diversity in the MOF, iron cations were added, requiring a full insertion of silver, a partial insertion of iron and a reduction to create a mixture of Fe^{3+} SAM and Ag^0_2 SNMC. For both cases only the silver atoms hosted in the octagonal pores were reduced, with the silver cations in the square pore remaining unreduced. In the case of the heterometallic SNCM, the iron cations were not reduced either.

In terms of catalysis, the Ag^0_2 SNMCs were able to efficiently catalyse the Buchner ring expansion reaction, allowing its reuse up to 6 times. While for **$Ag^0_2Fe^{3+}$@CuNi-Me_3mpba** an unmet reaction, the unprecedented direct conversion of styrene to phenylacetylene in one-pot, was achived with very high yields.

In Chapter 3, we have presented the synthesis and characterization of a novel MOF prepared with oxamidate ligands derived from the amino acid methylcysteine: **CuSr-Mecysmox**. The main features that differentiate it from the Me_3mpba-based MOF are the smaller size of its one-dimensional pores and the decoration of its channels by sulphur atom groups that have affinity for soft metals such as Pd. So it fulfilled the necessary requirements to form Pd SACs (instead of the Pd_4 SNMCs formed inside **Ni^{2+}@CuNi-Me_3mpba**): smaller pore size, di-

fferent chemical environment and high affinity for Pd. These Pd SACs formed inside **CuSr-Mecysmox** were able to catalyse, very efficiently, the reaction and oxidation of benzyl alkyl alkyls to benzoic acids.

In Chapter 4, I have taken up the use of the **Ni^{2+}@CuNi-Me_3mpba** MOFs, after (this time) complete insertion of Pd(II) cations, fluorinated bipyridinic ligands were inserted with the intention of forming SCCs inside the **Pd^{2+}@CuNi-Me_3mpba** MOF which were able to catalyse the aerobic oxidation of alkyl alcohols to carboxylic acids without the aid of any additives/bases and keeping their SCCs confined in the pores, with enhanced reuse and interesting selectivities.

In summary, in this thesis, we have gone deeper on the use of MOFs as chemical reactors for the preparation of unique and original catalytically active metal species. The compounds reported in the different chapters indeed constitute a step further on the applicability of MOFs in such an important field as industrial catalysis, as some of the reported compounds show outstanding catalytic properties and, in some cases, are capable to catalyse reactions that had not been achieved before. These results also open the gate to the development of novel metal nanosised species not achieved before. In particular, the preparation of ligands-free subnanometer heterometallic clusters is still a challenge. Some preliminary results have been achieved (Figure 5.1) and this thesis has has laid the foundations for future applications of these unique unprecedented species.

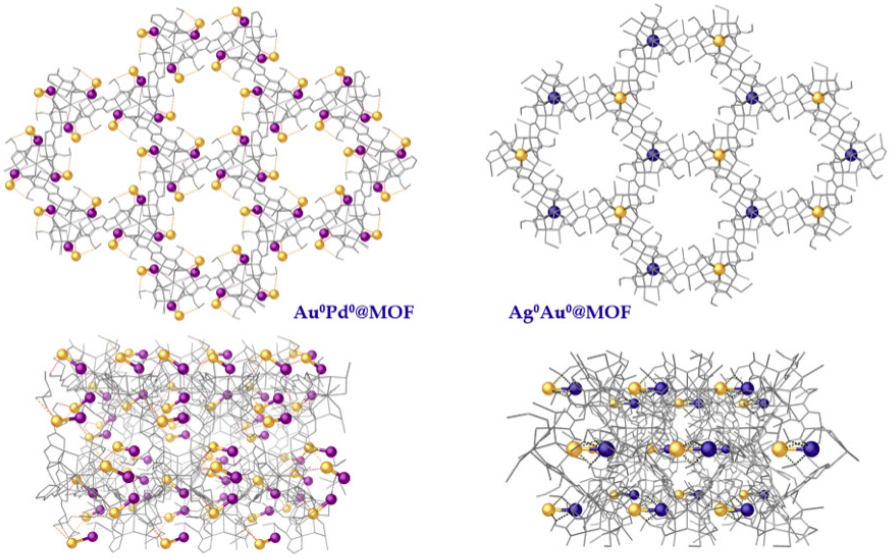

Figure 5.1. Crystal structure of **AuPd@CuSr-Mecysmox** and **AuAg@CuSr-Mecysmox.**

CHAPTER

6

Publications related to this Thesis

- Rossella Greco+, **Estefanía Tiburcio**+, Brenda Palomar-De Lucas, Jesús Ferrando Soria, Donatella Armentano, Emilio Pardo, Antonio Leyva-Perez. Click amidations, esterifications, and one–pot reactions catalyzed by Cu salts and multimetal–organic frameworks (M–MOFs). Molecular Catalysis 522 (**2022**) 112228.

- **Estefania Tiburcio**+, Rossella Greco+, Antonio Fernandez, Carlo Marini, Alejandro Vidal-Moya, Judit Oliver-Meseguer, Donatella Armentano, Emilio Pardo, Jesús Ferrando-Soria, and Antonio Leyva-Pérez. MOF-Stabilized Perfluorinated Palladium Cages Catalyze the Additive-Free Aerobic Oxidation of Aliphatic Alcohols to Chem. Eur. J. **2022**, 28, e202103781.

- **Estefanía Tiburcio**+, Rossella Greco+, Marta Mon, Jordi Ballesteros-Soberanas, Jesús Ferrando-Soria, Miguel López-Haro, Juan Carlos Hernández-Garrido, Judit Oliver-Meseguer, Carlo Marini, Mercedes Boronat, Donatella Armentano, Antonio Leyva-Pérez and Emilio Pardo. Soluble/MOF-Supported Palladium Single Atoms Catalyze the Ligand-, Additive-, and Solvent-Free Aerobic Oxidation of Benzyl Alcohols to Benzoic Acids. J. Am. Chem. Soc. **2021**, 143, 6, 2581–2592.

Other publications

o Cristina Bilanin, **Estefanía Tiburcio**, Jesús Ferrando-Soria, Donatella Armentano, Antonio Leyva-Pérez and Emilio Pardo. Crystallographic Visualization of a Double Water Molecule Addition on a Pt1-MOF during the Low-temperature Water-Gas Shift Reaction. ChemCatChem **2021**, 13, 1195– 1200.

o Marta Mon+, Rosaria Bruno+, **Estefanía Tiburcio**, Aida Grau-Atienza, Antonio Sepulveda-Escribano, Enrique V. Ramos-Fernandez, Alessio Fuoco, Elisa Esposito, Marcello Monteleone, Johannes C. Jansen, Joan Cano, Jesus Ferrando-Soria, Donatella Armentano, and Emilio Pardo. Efficient Gas Separation and Transport Mechanism in Rare Hemilabile Metal−Organic Framework. Chem. Mater. **2019**, 31, 5856−5866

o Marta Mon+,Rosaria Bruno+, **Estefanía Tiburcio**, Marta Viciano-Chumillas, Lucas H. G. Kalinke,Jesus Ferrando-Soria, Donatella Armentano, and Emilio Pardo. Multivariate Metal−Organic Frameworks for the Simultaneous Capture of Organic and Inorganic Contaminants from Water. J. Am. Chem. Soc. **2019**, 141, 13601−13609

o Lucas H. G. Kalinke, Danielle Cangussu, Marta Mon, Rosaria Bruno, **Estefanía Tiburcio**, Francesc Lloret, Donatella Armentano, Emilio Pardo, and Jesús Ferrando-Soria. Metal−Organic Frameworks as Playgrounds for Reticulate Single Molecule Magnets. Inorg. Chem. **2019**, 58, 14498−14506

- Marta Mon, Rosaria Bruno, **Estefanía Tiburcio**, Pierre-Edouard Casteran, Jesús Ferrando-Soria, Donatella Armentano and Emilio Pardo. Efficient capture of organic dyes and crystallographic snapshots by a highly crystalline amino acid-derived metal-organic framework. September **2018** Chemistry-A European Journal 24(67)

- Marta Mon, **Estefanía Tiburcio**, Jesús Ferrando-Soria, Rodrigo Gil San Millán, Jorge A. R. Navarro, Donatella Armentano and Emilio Pardo. Post-synthetic approach triggers selective and reversible sulphur dioxide adsorption on a metal-organic framework. Chem. Commun., [2018,] 54, 9063

CHAPTER

7

PUBLICATION 1

Click amidations, esterifications, and one–pot reactions catalyzed by Cu salts and multimetal–organic frameworks (M–MOFs).

Rossella Greco+, **Estefanía Tiburcio**+, Brenda Palomar-De Lucas, Jesús Ferrando Soria, Donatella Armentano, Emilio Pardo, Antonio Leyva-Perez.

Contents lists available at ScienceDirect

Molecular Catalysis

journal homepage: www.journals.elsevier.com/molecular-catalysis

Click amidations, esterifications and one–pot reactions catalyzed by Cu salts and multimetal–organic frameworks (M–MOFs)

Rossella Greco [a,1], Estefanía Tiburcio [b,1], Brenda Palomar-De Lucas [a], Jesús Ferrando-Soria [b], Donatella Armentano [c], Emilio Pardo [b,*], Antonio Leyva-Pérez [a,*]

[a] Instituto de Tecnología Química (UPV–CSIC), Universidad Politècnica de València–Consejo Superior de Investigaciones Científicas, Avda. de los Naranjos s/n, Valencia 46022, Spain
[b] Departamento de Química Inorgánica, Instituto de Ciencia Molecular (ICMol), Universidad de Valencia, Catedrático José Beltrán Martínez, 2, Paterna, Valencia 46980, Spain
[c] Dipartimento di Chimica e Tecnologie Chimiche (CTC), Università della Calabria, Rende, Cosenza 87036, Italy

ARTICLE INFO

Keywords:
Click reaction
Catalysis
Metal–organic frameworks
Cyclopropenones
esters
Amides
Copper
One–pot reactions

ABSTRACT

Amides and esters are prevalent chemicals in Nature, industry and academic laboratories. Thus, it is not surprising that a plethora of synthetic methods for these compounds has been developed along the years. However, these methods are not 100% atom economical and generally require harsh reagents or reaction conditions. Here we show a "spring–loaded", 100% atom–efficient amidation and esterification protocol which consists in the ring opening of cyclopropenones with amines or alcohols. Some alkyl amines react spontaneously at room temperature in a variety of solvents and reaction conditions, including water at different pHs, while other alkyl amines, aromatic amines and alcohols react in the presence of catalytic amounts of simple Cu^{2+} salts or solids. A modular reactivity pattern (alkyl amines >> alkyl alcohols >> phenols >> aromatic amines) enables to design orthogonal and one–pot reactions on well–defined catalytic Multimetal–Organic Frameworks (M–MOFs, M= Cu, Ni, Pd), to easily functionalize the resulting cinnamides and cinnamic esters to more complex molecules. The strong resemblance of the amidation and esterification reaction conditions here reported with the copper–catalyzed azide–alkyne cycloaddition (CuAAC) allows to define this fast, clean and flexible protocol as a click reaction.

1. Introduction

Click reactions are extremely fast and regiospecific couplings between two different functional groups, generally boosted by a favorable release of energy (ΔH^0 typically < -40 kcalmol^{-1}). These reactions operate under ambient conditions at different pHs, in the presence of other organic and inorganic (iclick) functional groups, and in many conventional solvents, including water [1–3]. This combination of high specificity and reaction condition ubiquity makes click reactions of great utility for the design and construction of bio–orthogonal reactions [4–6] and chemical libraries,[7,8] to name a couple of current applications Fig. 1. shows the CuAAC reaction, a very representative click reaction [9,10].

Amide and ester bonds are present at the core of chemistry. However, it is difficult to find a fast and full–atom economy protocol for the synthesis of these paramount functional groups. A paradigmatic example is the synthesis of cinnamides and cinnamic esters, also shown in Fig. 1, which still requires classical methods such as Claisen–type condensations and Wittig–type alkenylations of aldehydes [11–15], (trans)amidations and esterifications of preformed cinnamic esters and acids [16], or the intermolecular Heck coupling of acrylamides and acrylates [17–20]. However, these protocols start from a preformed amide or ester, typically use a high excess of reagent (i.e. strong base or amine/alcohol) to shift the equilibrium towards the desired carboxylate derivative, and, in many cases, do not tolerate sensitive functional groups in the molecule.

Cyclopropenones are highly energetic but stable aromatic ketones, with an increasing number of synthetic protocols in the last years [21–27]. The strained carbonyl group but not the conjugated alkene is expected to preferentially react with hard nucleophiles, in clear contrast

* Corresponding authors.
E-mail addresses: emilio.pardo@uv.es (E. Pardo), anleyva@itq.upv.es (A. Leyva-Pérez).
[1] These author contributed equally to this work.

https://doi.org/10.1016/j.mcat.2022.112228
Received 16 February 2022; Received in revised form 3 March 2022; Accepted 8 March 2022

to typical enones [22,28–30]. Besides, cyclopropenones will not suffer equilibrium shifts as esters or acids do after amine and alcohol addition, since the strongly thermodynamically favored strain release of the cyclopropane ring (-67 kcal·mol^{-1}) will drive the reaction irreversible towards the desired cinnamyl derivative [31]. This reactive hypothesis has, to our knowledge, been little explored in the open literature [32, 33], only for phenols [34] and, in some cases, to generate imines and trigger cyclic rearrangements [22,35,36], or for bio–orthogonal functionalization with phosphines [37]. With all these precedents in mind, and inspired by the archetypical click reaction (CuAAC), Fig. 1 also shows the novelty of this work, which consists in the ring–opening of cyclopropenones with amines and alcohols, which can also be named as hydroamination and hydroalkoxylation of cyclopropenones, respectively, as a potentially feasible and full–atom economy alternative reaction for a general synthesis of cinnamides and cinnamic esters. Besides, our work here will show that not only simple Cu^{2+}salts but also Cu^{2+}–containing metal–organic frameworks (MOFs) are catalytically competent for the reactions, and that other catalytic metals can be incorporated in the MOF structure and engage different reactions in one–pot.

2. Materials and methods

All chemicals were of reagent grade quality. Reagents and solvents were obtained from commercial sources and were used without further purification otherwise indicated. $Ni^{II}_2\{Ni^{II}_4[Cu^{II}_2(Me_3mpba)_2]_3\} \cdot 54H_2O$ (**NiCuMOF**) and $[Pd_4]_{0.5}@Na_3\{Ni^{II}_4[Cu^{II}_2(Me_3mpba)_2]_3\} \cdot 56H_2O$ (**PdCuMOF**) were prepared as reported previously (see main text). Cyclopropenones were prepared according to reported procedures (see SM). No unexpected or unusually high safety hazards were encountered.

Synthesis of $[Pd^{II}(NH_3)_4]\,Ni^{II}\{Ni^{II}_4\,[Cu^{II}_2(Me_3mpba)_2]_3\} \cdot 52H_2O$ (PdNiCuMOF). Well-formed dark green prisms of **PdNiCuMOF**, which were suitable for X-ray diffraction, were obtained by immersing crystals of **NiCuMOF** (*ca.* 5 mg, 0.0015 mmol) for 24 h in 5 mL of $[Pd(NH_3)_4]Cl_2$ aqueous solutions (0.003 mmol). Alternatively, a multigram scale procedure was also carried out by using the same synthetic procedure but with greater amounts of both, a powder sample of compound **PdNiCuMOF** (5 g, 1.45 mmol) and $[Pd(NH_3)_4]Cl_2$ (1.067 g, 2.9 mmol), with the same successful results and a high yield (4.91 g, 96%). Anal.: calcd (%) for $Cu_6Ni_5PdC_{78}H_{176}N_{16}O_{88}$ (**PdNiCuMOF**) (MW: 3527.45): C, 26.56; H, 5.03; N, 6.35. Found: C, 25.68; H, 5.01; N, 6.34. IR (KBr): ν = 3011, 2956 and 2917 cm^{-1} (C–H), 1607 cm^{-1} (C=O).

General procedure for the synthesis of cinnamates or cinnamamides. 0.7 mmol of the corresponding cyclopropenone were inserted in a glass vial with either $Cu(OAc)_2$ (1-2 mol%) or NiCuMOF (10 mol%), toluene (0.5 M final dilution respect to the cyclopropenone reactant) and the corresponding alcohol or amine (0.35 mmol). The solution was left overnight at 100 °C and at the end was quenched with water (5 ml). Then, the mixture was extracted with EtOAc (3 × 5 ml) and the organic layers were washed with water (5 ml) and brine (5 ml). Afterwards, the organic phase was dried over $MgSO_4$, filtered and concentrated under vacuum. The resulting mixture was purified by either thin-layer chromatography (TLC) or flash chromatography with the appropriate AcOEt/*n*-hexanes mixture.

3. Results and Discussion

3.1. Hydroamination and hydroalkoxylation of cyclopropenones with catalytic Cu^{2+} salts

3.1.1. Hydroamination reaction

Table 1 shows the results for the reaction between diphenylcyclopropenone **1a** and *n*–octylamine **2a** under ambient conditions, followed by gas chromatography (GC). The coupling reaction proceeds to the desired cinnamide **3a** in quantitative yields after 2–3 h, with similar reaction rates for all solvents tested (~0.03 s^{-1}), including water at pHs between 4.8 and 14.0, and brine, which supports the potential applicability of this reaction in biological systems [6,38,39]. The addition of catalytic amounts of $Cu(OAc)_2$ or the increase of the reaction temperature shortens the reaction time to just few minutes (reaction rate ~0.15 s^{-1}), while keeping a complete selectivity towards cinnamide **3a**. Notice that, under the heating reaction conditions, all reagents and catalyst are fully soluble. These results showcase the generality of the reaction under a plethora of reaction conditions, in line with typical click reactions.

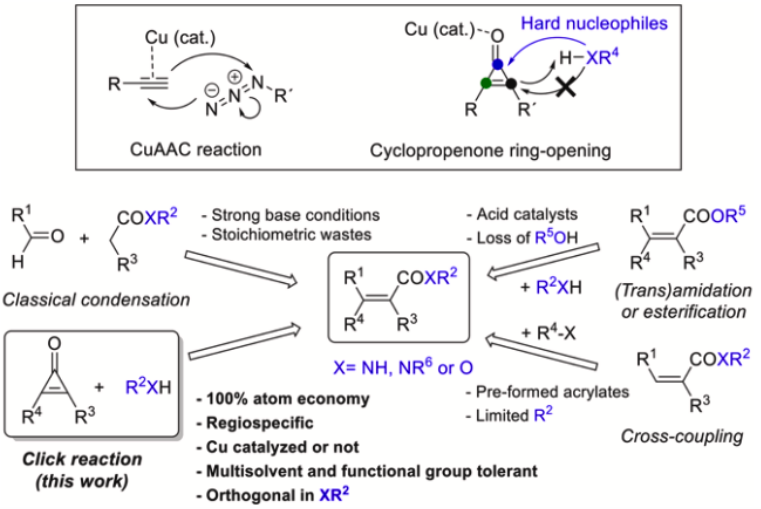

Fig. 1. Huisgen (or CuAAC) reaction and its parallelism with the here reported cyclopropenone ring–opening (click reaction), and comparison with the main synthetic methods for cinnamides and cinnamates.

Table 1
Ring–opening of diphenylcyclopropenone 1a with *n*–octylamine 2a. [a] $Cu(OAc)_2$ (2 mol%) as a catalyst. [b] pHs were set to the indicated values with HOAc/KOAc mixtures, except for pH 11.5 (Na_2CO_3) and pH 14 (KOH). GC yields.

Entry	Solvent	T (°C)	Time (min)	3a (%)
1	Toluene	25	210	94
2[a]		25	10	91
3		50	210	99
4		75	60	99
5		100	10	98
6	*n*–Hexane	25	135	>99
7	DCM			71
8	Diethyl ether			>99
9	CH_3CN			93
10	DMF			>99
11	EtOH			36
12	Water			99
13[a]	Water		10	99
14[b]	Water pH 2.4		135	22
15[b]	Water pH 4.8			99
16[b]	Water pH 9.3			92
17[b]	Water pH 11.5			99
18[b]	Water pH 14.0			99
18	Brine			82

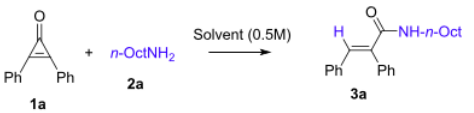

Fig. 2 shows that three different cyclopropenones **1a–c** and different alkyl amines **2a–g** react in the presence of catalytic $Cu(OAc)_2$ (2 mol%) to give cinnamides **3a–i** in moderate to good yields. In these cases, the presence of the Cu catalyst was needed not only to boost the reaction rate but also to increase the selectivity towards the cinnamide products, otherwise parasite reactions take over. *Cis*–olefins are exclusively formed because the reaction goes through a concerted addition of the amine to the double bond, with the Cu^{2+} catalyst coordinating the carbonyl rather than the alkene group, thus by-passing any final dehydrometalation reaction (see Fig. 8 ahead).

3.1.2. Hydroamination vs hydroalkoxylation reaction

Fig. 2 also shows that aniline **4a**, octyl alcohol **5a** and phenol **6a** react with **1a** only when $Cu(OAc)_2$ is added in catalytic amounts, to give 25%, >99% and 60% yield of cinnamyl derivatives **7a, 8a** and **9a**, respectively. Other Cu^{2+} and Cu^{+} salts were similarly effective for the hydroalkoxylation of **1a** with **5a** (Table S1). Notice that no reductant agents such as ascorbic acid are required, in contrast to the most representative CuAAC reaction protocol. The activation energy (E_a) for the coupling of each nucleophile with **1a** catalyzed by a 5 mol% of Cu $(OAc)_2$ was calculated by kinetic measurements at different temperatures (25, 50, 75 and 100 °C), based on the initial rates of the reaction, and the results show that the E_a = <1.0, 11.1, 13.9 and 34.8 kcal·mol^{-1} for octylamine **2a**, phenol **6a**, aniline **4a** and octyl alcohol **5a**, respectively. This reactive trend (alkyl amines >> phenols > aromatic amines >> alkyl alcohols) roughly follows the expected nucleophilicity of each partner and is inversely proportional to the corresponding pK_a (35, 18, 31 and 30, respectively). Notice that the E_a values do not mathematically correlate with the *p*Ka values, it is just an estimation, and that the E_a calculated for the uncatalyzed reaction of **1a** with **2a** is 5.0 kcal·mol^{-1}, thus the addition of catalytic Cu^{2+} decreases at least five times the E_a of the reaction. These significant reactivity differences among nucleophiles suggest that the hydroamination and hydroalkoxylation of cyclopropenones can be carried out in a modular way, by simply adjusting the amount of catalyst and reaction conditions Fig. 3. shows that, by using ethanolamine as a bidentate nucleophile, we could obtain the hydroaminated/alkoxylated product **10b** after two consecutive hydroadditions to cyclopropenones **1b** and **1a,** respectively, employing or not $Cu(OAc)_2$ as a catalyst. This result confirms the orthogonality of the hydroamination / hydroalkoxylation reaction of cyclopropenones under the present reaction conditions.

Fig. 4 shows that aromatic amines are less reactive and require a 10 mol% of Cu catalyst to engage reasonably well in the cyclopropenone–opening reaction, as shown for aromatic cinnamides **7a–i**.

3.1.3. Hydroalkoxylation reaction

Fig. 5 shows the results for the hydroalkoxylation of cyclopropenones catalyzed by a 2 mol% of $Cu(OAc)_2$ (results in parentheses). As it can be seen, water [hydration reaction, product (**8b**)], different benzyl alcohols (**8f–h**), allyl alcohol **8i**, and different propargyl, alkenyl, amine, ketal and halogen–substituted alkyl alcohols (**8i–p**), and also alcohols containing complex natural products such as estradiol (**8q**), cholesterol (**8r**) and sphingomyelin (**8s**), gave good yields of the corresponding esters with cyclopropenone **1a**. Complementary, cyclopropenones bearing a methyl instead of a phenyl group (**1b**), only one phenyl group (**1d**) and *p*–nitrosubstituted phenyl rings (**1e**) were also reactive with a variety of alcohols, including alkyl (**8t, 8w, 8y–z**), alkynyl (**8u, 8aa**), tertiary amine–substituted (**8v**), ketal protected (**8x**) and alkenyl (**8ab**) alcohols. These results strongly suggest that the reactivity and chemoselectivity of alcohols is enhanced respect to most of the amines (compare with the above results) in the presence of the Cu^{2+} catalyst. In view of this, we envisioned the preparation of a Cu^{2+} supported catalyst, able to perform the reaction, with improved recyclability/reusability.

3.2. Metal organic frameworks (MOFs) as suitable solid catalysts for the hydroalkoxylation of cyclopropenones

3.2.1. Synthesis and characterization of Cu^{2+}–MOFs

Aiming at confirming that the described catalytic activity of Cu^{2+} cations can be extended to heterogeneous catalysis and intending to extend such results to one–pot catalysis, we used a type of porous materials –the so–called Metal–Organic Frameworks (MOFs) [40–44] whose potential in catalysis has already been widely demonstrated [45–49] to encapsulate such catalytically active metal species. In particular, we have prepared novel Multimetal–Organic Frameworks (M–MOFs) [50–54] containing three potential different metal active sites (Cu, Ni, Pd), located in both, the framework and also hosted in their channels.

Fig. 6 shows the porous crystal structure of the starting $[Ni(H_2O)_6]^{2+}$–MOF of formula $Ni^{II}_2\{Ni^{II}_4[Cu^{II}_2(Me_3mpba)_2]_3\} \cdot 54H_2O$; Me_3mpba_{4-} = *N,N'*–2,4,6–trimethyl–1,3–phenylenebis(oxamate) (NiCu–MOF, Fig. 6a) [55], the new crystal structure of MOF $[Ni(H_2O)_6]^{2+}$/$[Pd(NH_3)_4]^{2+}$–MOF with formula: $[Pd^{II}(NH_3)_4]Ni^{II}\{Ni^{II}_4[Cu^{II}_2(Me_3mpba)_2]_3\} \cdot 52H_2O$ after the PS cation exchange(PdNiCuMOF, Fig. 6b), and also the structure of the previously reported MOF where all Ni^{2+} cations are substituted by Pd^{2+} ones and then reduced to form $[Pd_4]^{2+}$ nanoclusters with formula $[Pd_4]_{0.5}@Na_3\{Ni^{II}_4[Cu^{II}_2(Me_3mpba)_2]_3\} \cdot 56H_2O$ (PdCuMOF, Fig. 6C) [56]. The previously reported ox-amato–based [57–61] three–dimensional (3D) NiCuMOF possesses accessible Cu^{2+} sites, which are located in the anionic coordination framework and Ni^{2+} cations situated in the channels (Fig. 6a). Synchrotron single crystal X–ray crystallography (SC–XRC) could be employed to un-derpin $[Ni(H_2O)_6]^{2+}$ and $[Pd(NH_3)_4]^{2+}$ cationic complexes inside the new nanoporous PdNiCuMOF material, and its crystal structure unambiguously shows that the $[Pd(NH_3)_4]^{2+}$ and $[Ni(H_2O)_6]^{2+}$ units are hosted in the two types of channels present in the anionic framework (Fig. 6b).

The larger octagonal pores –also accessible for catalysis (*vide infra*)– host both $[Ni(H_2O)_6]^{2+}$ and $[Pd(NH_3)_4]^{2+}$ units with the latter stabilized in sites close to the walls of the network. This evidence further supports an intrinsic stabilizing effect of MOF's confined space. The small square hindered channels retains only $[Ni(H_2O)_6]^{2+}$ as in the structure of the precursor **NiCuMOF**, confirming the lesser accessibility of these pores for cation exchange. The tetra–ammonium Pd(II) monomers exhibit

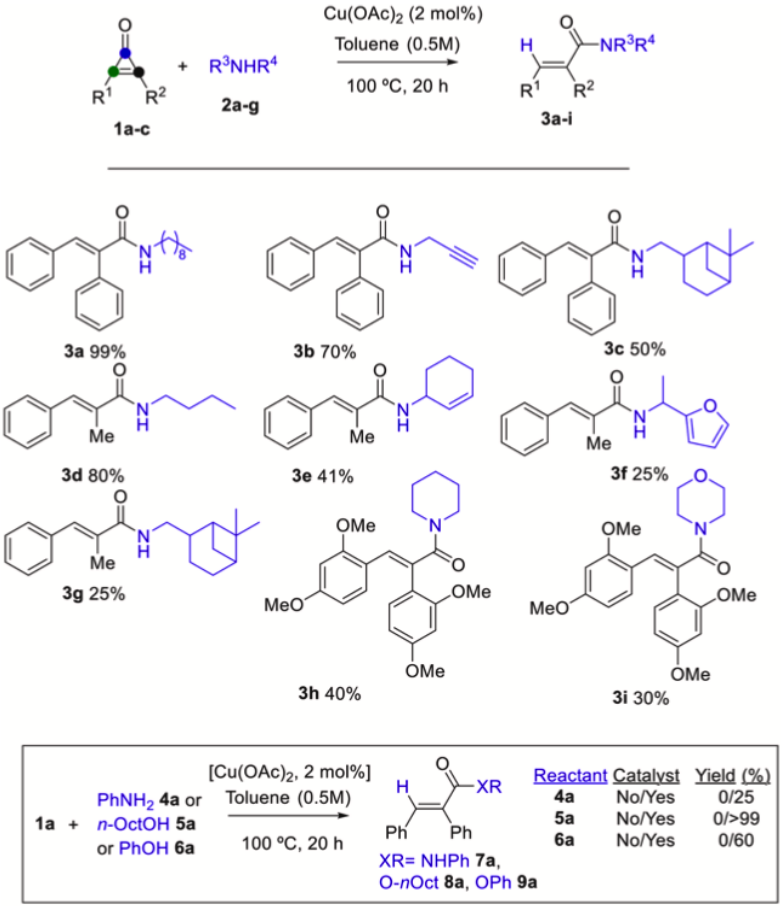

Fig. 2. Ring–opening of cyclopropenones **1a–c** with alkyl amines **2a–g** in the presence of $Cu(OAc)_2$ (2 mol%). The inset at the bottom shows the ring–opening of cyclopropenone **1a** with different nucleophiles. Isolated yields.

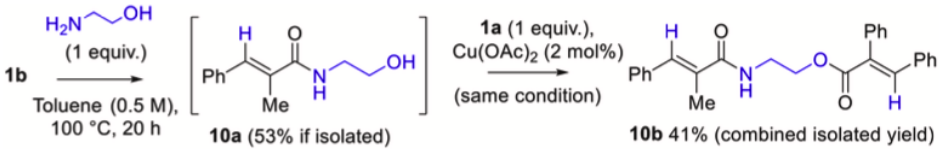

Fig. 3. Modular reactivity using ethanolamine as a bidentate nucleophile.

Pd–NH_3 bond distances [1.86(2) to 1.98(2) Å], very similar to those previously reported [56]. The larger octagonal hydrophilic channels of the MOF contain a much larger accessible void space (size of *ca.* 2.2 nm), which makes them as the first candidate to cation exchanges, leaving the small square channels fully occupied by the $[Ni(H_2O)_6]^{2+}$ monomers exactly as in **NiCuMOF** (Fig. 6a and b). Apart from electrostatic interactions between Pd(II) units and the anionic framework, all $[Pd(NH_3)_4]^{2+}$ cations are hydrogen–bonded through the carboxylate oxygen atoms of the framework and ammonia molecules of the Pd(II) environment [$N_{ammonia}\cdots O_{oxamate}$ varying in the range 2.93(2)–3.07(2) Å] to the anionic framework which further fixes and stabilizes them within the pores (dashed lines in Fig. 6b, see also Figs. S1–S6).

These direct crystallographic visualizations of the postsynthetic incorporation –within the channels of the MOF– of $[Pd(NH_3)_4]^{2+}$ cations, with a stoichiometrically–guided to be partial (50% of nickel) cation exchange, unquestionably underlines how the interplay between hydrophilic channels and the vastly solvated confined nanospace governs the exchange process, ensuring the maintenance of all kind of species, and safeguarding the final captured moieties stabilizations. Once more, synergies between MOF's crystallinity and cutting–edge crystallographic methods afford precious insights into the unorthodox chemistry with can be performed within confined spaces of MOFs.

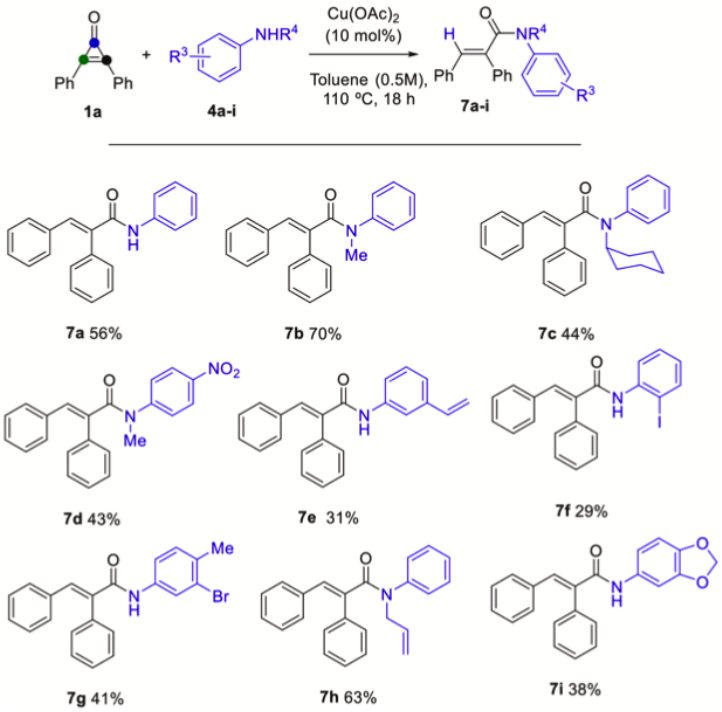

Fig. 4. Ring–opening of cyclopropenones **1a** with aromatic amines **4a–i** catalyzed by $Cu(OAc)_2$ (10 mol%). Isolated yields.

The chemical identity of **PdNiCuMOF** was further established by elemental analyses (C, H, S, N), inductively coupled plasm–mass spectrometry (ICP–MS), X–ray photoelectron spectroscopy (XPS) (Fig. 7a), electronic microscopy, powder X–ray diffraction (PXRD) (Fig. 7b), thermo–gravimetric (TGA) analyses (Fig. S7) and single crystal X–ray diffraction (Table S2).

Fig. 7a shows the XPS spectra of **PdNiCuMOF**. The Pd3d line is the typical doublet with binding energies (BE) for the $Pd3d_{5/2}$ and $Pd3d_{3/2}$ peaks of 338.6 and 343.0 eV, respectively, typical of Pd^{2+} cations, which is in good agreement to other reported values [56].

The experimental powder X–ray diffraction (PXRD) patterns of **PdNiCuMOF**, together with those of the previously reported **NiCuMOF** [55] and **PdCuMOF** [56] for the sake of comparison, can be observed in Fig. 7b. In each case, the experimental patterns (solid lines) are identical to the theoretical ones (bold lines), confirming the pureness and homogeneity of the samples. The solvent contents of **PdNiCuMOF** were confirmed by thermogravimetric analysis (TGA) (Fig. S7).

Fig. 7c shows the N_2 adsorption isotherm at 77 K of **PdNiCuMOF** (blue line) compared to those of compounds **NiCuMOF** and **PdCuMOF** (red and green lines, respectively), which confirms its permanent porosity. Remarkably, the permanent porosity for **PdNiCuMOF** is higher than **NiCuMOF** and approximately double that of **PdCuMOF**. This feature suggests higher accessible surface and structural stability for **PdNiCuMOF**. In contrast, the presence of the bulkier tetranuclear Pd clusters in **PdCuMOF** (Fig. 6c) may preclude access of the reactants to Cu^{2+} sites during the catalytic experiments.

3.2.2. *Hydroalkoxylation of cyclopropenones with Cu^{2+}–MOFs*

The isolated yields of different esters in Fig. 5 (without parentheses) show that **NiCuMOF** catalyzes the click reaction of cyclopropenone **1a** with water (**8b**), phenols (**9a–d**), benzyl (**8c,d** and **8f–h**), phenethyl (**8e**), allyl (**8i**), homopropargyl (**8j**) and linear primary alcohols containing sensitive functionalities (**8l–m**), secondary alcohols either linear or cyclic (**8n–o**), and natural products such as geraniol (**8p**). Bigger products do not penetrate in the microporous MOF solid. The alcohol is added in all cases selectively across the cyclopropenone bond in good to excellent yields, with easy–to–migrate alkenes and chiral carbon–oxygen bonds remaining untouched during the course of the reaction. Remarkably, we observed that the catalytic activity of the framework Cu^{2+} cations persisted in **PdNiCuMOF** but not in **PdCuMOF**, in line with the higher accessibility to the Cu^{2+} sites for the former, observed during the characterization measurements (vide supra). Other Ni and Pd catalysts including NiX_2 (X=OAc, NO_3, SO_4) and $PdCl_2(PPh_3)_2$, $Pd(PPh_3)_4$, $Pd[P(o–tolyl)_3]_4$, $PdOAc_2(SPhos)_2$, and also oxime palladacycles, were tested without success (yield <1%), strongly supporting that the Cu^{2+} cations of the MOFs are the catalytic active species for the hydroalkoxylation reaction. The fact of having the Cu^{2+} in the solid framework and using non–polar toluene as solvent of the reaction, precludes a significant leaching of the active species (Fig. S8), which allowed to reuse **NiCuMOF** at least five times without significant depletion in the final yield of product **8o** after 18 h reaction time (75% after 5 uses), however, accompanied by a significant decrease of the initial rate from use to use (kinetic points for the initial 1 h reaction time, Fig. S8). These results illustrate the advantages of using a Cu^{2+}–containing solid catalyst for the hydroalkoxylation of cyclopropenones.

3.3. *Proposed mechanism for the Cu^{2+}–catalyzed hydroalkoxylation of cyclopropenones*

Fig. 8 shows a plausible mechanism for the click amidations and esterifications on the basis of kinetic, isotopic, and reactivity experiments.

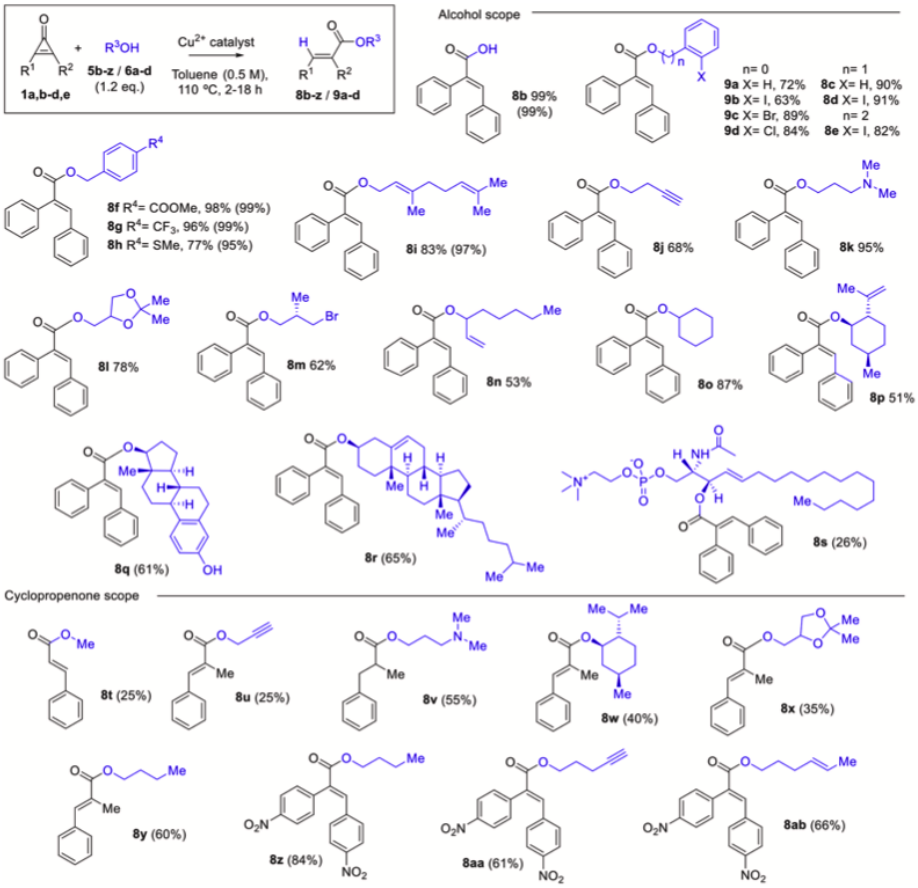

Fig. 5. Synthesis of cinnamate products by hydroalkoxylation of cyclopropenones, catalyzed by either soluble $Cu(OAc)_2$ (2 mol%, yields between parentheses) or insoluble **NiCuMOF** (10 mol%, yields without parentheses). Isolated yields. The major product for non–symmetric cyclopropenones is shown.

A kinetic isotopic effect (KIE)= 1.1 was calculated when CD_3OD was used as a reagent, which discards any role of the H atom during the rate–limiting step of the reaction. Considering that no inversed KIE value is found and the fact that the H atom of MeOH adds untouched on the final cinnamate product in the presence of additional D_2O, and complementary, the D atom of CD_3OD adds untouched when H_2O is present in the reaction mixture, a concerted rather than a stepwise addition across the C—C bond must be accepted.

3.4. One–pot hydroalkoxylation of cyclopropenones / cross coupling reactions

3.4.1. One–pot cyclopropenone hydration / Chan–Lam coupling reaction catalyzed by NiCuMOF

The presence of different catalytically active metal sites in **NiCuMOF** and **PdNiCuMOF** invites to carry out consecutive reactions where each metal catalyzes one step, *i.e.* one–pot hydroalkoxylation / cross coupling reactions Fig. 9. shows that the one–pot cyclopropenone hydration / Chan–Lam coupling reaction proceeds with catalytic amounts of **NiCuMOF** to give the corresponding aromatic esters **12a–d**, after formation of intermediate **8b** (Fig. S9). The Chan–Lam coupling is severelly inhibited after exchanging Ni^{2+} by either Fe^{3+} or Pd^{2+} in the MOF (Table S3)[60], which confirms the catalytic action of Ni^{2+} for the coupling [62]. Besides, the direct coupling of the boronic acid with neither the alkene moiety of **8b** [63] nor of **1a**,[64] to give products **13a–d**, occurs, and the latter only occured in great extent when Pd^{2+} was the exchanged cation (**PdNiCuMOF,** Table S3). KOH was the base of choice from all the bases tested (Table S3). Notice that despiste Cu^{2+} is traditionally active as a catalyst for the Chan–Lam reaction [65], the Cu^{2+} cations, from the framework in **NiCu@MOF**, can not accomodate two different aromatic molecules in its rigid metal coordination sphere and neither perform redox switches, thus being merely inactive for the coupling. Thus, **NiCuMOF** acts here as a bifunctional solid metal catalyst where Cu^{2+} catalyzes the hydration reaction and Ni^{2+} the Chan–Lam coupling.

3.4.2. One–pot cyclopropenone hydration / Mizoroki–Heck coupling reaction catalyzed by PdNiCuMOF

In view that **PdNiCuMOF** is catalytically active for the direct coupling of **1a** and **11a** to give **13a** (89%, entry 3 in Table S3), we tested a one–pot cyclopropenone hydration / Mizoroki–Heck coupling reaction. In this approach, the direct coupling of the alkene with the cyclopropenone cannot occur, thus giving an opportunity for the one–pot reaction to proceed.

Medium size lactones are difficult–to–synthesize molecules,

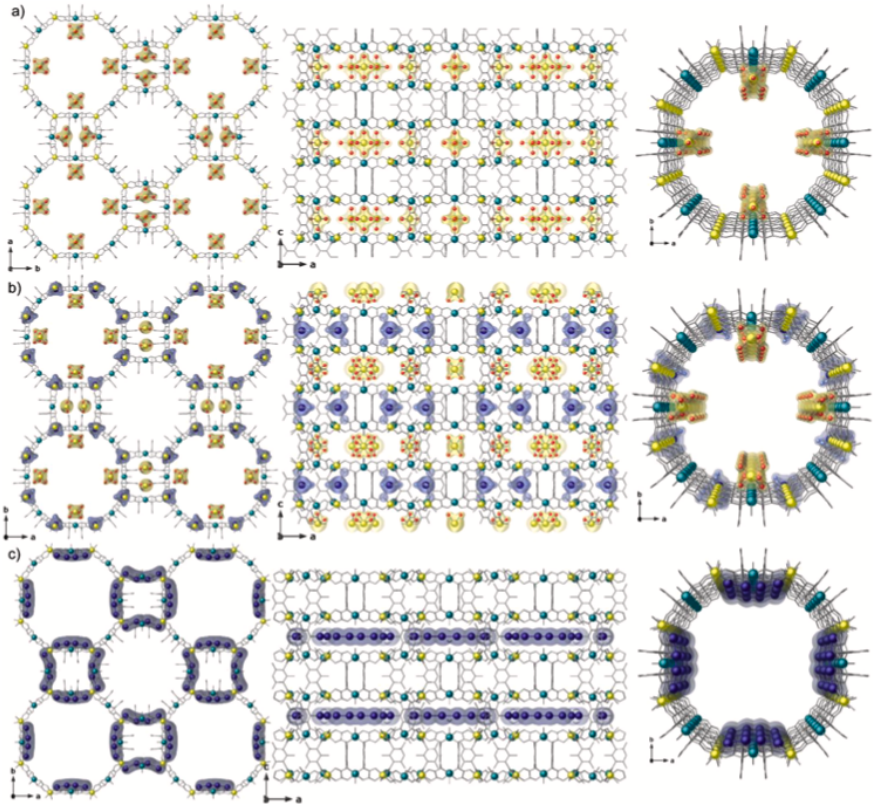

Fig. 6. Views along the *c* (left) and *b* (middle) axes of the crystal structures, determined by synchrotron X–ray diffraction, of the previously reported **NiCuMOF**[55] (a), the novel **PdNiCuMOF** (b) and the also reported **PdCuMOF**[56] (c). Perspective views of one single channel of **NiCuMOF** (a, right) and **PdNiCuMOF** (b, right). The ligands of the coordination 3D network are depicted as grey sticks whereas copper and nickel atoms are represented as cyan and yellow spheres. For the guest species hosted in the channels, nickel and palladium atoms and water and ammonia molecules are represented as yellow, dark blue, red and light blue spheres, respectively. Yellow and blue surfaces are used to highlight the guest Ni and Pd species, respectively, within MOFs channels.

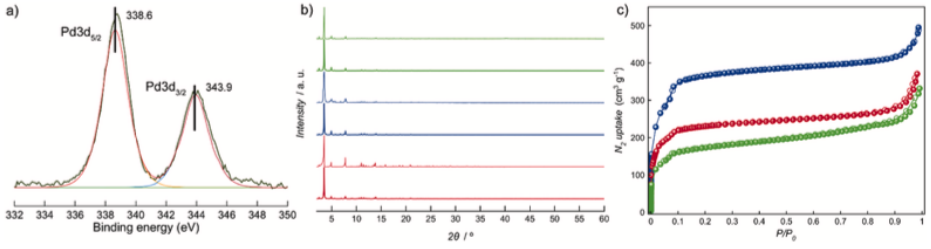

Fig. 7. (a) X–ray photoelectron spectroscopy (XPS) of **PdNiCuMOF**. (b) Calculated (bold lines) and experimental (solid lines) PXRD pattern profiles of **NiCuMOF** (red), **PdNiCuMOF** (blue) and **PdCuMOF** (green) in the 2θ range 2.0–60.0°. (c) N_2 (77 K) adsorption isotherms for the activated compounds **NiCuMOF** (red), **PdNiCuMOF** (blue) and **PdCuMOF** (green). Filled and empty symbols indicate the adsorption and desorption isotherms, respectively. The samples were activated at 70 °C under reduced pressure for 16 hprior to carry out the sorption measurements.

particularly by cross–coupling reactions [66–70]. The lack of straightforward, 100% atom economical and chemoselective synthetic methods for cinnamates translates into the unfeasibility of a straightforward synthesis for medium size lactones by intramolecular Heck reaction [71], since the preparation of cinnamates containing an aryl halide functionality at 5–8 carbon atom distance, ready for coupling, is difficult to find [72–75]. Thus, the one–pot hydroalkoxylation of phenyl cyclopropenone **1d** [21,76] with *ortho*–iodo benzyl and phenethyl alcohol to give products **8ac,d**, respectively, and the corresponding intramolecular Heck reaction, to give mainly the α–coupled exo alkenyl lactone **14a**, was attempted. This product is disfavored according to the cinnamate electronics,[77] however, Fig. 10 shows that the regioirregular Heck

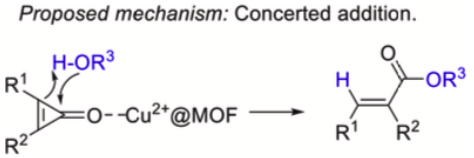

Fig. 8. Proposed mechanism for click amidations and esterifications on the basis of kinetic, isotopic and reactivity experiments.

products **14a** and **c** were the main products of the coupling when using reported conditions in solution. Then, the one–pot reactions with 10 mol % of **PdNiCuMOF** were attempted, and proceeded in reasonable yields to give the regioirregular Heck products, as also shown in Fig. 10. These last results confirm and significantly expands previous work [77,78] with sterically–hindered organopalladium complexes where the high electron–withdrawing nature of acrylates is overridden by the severe steric effects on the catalytic Pd site, which forces the coupling to occur on the electronically–disfavored alpha position [79–83].

Considering the irrelevant role of Ni^{2+} cations in the one–pot hydroalkoxylation / Mizoroki–Heck coupling reaction, seemed reasonable to replace, completely, Ni^{2+} cations by Pd^{2+} ones in order to enhance the efficiency of the catalyst. However, when the 100% of Ni^{2+} cations hosted in the pores are replaced by Pd^{2+} cations and reduced with $NaBH_4$, subnanometer Pd_4 clusters are formed, and the corresponding MOF **PdCuMOF** was not active even for the esterification, which did not proceed. This result is in line with the lack of activity of **PdCuMOF** for the hydration of the cyclopropenone, which can be ascribed to the inaccessibility of the reagents to the Cu^{2+} sites after the Pd cations have been reduced and agglomerated in clusters.

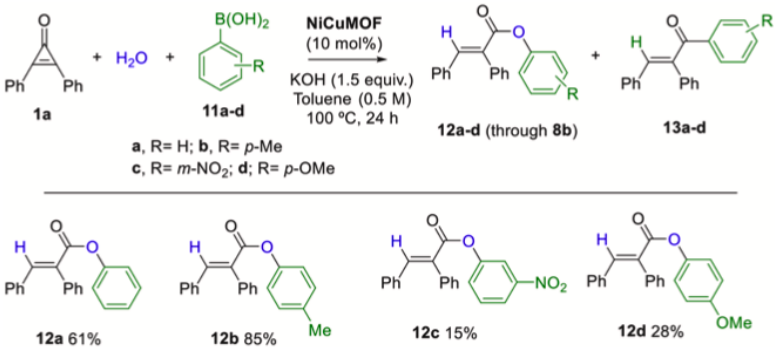

Fig. 9. NiCu@MOF–catalyzed one–pot cyclopropenone hydration / Chan–Lam reaction. Compounds **13a–d** were obtained in <10% yield in all cases.

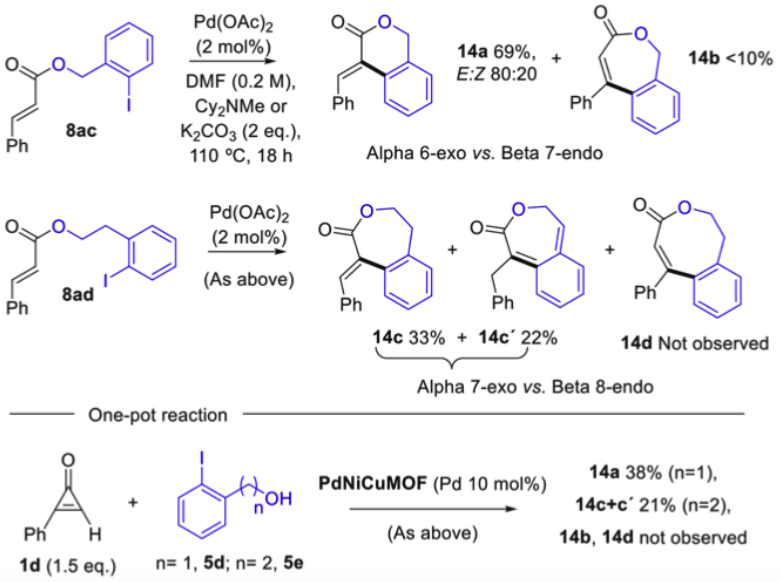

Fig. 10. Intramolecular Heck reaction of *ortho*–iodo substituted cinnamates **8ac** and **8ad** with different Pd catalysts and bases, and one–pot hydroalkoxylation of cyclopropenone **1d** / intramolecular Mizoroki–Heck reaction catalyzed by **PdNiCuMOF**.

4. Conclusions

Different Cu^{2+} salts and Cu^{2+}–MOFs catalyze the hydration, hydroalkoxylation and hydroamination of cyclopropenones to give the corresponding esters and amides in high yields, with 100% atom economy, wide solvent, atmospheric and functional group tolerance, and without any additive or by–product. Multimetallic MOFs (M–MOFs) allow cyclopropenone openings / cross–coupling reactions in one–pot [84–85]. We think that the results here significantly expand the available synthetic methodologies for essential chemicals such as esters and amides, and may open a new line of research in click chemistry.

CRediT authorship contribution statement

Rossella Greco: Methodology, Resources. **Estefanía Tiburcio:** Investigation. **Brenda Palomar-De Lucas:** Resources, Methodology. **Jesús Ferrando-Soria:** Investigation. **Donatella Armentano:** Methodology, Data curation. **Emilio Pardo:** Supervision, Writing – original draft. **Antonio Leyva-Pérez:** Supervision, Writing – original draft.

Declaration of Competing Interest

The authors have no competing interests to declare.

Acknowledgments

This work was supported by the Ministero dell'Istruzione, dell'Università e della Ricerca (Italy) and the MINECO (Spain) (Projects PID2019−104778GB−I00, RTC–2017–6331–5, Severo Ochoa program SEV–2016–0683 and Excellence Unit "Maria de Maeztu" CEX2019−000919−M) and MCIINN (Spain) (Project PID2020–115100GB–I00). D.A. acknowledgs the financial support of the Fondazione CARIPLO / "Economia Circolare: ricerca per un futuro sostenibile" 2019, Project code: 2019–2090, MOCA and Diamond Light Source for awarded beamtime and provision of synchrotron radiation facilities and thank Dr David Allan and Sarah Barnett for their assistance at I19 beamline (Proposal No. CY22411–1). Thanks are also extended to the "2019 Post–doctoral Junior Leader–Retaining Fellowship, la Caixa Foundation (ID100010434 and fellowship code LCF/BQ/PR19/11700011" and "Subvenciones concedidas a la excelencia científica de juniors investigadores, SEJI/2020/034" (J. F.–S.). E.P. acknowledgs the financial support of the European Research Council under the European Union's Horizon 2020 research and innovation programme / ERC Grant Agreement No 814804, MOF–reactors. R. G. thanks ITQ for a contract. E. T. acknowledgs MINECO for a predoctoral grant.

Supplementary materials

Supplementary material associated with this article can be found, in the online version, at doi:10.1016/j.mcat.2022.112228.

References

[1] J.C. Jewett, C.R. Bertozzi, Cu-free click cycloaddition reactions in chemical biology, Chem. Soc. Rev. 39 (2010) 1272–1279, https://doi.org/10.1039/B901970G.
[2] L. Xu, J. Dong, Click chemistry: evolving on the fringe, Chin. J. Chem. 38 (2020) 414–419, https://doi.org/10.1002/cjoc.201900421.
[3] H.C. Kolb, M.G. Finn, K.B. Sharpless, Click chemistry: diverse chemical function from a few good reactions, Angew. Chem. Int. Ed. Engl. 40 (2001) 2004–2021, https://doi.org/10.1002/1521-3773(20010601).
[4] E.M. Sletten, C.R. Bertozzi, Bioorthogonal chemistry: Fishing for selectivity in a sea of functionality, Angew. Chem. Int. Ed. Engl. 48 (2009) 6974–6998, https://doi.org/10.1002/anie.200900942.
[5] R.D. Row, J.A. Prescher, Constructing new bioorthogonal reagents and reactions, Acc. Chem. Res. 51 (2018) 1073–1081, https://doi.org/10.1021/acs.accounts.7b00606, 2018.
[6] A. Gutiérrez-González, P. Destito, J.R. Couceiro, C. Pérez-González, F. López, J. L. Mascareñas, Bioorthogonal azide–thioalkyne cycloaddition catalyzed by photoactivatable ruthenium(II) complexes, Angew. Chem. Int. Ed. 60 (2021) 16059, https://doi.org/10.1002/anie.202103645.
[7] F. Musumeci, S. Schenone, A. Desogus, E. Nieddu, D. Deodato, L. Botta, Click chemistry, a potent tool in medicinal sciences, Curr. Med. Chem. 22 (2015) 2022–2050, https://doi.org/10.2174/0929867322666150421110819.
[8] H.D. Agnew, M.B. Coppock, M.N. Idso, B.T. Lai, J. Liang, A.M. McCarthy-Torrens, C.M. Warren, J.R. Heath, Protein–catalyzed capture agents, Chem. Rev. 119 (2019) 9950–9970, https://doi.org/10.1021/acs.chemrev.8b00660.
[9] F. Himo, T. Lovell, R. Hilgraf, V.V. Rostovtsev, L. Noodleman, K.B. Sharpless, V. V. Fokin, Copper(I)–catalyzed synthesis of azoles. DFT study predicts unprecedented reactivity and intermediates, J. Am. Chem. Soc. 127 (2005) 210–216, https://doi.org/10.1021/ja0471525.
[10] B.T. Worrell, J.A. Malik, V.V. Fokin, Direct evidence of a dinuclear copper intermediate in Cu(I)–catalyzed azide–alkyne cycloadditions, Science 340 (2013) 457–460, https://doi.org/10.1126/science.1229506.
[11] G.A. Grasa, T. Güveli, R. Singh, S.P. Nolan, Efficient transesterification/acylation reactions mediated by N–heterocyclic carbene catalysts, J. Org. Chem. 68 (2003) 2812–2819, https://doi.org/10.1021/jo0267551.
[12] M. Arthuis, A. Lecup, E. Roulland, Pd0–catalyzed carbonylation of 1,1–dichloro–1–alkenes, a new selective access to Z–α–chloroacrylates, Chem. Commun. 46 (2010) 7810–7812, https://doi.org/10.1039/C0CC02517H.
[13] S.S. Weng, C.S. Ke, F.K. Chen, Y.F. Lyu, G.Y. Lin, Transesterification catalyzed by iron(III) β–diketonate species, Tetrahedron 67 (2011) 1640–1648, https://doi.org/10.1016/j.tet.2011.01.009.
[14] V. Lloret, M. Rivero-Crespo, J.A. Vidal-Moya, S. Wild, A. Doménech-Carbó, B.S. J. Heller, S. Shin, H.P. Steinrück, F. Maier, F. Hauke, M. Varela, A. Hirsch, A. Leyva-Pérez, G. Abellán, Few layer 2D pnictogens catalyze the alkylation of soft nucleophiles with esters, Nat. Commun. 10 (2019) 509, https://doi.org/10.1038/s41467-018-08063-3.
[15] D. Nakatake, R. Yazaki, T. Ohshima, Chemoselective transesterification of acrylate derivatives for functionalized monomer synthesis using a hard zinc alkoxide generation strategy, Eur. J. Org. Chem. 2016 (2016) 3696–3699, https://doi.org/10.1002/ejoc.201600737.
[16] B. Narasimhan, D. Belsare, D. Pharande, V. Mourya, A. Dhake, Esters, amides and substituted derivatives of cinnamic acid: synthesis, antimicrobial activity and QSAR investigations, Eur. J. Med. Chem. 39 (2004) 827–834, https://doi.org/10.1016/j.ejmech.2004.06.013.
[17] A.H.M. de Vries, J.M.C.A. Mulders, J.H.M. Mommers, H.J.W. Henderickx, J.G. de Vries, Homeopathic ligand–free palladium as a catalyst in the Heck reaction. A comparison with a palladacycle, Org. Lett. 5 (2003) 3285–3288, https://doi.org/10.1021/ol035184b.
[18] A. Leyva-Pérez, J. Oliver-Meseguer, P. Rubio-Marqués, A. Corma, Water–stabilized three– and four–atom palladium clusters as highly active catalytic species in ligand–free C–C cross–coupling reactions, Angew. Chem. Int. Ed. Engl. 52 (2013) 11554–11559, https://doi.org/10.1002/anie.201303188.
[19] E. Fernández, M.A. Rivero-Crespo, I. Domínguez, P. Rubio-Marqués, J. Oliver-Meseguer, L. Liu, M. Cabrero-Antonino, R. Gavara, J.C. Hernández-Garrido, M. Boronat, A. Leyva-Pérez, A. Corma, Base-controlled Heck, Suzuki, and Sonogashira reactions catalyzed by ligand-free platinum or palladium single atom and sub-nanometer clusters, J. Am. Chem. Soc. 141 (2019) 1928–1940, https://doi.org/10.1021/jacs.8b07884.
[20] A. Francais, A. Leyva, G. Etxebarria-Jardi, S.V. Ley, Total synthesis of the anti–apoptotic agents iso– and bongkrekic acids, Org. Lett. 12 (2010) 340–343, https://doi.org/10.1021/ol902676t.
[21] R. Breslow, J. Posner, A. Krebs, Synthesis of cyclopropenones by a modified Favorskii reaction, J. Am. Chem. Soc. 85 (1963) 234, https://doi.org/10.1021/ja00885a029. –234.
[22] K. Komatsu, T. Kitagawa, Cyclopropenylium cations, cyclopropenones, and heteroanalogues–recent advances, Chem. Rev. 103 (2003) 1371–1427, https://doi.org/10.1021/cr010011q.
[23] M. Nakamura, H. Isobe, E. Nakamura, Cyclopropenone acetals: synthesis and reactions, Chem. Rev. 103 (2003) 1295–1326, https://doi.org/10.1021/cr0100244.
[24] F. Wang, W. Zhang, J. Zhu, H. Li, K.-W. Huang, J. Hu, Chloride ion–catalyzed generation of difluorocarbene for efficient preparation of gem–difluorinated cyclopropenes and cyclopropanes, Chem. Commun. 47 (2011) 2411–2413, https://doi.org/10.1039/C0CC04548A.
[25] P. Rullière, P. Cyr, A.B. Charette, Difluorocarbene addition to alkenes and alkynes in continuous flow, Org. Lett. 18 (2016) 1988–1991, https://doi.org/10.1021/acs.orglett.6b00573.
[26] R.D. Row, H.-W. Shih, A.T. Alexander, R.A. Mehl, J.A. Prescher, Cyclopropenones for metabolic targeting and sequential bioorthogonal labeling, J. Am. Chem. Soc. 139 (2017) 7370–7375, https://doi.org/10.1021/jacs.7b03010.
[27] O.J. Curnow, G.M. Fern, R.J. Pipal, Synthesis of diisopropylcyclopropenone and X–ray structure of its dichlorodimethyltin(IV) adduct, Arkivoc iii (2006) 43–47. http://hdl.handle.net/10092/603.
[28] J. Ciabattoni, G.A. Berchtold, Cycloaddition reaction of enamines with diphenylcyclopropenone, J. Am. Chem. Soc. 87 (1965) 1404–1405.
[29] S. Cunha, A. Kascheres, A semiempirical quantum mechanical approach towards understanding of cyclopropenone reactivity, J. Mol. Struc. THEOCHEM 364 (1996) 45–49, https://doi.org/10.1016/0166-1280(95)04453-1.
[30] X. Li, C. Han, H. Yao, A. Lin, Organocatalyzed [3 + 2] annulation of cyclopropenones and β–ketoesters: an approach to substituted butenolides with a quaternary center, Org. Lett. 19 (2017) 778–781, https://doi.org/10.1021/acs.orglett.6b03737.

[31] A. Greenberg, R.P.T. Tomkins, M. Dobrovolny, J.F. Liebman, The strain energy of diphenylcyclopropenone: a reexamination, J. Am. Chem. Soc. 105 (1983) 6855–6858, https://doi.org/10.1021/ja00361a018.
[32] A. Kascheres, J.A.R. Rodrigues, Reaction of diphenylcyclopropenone with 2–aminopyridines. Synthetic and mechanistic implications, J. Org. Chem. 40 (1975) 1440–1444, https://doi.org/10.1021/jo00898a013.
[33] T. Eicher, R. Graf, H. Konzmann, R. Pick, Synthese und reaktionen von 2,3–diaryl– und 2,3–dialkylcyclopropenoniminen, Synthesis 1987 (1987) 887–892.
[34] T. Nanda, P.C. Ravikumar, A palladium–catalyzed cascade c–c activation of cyclopropenone and carbonylative amination: easy access to highly functionalized maleimide derivatives, Org. Lett. 22 (2020) 1368–1374, https://doi.org/10.1021/acs.orglett.9b04656.
[35] C. Kascheres, A. Kascheres, P.S.H. Pilli, Reaction of diphenylcyclopropenone with primary and secondary enaminones. Synthetic and mechanistic implications, J. Org. Chem. 45 (1980) 5340–5343.
[36] T.K. Heiss, J.A. Prescher, Cyclopropeniminium ions exhibit unique reactivity profiles with bioorthogonal phosphines, J. Org. Chem. 84 (2019) 7443–7448, https://doi.org/10.1021/acs.joc.9b00518.
[37] T. Eicher, S. Böhm, H. Ehrhardt, R. Harth, D. Lerch, Zur reaktion von diphenylcyclopropenon, seinen funktionellen derivaten und imoniumsalzen mit aminen, Liebigs Ann. 1981 (1981) 765–788.
[38] F. Friscourt, C.J. Fahrni, G.J. Boons, A fluorogenic probe for the catalyst–free detection of azide–tagged molecules, J. Am. Chem. Soc. 134 (2012) 18809–18815, https://doi.org/10.1021/ja309000s.
[39] C. Favre, L. de Cremoux, J. Badaut, F. Friscourt, Sydnone reporters for highly fluorogenic copper–free click ligations, J. Org. Chem. 83 (2018) 2058–2066, https://doi.org/10.1021/acs.joc.7b03004.
[40] O.M. Yaghi, G. Li, H. Li, Selective binding and removal of guests in a microporous metal–organic framework, Nature 378 (1995) 703–706, https://doi.org/10.1038/378703a0.
[41] H. Furukawa, K.E. Cordova, M. O'Keeffe, O.M. Yaghi, The chemistry and applications of metal–organic frameworks, Science 341 (2013), 1230444, https://doi.org/10.1126/science.1230444.
[42] G. Maurin, C. Serre, A. Cooper, G. Férey, The new age of MOFs and of their porous–related solids, Chem. Soc. Rev. 46 (2017) 3104–3107, https://doi.org/10.1039/C7CS90049J.
[43] A. Kirchon, L. Feng, H.F. Drake, E.A. Joseph, H.C. Zhou, From fundamentals to applications: a toolbox for robust and multifunctional MOF materials, Chem. Soc. Rev. 47 (2018) 8611–8638, https://doi.org/10.1039/C8CS00688A.
[44] S. Kitagawa, R. Matsuda, Chemistry of coordination space of porous coordination polymers, Coord. Chem. Rev. 251 (2007) 2490–2509, https://doi.org/10.1016/j.ccr.2007.07.009.
[45] M. Viciano-Chumillas, M. Mon, J. Ferrando-Soria, A. Corma, A. Leyva-Pérez, D. Armentano, E. Pardo, Metal–organic frameworks as chemical nanoreactors: synthesis and stabilization of catalytically active metal species in confined spaces, Acc. Chem. Res. 53 (2020) 520–531, https://doi.org/10.1021/acs.accounts.9b00609.
[46] R.J. Young, M.T. Huxley, E. Pardo, N.R. Champness, C.J. Sumby, C.J. Doonan, Isolating reactive metal–based species in metal–organic frameworks – viable strategies and opportunities, Chem. Sci. 11 (2020) 4031–4050, https://doi.org/10.1039/D0SC00485E.
[47] D. Yang, B.C. Gates, Catalysis by metal organic frameworks: perspective and suggestions for future research, ACS Catal. 9 (2019) 1779–1798, https://doi.org/10.1021/acscatal.8b04515.
[48] A. Dhakshinamoorthy, Z. Li, H. Garcia, Catalysis and photocatalysis by metal organic frameworks, Chem. Soc. Rev. 47 (2018) 8134–8172, https://doi.org/10.1039/C8CS00256H.
[49] J. Gascon, A. Corma, F. Kapteijn, F.X. Llabrés i Xamena, Metal organic framework catalysis: quo vadis? ACS Catal. 4 (2014) 361–378, https://doi.org/10.1021/cs400959k.
[50] C. Castillo-Blas, F. Gándara, Metal–organic frameworks incorporating multiple metal elements, Isr. J. Chem. 58 (2018) 1036–1043, https://doi.org/10.1002/ijch.201800085.
[51] M.J. Kalmutzki, N. Hanikel, O.M. Yaghi, Secondary building units as the turning point in the development of the reticular chemistry of MOFs, Sci. Adv. 4 (2018) eaat9180, https://doi.org/10.1126/sciadv.aat9180.
[52] M.Y. Masoomi, A. Morsali, A. Dhakshinamoorthy, H. Garcia, Mixed–metal MOFs: unique opportunities in metal–organic framework (MOF) functionality and design, Angew. Chem. Int. Ed. Engl. 58 (2019) 15188–15205, https://doi.org/10.1002/ange.201902229.
[53] R. Rajak, R. Kumar, S.N. Ansari, M. Saraf, S.M. Mobin, Recent highlights and future prospects on mixed–metal MOFs as emerging supercapacitor candidates, Dalton Trans. 49 (2020) 11792–11818, https://doi.org/10.1039/D0DT01676D.
[54] Z.H. Syed, F. Sha, X. Zhang, D.M. Kaphan, M. Delferro, O.K. Farha, Metal–organic framework nodes as a supporting platform for tailoring the activity of metal catalysts, ACS Catal. 10 (2020) 11556–11566, https://doi.org/10.1021/acscatal.0c03056.
[55] T. Grancha, J. Ferrando-Soria, H.C. Zhou, J. Gascon, B. Seoane, J. Pasán, O. Fabelo, M. Julve, E. Pardo, Postsynthetic improvement of the physical properties in a metal–organic framework through a single crystal to single crystal transmetallation, Angew. Chem. Int. Ed. Engl. 54 (2015) 6521–6525, https://doi.org/10.1002/ange.201501691.
[56] F.R. Fortea-Pérez, M. Mon, J. Ferrando-Soria, M. Boronat, A. Leyva-Pérez, A. Corma, J.M. Herrera, D. Osadchii, J. Gascon, D. Armentano, E. Pardo, The MOF–driven synthesis of supported palladium clusters with catalytic activity for carbene–mediated chemistry, Nat. Mater. 16 (2017) 760–766, https://doi.org/10.1038/nmat4910.
[57] T. Grancha, J. Ferrando-Soria, M. Castellano, M. Julve, J. Pasán, D. Armentano, E. Pardo, Oxamato–based coordination polymers: recent advances in multifunctional magnetic materials, Chem. Commun. 50 (2014) 7569–7585, https://doi.org/10.1039/C4CC01734J.
[58] R. Adam, M. Mon, R. Greco, L.H.G. Kalinke, A. Vidal-Moya, A. Fernandez, R.E. P. Winpenny, A. Doménech-Carbó, A. Leyva-Pérez, D. Armentano, E. Pardo, J. Ferrando-Soria, Self-assembly of catalytically active supramolecular coordination compounds within metal-organic frameworks, J. Am. Chem. Soc. 141 (2019) 10350–10360, https://doi.org/10.1021/jacs.9b03914.
[59] M. Mon, R. Adam, J. Ferrando−Soria, A. Corma, D. Armentano, E. Pardo, A. Leyva−Pérez, Stabilized $Ru[(H_2O)_6]^{3+}$ in confined spaces (MOFs and zeolites) catalyzes the imination of primary alcohols under atmospheric conditions with wide scope, ACS Catal. 8 (2018) 10401–10406, https://doi.org/10.1021/acscatal.8b03228.
[60] M. Tejeda-Serrano, M. Mon, B. Ross, F. Gonell, J. Ferrando-Soria, A. Corma, A. Leyva-Pérez, D. Armentano, E. Pardo, Isolated Fe(III)–O sites catalyze the hydrogenation of acetylene in ethylene flows under front–end industrial conditions, J. Am. Chem. Soc. 140 (2018) 8827–8832, https://doi.org/10.1021/jacs.8b04669.
[61] M.A. Rivero-Crespo, M. Mon, J. Ferrando-Soria, C.W. Lopes, M. Boronat, A. Leyva-Pérez, A. Corma, J.C. Hernández-Garrido, M. López-Haro, J.J. Calvino, E.V. Ramos-Fernandez, D. Armentano, E. Pardo, Confined Pt_1^{1+} water clusters in a MOF catalyze the low–temperature water–gas shift reaction with both CO_2 oxygen atoms coming from water, Angew. Chem. Int. Ed. Engl. 57 (2018) 17094–17099, https://doi.org/10.1021/jacs.0c12367.
[62] J. Wang, T. Qin, T.G. Chen, L. Wimmer, J.T. Edwards, J. Cornella, B. Vokits, S. A. Shaw, P.S. Baran, Nickel-catalyzed cross-coupling of redox-active esters with boronic acids, Angew. Chem. Int. Ed. Engl. 55 (2016) 9676–9679, https://doi.org/10.1002/anie.201605463.
[63] W. Chen, L. Sun, X. Huang, J. Wang, Y. Peng, G. Song, Ligand-free nickel-catalysed 1,4-addition of arylboronic acids to α,β-unsaturated carbonyl compounds, Adv. Synth. Catal. 357 (2015) 1474–1482, https://doi.org/10.1002/adsc.201400761.
[64] L. Shan, G. Wu, M. Liu, W. Gao, J. Ding, X. Huang, H. Wu, α,β-Diaryl unsaturated ketones via palladium catalyzed ring-opening of cyclopropenones with organoboronic acids, Org. Chem. Front. 5 (2018) 1651–1654, https://doi.org/10.1039/C8QO00241J.
[65] A. Vijayan, D.N. Rao, K.V. Radhakrishnan, P.Y.S. Lam, P. Das, Advances in carbon–element bond construction under Chan–Lam cross-coupling conditions: a second decade, Synthesis 53 (2021) 805–847, https://doi.org/10.1055/s-0040-1705971.
[66] A. Martins, U. Marquardt, N. Kasravi, D. Alberico, M. Lautens, Synthesis of substituted benzoxacycles via a domino ortho–alkylation/Heck coupling sequence, J. Org. Chem. 71 (2006) 4937–4942, https://doi.org/10.1021/jo06552l.
[67] M.P. Denieul, B. Laursen, R. Hazell, T. Skrydstrup, Synthesis of the benzophenone fragment of balanol via an intramolecular cyclization event, J. Org. Chem. 65 (2000) 6052–6060, https://doi.org/10.1021/jo000750r.
[68] X. Li, B. Zhou, R.Z. Yang, F.M. Yang, R.X. Liang, R.R. Liu, Y.X. Jia, Palladium–catalyzed enantioselective intramolecular dearomative Heck reaction, J. Am. Chem. Soc. 140 (2018) 13945–13951, https://doi.org/10.1021/jacs.8b09186.
[69] M. Lautens, J.F. Paquin, S. Piguel, Palladium–catalyzed sequential alkylation–alkenylation reactions. Application to the synthesis of 2–substituted–4–benzoxepines and 2,5–disubstituted–4–benzoxepines, J. Org. Chem. 67 (2002) 3972–3974, https://doi.org/10.1021/jo0107296.
[70] E. Coya, N. Sotomayor, E. Lete, Intramolecular direct arylation and heck reactions in the formation of medium–sized rings: selective synthesis of fused indolizine, pyrroloazepine and pyrroloazocine systems, Adv. Synth. Catal. 356 (2014) 1853–1865, https://doi.org/10.1002/adsc.201400075.
[71] M. Beller, A. Zapf, Intermolecular Heck reaction: palladium–catalyzed coupling reactions for industrial fine chemicals syntheses, in: E. Negishi (Ed.), Handbook of Organopalladium Chemistry for Organic Synthesis, John Wiley & Sons, Inc., 2002, pp. 1209–1222.
[72] M. Alami, F. Liron, M. Gervais, J.F. Peyrat, J.D. Brion, Ortho substituents direct regioselective addition of tributyltin hydride to unsymmetrical diaryl (or heteroaryl) alkynes: an efficient route to stannylated stilbene derivatives, Angew. Chem. Int. Ed. Engl. 41 (2002) 1578–1580, https://doi.org/10.1002/1521-3757(20020503).
[73] D.V. Kadnikov, R.C. Larock, Palladium–catalyzed carbonylative annulation of internal alkynes: synthesis of 3,4–disubstituted coumarins, J. Org. Chem. 68 (2003) 9423–9432, https://doi.org/10.1021/jo0350763.
[74] S.H. Kwak, S.J. Lim, H.J. Yoo, J.E. Ha, Y.D. Gong, Intramolecular Mizoroki–Heck reaction of 2–thiosubstituted acrylates for the synthesis of 3–substituted benzo[b] thiophene–2–carboxylates, Synthesis 48 (2016) 4131–4142, https://doi.org/10.1055/s-0035-1562613.
[75] H. Madhurima, J. Krishna, G. Satyanarayana, Concise three–step strategy for the synthesis of 2–benzoxepin–3(1H)–ones, Synthesis 47 (2015) 1245–1254, https://doi.org/10.1055/s-0034-1379901.
[76] C. He, S. Guo, L. Huang, A. Lei, Copper catalyzed arylation/C−C bond activation: an approach toward α–aryl ketones, J. Am. Chem. Soc. 132 (2010) 8273–8275, https://doi.org/10.1021/ja1033777.
[77] F. Garnes-Portolés, R. Greco, J. Oliver-Meseguer, J. Castellanos-Soriano, M. Consuelo Jiménez, M. López-Haro, J.C. Hernández-Garrido, M. Boronat, R. Pérez-Ruiz, A. Leyva-Pérez, Regioirregular and catalytic Mizoroki–Heck

Anex: publications related to this thesis

reactions, Nat. Catal. 4 (4) (2021) 293–303, https://doi.org/10.1038/s41929-021-00592-3.
[78] P. Wucher, L. Caporaso, P. Roesle, F. Ragone, L. Cavallo, S. Mecking, I. Göttker-Schnetmann, Breaking the regioselectivity rule for acrylate insertion in the Mizoroki–Heck reaction, Proc. Natl. Acad. Sci. USA 108 (22) (2011) 8955–8959, https://doi.org/10.1073/pnas.1101497108.
[79] I.P. Beletskaya, A.V. Cheprakov, Palladacycles in catalysis – a critical survey, J. Organomet. Chem. 689 (2004) 4055–4082, https://doi.org/10.1016/j.jorganchem.2004.07.054.
[80] C. Nájera, Oxime-derived palladacycles: applications in catalysis, ChemCatChem 8 (2016) 1865–1881, https://doi.org/10.1002/cctc.201600035.
[81] J. Mo, J. Xiao, The Heck reaction of electron–rich olefins with regiocontrol by hydrogen–bond donors, Angew. Chem. Int. Ed. Engl. 45 (2006) 4152–4157, https://doi.org/10.1002/anie.200600799.
[82] L. Qin, X. Ren, Y. Lu, Y. Li, J. Zhou, Intermolecular Mizoroki–Heck reaction of aliphatic olefins with high selectivity for substitution at the internal position, Angew. Chem. Int. Ed. Engl. 51 (2012) 5915–5919, https://doi.org/10.1002/anie.201201806.
[83] A. Fardost, J. Lindh, P.J.R. Sjöberg, M. Larhed, Palladium(II)–catalyzed decarboxylative heck arylations of acyclic electron–rich olefins with internal selectivity, Adv. Synth. Catal. 356 (2014) 870–878, https://doi.org/10.1002/adsc.201301004.
[84] A. Dhakshinamoorthy, A.M. Asiri, H. García, Metal–organic frameworks as multifunctional solid catalysts, Trends Chem. 2 (2020) 454–466, https://doi.org/10.1016/j.trechm.2020.02.00.
[85] A. Dhakshinamoorthy, A.M. Asiri, H. García, Mixed-metal or mixed-linker metal organic frameworks as heterogeneous catalysts, Catal. Sci. Technol. 6 (2016) 5238–5261, https://doi.org/10.1039/C6CY00695G.

PUBLICATION 2

Soluble/MOF-Supported Palladium Single Atoms Catalyze the Ligand-, Additive-, and Solvent-Free Aerobic Oxidation of Benzyl Alcohols to Benzoic Acids.

Estefanía Tiburcio+, Rossella Greco+, Marta Mon, Jordi Ballesteros-Soberanas, Jesús Ferrando-Soria, Miguel López-Haro, Juan Carlos Hernández-Garrido, Judit Oliver-Meseguer, Carlo Marini, Mercedes Boronat, Donatella Armentano, Antonio Leyva-Pérez and Emilio Pardo. J. Am. Chem. Soc. 2021, 143, 6, 2581–2592.

JACS
JOURNAL OF THE AMERICAN CHEMICAL SOCIETY
pubs.acs.org/JACS
Article

Soluble/MOF-Supported Palladium Single Atoms Catalyze the Ligand-, Additive-, and Solvent-Free Aerobic Oxidation of Benzyl Alcohols to Benzoic Acids

Estefanía Tiburcio,[▽] Rossella Greco,[▽] Marta Mon, Jordi Ballesteros-Soberanas, Jesús Ferrando-Soria, Miguel López-Haro, Juan Carlos Hernández-Garrido, Judit Oliver-Meseguer, Carlo Marini, Mercedes Boronat, Donatella Armentano,* Antonio Leyva-Pérez,* and Emilio Pardo*

Cite This: https://dx.doi.org/10.1021/jacs.0c12367
Read Online
ACCESS | Metrics & More | Article Recommendations | Supporting Information

ABSTRACT: Metal single-atom catalysts (SACs) promise great rewards in terms of metal atom efficiency. However, the requirement of particular conditions and supports for their synthesis, together with the need of solvents and additives for catalytic implementation, often precludes their use under industrially viable conditions. Here, we show that palladium single atoms are spontaneously formed after dissolving tiny amounts of palladium salts in neat benzyl alcohols, to catalyze their direct aerobic oxidation to benzoic acids without ligands, additives, or solvents. With this result in hand, the gram-scale preparation and stabilization of Pd SACs within the functional channels of a novel methyl-cysteine-based metal−organic framework (MOF) was accomplished, to give a robust and crystalline solid catalyst fully characterized with the help of single-crystal X-ray diffraction (SCXRD). These results illustrate the advantages of metal speciation in ligand-free homogeneous organic reactions and the translation into solid catalysts for potential industrial implementation.

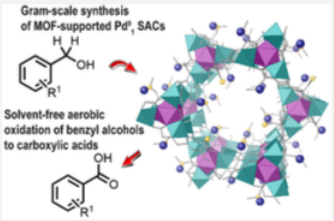

■ INTRODUCTION

Single-atom catalysts (SACs) attract great interest due to their unique catalytic properties in different reactions of capital importance.[1] However, various limitations linked with their real applications, such as the difficulties related to their gram-scale preparation, their challenging characterization, and the need to use protective ligands to stabilize these SACs, preventing their agglomeration, still need to be overcome.[2−4] In this context, the formation, stabilization, and catalytic action of soluble SACs in the neat reactant is still a quite unexplored field, since metals, even in very low amounts, tend to agglomerate in organic solutions after reduction.[5−7] However, this may not be the case for molecules able to concomitantly reduce, stabilize and be activated by the *in situ* formed SACs.[8]

Benzyl alcohols are fundamental starting materials in organic synthesis such as in the formation of benzaldehydes and benzoic acids after oxidation.[9,10] Figure 1 shows that the dehydrogenation of benzyl alcohols occurs under a variety of metal catalysts and reaction conditions[11−16] and that the radical oxidation of benzaldehydes occurs spontaneously under air for substrates with >98% purity; otherwise, just a >2% of remaining benzyl alcohol acts as a very good quencher of radical oxygen species (ROS).[17] With these results in mind, it is not surprising that in contrast to the stepwise process the direct aerobic oxidation of benzyl alcohols to benzoic acids is a challenging reaction that requires of harsh oxidation agents or

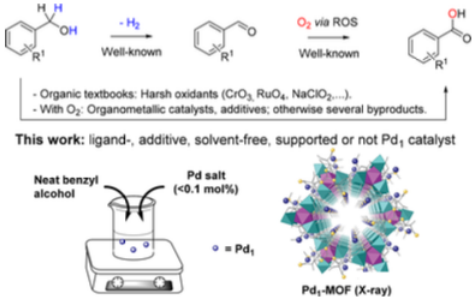

Figure 1. Stepwise and direct catalytic oxidation of benzyl alcohols to benzoic acids (top) and the catalytic systems used here (bottom).

Received: November 26, 2020

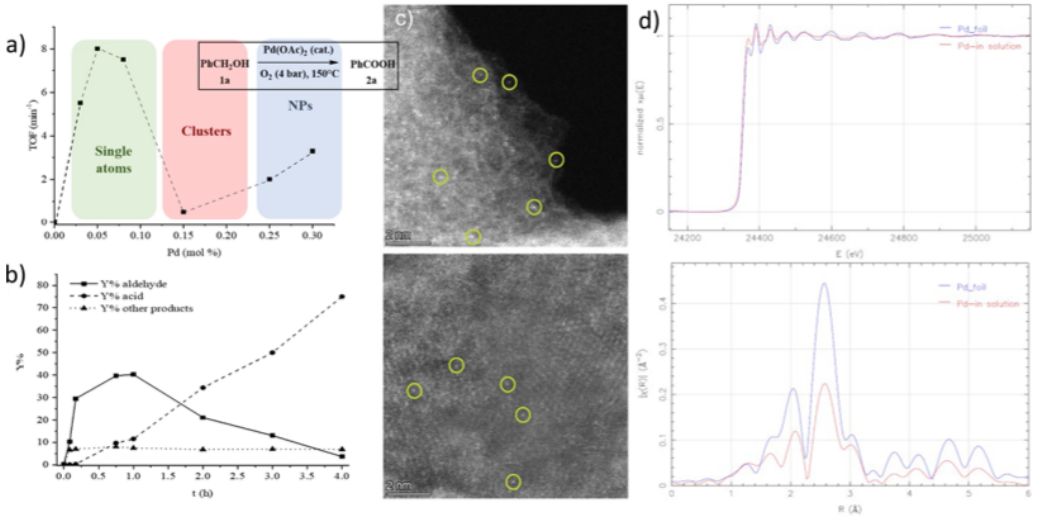

Figure 2. (a) Initial turnover frequency (TOF_0) for the aerobic oxidation of neat benzyl alcohol **1a** with increasing amounts of $Pd(OAc)_2$ at 150 °C under 4 bar of O_2. (b) Representative time−yield kinetic plot of the reaction for 0.05 mol % $Pd(OAc)_2$. (c) Two different AC-HAADF-STEM images of the Pd species in solution during reaction, after being trapped in active charcoal. Some Pd SACs are marked with yellow circles. (d) X-ray absorption near-edge structure (XANES, top) and extended X-ray absorption fine structure (EXAFS, bottom) spectra of the solution (red lines), compared to Pd foil (blue lines).

organometallic complex catalysts, additives, and solvents; otherwise, different undesired reactions such as ether and ester formation occurs.[18−28]

Benzyl alcohol is an industrial reagent for the reduction of noble metal salts (e.g., Pd, Au, etc.) to nanoparticles, with the concomitant formation of benzaldehyde.[29] Thus, we envisioned that perhaps the dissolution of a metal salt into tiny amounts of neat benzyl alcohols could generate a viable, self-stabilized redox single metal atom for the catalytic oxidation of benzyl alcohols to benzoic acid under air. This highly reactive single atom would, in principle, feature the empty coordinating sites required for the different chemical events during reaction, including dehydrogenation and oxygen activation,[19,20] while most likely circumventing severe benzyl alcohol poisoning. From a material synthesis point of view, the SAC could be considered an arrested state of the metal during the reduction/aggregation process into the benzyl alcohol, which keeps the metal seeds alive and catalytically active for the solvent-, ligand-, and additive-free oxidation reaction, beyond which some other metal species could be present.[30−33]

■ RESULTS AND DISCUSSION

Figure 2a shows the catalytic results for the aerobic oxidation of neat benzyl alcohol **1a** to benzoic acid **2a** with a 0.03−0.3 mol % of dissolved $Pd(OAc)_2$, and it can be observed that a high initial turnover frequency (TOF_0) for **2a** is achieved with <0.1 Pd mol % but not with higher amounts of Pd, with yields of **2a** around 50−80% after 4 h of reaction time (Figure S1). Similar results were observed with other Pd sources, including K_2PdCl_4, $Pd_2(dba)_3$, and $Pd(acac)_2$, but not with Pd complexes having a stronger ligand such as a phosphine, i.e., $Pd(PPh_3)_4$ or $Pd(PPh_3)_2Cl_2$ (Table S1 and Figure S2). Figure 2b shows that remarkably **2a** starts to form at intermediate conversions, when >50% of **1a** still remains in solution. These results confirm that the Pd catalyst formed under these conditions is able to override the poisoning of **1a** under aerobic conditions. An acceptorless dehydrogenation pathway can be ruled out since an open vial reaction gave very conversion of **1a**, thus confirming the need of O_2 to facilitate the one-pot oxidation.

Figure 2c shows aberration-corrected high-angle annular dark field scanning-transmission electron microscopy (AC-HAADF-STEM) measurements of the metal species in solution during reaction, trapped *in situ* with active charcoal. Since AC HAADF-STEM imaging is proportional in good approximation to the squared atomic number, Z^2, Pd species can be reliably identified as the brightest contrasts in the image (some of them have been marked with orange circles). While Pd single atoms are the main species present at <0.1 Pd mol %, only clusters and eventually NPs were found at >0.1 Pd mol (see Figures S3 and S4). Figure 2d shows X-ray absorption near edge structure (XANES) and extended X-ray absorption fine structure (EXAFS) measurements of the solution, which confirm the reduction of Pd and the generation of very small agglomerates, with an average number of ∼6 Pd−Pd bonds (see also Table S2), much lower than in Pd foil (12 Pd−Pd bonds). Ultraviolet−visible (UV−vis) spectrophotometric titrations with PPh_3 confirm the progressive disappearance of Pd^{2+} in solution during reaction (Figure S5 top). These results strongly support that partially reduced Pd1 species could be the catalytic active species for the direct aerobic oxidation of **1a** to **2a**.

The very low catalytic activity found with intermediate Pd amounts (0.1−0.25 mol %) is consistent with the formation of subnanometric Pd clusters, catalytically inactive in this case.[6] In order to check this hypothesis, subnanometric Pd clusters in

https://dx.doi.org/10.1021/jacs.0c12367
J. Am. Chem. Soc. XXXX, XXX, XXX−XXX

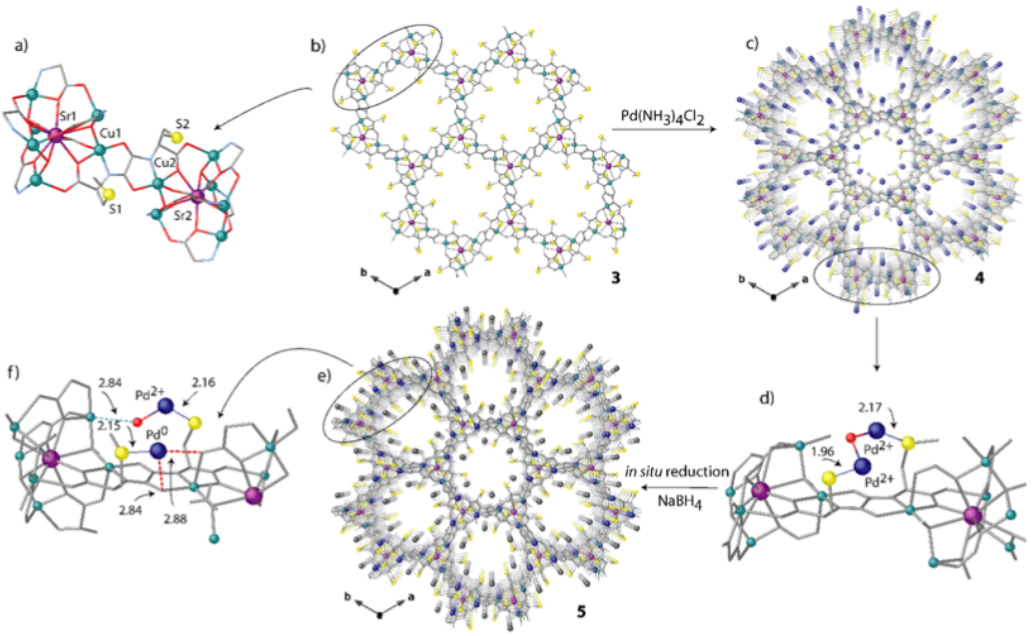

Figure 3. PS approach showing the structures of **3**−**5** determined by single-crystal X-ray diffraction which consists of two consecutive processes: first, the insertion of $[Pd(NH_3)_4]^{2+}$ cations within the channels of **3** (a, b) to give **4** (c, d) and, second, the reduction of Pd^{2+} cations to form the Pd^0_1 single atoms in **5** (e, f). Copper and strontium atoms from the network are represented by cyan and purple spheres, respectively, whereas organic ligands are depicted as gray sticks. Yellow and blue spheres represent S and Pd atoms (gray spheres in e represent Pd^0 atoms). Dotted lines represent the Pd···S interactions.

solution were independently prepared by two reported methods, i.e., endogenous reduction in aqueous *N*,*N*-dimethylformamide[6] and supporting solvent as well as reduction and leaching from ethylene vinyl alcohol polymer (EVOH),[8] and tested as catalyst for the oxidation of **1a** under the same conditions than Pd salts and complexes. The results (Figure S5, bottom) show that these clusters are inactive as catalysts for the oxidation of **1a** to **2a**, which strongly supports that Pd_1 is the main catalytic active species for the oxidation reaction. It is reasonable to think that the combination of a mild reductant agent (benzyl alcohol), which can at the same time act as a stabilizer, could have the same effect than a support/strong reductant system for the preferential formation of Pd_1 species.[1−3] In any case, the Pd clusters may be unable not only to catalyze the redox reaction but also to dislodge Pd single atoms, according to the canonical Ostwald ripening mechanism. In accordance with this hypothesis, the formation of **2a** starts to be observed again at Pd concentrations where NPs are formed (>0.3 mol %). This is in good agreement with the reported catalytic activity of some metal NPs for this reaction,[23−28] as well as with the ability of metal NPs to dissociate O_2 and dislodge single atoms in solution.[34] Commercially available samples of Pd/C with different Pd loadings (1−10 wt %) and particle size (5−50 nm average diameter) were tested as catalyst for the reaction and only the sample with highest loading and biggest NP size was active for the formation of **2a** (Figure S6). A quenching test with triphenylphosphine, under the indicated reaction conditions, showed that the catalytic activity comes from species in solution (Figure S7). These results strongly support that the oxidation of **1a** to **2a** in the neat reagent is catalyzed by soluble Pd1 species, regardless the amount of Pd employed.[35]

SACs are, by definition, supported metal species.[1−4] Thus, once we established the catalytic activity of *in situ* prepared Pd_1 SACs for the one-pot oxidation of **1a** to **2a**, it is of interest to find a solid able to generate and stabilize such Pd^0_1 species. However, this is a quite difficult task. The appropriate solid has to be able to preserve the required electronic and structural chemical nature of SACs, preventing their leaching out under reaction conditions and diffusing onto the solid to aggregate and, at the same time, enable a clear-cut characterization of the supported Pd_1 site and surroundings. In this context, metal−organic frameworks[36−41] (MOFs) are one of the most suitable platforms to overcome these difficulties. MOFs chemistry have reached high microporosity control, fine-tuning of the functionalities decorating their channels, and in-depth characterization of the final hosted metal species using single-crystal X-ray diffraction (SC-XRD).[42−48] As a direct consequence, MOFs have experienced rapid growth over the few last decades in catalysis, by means of their constituting building blocks, both organic linkers and open metal sites, and/or catalytically active guest species within their pores.[49−57]

Herein, we report a novel three-dimensional (3D) MOF, derived from the amino acid *S*-methyl-L-cysteine, with formula $\{Cu_6Sr[(S,S)\text{-Mecysmox}]_3(OH)_2(H_2O)\}\cdot 15H_2O$ (**3**) (Mecysmox = bis[*S*-methylcysteine]oxalyl diamide) (Figure 3a),

https://dx.doi.org/10.1021/jacs.0c12367
J. Am. Chem. Soc. XXXX, XXX, XXX−XXX

featuring pores densely decorated with dimethyl thioether groups, which allow the sequential formation and stabilization of Pd_1 SACs within their functional channels (Figure 3). In order to do so, a two-step postsynthetic (PS)[57] strategy has been applied, leading to the formation of two novel adsorbates with formulas $[Pd^{II}_2(H_2O)(NH_3)_6]_{0.5}Cl_2@\{Sr^{II}Cu^{II}_6[(S,S)\text{-Mecysmox}]_3(OH)_2\ CH_3OH)\}\cdot 12H_2O$ (**4**) (Figure 3c) and $(Pd^0_1)_{0.5}([Pd^{II}(H_2O)(NH_3)_3]Cl_2)_{0.5}@\{Sr^{II}Cu^{II}_6[(S,S)\text{-Mecysmox}]_3(OH)_2\ CH_3OH)\}\cdot 13H_2O$ (**5**), respectively, (Figures 1 bottom and 3e, Table S3). Figure 3 serves a dual purpose: shows the crystal structures of **3**−**5** and illustrates the SACs formation route. First, this consists of the insertion of $[Pd(NH_3)_4]Cl_2$ cations in the starting MOF (**3**) to form the Pd^{2+}-containing MOF (**4**) and the concomitant *in situ* reduction of half of the Pd^{2+} cations to form the mixed valence Pd^{2+}/Pd_1 hybrid compound (**5**) (see the Experimental Section). Notably, the sulfur-containing groups play a dual key role in this PS approach. They retain the Pd^{2+} cations in specific positions after the insertion process, which allows their homogeneous distribution along the channels and prevents their agglomeration and forming of NCs or NPs during the reduction process. Besides, the crystal structure of each phase could be unveiled by SC-XRD given the high crystallinity and robustness[58−64] of the pristine MOF (Figure 3 and Table S4).

Compounds **3**−**5** are isomorphous, crystallizing in the chiral $P6_3$ space group, and exhibit a chiral 3D strontium(II)−copper(II) network, featuring hexagonal channels where the dimethyl thioether chains from methylcysteine residues are confined. These functional arms exploit their intrinsic flexibility adopting different most stable conformations depending on the nature of target, i.e., solvent molecules in **3** (Figures S8−S10), Pd^{2+} in **4** (Figures 3c,d and S11) or both Pd^{2+} cations and Pd^0_1 SACs in **5** (Figures 3e,f, 4, and S14). The Pd^{2+}−S bond distances [1.96(4) and 2.17(2) Å (4)] (Figures 3d and S13a) are close enough to those observed previously,[65] and similar to the Pd^0−S bond distance observed in **5** 2.16(2) Å] (Figures 3f and S13b). In **3**−**5** the thioether chains from the Mecysmox ligand show as basic conformation one of the two distinct moieties in a distended conformation toward the center of the pores, and the other one regularly bent, with the terminal methyl groups pointing toward the smaller interstitial voids residing along the *a*-axis (Figures S10 and S14). Both conformations allow amino acid arms to efficiently target Pd^{2+} ions by S binding sites,[48,66−68] as confirmed by the crystal structure of **4**. However, only the Pd^{2+} ions residing in the most accessible pores [50% of total Pd^{2+} ions] could be chemically reduced to Pd^0, as confirmed by XPS spectrum of **5** (vide infra) (Figures 4b and S11−S14). This situation was observed previously.[62] In **5**, Pd_1 SACs are fixed to sulfur atoms in the larger hexagonal pores (Figure 4a and S12), whereas Pd^{2+} ions are still stabilized by sulfur atoms of dimethyl thioether located in interstitial voids (Figure S14). The water molecule acting as bridge between two-coordinated Pd^{2+} ions in **4**, still remains coordinated in **5** but as a terminal ligand, to only one of Pd^{2+} metal ions, as a consequence of the breaking linkage after Pd_1 SAC formation [Pd−Ow 2.00(6) and 3.03(7) Å in **4** and 1.99(2) Å in **5**] (Figure S13) (vide infra). Pd^0_1 weakly also interacts with oxamate moieties with Pt···O distances of 2.84(1) and 2.88(1) Å (see also Figures S12 and S13b). As far as we know, no examples of crystallographically precise Pd_1 SACs have been reported so far. Nevertheless, this Pd···O distance is close enough to that previously reported for Pd nanoclusters (2.9 Å).[64]

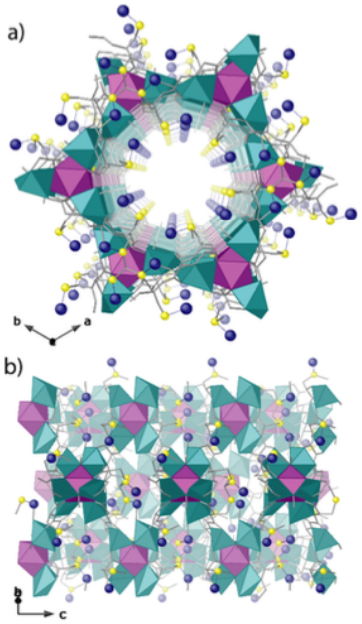

Figure 4. Perspective views of one single channel of **5** along the *c*- (a) and *b*-axes (b). Copper and strontium atoms from the network are represented by cyan and purple polyhedra, respectively, whereas organic ligands are depicted as gray sticks. Yellow and blue spheres represent S and Pd atoms. Dual color sticks represent the Pd···S interactions.

SC-XRD data also allows to suggest certain parameters of the Pd_1 formation mechanism. First, the bridging water molecule in $[Pd_2(H_2O)(NH_3)_6]$ units (**4**) (Figures 3d and S13a) might play a crucial role during the SACs formation process (**5**), acting synergistically with the flexible dimethyl thioether chains from methylcysteine residues stabilizing Pd^{2+} metal ions in **4**. The reduction process of Pd^{2+}−S units located inside the most accessible pores breaks water bonds from one side, which meanwhile generates the Pd^0−S ones in **5**. This leaves the water molecule still coordinated and stabilizing the unreduced mononuclear Pd^{2+} complexes residing in hindered interstitial voids (Figures 3f and S13b). Second, the length of the amino acid residue also seems to play a key role in the nuclearity of the metal species formed. Thus, in the present MOF, where Pd^{2+} cations are connected to shorter dimethyl thioether chains within the channels, Pd_1 SACs are formed during the reduction process. In turn, in a previously reported work with an isoreticular MOF prepared from the amino acid L-methionine,[66,67] the larger length of the ethylmethyl thioether chains decorating the channels allows a closer approach of the metal species, and dinuclear Pt_2 nanoclusters could be obtained.[62]

The virtual diameter of the channels only slightly decreases from ca. 0.9 nm in the precursor material **3** to ca. 0.7 nm in **4** and **5** (Figures S9, S11, and S12). This is in total agreement with adsorption measurements. Thus, the permanent porosity of the samples, particularly important in the case of **4** and **5** for catalytic applications, was verified by measuring their N_2

https://dx.doi.org/10.1021/jacs.0c12367
J. Am. Chem. Soc. XXXX, XXX, XXX−XXX

adsorption isotherms at 77 K. They confirm the permanent porosity for **3**−**5** (Figure S15), which is slightly lower for **4** and **5**, as expected from the decrease of their accessible void due to the presence of the Pd guests within the channels (calculated Brunauer−Emmett−Teller (BET) surface areas[69] for **3**, **4**, and **5** are 719, 548, and 572 m^2/g, respectively).

Besides the structural characterization, the chemical identities of **3**−**5** were also established by elemental analyses (C, H, S, and N), inductively coupled plasm−mass spectrometry (ICP−MS), powder X−ray diffraction (PXRD), electronic microscopy, X-ray photoelectron spectroscopy (XPS) and thermogravimetric (TGA) analyses (see the Supporting Information). Figure S16 shows the experimental powder X-ray diffraction (PXRD) patterns of **3**−**5**. They are identical to the theoretical ones (bold lines in Figure S16), which confirms that the bulk samples are pure and homogeneous. The solvent contents of **3**−**5** were, however, definitively established by TGA (see Figure S17). The XPS spectra of **4** and **5** are shown in Figure S18. The Pd 3d line of **2** is only one doublet with a binding energy (BE) of the Pd $3d_{5/2}$ peak of 337.8 eV, typical of Pd^{2+} cations (Figure S18a) which is close enough to other reported values.[64] In turn, Figure S18b clearly shows, apart from the same Pd $3d_{5/2}$ doublet with a BE of 337.7 eV, an additional peak at 335.8 eV, attributed to reduced Pd^0_1 SACs,[64] with a 1:1 ratio respect to Pd^{2+}. This feature indicates that only 50% of Pd^{2+}, those occupying accessible positions, are reduced when in contact with reducing agent, whereas those Pd^{2+} cations situated in inaccessible sheltered interstitial positions (see structural description) remain in their original oxidation state. These values are close enough to those observed for other Pd^{2+}/ Pd_1 species.[64] Therefore, they suggest that the thioether groups do not alter significantly either the native electronics nor the open-shell structure of the Pd_1 site, which is ready to catalyze the aerobic oxidation of **1** to **2**.

In order to further confirm the presence of partially reduced Pd SACs within **5**, Fourier transform infrared under CO (FTIR−CO), XANES, and EXAFS spectroscopic measurements and computational calculations based on the density functional theory (DFT) were carried out. Figure 5 shows the low-temperature (−196 °C) FTIR-CO results of **5**, where there are no signals above 2150 cm^{-1}, corresponding to bare

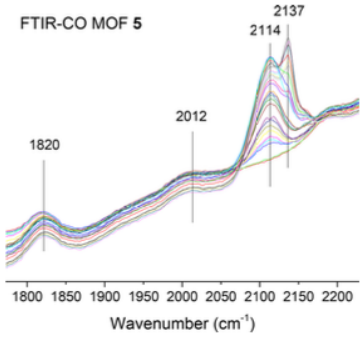

Figure 5. Low-temperature Fourier transform infrared spectrum, under CO (FTIR-CO), of fresh MOF **5**. Peak assignments: free CO (2137 cm^{-1}), Pd^{2+} (2114 cm^{-1}), $Pd^{\delta+}$ (2012 cm^{-1}, $\delta = 0-1$), and Pd^0 NPs (1820 cm^{-1}).

Pd^{2+}, can be observed, which supports the partial reduction of Pd. However, two clear broad signals centered at 2114 and 2012 cm^{-1}, attributable to unreduced Pd^{2+} and highly dispersed, partially reduced $Pd^{\delta+}$ atoms (δ = 0−1),[64] respectively, can be clearly seen, together with the increasing sharp signal of free CO (2137 cm^{-1}) at high CO doses. These peaks are accompanied by a very broad signal at 1820 cm^{-1}, which can be assigned to Pd(0) nanoparticles.[64]

Figure 6 shows the EXAFS and XANES spectra of MOF **5**, compared to Pd foil. The results confirm the partial reduction

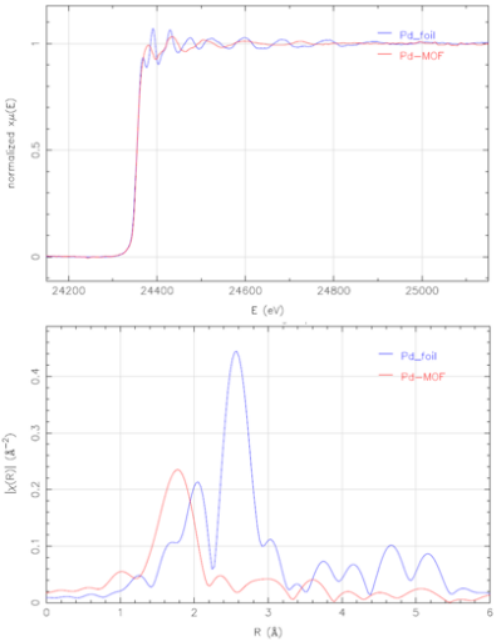

Figure 6. XANES (top) and EXAFS (bottom) spectra of fresh MOF **5** (red lines), compared to Pd foil (blue lines).

of Pd, as occurred for the Pd catalyst in solution (see Figure 2d above and Figure S19 for comparison and fitting). It can be observed in both cases, i.e., in solution and in MOF **5**, that the first oscillations beyond the edge are flattened respect to the foil due to quantum size effects of the single atoms, also indicating a large fraction of low coordination Pd atoms, more intensified in the case of MOF **5**. No Pd−Pd bond signals can be detected for the latter, but an average of 3 Pd−S bonds are detected (see also Table S2 and the Experimental Section in the Supporting Information, with references), in nice agreement with the SCXRD structure. Combined, these results strongly support the single-atom nature of Pd within MOF **5**.

In order to further support the stability of the Pd SACs in MOF **5**, DFT calculations were performed. Figure 7 shows the periodic DFT calculations through geometry optimization of Pd(0) in three different environments within the MOF (see also Figure S20 and Table S5), which support the crystallographic characterization of **5**. Pd(0) is always linearly coordinated to two ligands (O or S) with optimized Pd−O and Pd−S distances between 2.1 and 2.3 Å, as measured in the

https://dx.doi.org/10.1021/jacs.0c12367
J. Am. Chem. Soc. XXXX, XXX, XXX−XXX

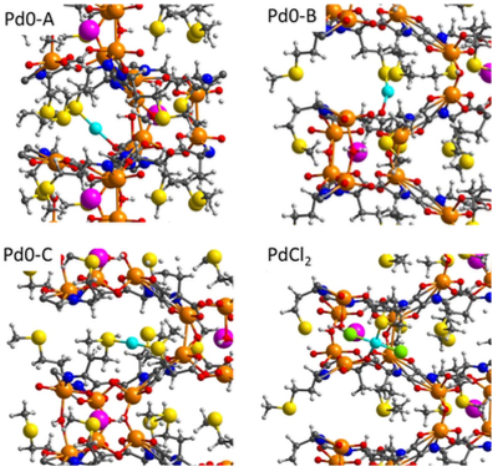

Figure 7. DFT-optimized structures of Pd(0) and $PdCl_2$ within the MOF, for three different coordination environments (Pd0−A−C, see also Figure S20 and Table S5). Pd, Cu, Sr, S, N, O, Cl, C, and H atoms are depicted as cyan, orange, pink, yellow, blue, red, green, gray, and white balls, respectively.

X-ray absorption spectroscopy (XAS) techniques (compare with Table S2). The calculated atomic charge on Pd in $PdCl_2$ within the MOF is nearly the same as in the gas phase calculated at the same level of theory (0.678 e), while the net atomic charges on two Pd(0) models are just slightly positive and slightly negative in the third one (see Table S5). With the optimized structure of MOF **5** in hand, the interaction of the Pd SACs with CO was simulated by DFT calculations, in order to compare with the experimental results in Figure 5. The results (Table S6 and Figure S21) show that CO interacts strongly with all models of Pd0 but not with $PdCl_2$, with calculated interaction energies between −28 and −40 kcal·mol^{-1} and with optimized Pd−CO distances around 1.8 Å. In particular, the interaction of Pd with CO in the Pd0−A system is so strong that the Pd−O bond is broken. The calculated ν(CO) frequency in this system, 1997 cm^{-1}, is similar to that obtained for CO adsorbed on top of a corner Pd atom in a small Pd_{13} cluster used as reference (1999 cm^{-1}) and nicely fits with the observed experimental peak at 2012 cm^{-1} (see above). In the other two models (Pd0−B−C), where the Pd(0) atom remains attached to two MOF ligands after CO coordination, the calculated ν(CO) frequency is slightly shifted to 1930−1945 cm^{-1}, in any case still assignable to the experimental peak observed.

The catalytic results for the aerobic oxidation of benzyl alcohol **1a** with MOFs **3**−**5** show that only Pd_1 SACs-MOF (**5**) catalyzes the oxidation with good efficiency (28% of benzaldehyde and 43% of benzoic acid **2a**). In contrast, **4** barely catalyzes the reaction, and **3** is completely inactive. The inactivity of **4** can be explained by the need of using a reducing agent stronger than **1a** to obtain the catalytically active Pd_1 species within the MOF, which then show a catalytic activity comparable to the Pd(0) complex $Pd_2(dba)_3$ (see Table S1). Figure 8a shows that MOF **5** is recyclable, without minimal depletion of the catalytic activity after 3 reuses. In order to verify the integrity of the SACs in MOF **5**, electronic

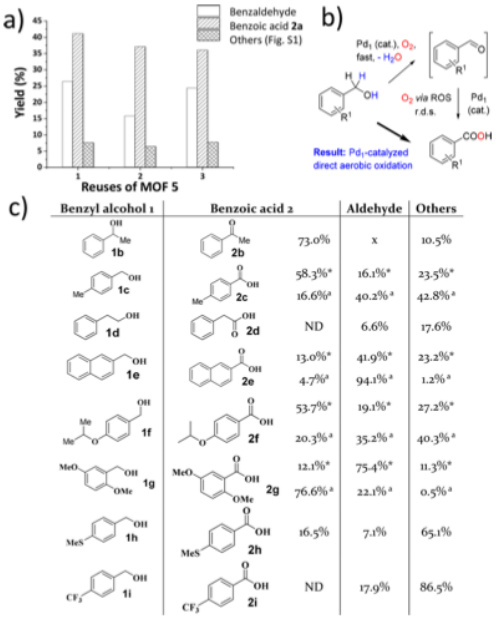

Figure 8. (a) Reusability of Pd^0_1 SACs-MOF (**5**); reaction conditions: 1.96 mmol substrate, 0.1% mol Pd^0_1 SACs-MOF, 4 atm O_2, 150 °C, 450 rpm, 15 h; GC yields. (b) Plausible reaction mechanism for Pd in solution. (c) Reaction scope with $Pd(OAc)_2$ (0.3 mol %). Reaction conditions: 1.96 mmol substrate, 0.3% mol $Pd(OAc)_2$, 4 atm O_2, 150 °C, 450 rpm, 4 h. GC yields. *15 h. [a]0.1% mol Pd^0_1 SACs-MOF, 24 h.

microscopy experiments were carried out after the catalytic experiments, where no SC-XRD measurements could be carried out due to the loss of the crystallinity of the material. Figures 9 and S22 show representative AC-HAADF-STEM images of **5**. Highly dispersed Pd species are clearly observed. In particular, they show a 0.135 nm average diameter, which is

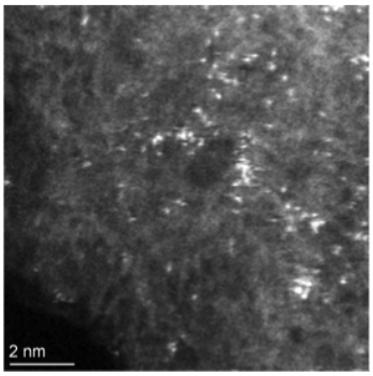

Figure 9. AC-HAADF-STEM image of reused MOF **5** showing the presence of Pd SACs.

https://dx.doi.org/10.1021/jacs.0c12367
J. Am. Chem. Soc. XXXX, XXX, XXX−XXX

in a good agreement with isolated atomic species. Only very scarce, small agglomerations could be observed in some areas, with diameters <0.5 nm, thus confirming that the Pd atoms do not aggregate into large NCs. In the same vein, PXRD pattern of **5**, recovered after catalysis (Figure S23a), confirm that the material remains crystalline and that no characteristic XRD peaks of Pd NPs or oxides are observed, further confirming the integrity of Pd_1 SACs. Moreover, the XPS spectra of **5** after catalytic experiments (**5′**) is very similar to that of the starting material (Figure S23b), confirming that a 1:1 ratio for Pd^0 and Pd^{2+} remains after catalysis. In accordance with all the characterization made to the used MOF **5** sample, leaching tests after filtration in hot of the catalyst (Figure S24) reveals that no reaction occurs after filtration of the solid catalyst, neither for the benzaldehyde intermediate nor product **2a**, which disproves the presence of catalytically active Pd species in solution from MOF **5**.

The potential cocatalysis by the Cu atoms in the MOF was discarded on the basis of comparative experiments (Table S7), since $Cu(OAc)_2$ merely does not catalyze the reaction (0.6% of **2a** and 2.8% of benzaldehyde under optimized reaction conditions), while a Cu-MOF treated under reduction conditions ($NaBH_4$ in methanol) and not having any Pd showed a similar catalytic activity than $Cu(OAc)_2$ (0.8% of **2a** and 5.0% of benzaldehyde). These results disprove Cu, on its own, as a catalyst of the reaction, and when $Cu(OAc)_2$ was put together with $Pd(OAc)_2$, the yield of benzoic acid **2a** was lower than that with Pd alone. These results together confirm that Pd is the only metal catalyst for the reaction here. Overall, these results nicely fit the observations during the reactions in solution and strongly support the idea that ligand-free Pd_1 are the catalytically active species during the one-pot oxidation of benzyl alcohols to benzoic acids under additive- and solvent-free conditions.

Kinetic experiments evidence that the rate equation for Pd_1 in solution is $v_0 = k_{exp}[Pd][O_2][\mathbf{1a}]^{-1}$ (Figure S25); this equation rate is similar if one starts from benzaldehyde rather than benzyl alcohol **1a** (Figure S26) and that the kinetic isotopic effect (KIE) is 2.6(7) when **1a-*d*$_2$** is used as the neat substrate. The inverse reaction order for **1a**, obtained by dilution experiments with *n*-hexadecane, is in accordance with the expected tendency of **1a** to poison the oxidation catalyst. The good linearity of the reaction rate with O_2 pressure supports the lack of diffusion effects and sufficient solubility in the neat reactant.[70] Trapping of benzaldehyde as an acetal with a diol, *in situ*, completely stops the formation of benzoic acid **2a**, and starting the reaction from the corresponding ester does not give any product **2a**, while dibenzyl ether does give **2a** (Figures S27 and S28). Moreover, the addition of the oxygen radical inhibitor DABCO to the reaction mixture stops the formation of **2a**, but it did not affect the formation of benzaldehyde (Figure S29). These kinetic, isotopic, and reactivity results together strongly support the reaction mechanism proposed in Figure 8b for Pd in solution, where the rate-determining step of the reaction is the oxidation of benzaldehyde to **2a**. This explains the catalytic activity of Pd_1 in the neat reactant, since the dehydrogenation of **1a** proceeds extremely well, and no base or additional stabilizing are needed. However, given that this is an early step in the reactive sequence, the addition of catalytic amounts of NaOAc did increase the reaction rate (Figure S30).[18−28] In contrast, the rate equation obtained with MOF **5** as a catalyst on the basis of initial rates (Figure S31) is $v_0 = k'_{exp}[\mathbf{5}][\mathbf{1a}]$, which differs from that of soluble Pd (compare with Figure S25). The lack of influence of O_2 for the solid catalyst can be explained by diffusion limitations; thus, the dehydrogenation step is slower than that in solution. Indeed, the experimental activation energy for the latter (7.7 kcal·mol^{-1}), also on the basis of initial rates, is much higher than that for the former (35.2 kcal·mol^{-1}), showcasing the more difficult access to the catalytic sites in the solid. The inhibiting effect with the strong ligand PPh_3 also occurs (Table S1).

The fact that different Pd sources work well as catalysts in solution (Table S1) suggests that the dynamic system drives to a common catalytically active reduced Pd species in variable amounts, while in contrast the reduced Pd species are directly obtained within the MOF **5** during the reduction treatment and not during reaction, since MOF **4** does not work well. These results illustrate the stability conferred by the MOF structure to the confined Pd single atoms, at expense of losing substrate availability. Nevertheless, Figure 8c shows the reaction scope for the Pd_1 catalyst in neat benzyl alcohols **1a−i**, which provides a limited number of benzoic acids **2a−i** in moderate yields, fairly comparable to most of the catalytic metal systems previously reported.[71] Besides, the calculated turnover frequency for product **2a** under optimized conditions is 7.95 min^{-1}, which is a 50-fold increase with respect to any other catalytic system previously reported for this reaction (Table S8).

■ CONCLUSIONS

In summary, we report, in the first part of the manuscript, the *in situ* formation of Pd_1 in neat benzyl alcohols which are able to catalyze the aerobic oxidation to benzoic acids. Then, we present the gram-scale preparation of well-defined Pd_1 SACs in a methyl-cysteine-based MOF, homogeneously distributed and stabilized along the functional channels. Synchrotron SC-XRD allows, for the first time, to clearly visualize the Pd_1 SACs and surroundings. The nature of Pd_1 in both solution and MOF is further supported by microscopic and XAS techniques, in addition to DFT calculations for the solid. The latter enable us to support SC-XRD results unveiling the main interactions between palladium atoms and the network, as well as to infer a plausible formation mechanism of Pd_1 SACs. The present results show a straightforward manner to obtain, on a multigram scale, well-defined ligand-free Pd_1 SACs, which can be effectively used in catalysis under industrially viable reaction conditions without additional reagents. This further demonstrates the great versatility of MOFs and represents a step closer to the real application of MOF-based materials in catalysis.

■ EXPERIMENTAL SECTION

Preparation of {Cu$_6$Sr[(*S*,*S*)-Mecysmox]$_3$(OH)$_2$(H$_2$O)}·15H$_2$O (3). $(Me_4N)_2\{Cu_2[(S,S)\text{-methox}](OH)_2\}\cdot 4H_2O$ (4.32 g, 6.0 mmol) was dissolved in 50 mL of water. Then, another aqueous solution (10 mL) containing $Sr(NO_3)_2$ (0.42 g, 2.0 mmol) was added dropwise under stirring. After further stirring for 10 h, at room temperature, a green polycrystalline powder was obtained and collected via filtration and dried with ethanol, acetone and diethyl ether. Yield: 2.91 g, 83%. Anal. calcd for $C_{30}Cu_6SrH_{70}S_6N_6O_{36}$ (1752.2): C, 20.56; H, 4.03; S, 10.98; N, 4.80%. Found: C, 20.51; H, 4.00; S, 10.99; N, 4.83%. IR (KBr): ν = 1605 cm^{-1} (C═O). Well-shaped hexagonal prisms of **1** suitable for X-ray structural analysis could be

https://dx.doi.org/10.1021/jacs.0c12367
J. Am. Chem. Soc. XXXX, XXX, XXX−XXX

obtained by slow diffusion in an H-shaped tube of H_2O/DMF (1:9) solutions containing stoichiometric amounts of $(Me_4N)_2\{Cu_2[(S,S)\text{-Mecysmox}](OH)_2\}\cdot 5H_2O$ (0.13 g, 0.18 mmol) in one arm and $Sr(NO_3)_2$ (0.012 g, 0.06 mmol) in the other. They were isolated by filtration on paper and air-dried.

Preparation of $[Pd_2(H_2O)(NH_3)_6]_{0.5}Cl_2$@$\{Sr^{II}Cu^{II}_6[(S,S)\text{-Mecysmox}]_3(OH)_2(CH_3OH)\}\cdot 12H_2O$ (4). Well-formed hexagonal green prisms of **2**, which were suitable for X-ray diffraction, were obtained by soaking crystals of **1** (ca. 25 mg, 0.015 mmol) in a H_2O/CH_3OH (1:1) solution of $[Pd(NH_3)_4]Cl_2$ (0.015 mmol) for 6 h. The process was repeated five times to ensure the maximum loading of $[Pd(NH_3)_4]Cl_2$. Crystals were washed with a H_2O/CH_3OH (1:1) solution several times, isolated by filtration on paper and air-dried. Anal. calcd for $C_{31}Cl_2Cu_6SrH_{76}PdS_6N_9O_{33.5}$ (1949.6): C, 19.10; H, 3.93; S, 9.87; N, 6.47%. Found: C, 19.07; H, 3.89; S, 9.91; N, 6.45%. IR (KBr): ν = 1603 cm−1 (C═O).

A multigram-scale procedure was also developed by using the same synthetic procedure but using a higher amount of a polycrystalline sample of **1** (2 g, 1.15 mmol), which were suspended a H_2O/CH_3OH (1:1) solution of $[Pd(NH_3)_4]Cl_2$ (1.1 mmol) for 1 h under a mild stirring. The process was repeated 5 times. Finally, the product was collected by filtration, washed with a H_2O/CH_3OH (1:1) solution and air-dried. Anal. calcd for $C_{31}Cl_2Cu_6SrH_{76}PdS_6N_9O_{33.5}$ (1949.6): C, 19.10; H, 3.93; S, 9.87; N, 6.47%. Found: C, 19.02; H, 3.87; S, 9.91; N, 6.47%. IR (KBr): ν = 1602 cm^{-1} (C═O).

$(Pd^0)_{0.5}([Pd^{II}(H_2O)(NH_3)_3]Cl_2)_{0.5}$@$\{Sr^{II}Cu^{II}_6[(S,S)\text{-Mecysmox}]_3(OH)_2(CH_3OH)\}\cdot 13H_2O$ (5). The same procedure was applied, with the same successful results to both crystals (ca. 25 mg) and a powder polycrystalline sample of **2** (ca. 2 g). They were suspended in H_2O/CH_3CH_2OH (1:1) solutions to which $NaBH_4$, divided in 15 fractions (0.4 mmol of $NaBH_4$ per mmol of MOF each), were added progressively in the space of 72 h. Each fraction was allowed to react for 1.5 h. After this period, samples were gently washed with a H_2O/CH_3OH solution and filtered on paper. Anal. calcd for $C_{31}ClCu_6SrH_{73.5}PdS_6N_{7.5}O_{34.5}$ (1906.6): C, 19.53; H, 3.89; S, 10.01; N, 5.51%. Found: C, 19.48; H, 3.87; S, 10.03; N, 5.49%. IR (KBr): ν = 1601 cm^{-1} (C═O).

Catalysis Details. All reactions were performed under aerobic solvent-free conditions. Palladium acetate (Sigma-Aldrich, >99.8% purity) was weighed (0.13−1.3 mg, which corresponds to 0.03 to 0.30%mol, respectively) in a double-walled 5 mL reactor equipped with a needle connected to a manometer. Then, the corresponding benzyl alcohol (0.2 mL, Sigma-Aldrich, > 98%) was added, and after setting an atmosphere of 4 bar O_2, the reactor was placed at 150 °C at a stirring rate of 450 rpm for the required reaction time. Aliquots were taken periodically to follow the course of the reaction by GC and by GC-MS, after adding mesitylene (3 μL) as an external standard. Supported Pd nanoparticles (Sigma-Aldrich, 98%) of different loadings 10, 5, and 1% in weight (3.1, 6.1, and 30.7 mg, respectively) and MOF **5** (1% in weight, 30.7 mg) were used as catalysts for the same purpose.

General procedure for the oxidation of 1a with palladium catalysts: In a 10 mL glass vial equipped with a stirring bar, the corresponding benzyl alcohol (1.96 mmol) was charged with the different amounts of the palladium catalyst. The vial was closed with a septum, an oxygen balloon was connected, and the mixture was placed in a preheated metal heating plate at 150 °C and stirred at 450 rpm for the indicated time. Alternatively, we used a lab-made double-walled vial connected to a manometer, where O_2 can be introduced at the desired pressure through a cannula. After the reaction time, the mixture was analyzed as above.

The following procedure was followed to get the active catalytic species trapped *in situ* after 60 min of reaction, at 150 °C and 4 bar O_2. Active charcoal was added after depressurization of the reaction, while the reaction mixture was being stirred at reaction temperature. While still hot, the reactor was set aside, and 2 mL of methanol was added to reactor. The mixture was kept in stirring for 10 min. Afterward, the whole mixture was transferred to a 2 mL vial, which was then centrifuged and washed 3 times with 2 mL of fresh methanol each time. After this procedure, the samples were dried at 70 °C under vacuum overnight and then analyzed by HR-TEM. The amount of charcoal used to trap the species (5−30 mg) was calculated in order to obtain a sample with approximately 2−3 wt % of Pd.

General Procedure for Ultraviolet−Visible (UV−Vis) Spectrophotometric Titrations. In a 10 mL glass vial equipped with a stirring bar, the corresponding benzyl alcohol (1.96 mmol) was charged with 0.006 mmol of palladium acetate. The vial was closed with a septum equipped with a manometer and charged with 4 bar of oxygen. Then, it was placed in a preheated metal heating plate at 150 °C and stirred at 450 rpm for the indicated time. Afterward the mixture was quenched with 4 mL of a 0.02 M triphenylphosphine solution in CH_2Cl_2 and analyzed by UV−vis spectrophotometry in quartz cuvettes with an optical path of 10 × 10 mm^2.

X-ray Crystallographic Details. Diffraction data for **3** were collected on a Bruker-Nonius X8APEXII CCD area detector diffractometer using graphite-monochromated Mo Kα radiation (λ = 0.71073 Å), whereas data for **4** and **5** were collected using synchrotron radiation at I19 beamline of the Diamond Light Source at λ = 0.6889 Å. Crystal data for **3**−**5**: hexagonal, space group $P6_3$, T = 100(2), Z = 2. **3**: $C_{30}Cu_6H_{70}N_6O_{36}S_6Sr$, a = 18.057(4) Å, c = 12.800(3) Å, V = 3614.6(17) $Å^3$; **4**: $C_{31}Cu_6H_{76}N_9O_{33.5}S_6SrPdCl_2$, a = 17.86780(10) Å, c = 12.80840(10) Å, V = 3541.34(5) $Å^3$; **5**: $C_{31}Cu_6H_{73.5}N_{7.5}O_{34.5}S_6SrPdCl$, a = 17.8206(2) Å, c = 12.7821(3) Å, V = 3515.42(11) $Å^3$. Further details can be found in the Supporting Information. CCDC 1995182, 1995183, and 1995184 for **3**, **4**, and **5**, respectively, contain the supplementary crystallographic data for this paper. These data can be obtained free of charge via www.ccdc.cam.ac.uk/conts/retrieving.html or from the Cambridge Crystallographic Data Centre, 12 Union Road, Cambridge CB21EZ, UK; fax: (+44)1223−336−033; or deposit@ccdc.cam.ac.uk.

X-ray Powder Diffraction Measurements. Polycrystalline samples of **3**, **4**, and **5** were introduced into 0.5 mm borosilicate capillaries prior to being mounted and aligned on a Empyrean PANalytical powder diffractometer, using Cu Kα radiation (λ = 1.54056 Å). For each sample, five repeated measurements were collected at room temperature (2θ = 2−60°) and merged in a single diffractogram. A polycrystalline sample of **5** was also measured after catalysis following the same procedure.

X-ray Photoelectron Spectroscopy (XPS) Measurements. Samples **4**, **5**, and **5′** (after catalysis) were prepared by sticking, without sieving, the MOF onto a molybdenum plate with cellophane tape, followed by air drying. Measurements were performed on a K-Alpha X-ray Photoelectron Spectrometer (XPS) System using a monochromatic Al K(alpha) source (1486.6 eV). As an internal reference for the peak

https://dx.doi.org/10.1021/jacs.0c12367
J. Am. Chem. Soc. XXXX, XXX, XXX−XXX

positions in the XPS spectra, the C 1s peak has been set at 284.8 eV.

FTIR Spectroscopy of Adsorbed CO. Fourier transform infrared (FTIR) using CO as a probe molecule was used to evaluate electronic properties of MOF **5**. Spectra were recorded once complete coverage of CO at the specified CO partial pressure was achieved. See the Supporting Information for details.

Computational Methods. Periodic DFT calculations were performed with the Vienna Ab-initio Simulation Package (VASP) code, using the Perdew–Burke–Ernzerhof (PBE) exchange-correlation functional. See Supporting Information for details.

XAS Techniques. XANES and EXAFS measurements of Pd foil, Pd acetate, and MOF **5** were carried out on CLAESS beamline at ALBA Synchrotron Light Source, Barcelona, Spain. See the Supporting Information for details.

■ ASSOCIATED CONTENT

Supporting Information

The Supporting Information is available free of charge at https://pubs.acs.org/doi/10.1021/jacs.0c12367.

Physical techniques. Crystallographic and catalytic details. Tables S1–S8. Figures S1–S31. (PDF)

Accession Codes

CCDC 1995182–1995184 contain the supplementary crystallographic data for this paper. These data can be obtained free of charge via www.ccdc.cam.ac.uk/data_request/cif, or by emailing data_request@ccdc.cam.ac.uk, or by contacting The Cambridge Crystallographic Data Centre, 12 Union Road, Cambridge CB2 1EZ, UK; fax: +44 1223 336033.

■ AUTHOR INFORMATION

Corresponding Authors

Donatella Armentano – *Dipartimento di Chimica e Tecnologie Chimiche (CTC), Università della Calabria, Rende 87036, Cosenza, Italy;* orcid.org/0000-0002-8502-8074; Email: donatella.armentano@unical.it

Antonio Leyva-Pérez – *Instituto de Tecnología Química (UPV–CSIC), Universitat Politècnica de València–Consejo Superior de Investigaciones Científicas, 46022 Valencia, Spain;* orcid.org/0000-0003-1063-5811; Email: anleyva@itq.upv.es

Emilio Pardo – *Instituto de Ciencia Molecular (ICMol), Universidad de Valencia, 46980 Paterna, Valencia, Spain;* orcid.org/0000-0002-1394-2553; Email: emilio.pardo@uv.es

Authors

Estefanía Tiburcio – *Instituto de Ciencia Molecular (ICMol), Universidad de Valencia, 46980 Paterna, Valencia, Spain*

Rossella Greco – *Instituto de Tecnología Química (UPV–CSIC), Universitat Politècnica de València–Consejo Superior de Investigaciones Científicas, 46022 Valencia, Spain*

Marta Mon – *Instituto de Tecnología Química (UPV–CSIC), Universitat Politècnica de València–Consejo Superior de Investigaciones Científicas, 46022 Valencia, Spain*

Jordi Ballesteros-Soberanas – *Instituto de Tecnología Química (UPV–CSIC), Universitat Politècnica de València–Consejo Superior de Investigaciones Científicas, 46022 Valencia, Spain*

Jesús Ferrando-Soria – *Instituto de Ciencia Molecular (ICMol), Universidad de Valencia, 46980 Paterna, Valencia, Spain*

Miguel López-Haro – *Departamento de Ciencia de los Materiales e Ingeniería Metalúrgica y Química Inorgánica, Facultad de Ciencias, Universidad de Cádiz, Campus Universitario de Puerto Real, 11510 Puerto Real, Cádiz, Spain; Instituto Universitario de Investigación en Microscopía Electrónica y Materiales (IMEYMAT), Facultad de Ciencias, Universidad de Cádiz, Campus Universitario de Puerto Real, 11510 Puerto Real, Cádiz, Spain;* orcid.org/0000-0003-2560-8015

Juan Carlos Hernández-Garrido – *Departamento de Ciencia de los Materiales e Ingeniería Metalúrgica y Química Inorgánica, Facultad de Ciencias, Universidad de Cádiz, Campus Universitario de Puerto Real, 11510 Puerto Real, Cádiz, Spain; Instituto Universitario de Investigación en Microscopía Electrónica y Materiales (IMEYMAT), Facultad de Ciencias, Universidad de Cádiz, Campus Universitario de Puerto Real, 11510 Puerto Real, Cádiz, Spain;* orcid.org/0000-0001-8499-0395

Judit Oliver-Meseguer – *Instituto de Tecnología Química (UPV–CSIC), Universitat Politècnica de València–Consejo Superior de Investigaciones Científicas, 46022 Valencia, Spain*

Carlo Marini – *CELLS–ALBA Synchrotron, E-08290 Barcelona, Spain*

Mercedes Boronat – *Instituto de Tecnología Química (UPV–CSIC), Universitat Politècnica de València–Consejo Superior de Investigaciones Científicas, 46022 Valencia, Spain;* orcid.org/0000-0002-6211-5888

Complete contact information is available at: https://pubs.acs.org/10.1021/jacs.0c12367

Author Contributions

[V]E.T. and R.G. contributed equally to this work.

Notes

The authors declare no competing financial interest.

■ ACKNOWLEDGMENTS

This work was supported by the Ministero dell'Istruzione, dell'Università e della Ricerca (Italy) and the MINECO (Spain) (Projects PID2019–104778GB–I00, CTQ 2017–86735–P, RTC–2017–6331–5, Severo Ochoa program SEV–2016–0683 and Excellence Unit "Maria de Maeztu" CEX2019–000919–M). E.T. and M.M. thank MINECO and ITQ for the concession of a contract. D.A. acknowledges the financial support of the Fondazione CARIPLO/"Economia Circolare: ricerca per un futuro sostenibile" 2019, Project code: 2019–2090, MOCA and Diamond Light Source for awarded beamtime and provision of synchrotron radiation facilities and thanks Dr. Sarah Barnett and David Allan for their assistance at I19 beamline (Proposal No. MT18768-1). Thanks are also extended to the "2019 Post-doctoral Junior Leader-Retaining Fellowship, la Caixa Foundation (ID100010434 and fellowship code LCF/BQ/PR19/11700011" (J.F.-S.) and "La Caixa" scholarship (ID 100010434) LCF/BQ/DI19/11730029 (J.B.-S). E.P. acknowledges the financial support of the European Research Council under the European Union's Horizon 2020 research and innovation programme/ERC Grant Agreement No 814804, MOF reactors. J.O.-M. acknowledges the Juan de la Cierva

https://dx.doi.org/10.1021/jacs.0c12367
J. Am. Chem. Soc. XXXX, XXX, XXX–XXX

program for the concession of a contract (IJC2018-036514-I). We gratefully acknowledge to ALBA synchrotron for allocating beamtime and CLÆSS beamline staff for their technical support during our experiment. The computations were performed on the Tirant III cluster of the Servei d'Informàtica of the University of Valencia.

■ REFERENCES

(1) Yang, X.-F.; Wang, A.; Qiao, B.; Li, J.; Liu, J.; Zhang, T. Single-Atom Catalysts: A New Frontier in Heterogeneous Catalysis. *Acc. Chem. Res.* **2013**, *46*, 1740−1748.
(2) Flytzani-Stephanopoulos, M.; Gates, B. C. Atomically Dispersed Supported Metal Catalysts. *Annu. Rev. Chem. Biomol. Eng.* **2012**, *3*, 545−574.
(3) Liu, L.; Corma, A. Metal Catalysts for Heterogeneous Catalysis: From Single Atoms to Nanoclusters and Nanoparticles. *Chem. Rev.* **2018**, *118*, 4981−5079.
(4) Chen, Z. W.; Chen, L. X.; Yang, C. C.; Jiang, Q. Atomic (Single, Double, and Triple Atoms) Catalysis: Frontiers, Opportunities, and Challenges. *J. Mater. Chem. A* **2019**, *7*, 3492−3515.
(5) Oliver-Meseguer, J.; Cabrero-Antonino, J. R.; Dominguez, I.; Leyva-Perez, A.; Corma, A. Small Gold Clusters Formed in Solution Give Reaction Turnover Numbers of 107 at Room Temperature. *Science* **2012**, *338*, 1452−1455.
(6) Leyva-Pérez, A.; Oliver-Meseguer, J.; Rubio-Marqués, P.; Corma, A. Water-Stabilized Three- and Four-Atom Palladium Clusters as Highly Active Catalytic Species in Ligand-Free C-C Cross-Coupling Reactions. *Angew. Chem., Int. Ed.* **2013**, *52*, 11554−11559.
(7) Oliver-Messeguer, J.; Liu, L.; García-García, S.; Canós-Giménez, C.; Domínguez, I.; Gavara, R.; Doménech-Carbó, A.; Concepción, P.; Leyva-Pérez, A.; Corma, A. Stabilized Naked Sub-Nanometric Cu Clusters within a Polymeric Film Catalyze C−N, C−C, C−O, C−S, and C−P Bond-Forming Reactions. *J. Am. Chem. Soc.* **2015**, *137*, 3894−3900.
(8) Fernández, E.; Rivero-Crespo, M. A.; Domínguez, I.; Rubio-Marqués, P.; Oliver-Meseguer, J.; Liu, L.; Cabrero-Antonino, M.; Gavara, R.; Hernández-Garrido, J. C.; Boronat, M.; Leyva-Pérez, A.; Corma, A. Base-Controlled Heck, Suzuki, and Sonogashira Reactions Catalyzed by Ligand-Free Platinum or Palladium Single Atom and Sub-Nanometer Clusters. *J. Am. Chem. Soc.* **2019**, *141*, 1928−1940.
(9) McCann, S. D.; Stahl, S. S. Copper-Catalyzed Aerobic Oxidations of Organic Molecules: Pathways for Two-Electron Oxidation with a Four-Electron Oxidant and a One-Electron Redox-Active Catalyst. *Acc. Chem. Res.* **2015**, *48*, 1756−1766.
(10) Parmeggiani, C.; Matassini, C.; Cardona, F. A Step Forward towards Sustainable Aerobic Alcohol Oxidation: New and Revised Catalysts Based on Transition Metals on Solid Supports. *Green Chem.* **2017**, *19*, 2030−2050.
(11) Dijksman, A.; Marino-González, A.; Mairata i Payeras, A.; Arends, I. W. C. E.; Sheldon, R. A. Efficient and Selective Aerobic Oxidation of Alcohols into Aldehydes and Ketones Using Ruthenium/TEMPO as the Catalytic System. *J. Am. Chem. Soc.* **2001**, *123*, 6826−6833.
(12) Partenheimer, W. The High Yield Synthesis of Benzaldehydes from Benzylic Alcohols Using Homogeneously Catalyzed Aerobic Oxidation in Acetic Acid. *Adv. Synth. Catal.* **2006**, *348*, 559−568.
(13) Enache, D. I.; Edwards, J. K.; Landon, P.; Solsona-Espriu, B.; Carley, A. F.; Herzing, A. A.; Watanabe, M.; Kiely, C. J.; Knight, D. W.; Hutchings, G. J. Solvent-Free Oxidation of Primary Alcohols to Aldehydes Using Au-Pd/TiO 2 Catalysts. *Science* **2006**, *311*, 362−365.
(14) Jiang, B.; Feng, Y.; Ison, E. A. Mechanistic Investigations of the Iridium(III)-Catalyzed Aerobic Oxidation of Primary and Secondary Alcohols. *J. Am. Chem. Soc.* **2008**, *130*, 14462−14464.
(15) Hoover, J. M.; Ryland, B. L.; Stahl, S. S. Copper/TEMPO-Catalyzed Aerobic Alcohol Oxidation: Mechanistic Assessment of Different Catalyst Systems. *ACS Catal.* **2013**, *3*, 2599−2605.
(16) Huang, K.; Fu, H.; Shi, W.; Wang, H.; Cao, Y.; Yang, G.; Peng, F.; Wang, Q.; Liu, Z.; Zhang, B.; Yu, H. Competitive Adsorption on Single-Atom Catalysts: Mechanistic Insights into the Aerobic Oxidation of Alcohols over Co N C. *J. Catal.* **2019**, *377*, 283−292.
(17) Sankar, M.; Nowicka, E.; Carter, E.; Murphy, D. M.; Knight, D. W.; Bethell, D.; Hutchings, G. J. The Benzaldehyde Oxidation Paradox Explained by the Interception of Peroxy Radical by Benzyl Alcohol. *Nat. Commun.* **2014**, *5*, 3332.
(18) Buffin, B. P.; Belitz, N. L.; Verbeke, S. L. Electronic, Steric, and Temperature Effects in the Pd(II)-Biquinoline Catalyzed Aerobic Oxidation of Benzylic Alcohols in Water. *J. Mol. Catal. A: Chem.* **2008**, *284*, 149−154.
(19) Schultz, M. J.; Adler, R. S.; Zierkiewicz, W.; Privalov, T.; Sigman, M. S. Using Mechanistic and Computational Studies To Explain Ligand Effects in the Palladium-Catalyzed Aerobic Oxidation of Alcohols. *J. Am. Chem. Soc.* **2005**, *127*, 8499−8507.
(20) Steinhoff, B. A.; Guzei, I. A.; Stahl, S. S. Mechanistic Characterization of Aerobic Alcohol Oxidation Catalyzed by Pd-(OAc) 2 /Pyridine Including Identification of the Catalyst Resting State and the Origin of Nonlinear [Catalyst] Dependence. *J. Am. Chem. Soc.* **2004**, *126*, 11268−11278.
(21) Steinhoff, B. A.; Stahl, S. S. Ligand-Modulated Palladium Oxidation Catalysis: Mechanistic Insights into Aerobic Alcohol Oxidation with the Pd(OAc) 2 /Pyridine Catalyst System. *Org. Lett.* **2002**, *4*, 4179−4181.
(22) Liu, C.; Fang, Z.; Yang, Z.; Li, Q.; Guo, S.; Guo, K. Highly Practical Sodium(I)/Azobenzene Catalyst System for Aerobic Oxidation of Benzylic Alcohols. *RSC Adv.* **2015**, *5*, 79699−79702.
(23) Abad, A.; Concepción, P.; Corma, A.; García, H. A Collaborative Effect between Gold and a Support Induces the Selective Oxidation of Alcohols. *Angew. Chem., Int. Ed.* **2005**, *44*, 4066−4069.
(24) Tsunoyama, H.; Sakurai, H.; Negishi, Y.; Tsukuda, T. Size-Specific Catalytic Activity of Polymer-Stabilized Gold Nanoclusters for Aerobic Alcohol Oxidation in Water. *J. Am. Chem. Soc.* **2005**, *127*, 9374−9375.
(25) Abad, A.; Corma, A.; García, H. Catalyst Parameters Determining Activity and Selectivity of Supported Gold Nanoparticles for the Aerobic Oxidation of Alcohols: The Molecular Reaction Mechanism. *Chem. - Eur. J.* **2008**, *14*, 212−222.
(26) García-Suárez, E. J.; Tristany, M.; García, A. B.; Collière, V.; Philippot, K. Carbon-Supported Ru and Pd Nanoparticles: Efficient and Recyclable Catalysts for the Aerobic Oxidation of Benzyl Alcohol in Water. *Microporous Mesoporous Mater.* **2012**, *153*, 155−162.
(27) Savara, A.; Chan-Thaw, C. E.; Rossetti, I.; Villa, A.; Prati, L. Benzyl Alcohol Oxidation on Carbon-Supported Pd Nanoparticles: Elucidating the Reaction Mechanism. *ChemCatChem* **2014**, *6*, 3464−3473.
(28) Karimi, B.; Khorasani, M.; Vali, H.; Vargas, C.; Luque, R. Palladium Nanoparticles Supported in the Nanospaces of Imidazolium-Based Bifunctional PMOs: The Role of Plugs in Selectivity Changeover in Aerobic Oxidation of Alcohols. *ACS Catal.* **2015**, *5*, 4189−4200.
(29) Juárez, R.; Concepción, P.; Corma, A.; Fornés, V.; García, H. Gold-Catalyzed Phosgene-Free Synthesis of Polyurethane Precursors. *Angew. Chem., Int. Ed.* **2010**, *49*, 1286−1290.
(30) Ananikov, V. P.; Beletskaya, I. P. Toward the Ideal Catalyst: From Atomic Centers to a "Cocktail" of Catalysts. *Organometallics* **2012**, *31*, 1595−1604.
(31) Eremin, D. B.; Ananikov, V. P. Understanding Active Species in Catalytic Transformations: From Molecular Catalysis to Nanoparticles, Leaching, "Cocktails" of Catalysts and Dynamic Systems. *Coord. Chem. Rev.* **2017**, *346*, 2−19.
(32) Polynski, M. V.; Ananikov, V. P. Modeling Key Pathways Proposed for the Formation and Evolution of "Cocktail"-Type Systems in Pd-Catalyzed Reactions Involving ArX Reagents. *ACS Catal.* **2019**, *9*, 3991−4005.

https://dx.doi.org/10.1021/jacs.0c12367
J. Am. Chem. Soc. XXXX, XXX, XXX−XXX

(33) Geiger, Y.; Achard, T.; Maisse-François, A.; Bellemin-Laponnaz, S. Hyperpositive Nonlinear Effects in Asymmetric Catalysis. *Nat. Catal.* **2020**, *3*, 422−426.
(34) Boronat, M.; Leyva-Pérez, A.; Corma, A. Theoretical and Experimental Insights into the Origin of the Catalytic Activity of Subnanometric Gold Clusters: Attempts to Predict Reactivity with Clusters and Nanoparticles of Gold. *Acc. Chem. Res.* **2014**, *47*, 834−844.
(35) Kaiser, S. K.; Fako, E.; Manzocchi, G.; Krumeich, F.; Hauert, R.; Clark, A. H.; Safonova, O. V.; López, N.; Pérez-Ramírez, J. Nanostructuring Unlocks High Performance of Platinum Single-Atom Catalysts for Stable Vinyl Chloride Production. *Nat. Catal.* **2020**, *3*, 376−385.
(36) Maurin, G.; Serre, C.; Cooper, A.; Férey, G. The New Age of MOFs and of Their Porous-Related Solids. *Chem. Soc. Rev.* **2017**, *46*, 3104−3107.
(37) Cui, Y.; Li, B.; He, H.; Zhou, W.; Chen, B.; Qian, G. Metal−Organic Frameworks as Platforms for Functional Materials. *Acc. Chem. Res.* **2016**, *49*, 483−493.
(38) Zhou, H.-C.; Kitagawa, S. Metal−Organic Frameworks (MOFs). *Chem. Soc. Rev.* **2014**, *43*, 5415−5418.
(39) Furukawa, H.; Cordova, K. E.; O'Keeffe, M.; Yaghi, O. M. The Chemistry and Applications of Metal-Organic Frameworks. *Science* **2013**, *341*, 1230444.
(40) Farha, O. K.; Hupp, J. T. Rational Design, Synthesis, Purification, and Activation of Metal−Organic Framework Materials. *Acc. Chem. Res.* **2010**, *43*, 1166−1175.
(41) Long, J. R.; Yaghi, O. M. The Pervasive Chemistry of Metal-Organic Frameworks. *Chem. Soc. Rev.* **2009**, *38*, 1213−1214.
(42) Inokuma, Y.; Arai, T.; Fujita, M. Networked Molecular Cages as Crystalline Sponges for Fullerenes and Other Guests. *Nat. Chem.* **2010**, *2*, 780−783.
(43) Mon, M.; Ferrando-Soria, J.; Verdaguer, M.; Train, C.; Paillard, C.; Dkhil, B.; Versace, C.; Bruno, R.; Armentano, D.; Pardo, E. Postsynthetic Approach for the Rational Design of Chiral Ferroelectric Metal−Organic Frameworks. *J. Am. Chem. Soc.* **2017**, *139*, 8098−8101.
(44) Rissanen, K. Crystallography of Encapsulated Molecules. *Chem. Soc. Rev.* **2017**, *46*, 2638−2648.
(45) Burgun, A.; Coghlan, C. J.; Huang, D. M.; Chen, W.; Horike, S.; Kitagawa, S.; Alvino, J. F.; Metha, G. F.; Sumby, C. J.; Doonan, C. J. Mapping-Out Catalytic Processes in a Metal-Organic Framework with Single-Crystal X-Ray Crystallography. *Angew. Chem., Int. Ed.* **2017**, *56*, 8412−8416.
(46) Mon, M.; Bruno, R.; Ferrando-Soria, J.; Bartella, L.; Di Donna, L.; Talia, M.; Lappano, R.; Maggiolini, M.; Armentano, D.; Pardo, E. Crystallographic Snapshots of Host−Guest Interactions in Drugs@metal−Organic Frameworks: Towards Mimicking Molecular Recognition Processes. *Mater. Horiz.* **2018**, *5*, 683−690.
(47) Young, R. J.; Huxley, M. T.; Pardo, E.; Champness, N. R.; Sumby, C. J.; Doonan, C. J. Isolating Reactive Metal-Based Species in Metal−Organic Frameworks − Viable Strategies and Opportunities. *Chem. Sci.* **2020**, *11*, 4031−4050.
(48) Mon, M.; Bruno, R.; Tiburcio, E.; Viciano-Chumillas, M.; Kalinke, L. H. G.; Ferrando-Soria, J.; Armentano, D.; Pardo, E. Multivariate Metal−Organic Frameworks for the Simultaneous Capture of Organic and Inorganic Contaminants from Water. *J. Am. Chem. Soc.* **2019**, *141*, 13601−13609.
(49) Lee, J.; Farha, O. K.; Roberts, J.; Scheidt, K. A.; Nguyen, S. T.; Hupp, J. T. Metal−Organic Framework Materials as Catalysts. *Chem. Soc. Rev.* **2009**, *38*, 1450.
(50) Farrusseng, D.; Aguado, S.; Pinel, C. Metal-Organic Frameworks: Opportunities for Catalysis. *Angew. Chem., Int. Ed.* **2009**, *48*, 7502−7513.
(51) Corma, A.; García, H.; Llabrés i Xamena, F. X. Engineering Metal Organic Frameworks for Heterogeneous Catalysis. *Chem. Rev.* **2010**, *110*, 4606−4655.
(52) Juan-Alcañiz, J.; Gascon, J.; Kapteijn, F. Metal−Organic Frameworks as Scaffolds for the Encapsulation of Active Species: State of the Art and Future Perspectives. *J. Mater. Chem.* **2012**, *22*, 10102.
(53) Valvekens, P.; Vermoortele, F.; De Vos, D. Metal−Organic Frameworks as Catalysts: The Role of Metal Active Sites. *Catal. Sci. Technol.* **2013**, *3*, 1435.
(54) Gascon, J.; Corma, A.; Kapteijn, F.; Llabrés i Xamena, F. X. Metal Organic Framework Catalysis: Quo Vadis ? *ACS Catal.* **2014**, *4*, 361−378.
(55) Dhakshinamoorthy, A.; Li, Z.; Garcia, H. Catalysis and Photocatalysis by Metal Organic Frameworks. *Chem. Soc. Rev.* **2018**, *47*, 8134−8172.
(56) Yang, D.; Gates, B. C. Catalysis by Metal Organic Frameworks: Perspective and Suggestions for Future Research. *ACS Catal.* **2019**, *9*, 1779−1798.
(57) Viciano-Chumillas, M.; Mon, M.; Ferrando-Soria, J.; Corma, A.; Leyva-Pérez, A.; Armentano, D.; Pardo, E. Metal−Organic Frameworks as Chemical Nanoreactors: Synthesis and Stabilization of Catalytically Active Metal Species in Confined Spaces. *Acc. Chem. Res.* **2020**, *53*, 520−531.
(58) Blay, G.; Fernández, I.; Giménez, T.; Pedro, J. R.; Ruiz, R.; Pardo, E.; Lloret, F.; Muñoz, M. C. Alkane Oxidation by a Carboxylate-Bridged Dimanganese (III) Complex. *Chem. Commun. (Cambridge, U. K.)* **2001**, *919*, 2102−2103.
(59) Adam, R.; Mon, M.; Greco, R.; Kalinke, L. H. G.; Vidal-Moya, A.; Fernandez, A.; Winpenny, R. E. P.; Doménech-Carbó, A.; Leyva-Pérez, A.; Armentano, D.; Pardo, E.; Ferrando-Soria, J. Self-Assembly of Catalytically Active Supramolecular Coordination Compounds within Metal−Organic Frameworks. *J. Am. Chem. Soc.* **2019**, *141*, 10350−10360.
(60) Mon, M.; Adam, R.; Ferrando-Soria, J.; Corma, A.; Armentano, D.; Pardo, E.; Leyva-Pérez, A. Stabilized $Ru[(H_2O)_6]^{3+}$ in Confined Spaces (MOFs and Zeolites) Catalyzes the Imination of Primary Alcohols under Atmospheric Conditions with Wide Scope. *ACS Catal.* **2018**, *8*, 10401−10406.
(61) Rivero-Crespo, M. A.; Mon, M.; Ferrando-Soria, J.; Lopes, C. W.; Boronat, M.; Leyva-Pérez, A.; Corma, A.; Hernández-Garrido, J. C.; López-Haro, M.; Calvino, J. J.; Ramos-Fernandez, E. V.; Armentano, D.; Pardo, E. Confined Pt 1 1+ Water Clusters in a MOF Catalyze the Low-Temperature Water-Gas Shift Reaction with Both CO_2 Oxygen Atoms Coming from Water. *Angew. Chem., Int. Ed.* **2018**, *57*, 17094−17099.
(62) Mon, M.; Rivero-Crespo, M. A.; Ferrando-Soria, J.; Vidal-Moya, A.; Boronat, M.; Leyva-Pérez, A.; Corma, A.; Hernández-Garrido, J. C.; López-Haro, M.; Calvino, J. J.; Ragazzon, G.; Credi, A.; Armentano, D.; Pardo, E. Synthesis of Densely Packaged, Ultrasmall Pt^0_2 Clusters within a Thioether-Functionalized MOF: Catalytic Activity in Industrial Reactions at Low Temperature. *Angew. Chem., Int. Ed.* **2018**, *57* (21), 6186−6191.
(63) Tejeda-Serrano, M.; Mon, M.; Ross, B.; Gonell, F.; Ferrando-Soria, J.; Corma, A.; Leyva-Pérez, A.; Armentano, D.; Pardo, E. Isolated Fe(III)−O Sites Catalyze the Hydrogenation of Acetylene in Ethylene Flows under Front-End Industrial Conditions. *J. Am. Chem. Soc.* **2018**, *140* (28), 8827−8832.
(64) Fortea-Pérez, F. R.; Mon, M.; Ferrando-Soria, J.; Boronat, M.; Leyva-Pérez, A.; Corma, A.; Herrera, J. M.; Osadchii, D.; Gascon, J.; Armentano, D.; Pardo, E. The MOF-Driven Synthesis of Supported Palladium Clusters with Catalytic Activity for Carbene-Mediated Chemistry. *Nat. Mater.* **2017**, *16*, 760−766.
(65) Saikia, K.; Dutta, D. K. Palladium Complexes of Heterobidentate Ligands: Active Catalysts for Direct Acylation of Aryl Halides with Aldehydes via C(Sp2)-H Activation. *J. Mol. Catal. A: Chem.* **2015**, *408*, 20−25.
(66) Mon, M.; Lloret, F.; Ferrando-Soria, J.; Martí-Gastaldo, C.; Armentano, D.; Pardo, E. Selective and Efficient Removal of Mercury from Aqueous Media with the Highly Flexible Arms of a BioMOF. *Angew. Chem., Int. Ed.* **2016**, *55*, 11167−11172.
(67) Mon, M.; Ferrando-Soria, J.; Grancha, T.; Fortea-Pérez, F. R.; Gascon, J.; Leyva-Pérez, A.; Armentano, D.; Pardo, E. Selective Gold

https://dx.doi.org/10.1021/jacs.0c12367
J. Am. Chem. Soc. XXXX, XXX, XXX−XXX

Recovery and Catalysis in a Highly Flexible Methionine-Decorated Metal−Organic Framework. *J. Am. Chem. Soc.* **2016**, *138*, 7864−7867.
(68) Mon, M.; Qu, X.; Ferrando-Soria, J.; Pellicer-Carreño, I.; Sepúlveda-Escribano, A.; Ramos-Fernandez, E. V.; Jansen, J. C.; Armentano, D.; Pardo, E. Fine-Tuning of the Confined Space in Microporous Metal−Organic Frameworks for Efficient Mercury Removal. *J. Mater. Chem. A* **2017**, *5*, 20120−20125.
(69) De Lange, M. F.; Vlugt, T. J. H.; Gascon, J.; Kapteijn, F. Adsorptive Characterization of Porous Solids: Error Analysis Guides the Way. *Microporous Mesoporous Mater.* **2014**, *200*, 199−215.
(70) Sato, T.; Hamada, Y.; Sumikawa, M.; Araki, S.; Yamamoto, H. Solubility of Oxygen in Organic Solvents and Calculation of the Hansen Solubility Parameters of Oxygen. *Ind. Eng. Chem. Res.* **2014**, *53*, 19331−19337.
(71) Chen, Y.; Guo, Z.; Chen, T.; Yang, Y. Surface-Functionalized TUD-1 Mesoporous Molecular Sieve Supported Palladium for Solvent-Free Aerobic Oxidation of Benzyl Alcohol. *J. Catal.* **2010**, *275*, 11−24.

https://dx.doi.org/10.1021/jacs.0c12367
J. Am. Chem. Soc. XXXX, XXX, XXX−XXX

PUBLICATION 3

MOF-Stabilized Perfluorinated Palladium Cages Catalyze the Additive-Free Aerobic Oxidation of Aliphatic Alcohols to Acids.

Rossella Greco+, **Estefania Tiburcio-Fortes+**, Antonio Fernandez, Carlo Marini, Alejandro Vidal-Moya, Judit Oliver-Meseguer, Donatella Armentano, Emilio Pardo, Jesús Ferrando-Soria, and Antonio Leyva-Pérez.

Chemistry–A European Journal | Research Article
doi.org/10.1002/chem.202103781

www.chemeurj.org

MOF-Stabilized Perfluorinated Palladium Cages Catalyze the Additive-Free Aerobic Oxidation of Aliphatic Alcohols to Acids

Rossella Greco[+],[a] Estefania Tiburcio-Fortes[+],[b] Antonio Fernandez,[c] Carlo Marini,[d] Alejandro Vidal-Moya,[a] Judit Oliver-Meseguer,[a] Donatella Armentano,*[e] Emilio Pardo,*[b] Jesús Ferrando-Soria,*[b] and Antonio Leyva-Pérez*[a]

Abstract: Extremely high electrophilic metal complexes, composed by a metal cation and very electron poor σ-donor ancillary ligands, are expected to be privileged catalysts for oxidation reactions in organic chemistry. However, their low lifetime prevents any use in catalysis. Here we show the synthesis of fluorinated pyridine-Pd^{2+} coordinate cages within the channels of an anionic tridimensional metal-organic framework (MOF), and their use as efficient metal catalysts for the aerobic oxidation of aliphatic alcohols to carboxylic acids without any additive. Mechanistic studies strongly support that the MOF-stabilized coordination cage with perfluorinated ligands unleashes the full electrophilic potential of Pd^{2+} to dehydrogenate primary alcohols, without any base, and also to activate O_2 for the radical oxidation to the aldehyde intermediate. This study opens the door to design catalytic perfluorinated complexes for challenging organic transformations, where an extremely high electrophilic metal site is required.

Introduction

Catalytic metal complexes with ancillary ligands – i.e. ligands that do not participate directly in the reaction, but keep the metal complex structurally operative- are paramount in organic synthesis. Aromatic C–H activation[1–3] and oxidation reactions[4] are usually catalyzed by electrophilic metal complexes where the ancillary ligand does not deplete much cationic charge from the metal site. However, a balance between metal complex lifetime and metal Lewis acidity is particularly difficult to achieve for sigma (σ) donor ancillary ligands. Figure 1a shows that, in general, the more electron donor the ligand is, the more stable the complex becomes, but at expenses of decreasing the metal Lewis acidity/catalytic activity. This dichotomy has been often overcome with different chemical manifolds; such as oxidizing the ligand[5] or the metal to a high-valence state,[6,7] and using non-coordinating counteranions or other donor-acceptor ligands, with anchimeric assistance or redox properties.[8–18] However, these approaches eventually increase the synthetic complexity and price of the final metal catalyst.

A straightforward synthetic strategy to decrease the electronic donation of the ligand to the metal is fluorination of the former, due to the strong inductive effect of fluoride.[19] Indeed, monofluorinated pyridine-Pd^{2+} complexes have been reported as extremely active catalysts for carbon-carbon cross-coupling reactions and oxidation reactions after aryl C–H activation.[20] On this basis, it is reasonable to think that perfluorinated pyridines will give even better results,[21] since are weaker electron σ-donor ligands, and consequently, they will increase more the electrophilicity of the metal catalyst, as shown in Figure 1b. Moreover, perfluoropyridines are one order of magnitude cheaper than the corresponding mono- and bis-fluorinated pyridines[22–26] – since pyridine fluorination is difficult to stop at one carbon and goes all through to the perfluorinated derivative skeleton. However, despite both suitable features, perfluorinated pyridines have not been profited in catalysis, as consequence of their inability to bind strongly enough metal cations and stabilize the resulting complex. Thus, it is difficult to find any literature example of a catalytically

[a] Dr. R. Greco,[+] Dr. A. Vidal-Moya, Dr. J. Oliver-Meseguer, Dr. A. Leyva-Pérez
Instituto de Tecnología Química (UPV-CSIC)
Universidad Politècnica de València-Consejo Superior de Investigaciones Científicas
Avda. de los Naranjos s/n, 46022 Valencia (Spain)
E-mail: anleyva@itq.upv.es

[b] E. Tiburcio-Fortes,[+] Prof. E. Pardo, Dr. J. Ferrando-Soria
Departamento de Química Inorgánica
Instituto de Ciencia Molecular (ICMol)
Universidad de Valencia
Catedrático José Beltrán Martínez, 2, 46980 Paterna, Valencia (Spain)
E-mail: Emilio.Pardo@uv.es
jesus.ferrando@uv.es

[c] Dr. A. Fernandez
Chemistry Department, Sir David Davies Building
Loughborough University
Loughborough LE11 3TU (UK)

[d] Dr. C. Marini
CELLS-ALBA Synchrotron
8290 Cerdanyola del Vallès, Barcelona (Spain)

[e] Prof. D. Armentano
Dipartimento di Chimica e Tecnologie Chimiche (CTC)
Università della Calabria
via P. Bucci, 12, Rende 87036, Cosenza (Italy)
E-mail: donatella.armentano@unical.it

[+] These authors contributed equally.

Supporting information for this article is available on the WWW under https://doi.org/10.1002/chem.202103781

Chemistry–A European Journal | Research Article
doi.org/10.1002/chem.202103781
Chemistry Europe
European Chemical Societies Publishing

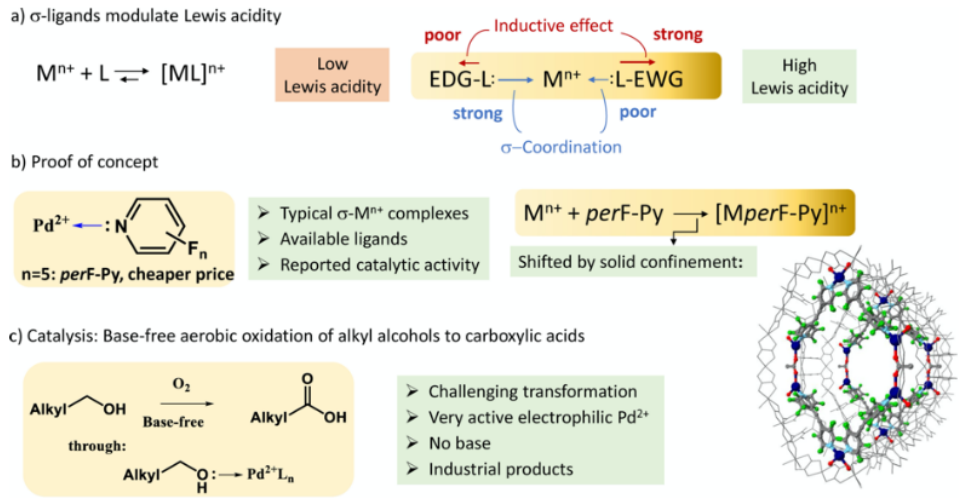

Figure 1. a) Modulation of the Lewis acidity in a metal cation by σ-coordinating ligands. Stronger ligands stabilize the metal complex but decrease Lewis acidity. b, c) Case study: catalytic perfluorinated pyridine Pd(II) complexes for the base-free aerobic oxidation of alkyl alcohols to carboxylic acids. Locking of the electrophilic σ-metal complex by formation of a coordination cage within a MOF.

efficient perfluorinated pyridine complex, despite all the precedents suggest that, if conveniently formed and stabilized, they may show an enhanced catalytic activity respect less fluorinated derivatives for selected organic reactions.[27,28]

Figure 1c shows that highly electrophilic complexes would be relevant for the aerobic oxidation of aliphatic alcohols to the corresponding carboxylic acids. Aliphatic alcohols are challenging alcohols to be oxidized in comparison with benzylic alcohols, and this is an industrial reaction which usually requires high amount of metal catalysts, stoichiometric bases and harsh oxidants, generating polluting and dangerous waste at the end of the reaction.[29–38] Despite many metal catalytic systems have been designed,[34,37,39–41] and those based on palladium metal – including pyridine-type molecular complexes[4,42–46] and heterogeneous catalysts[47–52] have proven to be successful, they generally need of bases and/or other additives. Only electrochemical methods seem to circumvent the use of bases with high efficiency.[53] The role of the base is to deprotonate the metal-coordinated primary alcohol, since the pK_a of the resulting metal alcoholate complex is still too low for a single metal-mediated deprotonation. This is particularly true for simple alkyl alcohols, where other electron withdrawing groups are not present to assist the deprotonation – i.e. benzyl alcohols.[54] However, if a very electrophilic metal site could be able to activate sufficiently the primary alkyl alcohol for spontaneous dehydrogenation, the base could be suppressed,[55,56] and the corresponding aldehyde would be formed after β-hydride elimination under aerobic conditions.[57–60] In addition, as no additional nucleophiles are present in the reaction medium – nor bases, nor additives and even nor electron donor ligands – the catalytic electrophilic Pd^{2+} could be regenerated back by activating O_2 in the presence of the so-formed aldehyde, and leading to the corresponding carboxylic acid after radical scission.[61,62] Thus, *a priori*, this additive-free mechanism constitutes a very simple and efficient way to convert abundant aliphatic primary alcohols into industrially relevant fatty carboxylic acids.[63] But, to this end, we will have to find the manner to form and stabilize highly electrophilic perfluorinated pyridine complexes.

In connection with the research lines of our groups, a type of crystalline porous materials[64–70] – so-called metal-organic frameworks (MOFs) – have been recently successfully used as platforms for the *in-situ* MOF-driven formation of robust and catalytically active supramolecular coordination compounds (SCCs) within their channels (SCCs@MOFs).[71,72] In particular, previously reported palladium SCCs@MOFs[71] exhibited high structural stability under reaction conditions – due to the formation of stabilizing mechanical interactions between the SCCs and the MOF network – and improved catalytic activities and selectivities for metal-catalysed reactions – i.e. coupling of boronics and/or alkynes –, as consequence of the limited, but tunable, accessible void space for catalysis. On this basis, with the aim to further expand this nascent synergetic hybridization between SCCs and MOFs, we wondered if it will be possible to take advantage of the same synthetic strategy and MOFs pore's chemistry to construct catalytically active fluorinated pyridine-type Pd^{2+} SCCs@MOFs, tentatively showing enhanced catalytic activity respect homogenous complexes in the base-free oxidation of aliphatic primary alcohols to carboxylic acids. Besides its interest from the point-of-view of developing

Chemistry–A European Journal | Research Article doi.org/10.1002/chem.202103781 | Chemistry Europe European Chemical Societies Publishing

efficient heterogenous catalyst in relevant industrial reactions, this will be also interesting from a fundamental perspective. This work represents one of the few reported examples where the confined space of the MOF is used to build up otherwise not accessible SCCs, which evidences the uniqueness of MOFs chemistry.

Results and Discussion

Synthesis and characterization of SCCs@MOF

We have chosen the highly crystalline MOF, of formula $[Pd^{II}(NH_3)_4][Pd^{II}_2(\mu\text{-}O)(NH_3)_6)(NH_4)_2]_{0.5}\{Ni^{II}_4[Cu^{II}_2(Me_3mpba)_2]_3\}\cdot 52H_2O$ (**1**),[73] as chemical *nano*reactor for the post-synthetic construction of fluorinated pyridine-Pd^{2+} SCCs inside the MOF's channels. Figure 2a shows its crystal structure, which features huge octagonal nano-pores (virtual diameter of ca. 2.0 nm) filled by Pd^{II} ions, either monomeric or self-assembled in dimers and stabilized by host-guest interactions. The crystals of **1** were soaked in an acetonitrile/water (2:1) solution of sodium acetate and different fluorinated pyridine ligands – L_{1-3}; L_1 = bis(3-fluoro-pyridin-4-yl)acetylene, L_2 = bis (2,3-difluoro-pyridin-4-ykl)acetylene and L_3 = bis(2,3,5,6-tetrafluoro-pyridin-4-yl)acetylene-, prepared by Sonogashira coupling/silane deprotection of the corresponding iodides and silyl acetylenes (see Supporting Information Figure S1), to led to the formation of SCCs@MOF **2**–**4**, respectively. The characterization of **2**–**4** was performed by different characterization techniques (see ahead): inductively coupled plasma-mass spectrometry (ICP-MS), elemental, thermo-gravimetric and powder X-ray diffraction (PXRD) analyses, N_2 adsorption isotherm, X-ray photoelectron (XPS), X-ray absorption and X-ray absorption near edge structure (XANES) spectroscopies, and also solid-state magic-spinning ^{19}F nuclear magnetic resonance (SS MAS ^{19}F-NMR).

The results of this multitechnique approach could be successfully confirmed for L_3, with single-crystal X-ray diffraction (SC-XRD) of **4** under synchrotron radiation, which evidenced the self-assembling of a novel supramolecular hexameric Pd^{II} square SCC within the biggest channels of **1**, to lead to a SCCs@MOF of formula $[Pd^{II}(NH_3)_4)]_{1.5}[Pd^{II}_6(\mu\text{-}HOAc)_2(H_2O)_{12}(L_3)_4]_{0.08333}\{Ni^{II}_4[Cu^{II}_2(Me_3mpba)_2]_3\}\cdot 28H_2O$ (**4**), as shown in Figures 2 and 3 (see also Figures S2-S7 and Table S1). Attempts to solve the crystal structure of **2** and **3** were unsuccessful. Despite not having the security of the atomic resolution provided by SCXRD, the multi-technique approach used – commonly applied in solving highly complex architectures, when SCXRD is not possible – and the similarities of the ligands allowed us to propose tentatively formulae for **2** and **3**, $[Pd^{II}(NH_3)_4)]_{1.5}[Pd^{II}_6(\mu\text{-}HOAc)_2(H_2O)_{12}(L_1)_4]_{0.08333}\{Ni^{II}_4[Cu^{II}_2(Me_3mpba)_2]_3\}\cdot 25H_2O$ (**2**) $[Pd^{II}(NH_3)_4)]_{1.5}[Pd^{II}_6(\mu\text{-}HOAc)_2(H_2O)_{12}(L_2)_4]_{0.08333}\{Ni^{II}_4[Cu^{II}_2(Me_3mpba)_2]_3\}\cdot 26H_2O$ (**3**). Conversely for **4**, application of cutting-edge X-ray crystallography techniques, allowed us to unveil that the 3D network of the anionic $Ni^{II}_4Cu^{II}_6$ porous framework acts in response to perfluorinated pyridine ligand insertion simply with a distortion of the pores' shape, accounting for a phase transition from the tetragonal (*P4/mmm* space group of **1**) to orthorhombic system. Indeed, **4** crystallizes in the *Cmmm* space group, with the $[Pd^{II}_6(\mu\text{-}HOAc)_2(H_2O)_{12}(L_3)_4]$ cages located in

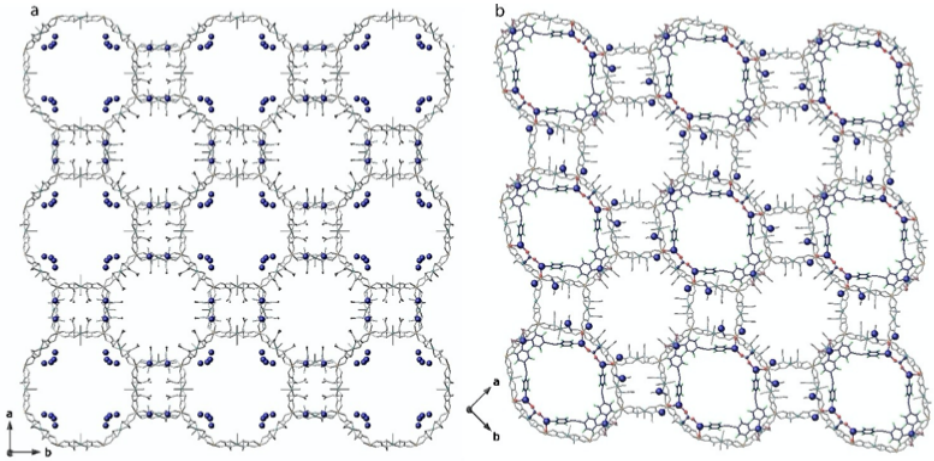

Figure 2. From MOFs 1 to 4. Comparative perspectives of the crystal structures of 1 and 4. (a) View along *c* crystallographic axis of crystal structure of the precursor **1**,[73] featuring channels filled by $[Pd^{II}(NH_3)_4][Pd^{II}_2(\mu\text{-}O)(NH_3)_6)(NH_4)_2]$. (b) View of the crystal structure, determined by synchrotron X-ray diffraction, of **4**, where $[Pd^{II}_6(\mu\text{-}HOAc)_2(H_2O)_{12}(L_3)_4]$ cages are self-assembled within the confined spaces by perfluorinated ligand L_3. Ligands atoms of the heterobimetallic $Ni^{II}_4Cu^{II}_6$ 3D anionic network are depicted as grey sticks, with cyan or orange spheres for copper and nickel metal ions, respectively. Pd(II) cations in the pores and ligands forming the cages, are represented by blue spheres and blue sticks (with fluorine in green), respectively, with oxygen atoms as red spheres.

Chemistry–A European Journal | Research Article
doi.org/10.1002/chem.202103781
Chemistry Europe
European Chemical Societies Publishing

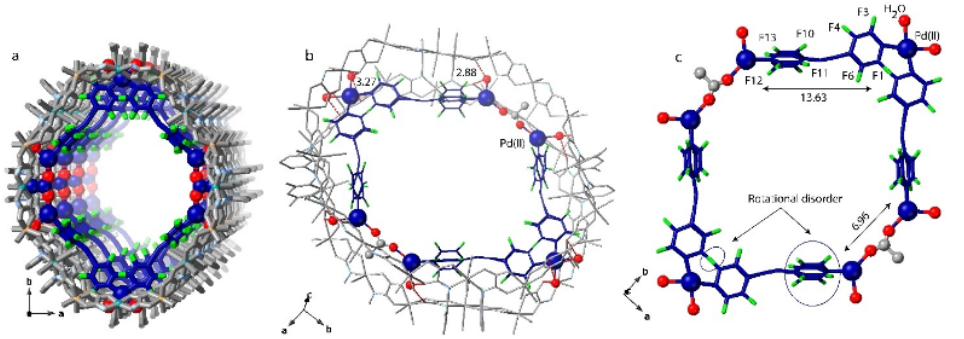

Figure 3. Details of a single pore in crystal structure of 4. Perspective views of a portion of single pores along the [001] direction showing the $[Pd^{II}_6(\mu\text{-}HOAc)_2(H_2O)_{12}(L_3)_4]$ cages (a) and (b) cages stabilized within MOF's pores by symmetric OH_2 ···O interactions. (c) View of the structure of the cages and related structural parameters. The heterobimetallic $Ni^{II}_4Cu^{II}_6$ 3D anionic network is depicted as grey sticks. Pd(II) cations in the pores and ligands forming the cages, are represented by blue spheres and blue sticks (with fluorine in green), respectively, with oxygen atoms as red spheres. Hydrogen-bonds are represented as red dashed lines.

the hydrophilic distorted octagonal pores [virtual diameter of ca. 2.2 nm] previously occupied by the Pd^{2+} dimers of **1**.

Monomeric $\{[Pd^{II}(NH_3)_4]^{2+}/[Pd^{II}(H_2O)_x(NH_3)_{4-x}]^{2+}\}$ complexes still reside both in the square smallest pores and octagonal hydrophobic pores (Figure S4). The nature and size of pores accounts for formulae uncertainties, indeed some NH_3 and H_2O molecules were not found from ΔF map (Figures S4 and S7). The confined assemblies are finely stabilized by interactions with the MOF network, which, due to their flexibility, *adapts* pores, in terms of shape (see crystallographic section in Supporting Information for structure refinement details) in relation to the nature of the linker of the cages.

Figure 3 shows that the $[Pd^{II}_6(\mu\text{-}HOAc)_2(H_2O)_{12}(L_3)_4]$ cages are self-assembled within the confined spaces of **4**, resulting from the reaction of half of the Pd^{2+} ions, from the mononuclear and dinuclear entities stabilized by the precursor (**1**), with the perfluorinated ligand. The templating action of the MOF is undersigned with the final polygon shape, which follows pore's distortion, exhibiting an elliptic geometry. The corners of the $[Pd^{II}_6(\mu\text{-}HOAc)_2(H_2O)_{12}(L_3)_4]$ cages can be located on $[Pd^{II}_2(\mu\text{-}HOAc)(H_2O)_2]$ dimeric fragments, which reside at the sides of the elliptic assembly (Figures S2–S3) and interact with the MOF by means of water-mediated H-bonds. Each Pd(II) exhibits regular square planar geometry, with Pd–N [2.13(2) and 2.077(11) Å for Pd-N_{L3} and 2.070(10) Å for detected Pd-NH_3, respectively], Pd-OH_2 [2.35(2) and 2.30(2) Å for detected Pd-OH_2] and Pd-OAc [2.34(2) Å] bond distances similar, or longer for the latter, to those found in the literature.[74] Figure 3c shows that Pd(II) separations through AcOH and L_3 bridges are 6.96(1) and 13.63(1) Å, respectively. Elliptic polygons are regularly pillared along *c* crystallographic axes, with a Pd(II)···Pd(II) separation among adjacent polygons of 14.94(1) Å (Figure S3 and S5b). Figure 3b shows that the polygons are well-stabilized by mechanical-bonds with the walls of the net, involving terminal H_2O molecules and oxamate residues belonging to the porous network [H_2O···$O_{oxamate}$ of 2.88(1) and 3.27(1) Å] (Figures S3 and S5). Figure 3b also shows that further stabilization is ensured by interactions involving terminal water molecules coordinated to copper metal ions of the network [H–OH···O_{water} 3.15(1) Å] (Figure S3c). The synergic stabilizations, ensured by a such MOF, allow the framework to act as impeccable platform to efficiently safeguard the robustness of the assembled cages, which in turn exhibit high activity in heterogeneous metal-based supramolecular catalysis (see below). Furthermore, it is worth to note that their size and shape, stabilized near to the walls of the hosting matrix, preserve the available nano-confined spaces, needed for reactants access (Figure S2 and S3a–d).

The experimental PXRD pattern of **4** is identical to the corresponding calculated one (Figure S8). This confirms the homogeneity of the bulk sample, which is isostructural to the crystal selected for single-crystal X-ray diffraction. **2** and **3** showed isostructural experimental diffractograms to **4**, which evidenced the similarities of these SCCs@MOF with the crystallographically resolved one. Metal analyses was performed by combined ICP-MS and SEM/EDX measurements (Table S2). The solvent contents of **2**–**4** were determined by TGA under a dry N_2 atmosphere and compared with pristine MOF **1** (Figure S9). All four materials showed a fast mass loss from room temperature, being lower for **2**–**4** than in **1**, which agree with the fact that the cavities of these materials are partially occupied by the *in-situ* constructed SCCs. Then, there is a pseudo plateau until decomposition starts in **1**–**4**. The observed weight losses were 25.72 (**1**), 13.96 (**2**), 14.65 (**3**) and 15.45 % (**4**), respectively, and correspond to 52, 25, 26 and 28 water molecules, respectively, which is in line with CHN analyses. N_2 adsorption isotherms of **2**–**4** at 77 K (Figure S10) are also consistent with the decrease in channels accessible void space as consequence of the formation of SCCs@MOF, which agrees with TGA and the crystal structure. Besides, the amount

Chemistry–A European Journal | Research Article doi.org/10.1002/chem.202103781 | Chemistry Europe European Chemical Societies Publishing

adsorbed is similar to the related non–fluorinated SCCs@MOF previously reported.[71]

XPS evidences a very slight shift of the Pd $3d_{5/2}$ peak of the Pd^{II} atoms in **2**–**4** (338.8, 338.9 and 338.8 eV, respectively) respect **1** (338.6 eV), as it was expected by the low coordination of fluorinated L_{1-3} ligands (Figure S11). XANES results confirm the electrophilicity of Pd^{II} in **2**, similar to **1** without any ligand (Figure S12). EXAFS results for **2** strongly support the formation of the SCCs inside the MOF, with coordination numbers (CN) and estimated distances (Å) for oxygen atoms (CN: 2.35±0.93 and 2.02 Å), nitrogen atoms (CN: 4.40±0.73 and 2.19 Å) and fluorine atoms (CN: 1.50±0.86 and 2.45 Å) in good agreement with the SC-XRD of **4** (Figure S13 and Table S3). Combined liquid NMR and SS MAS ^{19}F-NMR confirmed the complexation to the Pd^{II} site of the perfluorinated ligand L_1 within the SCCs@MOF **2**, since the expected downshift of the signal of free L_1 from ~−126 to ~−118 ppm when complexed to the metal, can be seen, beyond the presence of an impurity coming from the starting material (Figure S14).

These results, together, allowed us to have solid fundaments to establish formulae for **2** and **3** and to further confirm the results obtained with SCXRD for **4**, as well as give us tools to follow the catalytic experiments within SCCs@MOFs.

Catalytic experiments

Figure 4a shows the results for the aerobic oxidation of hexanol **5a** to caproic acid **6a** with $Pd(OAc)_2$/2-fluoro-pyridine (^{2}F-py)[30] as a catalyst and different solvents, atmospheres and pressures. The best results were obtained with dioxane as a solvent under 4 bars of O_2 (48.9% yield with >97% selectivity, entry 5). The intermediate aldehyde **7a** was barely detected at the end of the reaction under these conditions and, remarkably, the addition of NaOAc, a typical base for this reaction, does not significantly change neither the yield nor selectivity to **6a** (entry 11), in accordance with the potential ability of Pd^{2+} to catalyze the whole process without base assistance. The lack of base does not adversely affect the reaction progress, since the formed acid does not apparently poison the catalytic system and can be easily isolated after chromatographic separation. The N:Pd ratio in the MOF analyses, corresponding to the expected pyridine to Pd site stoichiometry, excludes the action of any excess of pyridine ligands as a base, which in any case would correspond to an amount of base marginal to improve the catalytic reaction.The formation of high-valence Pd complexes can be excluded on the basis of oxidation experiments with *m*-chloroperbenzoic acid (MCPBA), which do not show any increase in the oxidation yield (entry 8), and control experiments also exclude any role of water during reaction (entry 9). The reaction yield is proportional to the pressure of O_2 (compare entries 10–12). Thus, air can replace pure O_2 as an oxidant, provided that the right partial pressure of O_2 is set, otherwise the oxidation tends to stop in the intermediate aldehyde **7a**. Notice that the oxidation reaction does not evolve without O_2, which discards acceptorless dehydrogenative mechanisms.

Figure 4b shows the results for different pyridine-Pd^{2+} complexes under optimized reaction conditions, including fluorinated linear alkynyl bispyridines (L_1–L_3, see Table S4 for

Entry	Solvent	Additive	Atmosphere	TON	
				6a	7a
1	-*	-	O_2 (4atm)	0.2	0.2
2	toluene	-	O_2 (4atm)	8.6	n.d.
3	dodecane	-	O_2 (4atm)	5.6	0.4
4	THF	-	O_2 (4atm)	4.2	4.2
5	dioxane	-	O_2 (4atm)	48.9	0.8
6	butyric anhydride	-	O_2 (4atm)	n.d.	0.3
7	dioxane	NaOAc	O_2 (4atm)	57.0	2.2
8	dioxane	MCPBA	O_2 (4atm)	43.0	1.5
9	dioxane	H_2O	O_2 (4atm)	55.8	1.1
10	dioxane	-	N_2 (4atm)	2.1	3.3
11	dioxane	-	reflux	9.4	10.6
12	dioxane	-	air (4atm)	10.1	6.9

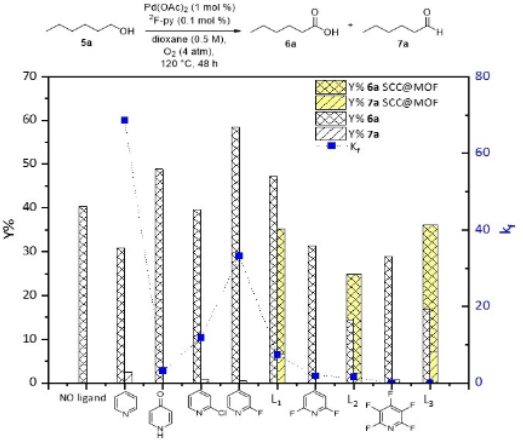

Figure 4. (a) Aerobic oxidation of hexanol **5a** to caproic acid **6a** with $Pd(OAc)_2$/^{2}F-py catalyst under different reaction conditions. Turnover number (TON) equals yield in this case (1 mol% catalyst). (b) Correlation between catalytic activity, pyridine σ electron donation and complex stability for different pyridine-Pd^{2+} complex catalysts. The yields obtained are correlated with the pK_a value of the ligand, which constitutes a valid estimation of the σ electron donation to the Pd^{2+} atom, and the constant of formation for each complex in solution (k_f, square points). Reaction conditions: **5a** 0.25 mmol; [Pd] 1% mol; [pyridine ligand] 0.1% mol; dioxane 0.5 M; 120 °C; 48 h; O_2 4 bar. * No solvent.

Chemistry–A European Journal | Research Article doi.org/10.1002/chem.202103781 | Chemistry Europe European Chemical Societies Publishing

numeric yields). Yields of **6a** can be correlated with the pK_a value of the ligand, which constitutes a valid estimation for the σ electron donation of the pyridine to the Pd^{2+} atom,[31] and the constant of formation for each complex in solution, calculated by ^{1}H- and ^{19}F-NMR measurements of each complex (Figures S15–S17, see also catalytic procedures). These correlations show that the catalytic activity increases linearly with the electron donor weakness of the pyridine ligand, reaching a maximum for ^{2}F-py, in accordance with previous reports for other reactions.[1,7] This volcano-type is explained by the lack of formation of the Pd^{2+}-pyridine complex beyond the monofluorinated pyridine, which is confirmed here by the formation constants of the different complexes, drastically decreasing for perfluorinated pyridines (blue squares). Notice that the relationship between k_f for electron-poor pyridines and catalytic activity is qualitative, just to confirm that the formation of the palladium complex is directly related to the catalytic activity, but not quantitative, and the better formation of the MOF-supported fluoropyridine Pd complexes is not assessed here with k_fs. The blank experiment without any ligand also gives a significant amount of oxidation product, since acetates are relatively low-coordinating ligands, however, a lower amount of oxidation products are found that for many of the electron poor ligands. It must be noticed that the formation of the corresponding fluorobispyridine-Pd^{2+} cages in solution did not occur under standard synthetic conditions for the non-fluorinated cage,[75] which contrast with their formation within MOFs channels (see above). Kinetic experiments with different amounts of NaOAc confirmed that the absence of NaOAc is beneficial for the formation of **6a** (Figure S18).

The catalytic results for the oxidation of **5a** to **6a** with the different MOFs **2**–**4** can also be found in Figure 4b. It can be seen that, in contrast to the corresponding fluoro-pyridine-Pd^{2+} complexes in solution, the yield of **6a** is kept to a maximum value with the perfluorinated cage in MOF **4**. Here, the catalytic activity is defined by a subtle balance between the number of F atoms in the pyridine ligand (electronic effect) and the associated limited diffusion within the microporous framework (steric and coordinating impediments). Indeed, the position of the F atoms in the pyridine ligand also can play a role, beyond the total number of F substituents. For that reason, 2,3-difluoropyridine and 2,3,5,6-tetrafluoropyridine were additionally tested as ligands in solution and the catalytic results (Figure S19 and Table S4) show that it is difficult to establish a sound relationship between number/position of F atoms on the pyridine ligand and catalytic activity in solution, beyond the rough increase in catalytic activity for F-substituted ligands. The formation of the cage is paramount for the catalytic activity within the MOF, since the combination of the ancestor MOF **1**,[73] with bare Pd^{2+} sites, and different soluble pyridine ligands, only catalyze properly the oxidation of **5a** when the appropriate ligand for cage formation is employed (Table S5). The catalytic results with SCC@MOFs **2**–**4** do not exceed the soluble monofluorobipyridine-Pd^{2+} complex, however, they reflect the higher activity of the perfluorinated ligand when forming SCCs@MOF. Also, it will showcase the advantages of translating unrecoverable homogenous catalysts into nanoparticulated recoverable solid catalysts (see below).[76–82]

Figure 5a shows the aerobic oxidation of different aliphatic alcohols of increasing chain length **5a**–**h** catalyzed by SCCs@MOF **4**, under optimized conditions (for numeric values see Table S6). It can be seen that ~30% and ~20% yields, in average, are obtained for <8 atom carbon acids **6a**–**d** and >8 atom carbon acids **6e**–**h**, respectively. These results are in accordance with the channels topology and dimensions (~0.8 nm) of SCCs@MOF **4**, which allows the better diffusion of small linear alkyl chain reactants and products not only through the MOF channels but also through the cages, and complicates the traffic of longer chain molecules. The aerobic oxidation of alkyl alcohols to carboxylic acids is plagued with multiple by-reactions such as ester or ether formation and decarboxylation, and moreover, the absence of base provokes the acidification of the reaction medium, which could trigger more undesired reactions. Thus, the final reaction yields obtanied here with a MOF solid catalyst can be considered reasonable. Figure 5b shows the hot filtration test for SCCs@MOF **4**, which excludes the presence of catalytically active species in solution, and Figure 5c shows that SCCs@MOF **4** keeps its catalytic activity throughout different reuses. PXRD analysis of the fresh and spent solid catalyst confirmed the integrity of the structure (Figure S20). It seems that the catalyst becomes more selective after the first use, nevertheless notice that the yield for **6a** is <10% and **6a** is a potential intermediate of **7a**, thus some variability in the final yield of **6a** may be expected. This variability could come, for instance, from different O_2 pressure during the reuses or slightly modifications of the solid catalyst material during reaction. However, it should be considered that the yields are 35, 45 and 42% for the three reuses, respectively, and a 7% by-product is found in the first use, and none in the second two uses. Thus, the variability for both yield and selectivity is <10% overall, thus it is a reasonable value for a reused solid catalyst. In addition, we have observed that the results with the catalytic SCCs@MOF **2** are not far from the parent monofluorinated complex in solution (Figure S21). These results showcase a clear practical advantage of the solid SCCs@MOFs respect to the homogeneous soluble counterparts, beyond the electronic effects imparted by the perfluorinated ligand.[83–86]

Figure 5d shows the kinetics for the oxidation of intermediate hexanal **7a**, catalyzed by SCCs@MOF **4**, under optimized conditions. Each point corresponds to an individual experiment, where O_2 is released and filled back to the reaction to keep the same starting pressure. The formation of caproic acid **6a** perfectly matches with the disappearance of hexanal **7a**, which explains that the intermediate aldehyde is not detected under reaction conditions, since **7a** rapidly oxidizes to **6a** as soon as the former is formed (indeed, the final yield of **6a** is >10% higher when starting from **5a** than **7a**, compare Figures 5b and 5d). These results suggest that the rate-determining step during the oxidation of **5a** to **6a** is the dehydrogenation of **5a** to **7a**. Blank experiments showed that no conversion for any of both reactions occurs if SCCs@MOF **4** is not present (not shown).

Chemistry–A European Journal | Research Article doi.org/10.1002/chem.202103781 | Chemistry Europe European Chemical Societies Publishing

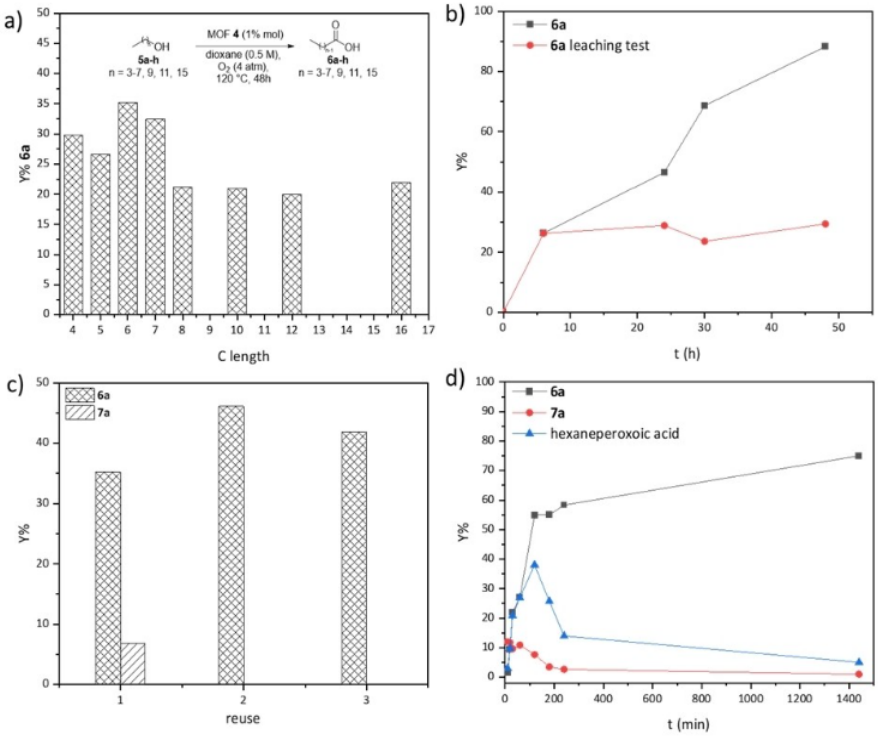

Figure 5. (a) Results for the aerobic oxidation of aliphatic alcohols of increasing chain length catalyzed by solid SCCs@MOF **4**. Selectivity to the carboxylic acid is >97%. Reaction conditions: **5a–h** 0.25 mmol; SCCs@MOF **4**, [Pd] 1% mol; dioxane 0.5 M; 120 °C; 48 h; O_2 4 bar. (b) and (c) Hot filtration test and reuses of SCCs@MOF **4** for the oxidation of **5a** under optimized conditions. (d) Time dependence for the formation of acid **6a** during the oxidation of intermediate aldehyde **7a**. Reaction conditions: **7a** 0.25 mmol; SCCs@MOF **4**, [Pd] 1% mol; dioxane 0.5 M; 120 °C; O_2 4 bar.

Figure 6 shows a plausible mechanism for the oxidation of **5a** to **6a**. Kinetic studies reveal that the rate for the oxidation of hexanol **5a** to caproic acid **6a** follows the equation $r_0 = [\mathbf{5a}][Pd][L]^{-1}$ at low concentrations of **5a** and for any pyridine ligand tested (Figures S22–S27; the error in the data fitting is significant, however, we think that a numerical reaction order can be assigned to, at least, show that the dependence of the reaction rate on the concentration of a particular component is positive, negative or insubstantial). A numerical reaction order O_2 pressure does not appear in the rate equation, in accordance with the rapid oxidation of hexanal **7a** to caproic acid **6a**, and the reaction order for hexanal **7a** matches **5a** under similar reaction conditions, which further confirms the intermediacy and rapid oxidation of **7a** (Figure S28). Besides, [**5a**] has no influence on the reaction rate at concentrations >3:1 respect to $[Pd^{2+}]$, thus when the Pd complex is already saturated by the alcohol (Figure S22). These results strongly suggest that the catalytic species corresponds to a Pd^{2+} complex where the alcohol has replaced the pyridine ligand, to be efficiently dehydrogenated by the electrophilic Pd^{2+} site. This cationic Pd site is now available to receive the hydroperoxy molecule (see ahead). The highly competitive coordination of the pyridine ligand explains why the perfluorinated Pd^{2+} cages in SCCs@MOFs **2**–**4**, despite having the optimal electronics in the

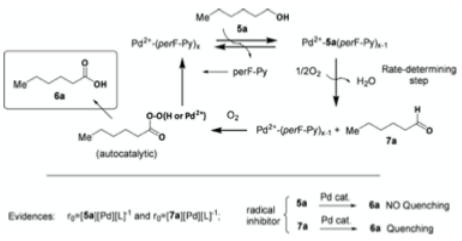

Figure 6. Plausible mechanism for the oxidation of **5a** to **6a**.

Chemistry–A European Journal | Research Article doi.org/10.1002/chem.202103781 | Chemistry Europe European Chemical Societies Publishing

ligands, are only slightly more efficient that the monofluoropyridine-Pd^{2+} complex in solution, since the forced ligand-to-metal interaction in the confined coordination cage must severely impede the coordination of alcohol **5a**. However, the catalytic results obtained by the solid SCCs@MOFs **2**–**4** have to be put in context and remarked, if one considers not only the intrinsic steric and coordination hindrance of the cage but also the lower mobility of the reactants/products inside the microstructured SCCs@MOFs compared to the open catalytic Pd^{2+} complexes in solution.

Considering that the aldehyde is the undiscussed precursor of the acid, and in order to unveil the rapid oxidation mechanism operating during the reaction, the rate equation and possible transient species during the oxidation of hexanal **7a** to caproic acid **6a** was studied (Figures S29–S34). The results with different fluoropyridine-Pd^{2+} catalysts show that hexanehydroperoxy acid is formed in all cases, and it rapidly collapses into the final acid **6a**, with a rate equation $r_0 = [\mathbf{7a}][Pd][L]^{-1}$. This rate equation is identical to the direct oxidation process, from hexanol **5a** to caproic acid **6a**. The use of radical inhibitors (Figure S35) quenches the oxidation of aldehyde **7a** to **6a**, and the dehydrogenation of alcohol **5a** to **7a**. These results strongly support alkylhydroperoxy acids as intermediates during the oxidation of the aldehyde, which are accepted intermediates during the autocatalyzed oxidation of aldehydes to carboxylic acids.[87] These peroxy acids join the potential formation of explosive peroxide intermediates with solvent dioxane under O_2, which probably makes the system unsuitable at the industrial level but certainly promising and worthy of further exploration.

Conclusions

SCCs of Pd^{2+} with (per)fluorinated pyridines are formed within the channels of an anionic tridimensional MOF and are able to catalyse the aerobic oxidation of alkyl alcohols to carboxylic acids without assistance of any additive/base. Related SCCs supported on MOFs but without (per)fluorinated pyridine ligands are not able to efficiently perform such transformation.[71] The structure of these new solid materials was determined by a multi-technique approach including single-crystal X-ray crystallography, allowing to unveiled how reticular chemistry and supramolecular chemistry are connecting in the task to produce highly stable and well-performing materials. These recoverable solid materials not only expand the Pd organometallic chemistry towards stable, extremely high electrophilic Pd^{2+} sites, but also open the door to their use as catalysts in challenging C–H activation reactions.

Deposition Number(s) 2107391 (for **4**) contain(s) the supplementary crystallographic data for this paper. These data are provided free of charge by the joint Cambridge Crystallographic Data Centre and Fachinformationszentrum Karlsruhe Access Structures service.

Acknowledgements

This work was supported by the Ministero dell'Istruzione, dell'Università e della Ricerca (Italy), the MICINN (Spain) (Projects PID2019-104778GB–I00, 2017-86735-P, PID2020-115100GB–I00, and Excellence Units "Severo Ochoa" and "Maria de Maeztu" SEV-2016-0683 and CEX2019-000919-M) and the Engineering and Physical Sciences Research Council (UK). The work has also been funded by Generalitat Valenciana, Prometeo Grupos de Investigación de Excelencia (PROMETEU/2021/054). R.G. thanks ITQ for a contract. J.O.-M. acknowledges the Juan de la Cierva program for the concession of a contract (IJC2018-036514-I). D.A. acknowledges the financial support of the Fondazione CARIPLO/"Economia Circolare: ricerca per un futuro sostenibile" 2019, Project code: 2019–2090, MOCA and Diamond Light Source for awarded beamtime and provision of synchrotron radiation facilities and thank Dr David Allan and Sarah Barnett for their assistance at I19 beamline (Proposal No. CY22411-1). Thanks are also extended to the 2019 Post-doctoral Junior Leader-Retaining Fellowship, la Caixa Foundation (ID100010434 and fellowship code LCF/BQ/PR19/11700011), the "Generalitat Valenciana" (SEJI/2020/034) and the "Ramón y Cajal" program (J.F.-S.). E.P. acknowledges the financial support of the European Research Council under the European Union's Horizon 2020 research and innovation programme/ERC Grant Agreement No 814804, MOF-reactors. E. T–F thanks the MICINN for a PhD FPI grant.

Conflict of Interest

The authors declare no conflict of interest.

Data Availability Statement

The data that support the findings of this study are available from the corresponding author upon reasonable request.

Keywords: aerobic alcohol oxidation to carboxylic acid · metal-organic frameworks · per-fluorinated palladium complexes · single-crystal X-Ray diffraction · supramolecular coordination cages

[1] D. Zhao, P. Xu, T. Ritter, *Chem* **2019**, *5*, 97–107.
[2] C. A. Salazar, K. N. Flesch, B. E. Haines, P. S. Zhou, D. G. Musaev, S. S. Stahl, *Science* **2020**, *370*, 1454–1460.
[3] J. Vercammen, M. Bocus, S. Neale, A. Bugaev, P. Tomkins, J. Hajek, S. Van Minnebruggen, A. Soldatov, A. Krajnc, G. Mali, et al., *Nat. Catal.* **2020**, *3*, 1002–1009.
[4] G. t. Brink, *Science* **2000**, *287*, 1636–1639.
[5] D. L. Bruns, D. G. Musaev, S. S. Stahl, *J. Am. Chem. Soc.* **2020**, *142*, 19678–19688.
[6] D. C. Powers, E. Lee, A. Ariafard, M. S. Sanford, B. F. Yates, A. J. Canty, T. Ritter, *J. Am. Chem. Soc.* **2012**, *134*, 12002–12009.
[7] C. C. Roberts, E. Chong, J. W. Kampf, A. J. Canty, A. Ariafard, M. S. Sanford, *J. Am. Chem. Soc.* **2019**, *141*, 19513–19520.
[8] J. A. Tunge, L. N. Foresee, *Organometallics* **2005**, *24*, 6440–6444.
[9] K. Li, Y. Zeng, B. Neuenswander, J. A. Tunge, *J. Org. Chem.* **2005**, *70*, 6515–6518.

Chemistry–A European Journal | Research Article doi.org/10.1002/chem.202103781 | Chemistry Europe European Chemical Societies Publishing

[10] J. K. Kirsch, J. L. Manske, J. P. Wolfe, *J. Org. Chem.* **2018**, *83*, 13568–13573.
[11] N. Lebrasseur, I. Larrosa, *J. Am. Chem. Soc.* **2008**, *130*, 2926–2927.
[12] R. Kudirka, S. K. J. Devine, C. S. Adams, D. L. Van Vranken, *Angew. Chem. Int. Ed.* **2009**, *48*, 3677–3680; *Angew. Chem.* **2009**, *121*, 3731–3734.
[13] M. S. Sigman, E. W. Werner, *Acc. Chem. Res.* **2012**, *45*, 874–884.
[14] Z. She, Y. Shi, Y. Huang, Y. Cheng, F. Song, J. You, *Chem. Commun.* **2014**, *50*, 13914–13916.
[15] A. C. Kruegel, S. Rakshit, X. Li, D. Sames, *J. Org. Chem.* **2015**, *80*, 2062–2071.
[16] J. R. Cabrero-Antonino, M. Tejeda-Serrano, M. Quesada, J. A. Vidal-Moya, A. Leyva-Pérez, A. Corma, *Chem. Sci.* **2017**, *8*, 689–696.
[17] T. U. Thikekar, C.-M. Sun, *Adv. Synth. Catal.* **2017**, *359*, 3388–3396.
[18] H. T. Kim, W. Lee, E. Kim, J. M. Joo, *Chem. Asian J.* **2018**, *13*, 2418–2422.
[19] T. Korenaga, R. Sasaki, K. Shimada, *Dalton Trans.* **2015**, *44*, 19642–19650.
[20] Y. Izawa, S. S. Stahl, *Adv. Synth. Catal.* **2010**, *352*, 3223–3229.
[21] L. I. Panferova, M. O. Zubkov, V. A. Kokorekin, V. V. Levin, A. D. Dilman, *Angew. Chem. Int. Ed.* **2021**, *60*, 2849–2854; *Angew. Chem.* **2021**, *133*, 2885–2890.
[22] R. P. Singh, G. V. Eggers, J. M. Shreeve, *Synthesis* **2003**, *2003*, 1009–1011.
[23] K. L. Hull, W. Q. Anani, M. S. Sanford, *J. Am. Chem. Soc.* **2006**, *128*, 7134–7135.
[24] F. Du, Q. Zhou, D. Liu, T. Fang, Y. Shi, Y. Du, G. Chen, *Synlett* **2018**, *29*, 779–784.
[25] G. S. Biggs, M. J. O'Neill, P. Carames Mendez, T. G. Scrase, Y. Lin, A. M. Bin-Maarof, A. D. Bond, S. R. Boss, P. D. Barker, *Dalton Trans.* **2019**, *48*, 6910–6920.
[26] Y. Y. See, M. T. Morales-Colón, D. C. Bland, M. S. Sanford, *Acc. Chem. Res.* **2020**, *53*, 2372–2383.
[27] I. Klemet, H. Lütjens, P. Knochel, *Angew. Chem. Int. Ed.* **1997**, *36*, 1454–1456; *Angew. Chem.* **1997**, *109*, 1605–1607.
[28] R. Boyaala, M. Peng, W.-S. Tai, R. Touzani, T. Roisnel, V. Dorcet, Y. Chi, V. Guerchais, H. Doucet, J.-F. Soulé, *Inorg. Chem.* **2020**, *59*, 13898–13911.
[29] A. Sen, M. Lin, *Direct Catalytic Oxidative Carbonylation of Lower Alkanes to Acids* (US08/357,437), **1996**.
[30] R. Sheldon, I. W. C. Arends, A. Dijksman, *Catal. Today* **2000**, *57*, 157–166.
[31] K. Noweck, W. Grafahrend, in *Ullmann's Encycl. Ind. Chem.*, Wiley-VCH Verlag GmbH & Co. KGaA, Weinheim, Germany, **2006**.
[32] V. Cherepakhin, T. J. Williams, *Synthesis* **2021**, *53*, 1023–1034.
[33] R. K. Sodhi, S. Paul, J. H. Clark, *Green Chem.* **2012**, *14*, 1649.
[34] T. Mallat, A. Baiker, *Catal. Today* **1994**, *19*, 247–283.
[35] S. Mannam, G. Sekar, *Synth. Commun.* **2010**, *40*, 2822–2829.
[36] Q. Gu, W.-H. Fang, R. Wischert, W.-J. Zhou, C. Michel, M. Pera-Titus, *J. Catal.* **2019**, *380*, 132–144.
[37] J. Sha, E.-J. Zheng, W.-J. Zhou, A. Liebens, M. Pera-Titus, *J. Catal.* **2016**, *337*, 199–207.
[38] B. Mahmoudi, A. Rostami, M. Kazemnejadi, B. A. Hamah-Ameen, *Green Chem.* **2020**, *22*, 6600–6613.
[39] X. Jiang, J. Zhang, S. Ma, *J. Am. Chem. Soc.* **2016**, *138*, 8344–8347.
[40] M. Zhao, X.-W. Zhang, C.-D. Wu, *ACS Catal.* **2017**, *7*, 6573–6580.
[41] H.-M. Liu, L. Jian, C. Li, C.-C. Zhang, H.-Y. Fu, X.-L. Zheng, H. Chen, R.-X. Li, *J. Org. Chem.* **2019**, *84*, 9151–9160.
[42] G.-J. ten Brink, I. W. C. E. Arends, R. A. Sheldon, *Adv. Synth. Catal.* **2002**, *344*, 355–369.
[43] M. J. Schultz, C. C. Park, M. S. Sigman, *Chem. Commun.* **2002**, 3034–3035.
[44] D. R. Jensen, M. J. Schultz, J. A. Mueller, M. S. Sigman, *Angew. Chem. Int. Ed.* **2003**, *42*, 3810–3813; *Angew. Chem.* **2003**, *115*, 3940–3943.
[45] M. Yang, K.-T. Yip, J.-H. Pan, Y.-C. Chen, N.-Y. Zhu, D. Yang, *Synlett* **2006**, *18*, 3057–3060.
[46] S. Gowrisankar, H. Neumann, D. Gördes, K. Thurow, H. Jiao, M. Beller, *Chem. Eur. J.* **2013**, *19*, 15979–15984.
[47] Y. Uozumi, R. Nakao, *Angew. Chem. Int. Ed.* **2003**, *42*, 194–197; *Angew. Chem.* **2003**, *115*, 204–207.
[48] D. Wang, J. N. Jaworski, S. S. Stahl, in *Liq. Phase Aerob. Oxid. Catal. Ind. Appl. Acad. Perspect.*, Wiley-VCH Verlag GmbH & Co. KGaA, Weinheim, Germany, **2016**, pp. 113–138.
[49] B. Karimi, S. Abedi, J. H. Clark, V. Budarin, *Angew. Chem. Int. Ed.* **2006**, *45*, 4776–4779; *Angew. Chem.* **2006**, *118*, 4894–4897.
[50] Z. Hou, N. Theyssen, W. Leitner, *Green Chem.* **2007**, *9*, 127–132.
[51] K. Mori, T. Hara, T. Mizugaki, K. Ebitani, K. Kaneda, *J. Am. Chem. Soc.* **2004**, *126*, 10657–10666.
[52] W. Hou, N. Dehm, R. Scott, *J. Catal.* **2008**, *253*, 22–27.
[53] M. Rafiee, Z. M. Konz, M. D. Graaf, H. F. Koolman, S. S. Stahl, *ACS Catal.* **2018**, *8*, 6738–6744.
[54] E. Tiburcio, R. Greco, M. Mon, J. Ballesteros-Soberanas, J. Ferrando-Soria, M. López-Haro, J. C. Hernández-Garrido, J. Oliver-Meseguer, C. Marini, M. Boronat, et al., *J. Am. Chem. Soc.* **2021**, *143*, 2581–2592.
[55] T. Wang, C.-X. Xiao, L. Yan, L. Xu, J. Luo, H. Shou, Y. Kou, H. Liu, *Chem. Commun.* **2007**, 4375.
[56] T. Wang, H. Shou, Y. Kou, H. Liu, *Green Chem.* **2009**, *11*, 562.
[57] J. A. Mueller, C. P. Goller, M. S. Sigman, *J. Am. Chem. Soc.* **2004**, *126*, 9724–9734.
[58] M. J. Schultz, R. S. Adler, W. Zierkiewicz, T. Privalov, M. S. Sigman, *J. Am. Chem. Soc.* **2005**, *127*, 8499–8507.
[59] M. Mon, R. Adam, J. Ferrando-Soria, A. Corma, D. Armentano, E. Pardo, A. Leyva-Pérez, *ACS Catal.* **2018**, *8*, 10401–10406.
[60] N. Riemer, M. Shipman, P. Wessig, B. Schmidt, *J. Org. Chem.* **2019**, *84*, 5732–5746.
[61] S. Ishikawa, N. Noda, M. Wada, S. Tsurumi, W. Ueda, *ACS Catal.* **2020**, *10*, 10535–10545.
[62] J. M. Hoover, S. S. Stahl, *J. Am. Chem. Soc.* **2011**, *133*, 16901–16910.
[63] D. Kong, P. J. Moon, E. K. J. Lui, O. Bsharat, R. J. Lundgren, *Science* **2020**, *369*, 557–561.
[64] H.-C. Zhou, J. R. Long, O. M. Yaghi, *Chem. Rev.* **2012**, *112*, 673–674.
[65] N. Stock, S. Biswas, *Chem. Rev.* **2012**, *112*, 933–969.
[66] H. Furukawa, K. E. Cordova, M. O'Keeffe, O. M. Yaghi, *Science* **2013**, *341*, 974.
[67] H.-C. Zhou, S. Kitagawa, *Chem. Soc. Rev.* **2014**, *43*, 5415–5418.
[68] Y. Cui, B. Li, H. He, W. Zhou, B. Chen, G. Qian, *Acc. Chem. Res.* **2016**, *49*, 483–493.
[69] A. Kirchon, L. Feng, H. F. Drake, E. A. Joseph, H.-C. Zhou, *Chem. Soc. Rev.* **2018**, *47*, 8611–8638.
[70] G. Maurin, C. Serre, A. Cooper, G. Férey, *Chem. Soc. Rev.* **2017**, *46*, 3104–3107.
[71] R. Adam, M. Mon, R. Greco, L. H. G. Kalinke, A. Vidal-Moya, A. Fernandez, R. E. P. Winpenny, A. Doménech-Carbó, A. Leyva-Pérez, D. Armentano, et al., *J. Am. Chem. Soc.* **2019**, *141*, 10350–10360.
[72] B. Li, Y. Zhang, D. Ma, T. Ma, Z. Shi, S. Ma, *J. Am. Chem. Soc.* **2014**, *136*, 1202–1205.
[73] F. R. Fortea-Pérez, M. Mon, J. Ferrando-Soria, M. Boronat, A. Leyva-Pérez, A. Corma, J. M. Herrera, D. Osadchii, J. Gascon, D. Armentano, et al., *Nat. Mater.* **2017**, *16*, 760–766.
[74] J.-H. Chu, Z.-H. Su, K.-W. Yen, H.-I. Chien, *Organometallics* **2020**, *39*, 3168–3179.
[75] M. Fujita, O. Sasaki, T. Mitsuhashi, T. Fujita, J. Yazaki, K. Yamaguchi, K. Ogura, *Chem. Commun.* **1996**, 1535.
[76] S. Mitchell, R. Qin, N. Zheng, J. Pérez-Ramírez, *Nat. Nanotechnol.* **2021**, *16*, 129–139.
[77] A. Abad, P. Concepción, A. Corma, H. García, *Angew. Chem. Int. Ed.* **2005**, *44*, 4066–4069; *Angew. Chem.* **2005**, *117*, 4134–4137.
[78] A. Abad, C. Almela, A. Corma, H. García, *Tetrahedron* **2006**, *62*, 6666–6672.
[79] D. I. Enache, J. K. Edwards, P. Landon, B. Solsona-Espriu, A. F. Carley, A. A. Herzing, M. Watanabe, C. J. Kiely, D. W. Knight, G. J. Hutchings, *Science* **2006**, *311*, 362–365.
[80] B. Karimi, F. Mansouri, H. Vali, *ACS Appl. Nano Mater.* **2020**, *3*, 10612–10627.
[81] B. A. Steinhoff, S. R. Fix, S. S. Stahl, *J. Am. Chem. Soc.* **2002**, *124*, 766–767.
[82] B. A. Steinhoff, S. S. Stahl, *J. Am. Chem. Soc.* **2006**, *128*, 4348–4355.
[83] A. Dhakshinamoorthy, H. Garcia, *ChemSusChem* **2014**, *7*, 2392–2410.
[84] A. Dhakshinamoorthy, A. M. Asiri, H. Garcia, *Chem. Commun.* **2017**, *53*, 10851–10869.
[85] A. Dhakshinamoorthy, A. M. Asiri, H. Garcia, *Trends Chem.* **2020**, *2*, 454–466.
[86] A. Dhakshinamoorthy, A. M. Asiri, H. Garcia, *ChemCatChem* **2020**, *12*, 4732–4753.
[87] M. Sankar, E. Nowicka, E. Carter, D. M. Murphy, D. W. Knight, D. Bethell, G. J. Hutchings, *Nat. Commun.* **2014**, *5*, 3332.

Manuscript received: October 20, 2021
Accepted manuscript online: December 20, 2021
Version of record online: January 12, 2022

AGRADECIMIENTOS

Tras un currículum químico físico y biofísico, nunca pensé que acabaría introduciéndome en la química de los materiales, en concreto, del mundo de los MOFs. Un mundo del que he acabado fascinada y sedienta de conocimiento, dado que la versatilidad de los MOFs es increíblemente amplia.

Todo esto no habría sido posible sin la confianza que depositaron mis directores Dr. Emilio Pardo y Dr. Jesús Ferrando para realizar este recorrido predoctoral de la mano de la FPI2017. Me gustaría expresarles mi gratitud por todo el tiempo que me han dedicado para enseñarme, retarme y apoyarme en cada etapa de mi crecimiento profesional. A Emilio, darle las gracias por el tiempo y la dedicación que ha invertido en ampliar mis conocimientos y mi confianza en mí misma. A Jesús, muchas gracias por su disponibilidad y predisposición, ya no solo en lo profesional, sino que también en lo personal.

Por otro lado, agradecer a los colaboradores externos imprescindibles para la realización de esta tesis, sobre todo su dedicación, y los conociemientos en cristalografía y catálisis que Donatella Armentano y Antonio Leyva me han aportado, enriqueciéndome profesionalmente.

También me gustaría agradecer a todos mis compañeros y vecinos de laboratorio por todos los momentos que hemos compartido. En especial, a Renato, por acogerme, escucharme y ayudarme desde el minuto cero en el que me conoció. A Cristina, por cuidarme y animarme; a Paula, por su simpatía y predisposición. A Ivana por su amistad incondicional desde que nos conocimos en pilates. A Nuria, por llegar en el momento en el que más necesitaba ayuda enriqueciendome con su inteligencia y sentido del humor. A Xavi que en el poco tiempo que lleva

en nuestro grupo me ha demostrado que es muy buena persona. A Nadia, por sus consejos y largas charlas. Y a Nicolás por ayudarme a buscar soluciones, compuestos y demás, muchas gracias.

Me gustaría agradecer el amor incondicional y apoyo recibido durante el desarrollo de esta tesis a mi familia y amigos: en especial, a mi madre Antonia, por todo lo que ha luchado para que llegue hasta aquí. A mis hermanos Jennifer y Rubén, por creer siempre en mí. A Melisa, por ser como una hermana; y a Clara y Simona, por su amistad inquebrantable.

En cuanto a la familia que he creado junto a mi mujer: Adela, y mis hijos Aitor y Matías a ellos no sólo les agradezco su amor, apoyo y paciencia, sino que también les dedico esta tesis pues intento ser cada día mejor por y para ellos. Además quiero agradecer a mi esposa el gran trabajo que ha realizado con la maquetación de esta tesis, así como el trabajo relizado en los pósters y presentaciones que he requerido en los congresos a los que he asistido. Familia, os amo con toda mi alma.

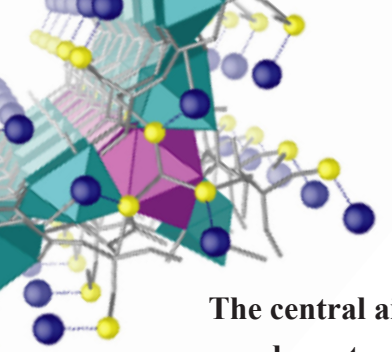

The central aim of this PhD thesis is to develop synthetic procedures to construct metal organic-frameworks (MOFs) able to host/build up molecular-based species, such as metal ions with particular coordination environments, single atom catalysts (SACs), sub-nanometric metal clusters (SNMCs) and supramolecular coordination complexes (SCCs), otherwise hardly accessible, with high catalytic reactivity and in a multigram scale.

The nature of the final assemblies has been characterised with a myriad of physical techniques, where taking advantage of the high crystallinity and structural robustness of the MOFs used as platforms, single-crsytal X-ray crystallography play a promienet role and provide us with unique snapshots of the novel hybrid materials assembled. Here, it is worth to remark that the obtention, stabilization and characterization of such unique hybrid species is an extraordinary challenge. Thus, this in itself reflects the success of the results presented in this PhD thesis.

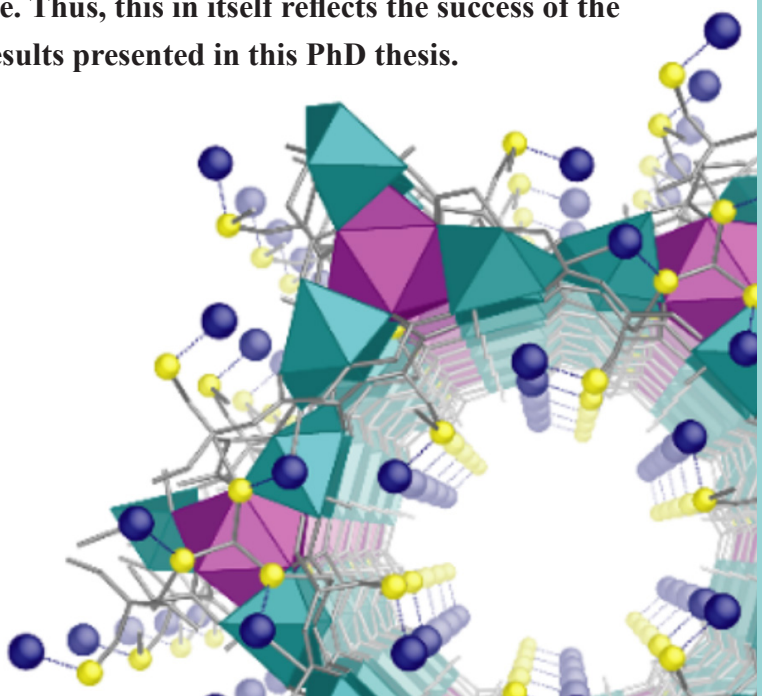

VNIVERSITAT DE VALÈNCIA